ISSN 2188-5001

MATERIALS DESIGN AND
CHARACTERIZATION LABORATORY
SUPERCOMPUTER CENTER

ACTIVITY REPORT
2020

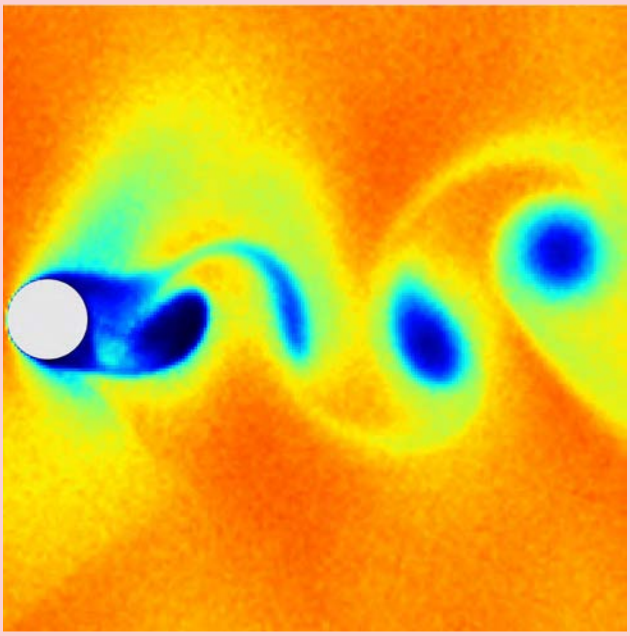

THE UNIVERSITY OF TOKYO

Materials Design and Characterization Laboratory (MDCL)

The MDCL was established as the third research facility of the Institute for Solid State Physics (ISSP) when the latter was reorganized in May 1996. Its aim is to promote material science with an emphasis on the “DSC cycle”, where DSC stands for design, synthesis and characterization, three processes for developing new materials.

The MDCL consists of two sections, Materials Design (MD) section and Materials Synthesis and Characterization (MSC) section. The Supercomputer Center of the ISSP (SCC-ISSP) is placed in the MD section, while in the MSC section there are seven laboratories for joint use; Materials Synthesis Laboratory, Chemical Analysis Laboratory, X-ray Diffraction Laboratory, Electron Microscope Laboratory, Electromagnetic Measurement Laboratory, Spectroscopy Laboratory, and High-Pressure Synthesis Laboratory.

Almost all the facilities of the MDCL are open to scientists in Japan through the User Programs conducted by two steering committees of the MDCL. One is the steering committee of the SCC-ISSP, under which the Supercomputer Project Advisory Committee is placed for reviewing proposals. The other is the steering committee of the MSC facilities. More than half of the members of these committees are from the outside of ISSP.

COVER FIGURE

Karman Vortex with cavilation
See Y. Asano et al. Page 36–46, ”Large-Scale Molecular Dynamics Simulations of Karman Vortex and Sound Wave: Cavitation and Polymer Effects”.

PREFACE

The Supercomputer Center (SCC) is a part of the Materials Design and Characterization Laboratory (MDCL) of ISSP. Its mission is to serve the whole community of computational condensed-matter physics of Japan providing it with high performance computing environment. In particular, the SCC selectively promotes and supports large-scale computations. For this purpose, the SCC invites proposals for supercomputer-aided research projects and hosts the Steering Committee, as mentioned below, that evaluates the proposals.

The ISSP supercomputer system consists of two subsystems: System B, which was replaced recently (Oct. 2020), is intended for larger total computational power and has more nodes with relatively loose connections. System B (ohtaka) consists of 1680 CPU nodes of AMD EPYC 7702 (64 cores) and 8 FAT nodes of Intel Xeon Platinum 8280 (28 cores) with total theoretical performance of 6.881 PFlops. System C (enaga, installed in Jan. 2018) consists of 252 nodes of HPE SGI 8600 with 0.77 PFLOPS. Replacement of the System C is scheduled in Spring 2022.

In addition to the hardware administration, the SCC puts increasing effort on the software support. Since 2015, the SCC has been conducting “Project for advancement of software usability in materials science (PASUMS).” In this project, for enhancing the usability of the ISSP supercomputer system, we conduct several software-advancement activities: developing new application software that runs efficiently on the ISSP supercomputer system, adding new functions to existing codes, help releasing private codes for public use, creating/improving manuals for public codes, etc. Three target programs were selected in fiscal year 2020 and developed or enhanced the ustablity of software were released as (1) PHYSBO (proposal made by R. Tamura (NIMS)), (2) 2DMAT (proposal made by T. Hoshi (Tottori Univ.)), and (3) MateriApps Installer (proposal made by S. Todo (Univ. of Tokyo)). In 2021, we also started the data repository service.

All staff members of university faculties or public research institutes in Japan are invited to propose research projects (called User Program). The proposals are evaluated by the Steering Committee of SCC. Pre-reviewing is done by the Supercomputer Project Advisory Committee. In fiscal year 2020, totally 387 projects were approved. The total points applied and approved are listed on Table. 1 below. Additionally, we supported FUGAKU and other computational materials science projects through Supercomputing Consortium for Computational Materials Science (SCCMS).

The research projects are roughly classified into the following three (the number of projects approved):

First-Principles Calculation of Materials Properties (189)
Strongly Correlated Quantum Systems (40)
Cooperative Phenomena in Complex, Macroscopic Systems (137)

In all the three categories, most proposals involve both methodology and applications. The results of the projects are reported in 'Activity Report 2020' of the SCC. Every year 3-4 projects are selected for “invited papers” and published at the beginning of the Activity Report. In the Activity Report 2020, the following three invited papers are included:

"Some Recent Developments in ab initio Thermodynamics of Ion Disorder in Solids",
Shusuke KASAMATSU (Yamagata Univ.)

"High precision study of the Anderson transition",
Tomi OHTSUKI (Sophia Univ.) and Keith SLEVIN (Osaka Univ.)

"Large-Scale Molecular Dynamics Simulations of Karman Vortex and Sound Wave: Cavitation and Polymer Effects",
Yuta ASANO (ISSP), Hiroshi WATANABE (Keio Univ.) and Hiroshi NOGUCHI (ISSP)

June 1, 2021

Naoki Kawashima
(Chairman of the steering committee, SCC, ISSP)

CONTENTS

PREFACE

1 OUTLINE

1.1 Supercomputer System

At the beginning of School Year 2020 (SY2020), the ISSP supercomputer center provided users with two supercomputer systems: SGI ICE XA/UV hybrid system named "sekirei" (System B) and HPE SGI 8600 system named "enaga" (System C). In Oct. 2020, Systems B was replaced by Dell PowerEdge C6525/R940 system named "ohtaka", and this system will be called System B for the next six years. System B is a massively-parallel supercomputer with two types of compute nodes: 8 "Fat" nodes and 1680 "CPU" nodes. "Fat" nodes are each comprised of four Intel Xeon Platinum 8280 CPUs (28 cores/CPU) and 3 TB of memory per node. "CPU" nodes have two AMD EPYC 7702 CPUs (64 cores/CPU) and 256 GB of memory per node. System B achieves about 6.881 PFLOPS in theoretical peak performance with high power efficiency. The subsystem comprised of only CPU nodes ranks 87st in the Nov. 2020 Top 500 List, which is a ranking based on total performance measured by the HPL benchmark. The compute nodes communicate to each other through HDR100 Infiniband and are connected in fat tree topology. System B entered official operation on Oct. 16th, 2020. Trial operation of System B continued until Nov. 26th, 2020. 2020 was the first year of the operation of the current System B. System C is a massively-parallel supercomputer with 252 "CPU" nodes, which have two Intel Xeon Gold 6148 CPUs (20 cores/CPU) and 192 GB of memory. System C achieves 774 TFLOPS in theoretical peak performance. 2020 was the third year of the operation of the current System C. For further details, please contact ISSP Supercomputer Center (SCC-ISSP).

[Correspondence: center@issp.u-tokyo.ac.jp]

1.2 Project Proposals

The ISSP supercomputer system provides computation resources for scientists working on condensed matter sciences in Japan. All scientific staff members (including post-docs) at universities or public research institutes in Japan can submit proposals for projects related to research activities on materials and condensed matter sciences. These proposals are peer-reviewed by the Advisory Committee members (see Sec. 1.3), and then the computation resources are allocated based on the review reports. The leader of an approved project can set up user accounts for collaborators. Other types of scientists, including graduate students, may also be added. Proposal submissions, peer-review processes, and user registration are all managed via a web system.

The computation resources are distributed in a unit called "point", determined as a function of available CPU utilization time and consumed disk resources. There were calls for six classes of research projects in SY 2020. The number of projects and the total number of points that were applied for and approved in this school year are listed in Table 1.

Table 1: Classes of research projects in SY 2020

First semester (Apr.-Sep.)

Class	Maximum Points		Application	# of Proj.	Total points			
					Applied		Approved	
	Sys–B	Sys–C			Sys–B	Sys–C	Sys–B	Sys–C
A	100	50	any time	8	0.8k	0.4k	0.8k	0.4k
B	500	100	twice a year	61	28.4k	4.0k	22.8k	3.9k
C	5k	1k	twice a year	115	446.5k	80.1k	239.8k	42.4k
D	10k	1k	any time	3	22.5k	2.0k	15.0k	2.0k
E	15k	3k	twice a year	9	127.4k	27.0k	88.5k	21.4k
S	–	–	twice a year	0	0	0	0	0
SCCMS				11	23.7k	4.6k	23.7k	4.6k
Total				207	649.3k	118.0k	390.6k	74.6k

Second semester (Oct.-Mar.)

Class	Maximum Points		Application	# of Proj.	Total points			
					Applied		Approved	
	Sys–B	Sys–C			Sys–B	Sys–C	Sys–B	Sys–C
A	100	50	any time	10	1.0k	0.4k	1.0k	0.4k
B	1k	100	twice a year	57	46.6k	3.2k	22.0k	2.0k
C	8k	1k	twice a year	96	595.8k	59.0k	226.0k	22.3k
D	10k	1k	any time	0	0	0	0	0
E	25k	3k	twice a year	7	175.0k	18.0k	87.0k	8.4k
S	–	–	twice a year	0	0	0	0	0
SCCMS				10	50.0k	4.5k	50.0k	4.5k
Total				180	868.3k	85.0k	386.0k	37.5k

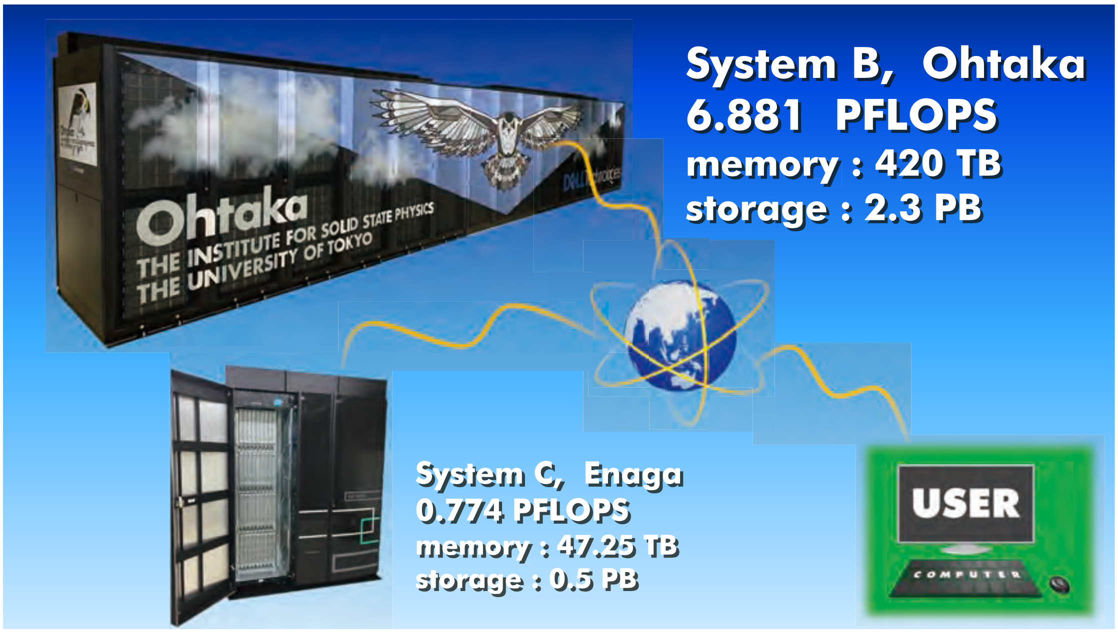

Figure 1: Supercomputer System at the SCC-ISSP

- Class A is for trial use by new users; proposals for Class A projects are accepted throughout the year.

- Proposals for projects in Classes B (small), C (mid-size), E (large-scale), and S (exceptional) can be submitted twice a year. Approved projects in Classes A, B, C, and E continue to the end of the school year.

- In Class D, projects can be proposed on rapidly-developing studies that need to perform urgent and relatively large calculations. An approved project continues for 6 months from its approval.

- Class S is for projects that are considered extremely important for the field of condensed matter physics and requires extremely large-scale computation. The project may be carried out either by one research group or cooperatively by several investigators at different institutions. A project of this class should be applied with at least 10,000 points; there is no maximum. We require group leaders applying for Class S to give a presentation on the proposal to the Steering Committee of the SCC-ISSP. Class S projects are carried out within one year from its approval.

- Project leaders can apply for points so that the points for each system do not exceed the maximum point shown in this table.

In addition, from SY 2016, ISSP Supercomputer has been providing 20% of its computational resources for Supercomputing Consortium for Computational Materials Science (SCCMS), which aims at advancing parallel computations in condensed matter, molecular, and materials sciences on the 10-PFlops K Computer and the exascale post-K project. From SY 2020, about 10% of the computational resources have been provided for SCCMS. Computational resources have also been allotted to Computational Materials Design (CMD) workshops, as well as CCMS hands-on workshops.

1.3 Committees

In order to fairly manage the projects and to smoothly determine the system operation policies, the Materials Design and Characterization Laboratory (MDCL) of the ISSP has organized the Steering Committee of the MDCL and the Steering Committee of the SCC-ISSP, under which the Supercomputer Project Advisory Committee (SPAC) is formed to review proposals. The members of the committees in SY 2020 were as follows:

Steering Committee of the MDCL

KAWASHIMA, Naoki	ISSP (Chair person)
HIROI, Zenji	ISSP
OZAKI, Taisuke	ISSP
NOGUCHI, Hiroshi	ISSP
UWATOKO, Yoshiya	ISSP
SUGINO, Osamu	ISSP
KUBO, Momoji	Tohoku Univ.
ONO, Tomoya	Kobe Univ.
YAMAURA, Jun-ichi	Tokyo Tech.
TAKAHASHI, Hiroki	Nihon Univ.
MOTOME, Yukitoshi	Univ. of Tokyo
HOSHI, Takeo	Tottori Univ.
KIMURA, Kaoru	Univ. of Tokyo
HASEGAWA, Masashi	Nagoya Univ.
NAKATSUJI, Satoru	ISSP

Steering Committee of the SCC-ISSP

KAWASHIMA, Naoki	ISSP (Chair person)
NOGUCHI, Hiroshi	ISSP
OZAKI, Taisuke	ISSP
SUGINO, Osamu	ISSP
TSUNETSUGU, Hirokazu	ISSP
KATO, Takeo	ISSP
YAMASHITA, Minoru	ISSP
MORITA, Satoshi	ISSP
HIGUCHI, Yuji	ISSP
FUKUDA, Masahiro	ISSP
IDO, Kota	ISSP

KAWAMURA, Mitsuaki	ISSP
NAKAJIMA, Kengo	Univ. of Tokyo
HATANO, Naomichi	Univ. of Tokyo
MOTOME, Yukitoshi	Univ. of Tokyo
ONO, Tomoya	Kobe Univ.
TODO, Synge	Univ. of Tokyo
KUBO, Momoji	Tohoku Univ.
OBA, Fumiyasu	Tokyo Tech.
WATANABE, Hiroshi	Keio Univ.
YOSHINO, Hajime	Osaka Univ.
OKUMURA, Hisashi	NINS-RSCS
HOSHI, Takeo	Tottori Univ.
YOSHIMI, Kazuyoshi	ISSP
YATA, Hiroyuki	ISSP
FUKUDA, Takaki	ISSP

Supercomputer Project Advisory Committee

KAWASHIMA, Naoki	ISSP (Chair person)
NOGUCHI, Hiroshi	ISSP
OZAKI, Taisuke	ISSP
SUGINO, Osamu	ISSP
TSUNETSUGU, Hirokazu	ISSP
KATO, Takeo	ISSP
YAMASHITA, Minoru	ISSP
MORITA, Satoshi	ISSP
HIGUCHI, Yuji	ISSP
FUKUDA, Masahiro	ISSP
IDO, Kota	ISSP
KAWAMURA, Mitsuaki	ISSP
NAKAJIMA, Kengo	Univ. of Tokyo
HATANO, Naomichi	Univ. of Tokyo
MOTOME, Yukitoshi	Univ. of Tokyo
ONO, Tomoya	Univ. of Tsukuba
TODO, Synge	Univ. of Tokyo
KUBO, Momoji	Tohoku Univ.
OBA, Fumiyasu	Tokyo Tech.
WATANABE, Hiroshi	Keio Univ.
YOSHINO, Hajime	Osaka Univ.
OKUMURA, Hisashi	NINS-RSCS
HOSHI, Takeo	Tottori Univ.
TSUNEYUKI, Shinji	Univ. of Tokyo
SUZUKI, Takafumi	Univ. of Hyogo
YOSHIMOTO, Yoshihide	Univ. of Tokyo
TOHYAMA, Takami	Tokyo Univ. of Sci.

KITAO, Akio	Tokyo Tech.
ARITA, Ryotaro	Univ. of Tokyo
IKUHARA, Yuichi	Univ. of Tokyo
SHIBATA, Naokazu	Tohoku Univ.
AKAGI, Kazuto	Tohoku Univ.
YANASE, Yoichi	Kyoto Univ.
HATSUGAI, Yasuhiro	Univ. of Tsukuba
OKADA, Susumu	Univ. of Tsukuba
KOBAYASHI, Nobuhiko	Univ. of Tsukuba
NAKAYAMA, Takashi	Chiba Univ.
HOTTA, Takashi	Tokyo Metropolitan Univ.
MATSUKAWA, Hiroshi	Aoyama Gakuin Univ.
YAMAUCHI, Jun	Keio Univ.
HAGITA, Katsumi	National Defense Academy
KONTANI, Hiroshi	Nagoya Univ.
SAITO, Mineo	Kanazawa Univ.
KAWAKAMI, Norio	Kyoto Univ.
YUKAWA, Satoshi	Osaka Univ.
SUGA, Seiichiro	Univ. of Hyogo
TATENO, Masaru	Univ. of Hyogo
YASUDA, Chitoshi	Univ. of the Ryukyus
OGATA, Masao	Univ. of Tokyo
WATANABE, Satoshi	Univ. of Tokyo
HUKUSHIMA, Koji	Univ. of Tokyo
NEMOTO, Koji	Hokkaido Univ.
YABANA, Kazuhiro	Univ. of Tsukuba
FURUKAWA, Nobuo	Aoyama Gakuin Univ.
KUROKI, Kazuhiko	Osaka Univ.
YASUOKA, Kenji	Keio Univ.
TANAKA, Yukio	Nagoya Univ.
MASUBUCHI, Yuichi	Nagoya Univ.
KUSAKABE, Koichi	Osaka Univ.
SHIRAI, Koun	Osaka Univ.
SAKAI, Toru	Univ. of Hyogo
ISHIBASHI, Shoji	AIST
OTANI, Minoru	AIST
TOMITA, Yusuke	Shibaura Inst. Tech.
MIYASHITA, Seiji	JPS
SHIRAISHI, Kenji	Nagoya Univ.
OGUCHI, Tamio	Osaka Univ.
KAWAKATSU, Toshihiro	Tohoku Univ.
KOBAYASHI, Kazuaki	NIMS
TATEYAMA, Yoshitaka	NIMS
KIM, Kang	Osaka Univ.
OTSUKI, Tomi	Sophia Univ.

MORIKAWA, Yoshitada	Osaka Univ.
ODA, Tatsuki	Kanazawa Univ.
OTSUKI, Junya	Okayama Univ.
KOGA, Akihisa	Tokyo Tech.
SHIMOJO, Fuyuki	Kumamoto Univ.
TAKETSUGU, Tetsuya	Hokkaido Univ.
TSURUTA, Kenji	Okayama Univ.
HAMAGUCHI, Satoshi	Osaka Univ.
NISHIDATE, Kazume	Iwate Univ.
KAGESHIMA, Hiroyuki	Shimane Univ.
SATO, Tetsuya	Keio Univ.
ISHII, Fumiyuki	Kanazawa Univ.
TATETSU, Yasutomi	Meio Univ.
YANAGISAWA, Susumu	Univ. of the Ryukyus
SHUDO, Ken-ichi	Yokohama Natl. Univ.
OHMURA, Satoshi	Hiroshima Inst. Tech.
NOGUCHI, Yoshifumi	Shizuoka Univ.
NAKAMURA, Kazuma	Kyushu Inst. Tech.
GOHDA, Yoshihiro	Tokyo Tech.
HAMADA, Ikutaro	Osaka Univ.
RAEBIGER, Hannes	Yokohama Natl. Univ.
TADA, Tomofumi	Tokyo Tech.

1.4 Staff

The following staff members of the SCC-ISSP usually administrate the ISSP Supercomputer.

KAWASHIMA, Naoki	Professor (Chair person)
NOGUCHI, Hiroshi	Associate Professor
OZAKI, Taisuke	Professor
SUGINO, Osamu	Professor
IDO, Kota	Research Associate
FUKUDA, Masahiro	Research Associate
HIGUCHI, Yuji	Research Associate
KAWAMURA, Mitsuaki	Research Associate
MORITA, Satoshi	Research Associate
YOSHIMI, Kazuyoshi	Project Researcher
MOTOYAMA, Yuichi	Project Researcher
YATA, Hiroyuki	Technical Associate
FUKUDA, Takaki	Technical Associate
ARAKI, Shigeyuki	Technical Associate

2 STATISTICS (SCHOOL YEAR 2020)

2.1 System and User Statistics

In the following, we present statistics for operation time taken in the period from April 2020 to March 2021 (SY 2020). In Table 2, we show general statistics of the supercomputer system in SY 2020. The total numbers of compute nodes in System B “sekirei”, System B “ohtaka” and System C “enaga” are 1891, 1688 and 252, respectively. Consumed disk points amount to about a few percent of the total consumed points in both System B and System C.

Table 2: Overall statistics of SY 2020

	System B sekirei (Apr.–Jun.)	System B ohtaka (Oct.-Mar.)	System C enaga (Apr.–Mar.)
total service time ($\times 10^3$ node·hours)	4060	7252	1734
number of executed jobs	179504	191483	82484
total consumed points ($\times 10^3$ point)	164	188	55
CPU points ($\times 10^3$ point)	158	185	54
disk points ($\times 10^3$ point)	6	4	2
total exec. time ($\times 10^3$ node·hours)	3626	5935	1454
availability	98.29 %	98.37%	94.59%
utilization rate	89.31 %	80.43%	83.40%

In Fig. 2, availabilities, utilization rates, and consumed points in Systems B and C are plotted for each month. Throughout the school year, the availability and the utilization rates were very high, while these were reduced from July to October due to the replacement of System B and the construction of the water cooling equipment.

The user statistics are shown in Fig. 3. The horizontal axis shows the rank of the user/group arranged in the descending order of the execution time (hour×nodes). The execution time of the user/group of the first rank is the longest. The vertical axis shows the sum of the execution time up to the rank. From the saturation points of the graphs, the numbers of “active” users of Systems B and C are around 200 and 150, respectively. The maximum ranks in the graphs correspond to the number of the users/groups that submitted at least one job.

2.2 Queue and Job Statistics

Queue structures of Systems B and C in SY2020 are shown in Tables 3 and 4, respectively. In System B “ohtaka”(“sekirei”), users can choose from two (three) types of compute nodes; jobs submitted to queues with “cpu” and “fat” (“cpu”, “acc”, and “fat”) at the end of their queue names are submitted to CPU and

Fat nodes (CPU, ACC, and Fat nodes), respectively, while only CPU nodes are available in System C "enaga". See Sec. 1.1 for a description of each type of compute node. The user then has to choose the queue according to the number of nodes to use and the duration of their calculation jobs. Queue names starting with "F" are for jobs taking 24 hours or less, while those starting with "L" can run much longer up to 120 hours. More nodes are allotted to "F" queues in order to maximize the turnaround time of user jobs. The queue names starting with "i" are used for interactive debugging of user programs and the elapsed time limit is 30 minutes. The number following "F", "L", or "i" correspond to the number of nodes that can be used by one user job. Although we do not mention here in detail, to promote utilization of the massively parallel supercomputer, background queues (queue name starting with "B") for Systems B and C which charge no points for the jobs have also been open.

To prevent overuse of the storage, points are charged also for usage of disk quota in the three systems, as shown in Table 5. Disk points are revised often for optimal usage of the resources by examining usage tendencies each year.

The number of jobs, average waiting time, and total execution time in each queue are shown in Tables 6 and 7. In System B, a large portion of jobs have been executed in "F" queues. The largest amount of the execution time has been consumed in the large-scale "F144cpu" and "F72cpu" queues for sekirei and ohtaka, respectively. However, substantial number of jobs were run in every queue, suggesting that a wide variety of user needs are met by this queuing scheme. In most of these queues, the queue settings meet the user's tendencies in that the waiting times are on the order of the elapsed-time limit.

2.3 Project for Advancement of Software Usability in Materials Science

From School Year 2015, the supercomputer center (SCC) has started "Project for advancement of software usability in materials science". In this project, for enhancing the usability of the supercomputer system in ISSP, we perform some software-advancement activity such as implementing a new function to an existing code, releasing a private code on Web, writing manuals. Target programs are publicly offered in December and selected in the review by the Steering Committee of SCC. The projects are carried out by the software development team composed of three members in ISSP. In SY 2020, three projects were selected as listed in Table 8.

Acknowledgments

The staffs would like to thank Prof. Takafumi Suzuki (now at University of Hyogo) for developing WWW-based system (SCM: SuperComputer Management System) for management of project proposals, peer-review reports by the SPAC committee, and user accounts. We also thank Ms. Reiko Iwafune for creating and maintaining a new WWW page of the ISSP Supercomputer Center.

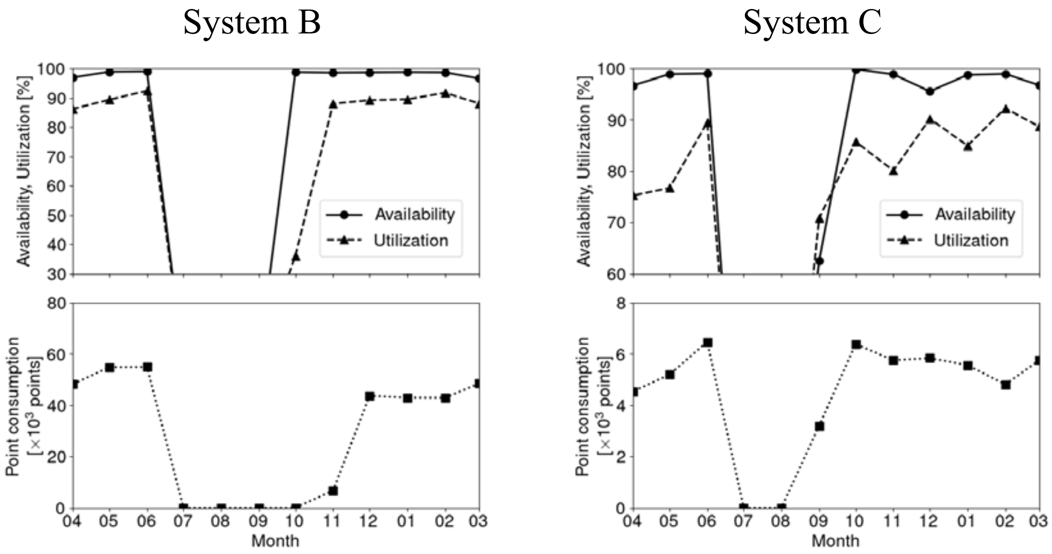

Figure 2: Availabilities, utilization rates and point consumptions of each month during SY 2020.

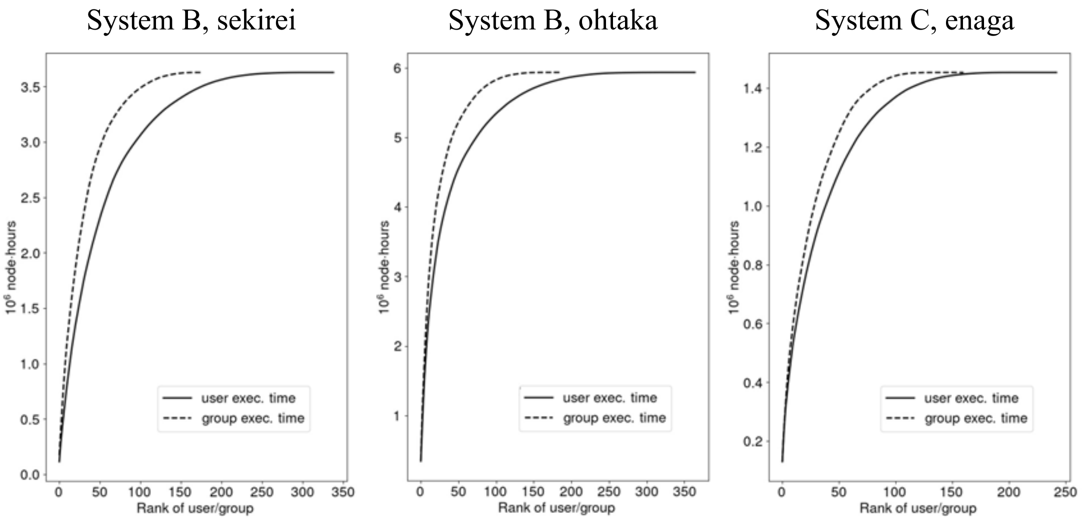

Figure 3: User statistics. The horizontal axis shows the rank of the user/group arranged in the descending order of the execution time (hour×nodes). The vertical axis shows the sum of the execution time up to the rank.

Table 3: Queue structures of System B in SY 2020

System B, sekirei

queue name	Elapsed time limit (hr)	# of nodes /job	# of nodes /queue	Memory limit (GB)	job points /(node·day)
F4cpu	24	1–4	216	120/node	1
L4cpu	120	1–4	108	120/node	1
F36cpu	24	5–36	288	120/node	1
L36cpu	120	5–36	144	120/node	1
F144cpu	24	37–144	1008	120/node	72(144)/(# of nodes)*
L144cpu	120	37–144	144	120/node	72(144)/(# of nodes)*
i18cpu	0.5	1–18	72	120/node	1
F18acc	24	1–18	180	120/node	2
L18acc	120	1–18	90	120/node	2
i9acc	0.5	1–9	36	120/node	2
F2fat	24	1–2	17	1000/node	4
L2fat	120	1–2	6	1000/node	4
i1fat	0.5	1	2	1000/node	4

* For F/L144cpu queue, the number of occupied node increases in increments of 72 nodes.

System B, ohtaka

queue name	Elapsed time limit (hr)	# of nodes /job	# of nodes /queue	Memory limit (GB)	job points /(node·day)
F1cpu	24	1	600	230/node	1
L1cpu	120	1	300	230/node	1
F4cpu	24	2–4	216	230/node	1
L4cpu	120	2–4	108	230/node	1
F16cpu	24	5–16	288	230/node	1
L16cpu	120	5–16	144	230/node	1
F36cpu	24	17–36	72	230/node	1
L36cpu	120	17–36	36	230/node	1
F72cpu	24	72	576	230/node	1
L72cpu	120	72	288	230/node	1
F144cpu	24	144	432	230/node	1
L144cpu	120	144	144	230/node	1
i8cpu	0.5	1–8	72	230/node	1
F2fat	24	1–2	7	2900/node	4
L2fat	120	1–2	3	2900/node	4
i1fat	0.5	1	1	2900/node	4

Table 4: Queue structures of System C in SY 2020

System C, enaga

queue name	Elapsed time limit (hr)	# of nodes /job	# of nodes /queue	Memory limit (GB)	job points /(node·day)
F4cpu	24	1–4	54	170/node	1
L4cpu	120	1–4	18	170/node	1
i4cpu	0.5	1–4	18	170/node	1
F9cpu	24	5–9	36	170/node	1
L9cpu	120	5–9	18	170/node	1
F36cpu	24	10–36	144	170/node	18(36)/(# of nodes)*
L36cpu	120	10–36	36	170/node	18(36)/(# of nodes)*

* For F/L36cpu queue, the number of occupied node increases in increments of 18 nodes.

Table 5: Disk points of Systems B and C

		point/day
System B sekirei	`/home`	$0.001 \times \theta(q-300)$
	`/work`	$0.0001 \times \theta(q-3000)$
System B ohtaka	`/home`	$0.001 \times \theta(q-600)$
	`/work`	$0.0001 \times \theta(q-6000)$
System C enaga	`/home`	$0.001 \times \theta(q-150)$
	`/work`	$0.0001 \times \theta(q-1500)$

* q is denoted in unit of GB.

* $\theta(x)$ is equal to the Heaviside step function $H(x)$ multiplied by x, i.e., $xH(x)$.

Table 6: Number of jobs, average waiting time, total execution time, and average number of used nodes per job in each queue of System B.

System B, sekirei

queue	# of Jobs	Waiting Time (hour)	Exec. Time ($\times 10^3$ node·hour)	# of nodes
F4cpu	58198	6.68	305.49	1.35
L4cpu	2563	27.32	147.35	1.52
F36cpu	4617	18.02	332.16	10.87
L36cpu	720	43.54	210.52	8.52
F144cpu	2434	27.52	1799.18	95.31
L144cpu	59	131.70	234.02	106.17
i18cpu	16181	0.32	21.10	8.61
F18acc	28444	3.36	245.80	3.23
L18acc	1334	7.72	85.87	1.83
i9acc	458	0.06	0.13	3.40
F2fat	1667	11.92	15.90	1.33
L2fat	417	23.29	7.78	1.09
i1fat	492	0.03	0.09	1.00

System B, ohtaka

queue	# of Jobs	Waiting Time (hour)	Exec. Time ($\times 10^3$ node·hour)	# of nodes
F1cpu	79020	25.58	156.19	1.00
L1cpu	3130	80.84	100.34	1.00
F4cpu	39592	14.36	557.68	2.58
L4cpu	2325	24.48	183.46	2.84
F16cpu	8550	33.61	607.91	9.72
L16cpu	1041	87.90	422.01	10.46
F36cpu	715	84.88	174.38	26.47
L36cpu	46	94.17	37.22	24.78
F72cpu	3215	17.44	1782.87	72.00
L72cpu	80	49.64	190.69	72.00
F144cpu	1236	27.96	1156.23	144.00
L144cpu	47	169.13	325.44	144.00
i8cpu	36070	0.12	22.44	3.63
F2fat	4476	8.87	13.11	1.05
L2fat	268	22.37	5.54	1.03
i1fat	400	0.47	0.05	1.00

Table 7: Number of jobs, average waiting time, total execution time, and average number of used nodes per job in each queue of System C.

System C, enaga

queue	# of Jobs	Waiting Time (hour)	Exec. Time ($\times 10^3$ node·hour)	# of nodes
F4cpu	44830	9.74	221.91	1.31
L4cpu	1620	46.22	86.90	1.70
i4cpu	13624	0.13	3.15	2.26
F9cpu	4688	23.12	113.76	6.32
L9cpu	249	45.02	55.75	6.92
F36cpu	4203	19.08	643.73	22.76
L36cpu	145	148.48	162.70	29.30

Table 8: List of Project for advancement of software usability in materials science for SY 2020.

Project Proposer	Project Name
Ryo Tamura NIMS	Bayesian optimization library COMBO
Synge Todo The University of Tokyo	MateriApps Installer - Installation Tool for Open-source Software
Takeo Hoshi Tottori University	Advancement of the experimental data analysis for 2D material structure

3 RESEARCH REPORTS

3.1 Invited Articles

Some Recent Developments in ab initio Thermodynamics of Ion Disorder in Solids

Shusuke KASAMATSU
Academic Assembly (Faculty of Science), Yamagata University
Kojirakawa, Yamagata-shi, Yamagata, JAPAN 990-8560

Abstract

Configurational disorder of ions in solids often play key roles in determining the properties of functional materials. A natural way to obtain thermodynamically relevant structures from the combinatorially increasing number of configurations in multicomponent systems is to combine computational statistical physics methods such as Metropolis sampling with *ab initio* methods. Since *ab initio* methods incur high computational costs, the usual approach is to fit *ab inito* datasets to low-cost models such as cluster expansion, then use those models for sampling. However, obtaining reliable low-cost models for complex oxide systems have turned out to be challenging. To circumvent this problem, we have recently been examining the feasibility of direct sampling on *ab initio* energies, as well as turning to more flexible neural network models as an alternative to cluster expansion. Here, we review some of our recent works in this direction; we also introduce our open source code *abICS*, which is designed to harness the computational capacity of modern supercomputers to perform configurational sampling on complex multicomponent systems.

1 Introduction

Functional materials for various applications including energy conversion, nanoelectronics devices, and structural materials exhibit varying levels of configurational disorder which depend on the details of materials processing including temperature and chemical potentials. Such disorder often plays significant roles in determining materials properties, and many materials in e.g., battery or magnet applications utilize impurities to cause disorder on purpose so as to obtain desirable properties. Thus, the ability to simulate such disorder as a function of temperature should be immensely helpful for prediction and design of properties in materials with realistic levels of disorder. To achieve this, it is necessary to perform sufficient thermodynamic sampling based on statistical mechanics. First-principles molecular dynamics is the method of choice for sampling quickly-relaxing (e.g., liquid) systems, but it is nearly useless for sampling solid state systems with very high energy barriers between different configurations. On the other hand, Monte Carlo methods are not limited by realistic relaxation time scales since they can employ “unphysical” trial steps such as swapping of atom positions. However, standard Metropolis Monte Carlo sampling can still get trapped in local minima, and it is usually not efficient enough to allow for a direct combination with first-principles calculations. Thus, many workers have opted to first derive lightweight models from first-principles calculations, then use those models for Monte Carlo sampling.

For modeling of systems that can be mapped to a lattice (i.e., crystalline systems with configurational disorder), the cluster expansion approach has seen much success [1–8]. This method expands the total energy in terms of “clusters” of

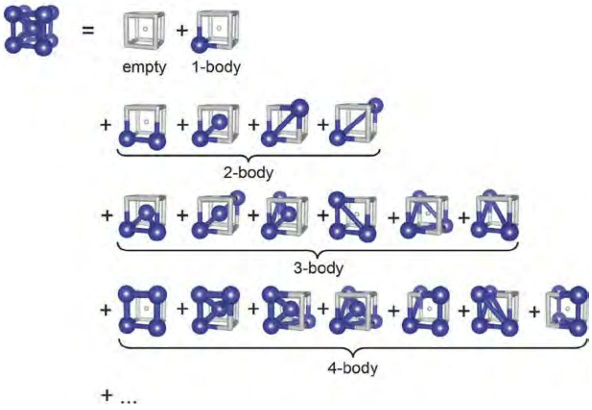

Figure 1: Clusters within the conventional BCC cell. From Chang et al. [8] (Creative Commons Attribution License 3.0, `https://doi.org/10.1088/1361-648X/ab1bbc`).

atoms (Fig. 1):

$$E(\vec{\sigma}) = \sum_{\alpha} m_\alpha V_\alpha \Phi_\alpha(\vec{\sigma}), \tag{1}$$

where α denotes empty, single, and multi-component clusters, m_α is the cluster multiplicity, and $\vec{\sigma}$ is the occupation vector. Φ_α is the cluster basis function, which for a binary system takes the simple form of

$$\Phi_\alpha(\vec{\sigma}) = \prod_{p \in \alpha} \sigma_p, \tag{2}$$

where p are site indices and $\sigma_p = \pm 1$ depending on which component occupies site p. V_α is the effective cluster interaction (ECI), which represents the contribution of each cluster to the total energy. This model reduces to the classical Ising model when considering only nearest neighbor pair clusters. The ECIs are usually obtained by fitting to energies of relaxed structures from many small-scale first-principles density functional theory (DFT) calculations, then used to perform Monte Carlo sampling on a larger cell.

The efficiency of the cluster expansion approach depends on the ability to quantitatively reproduce configuration energies using as few clusters (and corresponding ECIs) as possible. This is rarely an issue for simple two-component metallic alloys where considering only near-neighbor interactions often leads to sufficient accuracy. However, complex systems such as multicomponent oxides often require many clusters due to longer range coulomb interactions as well as complicated strain patterns. In addition to this, increasing the number of components (i.e., ion types) leads to a combinatorial increase in the number of clusters which makes cluster expansion computationally unfeasible. Another issue that has been recognized when using cluster expansion is that surface calculations require many more clusters than bulk calculations for sufficient accuracy [9].

There are two possible ways to tackle the above issue. One approach is to bypass the use of models and sample directly on first-principles energies. Although this approach is computationally expensive as mentioned above, the use of parallel sampling algorithms combined with modern-day supercomputers have made it just barely feasible in recent years. Another approach is to utilize recently-developed machine-learning models which is expected to be more flexible than the cluster expansion model. We have been working on both fronts; we will review some of the literature as well as our recent developments on the former approach in Sec. 2 and the latter approach in Sec. 3. A software framework that incorporates these developments, which we have named ab Initio Configuration Sampling Toolkit, or *abICS* for short, is introduced in Sec. 5.

2 Direct coupling of first-principles calculations with replica exchange sampling [10]

There have already been some reports of first-principles Monte Carlo simulation in the literature, but they were limited to relatively simple and quickly relaxing systems where first-principles molecular dynamics may be just as efficient [11, 12]. The issue, as noted above, is the tendency to get stuck in local minima, especially at low temperatures. One may think that with the increase in computer power available to researchers today, simply performing many Metropolis sampling calculations in parallel would lead to a sufficient number of samples for obtaining statistically relevant results. However, such embarrassingly parallel sampling is useless if each parallel image cannot achieve equilibrium. The reason for getting trapped in local minima is that the Metropolis algorithm samples the canonical ensemble; a given configuration is sampled with a probability proportional to $\exp(-\beta E)$, where β is the inverse temperature and E is the energy of the configuration. Thus, configurations residing at or near energy barriers on the potential energy surface will rarely be accepted and the difficulty to cross such energy barriers increases exponentially with βE.

This is where the so-called *extended ensemble* sampling comes to the rescue. Using histogram reweighting [13], it is possible, in theory, to convert between arbitrary ensembles. Thus, we are not limited to sampling in a single canonical ensemble at a given temperature, and this allows for choosing ensembles that can avoid the minima trapping issue. For example, one can choose to sample an ensemble where each configuration is realized with probabilities proportional to the inverse of the density of states. This is the idea behind multicanonical [14] and Wang-Landau [15] methods. In fact, the Wang-Landau method was recently used successfully in combination with order-N first-principles Korringa-Kohn-Rostoker approach (albeit without structural relaxation) to calculate the order-disorder transition in a 250-atom CuZn supercell [16].

On the other hand, we have been working extensively on combining first-principles calculation with another popular extended ensemble method, i.e., the replica exchange Monte Carlo (RXMC) method [17]. This approach considers an ensemble of N_{rep} replicas of a given system at N_{rep} different temperatures. Each replica is simulated in the canonical ensemble, so the low temperature replicas would still have the minima trapping issue. However, the problem is alleviated by allowing swaps of temperatures between replicas according to the following Metropolis criterion for the ensemble of N_{rep} replicas:

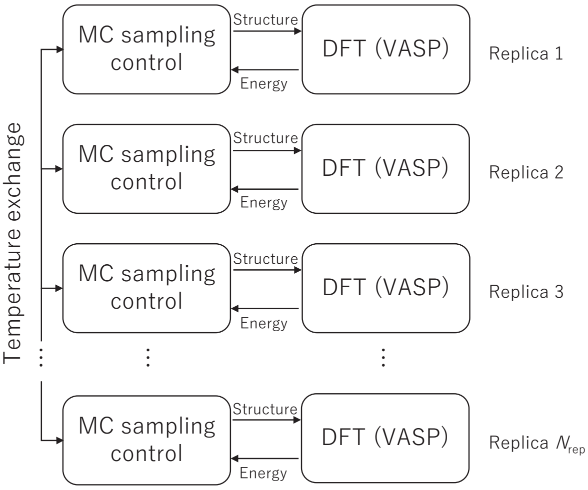

Figure 2: Schematic of our scheme for coupling the RXMC method with DFT codes. Reproduced from Ref. [10]

$$P = \min\{1, \exp[(\beta_i - \beta_j)(E_i - E_j)]\}. \quad (3)$$

Here, i and j are the indices of the replicas attempting the swap, and $\beta_{i(j)}$ and $E_{i(j)}$ are the inverse temperatures and energies of each replica. According to this criterion, a replica with lower energy will be assigned progressively lower energies, and vice versa. Essentially, a high-temperature replica is given the task of a global scan of configuration space; when it finds a new local minimum, it will be assigned a lower temperature and will perform a more careful search within the newly found energy basin. In this manner, the RXMC method provides a good balance between global search and local optimization. At the same time, the canonical ensembles are easily recovered by collecting the replicas at each temperature.

Figure 2 shows our computational scheme. There are N_{rep} Metropolis samplers running at different temperatures; the samplers are coded using python and parallelized using mpi4py [18–20]. At each Metropolis step, each sampler performs a swap between atoms of different types (possibly including vacancies), prepares input files for the specified DFT code, and spawns parallel DFT processes using MPI-2 dynamic process management, i.e., the MPI_COMM_SPAWN function. The DFT

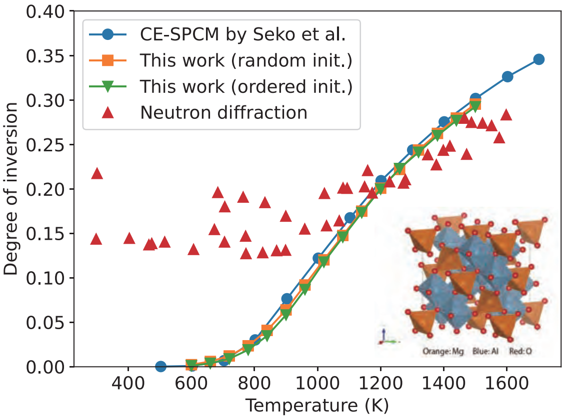

Figure 3: Comparison of the degree of inversion as a function of temperature calculated by CE-SPCM (Seko et al. [21]; circles), the present approach (randomly initialized: squares; initialized with an ordered spinel structure: triangles and experimental neutron diffraction data [22]). The spinel structure is shown in the inset. Reproduced from Ref. [10] with addition of neutron diffraction data.

processes perform local structural relaxation and energy calculation, then the results are read automatically by the sampler to determine whether to accept or reject the new configuration. The samplers also attempt temperature swaps between replicas at preset intervals according to Eq. 3. This multilayered parallelism over replicas and DFT processes makes it ideal for harnessing the power of modern-day parallel supercomputers.

As a first benchmark for testing the feasibility of this approach, we chose to calculate the degree of cation disorder in $MgAl_2O_4$ spinel oxide [10]. Spinel oxides have a general formula of $A(II)B(III)_2O_3$ with A (B) representing a divalent (trivalent) cation, and are of interest in magnetic (spintronic) and electronic applications as well as mineralogy. The structure is shown in Fig. 3. Usually, the divalent cation occupies the tetrahedral sites and the trivalent cation occupies the octahedral sites. However, some inversion between the sites can occur, and some A(II)–B(III) combinations are known to exhibit completely inverse ordering, where all trivalent cations occupy the octahedral sites. The degree of inversion (DOI) is quantified by the ratio of divalent cations at octahedral sites. Seko and coworkers have performed calculations of the DOI in several spinels using cluster expansion [4, 21], and we took their result for $MgAl_2O_4$ as reference. We employed a calculation supercell containing 16 Mg, 32 Al, and 64 O atoms, and sampled the configuration of Mg and Al on the cation sublattice. No disorder on the O sublattice was considered. We performed two separate RXMC runs to check for convergence and initial configuration dependence; one run was initialized with random configurations and another was initialized from the ordered spinel configuration. We used 16 replicas spaced evenly between 600 and 1500 K and performed 16750 steps for the randomly initialized run and 13000 steps for the run initialized from the ordered configuration. This amounts to roughly 4000 node hours for each run on System C (enaga) at ISSP which has two Xeon Gold 6148 processors per node. Figure 3 compares the calculated DOI vs. temperature for the two runs as well as that obtained by a cluster expansion model augmented by a screened point charge model. We find the results to be virtually identical, showing that sufficient sampling steps were performed and it is indeed feasible to perform such calculations on meaningfully large supercells without resorting to fitted models. Moreover, the RXMC calculation initialized in the random configuration discovered the ground state ordered spinel configuration within 300 steps. We think this is rather impressive considering that there are ${}_{48}C_{16}$ = 2254848913647 possible configurations, and attests to the efficiency of the RXMC method not only as a sampler but also as an optimizer. We also note that the deviation from experiment at lower temperature is seen in both our calculation and Seko's. This is most likely due to the low mobility of cations at low temperature which inhibits the equilibration in the experiment.

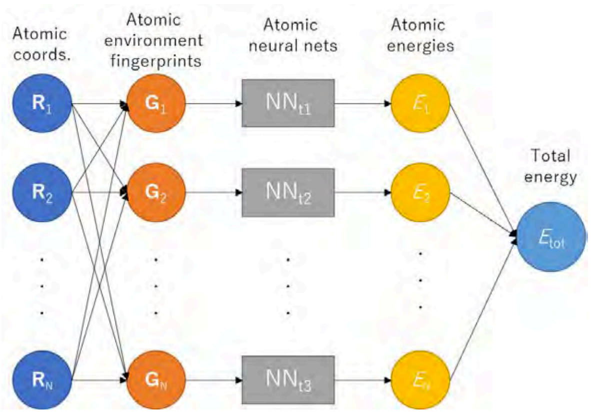

Figure 4: The structure of the HDNNP. The atomic coordinates are converted to a rotationally and translationally invariant environment descriptor before feeding in to the neural network.

3 Accelerated sampling utilizing a neural network model combined with active learning [23]

Although direct sampling using DFT-relaxed energies was shown to be feasible as detailed above, the amount of required computer resources is quite large, taking several days to a week to sample just one composition on a modern supercomputer. A much higher throughput is necessary to enable materials design based on such simulations. Also, because of the computational cost of DFT calculations, it is not feasible to go beyond a system size of about one hundred atoms and perform sufficient numbers of sampling steps. This is a problem when treating systems with, e.g., dilute doping or long correlation lengths. To provide the necessary acceleration, we have no choice at this point but to go back to lightweight models. However, as mentioned above, the *de facto* standard cluster expansion approach has difficulty handling complex multicomponent systems that are of interest for various applications.

To overcome this issue, we turned to the high-dimensional neural network potential (HDNNP) approach pioneered by Behler and Parinello [24, 25]. This approach relies on the ansatz that the total energy can be expressed as a sum of atomic energies determined by the environment around each atom and uses a a feed-forward neural network to represent those atomic energies (Fig. 4). The network weights are trained to reproduce DFT energies and forces (i.e., energy derivatives). Acceleration by 2–4 orders of magnitude compared to DFT has been achieved while maintaining similar levels of accuracy.

The HDNNP approach was developed for accelerating molecular dynamics simulations. There, it is necessary to accurately reproduce the energy and forces in continuous coordinate space. This is overkill when considering the lattice configuration problem; we only need to map the ideal lattice structure with configurational disorder to the energy after local relaxation. Thus, we proposed to train the HDNNP model to predict the relaxed energies from the set of atom coordinates and atom species on the ideal lattice [23]. The new ansatz here is that the total energy of a *relaxed* configuration can be expressed as a sum of atomic energies determined from atom environment descriptors calculated on the ideal lattice *before relaxation*. This may be expressed as follows:

$$E_{\mathrm{rel}}(\vec{\sigma}) = \sum_{i}^{\mathrm{atoms}} \mathrm{NNP}^{\mathrm{rel}}_{t_i}(f[\vec{\sigma}_i^{R_\mathrm{c}}]) \text{ for } \vec{\sigma} \in \{\vec{\sigma}_{\mathrm{lattice}}\}, \tag{4}$$

where $\vec{\sigma}$ represents the coordinates of all atoms in the system, which is restricted, in our scheme, to those on the ideal lattice. i represents atom indices, t_i is the corresponding atom type, and $\vec{\sigma}_i^{R_\mathrm{c}}$ represents the configuration of atoms within a cutoff radius from atom i. A separate neural net NNP_{t_i} is trained for each atom type; it takes as input a rotationally and translationally invariant fingerprint of the atomic environment $f[\vec{\sigma}_i^{R_\mathrm{c}}]$ and outputs the contribution of the atom i to the *relaxed* total energy. In this work, we employed the Chebychev fingerprint proposed by Artrith and coworkers [26]. In this fingerprinting scheme, Chebychev expansion coefficients of the radial and angular distribution functions are used as the fingerprint. The atom type is encoded by multiplying with type-dependent factors when calculating the radial/angular distributions. We use ænet code (`http://ann.atomistic.net/`) for the training and evaluation of the neural network model.

An issue with neural network approaches in general is that they are good at interpolating between training data but not at extrapolating. To overcome this problem, we adopted the so-called “active learning” approach, where the neural network is retrained on-the-fly when the simulation wanders into regions of structure space that were not included in the original training data set [27–35]. Our approach is summarized as follows:

1. Prepare a training set consisting of DFT-relaxed energies of randomly generated configurations.
2. Perform neural network training.
3. Perform RXMC sampling using the trained neural network model.
4. Perform DFT relaxations on a subset of configurations that appeared during RXMC sampling and check the prediction accuracy. If sufficient accuracy is achieved, stop here.
5. If the accuracy is found to be insufficient, add those configurations to the training set and repeat from step 2.

We benchmarked this approach, again, on the temperature dependence of the DOI in $MgAl_2O_4$. We used a supercell with 192 cation sites compared to 48 in the previous section. The supercell size combined with the explosion of the possible number of configurations (${}_{192}C_{64} \sim 10^{51}$) makes this calculation completely out of reach for direct sampling on DFT energies.

Figure 5 shows the correlation plot between the neural network predictions vs. reference DFT energies. The model trained on randomly generated configurations performs well in the high energy region but shows a sizable deviation at lower energies. This is because the lower energy structures with more ordering were obviously not included in the original training data set. In our active learning scheme, these structures are then added to the training set and the model is retrained. The resulting correlation after active learning is nearly perfect with deviations of less than a few meV/atom. The active-learned neural network model was used to sample the DOI vs. temperature (Fig. 6) from 480,000 RXMC steps with 15 replicas, and good agreement was obtained with cluster expansion and direct sampling on DFT energies explained in the previous section.

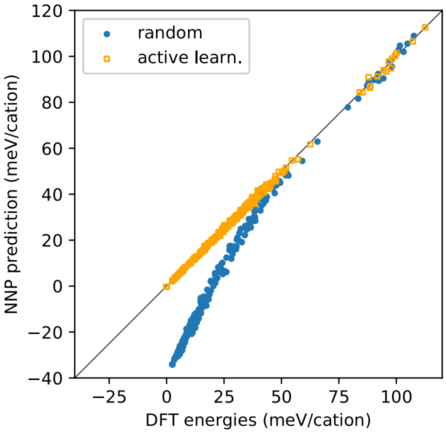

Figure 5: The correlation between reference DFT energies and neural network predictions when training was performed on randomly generated configurations (closed circles) and after performing active learning (open squares).

4 Applications

We have only just started to apply the thermodynamic sampling methods outlined in previous sections to complex oxide systems that were difficult to treat using previously available methods. Here, we briefly present some results obtained for a couple of systems of interest in solid state ionics and electrochemistry.

Acceptor-doped $BaZrO_3$

Ceramic-based electrolytes are under intense research for application in battery, fuel cell, and electrolyzer applications. Recently, we have been focusing on acceptor-doped $BaZrO_3$, which is known as a promising material to be used as the

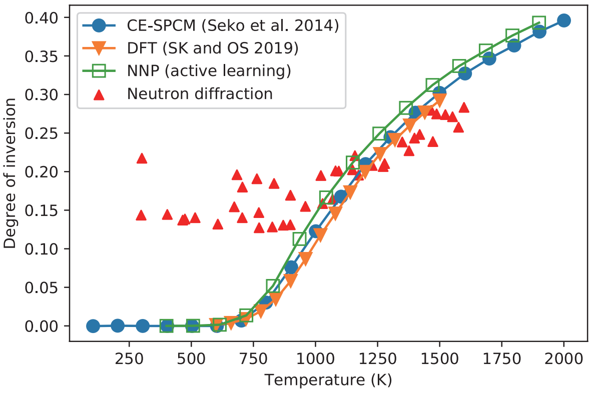

Figure 6: Comparison of the DOI calculated using cluster expansion (blue circles), direct sampling on DFT energies (orange triangles), and the neural network model (open green squares) compared to experiment (red triangles).

proton conducting electrolyte in solid oxide fuel cells. The material is an insulator without doping, but oxygen vacancies with an effective charge of +2 can be induced by substituting Zr^{4+} by trivalent acceptor cations such as Y^{3+}. This is expressed in Kröger-Vink notation as follows:

$$2\mathrm{Zr}_{\mathrm{Zr}}^{\times} + \mathrm{O}_{\mathrm{O}}^{\times} + \mathrm{Y}_2\mathrm{O}_3 \rightarrow 2\mathrm{Y}_{\mathrm{Zr}}' + \mathrm{V}_{\mathrm{O}}^{\bullet\bullet} + 2\mathrm{ZrO}_2. \quad (5)$$

These oxygen vacancies are immobile in the temperature range of interest, but highly mobile protons can be induced by a hydration reaction with these vacancies:

$$\mathrm{H}_2\mathrm{O} + \mathrm{V}_{\mathrm{O}}^{\bullet\bullet} + \mathrm{O}_{\mathrm{O}}^{\times} \rightarrow 2(\mathrm{OH}_{\mathrm{O}}^{\bullet}). \quad (6)$$

The maximum dopant concentration can reach up to 60% depending on the dopant species [36] (although it may be questionable whether it is appropriate to refer to such high concentrations as “doping”). Conventionally, dopants were assumed to distribute randomly on the Zr sites. On the other hand, some recent works have pointed out that the configuration of dopants can impact the proton mobility in both positive and negative ways [37–39]. For example, an isolated dopant or a cluster of dopants can act as a trapping site for protons due to coulomb attraction. On the other hand, dopants may form a long-range percolating pathway along which protons can diffuse relatively freely. Thus, we performed RXMC sampling combined directly with DFT for revealing what the realistic dopant configurations will be under processing conditions in Y-doped BaZrO_3 with dopant concentration up to 30%. We note that many works have discussed the interaction between few dopants and O vacancies or protons, but none have treated such highly doped systems rigorously within a statistical thermodynamics framework like ours. Our approach revealed that the dopant configurations are far from random even at the usual sintering temperature of $\sim$ 1800 K. This originates from complex many-body interactions that cannot be explained simply in terms of coulomb interactions between charged defects. Detailed analysis based on the statistics obtained from RXMC samples can be found in Ref. [40]. We also fed the obtained configurations into a master equation model for proton diffusion [41] and found that the realistic dopant configurations obtained by RXMC sampling predicts slightly higher conductivities compared to random configurations [42]. Another insight obtained there is that in general, the formation of deep trapping sites due to dopant clustering has much more profound effect than the formation of a percolating pathway. Thus, avoiding dopant clustering would be the route to higher conductivity in this system.

We are now performing the active learning NN-RXMC approach of Sec. 3 to understand the hydration behavior and the recently reported high conductivity of 0.01 S/cm at 400 °C in 60% Sc-doped BaZrO_3 [36]. Prior to this report, Y doping of $\sim$ 20% was reported to result in the highest proton conductivity using BaZrO_3 as the parent material. An issue was that further doping results in the decline of proton conductivity, which was also reproduced by our work mentioned above [42]. In the case of Sc, however, the conductivity continues to increase up to 60% doping, which is the solubility limit for this system. It will be interesting and insightful to see how the character of different dopants with the same formal charge can lead to such different behavior. We are working to contribute in this regard using *ab initio* thermodynam-

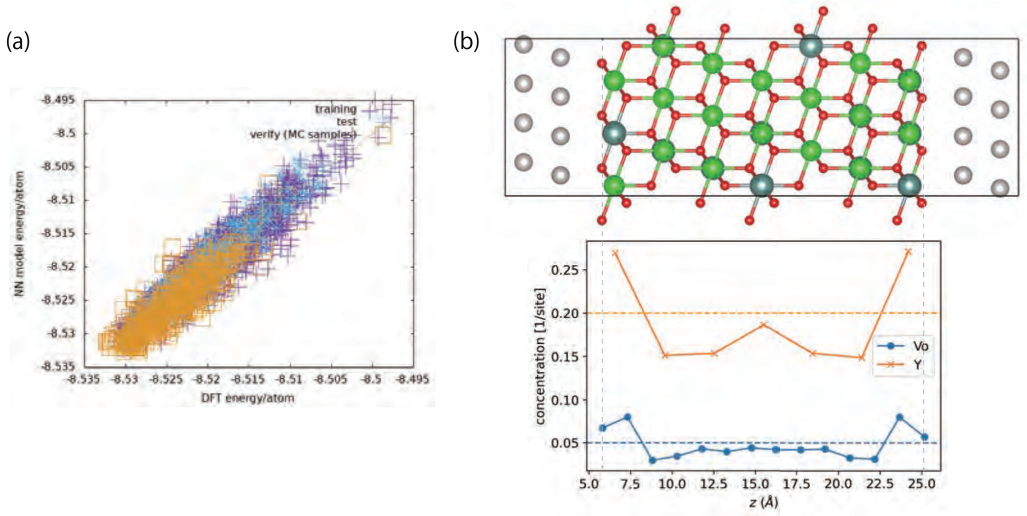

Figure 7: (a) Evaluation of NN accuracy after active learning on The Pt/YSZ slab model and (b) the obtained Y and O vacancy concentration profiles.

ics.

The ionic space charge layer

Another issue we are currently working on is the ionic space charge effect at solid-solid interfaces. The space charge concept is a central idea of semiconductor device physics, where a depletion or accumulation of holes or electrons occurs to align the Fermi level across the interface. The concept should naturally be extended to mobile ions, which are abundant in solid electrolytes, but the situation is now much more complicated because various ionic species can contribute to the effect, and ions can even be introduced spontaneously (e.g., hydrogen in the atmosphere can spontaneously dope oxides [43]). A related (or maybe equivalent) concept in electrochemistry of liquid electrolytes is the electrical double layer. The nanoscale atomistic details of the space charge layer is expected to modify the ion dynamics in various ways. It should impact the performance of solid state electrochemical devices such as solid-state batteries, fuel cells, and electrolyzers, or may even lead to novel functionalities. Because of this, the topic is under intense study from both experimental and theoretical standpoints (see, e.g., `https://interface-ionics.jp/en/index.html`).

In the past, we have combined ion defect formation energetics calculated using DFT with a Poisson-Boltzmann type model to calculate the ion distribution near metal/solid electrolyte interfaces [44–46]. However, the energetics were calculated in the bulk and do not include effects such as the chemical characteristics of the interface or the concentration dependencies of the dielectric constant. Also, the interactions between defects were modeled considering only ideal point charge electrostatics. In other words, it is a mean field model with many assumptions and may not be reliable enough for certain cases.

ab initio statistical thermodynamics approaches introduced above are ideal for tackling this issue and going beyond the simple mean-field picture. As a first step, we calculated the ion distribution in the Pt (111)/Yttria-stabilized zirconia (YSZ) (111) slab model (Fig. 7). Note that YSZ is a well-studied oxide ion conductor for application in solid oxide fuel cells. The parent lattice is cubic fluorite ZrO_2 with 68 Zr sites and 126 O sites, and configurations of 12 Y ions on Zr sites and 6 O vacancies residing on the O sites were sampled using our active learning NN-RXMC approach (Sec. 3). The correlation between the DFT energies and NN predictions of the training, test, and verification sets seems to be good enough, although not as perfect as the bulk $MgAl_2O_4$ case (Fig. 5). The calculated concentration profiles show a segregation of Y on the outermost Zr layer and depletion on the second and third Zr layers. There is also an increase in the vacancy concentration on the second O layer. The next challenge would be to consider variations in the number of oxygen vacancies and perform grand canonical sampling, so that the results can be compared directly with experiments which control the oxygen partial pressure. We expect these calculations to be immensely useful for understanding the thermodynamics of space charge layer formation, and also to serve as a basis for understanding the modification of various materials properties due to formation of interfaces.

5 ab Initio Configuration Sampling Toolkit (abICS)

The software framework for direct coupling of RXMC sampling with DFT (Sec. 2) was selected as an ISSP Project for Advancement of Software Usability in Materials Science for SY2019. Parts of the prototype code developed by the author (S.K.) were rewritten in modular fashion so as to enable easy extension of the framework. The original prototype only supported VASP as the energy calculator, but interfaces for OpenMX and Quantum Espresso are now supported. In addition, a user interface employing the human-readable and computer-friendly TOML format (`https://toml.io/en/`) was developed for setting up the calculations. The code has been named ab Initio Configuration Sampling Toolkit, or *abICS* for short, and released to the public under an open source license (GPL ver. 3), along with a user manual. It is under continous development (`https://www.pasums.issp.u-tokyo.ac.jp/abics/`, `https://github.com/issp-center-dev/abICS`), and we are in the process of implementing the active learning approach explained in Sec. 3.

6 Summary and outlook

In this report, we presented our recent efforts in enabling configurational sampling in complex oxide systems from first principles. By harnessing the power of modern day supercomputers in combination with extended ensemble sampling, it has now become just barely feasible to perform sampling directly on DFT energies on unit cells of ~ 100 atoms. We also demonstrated that similar accuracy can be achieved with a speedup by a factor of $\sim 10^4$ by the use of a neural network model that reproduces the configuration energetics. This has made possible routine sampling on unit cells of a few hundred atoms with *ab initio* accuracy.

We have been implementing these approaches in an open source framework *abICS*. We believe that this framework will be immensely useful for making efficient use of the ever-increasing capacity of modern supercomputers. We are also aiming to bring together information science, materials simulation, and statistical physics using *abICS* as a hub. Because of modular coding practices employed in our project, it should be relatively easy to implement interfaces for other solvers, or to implement new sampling schemes. Please and do not refrain from contacting us if you are interested in using or extending this software.

Acknowledgements

abICS is developed by Yuichi Motoyama, Kazuyoshi Yoshimi, Yoshiyuki Yamamoto, Osamu Sugino, Taisuke Ozaki, and the author (S.K.) as part of the ISSP Project for Advancement of Software Usability in Materials Science. The calculations presented in this work were performed on the ISSP Joint-Use Supercomputer Systems “sekirei”, “enaga”, and “ohtaka” as well as on the supercomputer Fugaku provided by RIKEN for the Fugaku Battery and Fuel Cell Project. This report reviewed works supported over the years by KAKENHI (Grant numbers JP18H05519, 19K15287, 20H05284), MEXT LEADER program, and JST CREST (JPMJCR15Q3) and

FOREST (JPMJFR2037) programs. Atomic structure figures were drawn using VESTA [47].

References

[1] J. M. Sanchez, F. Ducastelle, and D. Gratias, Physica A **128A**, 334 (1984).

[2] G. Ceder, Comput. Mater. Sci. **1**, 144 (1993).

[3] A. van de Walle, M. Asta, and G. Ceder, Calphad **26**, 539 (2002).

[4] A. Seko, Y. Koyama, and I. Tanaka, Phys. Rev. B **80**, 165122 (2009).

[5] J. M. Sanchez, Phys. Rev. B **81**, 224202 (2010).

[6] J. M. Sanchez, J. Phase Equilib. Diffus. **38**, 238 (2017).

[7] Q. Wu, B. He, T. Song, J. Gao, and S. Shi, Comput. Mater. Sci. **125**, 243 (2016).

[8] J. H. Chang, D. Kleiven, M. Melander, J. Akola, J. M. Garcia-Lastra, and T. Vegge, J. Phys.: Condens. Matter **31**, 325901 (2019).

[9] K. Yuge, A. Seko, A. Kuwabara, F. Oba, and I. Tanaka, Phys. Rev. B **76**, 045407 (2007).

[10] S. Kasamatsu and O. Sugino, J. Phys.: Condens. Matter **31**, 085901 (2019).

[11] J. Jellinek, S. Srinivas, and P. Fantucci, Chem. Phys. Lett. **288**, 705 (1998).

[12] S. Wang, S. J. Mitchell, and P. A. Rikvold, Comput. Mater. Sci. **29**, 145 (2004).

[13] A. M. Ferrenberg and R. H. Swendsen, Phys. Rev. Lett. **61**, 2635 (1988).

[14] B. A. Berg and T. Neuhaus, Phys. Rev. Lett. **68**, 9 (1992).

[15] F. Wang and D. P. Landau, Phys. Rev. Lett. **86**, 2050 (2001).

[16] S. N. Khan and M. Eisenbach, Phys. Rev. B **93**, 024203 (2016).

[17] K. Hukushima and K. Nemoto, J. Phys. Soc. Jpn. **65**, 1604 (1996).

[18] L. Dalcín, R. Paz, and M. Storti, J. Parallel Distrib. Comput. **65**, 1108 (2005).

[19] L. Dalcín, R. Paz, M. Storti, and J. D'Elía, J. Parallel Distrib. Comput. **68**, 655 (2008).

[20] L. D. Dalcin, R. R. Paz, P. A. Kler, and A. Cosimo, Adv. Water Resour. **34**, 1124 (2011).

[21] A. Seko and I. Tanaka, J. Phys.: Condens. Matter **26**, 115403 (2014).

[22] S. A. T. Redfern, R. J. Harrison, H. S. C. O'Neill, and D. R. R. Wood, Am. Mineral. **84**, 12 (1999).

[23] S. Kasamatsu, Y. Motoyama, K. Yoshimi, U. Matsumoto, A. Kuwabara, and T. Ogawa, (2020), arXiv preprint: 2008.02572.

[24] J. Behler, Int. J. Quantum Chem. **115**, 1032 (2015).

[25] S. Watanabe, W. Li, W. Jeong, D. Lee, K. Shimizu, E. Mimanitani, Y. Ando, and S. Han, J. Phys.: Energy **3**, 012003 (2020).

[26] N. Artrith, A. Urban, and G. Ceder, Phys. Rev. B **96**, 014112 (2017).

[27] E. V. Podryabinkin and A. V. Shapeev, Comput. Mater. Sci. **140**, 171 (2017).

[28] E. V. Podryabinkin, E. V. Tikhonov, A. V. Shapeev, and A. R. Oganov, Phys. Rev. B **99**, 064114 (2019).

[29] K. Gubaev, E. V. Podryabinkin, G. L. Hart, and A. V. Shapeev, Comput. Mater. Sci. **156**, 148 (2019).

[30] J. S. Smith, B. Nebgen, N. Lubbers, O. Isayev, and A. E. Roitberg, J. Chem. Phys. **148**, 241733 (2018).

[31] L. Zhang, D.-Y. Lin, H. Wang, R. Car, and W. E, Phys. Rev. Mater. **3**, 023804 (2019).

[32] T. Kostiuchenko, F. Körmann, J. Neugebauer, and A. Shapeev, npj Comput. Mater. **5**, 1 (2019).

[33] T. D. Loeffler, T. K. Patra, H. Chan, M. Cherukara, and S. K. R. S. Sankaranarayanan, J. Phys. Chem. C **124**, 4907 (2020).

[34] J. Vandermause, S. B. Torrisi, S. Batzner, Y. Xie, L. Sun, A. M. Kolpak, and B. Kozinsky, npj Comput. Mater. **6**, 20 (2020).

[35] R. Jinnouchi, K. Miwa, F. Karsai, G. Kresse, and R. Asahi, J. Phys. Chem. Lett. **11**, 6946 (2020).

[36] J. Hyodo, K. Kitabayashi, K. Hoshino, Y. Okuyama, and Y. Yamazaki, Adv. Energy Mater. **n/a**, 2000213 (2020).

[37] K. Toyoura, W. Meng, D. Han, and T. Uda, J. Mater. Chem. A **6**, 22721 (2018).

[38] K. Toyoura, T. Fujii, N. Hatada, D. Han, and T. Uda, J. Phys. Chem. C **123**, 26823 (2019).

[39] F. M. Draber, C. Ader, J. P. Arnold, S. Eisele, S. Grieshammer, S. Yamaguchi, and M. Martin, Nature Mater. (2019).

[40] S. Kasamatsu, O. Sugino, T. Ogawa, and A. Kuwabara, J. Mater. Chem. A **8**, 12674 (2020).

[41] K. Toyoura, T. Fujii, N. Hatada, D. Han, and T. Uda, J. Phys. Chem. C **123**, 26823 (2019).

[42] T. Fujii, K. Toyoura, T. Uda, and S. Kasamatsu, Phys. Chem. Chem. Phys. **23**, 5908 (2021).

[43] C. G. Van de Walle, Phys. Rev. Lett. **85**, 1012 (2000).

[44] S. Kasamatsu, T. Tada, and S. Watanabe, Solid State Ionics **183**, 20 (2011).

[45] S. Kasamatsu, T. Tada, and S. Watanabe, Solid State Ionics **226**, 62 (2012).

[46] K. Shimizu, W. Liu, W. Li, S. Kasamatsu, Y. Ando, E. Minamitani, and S. Watanabe, Phys. Rev. Mater. **4**, 015402 (2020).

[47] K. Momma and F. Izumi, J. Appl. Crystallogr. **41**, 653 (2008).

High precision study of the Anderson transition

TOMI OHTSUKI[1]
KEITH SLEVIN[2]
1) Dept. Phys., Sophia University, Chiyoda-ku, Tokyo 102-8554, Japan
2) Dept. Phys., Osaka University, Toyonaka, Osaka 560-0043, Japan

(Dated: May 3, 2021)

INTRODUCTION

More than six decades have passed since Anderson's seminal paper on localisation was published[1]. During the subsequent decades, there have been numerous important discoveries including weak localisation, universal conductance fluctuations, and the scaling theory of localisation[2]. Localisation phenomena are observed not only in electron systems, but also in optical [3–9], acoustic [10–12], and cold atom systems [13–18].

Since the proposal of the scaling theory of localisation[19–23], determining the critical behavior of the localisation-delocalisation transition, which is usually referred to as the Anderson transition (AT), has continued to attract considerable attention. Depending on the symmetry of the Hamiltonian, systems are classified into orthogonal, unitary and symplectic symmetry classes, cf. the classification of random matrices[24, 25]. This classification was extended to include three classes with chiral symmetry[26, 27], and four classes with particle-hole symmetry[28]. These ten classes have also proven useful in the discussion of whether or not there is a topological phase and, if there is, what type of topological phase is realized, given the symmetry class and the dimensionality of the system.[29, 30]

In this activity report, we review the numerical approach for the study of the Anderson transition, and also another type of transition, the metal to semimetal transition. We emphasize the importance of the concept of universality class, and the scaling analysis of high precision numerical data.

The rest of this report is organized as follows. In the next section, we explain the method, followed by the results for our recent high precision studies of three dimensional (3D) Anderson transitions with and without time reversal symmetry. We then review the recent progress on the novel symmetry classes with chiral and particle-hole symmetries as well as the extension to non-Hermitian systems. We conclude this report by discussing the metal to semimetal transition and the scaling behavior of the density of states.

METHODS

We start with the Anderson's model of localisation[1],

$$H = \sum_i E_i \left| i \right\rangle \left\langle i \right| - \sum_{\langle ij \rangle} \left| i \right\rangle V_{i,j} \left\langle j \right| . \qquad (1)$$

where $|i\rangle$ is an orbital localised on site i of a 3D cubic lattice. The first sum is over all sites on the lattice and the second sum is over pairs of nearest neighbours. The unit of energy is the nearest neighbour transfer energy $V = |V_{i,j}|$, which we set to unity $V = 1$. The orbital energies E_i are assumed to be identically and independently distributed with a uniform distribution

$$p\left(E_i\right) = \begin{cases} 1/W, & |E_i| \le W/2\,, \\ 0, & \text{otherwise}\,. \end{cases} \qquad (2)$$

The parameter W determines the strength of disorder. The Hamiltonian commutes with the complex conjugation operator, i.e. a time reversal operator that squares to $+1$, and this model belongs to the orthogonal symmetry class [21, 22, 24, 25] (see Table I).

We can extend the Anderson model by including Peierls phases $V_{i,j} = \exp(i\theta_{i,j})$, which describe magnetic fields, in the nearest neighbour hoppings. Here $\theta_{i,j}$ with $i > j$ are randomly and uniformly distributed between $[0, 2\pi]$ and and $\theta_{i,j} = -\theta_{j,i}$. We call this the U(1) model. In this case the Hamiltonian does not commute with a time reversal operator, and the model belongs to the unitary symmetry class.

Symmetry classification

We can further extend the model to include spin/orbital degree of freedom by modifying $V_{i,j}$ and E_i and can realize different symmetry classes.

Class	Symbol	TRS	PHS	CS
Unitary	A	No	No	No
Orthogonal	AI	1	No	No
Symplectic	AII	-1	No	No
Chiral Unitary	AIII	No	No	Yes
Chiral Orthogonal	BDI	1	1	Yes
Chiral Symplectic	CII	-1	-1	Yes
BdG	D	No	1	No
	C	No	-1	No
	DIII	-1	1	Yes
	CI	1	-1	Yes

TABLE I. Classification according to TRS, PHS and CS. For TRS (PHS), 1 means $C^T = C$ ($C'^T = C'$) whereas -1 means $C^T = -C$ ($C'^T = -C'$). BdG means Bogoliubov-de Gennes class.

Using the unitary operators C, C' and P, we can classify the Hamiltonian according to whether it satisfies the following symmetries[29],

$$H = CH^*C^{-1}\,, \tag{3}$$

for time reversal symmetry (TRS), and

$$H = -C'H^*C'^{-1}\,. \tag{4}$$

for particle-hole symmetry (PHS). Systems with TRS and PHS are further classified according to whether C or C' is symmetric or antisymmetric.

We also have chiral symmetry

$$H = -PHP^{-1}, P^2 = 1\,. \tag{5}$$

Note that chiral symmetry is automatic when we have both TRS and PHS.

The classification[29] is summarized in Table I.

The transfer matrix method

One of the ways to study the Anderson transition with high precision is to calculate the quasi-one dimensional localisation length and perform a finite size scaling analysis [31–35].

We consider a system with a square cross section $L \times L$, which we divide into layers labelled by their x coordinate. Then the Schrödinger equation for a state vector $|\Psi\rangle$ and energy E

$$H\,|\Psi\rangle = E\,|\Psi\rangle\ , \tag{6}$$

is expressed in the following form

$$\begin{pmatrix}\psi_{x+1}\\ V_{x+1,x}\psi_x\end{pmatrix} = M_x \begin{pmatrix}\psi_x\\ V_{x,x-1}\psi_{x-1}\end{pmatrix}, \tag{7}$$

where ψ_x is the wavefunction on the slice at position x,

$$(\psi_x)_{y,z} = \langle x,y,z\,|\Psi\rangle\ . \tag{8}$$

M_x is the transfer matrix defined by,

$$M_x = \begin{pmatrix}V^{-1}_{x,x+1}(E-H_x) & -V^{-1}_{x,x+1}\\ V_{x+1,x} & 0_N\end{pmatrix}. \tag{9}$$

For the Anderson model where we set $V_{i,j} = -1$, we have

$$\begin{pmatrix}\psi_{x+1}\\ -\psi_x\end{pmatrix} = \begin{pmatrix}H_x - E & 1_N\\ -1_N & 0_N\end{pmatrix}\begin{pmatrix}\psi_x\\ -\psi_{x-1}\end{pmatrix}. \tag{10}$$

H_x is the following sub-matrix of the Hamiltonian

$$(H_x)_{y,z,y',z'} = \langle x,y,z|\ H|\ x,y',z'\rangle\ . \tag{11}$$

0_N and 1_N are the $N \times N$ ($N = L^2$) zero and unit matrices, respectively. The boundary conditions in the transverse directions influence some of the critical behavior[36]. In this report, we impose periodic boundary conditions in the transverse directions. We set the energy at the band centre, i.e. $E = 0$.

We note that the transfer matrix must satisfy the following relation

$$M_x^T \Sigma M_x = \Sigma\,, \tag{12}$$

where

$$\Sigma = \begin{pmatrix}0_N & -i1_N\\ i1_N & 0_N\end{pmatrix}. \tag{13}$$

The wave-function amplitudes on the first two layers are related to the wave-function amplitudes on the last two layers as follows

$$\begin{pmatrix}\psi_{L_x+1}\\ -\psi_{L_x}\end{pmatrix} = M_{L_x}\cdots M_1 \begin{pmatrix}\psi_1\\ -\psi_0\end{pmatrix}, \tag{14}$$

which involves the product of L_x independently and identically distributed random matrices $M = M_{L_x}\cdots M_1$.

The following limiting matrix exists[37],

$$\Omega = \lim_{L_x\to\infty} \frac{\ln M^T M}{2L_x}\,. \tag{15}$$

The limit depends on the particular sequence of random matrices, but the eigenvalues $\{\gamma_i\}$ of Ω are the same for all sequences ("all" means with probability one). These values are called Lyapunov exponents. From Eq. (12) these eigenvalues occur in pairs of opposite sign. It is usual to number them as follows

$$\gamma_1 > \cdots > \gamma_N > \gamma_{N+1} = -\gamma_N > \cdots > \gamma_{2N} = -\gamma_1 \,. \tag{16}$$

This ± symmetry can be derived from Eq. (12).

To estimate the Lyapunov exponents we start with a $2N \times 2N$ orthogonal matrix, truncate the matrix product at a very large but finite L_x, and perform a QR decomposition of the result

$$QR = MQ_0 \,. \tag{17}$$

Here, Q_0 and Q are a $2N \times 2N$ orthogonal matrix and R is a $2N \times 2N$ upper triangular matrix with positive diagonal elements. We then define

$$\tilde{\gamma}_i = \frac{1}{L_x} \ln R_{i,i} \,. \tag{18}$$

In the limit of infinite length

$$\gamma_i = \lim_{L_x \to \infty} \tilde{\gamma}_i \,. \tag{19}$$

For sufficiently large L_x, the $\{\tilde{\gamma}_i\}$ may be used to estimate the Lyapunov exponents.

This method requires the simulation of a single very long sample. While this method has been employed very successfully in numerous simulations over the preceding decades, the calculations are inherently serial and do not allow us to take advantage of massively parallel computers.

Parallel transfer matrix method

An alternative way is to simulate an ensemble of much shorter samples and consider an ensemble average. While for simplicity we consider cubes with $L_x = L$, the method is also applicable when $L_x \neq L$.

We note here that the matrix Q_0 should be a $2N \times 2N$ random matrix with orthogonal columns sampled from a probability distribution that is invariant under convolution with the transfer matrix distribution, i.e., with a distribution that is invariant under the operation[38]

$$Q'R = M_x Q \,. \tag{20}$$

For such a distribution, it immediately follows that [39]

$$\gamma_N = \langle \tilde{\gamma}_N \rangle \,, \tag{21}$$

where $\langle \cdots \rangle$ is the sample average. To generate such matrices, we have found that the following procedure works well. We start with Q_0 given by the $2N$-dimensional unit matrix,

$$Q_0 = 1_{2N} \tag{22}$$

and calculate

$$Q'R = M_q \cdots M_1 Q_0 \,. \tag{23}$$

The matrix R is then discarded and we set $Q_0 = Q'$. This procedure is then repeated a sufficient number of times.

For a given L, we have found that, when a sufficient number of randomizing multiplications are performed, the distribution of $\tilde{\gamma}_N$ becomes independent of the number of such multiplications[39]. We assess this by applying the Kolmogorov-Smirnov test to the data for $\tilde{\gamma}_N$ with different numbers of randomizing multiplications. For sufficiently large number of randomizing multiplications we find that the Kolmogorov-Smirnov test is unable to distinguish the distribution of $\tilde{\gamma}_N$ obtained[39].

Fitting

Once we calculate γ_N, which is a function of the cross section size L and the strength of disorder W, we define

$$\Gamma(W, L) = L\gamma \,, \tag{24}$$

and assume the scaling form,

$$\Gamma(W, L) = F(\phi_1, \phi_2, \phi_3, \cdots). \tag{25}$$

Each scaling variable ϕ_i on the right hand side has a power law dependence on L

$$\begin{aligned} \phi_1 &\equiv u_1(w) L^{1/\nu}, \\ \phi_2 &\equiv u_2(w) L^{-y}, \\ \phi_3 &\equiv u_3(w) L^{-y'}, \\ &\cdots . \end{aligned}$$

Here $1/\nu\,(> 0)$ is the scaling dimension of the relevant scaling variable and $-y$ is the scaling dimension of the least irrelevant scaling variable; $\cdots < -y' < -y\,(< 0)$.

In this report, we use the disorder strength W to tune the system through the transition. We denote the critical disorder where the transition occurs as

W_c. We define $w \equiv (W - W_c)/W_c$. The functions $u_j(w)$ $(j = 1, 2, \cdots)$ obey $u_1(w = 0) = 0$ and $u_j(w = 0) \neq 0$ $(j = 2, 3, \cdots)$. When w is sufficiently small, the u's can be expanded in powers of w

$$u_i(w) \equiv \sum_{j=0}^{m_i} b_{i,j} w^j \tag{26}$$

with $i = 1, 2, \cdots$, $b_{1,0} = 0$, and $b_{j,0} \neq 0$ $(j = 2, 3, \cdots)$[35, 40]. When the ϕ's are sufficiently small, the universal scaling function F can also be expanded[41]. We keep only the relevant scaling variable ϕ_1 and the least irrelevant scaling variable ϕ_2, while assuming the other irrelevant scaling variables to be zero, $\phi_3 = \cdots = 0$. This should be reasonable for w sufficiently small and L sufficiently large. We expand F in terms of ϕ_1 and ϕ_2 as

$$F = \sum_{j_1=0}^{n_1} \sum_{j_2=0}^{n_2} a_{j_1,j_2} \phi_1^{j_1} \phi_2^{j_2} \,. \tag{27}$$

To remove the ambiguity of fitting parameters, we set $a_{1,0} = a_{0,1} = 1$. The parameter $a_{0,0}$ is sometimes related to quantities of interest such as multifractal exponents[42], and we write it as Γ_c.

Whether the fit is plausible is determined by calculating the goodness of fit probability. When the fit is plausible, we check the stability of the fit against changes of the range of data being fitted and of the orders of the polynomial expansions. Fig. 1 shows an example of simulation data Γ and the results of the fitting.

The confidence intervals of the fitting parameters are determined by Monte Carlo simulations. From the fitting function $F_i = F(W_i, L_i)$ for the i-th data $(1 \leq i \leq N_D$, N_D the number of data points), we produce an ensemble of synthetic data sets with $\tilde{\Gamma}_i = F_i + \sigma_i$ where σ_i is a random number, the variance is the same as that of i-th data and the mean zero. By fitting the synthetic data sets $\{\tilde{\Gamma}_i\}$'s we obtain the distribution of the critical parameters such as W_c and ν, and estimate their confidence intervals.

NUMERICAL STUDIES OF THE ANDERSON TRANSITION

Wigner-Dyson classes

For the Wigner-Dyson (WD) classes, neither the particle-hole (PHS) or chiral (CS) is present. There are 3 WD classes (see Table I). Using System B and simulating the Anderson and U(1) models, we have determined the critical exponents of the 3D orthogonal and unitary universality classes. The results are summarized in Fig. 1 and Table II.

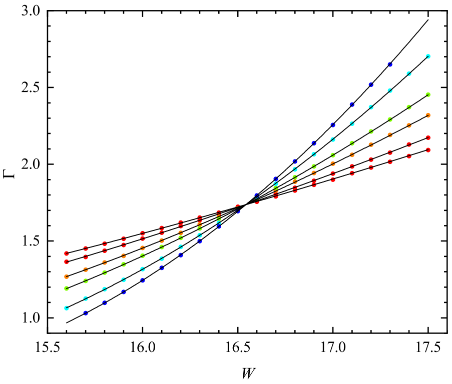

(a) 3D class AI

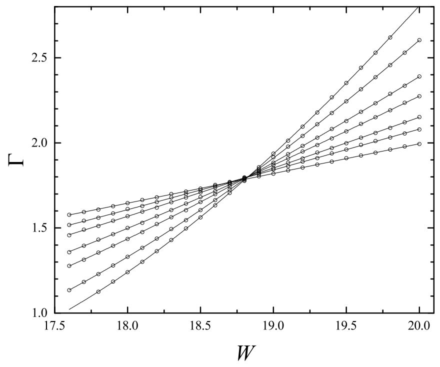

(b) 3D class A

FIG. 1. Γ as a function of the disorder strength W for various cross section size L. (a) 3D class AI, where $L = 12.18, 24, 32, 48$ and 64. $L = 96$ is underway using new System B. (b) 3D class A, where $L = 4, 6, 8, 12, 16, 20$ and 24. In the delocalised (localised) phase, Γ decreases (increases) with L. (a) is taken from [39] and (b) from [43].

The calculation time is proportional to the time for the QR decomposition and the number of transfer matrix multiplications. The dimension of transfer matrix is proportional to $L^{(d-1)}$, hence QR decomposition takes time proportional to $L^{3(d-1)}$, d being the space dimension. In addition, to obtain the same precision for larger L, we need to increase the length L_x proportional to L. The calculation time, therefore, is proportional to L^{3d-2}. This rapid increase of calculation time for higher dimen-

class	ν	Γ_c	W_c	N_D	N_P	p	$-y$
3D AI	1.572[1.566,1.577]	1.7372[1.7359,1.7384]	16.543[16.541,16.545]	117	7	0.5	–
3D A	1.443[1.437,1.449]	1.805[1.803,1.808]	1.805[1.803,1.808]	171	10	0.4	-3.1[-3.9,-2.4]

TABLE II. Results of the finite size scaling fits. Numbers are taken from Refs. [39, 43]. The systems sizes are $L = 24, 32, 48$ and 64 for 3D orthogonal class (Anderson model, class AI), whereas they are $L = 4, 6, 8, 12, 16, 20$ and 24 for 3D unitary class (U(1) model, class A). The precision is expressed by 95% confidence intervals, N_D is the number of data points, N_P the number of fitting parameters, and p the goodness of fit probability. For the 3D orthogonal case, irrelevant scaling variables are not necessary. This is because we use only $L \geq 24$ where corrections to scaling are smaller than the precision of the data [35].

sion, at first sight, gives the impression that higher dimensional simulation is almost impossible. However, the corrections to scaling are smaller in higher dimensions, and the critical behavior in dimensions higher than three has also been studied[43–45]. On the other hand, the critical behavior of the quantum Hall transition, which occurs in two dimensions, is still controversial due to the very slowly converging corrections to scaling[46].

Distribution of Kondo temperature

At the critical point, eigenstates exhibit multifractality. This is reflected in the fluctuations of the local density of states. As a result, when we consider magnetic impurities, the Kondo temperature T_K has a broad distribution. It has been predicted that the distribution of T_K has a power law tail at small T_K with a universal exponent whose value is related to the multifractal exponent η [47]. Using the kernel polynomial method [48], we calculated the local density of states at the Anderson transition, and determined the distribution of T_K. The massively parallel calculations on System B enabled us to reach the small T_K needed to check the analytic prediction [49]. Experimental verification may be possible by comparing with measurements of the temperature dependence of the magnetic susceptibility.

Beyond the Wigner-Dyson classes

Systems with CS/PHS symmetries have attracted much attention recently, because many of them are topological insulators or topological superconductors[29]. We note that these unconventional universality classes, i.e. classes other than Wigner-Dyson, are realized only at $E = 0$.

One way to realize a model with chiral symmetry is to set all the orbital energies $E_i = 0$, and consider random hopping, $V_{i,j}$. Setting $E = 0$, we may then vary the strength of the randomness of the hopping and study the Anderson transition. This approach, however, has proven to be difficult to handle numerically because an unphysically large disorder in the hopping is needed to cause an Anderson transition[50].

Fixing the hopping and changing the diagonal disorder is easier for numerical calculations. This can be realized by considering, for example, the following Hamiltonian, which corresponds to 3D class CI (see Table I). It is a two-orbital cubic lattice model,

$$\begin{aligned}\mathcal{H} \equiv & \sum_{\boldsymbol{i},\boldsymbol{j}} \sum_{d,d'} |\boldsymbol{i}, d\rangle [\mathbb{H}]_{(\boldsymbol{i},d|\boldsymbol{j},d')} \langle \boldsymbol{j}, d'| \\ = & \sum_{\boldsymbol{i}} \Big\{ \big(E_{\boldsymbol{i}} + \Delta\big)\big(|\boldsymbol{i}, a\rangle\langle \boldsymbol{i}, a| - |\boldsymbol{i}, b\rangle\langle \boldsymbol{i}, b|\big) \\ & + t_{\|}\big(|\boldsymbol{i}, a\rangle\langle \boldsymbol{i}, b| + |\boldsymbol{i}, b\rangle\langle \boldsymbol{i}, a|\big) \\ & + t_{\perp} \sum_{\mu=x,y} \sum_{d=a,b} \big(|\boldsymbol{i} + \boldsymbol{e}_\mu, d\rangle + |\boldsymbol{i} - \boldsymbol{e}_\mu, d\rangle\big)\langle \boldsymbol{i}, d| \\ & + t'_{\|}\big(|\boldsymbol{i} + \boldsymbol{e}_z, a\rangle\langle \boldsymbol{i}, a| - |\boldsymbol{i} + \boldsymbol{e}_z, b\rangle\langle \boldsymbol{i}, b| + \text{h.c.}\big)\Big\}. \end{aligned} \tag{28}$$

Here $d, d' = a, b$ denotes the orbital index, $\boldsymbol{i} \equiv (i_x, i_y, i_z)$ with $\boldsymbol{e}_x = (1, 0, 0)$, $\boldsymbol{e}_y = (0, 1, 0)$ and $\boldsymbol{e}_z = (0, 0, 1)$ is the site index on the 3D cubic lattice. The orbital energies at two different lattice sites have no correlation; $\overline{E_{\boldsymbol{i}} E_{\boldsymbol{j}}} = \delta_{\boldsymbol{i},\boldsymbol{j}} W^2/12$. The model has a particle-hole symmetry ($\mathbb{P}\mathbb{H}\mathbb{P}^{-1} = -\mathbb{H}$) as well as the time-reversal symmetry ($\mathbb{H}^* = \mathbb{H}$) with $[\mathbb{P}]_{(\boldsymbol{i},d|\boldsymbol{j},d')} \equiv (-1)^{i_x+i_y} \delta_{\boldsymbol{i},\boldsymbol{j}} [\sigma_y]_{d,d'}$ with the 2 by 2 Pauli matrices, σ_x, σ_y and σ_z. Since $\mathbb{P}^{\mathrm{T}} = -\mathbb{P}$, the Hamiltonian has a set of doubly degenerate real-valued eigenstates at zero energy, which results in the degeneracy of the Lyapunov exponents at $E = 0$; the degeneracy is protected by the particle-hole symmetry. For simplicity, we set $\Delta = t_{\|} = t'_{\|} = t_{\perp} = 1$. As in the previous subsection, the localisation length of the zero-energy eigenstates along the z-direction (λ_z) is calculated via the transfer matrix method. The periodic boundary condition is imposed along x and y directions. The density of states (DOS) of $\mathbb{H}$ with finite disorder strength W is calculated in terms of kernel polynomial expansion (KPE) method [48]. Due to the particle-hole symmetry, the calculated DOS is symmetric about $E = 0$, while the DOS at $E = 0$ remains finite at the critical point[51]. The exponent of 3D class CI thus estimated is $\nu = 1.16 \pm 0.02$.

We can construct a similar Hamiltonian for the 3D class BDI, which is a model for disordered nodal-line Weyl semimetal [51].

SUMMARY AND CONCLUDING REMARKS

phase diagram

In this review, we focused on the Anderson transition at $E = 0$ (center of the band). Once we know the critical disorder $W_c \approx 16.54$ at $E = 0$ (see Table II), we can prepare thousands of delocalised ($W < W_c$) and localised ($W > W_c$) wave functions. Then we can let a convolutional neural network (CNN) learn the features of these wave functions[52, 53], and draw the phase diagram in $W - E$ parameter plane[54, 55].

Fig. 2(a) is an example. We take the training regions indicated by the arrows in Fig. 2(a), and let the neural network calculate the probability that the states are delocalised in the rest of the parameter region. We can also draw the phase diagram for quantum percolation, where sites are present with probability p and absent with probability $1 - p$, and all the orbital energies are set to zero, $E_i = 0$. From the training in the Anderson model where the transfer matrix method is applicable, we can draw the phase diagram for the quantum percolation problem where the transfer matrix method is not applicable. Fig. 2(b) is the phase diagram for the quantum percolation problem drawn by the neural network trained using the Anderson model.

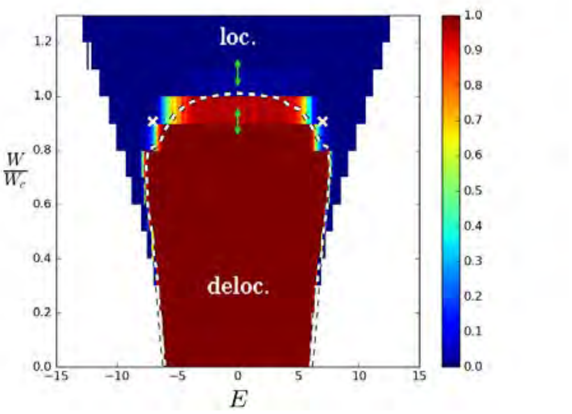

(a) 3D Anderson model

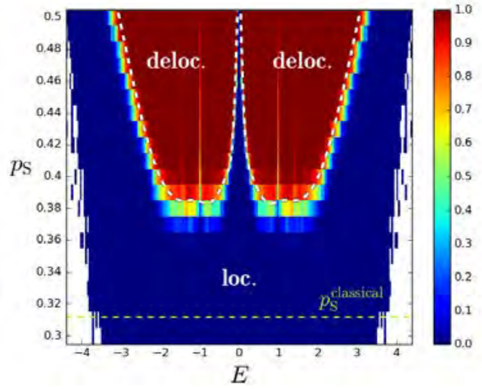

(b) 3D quantum percolation

FIG. 2. Phase diagram of 3D Anderson transitions. (a) is for Anderson model. The green arrows in (a) indicate the regions where the CNN is trained, whereas the white dashed line and crosses indicate the phase boundary estimated by other methods [56, 57]. (b) is for site-type quantum percolation. The white dashed line is from the estimates by Ref.[58], whereas the green horizontal dashed line indicates the classical percolation threshold. Taken from Refs.[54, 55].

Beyond Hermitian classes

The symmetry classification according to TRS and PHS can be extended to non-Hermitian (NH) systems [59]. For example, for TRS for Hermitian systems we have $H = CH^*C^{-1} = CH^TC^{-1}$ [Eq. (3)], but for non-Hermitian systems there are two possibilities,

$$H = CH^*C^{-1}\,, H = CH^TC^{-1}\,. \tag{29}$$

The latter symmetry is straightforwardly realized for the Anderson model [Eq. (1)] by making the orbital energies E_j random complex numbers. We then have $H = H^T$ but $H \neq H^*$. The system is called NH class AI†. Making the E_j complex in the U(1) model realizes NH class A. The critical behaviors have been shown to be different from the Hermitian classes AI and A[60, 61] via the finite size scaling analyses.

These two classes are only a part of the 38 symmetry classes[59] in non-Hermitian disordered systems. The critical behavior for these classes is an interesting topic left for the future.

Density of states scaling

So far, we have discussed the Anderson transition. There are other transitions in the same symmetry classes. For example, the semimetal to metal transition[62] occurs in 3D Dirac and Weyl systems, where the systems remains semimetal up to certain strength of disorder, then undergoes semimetal to metal transition. (Further increase of disorder leads to an Anderson transition.) Though the symmetry classes are AII (Dirac) and A (Weyl), the critical behaviors described by the scaling of the density of states[63, 64] is different from the Anderson transition, i.e., both the exponent ν and the dynamical exponent z differ from those of the Anderson transition in the same symmetry class and dimensionality.

Experiments

Interpreting the critical behavior found experimentally in doped semiconductors remains difficult because the role of the electron-electron interaction, which may be relevant in the renormalisation group sense, is not well understood. In experiments, the critical exponent s, which describes how the zero temperature conductivity vanishes as the critical point is approached from the metallic side, is measured. This exponent is related to the critical exponent ν by Wegner's relation $s = (d-2)\nu$[19]. As yet there is no agreement between theory and experiment and understanding the critical behaviour at the metal-insulator transition in doped semiconductors remains an open problem[65, 66].

The quantum kicked rotor with suitable quasi-periodic modulation exhibits an Anderson transition in the the same universality class as that in Anderson's model of localisation in 3D. This experimental realisation of the quantum kicked rotor has provided an alternative avenue for experimental investigation of the Anderson transition.[13–15]. The value $\nu = 1.63 \pm 005$ [15] found in these experiments agrees well with our numerical estimate.

Light waves [3, 4, 7–9] and acoustic waves [10–12] also localize and interaction effects play less of a role. For small loss, such systems are described by the 3D class AI. When the loss is not negligible, the system might show the critical behavior in 3D class $\mathrm{AI}^{\dagger}$. Quantitative studies and detailed comparisons between theory and experiment are interesting topics left for the future.

Acknowledgement The work was partly supported by JSPS KAKENHI Grants 19H00658.

[1] P. W. Anderson, Absence of diffusion in certain random lattices, Phys. Rev. **109**, 1492 (1958).

[2] E. Abrahams, ed., *50 Years of Anderson Localization* (World Scientific Publishing Company, 2010).

[3] S. John, Strong localization of photons in certain disordered dielectric superlattices, Phys. Rev. Lett. **58**, 2486 (1987).

[4] D. S. Wiersma, P. Bartolini, A. Lagendijk, and R. Righini, Localization of light in a disordered medium, Nature **390**, 671 (1997).

[5] M. Segev, Y. Silberberg, and D. N. Christodoulides, Anderson localization of light, Nature Photonics **7**, 197 (2013).

[6] A. Mafi, Transverse anderson localization of light: a tutorial, Advances in Optics and Photonics **7**, 459 (2015).

[7] T. Schwartz, G. Bartal, S. Fishman, and M. Segev, Transport and anderson localization in disordered two-dimensional photonic lattices, Nature **446**, 52 (2007).

[8] S. E. Skipetrov and I. M. Sokolov, Magnetic-field-driven localization of light in a cold-atom gas, Phys. Rev. Lett. **114**, 053902 (2015).

[9] S. E. Skipetrov, Localization transition for light scattering by cold atoms in an external magnetic field, Phys. Rev. Lett. **121**, 093601 (2018).

[10] T. R. Kirkpatrick, Localization of acoustic waves, Phys. Rev. B **31**, 5746 (1985).

[11] R. Weaver, Anderson localization of ultrasound, Wave Motion **12**, 129 (1990).

[12] H. Hu, A. Strybulevych, J. H. Page, S. E. Skipetrov, and B. A. van Tiggelen, Localization of ultrasound in a three-dimensional elastic network, Nature Physics **4**, 945 (2008).

[13] J. Chabé, G. Lemarié, B. Grémaud, D. Delande, P. Szriftgiser, and J. C. Garreau, Experimental observation of the anderson metal-insulator transition with atomic matter waves, Phys. Rev. Lett. **101**, 255702 (2008).

[14] G. Lemarié, J. Chabé, P. Szriftgiser, J. C. Garreau, B. Grémaud, and D. Delande, Observation of the anderson metal-insulator transition with atomic matter waves: Theory and experiment, Phys. Rev. A **80**, 043626 (2009).

[15] M. Lopez, J.-F. Clément, P. Szriftgiser, J. C. Garreau, and D. Delande, Experimental test of universality of the anderson transition, Phys. Rev. Lett. **108**, 095701 (2012).

[16] J. Billy, V. Josse, Z. Zuo, A. Bernard, B. Hambrecht, P. Lugan, D. Clément, L. Sanchez-Palencia, P. Bouyer, and A. Aspect, Direct observation of anderson localization of matter waves in a controlled disorder, Nature **453**, 891 (2008).

[17] G. Modugno, Anderson localization in bose–einstein condensates, Reports on Progress in Physics **73**, 102401 (2010).

[18] L. Sanchez-Palencia, D. Clément, P. Lugan, P. Bouyer, and A. Aspect, Disorder-induced trapping versus anderson localization in bose–einstein condensates expanding in disordered potentials, New Journal of Physics **10**, 10.1088/1367-2630/10/4/045019 (2008).

[19] F. J. Wegner, Electrons in disordered systems. scaling near the mobility edge, Zeitschrift fur Physik B **25**, 327 (1976).

[20] E. Abrahams, P. W. Anderson, D. C. Licciardello, and T. V. Ramakrishnan, Scaling theory of localization: Absence of quantum diffusion in two dimensions, Phys. Rev. Lett. **42**, 673 (1979).

[21] K. B. Effetov, A. I. Larkin, and D. E. Khmel'nitsukii, Soviet Phys. JETP **52**, 568 (1980).

[22] S. Hikami, A. I. Larkin, and Y. Nagaoka, Spin-orbit interaction and magnetoresistance in the two dimensional random system, Progress of Theoretical Physics **63**, 707 (1980).

[23] S. Hikami, Anderson localization in a nonlinear-σ-model representation, Phys. Rev. B **24**, 2671 (1981).

[24] E. P. Wigner, On the statistical distribution of the widths and spacings of nuclear resonance levels, Mathematical Proceedings of the Cambridge Philosophical Society **47**, 790–798 (1951).

[25] F. J. Dyson, Threefold way - algebraic structure of symmetry groups and ensembles in quantum mechanics, Journal of Mathematical Physics **3**, 1199 (1962).

[26] R. Gade and F. Wegner, The n = 0 replica limit of u(n) and u(n)so(n) models, Nuclear Physics B **360**, 213 (1991).

[27] R. Gade, Anderson localization for sublattice models, Nuclear Physics B **398**, 499 (1993).

[28] A. Altland and M. R. Zirnbauer, Nonstandard symmetry classes in mesoscopic normal-superconducting hybrid structures, Phys. Rev. B **55**, 1142 (1997).

[29] A. P. Schnyder, S. Ryu, A. Furusaki, and A. W. W. Ludwig, Classification of topological insulators and superconductors in three spatial dimensions, Phys. Rev. B **78**, 195125 (2008).

[30] A. Kitaev, Periodic table for topological insulators and superconductors, AIP Conference Proceedings **1134**, 22 (2009).

[31] A. MacKinnon and B. Kramer, One-parameter scaling of localization length and conductance in disordered systems, Phys. Rev. Lett. **47**, 1546 (1981).

[32] A. MacKinnon and B. Kramer, The scaling theory of electrons in disordered solids: Additional numerical results, Zeitschrift für Physik B Condensed Matter **53**, 1 (1983).

[33] J.-L. Pichard and G. Sarma, Finite size scaling approach to anderson localization, J. Phys. C: Solid State Phys. **C14**, L127 (1981).

[34] B. Kramer and A. MacKinnon, Localization: theory and experiment, Reports on Progress in Physics **56**, 1469 (1993).

[35] K. Slevin and T. Ohtsuki, Critical exponent for the anderson transition in the three-dimensional orthogonal universality class, New Journal of Physics **16**, 015012 (2014).

[36] K. Slevin, T. Ohtsuki, and T. Kawarabayashi, Topology dependent quantities at the anderson transition, Phys. Rev. Lett. **84**, 3915 (2000).

[37] V. I. Oseledec, A multiplicative ergodic theorem. characteristic ljapunov, exponents of dynamical systems, Trans. Moscow Math. Soc. **19**, 197 (1968).

[38] K. Slevin, Y. Asada, and L. I. Deych, Fluctuations of the lyapunov exponent in two-dimensional disordered systems, Phys. Rev. B **70**, 054201 (2004).

[39] K. Slevin and T. Ohtsuki, Critical exponent of the anderson transition using massively parallel supercomputing, Journal of the Physical Society of Japan **87**, 094703 (2018), https://doi.org/10.7566/JPSJ.87.094703.

[40] K. Slevin and T. Ohtsuki, Corrections to scaling at the anderson transition, Phys. Rev. Lett. **82**, 382 (1999).

[41] K. Binder, Critical properties from monte carlo coarse graining and renormalization, Phys. Rev. Lett. **47**, 693 (1981).

[42] M. Janssen, Statistics and scaling in disordered mesoscopic electron systems, Physics Reports **295**, 1 (1998).

[43] K. Slevin and T. Ohtsuki, Estimate of the critical exponent of the anderson transition in the three and four-dimensional unitary universality classes, Journal of the Physical Society of Japan **85**, 104712 (2016).

[44] A. M. García-García and E. Cuevas, Dimensional dependence of the metal-insulator transition, Phys. Rev. B **75**, 174203 (2007).

[45] Y. Ueoka and K. Slevin, Dimensional dependence of critical exponent of the anderson transition in the orthogonal universality class, Journal of the Physical Society of Japan **83**, 084711 (2014), http://dx.doi.org/10.7566/JPSJ.83.084711.

[46] K. Slevin and T. Ohtsuki, Critical exponent for the quantum hall transition, Phys. Rev. B **80**, 041304 (2009).

[47] S. Kettemann, E. R. Mucciolo, I. Varga, and K. Slevin, Kondo-anderson transitions, Phys. Rev. B **85**, 115112 (2012).

[48] A. Weiße, G. Wellein, A. Alvermann, and H. Fehske, The kernel polynomial method, Rev. Mod. Phys. **78**, 275 (2006).

[49] K. Slevin, S. Kettemann, and T. Ohtsuki, Multifractality and the distribution of the kondo temperature at the anderson transition, The European Physical Journal B **92**, 281 (2019).

[50] A. M. García-García and E. Cuevas, Anderson transition in systems with chiral symmetry, Phys. Rev. B **74**, 113101 (2006).

[51] X. Luo, B. Xu, T. Ohtsuki, and R. Shindou, Critical behavior of anderson transitions in three-dimensional orthogonal classes with particle-hole symmetries, Phys. Rev. B **101**, 020202 (2020).

[52] T. Ohtsuki and T. Ohtsuki, Deep learning the quantum phase transitions in random two-dimensional electron systems, Journal of the Physical Society of Japan **85**, 123706 (2016), http://dx.doi.org/10.7566/JPSJ.85.123706.

[53] T. Ohtsuki and T. Ohtsuki, Deep learning the quantum phase transitions in random electron systems: Applications to three dimensions, Journal of the Physical Society of Japan **86**, 044708 (2017), http://dx.doi.org/10.7566/JPSJ.86.044708.

[54] T. Mano and T. Ohtsuki, Phase diagrams of three-dimensional anderson and quantum percolation models using deep three-dimensional convolutional neural network, Journal of the Physical Society of Japan **86**, 113704 (2017), https://doi.org/10.7566/JPSJ.86.113704.

[55] T. Ohtsuki and T. Mano, Drawing phase diagrams of random quantum systems by deep learning the wave functions, J. Phys. Soc. Jpn. **89**, 022001 (2020).

[56] S. L. A. de Queiroz, Reentrant behavior and universality in the anderson transition, Phys. Rev. B **63**, 214202 (2001).

[57] G. Schubert, A. Weiße, G. Wellein, and H. Fehske, Hqs@hpc: Comparative numerical study of anderson localisation in disordered electron systems, in *High Performance Computing in Science and Engineering, Garching 2004*, edited by A. Bode and F. Durst (Springer Berlin Heidelberg, Berlin, Heidelberg, 2005) pp. 237–249.

[58] L. Ujfalusi and I. Varga, Quantum percolation transition in three dimensions: Density of states, finite-size scaling, and multifractality, Phys. Rev. B **90**, 174203 (2014).

[59] K. Kawabata, K. Shiozaki, M. Ueda, and M. Sato, Symmetry and topology in non-hermitian physics, Phys. Rev. X **9**, 041015 (2019).

[60] X. Luo, T. Ohtsuki, and R. Shindou, Universality classes of the anderson transitions driven by non-hermitian disorder, Phys. Rev. Lett. **126**, 090402 (2021).

[61] X. Luo, T. Ohtsuki, and R. Shindou, Transfer matrix study of the anderson transition in non-hermitian systems (2021), arXiv:2103.05239.

[62] E. Fradkin, Critical behavior of disordered degenerate semiconductors. ii. spectrum and transport properties in mean-field theory, Phys. Rev. B **33**, 3263 (1986).

[63] K. Kobayashi, T. Ohtsuki, K.-I. Imura, and I. F. Herbut, Density of states scaling at the semimetal to metal transition in three dimensional topological insulators, Phys. Rev. Lett. **112**, 016402 (2014).

[64] S. Liu, T. Ohtsuki, and R. Shindou, Effect of disorder in a three-dimensional layered chern insulator, Phys. Rev. Lett. **116**, 066401 (2016).

[65] Y. Harashima and K. Slevin, Critical exponent of metal-insulator transition in doped semiconductors: The relevance of the coulomb interaction, Phys. Rev. B **89**, 205108 (2014).

[66] E. G. Carnio, N. D. M. Hine, and R. A. Römer, Resolution of the exponent puzzle for the anderson transition in doped semiconductors, Phys. Rev. B **99**, 081201 (2019).

Large-scale molecular dynamics simulations of Kármán vortex and sound wave: cavitation and polymer effects

Yuta Asano [1], Hiroshi Watanabe [2], and Hiroshi Noguchi [1]
[1] *Institute for Solid State Physics,*
The University of Tokyo, Kashiwa-no-ha, Kashiwa, Chiba 277-8581, Japan
[2] *Department of Applied Physics and Physico-Informatics,*
Keio University, Yokohama, Kanagawa 223-8522, Japan

Abstract

In many industrial flows, microscale effects have a significant impact on their macroscale flows. Turbulent drag reduction by polymer addition and cavitation around rotating turbines in water are typical examples. In these flows, phenomena in a wide range of scales coexist, from molecular scale motion to macroscale fluid motion, and these interact with each other under strongly non-equilibrium. Therefore, it is challenging to clarify the underlying mechanism by its complexity.

We have performed large-scale molecular dynamics (MD) simulations of complex flows, such as polymer solutions and cavitating flow, as well as MD of sound propagation, using the ISSP supercomputer. In this activity report, we present a brief overview of these studies [1-4].

1. Introduction

Fluid flows play a vital role in a wide range of fields, from tap water familiar to our daily lives to fuel pipelines in energy supply systems. It is no exaggeration to say that flow sustains our lives. Therefore, a thorough understanding of the flow phenomena will improve our lives, also significantly contributes to global environmental protection. Flow control in industrial processes is an essential topic in fluid engineering, such as turbulence drag reduction by polymer addition [5] and gas-liquid multi-phase flow due to the cavitation [6]. Thus, many researchers have conducted experiments and numerical simulations based on the Navier—Stokes equation to clarify the mechanisms. However, since various phenomena in a wide range of scales coexist and interact with each other in non-equilibrium, the analyses are challenging issues. Therefore, it is crucial to analyze all phenomena simultaneously, from molecular-scale dynamics to fluid motion to understand the complex flows.

Mesoscale analysis methods such as the lattice Boltzmann method [7] and Multi-particle collision dynamics [8,9] have been developed to analyze the flow considering the effects of molecular-scale dynamics. Also, the micromacro coupling approaches [10,11] have been proposed to investigate more detailed molecular-scale information. However, in light of today's computational power, it is possible to simulate flows by all-particle simulations, namely a molecular dynamics (MD) simulation. In the MD simulation, molecular-scale dynamics, such as phase transition and polymer motion, naturally appear in the flow by simply solving the Newtonian equations of motion, only providing the interparticle interactions. In conventional fluid analysis methods, phenomenological models, such as constitutive equations and an equation of state, are required to describe these phenomena. Instead, we have to prepare a sufficiently large computational cell that can resolve the macroscale flow characteristics. Therefore, although it is inevitably a large-scale simulation, it will help us understand complex flow phenomena.

In this report, we present a brief overview of flow analysis by using large-scale MD simulations. We explain the effect of polymer addition and cavitation on the flow around a cylinder in sections 2 and 3, respectively. In section 4, we describe the application to soundwave propagation in a simple fluid. In section 5, we explain the recent study of cavitating flow in a polymer solution. Section 6 is a summary.

2. Effects of polymer addition on Kármán Vortex [1]

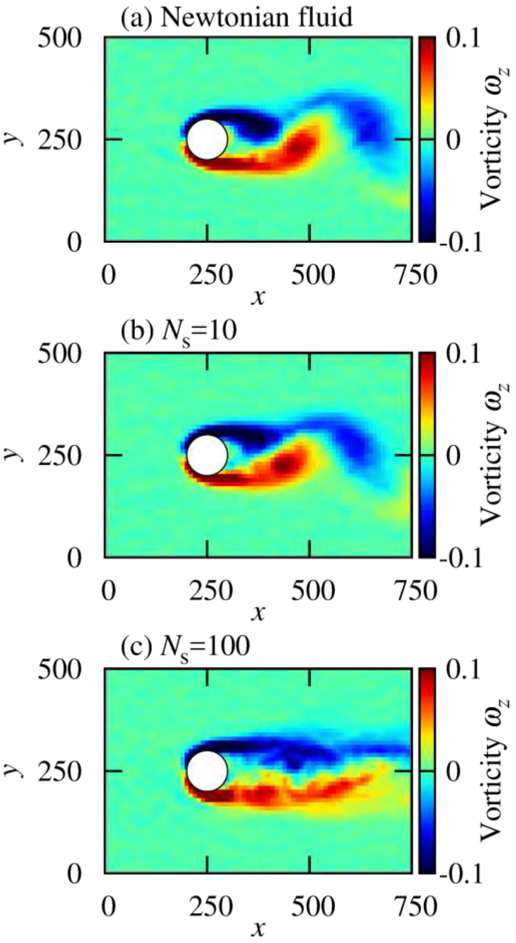

Fig. 1: Instantaneous vorticity fields for (a) the Newtonian fluid, (b) polymer solution with the number of segments $N_s = 10$, and (c) polymer solution with $N_s = 100$ at the Reynolds number $Re = 64$ [1].

Adding a tiny amount of polymer into a Newtonian fluid involves significant changes in the flow characteristics, such as a dramatic reduction in frictional drag [5] and suppression of the Kármán vortex [12]. Since most industrial flows are turbulent, the flow control by adding polymers is an attractive method in engineering applications because it saves energy

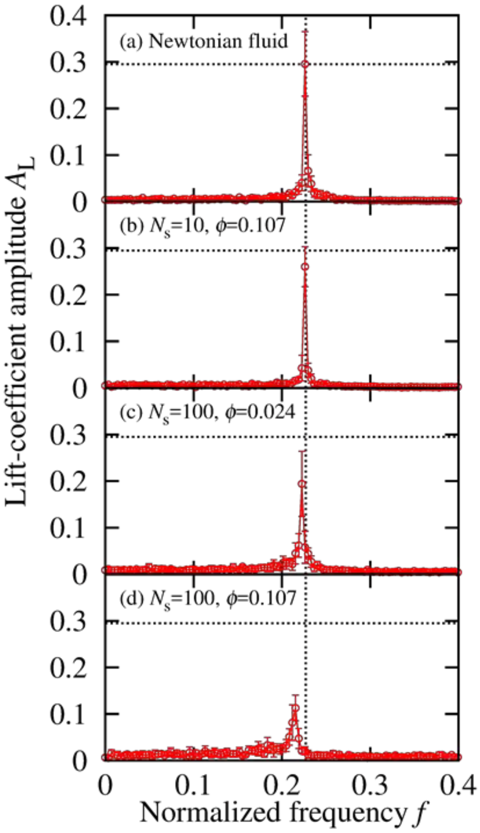

Fig. 2: Fourier spectra of the lift coefficient at $Re = 64$ [1]. (a) Newtonian fluid. (b) Polymer solution with $N_s = 10$ and volume fraction $\phi = 10$. (c) Polymer solution with $N_s = 100$ and $\phi = 0.02$.(d) Polymer solution with $N_s = 100$ and $\phi = 0.107$. The vertical and horizontal dotted lines denote the peak position and height for the Newtonian fluid, respectively.

consumption. However, the mechanism is not well understood because the polymer rheology in a flow is unclear.

The interaction between polymers and vortices presumably plays a significant role in the changes in flow characteristics. Therefore, it is necessary to elucidate the effects of polymers on vortices from the molecular scale. We focus on the flow around a cylinder, which is the most typical flow accompanied by vortices and is suitable for analysis due to its periodicity. We investigate the effects of polymers on vortices in the two-dimensional flow around a circular cylinder by MD simulations.

Figure 1 shows typical snapshots of the vorticity field. As for the Newtonian fluid, an alternating vortex street, the Kármán vortex street, appears behind the cylinder. Similar vortices appear for the short-chain polymers. However, for long-chain polymers, the vortices are blurred. Therefore, the chain length of the polymer significantly affects vortex formation.

Figure 2 shows the Fourier spectra of the lift coefficient. For the Newtonian fluid, a sharp peak appears, which indicates periodic vortex shedding. Note that the peak frequency is slightly increased by the finite size effects we reported in Ref. 13. The short-polymer solution shows a similar sharp peak. On the other hand, the peak position shifts to a lower frequency, and the spectrum broadens for the long-polymer solution. These effects enhance with increasing polymer concentration. The effects of polymer addition on the flow, (1) vortex blurring, (2) frequency reduction, and (3) chain length effect, obtained by MD simulations, are in good agreement with experimental results [12].

Figures 3(a) and 3(b) show the gyration radius of short- and long-chain polymers,

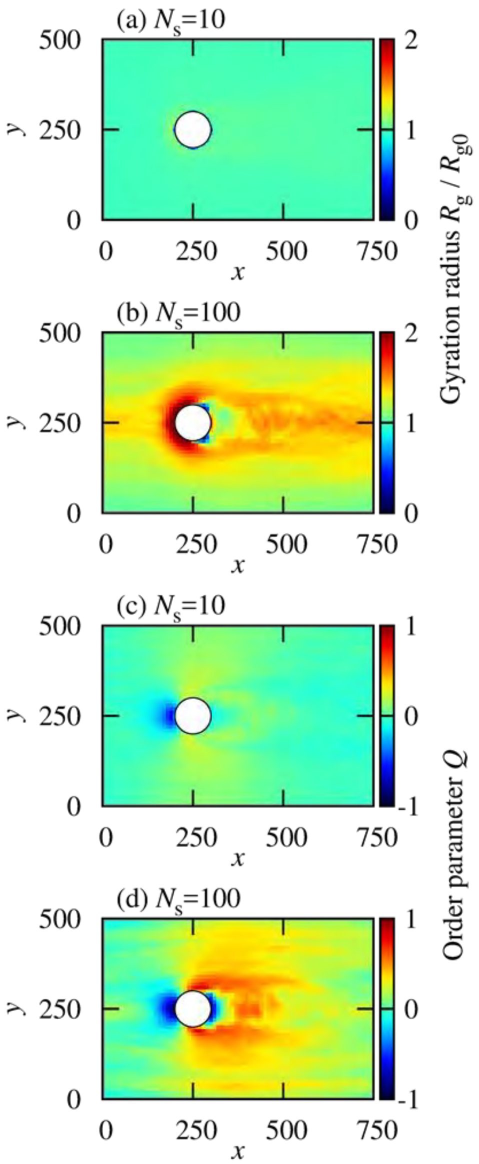

Fig. 3 Spatial distributions of the gyration radius R_g and orientational order Q for the polymer solutions with (a, c) $N_s = 10$ and (b, d) $N_s = 100$ at $Re = 64$ and $\phi = 0.107$[1]. R_{g0} is the gyration radius in the absence of the flow.

respectively. For short-chain polymer, the gyration radius is virtually identical to that in the stationary fluid. Therefore, the polymer flows with an almost spherical shape as a particle. On the other hand, long-chain polymers are significantly stretched near the cylinder and in the vortex behind the cylinder. Furthermore, the vortex also entrains the polymer in its vicinity.

Figures 3(c) and 3(d) show the orientational order Q of the short- and long-chain polymers, respectively. When the polymer aligns in the flow direction, $Q = 1$ the polymer aligns perpendicular to the flow, $Q = -1$ the polymer directs randomly, $Q = 0$. For the short-chain polymer, polymers orient randomly in the entire area. However, for long-chain polymers, the polymers are aligned in the flow direction near the cylinder. Furthermore, the polymers also tend to align in the flow direction in the vortices behind the cylinder. The reduction of the orientational order behind the cylinder is due to the entrainment by the vortex. Therefore, the stretching and entrainment of the polymer play a significant role in vortex suppression. As a consequence, the shapes of the vortices become blurred.

3. Effects of cavitation on the Kármán vortex behind circular-cylinder arrays [2]

Cavitation is a phenomenon of forming bubbles due to local pressure drop in a flowing liquid with high velocity [14]. When cavitation occurs in fluid machinery, such as pumps and turbines, it causes various adverse effects such as performance degradation, noise and vibration, and erosion. Therefore, it is vital in fluid

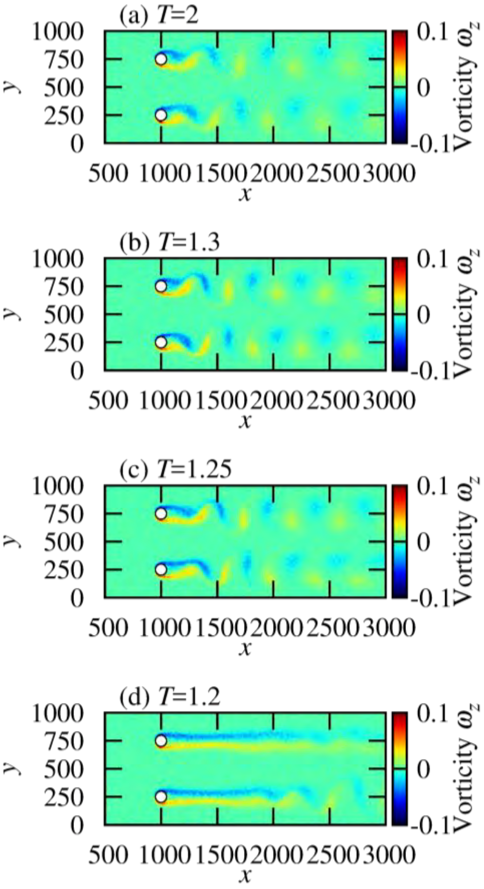

Fig 4: Instantaneous vorticity fields for the (a) non-cavitating flow ($T = 2$) and (b-d) cavitating flows ($T = 1.5$, 1.25, and 1.2) [2].

engineering to clarify the cavitation mechanism for appropriate control of the cavitating flow. However, because of the limitations of discussing the dynamics of microscopic bubble nuclei in a macroscopic flow, the cavitation mechanism is still not understood well. To clarify the effects of cavitation on the flow, we performed a large-scale MD simulation of the flow for the Lennard-Jones (LJ) around cylinders in a side-by-side arrangement.

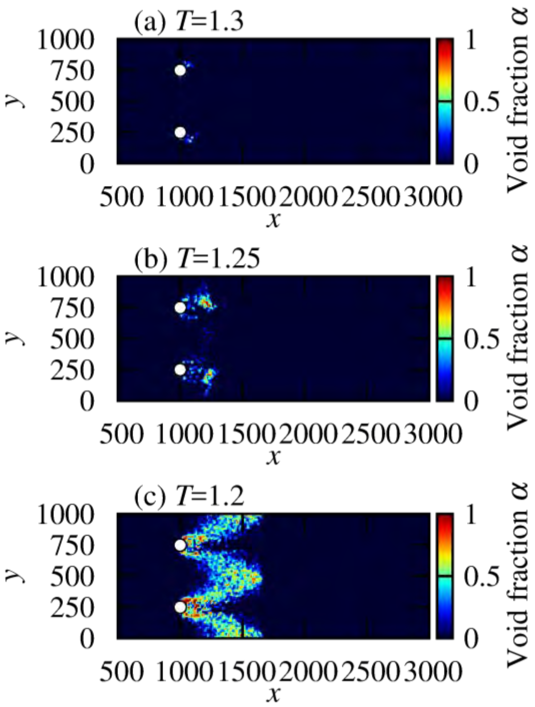

Fig. 5: Instantaneous void fraction fields for (a) $T = 1.3$, (b) $T = 1.25$, and (c) $T = 1.2$ [2].

Figures 4 and 5 show the typical snapshots of the vorticity and void fraction field, respectively. At high temperature ($T = 2$), no bubbles appear (i.e., non-cavitating flow). The Kármán vortex appears behind the cylinders, and the upper and lower vortex streets synchronize in anti-phase. As temperature decreases, bubbles appear in the vicinity of the cylinder at $T = 1.3$ in conjunction with vortex shedding (Fig. 5 (a)). The vortex streets behind the cylinder synchronize in anti-phase, as in the case of $T = 2$ (Figs. 4(a) and 4(b)).

At $T = 1.25$, the gas phase region is formed behind the cylinder and is attached to the cylinder (Fig. 5(b)). Also, the phase difference between the upper and lower vortex streets

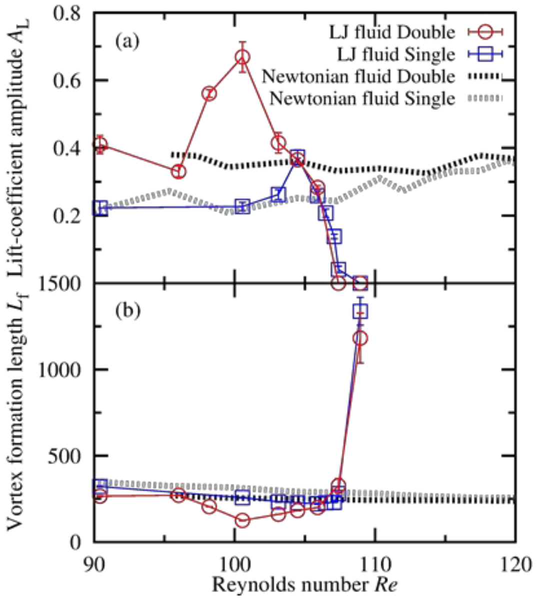

Fig. 6: Re dependence of (a) the lift coefficient amplitude and (b) vortex formation for the LJ fluid and Newtonian fluid [2]. Double and Single in the legend denote two- and one-cylinder systems, respectively.

slightly shifts (Fig. 4(c)). At $T = 1.2$, the gas phase region behind the cylinder expands further (Fig. 5. (c). In addition, the upper and lower vortex structures become asymmetric (Fig. 4(d)). This asymmetric vortex structure switches over a long period. For the fluid without phase transition, such a change in the flow field does not occur with temperature change. We found that the density fluctuation caused by the bubble generation has a significant effect on the vortex structure.

As the vortex structure changes, the lift force acting on the cylinder is also affected. Figure 6(a) shows the Redependence of the amplitude of the lift coefficient A_{L} and the vortex formation length L_{f}. For comparison, the figure also shows the results for the Newtonian fluid. For the reference liquid, A_{L} and L_{f} tend to increase and decrease with increase Re, respectively. However, in the case of LJ fluids, they exhibit non-monotonic behavior to Re. This behavior is probably due to the conflicting effects of increasing Re and bubble generation. A_{L} rapidly decreases and finally disappears due to the bubble generation. Simultaneously with the disappearance of A_{L}, L_{f} rapidly increases.

For the Newtonian fluid, A_{L} and L_{f} show almost the same trend for the two-cylinder system and the one-cylinder system, which has only one cylinder with the same distance between the neighboring (periodic image) cylinders (the vortex streets are always synchronized in-phase). In the case of LJ fluid, however, the behavior before bubble generation is different. The upward and downward peaks appear in A_{L} and L_{f}, respectively. Their positions for one- and two-cylinder systems are $Re = 105$ and 101, respectively. These peaks are probably due to a small nucleus generation which is the precursor of the cavitation or density fluctuations originating from the critical phenomena. Since the phase retraction amplifies the oscillation amplitude, the peak appears at a higher temperature in the two-cylinder system than in the one-cylinder system. After bubble generation, the bubbles weaken the interference between the vortex street, and the effect of the

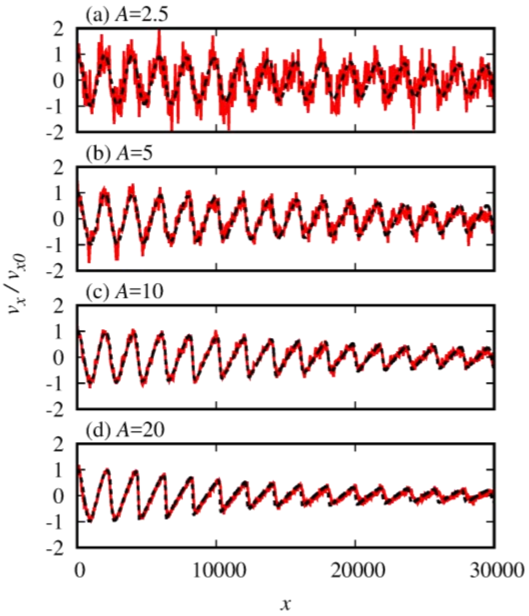

Fig 7: Waveforms of the LJ fluid for the (a) amplitude $A = 2.5$ (b) $A = 5$ (c) $A = 10$, and (d) $A = 20$ at frequency $f = 0.001$ [3]. The red and black lines represent the results of MD simulation and the Burgers' equation, respectively.

phase difference is almost negligible. We found that the bubble generation significantly affects the vortex structures, vortex interference, and lift due to vortex shedding.

4. Soundwave propagation in simple fluid [3]

Sound waves are a familiar phenomenon in our daily lives, such as the voices and sound of musical instruments. Because of the sound properties of propagating a wide range of solid, liquid, and gaseous materials, their application exists in a wide range of engineering fields. In particular, applications of ultrasonic cavitation

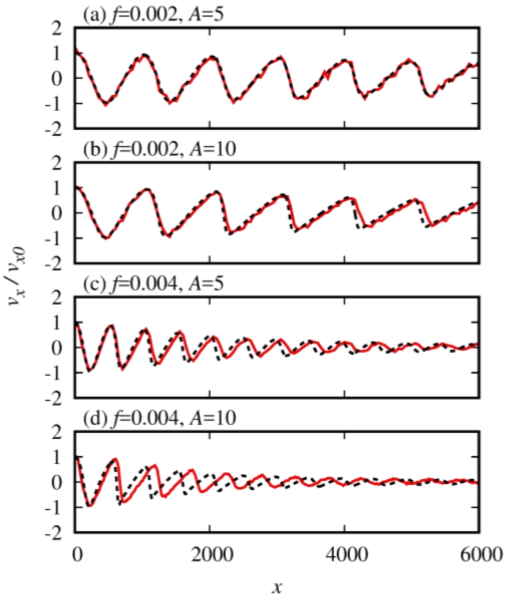

Fig. 8: Waveforms of the LJ fluid for the (a) $f = 0.002$ and $A = 5$, (b) $f = 0.002$ and $A = 10$ (c) $f = 0.004$ and $A = 5$, and (d) $f = 0.004$ and $A = 10$ [3]. The red and black lines represent the results of MD simulation and the Burgers' equation, respectively.

extend in a wide range of applications, such as medical treatment and food processing. For these applications, it is crucial to understand the characteristics of ultrasonic cavitation and the propagation in complex fluids. Therefore, it is necessary to analyze the sound wave propagation from the molecular scale.

We apply the MD simulation to the sound propagation in the LJ fluid. Moreover, we perform the fluid dynamics calculation utilizing Burgers' equation to justify the validity of the MD simulation for the sound waves. When the same fluid is analyzed, the two results should

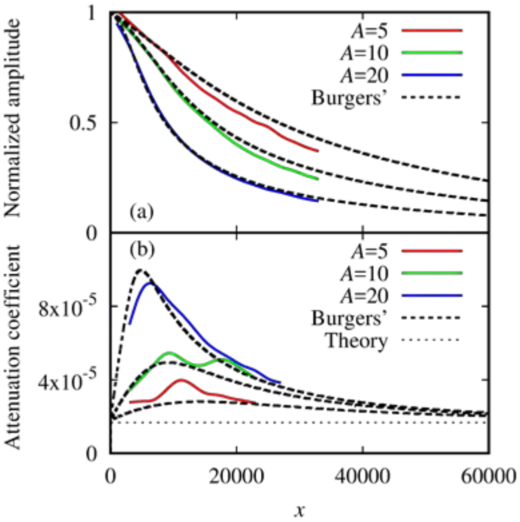

Fig. 9: x dependences of the (a) normalized amplitude and (b) attenuation coefficient of the LJ fluid [3]. The solid and broken lines represent the results of MD simulation and Burgers' equation, respectively. The dotted line in panel (b) shows the classical attenuation coefficient.

agree within the statistical error.

Figure 7 shows the amplitude dependence of the waveform of the LJ fluid at frequency $f = 0.001$. For small amplitudes, the waveform is sinusoidal owing to the weak nonlinearity. As the amplitude increases, the waveform becomes a sawtooth waveform (Figs. 7(c) and 7(d)). The black dotted lines in Fig. 7 are the numerical solutions of Burgers' equation, which is in good agreement with the results of the MD simulation.

Figure 8 shows the frequency dependence of the waveform at higher frequencies. As the frequency increases, the waveforms of the MD simulation and Burgers' equation become deviate the magnitude of the deviations becomes greater for higher amplitudes. This deviation is due to the acoustic flow that occurs by the high nonlinearity owing to high frequency. Since Burgers' equation is not applicable in the region where acoustic flow occurs, a fluid analysis involving higher-order terms is necessary for a quantitative discussion. The MD simulation provides a waveform reflecting the nonlinearity, thus obtaining a frequency-dependent sound speed.

The attenuation coefficient of a sound wave is estimated from the decrement in amplitude. Figure 9(a) shows the amplitude decrement at $f = 0.001$. When the amplitude is small, the deviation of the MD simulation from the Burgers’ equation is slightly different due to the thermal fluctuations. As the amplitude increases, the agreement between them becomes better. We estimate the attenuation coefficient by the logarithmic decrement rate of the amplitude at each position x. Figure 9(b) shows the attenuation coefficient as a function of x. The dotted line shows the value of the attenuation coefficient evaluated from the classical theory. The results of the Burgers’ equation approach asymptotically to the classical attenuation coefficient at a sufficient distance from the sound source position ($x = 0$). Although the results of the MD simulation are in good agreement with the results of Burgers' equation when the amplitude is large, the attenuation is overestimated by the nonlinearity. On the other

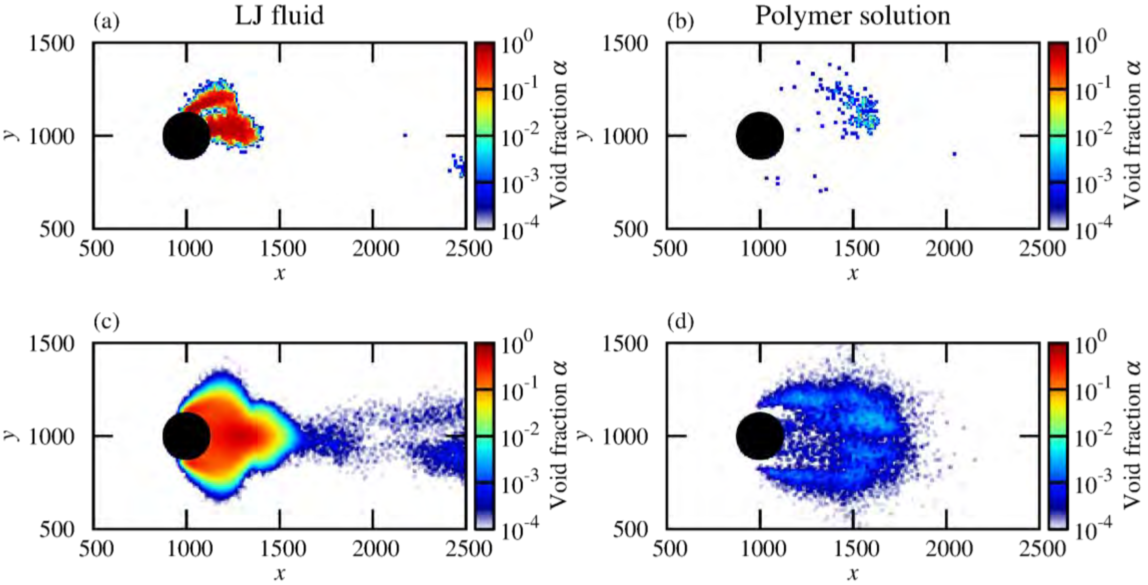

Fig. 10: Instantaneous void fraction fields of the (a) LJ fluid and (b) polymer solution, and time-averaged void fraction of the (c) LJ fluid and (d) polymer solution at $T = 1.25$ [4].

hand, the attenuation coefficient is hardly estimated for small amplitudes due to thermal fluctuation. Therefore, to obtain the classical attenuation coefficient by the MD simulation, the practical method is to estimate the parameters of the Burgers' equation from the waveform of MD simulation.

5. Effects of the polymer addition on the cavitating flow [4]

Finally, we briefly describe our recent analysis on the cavitating flow. In extreme cases, the adverse effects on fluid machinery caused by cavitation are prevented by controlling the flow to suppress cavitation. However, in general, most industrial flows are highly irregular turbulent fields, and it is difficult to achieve such flows by mechanical design. Since polymer addition is one of the methods to realize such flows, it has attracted attention. Although it is challenging to simultaneously analyze polymer motion, bubble nucleus dynamics, and macroscopic flow, the analysis should be possible by integrating the methods described in Sections 2 and 3. Here we briefly describe only the main results.

We investigate the effect of the polymer addition on the cavitating flow around a circular cylinder. Figure 10 shows the distribution of void fraction in the cavitating flow of the LJ fluid at $T = 1.25$, at which the cavitation occurs as described in Sec. 3. The polymer addition dramatically suppresses the formation of bubbles. Note that the polymer addition has negligible effects on the phase transition in the absence of the flow. From the temperature change in the fluid element and the conformation change in the polymer, we found that the vortex suppression and the entropic elasticity by the polymer have essential roles in the suppression of cavitation.

6. Summary

We performed large-scale MD simulations for complex fluids involving polymers, gas-liquid multi-phase flows owing to cavitation, and sound waves. The direct analysis from the molecular scale enables us to analyze the flow field reflecting the micro-scale effects, such as the elongation properties of polymers, phase transitions that are difficult to model by conventional computational fluid dynamics. In particular, we were able to analyze cavitation in complex fluids, which was one of the main objectives at the beginning of our research. This achievement would not have been possible without using the ISSP supercomputer system B (Ohtaka).

Compared to conventional fluid analysis methods, MD simulation does not require phenomenological models such as equations of state. The advantage of MD simulations is that all physical quantities and phenomena are obtained from molecular motion. Therefore, the MD simulation is a suitable tool to analyze complex flow phenomena, such as the multi-phase and multi-component flow around a propeller.

Acknowledgment

We thank Toshihiro Kawakatsu, Youhei Morii, Shinichi Tsuda, Yuichi Kunishima, and Yuji Higuchi for helpful discussions. This research was supported by MEXT as "Exploratory Challenge on Post-K computer" (Challenge of Basic Science Exploring Extremes through Multi-Physics and Multi-Scale Simulations) and JSPS KAKENHI (Grant No. JP19H05718). We acknowledge the Supercomputer Center, Institute for Solid State Physics (ISSP), University of Tokyo, Research Center for Computational Science (RCCS), Okazaki, Japan, and Center for Computational Materials Science, Institute for Materials Research (IMR), Tohoku University for the use of their supercomputers (Project No.20S0026 for MASAMUNE-IMR in IMR).

References

[1] Y. Asano, H. Watanabe, and H. Noguchi, J. Chem. Phys. **148** (2018) 144901.

[2] Y. Asano, H. Watanabe, and H. Noguchi, J. Chem. Phys. **152** (2020) 034501.

[3] Y. Asano, H. Watanabe, and H. Noguchi, J. Chem. Phys. **153** (2020) 124504.

[4] Y. Asano, H. Watanabe, and H. Noguchi, J. Chem. Phys. **155** (2021) 014905.

[5] G. E. Gadd, Nature **206** (1965) 463.

[6] R. E. Arndt, Ann. Rev. Fluid Mech. **34** (2002) 143.

[7] S. Succi, *The Lattice Boltzmann Equation: For Fluid Dynamics and Beyond*, Oxford University Press Inc., New York (2001).

[8] R. Kapral, Adv. Chem. Phys. **140** (2008) 89.

[9] G. Gompper, T. Ihle, D. M. Kroll, and R. G. Winkler, Adv. Polym. Sci. **221** (2009) 1.

[10] T. Murashima, ISSP Supercomputer Activity Report 2015 (2015) 35.

[11] X. Xu and P. Yu, J. Non-Newtonian Fluid Mech. **229** (2016) 27.

[12] J. R. Cressman, Q. Bailey, and W. I. Goldburg, Phys. Fluids **13** (2001) 867.

[13] Y. Asano, H. Watanabe, and H. Noguchi, J. Phys. Soc. Jpn. **88**, 075003 (2019).

[14] C. E. Brennen, *Cavitation and Bubble Dynamics*, Oxford University Press, (1995).

3.2 First-Principles Calculation of Material Properties

Simulation of electrochemical interfaces

Osamu Sugino
Institute for Solid State Physics,
The University of Tokyo, Kashiwa-no-ha, Kashiwa, Chiba 277-8581

The electrochemical interface provides a unique environment for efficient redox reactions. The platinum-electrolyte interface has long been focused on the fuel-cell study because of the efficient oxygen reduction reaction (ORR), but defective TiO_2 has attracted attention for its enhanced reactivity and durability. It was explained in our previous first-principles study that the various adsorption forms taken by the ORR intermediates, such as OH and O_2H, is the reason for the reactivity [1]. This contrasts to the metal electrocatalysts where the variety in the adsorption is quite small and thus the ORR activity is limited thereby [2]. Further investigation of the oxide electrocatalyst is the target of this project.

Together with experimentalists, we modeled a ZrO_2 surface introduced with oxygen vacancies and foreign dopants to study the ORR reactivity. To make the model realistically mimic the experiment, we have performed the first-principles Monte Carlo simulation using abICS [2] and obtained equilibrium structures for the interface at the annealing condition. The calculated results are used then to investigate the activity. So far various structures with different stability and activity are obtained and this variety can be recognized as the characteristics of this material. Comparison with experiment is now underway.

Through the abICS calculation, we have constructed a machine learning model of the interface, and we plan to predict the activity after obtaining sufficient number of samplings.

References

[1] Y. Yamamoto et al., J. Phys. Chem. C 2019, 123, 32, 19486–19492.

[2] A. Kulkarni et al., Chem. Rev. 2018, 118, 2302– 2312.

[2] abICS is a software of first-principles Monte Carlo simulation developed by Dr. S. Kasamatsu. https://github.com/issp-center-dev/abICS

Mechanisms of Semiconductor Interface Formation and its Electronic Properties based on Quantum Theory

Atsushi Oshiyama
Institute of Materials and Systems for Sustainability, Nagoya University
Furo-cho, Chikusa-ku, Nagoya 464-8601

In the fiscal year of 2020, on the basis of the total-energy electronic-structure calculations and molecular dynamics simulations within the density-functional theory, we have studied the epitaxial growth of power semiconductors, atomic and electronic structures of semiconductor-insulator interfaces, and the complex of line defects and impurities. The main computational tools are our RSDFT (Real Space Density Functional Theory) code and RS-CPMD (Car-Parrinello Molecular Dynamics) code. We have clarified 1) the atom-scale mechanism of GaN epitaxial growth [1], 2) the mechanism of the adatom diffusion on SiC stepped surface[2], 3) the formation of dangling-bond free interface of GaN and a gate insulator[3,4], and 4) atomic and electronic structures of the dislocation-impurity complex in GaN [5].

The group identification codes for the achievements above are k0042 and m0001. The below is the explanation of the issue 1) above.

Step-flow epitaxial growth of GaN

Growth of high-quality epitaxial thin films of GaN is indispensable for the energy-saving power electronics and the clarification of the mechanism of the epitaxial growth is essential to advance nanoscience and technology. We have performed first-principles calculations that elucidate atomic structures and formation energies of the surface steps of GaN (0001) surfaces, unveil atom-scale elementary processes of N incorporation at the step edges, and then provide a microscopic picture of the step-ow epitaxial growth of GaN.

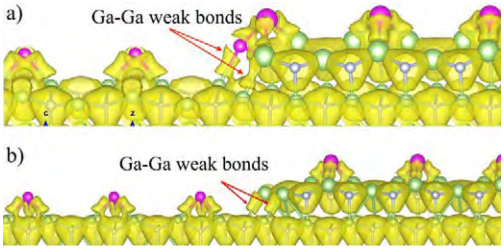

Fig.1: Calculated electron densities near the GN step (a) and the Ga2 step (b). The densities are represented by the yellow isovalue surfaces. The small yellow clouds reflect the presence of the low electron density, indicating that the Ga-Ga weak bonds are formed at the step edges. The Ga, Ga-ad (Ga adatom), and N atoms are represented by the green, pink, and blue balls, respectively.

Epitaxial growth usually takes place on Ga-rich vicinal surfaces in which the (0001) surface is slightly inclined toward [1100] or [11-20] direction. There are five distinct mono-bilayer steps on such vicinal surfaces depending on the atomic species, Ga or N, at the step edges and the inclined directions. We have performed the geometry optimization for all the possible step edges and calculated the step formation energies.

Typical structures of the step edges are shown in Fig. 1 along with the electron density. The characteristics is the presence of Ga-Ga bonds at the step edges. As is clear from the small electron clouds in Fig. 1, the Ga-Ga bonds are relatively weak and thus become hot spots for the epitaxial growth.

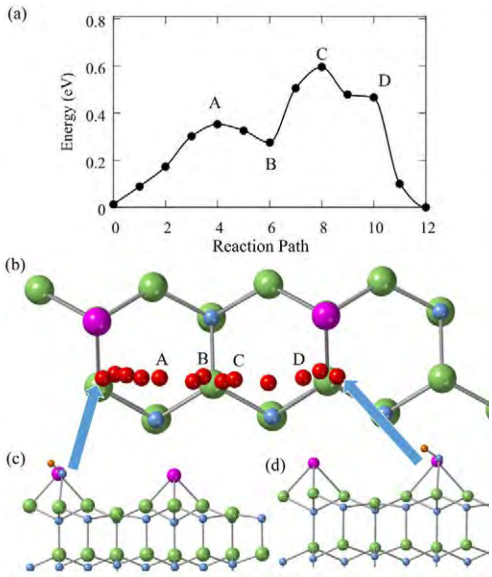

Fig. 2: Diffusion pathway and the corresponding energy barrier of an NH unit on the terrace of GaN(0001) surface. (a) The total-energy landscape along the diffusion pathway. The left and the right ends correspond to the initial and the final geometries, respectively. (b) Diffusion pathway in a top view represented by the small red balls which denote the lateral positions of the N atom in the NH during the diffusion. (c) An initial geometry of the NH unit which intervenes in the weak bond between the Ga adatom and the top Ga atom. (d) A final geometry of the NH unit which intervenes in the adjacent Ga-Ga weak bond. Burgandy, green, and blue balls depict Ga adatom, Ga and N atoms, respectively.

We have previously shown that the NH_3 provided in Metal-Organic Vapor Phase Epitaxy (MOVPE) arrives at the terrace of the growing Ga-rich surface and is decomposed into the NH unit [Fig. 2(c)] [6]. Now we have found this NH unit diffuses on the surface terrace with the activation energy of 0.6 eV (Fig. 2).

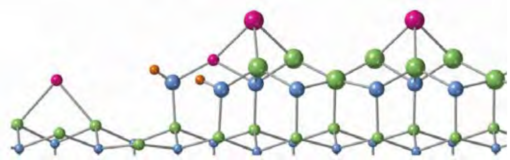

Fig. 3: The GN step-edge structure with two NH units intervening in the Ga-Ga bonds. Burgandy, green, blue and orange balls depict Ga adatom, Ga, N and H atoms, respectively.

This indicates that the NH units wander on the terrace and occasionally reach the surface step edges. We have indeed examined the energetics of the reaction in which two isolated NH units on the terrace diffuse toward a step edge and intervene into the adjacent Ga-Ga bonds as in Fig. 3. We have found this reaction is exothermic with the energy gain of 0.45 eV.

Then the next step is the incorporation of Ga atom at the step edge. Since the growing surface is Ga rich, it is highly likely that an additional Ga atom approaches the step edge where the two NH units are incorporated [Fig. 4(a)]. We have then examined a reaction in which the two H atoms are desorbed as an H2 molecule and the arriving Ga is incorporated at the step edge [Fig. 4(b)]. We have identified a pathway of this reaction, and calculated the energy profile [Fig. 4(d)]. We have

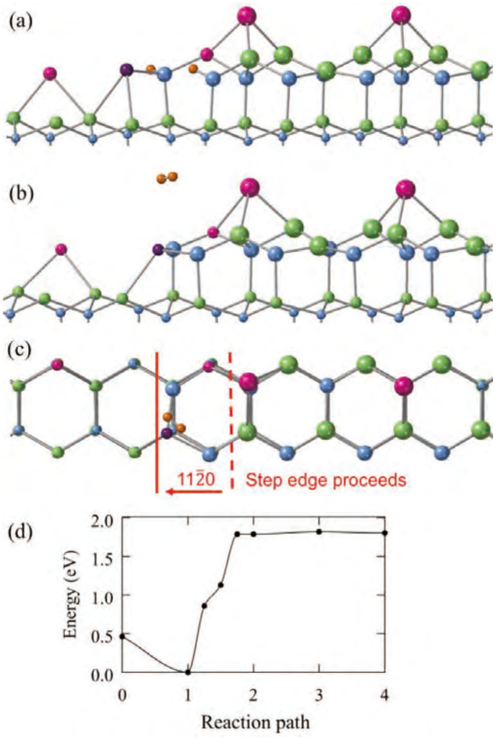

Fig.4: An elementary process in the step-flow growth of GaN. (a) Stable structure of the GN step edge attached with 2 NH units and an additional Ga atom nearby. (b) Stable structure of the GN step with H2 desorbed from the structure (a). (c) The top view of the stable structure shown in (b). Color code of the balls depicting atoms are the same as in Fig. 3. The additional Ga adatom is shown by purple. (d) Calculated energy profile for the reaction from (a) to (b).

found that the energy cost of this reaction is 1.8 eV. However, by examining the obtained energy profile in Fig. 4(d), this is the cost to make 2H atoms on the surface an H2 molecule in the gas phase. In the gas phase, the H2 molecule gains the free energy owing to its translational, vibrational and rotational motions. We have evaluated such free-energy gain at growth temperature and under the typical H2 partial pressure. It is evaluated to be 2.1 eV. This certainly compensates the obtained zero-temperature energy cost of 1.8 eV, indicating that this reaction is favorable.

The top view of the final structure is shown in Fig. 4(c). The step edge before this reaction proceeds one unit by incorporating two N atoms from the NH units and a new Ga atom. This is the elementary process of the step-flow epitaxial growth.

Related Publications

[1] K. M. Bui, K. Shiraishi and A. Oshiyama, Appl. Surf. Sci. **557**, 149542 (2021).

[2] K. Seino and A. Oshiyama, Appl. Surf. Sci. (2021) to be published.

[3] K. Chokawa, T. Narita, D. Kikuta, T. Kachi, K. Shiozaki, A. Oshiyama and K. Shiraishi, Phys. Rev. Applied **14**, 014034 (2020).

[4] K. Chokawa, K. Shiraishi and A. Oshiyama, Appl. Phys. Lett. (2021) to be published.

[5] T. Nakano, Y. Harashima, K. Chokawa, K. Shiraishi, A. Oshiyama, Y. Kangawa, S. Usami, N. Mayama, K. Toda, A. Tanaka, Y. Honda, and H. Amano, Appl. Phys. Lett. **117**, 012105 (2020).

[6] K. M. Bui, J.-I. Iwata, Y. Kangawa, K. Shiraishi, Y. Shigeta, and A. Oshiyama, J. Phys. Chem. C **122**, 24665 (2018).

Analyses on electronic structure and magnetoelectric effect in high-performance spintronics and magnetic materials

Tatsuki ODA[1,2], Indra PARDEDE[1], Daiki YOSHIKAWA[2], Tomosato KANAGAWA[2], Nurul IKHSAN[2], Hasan Al RASYID[2], Marleni WIRMAS[2], Masao OBATA[1,2]

[1]*Institute of Science and Engineering, Kanazawa University, Kanazawa, Ishikawa 920-1192*

[2]*Graduate School of Natural Science and Technology, Kanazawa University, Kanazawa, Ishikawa, 920-1192*

We studied the magnetic anisotropy and its electric field (EF) effect in the thin film related with spintronic devices [1]. We obtained an qualitative agreement between theory and experiment on magnetic anisotropy of the magnetic thin film including the Fe/MgO interface with Cr underlayer, by taking into account an alloying effect of Fe-Cr. Without alloying in the theoretical calculation, the total magnetic anisotropy indicates an in-plane magnetization. Such theoretical consequence had been solved in the comparison with the experimental result [2] that showed a perpendicular anisotropy. The introduction of alloying effect may be consistent with the fabrication condition in the experiment. As a result, our first-principles approach reveals a potential to describe magnetic anisotropies of magnetic thin film.

In the computational approach, we employed the plane-wave basis electronic structure calculation with using a scheme of non-collinear spin density and fully relativistic ultra-soft pseudopotential (including spin-orbit coupling). This scheme can provide the magnetocrystalline anisotropy energy (MCAE) from the difference between the total energy calculations for the different magnetization directions. In addition, the non-collinear spin density can estimate the shape magnetic anisotropy energy (SMAE) by using the scheme developed before in our research group [3]. In the present applications, the contributions of MCAE and SAME have different sign in the numerical values. Therefore, an accurate numerical computation is required for obtaining a realistic result.

We used the thin films in the followings; vacuum/Cr(6ML)/Fe(4ML)/MgO(5ML)/vacuum(S-I) and vacuum /Cr(6ML)/Fe(1ML)/Cr (1ML)/Fe(3ML)/MgO(5ML)/vacuum(S-II). The magnetic anisotropy energy (MAE) was calculated from the total energy difference between in-plane magnetization ([100]) and out-of-plane magnetization ([001]), MAE = $E[100]-E[001]$. To apply an EF, we used the effective screening medium (ESM) method.

Sys.	VCMA (fJ/Vm)	MCAE (mJ/m^2)	SMAE (mJ/m^2)	MAE (mJ/m^2)
S-I [1]	85	0.586	−1.336	−0.750
S-II [1]	89	1.280	−1.053	0.227
Exp. [2]	~300	–	–	~ 0.500

Table I. Results of VCMA, MCAE, SMAE, MAE(=MACE+SDA) and comparisons with experimental results.

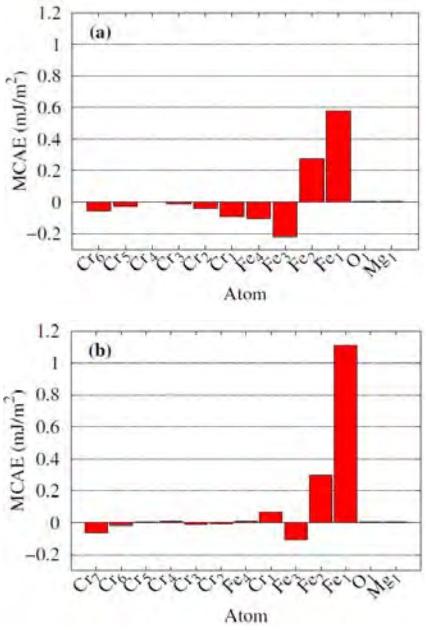

Figure 1. Atom resolved MCAE in (a)S-I and (b) S-II.

To obtain the EF inside the MgO layer, we took into account the dielectric constant (9.8 for MgO).

As shown in Table 1, the alloying system (S-II) shows a perpendicular anisotropy (positive value for MAE). The most important key for the perpendicular is that the MCAE increases by the alloying of Fe-Cr. As depicted in Fig. 1, the increase appears at the interface with MgO layer. This means that the magnetic anisotropy energy at the Fe/MgO interface is sensitive to the termination of Fe layer in the thin film.

Quasi-particle self-consistent GW (QSGW) ele-ctronic structure calculation [4] was performed in the spinel structures of ternary magnetic compound $NiCo_2O_4$, using the software *ecalj*. The QSGW method is state-of-the-art on electronic structure investigation without using any empirical parameter. The results were also compared with those from the density functional theory (DFT) based on generalized gradient approximation (GGA). Half-metallicity was observed, where the band energy gap appears in the majority spin state. Such property at the Fermi level is the reason why the material has been considered as a candidate of spintronics application. The QSGW indicated that the gap is larger than that of the corresponding GGA case. The QSGW may yield more localized 3d-orbitals, compared with those from the GGA. Based on the projected density of states (PDOS) analysis, Co atoms of the octahedral site [Co(oct)] were found to be a nonmagnetic/weak magnetic configuration (low spin state) among them, resulting in a negligible contribution to the total magnetization. The largest contribution to the total magnetization is provided by Co atoms of tetrahedral [Co(tet)] site (high spin state). The QSGW indicated the difference of octahedral crystal fields on the different cation sites of Co(oct) and Ni(oct). The electronic states near the Fermi level consist mainly of Co(tet) 3d e_g-orbitals. The comparison with the results of one-shot GW reveals that the self-consistent treatment introduces visible changes in the electronic structures.

References

[1] I. Pardede *et al.*, Crystals **10** (2020) 1118.

[2] T. Nozaki *et al.*, Phys. Rev. Appl. 5 (2016) 044006.

[3] T. Oda and M. Obata, JPSJ **87** (2018) 064803.

[4] T. Kotani *et al.*, PRL 96 (2006) 226402.

Development of first-principles electronic-structure and transport calculation code RSPACE and simulations for device

Tomoya ONO
Graduate School of Engineering, Kobe University
Rokkodai-cho, Nada, Kobe 657-8501

4H-SiC is one of the major enabling materials for advanced high power and high temperature electronics applications. However, the performance of the metal-oxide-semiconductor field-effect-transistor (MOSFET) using SiC is severely limited due to their field-effect mobility being much lower than the ideal electron mobility. SiC based MOSFETs are usually fabricated on the front side of 4H-SiC(0001) wafer (Si face) by the thermal oxidation in dry O_2 ambience. On the other hand, it is reported that MOSFETs fabricated on the C face, which is the back side of the same wafer, by wet oxidation in H_2O ambience contain low density of interface defects and exhibit higher carrier mobility than that on the Si face. Electrically detected magnetic resonance (EDMR) spectroscopy revealed that characteristic defects, which are called "C-face defects", are observed in the wet-oxidized C face[1]. However, the details of the generation of C-face defects are unclear.

In this project, we have conducted first-principles study on the formation energy of C-face defects at SiO_2/SiC(0001) interface. RSPACE code[2, 3, 4], which is also developed in this project is used for the first-principles calculations. The lateral lengths of the supercell are chosen to be $2\sqrt{3}a$ and $4a$ along the $[1\bar{1}00]$ and $[11\bar{2}0]$ directions of the 4H-SiC(0001) surface, where a is the lattice constant of SiC, and integration over the Brillouin zone is carried out using a 2 × 2 $\vec{k}$-point mesh. The surface C atoms are connected to OH groups to imitate oxide and the Si atoms are terminated by H atoms. For comparison, the formation energy of the defects in 4H-SiC bulk is also calculated. The dimension of the supercell is $2\sqrt{3}a$, $4a$, and c along the $[1\bar{1}00]$, $[11\bar{2}0]$ and [0001] directions, respectively, with c being the lattice constant of 4H-SiC bulk.

The C face defects are $\mathrm{C_{Si}V_C}$ c-axial, $\mathrm{C_{Si}V_C}$ basal, $\mathrm{V_{Si}V_C}$ c-axial, and $\mathrm{V_{Si}V_C}$ basal defects. It has been reported that only $\mathrm{C_{Si}V_C}$ c-axial and $\mathrm{V_{Si}V_C}$ basal are observed at the wet-oxidized C face among them. The $\mathrm{C_{Si}V_C}$ defects are generated by removing a Si atom and moving C atom to $\mathrm{V_C}$ site from the neighboring C site. We remove Si atom from the first or second SiC bilayer. In addition, $\mathrm{V_{Si}V_C}$ defects are created by removing C atoms at the Si site from the $\mathrm{C_{Si}V_C}$ defects. The computational model for the case of the $\mathrm{C_{Si}V_C}$ c-axial defect is shown in Fig. 1. Table 1 corrects the formation energies and magnetic moments of the defects.

When Si atom in the first SiC bilayer of the interface is removed, $\mathrm{C_{Si}V_C}$ basal, $\mathrm{V_{Si}V_C}$ c-axial, and $\mathrm{V_{Si}V_C}$ basal defects are hardly generated because the dangling bonds of C atom are passivated by the O atom which comes from the oxide layer. As a result, the formation energy of $\mathrm{C_{Si}V_C}$ c-axial defect, in which Si atom at the first bilayer is removed, is the most stable among $\mathrm{C_{Si}V_C}$ defects. In the case of the $\mathrm{V_{Si}V_C}$ defects, the formation energy

Table 1: Formation energies E_f and magnetic moments of C-face defects. The zero of the formation energy is set at the lowest models among $\mathrm{C_{Si}V_C}(+)$ at the interface, $\mathrm{C_{Si}V_C}(+)$ in bulk, $\mathrm{V_{Si}V_C}$ at the inerface, and $\mathrm{V_{Si}V_C}$ in bulk.

Defects	Formation energy (eV)	Magnetic moment (μ_B)
$\mathrm{C_{Si}V_C}(+)$ c-axial @ 1st layer	0.0	1
$\mathrm{C_{Si}V_C}(+)$ c-axial @ 2nd layer	+0.92	1
$\mathrm{C_{Si}V_C}(+)$ basal @ 2nd layer	+0.49	0
$\mathrm{C_{Si}V_C}(+)$ c-axial @ bulk	+0.10	1
$\mathrm{C_{Si}V_C}(+)$ basal @ bulk	0.0	1
$\mathrm{V_{Si}V_C}$ c-axial @ 2nd layer	+0.96	1
$\mathrm{V_{Si}V_C}$ basal @ 2nd layer	+0.49	2
$\mathrm{V_{Si}V_C}$ c-axial @ bulk	0.0	2
$\mathrm{V_{Si}V_C}$ basal @ bulk	+0.09	2

of the c-axial structure is lower than that of the basal one. Although this result is not in agreement with the experimental result, the magnetic moment of the basal defect at the interface corresponds with that in bulk while the magnetic moment of the c-axial does not. This indicats that our calculated results support the experimental situation.

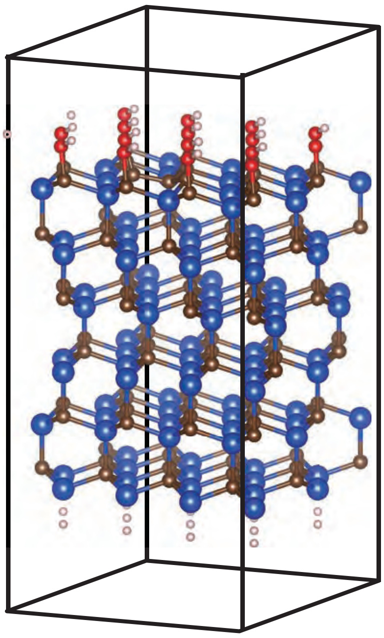

Figure 1: Computational model for SiC/$\mathrm{SiO_2}$ interface with $\mathrm{C_{Si}V_C}$ c-axial defect. Blue, brown, and red balls are Si, C, and O atoms, respectively. The supercell contains 95 Si, 96 C, 16 O, and 32 H atoms. H atoms are used for termination of dangling bonds at the surfaces.

References

[1] T. Umeda, Y. Kagoyama, K. Tomita, Y. Abe, M. Sometani, M. Okamoto, S. Harada, and T. Hatakeyama, Appl. Phys. Lett. **115**, 151602 (2019).

[2] K. Hirose, T. Ono, Y. Fujimoto, and S. Tsukamoto: First Principles Calculations in Real-Space Formalism (Imperial College, London, 2005).

[3] T. Ono, M. Heide, N. Atodiresei, P. Baumeister, S. Tsukamoto, and S. Blügel, Phys. Rev. B **82**, 205115 (2010).

[4] Y. Egami, S. Tsukamoto, and T. Ono, Phys. Rev. Research **3**, 013038 (2021).

Analyses related to atomic structures and atom dynamics at complex structures such as surfaces, interfaces and defects

Satoshi WATANABE
Department of Materials Engineering, the University of Tokyo
7-3-1 Hongo, Bunkyo-ku, Tokyo, 113-8656

1 Introduction

The understanding on structures and dynamics at surfaces, interfaces and defects on nanoscale is crucial to facilitate developments of novel information and energy devices. First-principles calculation has sufficient accuracy of prediction for this purpose, but its computational cost is often too high to model such devices realistically.

Keeping the above in minds, we have been investigating atomic structures and atom dynamics in various systems via first-principles calculations combined with multi-scale or machine-learning approaches. In the following, some of our results in the fiscal year 2020 are described.

2 Phase stability of Au-Li binary systems

Aiming to deepen our understanding on the operation mechanisms of novel memory device named VolRAM [1] and all-solid-state Li-ion batteries, we examined Li ion distribution at the interfaces between γ-Li_3PO_4 and metal electrodes by combining first-principles data of defect formation energies with a one-dimensional continuum model [2] in the previous year. However, we have not achieved thorough understanding because of alloy formation between Au and Li: The Au-Li binary system is known to exhibit various alloy phases over a wide range of compositional ratios. Therefore, in the fiscal year 2020, we have explored the alloying properties of Au and Li [3].

For this purpose, we constructed a high-dimensional neural network potential (HDNNP) [4] based on density functional theory (DFT) calculations. The predictions by the constructed HDNNP on lattice parameters and phonon properties agree well with those obtained by DFT calculations. The predictions on the mixing energy of $Au_{1-x}Li_x$ also show excellent agreement with DFT verifications. The lack of consensus on the Au-Li stable phases in previous studies can be understood from the existence of various compositions with structures on and slightly above the convex hull.

We have also examined the alloying process starting from the phase separated structure to the complete mixing phase by performing molecular dynamics simulations with the constructed HDNNP. Our results reveal that when multiple adjacent Au atoms dissolved into Li, the alloying of the entire Au/Li interface started from the dissolved region.

3 Band alignment tuning via thin-film insertion

Recently, interfacial resistance between the Nb-doped $SrTiO_3$ (STO) metal and a $LiCoO_2$ (LCO) mixed conductor has been found to de-

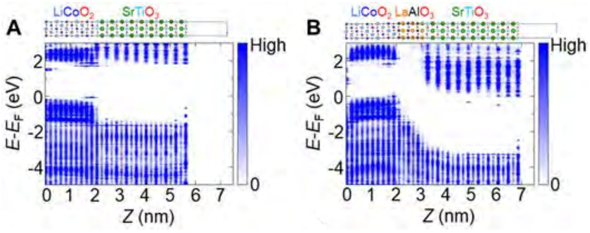

Figure 1: Calculated local density of states of (A) $LiCoO_2$(104)/$SrTiO_3$(001) and (B) $LiCoO_2$(104)/three unit cells of $LaAlO_3$/$SrTiO_3$(001) along the Z-axis direction perpendicular to the interfaces [5].

crease significantly (by more than five orders of magnitude) upon the insertion of a 1 nm thick insulating $LaAlO_3$ (LAO) layer at the interface [5]. To clarify the origin of this behavior, we have performed DFT+U calculations for LCO/STO and LCO/LAO/STO heterostructures. In our calculation, we have adopted the undoped system for both LCO and STO, considering the fact that Nb-doping shifts only the Fermi level, and the position of the conduction band minimum, measured from the vacuum level, is nearly the same between the undoped and Nb-doped STO.

Figure 1 shows the local density of states of the structurally optimized LCO/STO and LCO/3 unit cells of LAO/STO systems along the Z-axis direction perpendicular to the interface. In the LCO/STO model, upward (downward) band bending of $\sim$0.20 eV (0.06 eV) near the interface on STO (LCO) is seen. The difference in the valence band maximum energy of LCO and the conduction band minimum energy of STO was $\sim$1.8 eV. In contrast, the energy level difference decreased to 0.28 eV when 3 LAO unit cells were inserted at the interface. The linear change in the LAO band level along the Z-axis shows the presence of a built-in electric field. The electric field was 2.2 eV/nm (0.67 eV per LAO unit cell), which is comparable to the values deduced from the experiments [5] (0.4 eV per LAO unit cell). The shift in the energy level via LAO insertion suggests a reduction in the Schottky barrier height.

We have also performed quantum mechanical calculations for electron tunneling by solving the time-independent one-dimensional Schrödinger equation with a simple model constructed based on the above behavior of band alignment change due to the LAO layer insertion. The result reproduced the observed interfacial resistance change with the LAO layer thickness: The 4 u.c. LAO case had a minimum resistance.

This study provides a proof-of-concept demonstration of an approach to reduce the interfacial resistance by tuning the Schottky barrier at the interfaces of metals and mixed conductors.

References

[1] I. Sugiyama, R. Shimizu, T. Suzuki, K. Yamamoto, H. Kawasoko, S. Shiraki, and T. Hitosugi: APL Mater. **5** (2017) 046105.

[2] K. Shimizu, W. Liu, W. Li, S. Kasamatsu, Y. Ando, E. Minamitani, and S. Watanabe: Phys. Rev. Mater. **4** (2020) 015402.

[3] K. Shimizu, E. F. Arguelles, W. Li, Y. Ando, E. Minamitani, and S. Watanabe: Phys. Rev. B **103** (2021) 094112.

[4] J. Behler and M. Parrinello: Phys. Rev. Lett. **98** (2007) 146401.

[5] K. Nishio, T. Shirasawa, K. Shimizu, N. Nakamura, S. Watanabe, R. Shimizu, and T. Hitosugi: ACS Appl. Mater. Interfaces **13** (2021) 15746.

Theoretical Approach to Reduce the Interface-State Density in SiC-MOS Devices

Yu-ichiro MATSUSHITA

Tokyo Institute of Technology, Ookayama Meguro-ku, Tokyo 152-8550

SiC power MOSFETs have shown remarkable energy-saving effects and have already been commercialized. However, the SiC/SiO2 interface, which plays a fundamental role in SiC power MOSFETs, still has a high interfacial defect density, and most of the inversion layer carriers induced by the gate voltage are trapped in the interfacial defects. In fact, only 10% of the theoretical electron mobility has been achieved in SiC-MOSFETs. In order to reduce the interface-state density, microscopic identification of them is needed.

We have performed density-functional calculations to investigate the microscopic structure of interface defects. One of the most promising candidates of interface defects is the residual carbon-related defects at the interface. In this study, the stability of carbon-related defects distributed in three regions (SiC bulk, SiO2 film, and SiC/SiO2 just interface) and their dependence on temperature and oxygen partial pressure were clarified by theoretical calculations based on density-functional theory [1]. Theoretical calculations showed that carbon-related defects were generated near the interface under the temperature and oxygen partial pressure conditions used in the actual experiments. In particular, the residual carbon defects distributed just at the interface were found to be stabilized and present in large amounts. This calculation result indicates that the formation of residual carbon defects at the interface is energetically stable and that thermal oxidation inevitably produces residual carbon defects at the interface.

Therefore, we thought that the formation of carbon defects due to thermal oxidation of SiC was unavoidable, and we sought a way to overcome this problem. As a result, we succeeded in forming a high-quality interface by using a process that eliminates the thermal oxidation of SiC and removes the carbon defects near the SiC surface, followed by the formation of an oxide film [2]. In the proposed process, a Si thin film is deposited after hydrogen etching and oxidized to SiO_2 at a temperature where the oxidation of SiC does not proceed. Subsequent nitridation after the oxide film formation is effective in reducing defects. The effectiveness of the proposed method was confirmed experimentally, and a high-quality interfacial structure with an interfacial level density of (1-4) × 10^{10} $cm^{-2}eV^{-1}$, which is one order of magnitude smaller than the conventional 10^{11} $cm^{-2}eV^{-1}$, was achieved.

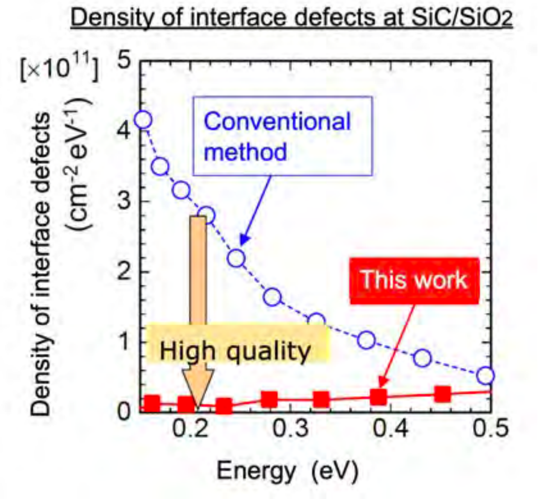

Fig. 1: Successful reduction in interface-state density in SiC/SiO_2

References

[1] T. Kobayashi and Y. Matsushita, JAP, **126**, 145302 (2019).

[2] T. Kobayashi, T. Okuda, K. Tachiki, K. Ito, Y. Matsushita, T. Kimoto, APEX, **13**, 091003 (2020).

First-Principles Molecular-Dynamics Study of Structural and Electronic Properties of Covalent Liquids and Glasses under Pressure

Fuyuki SHIMOJO

Department of Physics, Kumamoto University, Kumamoto 860-8555

For the investigation of the dynamic properties of covalent liquids and glasses under pressure, it is important to consider the stability of materials states under various conditions from the viewpoint of free energy. We have been using the thermodynamic integration (TI) method [1] for this purpose. The first-principles molecular dynamics (FPMD) simulations would be the most powerful and accurate tool to perform TI calculations. Due to the high calculation cost, however, FPMD simulations have been carried out only for small-sized systems. One of the solutions to solve this cost problem is to use machine-learning interatomic potential based on artificial neural networks (ANN) trained from the results of FPMD simulations.

This study aims to establish the training requirements for the ANN potential to reproduce the phase properties of sodium as an example. Figure 1 shows the temperature dependence of calculated volume *V*. The black circles show *V* obtained by FPMD. It is seen that, only when the virial stress tensor, as well as the potential energy and atomic forces, is taken into account in the training (EFP-fit), the constructed ANN potential precisely reproduces the FPMD results. The *V*-*T* relation calculated by the ANN potential trained with potential energy only (E-fit) or with potential energy and atomic forces (EF-fit) is completely different from that by FPMD, though the E-fit method gives almost correct *V* before melting. We also found that the 128-atom system with 4*k* points for Brillouin zone integration gives nearly converged results for the melting temperature.

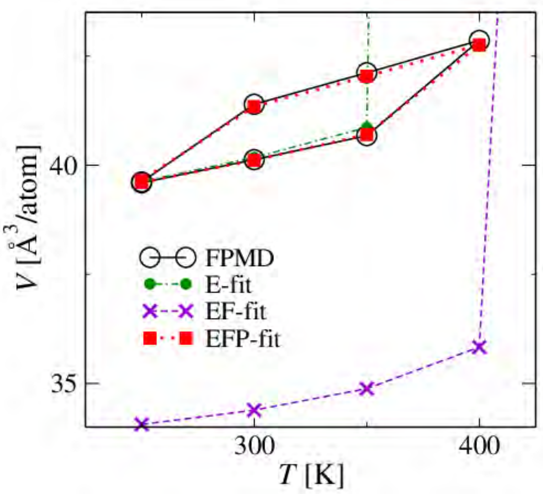

Fig. 1: Temperature dependence of volume *V* of Na obtained by FPMD and ANN-MD simulations.

References

[1] D. Frenkel and A. J. C. Ladd, J. Chem. Phys. **81**, 3188 (1984).

Quantum Simulations on Dynamical Heterogeneous Catalysts

J. I. ENRIQUEZ, H. H. HALIM, S. E. M. PUTRA, T. N. PHAM, Y. J. WONG,
Y. HAMAMOTO, K. INAGAKI, I. HAMADA, and Y. MORIKAWA
Department of Precision Engineering, Graduate School of Engineering,
Osaka University, 2-1 Yamadaoka Suita, Osaka 565-0871

In 2020-2021, we carried out theoretical investigation of chemical processes at surfaces and interfaces, oxidative etching process of diamond [1], multi-scale simulation of Cu adatom diffusion on Cu surfaces [2], formic acid adsorption in polymeric form and decomposition on Cu(111) [3], oxygen vacancy induced metal-insulator transition of $LaNiO_3$ thin film over SrTiO3 [4].

In this report, we report the oxidative etching process of the diamond (100) surface [1]. Diamond possesses a unique combination of superlative properties that makes it an attractive material for several novel applications. Of all semiconductors, diamond has the highest dielectric breakdown field, saturated electron drift velocity, and thermal conductivity which make it an ideal material for next-generation electronics that will outperform current systems in terms of operating frequency and power handling capacity. In addition, diamond's wide band gap, optical transparency, chemical inertness, hardness, and low thermal expansion have led to a number of specialized photonics applications including spacecraft window, optoelectronic microlens, photodetector, high energy particle detector, UV and infrared LED, and Raman laser. Diamond has color centers that functions as bright single photon source (SPS) at room temperatures and can be potentially implemented in quantum metrology and quantum information science.

At present, a theoretical study that investigates the entire oxidation process, starting from the adsorption of gas phase O_2 up to the desorption of CO and etching of the surface, has never been done. This kind of study is necessary to develop a comprehensive knowledge of diamond oxidation mechanism. For this reason, van der Waals-corrected density functional theory simulations of the oxidation of the C(100) surface have been performed.

Density functional theory (DFT) calculations have been performed using STATE code package (Simulation Tool for Atom TEchnology) with generalized gradient exchange-correlation functional (GGA) based on the work of Perdew, Burke and Ernzerhof (PBE). Semi-empirical van der Waals correction was implemented. Core electrons were treated using ultra-soft pseudopotentials. Wave functions were expanded using plane-wave basis with wave function and augmentation charges cutoff of 36 Ry and 400 Ry, respectively.

We simulated the succeeding desorption of CO up to the complete etching of the top C layer. The reaction paths and optimized structures are shown in Fig. 1. Following the desorption of the first CO, there are two possible locations where the second CO could desorb, the adjacent CO_{bridge} towards the $[01\bar{1}]$ direction where O is on top site and the CO from the adjacent ether group towards the [011] direction. The former and the latter have E_{barrier} of 4.53 eV and 3.62 eV, respectively. Succeeding CO desorptions along [011] (Fig. 1 B-E) all have lower E_{barrier} compared to $[01\bar{1}]$, suggesting a preferred etching direction. The calculated desorption activation energies vary between 1.01 - 4.68 eV. Initial desorption of CO along a given row in [011] direction has the highest desorption activation energy (reaction A→ B and E → F), while succeeding energy barriers are lower (Fig. 1 A-E, E-I). Analysis of the reaction path geometries shows that for these two reactions, the initial CO desorption proceeds by the near-simultaneous breaking of two CObridge-C bond. The point defect left by the initial desorption allows the next $\mathrm{CO}_{\mathrm{bridge}}$ to break one bond with second layer C and form CO on top ($\mathrm{CO}_{\mathrm{top}}$) structure. The non-simultaneous bond breaking reduces the heat released by the reaction and the desorption activation barrier. This suggests that the point defect functions as nucleation point for CO desorption along [011] direction. This nucleation function was first proposed by John et al. based on their observation that the surface roughness of diamond (100) did not increase even after removal of over 5300 atomic layers, suggesting that the removal rate of rows of atoms is more rapid than the removal rate of layers. Our work is the first theoretical study to support their prediction.

In summary, we performed density functional theory calculations with van der Waals corrections to elucidate diamond oxidation mechanism on the atomic-level which could lead to insights that will advance the improvement of nascent nanofabrication technologies. We developed a comprehensive theory of oxidative etching of the diamond (100) surface, from the adsorption of gas phase O_2, including details of metastable adsorption states, intersystem crossing, and induced surface dereconstruction, to the desorption of CO and CO_2, complete etching of the top surface layer and its subsequent stabilization.

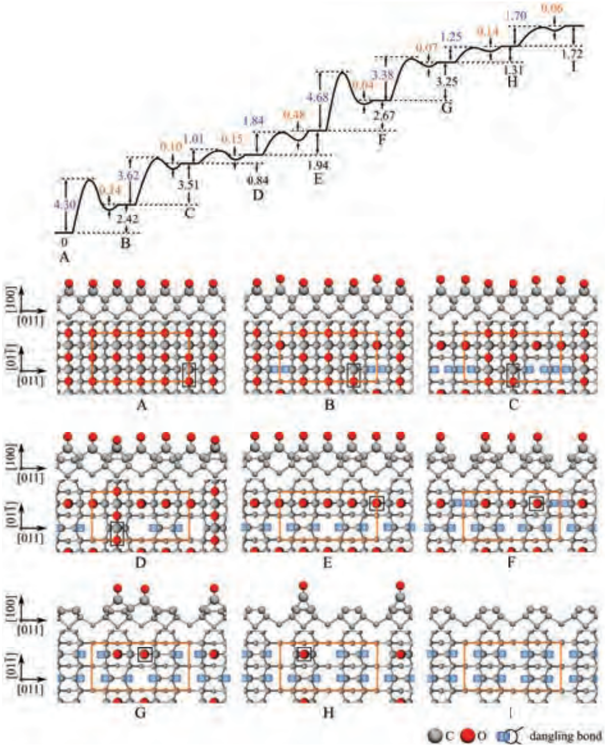

Figure 1: Etching of the top-layer atoms of C(100)-(1 × 1): $\mathrm{O}_{\mathrm{bridge}}$ surface through successive CO desorption. The heat of reactions and activation energies in electron-volts are shown in black and blue texts, respectively. Physisorption energies of CO are shown in orange text. Grey and red spheres correspond to carbon and oxygen atoms, respectively, while the dangling bonds are represented by blue cylinder.

References

[1] J. I. Enriquez, F. Muttaqien, M. Michiuchi, K. Inagaki, M. Geshi, I. Hamada, and Y. Morikawa: Carbon **174** (2021) 36-51.

[2] H. H. Halim, *et al.*, : ACS Omega **6** (2021) 5183.

[3] A. Shiotari, S. E. M. Putra, *et al.*, : Small, in press.

[4] H. D. Nguyen, *et al.*, : Phys. Rev. B **102** (2020) 165411.

Development and application of first-principles algorithms for long-range electron transport simulation

Yoshiyuki EGAMI
Division of Applied Physics, Faculty of Engineering, Hokkaido University
Kita 13, Nishi 8, Kita-ku, Sapporo, Hokkaido 060-8628

In recent years, a lot of first-principles studies on various materials have been energetically performed toward the development of novel devices. First-principles calculations generally require a computational cost proportional to the cube of the system size. In order to perform large-scale simulations, the development of $\mathcal{O}(N)$ algorithms and the improvement of parallelization efficiency of parallel calculations have been promoted. So far, great progress has been made in atomic structure calculations and electronic structure calculations, but reducing the computational cost remains a major issue in electron-transport property calculations.

In this subject, an efficient computational procedure based on the real-space finite-difference formalism[1] was developed to evaluate the electron-transport properties of long systems containing more than 10^5 atoms under the zero temperature and zero bias limits in the steady state without accuracy deterioration. In the procedure, a transition region is represented by arranging multiple parts along the transport direction. The Green's function of the whole transition region extended towards the transport direction was obtained by recursively combining the Green's functions of the adjoining parts one by one. The computational cost for calculating the submatrices of the Green's functions required to estimate the transport properties can be suppressed linearly for the number of the combined parts.

To exemplify the efficiency of the proposed procedure we demonstrate large-scale electron-transport calculations for BN-doped double-walled carbon nanotubes composed of 196,608 atoms (Fig. 1), which make, to the best of our knowledge, the largest system in the first-principles electron-transport calculation. These works have been performed on System B and System C of the Supercomputer Center, the Institute for Solid State Physics, the University of Tokyo.

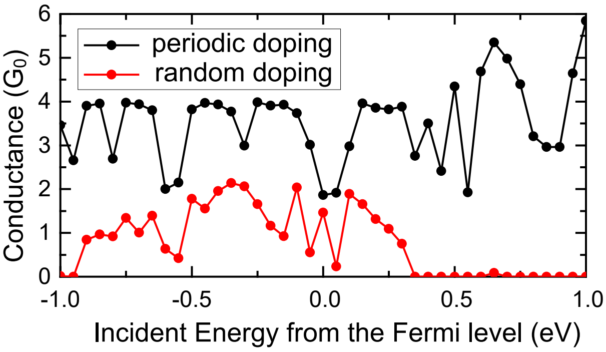

Figure 1: Conductance trace of BN-doped double-walled carbon nanotubes consisting of 196,608 atoms.

References

[1] Y. Egami, S. Tsukamoto and T. Ono: Phys. Rev. Res. **3**, 013038 (2021).

"Prediction of hydrogen function by advanced calculation of solids containing hydrogen"
"Development of data assimilation method for crystal structure prediction and its application to hydrogen-containing compounds"

Shinji TSUNEYUKI
Department of Physics, School of Science,
The University of Tokyo, 7-3-1 Hongo, Bunkyo-Ku, Tokyo 113-0033
Institute for Solid State Physics,
The University of Tokyo, Kashiwa-no-ha, Kashiwa, Chiba 277-8581

One of the most challenging problems in first-principles simulations of materials is to predict crystal structure by searching the global minimum in multi-dimensional potential energy surface (PES). It takes a sizeable computational cost to calculate the electronic energy of even a single atomic configuration from first principles. It is, therefore, practically difficult to find the most stable crystal structure when the number of atoms in the unit cell is large and when PES has many local minima.

The problem is partially solved by a data assimilation method which we have proposed [1]. In the data assimilation method, we incorporate powder diffraction data to constrain search space based on Bayes' theorem, by which we can drastically accelerate finding a probable crystal structure. The method is valid even if the diffraction data is incomplete and is insufficient for structure determination by ordinary data analysis methods. Typical applications are crystal structure determination of materials found by high-pressure experiments where the range of the diffraction angle is limited or those containing hydrogen atoms whose positions are difficult to be determined by X-ray diffraction. The data assimilation method might accelerate materials exploration in combination with combinatorial synthesis and measurement.

This year, we showed that the method is very robust against noise in the experimental data if we tune the control parameter representing the weight of the data assimilation [2].

We also extended the method to assimilate multiple experimental data, such as X-ray and neutron diffraction data, at the same time. Both reflect the same interlayer distances of the crystal but with different peak intensities, giving us more information. We applied this method to $Zn(OH)_2$ to confirm that using both sets of data significantly improved the success rate of crystal structure prediction [2].

Then we applied the method to two systems containing a considerable number of atoms in a unit cell. The first one is a Li-ion conductor $LiCB_9H_{10}$. The Li-ion conductivity of this material is known to increase two orders of magnitude at around 330-360K. Still, the mechanism and associated crystal-structure change have not been clarified yet. From our simulation, the difference in the crystal structure below and above the transition temperature is essentially the orientation and rotative motion of the $(CB_9H_{10})^-$ complex ions. Since the diffusive motion of Li ions is strongly correlated with the rotation of a nearby complex ion $(CB_9H_{10})^-$, it is greatly enhanced by its rotation in the high-temperature phase [3].

The second is a metal hydride $Ca_xAl_yH_z$ newly synthesized at high pressure. Although powder X-ray diffraction data is available, the unit cell seems to be quite large, and neither its accurate chemical composition nor the crystal structure is clarified experimentally. We tried its structure determination and found a plausible model containing more than one hundred atoms in a unit cell, as shown in Fig.1 [2,4]

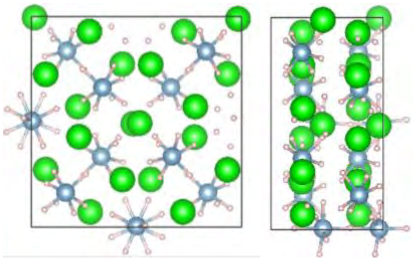

Fig. 1 Top and side views of a theoretically predicted structure of $Ca_xAl_yH_z$. Large, middle and small spheres denote Ca, Al and H atoms.

These works have been done in collaboration with the experimental groups of the Grant-in-Aid for Scientific Research on Innovative Areas "Hydrogenomics: Creation of Innovative Materials, Devices, and Reactive Processes using Higher-Order Hydrogen Functions" (FY 2018-2022).

References

[1] N. Tsujimoto, D. Adachi, R. Akashi, S. Todo and S. Tsuneyuki, Phys. Rev. Materials 2, 053801 (2018).

[2] S. Yoshikawa, Ph.D. dissertation (The University of Tokyo, 2021); S. Yoshikawa et al., in preparation.

[3] R. Sato et al., in preparation.

[4] R. Sato et al., in preparation.

First Principles Studies on Atomic and Electronic Structures of Impurity-Screw Dislocation Complexes in GaN

Kenji Shiraishi

Institute for Materials and Systems for Sustainability,

Nagoya University, Furo-cho, Chikusa-ku, Nagoya, Aichi 464-8601

Recent experiments suggest that Mg condensation at threading screw dislocations (TSD) induces current leakage, leading to degradation of GaN-based power devices. To investigate this, we performed first-principles total-energy calculations for various Mg and dislocation complexes. Figure 1(a) shows an atomistic configuration of a TSD. The dislocation has the Burgers vector of [0001]. To model the TSD, the atoms are initially aligned in a helical manner along the [0001] dislocation line.34,35 A periodic boundary condition is then imposed on all axes of the system. The system contains 812 Ga and N atoms in total, and a vacuum layer is added on lateral planes perpendicular to the [0001] direction [Fig. 1(b)].

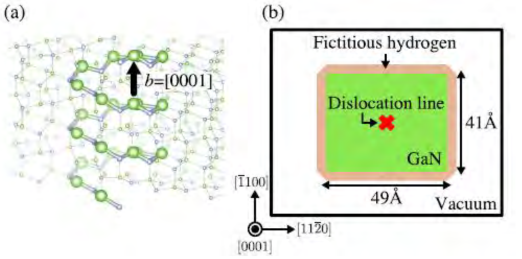

Fig. 1. (a) Model of a TSD. The Burgers vector is [0001], and the dislocation line runs along [0001]. Green and blue spheres are Ga and N atoms, respectively. Thelarger spheres highlight the dislocation core. (b) Schematic of the [0001] plane of the unit cell. The green region represents GaN, surrounding which is the fictitioushydrogen. The outermost region is vacuum. The red cross indicates the position ofthe dislocation line.

We find that threading screw dislocations indeed attract Mg impurities as shown in Fig.2.

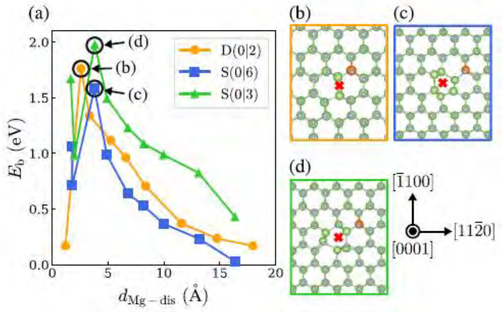

Fig. 2. (a) Binding energies of the Mg-TSD complexes of the D<0|2>, S<0|6>, and S<0|3> cores. d_{Mg-dis} is the distance of the Mg from the dislocation line. (b)–(d). The most stable core structures of the Mg–TSD complexes of the D<0|2>, S<0|6>, and S<0|3> cores, respectively. The position of the Mg atom is inindicated by the orange sphere. A red cross denotes the position of a dislocation line.

These findings provide a picture in which the Mg, being a p-type impurity in GaN, diffuses toward the TSD and then locally forms an n-type region. The appearance of this region along the TSD resultsin local formation of an n–n junction and leads to an increase in the reverse leakage current.

References

[1] T. Nakano,Y. Harashima, K. Chokawa, K. Shiraishi, A. Oshiyama, Y. Kangawa, S. Usami,N. Mayama, K. Toda, A. Tanaka, Y. Honda, and H. Amano, Appl. Phys. Lett., 117, 012105 (2021).

Theoretical Studies on Semiconductor MOVPE Growth Based on Multi-Physics Simulation

Kenji Shiraishi

Institute for Materials and Systems for Sustainability,

Nagoya University, Furo-cho, Chikusa-ku, Nagoya, Aichi 464-8601

We examined the main reaction pathway of the TMG ($Ga(CH_3)_3$) decomposition processes [1]. We calculated and compared the decomposition rate from the Gibbs energy of activation and calculated the mole fraction of each chemical species. Asa result, in B3LYP, the decomposition pathway of TMG is the sequential reaction with NH3followed by the reaction with H_2. In M062X, the decomposition proceeds through repeated reactions with NH_3 as in the previous study. Using the reaction rates we obtained, we calculated the mole fractions of each chemical species at 1300 K. It was found that GaH_3 was the most abundant species in B3LYPand $Ga(NH_2)_3$ in M062X. When we tested the difference between the two exchange-correlation functions using the high precision CCSD method, it was found that the results of the CCSD method were closer to those of B3LYP. Moreover, the experiment also supports the reaction paths obtained byB3LYP. Therefore, the main reaction pathway of TMG decomposition is shown in Fig.1: $Ga(CH_3)_3 \rightarrow Ga(CH_3)_2NH_2 \rightarrow Ga(CH_3)_2H \rightarrow GaCH_3HNH_2 \rightarrow GaCH_3H_2 \rightarrow GaH_2NH_2 \rightarrow GaH_3$. The main reaction pathway obtained in our study shows that when H_2 is sufficiently present as a carrier gas, amino groups, which are responsible for the formation of a wide variety of polymers, are difficult to form. Therefore, we were able to reduce the number of chemical reactions considered in conventional fluid simulations. GaH_3 molecules must be considered in the surface reaction of GaN MOVPE. Furthermore, it may be effective to decompose TMG at ahigh temperature of about 1300 K for a certain period of timet o control carbon contamination..

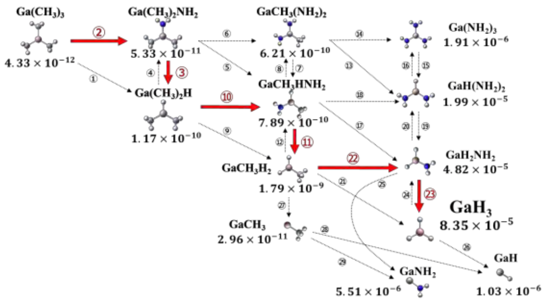

Fig. 1: Mole fraction of each chemical species after 1s at 1300 K and main reaction pathway of TMGa decomposition written in red obtained by the first principles calculations. [Ref.1]

References

[1] S. Sakakibara, K. Chokawa, M. Araidai, A. Kusaba, Y. Kangawa, and K. Shiraishi, Jpn. J. Appl. Phys. 60, 045507 (2021).

Mechanisms of Chemical Reaction of β-diketones Molecules with a Metallic Nickel Surface in Thermal Atomic Layer Etching Processes

Satoshi HAMAGUCHI

Center for Atomic and Molecular Technologies,

Osaka University, 2-1 Yamadaoka, Suita, Osaka 567-0871

Thermal atomic layer etching (ALE) is one of the key manufacturing technologies for nano-scale electronic devices [1] as it can be used for precise and damageless etching of metals. Thermal ALE of Ni with hfacH starts with the deprotonation of hfacH molecules after oxidizing the Ni surface. By increasing the surface temperature in the range of 300 ~ 400 °C, volatile nickel complex $Ni(hfac)_2$ and water H_2O molecules are formed on the surface and remove the NiO layer. In this process, once a new metallic Ni surface appears, no further etching occurs, which ensures the self-liming nature of the thermal ALE process [2-5]. It has been known experimentally [5,6] that, when hfacH molecules are supplied to a metallic Ni surface, they decompose and form neither $Ni(hfac)_2$ nor H_2O molecules, and as a result no etching of Ni takes place. The origin of the self-limiting process in the thermal ALE of Ni with hfacH exposure was discussed in an earlier study[4]. The aim of this work is to clarify the mechanisms of decomposition of β–diketones molecules – such as; hexa-fluoroacetylacetone (hfacH), trifluoro-acetylacetone (tfacH), and acetylacetone (acacH) – on a metallic Ni surface and the effect of surface roughness on the decomposition concerning thermal ALE.

My research assistant A. H. Basher has used ISSP supercomputer to study the chemical reaction of hfacH, tfacH, and acacH molecules on flat and rough metallic Ni surfaces. In this study, we employ van der Waals (vdW) inclusive [7] periodic density functional theory (DFT) to investigate the adsorption and reaction of hfacH on a metallic Ni surface, and clarify the surface chemistry in the atomic layer etching (ALE) process of Ni. We used our in-house plane-wave pseudopotential code STATE [8]. In our calculation, we have used 5 nodes for each submitted jobs to run the calculations on 120 processors parallelly and more than 1800 hours has been consumed.

We have investigated several adsorption sites to find the most stable one thermodynamically with and without vdW forces. Second, the dissociation C-F bond in hfacH was investigated using nudged elastic band (NEB) method as well as climbing image NEB (ciNEB) to get more accurate results. Third, the dissociation bond of O-H in hfacH (deprotonation) was studied by two methods: a) checking the deprotonation manually by increasing the distance between O and H atoms. b) using NEB then ciNEB methods that is still running.

It has been found that the physisorption energies of those β–diketones are almost the same while the chemisorption energy is higher for a β–diketone with a higher polarity and the van der Waals forces play a decisive role in determining the adsorption energy. The dissociation processes of β–diketones have been studied with a climbing image nudged elastic band method, which has shown the cleavage of a C-F bond of a β–diketone is more likely to take place than the deprotonation. The surface roughness can also help to form C-Ni bonds, which were also observed in experiments. In this way, our simulations have demonstrated the self-limiting nature of thermal ALE for Ni with β–diketone gases in general, which is consistent with earlier experimental observations [5,6].

References

[1] G. S. Oehrlein and S. Hamaguchi, Plasma Sources Sci. Technol. **27**, 023001 (2018).

[2] A. H. Basher, M. Krstić, T. Takeuchi, M. Isobe, T. Ito, M. Kiuchi, K. Karahashi, W. Wenzel, and S. Hamaguchi, J. Vac. Sci. Technol. A **38**, 022610 (2020).

[3] A. H. Basher, M. Krstić, F. Karin, T. Ito, K. Karahashi, W. Wenzel, and S. Hamaguchi, J. Vac. Sci. Technol. A **38**, 052602 (2020).

[4] A. H. Basher, I. Hamada, and S. Hamaguchi,, Jpn. J. Appl. Phys. **59**, 090905 (2020).

[5] T. Ito, K. Karahashi, and S. Hamaguchi, Proc. of the 39th Int. Symp. on Dry Process (DPS2017) (Tokyo, Japan, 2017) **45**, 2017.

[6] H. L. Nigg and R. I. Masel, J. Vac. Sci. Technol. A **17**, 3477, (1999).

[7] I. Hamada, Phys. Rev. B **89**, 121103 (2014).

[8] Y. Morikawa, H. Ishii and K. Seki, Phys. Rev. B, **69** (2004) 041403.

Thermodynamic properties of icy materials in the interior of planets and satellites

Yu Komatsu
Astrobiology Center / National Astronomical Observatory of Japan,
Osawa 2-21-1, Mitaka, Tokyo, Japan.

In this study, the equation of state (EOS) of hydrogen sulfide under high pressure is investigated, which is applicable to predicting the internal structure of icy satellites, such as Europa, and icy planets. H_2O, NH_3, CH_4 and H_2S are thought to be the typical icy materials, reflecting conditions before establishing the planetary system [1]. We focus on thermodynamical properties of hydrogen sulfide as the component, whose property under high pressure and low temperature has been investigated well due to its superconductivity, but there are no studies under a wider range of temperature and pressure.

DFT-MD calculations of hydrogen sulfide systems with a large parameter space with temperature and density were performed using Quantum ESPRESSO. As initial configurations, not only typical structures of hydrogen sulfide but also the Cmca and P1 structures, which were obtained by the structure prediction, were selected because they were suggested to be stable under higher pressure [2].

Figure 1 shows self-diffusion coefficients caluculated for the Cmca structure from 500 to 10,000 K, as a function of the density. In high temperature ranges above 5,000K, the diffusion coefficients as well as radial distribution functions starting from different initial structures converged to nearly identical values at given temperature and density. These analyses would be a good basis for further refinement of the new EOS for icy bodies, as the next step of our study.

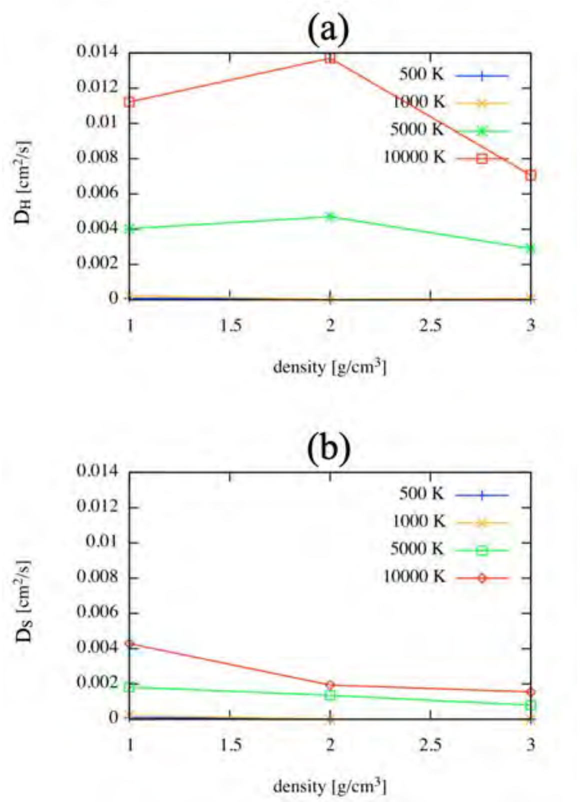

Figure 1: The self-diffusion coefficient for the hydrogen atom (a) and the sulfur atom (b) as function of the density of the Cmca structure with four different temperatures (500, 1,000, 5,000 and 10,000 K).

References

[1] T. V. Johnson *et al.*, ApJ **752**, 192 (2012).

[2] Y. Li, *et al.*, J. Chem. Phys. **140**, 174712 (2014).

Electrochemical reaction analysis using density functional calculation + implicit solvation model 2

Jun HARUYAMA

Institute for Solid State Physics,

The University of Tokyo, Kashiwa-no-ha, Kashiwa, Chiba 277-8581

The rechargeable Li-ion battery (LIB) is a successful energy storage device due to its high energy density and long cycle life. In order to improve its performance, quantitative understanding of elementary reactions in the LIB such as the reaction of Li intercalation from electrolyte solution into graphite and crystal structure change in graphite during the reaction must be a great help. In previous studies, we have studied charge transfer reactions at electrode/solution interfaces in Li-ion batteries (LIB) using density functional theory (DFT) calculations combined with implicit solvation model. [1–4]

Structure change of Li-intercalated graphite (LIG) during the charge/discharge processes was recently observed by operando X-ray diffraction measurements using a synchrotron radiation at SPring-8. [5, 6] The operando XRD data cannot explained by conventional staging model for LIG. To compare and discuss these experimental results, we conduct first-principles calculations for the phase stability of LIG.

Formation free energy ΔF_f is defined as

$$\Delta F_\mathrm{f}\,(\mathrm{Li}_x\mathrm{C}_6) = F(\mathrm{Li}_x\mathrm{C}_6) - xF(\mathrm{Li}) - F(\mathrm{C}_6) \quad (1)$$

$$F = E_\mathrm{DFT} + F_\mathrm{vib} - TS_\mathrm{conf} \quad (2)$$

where F are the free energies of LIG at composition $\mathrm{Li}_x\mathrm{C}_6$, metal Li, and AB stacked graphite C_6. Free energy is represented as the following three terms: DFT total energy E_DFT, vibrational free energy F_vib, and configurational entropy term TS_conf.

Atomic configurations and cell parameters of Li/6C, Li/9C, Li/12C, Li/18C, Li/24C, and Li/36C in-plane structures (see Fig. 1a) were investigated within van-der-Waals (vdW) level DFT calculations. Interlayer configurations were set to AA, AB, and mix stacking (Fig. 1b). Mix stacking is defined that Li-intercalated layers were set to AA stacking and the other layers were AB stacking. We performed spin-unpolarized density functional theory (DFT) calculations with Quantum ESPRESSO (QE) package. [7]

The vibrational free energy was approximated by using independent harmonic oscillators representation. In this representation, phonon density of state (DOS) was obtained from density functional perturbation theory (DFPT) implemented in QE. Lattice gas model of suitable constraint was applied to the configurational entropy term.

Figure 1c shows the calculated formation free energies. LiC$_6$, Li$_{1/2}$C$_6$, and Li$_{1/3}$C$_6$ stable structures are AA-stack Li/6C stage1, stage2, and AA stack Li/9C stage2, these structures are consistent with experiment. [1] AB stacking is stable at the region of $x < 0.05$ in Li$_x$C$_6$. We emphasize that formation energies using only DFT term failed to describe higher stage region (C$_6$ – Li$_{1/3}$C$_6$) especially Li$_{1/3}$C$_6$ and AB stacking cannot become convex hull. The calculation also shows the existence of mix stacking at intermediate region ($0.05 < x < 0.3$). The expected AB–mix phase transition is slightly different from AA–AB phase transition at $x \approx 0.1$ suggested from X-ray diffraction analysis. [1] Finally, the computational AB–mix phase transition well explained the entropy behavior comparing with electrochemically observed entropy. [8, 9]

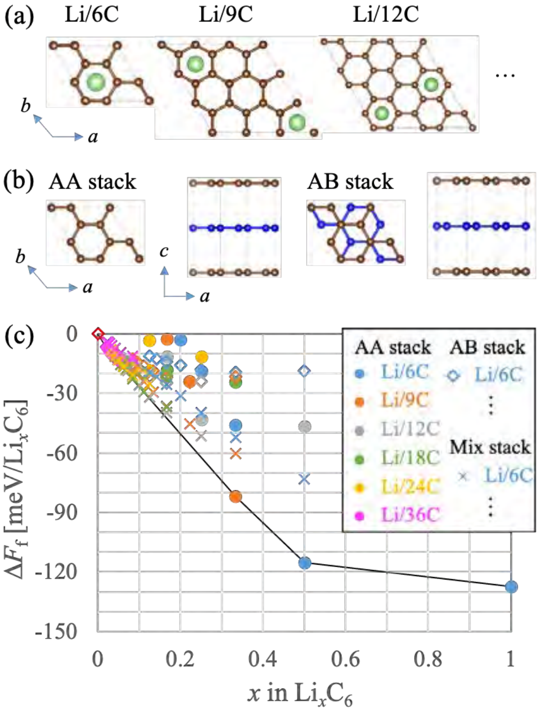

Figure 1: (a) In-plane configurations of Li/6C, Li/9C, Li/12C, … structures. (b) Interlayer configurations of AA and AB stackings. (c) Formation free energies (closed circles, diamonds, and crosses) and convex hull (black solid line) obtained from eq. (1).

References

[1] J. Haruyama, T. Ikeshoji, and M. Otani, J. Phys. Chem. C **122**, 9804 (2018).

[2] J. Haruyama, T. Ikeshoji, and M. Otani, Phys. Rev. Mater. **2**, 095801 (2018).

[3] M. Otani and O. Sugino, Phys. Rev. B **73**, 115407 (2006).

[4] S. Nishihara and M. Otani, Phys. Rev. B **96**, 115429 (2017).

[5] S. Takagi *et al.*, The 60th Battery Symposium, 1B20 (2019).

[6] H. Fujimoto *et al.*, The 59th Battery Symposium, 2E16 (2018).

[7] P. Giannozzi *et al.*, J. Phys.: Condens. Matter **21**, 395502 (2009); *ibid* **29**, 465901 (2017).

[8] R. Yazami and Y. Reynier, J. Power Sources **153**, 312 (2006).

[9] J. Haruyama, S. Takagi, K. Shimoda, I. Watanabe, K. Sodeyama, T. Ikeshoji, and M. Otani, in preparation.

Study of ferromagnetism in Pt(100) thin films by first-principles calculation

Tatsuru Yamada[1], Hiroyuki Kageshima[2], and Tetsuya Sato[1]
1Department of Applied Physics and Physico-Informatics, Keio University, 3-14-1 Hiyoshi, Kohoku-ku, Yokohama 223-0061, Japan
2Graduate School of Natural Science and Technology, Shimane University, 1060 Nishikawatsu-cho, Matsue 690-8504, Japan

Recently, It was reported that ferromagnetism appears in an oscillatory manner in the Pt(100) thin films depending on the film thickness[1][2]. However, few studies have focused in the ferromagnetism in Pt(100) thin film and the mechanism for appearance of ferromagnetism in Pt(100) thin film remains unclear. In this study, we performed the first-principles calculations of freestanding Pt(100) thin films to understand the mechanism for appearance of ferromagnetism in Pt(100) thin film. We performed first-principles calculations based on the density-functional theory with the generalized gradient approximation. Projector-Augmented Wave method was adopted as the pseudopotential of Pt. We used 88×88×1 k points (based on Monkhorst-Pack) and a cutoff energy of 36 Rydberg.

We calculated lattice constant that minimizes the energy. Using the obtained lattice constant, we calculated the Pt layer thickness dependence of the magnetic moment of Pt. As a result of the calculations of electronic structures for the free-standing Pt(100) thin films from 2 monolayers(ML) up to 17 ML, it was confirmed that ferromagnetism appeared in an oscillatory manner with a period of 6 ML (Fig. 1). By examining the energy band structure, we found that the flat band near the Γ point composed of $5d_{xz,yz}$ orbitals overlaps with Fermi energy(E_F) when ferromagnetism appears. This flat band is the quantum well band (Fig. 2).

From the phase model, the period at which the quantum well band in Pt(100) thin film overlaps with E_F is 5.7 ML[1]. This is consistent with experimental result of the previous research[2] and calculated results. So, it was concluded that oscillatory magnetic behavior in Pt(100) thin film can be explained by quantum well states.

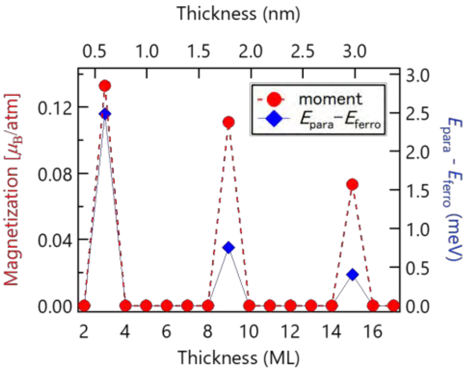

Fig. 1: Magnetic moment per Pt atom in Pt(100) thin films (circles) and total energy differences between the paramagnetic (para) and ferromagnetic (ferro) states (diamonds).

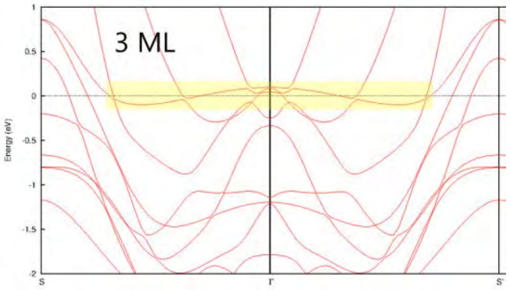

Fig. 2: Band structure of 3ML Pt(100) thin film.

References

[1] A. M. N. Niklasson *et al.*: Phys. Rev. **B** 75, 172402 (2007).

[2] K. Ochiai *et al.*: JPS2019, Gifu, 10aPS27 (2019).

Born-Oppenheimer MD Simulations of Excited States for Firefly Oxyluciferin Anions in Aqueous Solutions

Yoshifumi NOGUCHI

Department of Applied Chemistry and Biochemical Engineering, Graduate School of Engineering, Shizuoka University, Johoku 3-5-1, Hamamatsu, Shizuoka 432-8561, Japan

Firefly oxyluciferin anion, known as the light emitter in firefly bioluminescence process, has garnered significant attention because obtaining a deep insight on oxyluciferin anions could be an essential first step towards understanding the mechanism of the firefly bioluminescence process. However, majority of stabilizing and optical properties of oxyluciferin anions in the external environments are still a mystery.

We have performed first-principles Born-Oppenheimer molecular dynamics simulations (BOMD) for three possible isomers of firefly oxyluciferin anions (phenolate-keto, phenolate-enol, and phenol-enolate) surrounded by 64 explicit water molecules and elucidated their stabilizing mechanism in the aqueous solutions in the excited states. To attain the equilibrium conditions, we had to run BOMD up to 1.8 ns (corresponding to 3.7 million MD steps). Figure 1 shows the cumulative average for BLYP total energies simulated for phenolate-keto, phenolate-enol, and phenol-enolate. Unlike similar level BOMD simulations in the ground state in which the phenolate-enol form was the most stable [1,2], the current excited states BOMD simulations showed that phenolate-keto was the most stable isomers, whose energy was 0.38 eV and 0.57 eV lower than that of the phenolate-enol and phenol-enolate, respectively [3]. We analyzed the trajectories in detail and elucidated that the stabilizing mechanism of the oxyluciferin anions in the explicit aqueous solutions is the difference between at the ground and excited states.

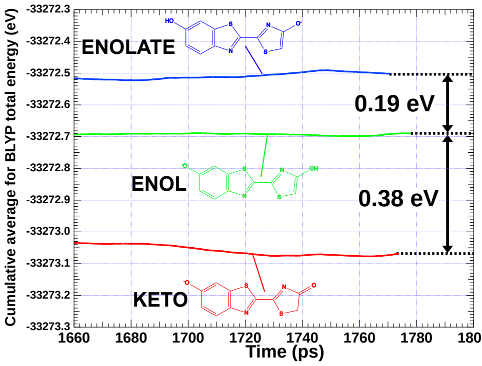

Fig. 1. Cumulative average for BLYP total energies.

References

[1] Y. Noguchi, et al., J. Phys. Chem. B, **120**, 8776 (2016).

[2] Y. Noguchi, et al., J. Chem. Theor. Comput., **15**, 5474 (2019).

[3] Y. Noguchi, et al., J. Chem. Phys., **153**, 201103 (2020).

Analysis of Thermoelectric Properties of Clathrate Compounds with Ab Initio Calculations

Masato OHNISHI
Department of Mechanical Engineering,
The University of Tokyo, 7-3-1, Hongo, Bunkyo-ku, Tokyo 113-8656

Clathrate compounds are promising candidates for thermoelectric materials in terms of the "electron-crystal phonon-glass" concept. Clathrate compounds are composed of guest atoms encapsulated in cagelike structures. It is expected that electrons can smoothly transport in the frame work while phonons are scattered by guest atoms. Particularly, in type-I clathrate compounds, guest atoms vibrate in a strong anharmonic potential because they are composed of a Weaire-Phelan structure, which divides a space with the maximum volume with the same cross-sectional area. While off-center clathrates such as type-I $Ba_8Ga_{16}Sn_{30}$, in which guest atoms vibrate in a double-well anharmonic potential, have low thermal conductivity, silicon-based clathrates are preferable for actual use in terms of the material cost.

In this study, we show that aluminum substitutions can enhance thermoelectric performance of silicon-based clathrates, type-I $Ba_8Ga_{16}Si_{30}$ (Fig. 1(a)). Comparing calculated thermoelectric figure of merits (ZT) with those obtained in experiment, we concluded that (a) aluminum additive enhances ZT with lowering doping level and (b) further suppression of doping level can enhance ZT significantly. To investigate thermoelectric properties, we obtained possible structures at finite temperatures with using a cluster expansion and Monte Carlo methods [1] and thermoelectric properties were averaged for different possible structures. As shown in Fig. 1(b), formation energies of arbitrary structures can be accurately predicted with the cluster expansion method. Phonon properties of the clathrates were calculated with using a self-consistent phonon (SCP) theory based on first-principles calculations [2]. While experimentally-observed carrier concentrations are around 10^{22} cm^{-3} for Si-based clathrates, our analysis shows that thermoelectric properties of the clathrate can be improved by suppressing carrier concentration, as shown in Fig. 1(c).

References

[1] M. Ångqvist, P. Erhart et al., Chem. Mater. 29, 7554 (2017) and 28, 6877 (2016).

[2] Tadano *et al.* Phys. Rev. Lett 120, 105901 (2018).

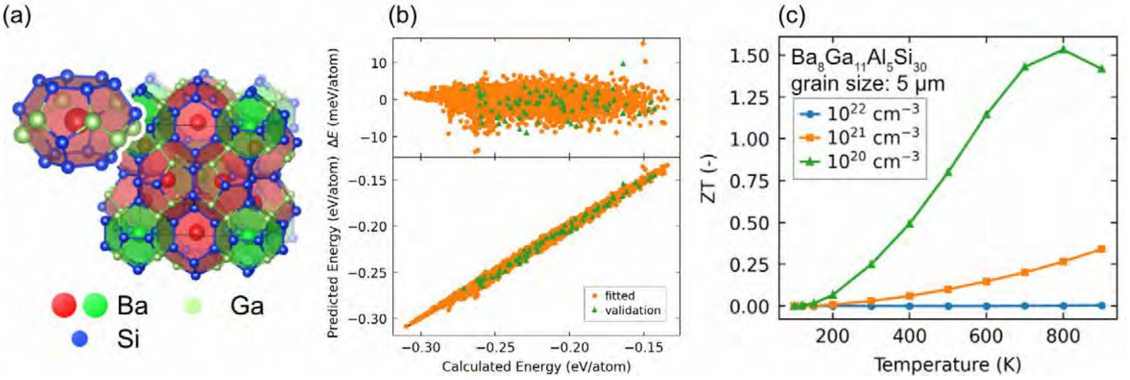

Fig. 1. Enhancement of thermoelectric properties of Si-based Clathrate. (a) Crystal structure of $Ba_8Ga_{16}Si_{30}$. (b) Prediction of formation energy with a cluster expansion method. (c) Dimensionless thermoelectric figure-of-merit (ZT) of the clathrate at different carrier concentrations.

First-principles calculation for low-temperature oxygen transfer in metal oxide

Akira Yoko

WPI-Advanced Institute for Materials Research,
Tohoku University, Katahira 2-1-1, Sendai, Miyagi 980-8577

We have studied oxygen storage and release materials experimentally and computationally. This term CeO_2 and Cr-doped CeO_2 were studied with first-principles calculations.

Plane-wave basis density functional theory (DFT) calculations were conducted to elucidate the Cr doping effects on CeO_2 structure using the VASP code [1,2]. The generalized gradient approximation (GGA) proposed by Perdew, Burke, and Ernzerhof (PBE) [3] was employed as the exchange correlation energy functional. The DFT+U method introduced by Dudarev et al. [4] was used to treat the electron localization. The parameter, U-J was set as 3.5 eV for Cr3d, 5.0 eV for Ce4f, and 5.5 eV for O2p states, respectively, based on the previous studies of Cr_2O_3 and CeO_2 [5,6]. The valence configurations of the pseudopotentials were $3\boldsymbol{s}^{2}3\boldsymbol{p}^{6}3\boldsymbol{d}^{5}4\boldsymbol{s}^{1}$ for Cr, $5\boldsymbol{s}^{2}5\boldsymbol{p}^{6}4\boldsymbol{f}^{1}5\boldsymbol{d}^{1}6\boldsymbol{s}^{2}$ for Ce and $2\boldsymbol{s}^{2}2\boldsymbol{p}^{4}$ for O. The energy cutoff for the plane-wave basis was set at 500 eV for all the calculations and provided the convergence of the total energy in the unit cell of CeO_2 (12 atoms). Defect calculations were conducted using the 2 × 2 × 2 extension (96 atoms) of CeO_2 unit cell with Monkhorst–Pack k-point mesh of 4 × 4 × 4. Atomic positions were relaxed within a cubic cell, and the lattice parameters of perfect CeO_2 and Cr-doped CeO_2 were obtained using the Murnaghan equation of state. Forces were converged to 0.01 eV/Å in all calculations.

Nudged elastic band (NEB) calculations were performed to obtain diffusion paths and barrier energies with seven replicas, including five nudged intermediate images. The spring constant linking images was 5.0 eV/Å and the conversion criteria were defined that resultant forces, including the spring forces, were less than 0.01 eV/ Å. The energy barrier was obtained by applying the climbing image algorithm [7], which allowed the determination of the saddle point at the transition state.

To elucidate the mobility of oxygen for pure and Cr-doped CeO_2, nudged elastic band calculation was conducted. Figures 1a and 1b show the diffusion path of an oxygen atom to the vacancy site and migration barrier. Compared to pure CeO_2 (0.41 eV), a much lower migration barrier was observed in Cr-doped CeO_2 (0.28 eV). In the case of the pure CeO_2, electron polaron (Ce^{3+}) exists at the next nearest neighbor of the oxygen vacancy, and diffusion of the polaron accompanied with oxygen diffusion was observed; Rapid polaron diffusion in reduced CeO_2 has been discussed previously [11]. As a result of the NEB calculation, diffusion constants at 400 °C are 5×10^{-11} m^2 s^{-1} for CeO_2 and 5×10^{-10} m^2 s^{-1} for Cr-doped CeO_2. The high diffusivity of oxygen in Cr-doped CeO_2 is one of the origins to cause high oxygen mobility at low temperature observed in the experiments. This result was published in ref. [12].

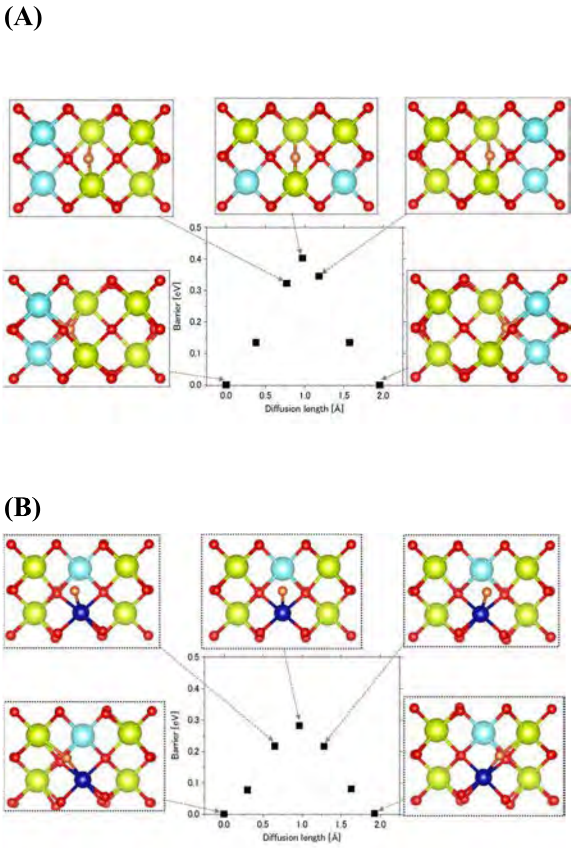

Figure 1 Energy barrier of oxygen atom diffusion to a vacancy site obtained by NEB calculation for (A) CeO_2 and (B) Cr-doped CeO_2. Light green, sky blue, dark blue, red, and orange balls represent Ce^{4+} ion, Ce^{3+} ion, Cr, O, and diffusing oxygen, respectively.

References

[1] Kresse, G.; Furthmuller, J., *Phys. Rev. B* 1996, 54 (16), 11169-11186.

[2] Kresse, G.; Joubert, D., *Phys. Rev. B* 1999, 59 (3), 1758-1775.G. [3] Perdew, J. P.; Burke, K.; Ernzerhof, M., *Phys Rev Lett* 1996, 77 (18), 3865-3868.

[4] Dudarev, S. L.; Botton, G. A.; Savrasov, S. Y.; Humphreys, C. J.; Sutton, A. P., *Phys. Rev. B* 1998, 57 (3), 1505-1509.

[5] Wang, J.; Gong, X.-Q., *Appl. Surf. Sci.* 2018, 428, 377-384.

[6] Keating, P. R. L.; Scanlon, D. O.; Morgan, B. J.; Galea, N. M.; Watson, G. W., *J. Phys. Chem. C* 2012, 116, 2443-2452.

[7] Henkelman, G.; Uberuaga, B.P.; Jonsson, H., *J. Chem. Phys.* 2000, 113 (22), 9901-9904.

[8] Wang, B.; Xi, X.; Cormack, A. N., *Chem. Mater.* 2014, 26, 3687-3692.

[9] M.V. Ganduglia-Pirovano, J.L. Da Silva, J. Sauer, Phys. Rev. Lett., 102 (2009), Article 026101

[10] Yu, M.; Trinkle, D. R., *J. Chem. Phys.* 2011, 134, 064111.

[11] Nakayama, M.; Ohshima, H.; Nogami, M.; Martin, M., *Phys. Chem. Chem. Phys.,* 2012, 14, 6079-6084.

[12] X. Hao, A. Yoko, K. Inoue, Y. Xu, M. Saito, C. Chen, G. Seong, T. Tomai, S. Takami, A.L. Shluger, B. Xu, T. Adschiri, Y. Ikuhara,, Acta Materialia, 203, 116473 (2021)

Reduction of Rare Metals in Formic Acid Decomposition Catalysts and Oxygen Storage Materials

Yuji KUNISADA

Center for Advanced Research of Energy and Materials, Faculty of Engineering,
Hokkaido University, Sapporo, Hokkaido 060-8628

We investigated the catalyst adsorption and diffusion properties on light-element element doped graphene with the aid of the first-principles calculation based on the density functional theory (DFT). Besides, we investigated the oxygen absorption properties of heteroatom-substituted brownmillerite-type oxides.

At first, we investigated the stabilities of Cu atoms embedded in light-element doped graphene. We considered embedded Cu atoms coordinated with various substituted dopants. We performed the total energy and electronic structure calculations using The Vienna Ab initio simulation package (VASP). We installed a parallelized VASP with Intel® MPI Library and Intel® Math Kernel Library. We revealed that the stabilities of Cu atoms embedded in light-element doped graphene strongly depend on the coordinated atoms. In the cases of large coordinated atoms, The Cu atoms protrude from graphene basal planes. We also investigated the catalytic activity using a theoretical volcano plot reported in the previous study.[1] From the adsorption energy of intermediates, we estimated the reaction activities. We found that the stable Cu atoms embedded in graphene show higher activity than unstable Cu clusters on graphene.

We investigated the oxygen absorption properties of partially substituted Ca_2AlMnO_5. We revealed that rotation of coordination polyhedra of cations releases the distortion induced by heteroatom doping. In addition, we investigated the effects of Pt addition on oxygen storage properties.

We also studied the adsorption properties and catalytic activities [3] and chemical bonding states [4] of Pt sub-nano clusters on light-element element doped graphene.

References

[1] J. S. Yoo, F. A.-Pedersen, J. K. Nørskov, F. Studt, ACS Catal. 4 (2014) 1226.

[2] A. Sato, G. Saito, K. Abe, Y. Kunisada, N. Sakaguchi, T. Akiyama, T. Nomura, J. Alloys Compd. 851 (2021) 156817.

[3] S. Hasegawa, Y. Kunisada, N. Sakaguchi, Vac. Surf. Sci. 63 (2020) 413.

[4] R. Sugimoto, Y. Segawa, A. Suzuta, Y. Kunisada, T. Uchida, K. Yamazaki, K. Gohara, J. Phys. Chem. C 125 (2021) 2900.

Ab initio analysis on the stability of magnetic ternary alloys

Yasutomi TATETSU

Meio University, Biimata, Nago, Okinawa 905-8585

Adding a small amount of third elements in binary systems not only stabilizes system but also changes these physical properties. Recently, a new ternary alloy was discovered by introducing a third element of In into $L1_2$-FePd$_3$ by Teranishi's group in Kyoto University [1]. Other interesting example is Nd–Fe amorphous phases which can be crystalized after adding Ga in Nd–Fe–B sintered magnets. Although the physical aspects of these added elements are unclear and cannot be understood deeply only through experiments.

In this study, we conducted theoretical analyses for the stability of an In-doped novel Fe–Pd and Ga-dope Nd–Fe ternary alloys using OpenMX. The model structures for the calculations were based on the chemical composition ratio obtained from experiments.

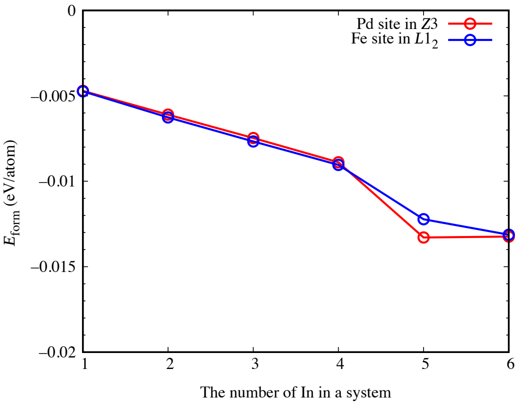

Figure: Formation energies for $L1_2$-(Fe, In)Pd$_3$ and $Z3$-Fe(Pd, In)$_3$.

For In-doped Fe–Pd ternary alloys, the In sites were chosen by replacing Fe or Pd sites with a special-quasirandom-structure method implemented in the Alloy Theoretic Automate Toolkit [3]. The figure illustrates the formation energies of $L1_2$-(Fe, In)Pd$_3$ and $Z3$-Fe(Pd, In)$_3$ when the number of In in a system takes from 1 to 6. By comparing these formation energies, $Z3$-Fe(Pd, In)$_3$ can be more stable than $L1_2$-(Fe, In)Pd$_3$ only in a narrow range of the In content. This tendency can be seen in the experimental results from XRD, EXAFS, and STEM-EDS analyses.

In Ga-doped Nd–Fe ternary alloys, we found that Ga is a key not only to stabilizing the fluorite-type crystal structure but also to suppressing its Curie temperature, which might be one of the reasons to explain why Ga-added Nd–Fe–B sintered magnets have high coercivity [4].

References

[1] K. Matsumoto, R. Sato, Y. Tatetsu, T. Teranishi, *et al.*, submitted.

[2] http://www.openmx-square.org

[3] A. van de Walle *et al.*, Calphad Journal **42**, 13 (2013).

[4] Yuta Ainai *et al.*, Jpn. J. Appl. Phys., **59**, 06094 (2020)

Fusion of computational material science and data-driven science with massively parallel computation

Takeo Hoshi

[1]*Department of Applied Mathematics and Physics, Tottori University,*

4-101 Koyama-Minami, Tottori 680-8550, Japan.

The present project was carried out for several topics in the fusion of computational material science and data-driven science on the ISSP supercomputer. The main collaborators are I. Mochizuki, T. Hyodo (KEK-IMSS-SPF), T. Hanada (Tohoku U), K. Hukushima (U Tokyo), K. Yoshimi, Y. Motoyama (ISSP), T. Fujita (IMS), Y. Yamamoto (UEC), Y. Miyatake (U. Tokyo).

The first topic is the development of the data analysis software of total-reflection high-energy positron diffraction (TRHEPD), a novel experimental technique for surface structure determination [1-6]. Experiments are being conducted intensively at the Slow Positron Facility, Institute of Materials Structure Science, High Energy Accelerator Research Organization. Figure 1 shows the structure determination of the $Si_4O_5N_3$ / 6H-SiC (0001)-($\sqrt{3}\times\sqrt{3}$) R30° (SiON) surface structure [3]. The software development activity was promoted to Project for Advancement of Software Usability in Materials Science in ISSP (https://www.pasums.issp.u-tokyo.ac.jp) in FY2020 and FY2021. Our software was called '2DMAT' and was published as an open-source software [4,5]. A TRHEPD simulator was required for the data analysis by 2DMAT and we used the simulator program 'sim-trhepd-rheed' originally developed by T. Hanada. [4,6].

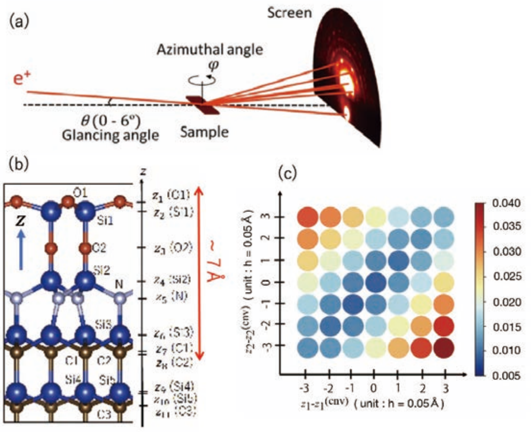

Fig.1 (a) Schematic figure of TRHEPD experiment. (b) The side view of $Si_4O_5N_3$ / 6H-SiC (0001)-($\sqrt{3}\times\sqrt{3}$) R30° (SiON) surface structure. (c) TRHEPD data analysis of the SiON surface structure [3]. The z-coordinate of the surface atom layers is denoted as $z_1, z_2, \ldots, z_7$. The color-coded isovalue plots of the R-factor, the residual function between the experimental and calculated data, on the local grid of the $z_1 - z_2$ plane [3].

The second topic is the method and application of large-scale electronic structure calculations for organic and other materials [7-10]. The study was carried out by our original code ELSES (http://www.elses.jp/), an order-*N* electronic state calculation code with an *ab-initio*-based tight-binding method and a fragment-molecular-orbital-based method. In particular, an excited-state theory was constructed for disordered Pentacene/C60 Interfaces [9-10]. The third topic is the development of several fundamental numerical algorithms [11-12].

References

[1] Development of data-analysis software for total-reflection high-energy positron diffraction (TRHEPD), K. Tanaka, T. Hoshi, I. Mochizuki, T. Hanada, A. Ichimiya, T. Hyodo, Acta. Phys. Pol. A 137, 188-192 (2020).

[2] Two-stage data-analysis method for total-reflection high-energy positron diffraction (TRHEPD), K. Tanaka, I. Mochizuki, T. Hanada, A. Ichimiya, T. Hyodo, T. Hoshi, JJAP Conf. Series, in press; Preprint: https://arxiv.org/abs/2002.12165

[3] Data-driven sensitivity analysis in a total-reflection high-energy positron diffraction (TRHEPD) experiment of the $Si_4O_5N_3$ / 6H-SiC (0001)-($\sqrt{3} \times \sqrt{3}$) R30° , T. Hoshi, D. Sakata, S. Oie, I. Mochizuki, S. Tanaka, T. Hyodo, K. Hukushima, Submitted; Preprint: https://arxiv.org/abs/2103.04875

[4] T. Hoshi, Y. Motoyama, T. Hanada, Y. Konishi and K. Yoshimi, poster presentation, CCMS Workshop of the data science in material science, online, 22-24. Feb. (2021).

[5] https://www.pasums.issp.u-tokyo.ac.jp/2DMAT; https://github.com/issp-center-dev/2DMAT

[6] https://github.com/sim-trhepd-rheed/

[7] Computational study for electrical conductivity properties of organic semiconducting polymers and metal complex-host systems, M. Ishida, M. Arita, S. Nishino, T. Hoshi, HPCI Research Report, to appear.

[8] Recent progress in large-scale electronic state calculations and data-driven sciences, T. Hoshi, S. Ito in *Handbook of Silicon Based MEMS Materials and Technologies 3rd Ed.*, Elsevier, 2020.

[9] Revisiting the Charge-Transfer States at Pentacene/C60 Interfaces with the GW/Bethe–Salpeter Equation Approach, T. Fujita, Y. Noguchi and T. Hoshi, Materials 13, 2728 (2020).

[10] FMO-based excited state dynamics in molecular aggregates, T. Fujita and T. Hoshi, in *Recent advances of the fragment molecular orbital method Subtitle: Enhanced performance and applicability, ed. Y. Mochizuki, S. Tanaka, and K. Fukuzawa,* Springer, 2021.

[11] Kω - Open-source library for the shifted Krylov subspace method of the form $(zI - H)x = b$, T. Hoshi, M. Kawamura, K. Yoshimi, Y. Motoyama, T. Misawa, Y. Yamaji, S. Todo, N. Kawashima, T. Sogabe, Comp. Phys. Comm. 258, 107536 (2021).

[12] A parallelizable energy-preserving integrator MB4 and its application to quantum-mechanical wavepacket dynamics, T. Sakai, S. Kudo, H. Imachi, Y. Miyatake, T. Hoshi, Y. Yamamoto, Japan J. Indust. Appl. Math. 38, 105 (2020).

Reduction of Rare Metals in Fuel Cell Catalysts and Hydrogen Permeable Membrane

Norihito Sakaguchi

Center for Advanced Research of Energy and Materials, Faculty of Engineering,

Hokkaido University, Sapporo, Hokkaido 060-8628

We investigated the catalytic properties of Pt sub-nano clusters on light-element doped graphene and hydrogen dissolution and diffusion properties in the interfaces of ceramic materials, with the aid of the first-principles calculation based on the density functional theory (DFT).

At first, we investigated the adsorption and catalytic properties of Pt single atoms and Pt sub-nano clusters on light-element doped graphene. We performed the total energy and electronic structure calculations using The Vienna Ab initio simulation package (VASP). We installed a parallelized VASP with Intel® MPI Library and Intel® Math Kernel Library. In this study, we focused on oxygen reduction reactions (ORR). In order to evaluate the catalytic properties, we calculated the energy diagrams of whole ORR paths. We also made a volcano-plot to show relationship between the adsorption energy of catalytic activities and intermediate species of chemical reactions.[1] We found that ORR activity of Pt_1 is higher than those of Pt_2 and Pt_3. From the viewpoint of a support effect caused by light-element doped graphene, the catalytic activity of Pt_1 more strongly depends on the light-element dopants in graphene lattice than those of Pt_2 and Pt_3. Therefore, Pt single atoms on light-element doped graphene support is a promising candidate for a new catalyst which is better than the current fuel cell catalyst, i.e., bulk Pt catalyst.

We also investigated the chemical bonding between N-doped graphene and Pt single atoms using DFT calculations and transmission electron microscopy combining with electron energy loss spectroscopy, and the hydrogen dissolution and diffusion properties in the interfaces of TiN with residual impurity gasses.

References

[1] J. K. Nørskov, J. Rossmeisl, A. Logadottir, L. Lindqvist, J. R. Kitchin, T. Bligaard, H. Jónsson, J. Phys. Chem. B, 108 (2004) 17886.

[2] S. Hasegawa, Y. Kunisada, N. Sakaguchi, Vac. Surf. Sci. 63 (2020) 413.

[3] R. Sugimoto, Y. Segawa, A. Suzuta, Y. Kunisada, T. Uchida, K. Yamazaki, K. Gohara, J. Phys. Chem. C 125 (2021) 2900.

First-principles study on physics of gap-state control at metal/semiconductor interfaces: II & III

Takashi NAKAYAMA
Department of Physics, Chiba University
1-33 Yayoi, Inage, Chiba 263-8522

Due to the break of atomic bonds and the lack of translational symmetry, gap states appear in semiconductor layers around metal/semiconductor interfaces, which have the energy position in the band gap and are localized around the interface. These states induce the electron transfer between metal and semiconductor layers and determine a variety of physical properties at the interface, such as Schottky barrier (SB) and carrier transport. However, it is still unclear how to control these gap states. In this works, we studied the SB and tunneling current at various interfaces and clarify the origins of gap-state generation/annihilation and deformation using the first- principles calculations.

First, we consider metal/Ge interfaces, where Fermi energies of most of simple metals are located around the valence-band top of Ge not depending on the kinds of metals. This is called the Fermi-level (FL) pinning and interrupts desirable low-resistive metal/n-Ge contacts. Although the breakdown of FL pinning was recently observed at the Bi/Ge(001) interface, its origin has not been clarified. To simulate the interfaces, we adopt (2×2) (Bi, Al)/Ge(001) repeated-slab models with various interface structures and calculate their SBs using local potential profiles.

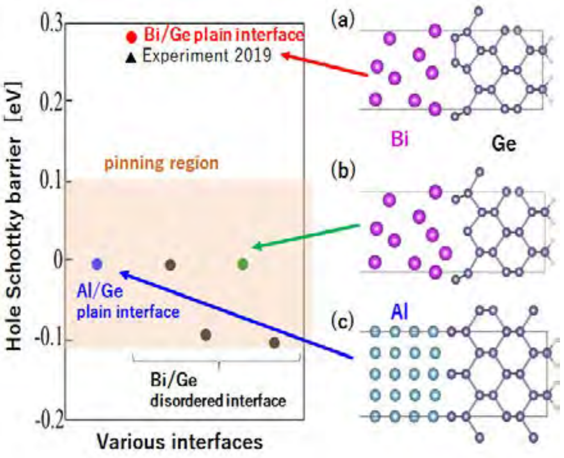

Fig.1. Left: calculated Schottky barriers for hole carriers at various (Bi, Al)/Ge interfaces. Right: schematic pictures of interface structures. (a): abrupt plain Bi/Ge interface, (b): disordered Bi/Ge interface, and (c): plain Al/Ge interface.

Figure 1 shows calculated SBs for hole carriers ate various interfaces. The SBs at (b) disordered Bi/Ge and (c) plain Al/Ge interfaces are around 0.0eV corresponding to the FL pinning, while the SB at (a) plain Bi/Ge interface has a large value around above 0.3eV, which is in good agreement with experiments. The origin of such SB variation is understood by observing the projected densities of states (PDOS) of interface Ge atoms, which are shown in Fig.2. For (b) and (c) interfaces, the continuous PDOS, thus the gap states, appear around 0.0eV due to the orbital hybridization between metal and Ge atoms, which induces the electron transfer from metal to Ge and realizes the FL pinning. On the other hand, we can see the suppression of gap states in the PDOS of interface Ge for the (a) interface, which realizes the FL-depinning. This suppression occurs due to the weak contact of Bi and Ge layers, which is caused by the lattice mismatch originating from the large atomic radius of Bi and produces the Ge-Ge dimer bonds at the interface as shown in the right of Fig. 1. In this way, the interface Ge-Ge dimer bonds annihilates the gap states in interface Ge layers and produces the large change of the SB values.

Next, we consider how the gap states change in electric fields. We consider the tunneling current at indirect-band-gap Si and GaP, and direct-band-gap GaAs and InP p/n junctions, in the cases without

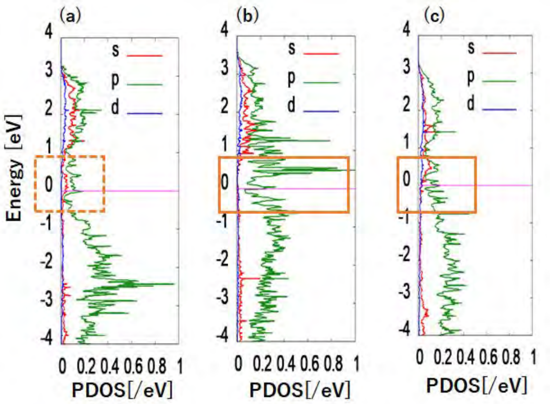

Fig.2. Calculated projected densities of states of interface Ge atoms around (a) plain Bi/Ge, (b) disordered Bi/Ge, and (c) plain Al/Ge interfaces, which respectively correspond to interfaces shown in Fig.1. Orange boxes indicate the band-gap region of Ge.

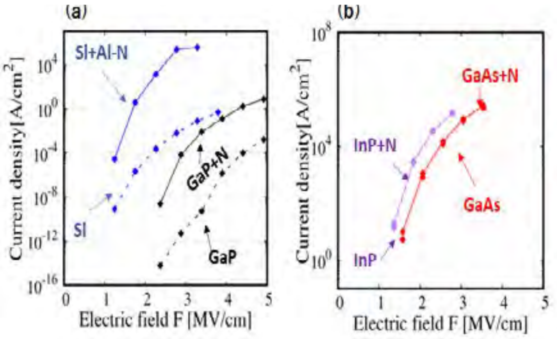

Fig.3. Calculated tunneling currents at (a) indirect-band-gap Si and GaP, and (b) direct-band-gap GaAs and InP p/n junctions, as a function of electric field. The cases without and with N-atom dopants are shown.

and with N-atom dopants. Figures 3(a) and 3(b) show calculated currents for these interfaces as a function of applied electric field. It is clearly seen that the current is much larger for the latter junctions, which is because the latter system have direct band gap and have larger interband tunneling transitions.

When N-atom dopants are embedded in p/n junctions, the current is markedly enhanced in the cases of indirect band-gap systems, i.e., Si and GaP. This enhancement occurs because the dopant gap state produces the resonance states with the conduction-band states of host Si layers around the junction in electric field as shown in Fig.4(b), and such resonance remarkably increases the tunneling probability across the junction as shown in Fig.4(a). On the other hand, in the cases of direct band-gap systems, as seen in Fig.3(b), there is no increase in the current by the dopants. This is because the dopant gap state is strongly localized as in Fig.4(d) and the increase of tunneling is small as in Fig.4(c). By analyzing electronic structures, we found that the difference in the dopant effects on tunneling currents between indirect and direct band-gap systems reflects the characters of conduction-band states in these systems.

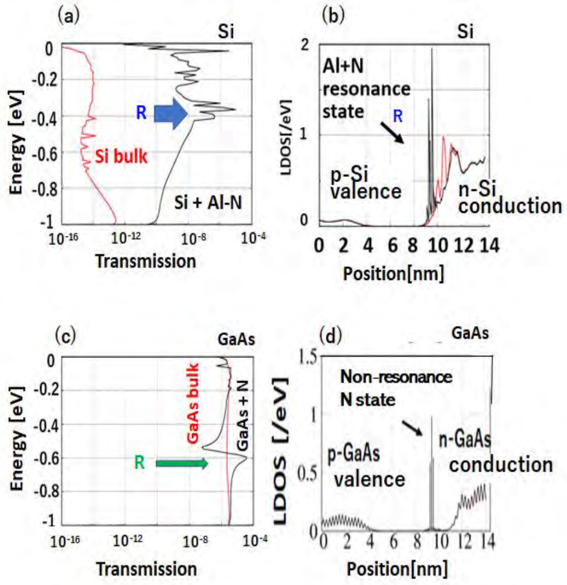

Fig.4. Calculated transmission spectra of electrons and local density of N-atom dopant states at the Si p/n junction ((a) and (b)), and the GaAs p/n junction ((c) and (d)). The cases of junctions without dopants are also shown by red lines.

All these calculations were performed using the xTAPP, VASP, and our original pspwf codes. In order to realize the calculations for the present interface systems, because the system is made of a large number of atoms (500-2000 atoms), the advanced computing facility having multi-task and higher-speed CPU (more than 1280 cores × 2.0GHz), larger-size memory (around 256GB), and larger-size strange (more than 2 TB) is indispensable. These conditions are realized only by the present ISSP supercomputing systems.

First-principles Calculations on Magnetism in 2D Magnetic Materials

Kunihiko Yamauchi

Institute of Scientific and Industrial Research (ISIR-SANKEN), Osaka University, 8-1 Mihogaoka, Ibaraki, Osaka 567-0047

We have studied the magnetism in 2D magnetic materials and discussed our current understanding of the mechanisms using the first-principles density functional theory (DFT) calculations.

First, we systematically investigated the magnetocrystalline anisotropy energy (MAE) of the Co-based transition-metal thin films using DFT HiLAPW code at the ISSP *seikirei* supercomputer. The results show that the large perpendicular MAE can be achieved by tuning atomic-layer stacking in Ni-Co thin film. The MAE is decomposed into single-layer contributions and inter-layer contributions to reveal the fact that not only the on-site SOC of 3*d* elements but also the strong hybridization between these elements play an important role to determine the MAE. The small effect of electric fields on the magnetocrystalline anisotropy also has been found in Ni-Co thin film, making this system becomes the potential for future spintronics applications [1].

Secondly, we investigated the magnetic stability in 2D magnetic material VI_3 making a comparison with CrI_3 using the VASP code at the ISSP *ohtaka* supercomputer. VI_3 is a Mott insulator with an energy band gap is 0.34 eV. In VI_3, under the trigonal crystal field with D_{3d} point group, the t_{2g} orbital state is split into a_{1g} and e_g' states. The a_{1g} orbital state plays an important role in inter-layer magnetic exchange interaction in a bilayer structure. By using Wannier90 code that is interfaced with the VASP code, we estimated the hopping integral and discussed the inter-layer magnetic exchange interaction based on the virtual-hopping mechanism. In the bilayer VI_3 case, we studied two structures corresponding to *R3* and *C2/c* phases in bulk VI_3, namely AB and AB' stacking. The application of electric field enables to switch the magnetic ordering from inter-layer AFM to FM in AB' stacking. This finding may pave a way to the spintronics application with 2D materials [2].

References

[1] T. P. T. Nguyen, K. Yamauchi, K. Nakamura, T. Oguchi, Journal of the Physical Society of Japan, **89**, 114710 (2020).

[2] T. P. T. Nguyen, K. Yamauchi, T. Oguchi, D. Amoroso, S. Picozzi, arXiv:2102.04173 (2021).

Band structure calculation based on the group theory

Mineo SAITO
Institute of Science and Technology, Kanazawa University
Kakuma, Kanazawa, 920-1192 Japan

In the field of spintronics, the spin-orbit coupling (SOC) is considered to generate new functions. One of the most important phenomena is concerning topological insulators. We emphasize that the group theoretical analysis is necessary to deeply understand the SOC effect on electronic structures but the analysis has been insufficient so far. We have developed a method to identify irreducible representations (IR) for the SOC bands which are obtained by using first-principles plane wave base calculations. The identification can be done by using computers and thus mis-identification can be avoided.

The IR of the band having the q-degeneracy is determined by using the following expression :

$$Q^{\alpha} = \frac{1}{l} \sum_{j=p}^{p+q-1} \sum_{m=1}^{l} \chi^{\alpha}(C_m)^{*} < \Psi_{\vec{k}}^{\ j} \,|\, C_m \,|\, \Psi_{\vec{k}}^{\ j} >$$

Where l and $\chi^{\alpha}(C_m)$ are the order of the k group and the character for the $m-$th symmetry operation C_m, respectively. $\Psi_{\vec{k}}^{\ j}$ is the Bloch function for the band index j and the wavenumber $\vec{k}$. The wavefunction (does not) belong to the IR of α when $Q^{\alpha} = 1$ ($Q^{\alpha} = 0$).

In this report, we focus on our results on group-IV two dimensional materials.

In the case of graphene, the Dirac cone is found to belong to the two-dimensional IR of E” in the D_{3h} group. The SOC is found to split the doubly degenerated level into $E_{1/2}$ and $E_{3/2}$ levels. The former level is found to be higher than the latter level and we clarify the reason for this energetical order by using a tight binding model. We evaluate the topological invariant and confirm that the values for both buckled and non-buckled structures are 1, suggesting the possibility of topological insulators.

Effects of solvents on properties of artificial-retina molecule: ab initio molecular dynamics simulations

Satoshi OHMURA

Research Center for Condensed Matter Physics / Department of Environmental and Civil Engineering

Hiroshima Institute of Technology, Saeki-ku, Hiroshima, 731-5143

Molecular dyes are attractive great attention because of their application for various optical devices such as solar cell and artificial retina. To improve functionality of the dye molecule, it is used to control the band gap. Therefore, theoretical studies based on the density functional theory tried to understand the structural and photoelectrical properties such as absorption and emission properties in the gas phase. However, the working conditions of such dye molecules in nature and in the industrial applications entail their solvation. We have systematically investigated the effects of solvent, H_2O, acetonitrile, tetrahydrofuran, and chlorobenzene on light-absorption properties in a photoelectric dye (NK-5962) which is better candidate for retinal prostheses by means of ab initio molecular-dynamics simulations. To calculate absorption spectra, we adopted the Time-Dependent Density-Functional linear-Response Theory (TDDFLRT), proposed and formulated by Casida. The simulation reveals that all solvents slightly affect the light-absorption spectrum but all systems has a main peak at visible light region. However, the excited charge dynamics after light absorption is influenced a great deal by H_2O. Without H_2O, the generated hole by light-absorption in NK-5962 transfers to counter-ion cite at less than 100 fs. On the other hand, in the case of the system with H_2O, the hole stays in NK-5962 site. Our simulation clarified that these effects are attributed to interaction between H_2O and counterion of NK5962. In addition to retina molecule, we have investigated the dissociation mechanisms from highly charged bromophenol $(C_6H_5OHBr)^{n+}$ ($n \leq 10$) by ab initio MD simulations [1]. The charge state dependence of dissociation mechanisms is observed by this simulation. We also investigated the intramolecular charge transfer time by using nonadiabatic quantum-mechanical molecular-dynamics with surface hopping approach. It is found that the hole transfer from the Br site to the molecular counterpart in ~5 fs.

References

[1] S. Ohmura, K. Nagaya, F. Shimojo and M Yao ; Z. Phys. Chem. 2021; 235(1–2): 169–187

Structural and transport properties of multi-component liquid Fe mixtures under high pressure

Satoshi OHMURA

Research Center for Condensed Matter Physics / Department of Environmental and Civil Engineering

Hiroshima Institute of Technology, Saeki-ku, Hiroshima, 731-5143

We have investigated the effects of light elements (LE) such as H, C, O, Si, and S on the structural and transport properties of liquid Fe under high pressure by ab initio molecular dynamics (MD) simulations. It is believed that Earth's outer core consists of liquid iron (or liquid-nickel alloy) with LE impurities. LE have a strong influence on structural and transport properties of liquid iron under high pressure. However, there are still many uncertainties regarding the influence of LE. For Fe-LE binary systems, we clarified the structural properties and interactions between LE atoms at core-mantle boundary condition [1]. The simulations clarify that H, C, and O are incorporated into liquid Fe interstitially while Si and S are "substitutional" type impurities. Under these circumstances, in this study, we have studied structural and transport properties of liquid ternary system consisting of liquid Fe and two types of LE by using ab initio MD simulations. From our simulations, it is found that Si and S atoms show "substitutional" behavior while H and O atoms show "interstitial" behavior even in ternary systems. For the transport properties, LE in the ternary systems decrease electric conductivity of liquid Fe as same as binary systems. The decreasing rates are between those of binary systems as shown in Fig. 1.

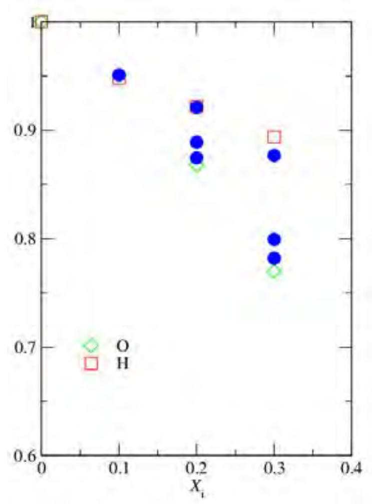

Fig. 1: Change of electrical conductivity of liquid Fe-H-O as a function of concentration of LE. Blue circles show ternary systems. Red and green squares show binary system.

References

[1] S. Ohmura, T. Tsuchiya and F. Shimojo: Physica Status Solidi B, **257**, 2000098 (2020)

Impact of the molecular quadrupole moment in the molecularly mixed film of organic semiconductors

Susumu Yanagisawa
Faculty of Science, Department of Physics and Earth Sciences, University of the Ryukyus
Nishihara, Okinawa, 903-0213

The energy levels of organic semiconductors are primarily determined by the molecular orbital energies of constituent molecules. Recent studies have, however, shown that the energy levels can be changed by the mixing ratio of two molecules which have different permanent quadrupole moments. From the good correlation between the magnitude of the mixed film's energy shift and the constituent molecules' permanent quadrupole moment, it was noted that the molecular quadrupole plays an important role in the energy shift.

In this study, I theoretically examined the mixed films of zinc phthalocyanine (ZnPc) and perfluorinated ZnPc (F_{16}ZnPc), which have permanent quadrupole moments with opposite directions. Here, as was successfully applied to organic semiconductor thin films[1, 2], a combination of the *GW* approximation suitable in general to solid or bulk systems and a periodic slab approach at the DFT-GGA level was employed. From the theoretical electronic polarization energy D and electrostatic energy S as a function of mixing ratio, ionization energies and electron affinities were estimated.

I performed first-principles electronic structure calculations with the STATE program code to determine the optimized geometries of the pristine crystals as well as 1:1 mixed thin films of ZnPc and F_{16}ZnPc. To check the convergence of the electrostatic energy on the number of the layers in the simulation cell, one, two, and three monolayers (1−3 ML) films were modeled by periodic slabs. For the pristine crystals, I fixed the lattice constants to experimental values of the monoclinic and triclinic forms for ZnPc and F_{16}ZnPc, respectively. The two stable facets are denoted by "edge-on" and "face-on" for each of the crystals, depending on the orientation of the molecules at the surface (see Fig. 1). Since the experimental lattice constants were not available for the mixed film, those of the pristine crystals were used for the mixed films.

The 1 ML slabs for the pristine ZnPc and F_{16}ZnPc films consisted of 2 molecules, and 4 molecules comprised the 1 ML mixed film in the ratio 1:1. The vacuum layer with a thickness of 2.0 nm was inserted. I optimized the geometric structures of the standing 1−3 ML slabs by taking into account the van der Waals forces within PBE-D2. To describe the orientation dependence of the electrostatic interaction, I took the difference in the HOMO or the LUMO energy of ZnPc and F_{16}ZnPc between the slab and an isolated gas-phase molecule.

The electronic polarization energy was described by the many-body perturbation theory, within the G_0W_0 approximation with the *GW* space-time code. The fundamental gaps were obtained as the difference between the highest occupied and lowest unoccupied band energies averaged over the Brillouin zone. The numbers of cores used in the calculations were 256∼512.

The gaps were determined to be 2.26 eV and 2.19 eV for the monoclinic ZnPc and the triclinic F_{16}ZnPc bulks, respectively. For the gas phase fundamental gap, I estimated the electron affinity (A_g) and the ionization energy (I_g) at the HSE06/spaug-cc-pVTZ level of theory with the delta self-consistent field approach using Gaussian16 Revision B.01 installed in my own computer resources. I did not use the gas-phase fundamental gap at the G_0W_0 level, since the G_0W_0 treatment tends to over-screen the injected charge in gas-phase molecules[3]. The electrostatic energy S was estimated as the difference in HOMO/LUMO energy between the surface slab and the gas phase estimated with the GGA-PBE level of theory[1, 2]. Based on the bulk fundamental gap obtained with G_0W_0 and the theoretical gas phase ionization energy I_g and electron affinity A_g, the electronic polarization D was obtained.

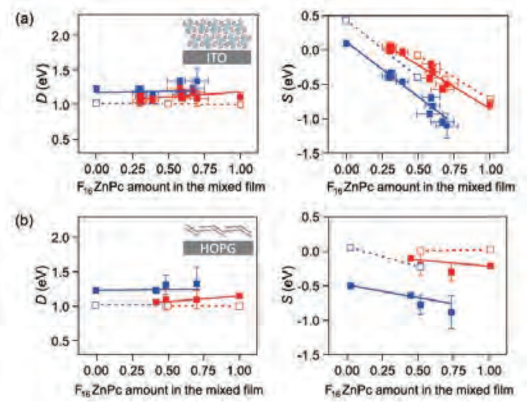

Figure 1: Theoretical polarization energy D and electrostatic energy S as a function of molar mixing ratio of F_{16}ZnPc in the mixed film. The calculated results are displayed by dashed lines and the experimental values are by solid lines.

Figure 1 displays the calculated D and S, along with the experimental values[4]. Overall, the theoretical polarization energies are in good agreement with experiments. In case of the electrostatic energies, the qualitative trend depending on the F_{16}ZnPc amount in the mixed film is similar.

It is found that the polarization energies are almost the same in the ”edge-on” and ”face-on” configurations. The result implies the nature of the electronic polarization originating from the stabilized injected charge surrounded by the induced polarization clouds inside the bulk, and thus does not depend on the molecular orientation at the surface of the films.

On the other hand, the electrostatic energy changes more rapidly as a function of the mixing ratio in the ”edge-on” configuration than in ”face-on”. The different trend comes from the different orientation of the molecules at the surfaces of the mixed thin film: in the ”edge-on” configuration in which the constituent molecules are standing on the surface of the film, the orientation angle is very sensitive to the mixing ratio, while in the ”face-on” configuration, the molecular planes are parallel to the film surface and the orientation angle does not change significantly with respect to change in the mixing ratio. The change in the electrostatic energy in the molecular crystal film comprised of molecules with appreciable quadrupole moment such as ZnPc and F_{16}ZnPc may be elucidated in terms of the electrostatics[5]. The present finding may lead to the insight into tuning of the charge injection energy levels at the surfaces of organic semiconductors.

References

[1] S. Yanagisawa: Jpn. J. Appl. Phys. **59** (2020) 031002.

[2] K. Yamada, S. Yanagisawa, T. Koganezawa, K. Mase, N. Sato and H. Yoshida: Phys. Rev. B **97** (2018) 245206.

[3] S. Rafaely-Abramson et al., Phys. Rev. B **88** (2013) 081204(R).

[4] Y. Uemura, S. A. Abd-Rahman, S. Yanagisawa and H. Yoshida: Phys. Rev. B **102** (2020) 125302.

[5] B. J. Topham and Z. G. Soos, Phys. Rev. B **84** (2011) 165405.

First principles exploration of the metastable phases of hydrides and their superconductivity

Ryosuke AKASHI
Institute for Solid State Physics, University of Tokyo
Kashiwa-no-ha, Kashiwa, Chiba 277-8581

Superhydrides that crystallize under extremely high pressure have attracted lots of interest since the discovery of high temperature superconductivity in solid hydrogen sulfide [1]. Recently, the domain of searching for new hydrides that possibly exhibit higher transition temperatures is getting broadened to ternary hydrides $AB\mathrm{H}_x$, resulting in the discovery of superconductivity in a C-S-H system with record of $T_\mathrm{c} = 286$ K [2].

We conducted exploration of the novel (meta)stable hydrides and calculations of superconducting properties of them. In particular, we contributed to an international theoretical-experimental study of a La-Y-H ternary hydride system. In their pure binary compositions LaH_x and YH_x, LaH_{10} and YH_6 have been discovered to form under pressure, both of which exhibit different forms hydrogen cage structures. The inverse, YH_{10} and LaH_6, are metastable according to simulations. Interestingly, it is predicted that their mixtures LaYH_{20} and LaYH_{12} can become stable at certain conditions, the origin of which may be a synergetic effect of La and Y. This prediction was verified by the experimentally observed diffraction patterns. We calculated their possible values of T_c, using the density functional theory for superconductors (SCDFT) [3, 4] to compare them with the experimentally observed T_c.

Here we append the the scheme of calculating T_c on the basis of SCDFT. First, the Kohn-Sham electronic and phononic structure calculations were performed using an open source code package QUANTUM ESPRESSO [5]. The generalized gradient approximation [6] for the exchange-correlation potential was employed. The optimized norm-conserving Vanderbilt pseudopotentials [7] was used for the calculations. Next, the dielectric matrix and matrix elements of the effective electron-electron Coulomb interaction were calculated with an in-house code. Finally using those data, the superconducting transition temperature was evaluated by solving the following SCDFT gap equation[3, 4, 8]

$$\Delta_{n\mathbf{k}} = -\mathcal{Z}_{n\mathbf{k}}\Delta_{n\mathbf{k}} - \frac{1}{2}\sum_{n'\mathbf{k}'}\mathcal{K}_{n\mathbf{k}n'\mathbf{k}'}\frac{\tanh[(\beta/2)E_{n'\mathbf{k}'}]}{E_{n'\mathbf{k}'}}\Delta_{n'\mathbf{k}'} \quad (1)$$

β denotes the inverse temperature. The exchange-correlation kernels $\mathcal{K}$ and $\mathcal{Z}$, which represents the effects of the electron-phonon and electron-electron interactions, are formulated in terms of the Kohn-Sham electronic and phononic properties.

Solutions of the Kohn-Sham equation was parallelized by MPI as implemented in pw.x code of QUANTUM ESPRESSO. The in-house code for calculating the dielectric matrix has been thread-parallelized by openmp. The SCDFT gap equation was solved without parallelization since it was less time-consuming. Calculations were mainly performed in System B.

Various synthesis protocols were executed for the La-Y-H samples and maximum T_c of $\sim$

Table 1: Superconducting transition temperature T_c calculated with the SCDFT gap equation Eq. (1). Coupling constant λ and typical frequency $\omega_{\ln}$ ([9]) of the electron-phonon coupling spectra are also presented.

	$LaYH_{12}$	$LaYH_{20}$
$T_c(SCDFT)$ (K)	191	252
λ	2.82	3.87
$\omega_{\ln}$	847	868

250 K was observed. The calculated superconducting transition temperatures, especially in LYH_{20}, show good agreement with this experiment (Table 1). This shows that the phonon-mediated pairing mechanism explains the superconductivity in the current ternary system. This result is to be published [10].

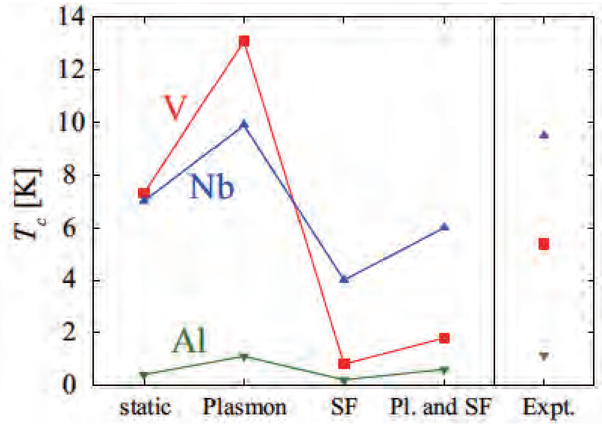

Figure 1: Impacts of the charge (plasmon) and spin fluctuations on superconducting T_c in V, Nb, and Al, taken from Ref. [11].

We also developed an extension of the SCDFT scheme to include the spin fluctuation effect, which is a continuous subject since a ISSP project in the fiscal year of 2018 [Project ID: H30-Ca-0046]. We examined the effects of the spin fluctuation and charge fluctuation on T_c in elemental metals, V and Nb. We found that the spin fluctuation strongly suppresses T_c. Experimentally observed T_c is smaller in V than in Nb, whereas the degree of the suppression effect depends on the character of atomic orbitals. This dependence results in correct reproduction of the T_c relation in those systems (Fig.1). This result has been published as a paper [11].

References

[1] A. P. Drozdov, M. I. Eremets, and I. A. Troyan, V. Ksenofontov, and S. I. Shylin, Nature (London) **525**, 73 (2015)

[2] E. Snider *et al.*, Nature (London) **586**, 373 (2020).

[3] M. Lüders, *et al.*, Phys. Rev. B **72**, 024545 (2005).

[4] M. A. L. Marques, *et al.*, Phys. Rev. B **72**, 024546 (2005).

[5] P. Giannozzi *et al*, J. Phys.: Condens. Matter **29**, 465901 (2017); http://www.quantum-espresso.org/.

[6] J. P. Perdew, K. Burke, and M. Ernzerhof, Phys. Rev. Lett. **77**, 3865 (1996).

[7] D. R. Hamann, Phys. Rev. B **88**, 085117 (2013); **95**, 239906 (2017).

[8] R. Akashi, M. Kawamura, S. Tsuneyuki, Y. Nomura, and R. Arita, Phys. Rev. B **91**, 224513 (2015).

[9] P.B. Allen and R.C. Dynes, Phys. Rev. B **12**, 905 (1975)

[10] D. V. Semenok *et al.*, arXiv:2012.04787; Mater. Today, in press.

[11] K. Tsutsumi, Y. Hizume, M. Kawamura, R. Akashi, and S. Tsuneyuki: Phys. Rev. B **102** (2020) 214515.

Helical channel at twin boundary of a boron-nitride atomic layer

Tatsuya ISHIKAWA, Yoshiyuki EGAMI and Hiroshi AKERA
Division of Applied Physics, Faculty of Engineering, Hokkaido University
Sapporo, Hokkaido, 060-8628

Helical channels, which suffer little from backscattering, have attracted much attention in valleytronics and theoretically studied in graphene on a boron nitride substrate [1, 2] and in a boron-nitride atomic layer (BNaL) with a twin boundary [3]. We focus on the BNaL twin boundary which can support a narrower helical channel. Twin boundaries of the BNaL are classified into unpolarized and polarized boundaries such as shown in Fig. 1 in which carbon chains are inserted at each twin boundary to relax the repulsion between cations and that between anions. In this work we have studied differences in electronic properties of helical channels between polarized and unpolarized twin boundaries.

We have made a first-principles calculation of the energy band of helical channels formed along BNaL twin boundaries (Fig. 1). We impose the periodic boundary condition perpendicular to channels so that the unit cell contains two twin boundaries. We have found that polarized and unpolarized twin boundaries have quite different helical channel bands: the distance in k space between helical channels belonging to K and K' valleys is much shorter in the polarized BCCB-NCCN arrangement [Fig. 1(b)] compared to that in the unpolarized NCB arrangement [Fig. 1(a)]. This result suggests a possibility of largely modifying transport properties through a helical channel by changing the atomic arrangement in the vicinity of the channel.

The computation in this work has been done using the facilities (system B and C) of the Supercomputer Center, the Institute for Solid State Physics, the University of Tokyo.

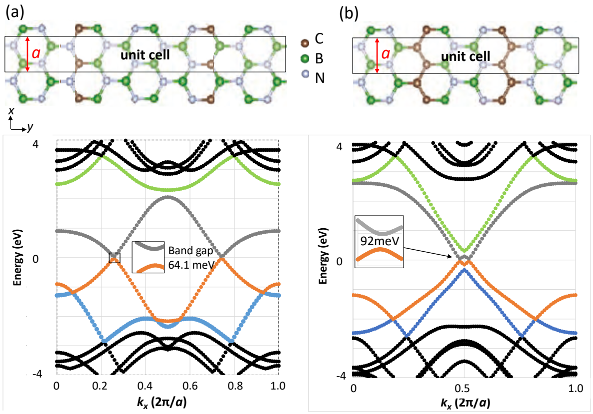

Figure 1: Helical channels at twin boundaries with (a) unpolarized NCB arrangement (b) polarized BCCB-NCCN arrangement. The periodic boundary condition is imposed in the y direction with periodicity of one unit cell. The zero of energy is taken at the Fermi energy.

References

[1] G.W. Semenoff, V. Semenoff, and Fei Zhou: Phys. Rev. Lett. **101** (2008) 087204.

[2] C. Hu, V. Michaud-Rioux, W. Yao, and H. Guo: Phys. Rev. Lett. **121** (2018) 186403.

[3] J. Jung, Z. Qiao, Q. Niu, and A. H. MacDonald: Nano Lett. **12** (2012) 2936.

First-principles study of quantum transport in nanostructures

NOBUHIKO KOBAYASHI
Department of Applied Physics, University of Tsukuba
1-1-1 Tennodai Tsukuba Ibaraki 305-8573

Theoretical investigations on transport properties are important not only for the fundamental research of science but also for the applications of electronics. We have developed the nonequilibrium Green's function (NEGF) method, and the O(N) time dependent wave-packet diffusion (TD-WPD) method on the basis of the density functional theory (DFT). By using these methods, we have investigated charge, head and spin transport properties of materials. [1]

We have developed a Simulation code for Atomistic Kohn-sham Equation (SAKE) for the ab-initio electron transport calculation based on the DFT and NEGF formalism. We have applied the method to analyses of thermoelectricity of magnetic semiconductors $CuFeS_2$. The electronic transport properties, Seebeck coefficient, and the figures of merit are estimated. We theoretically demonstrate the enhancement in the figure of merit by doping, which is in agreement with experimental work, and design doped systems for higher performance. [2]

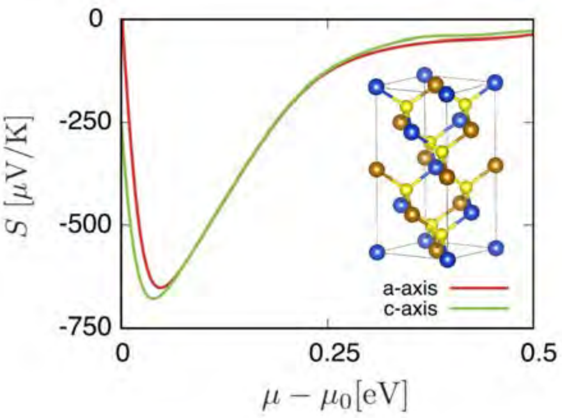

Figure 1: Seebeck coefficient of $CuFeS_2$ as a function of the chemical potential.

We developed the O(N) TD-WPD method for the quantum transport calculation of huge systems of up to 100 million atoms a decade ago. It is possible to calculate the conductivity and the mobility of the system with micron-order lengths at room temperature at the atomistic levels. We have proposed a prediction methodology to obtain charge transport properties of organic single crystals from their structural formula using TD-WPD method. We applied the method to C_{10}-DNBDT molecule, and succeeded in quantitative evaluation of charge mobility of the single crystal using our quantum wave-packet dynamical simulation method. It is shown that the proposed methodology is an effective theoretical design technique for efficiently developing new high-performance organic semiconductors. [3]

References

[1] N. Kobayashi, H. Ishii, K. Hirose, in *3D Local Structure and Functionality Design of Materials* eds H. Daimon, Y. C. Sasaki (World Scientific, 2018) p133.

[2] H.Takaki, N.Kobayashi, K.Hirose, *J. Phys.: Condens. Matter.* 32 325901(2020)

[3] H. Ishii, S. Obata, N. Niitsu, S. Watanabe, H. Goto, K. Hirose, N. Kobayashi, T. Okamoto, and J. Takeya, *Sci. Rep.* 10, 2524 (2020)

Magnetocaloric Effect of Transition-Metal Alloys

Hung Ba TRAN, Hiroyoshi MOMIDA, and Tamio OGUCHI
Institute of Scientific and Industrial Research, Osaka University,
8-1 Mihogaoka, Ibaraki, Osaka 567-0047, Japan

We study the magnetocaloric effect of transition-metal alloys by combining first-principles calculations and Monte-Carlo simulations. The parameters of the Monte-Carlo simulation are estimated from first-principles calculations. Several types of the magnetocaloric effect such as conventional (direct) magnetocaloric effect, giant magnetocaloric effect, anisotropic magnetocaloric effect, and inverse magnetocaloric effect can be considered by using our original program[1, 2, 3, 4]. The isothermal magnetic entropy change of $\mathrm{Mn}_{1-x}\mathrm{Cu}_x\mathrm{CoGe}$ alloy is shown in Fig. 1 (a). Stoichiometric MnCoGe has two phases, the low-temperature phase is orthorhombic while the high-temperature phase is hexagonal. Both the phases are ferromagnetic below different Curie temperatures. When there is a structural coupling between magnetic and structure part, the isothermal magnetic entropy change becomes gigantic as the $\mathrm{Mn}_{0.89}\mathrm{Cu}_{0.11}\mathrm{CoGe}$ case. We also perform speed-up tests for our massively parallel Monte-Carlo program with hybrid MPI and OpenMP in new System B as shown in Fig. 1 (b) and (c). We obtain a good scaling in the tests of OpenMP and MPI, that is quite important for further study such as virtual screening of magnetocaloric materials.

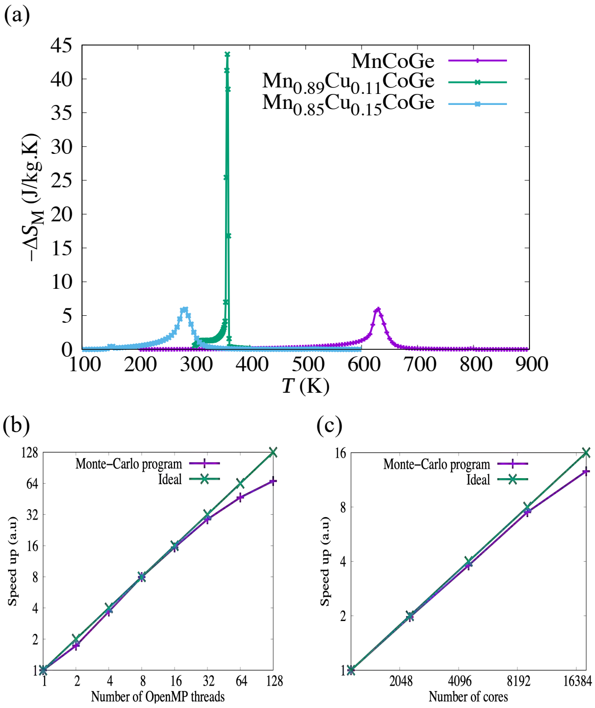

Figure 1: (a) Isothermal magnetic entropy change of $\mathrm{Mn}_{1-x}\mathrm{Cu}_x\mathrm{CoGe}$ ($x = 0.00$, 0.11, 0.15) [1]. (b) and (c) Speed-up tests of our Monte-Carlo program in the new System B (Ohtaka).

References

[1] H. B. Tran, T. Fukushima, K. Sato, Y. Makino, and T. Oguchi, J. Alloys Compd. **854**, 157063 (2021).

[2] H. B. Tran, T. Fukushima, Y. Makino, and T. Oguchi, Solid State Commun. **323**, 114077 (2021).

[3] H. B. Tran, T. Fukushima, H. Momida, K. Sato, Y. Makino, and T. Oguchi, Comput. Mater. Sci. **188**, 110227 (2021).

[4] H. B. Tran, T. Fukushima, H. Momida, K. Sato, Y. Makino, and T. Oguchi, Direct and Inverse Magnetocaloric Effects in FeRh Alloy: A Theoretical Study, http://dx.doi.org/10.2139/ssrn.3799705.

Theoretical analysis of molecular motions in proton-conducting organic materials

Yuta HORI

Center for Computational Sciences,

University of Tsukuba, Tennodai, Tsukuba, Ibaraki 305-8577

Anhydrous proton conduction materials have been investigated for use in electrolytes in fuel cells. The composite materials including imidazole have especially gained much attention because of the lack of humidity. Poly(vinylphosphonic acid)-imidazole (PVPA-*x*Im) has shown the increase of proton conductivity with *x* [1]. Understanding the proton conduction mechanism leads to the improvement of proton conduction materials.

In this study, we discussed the proton conduction mechanism in PVPA-*x*Im in terms of the microscopic characters of the hydrogen bond and imidazole motions as investigated by molecular dynamics simulations. The simulations were performed by the GROMACS package.

We calculated the translational diffusion coefficients of imidazole, imidazolium cation, and PVPA oligomer in PVPA-*x*Im to investigate their translational motion. All diffusion coefficients increased with temperature. The intercalation of imidazole into PVPA reduces the imidazole diffusion, because the diffusion coefficient of imidazole significantly decreased in PVPA-2Im compared to that in pure imidazole system. The diffusion coefficients of imidazoleium cation and PVPA oligomer in PVPA-2Im further decreased and were similar values each other. Therefore, we find that the imidazolium cation motion was interlocked by PVPA because of the strong hydron bond interaction between imidazolium cation and phosphonic acid in PVPA.

We estimated the rotational correlation time of imidazole and imidazolium cation to investigate their internal motions. The obtained results showed the similar dynamical behavior of the translational diffusions. We compared the activation energies of transrational and rotational motions of imidazole. The calculated energies of rotational motions were lower than those of translational motions. Therefore, it is expected that proton conduction obeys Grotthuss-type mechanism.

References

[1] M. Yamada, I. Honma, Polymer, **46**, 2986 (2005).

[2] Y. Hori, *et al.*, ACS Appl. Polym. Mater. **2**, 1561 (2020).

[3] Y. Hori, *et al.*, Chemistry Letters **50**, 17 (2021).

Development of molecular crystal structure prediction methods

Tomoki YAMASHITA
Top Runner Incubation Center for Academia-Industry Fusion,
Nagaoka University of Technology
1603-1 Kamitomioka-machi, Nagaoka, Niigata, 940-2188

We have developed a crystal structure prediction tool, CrySPY as an open source software [1]. CrySPY is interfaced with VASP[2], Quantum ESPRESSO[3], soiap[4], and LAMMPS code for structure optimization. Several searching algorithms are available in CrySPY, such as random search (RS), evolutionary algorithm (EA), Bayesian optimization (BO), and LAQA. RS is a basic algorithm and widely used. EA[5, 6, 7] is currently very popular. Previously we have developed selection-type algorithms with machine learning. BO can efficiently select potential candidates from a large number of candidate structures by machine learning[8]. LAQA is one of the refinforcement learning, which can reduce the computation time[9]. CrySPY enables us to find stable structures for bulk systems. However, CrySPY did not support molecular crystal, surface and interface structures. The original plan was to develop a method for surface structure prediction, but we changed the plan and developed a method for molecular crystal structure prediction.

We employed the PyXtal library [10] to generate molecular crystal structure generation, and developed the interface between CrySPY and PyXtal. We tested molecular crystal structure prediction for Li_3PS_4 using CrySPY. The most stable structure of Li_3PS_4 is known as $\gamma-Li_3PS_4$ [11], which is composed of six Li atoms and two PS_4 molecules shown in Fig. 1. Fifty molecular crystal structures of two formula units of Li_3PS_4 were randomly generated. Structure optimizations were performed using the density functional theory with the projector-augmented wave [12] method as implemented in the VASP code [2]. The generalized gradient approximation by Perdew, Burke, and Ernzerhof [13] was employed for exchange-correlation functional. A cutoff energy of 625 eV for the plane-wave expansion of the wave function and k-point mesh density of 80 $Å^{-3}$ were used.

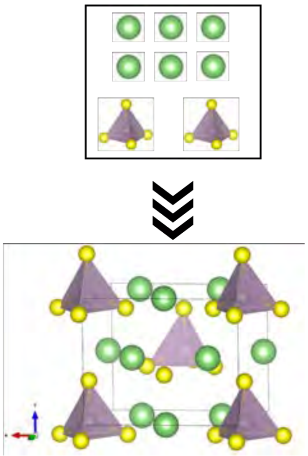

Figure 1: Crystal structure prediction of Li_3PS_4. The stable structure is $\gamma-Li_3PS_4$.

Crystal parameters of the lowest-energy structure perfectly agree with the experimental ones of $\gamma-Li_3PS_4$ except for the tiny amount of differences in lattice constants and atomic positions. These results indicate that the molecular structure generation method is quite useful for stable structure predictions of molecular crystals.

References

[1] https://github.com/Tomoki-YAMASHITA/CrySPY.

[2] G. Kresse and J. Furthmüller, Phys. Rev. B **54**, 11169 (1996).

[3] P. Giannozzi et al., J.Phys.:Condens.Matter **21**, 395502 (2009).

[4] https://github.com/nbsato/soiap.

[5] A. R. Oganov and C. W. Glass, J. Chem. Phys. **124**, art. 244704 (2006).

[6] A. R. Oganov, A. O. Lyakhov and M. Valle, Acc. Chem. Res. **44**, 227 (2011).

[7] A. O. Lyakhov, A. R. Oganov, H. T. Stokes, and Q. Zhu, Comp. Phys. Comm. **184**, 1172 (2013).

[8] T. Yamashita, N. Sato, H. Kino, T. Miyake, K. Tsuda, and T. Oguchi, Phys. Rev. Materials **2**, 013803 (2018).

[9] K. Terayama, T. Yamashita, T. Oguchi, and K. Tsuda, Npj Comput. Mater. **4**, 32 (2018).

[10] S. Fredericksa, D. Sayrea, and Q. Zhua, Comput Phys Commun. **261**, 107810 (2021).

[11] K. Homma et al., Solid State Ionics **182**, 53 (2011).

[12] P. E. Blöchl, Phys. Rev. B **50**, 17953 (1994).

[13] J. P. Perdew, K. Burke, and M. Ernzerhof, Phys Rev Lett. **77**, 3865 (1996).

Density Functional Theory and Polarizable Continuum Model for Developing High-Performance Polymer Electret

Yucheng ZHANG, Zetian MAO, and Yuji SUZUKI
Department of Mechanical Engineering
The University of Tokyo, Hongo, Bunkyo-ku, Tokyo 113-8656

Electret is a dielectric material, where trapped charges can generate electrostatic field for tens of years. Vibrational electret energy harvester (VEEH) can convert kinetic energy into electricity efficiently by electrostatic induction. Because the output power can be increased by four times with bipolar (negative and positive) charging, development of high-performance electret material for both positive and negative charging is crucial.

CYTOP (AGC Co. Ltd.) is an amorphous fluorinated polymer, with its chemical structures shown in Figure 1. There are three kinds of commercialized CYTOP, CTX-S, A and M. Recently, S Kim et al. [1] utilized quantum chemical analysis for evaluating charge trap of CYTOP electrets. It is shown that, although number of repeat unit of CYTOP is over 500, the trapped electron is localized at the end group. In addition, the computed electron affinities (EA) for CYTOP with different end groups are in qualitative agreement with surface charge density and charge stability obtained in experiments. Therefore, we investigate charge stability of molecule candidates with free amine functional group which can react with -COOH end group of CTX-A. EA and ionization potential (IP) obtained from DFT calculations with polarizable continuum model (PCM) are used to evaluate the electron trap energy and hole trap energy of possible candidates after dehydration condensation respectively. The above strategy is shown in Figure 2.

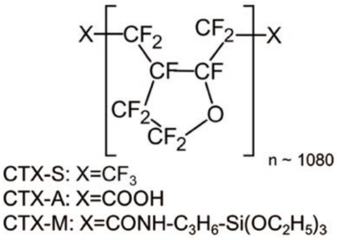

Fig. 1. Chemical structure of CYTOP series.

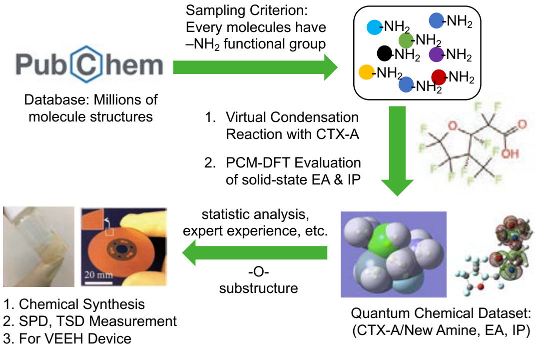

Fig. 2. Framework of simulation (PCM-DFT) guided material development.

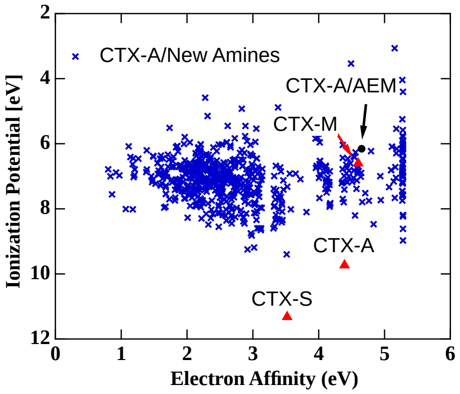

Fig. 3. PCM-DFT EA-IP computation of 600 CTX-A/new amines with comparison to CTX-S, A, M, and CTX-A/AEM.

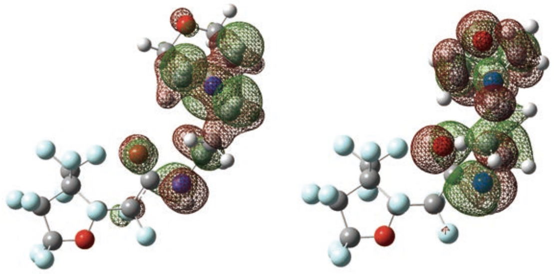

Fig. 4. Singly Occupied Orbital in negatively (left) and positively (right) charged monomer of CTX-A/AEM.

Firstly, EA and IP for monomer CTX-S, A, M are computed with PCM-DFT as follows. EA: 3.52 eV, 4.39 eV, and 4.60 eV, respectively. IP: 11.32 eV, 9.73 eV, and 6.60 eV, respectively. PCM-DFT EA gave good agreement with previous MD-DFT EAs: 3.42 eV, 3.94 eV, and 4.56 eV. It is also shown that EA of CTX-S is in quantitative agreement with experimentally measured value by LEIPS of 3.60 eV [1].

Within the framework of Fig. 2, 600 EA and IP for molecules of CTX-A/Amines are computed by PCM-DFT, as shown in Fig. 3. CYTOP dataset is then built based partially on these calculations.

In addition to using this dataset for machine learning, statistical analysis of the dataset itself extracts several useful information. For example, -O- is an important factor for enhancing the charge stability, while singly-occupied orbital is usually localized at the end-group for high-ranking molecules (Figure 4). More analysis and experiments are on-going.

This work was partially supported by JST CREST Grant Number JPMJCR15Q3 and JPMJCR19Q1. The calculation is performed with SGI ICE XA ISSP system B and every calculation is held with 1 node (24 CPUs). The energy of the molecule is computed mainly by DFT at the level of CAM-B3LYP/6-31+G(d,p), with solvation effect added by PCM, by using quantum chemical simulation software GAUSSIAN [2]. In addition, different basis sets such as STO-3G and 3-21G are used for determining a good balancing point between calculation cost and accuracy. As for the computation cost, CYTOP hexamers: 2500 CPU hours per molecule; CYTOP monomer: 36 hours per molecule.

References

[1] Kim S., et al., J. Phys. Chem. B, Vol. 124, No. 46, pp. 10507-10513 (2020).

[2] M. Frisch et al., “Gaussian 09, Rev. A. 1,” Gaussian, Inc. Wellingford, CT, 2009.

First principles calculation of fluorocarbon layer in dry etching process and exciton self-trapping in low-dimensional perovskites

Hannes Raebiger and Soungmin Bae

Department of Physics,

Yokohama National University, Yokohama 240-8501

First principles calculation of fluorocarbon layer in dry etching process–Plasma dry etching using fluorocarbon gas is the most powerful tool to achieve sub-nm high aspect ratio hole contact (HARC) in silicon oxide and nitride which is indispensable for the current semiconductor industry. One of the main obstacle for HARC process is the 'charge-up' effect where accumulated incident ions in the FC layer exerts electrostatic repulsion and bents the ion trajectories, which prominently twists the etching profile of HARC with ultrahigh aspect ratio. Although many attempts of profile simulation in mesoscopic scale for resolving 'charge-up' problem have been devoted, the atomic understanding of FC layer in terms of their bonding character, dielectric property and environment dependence (for instance, flux ratio of ion and FC neutrals and bias power) were hardly known. Here, we report our progress on ab initio simulation of FC layer on silicon under low pressure non equilibrium plasma condition obtained by density-functional calculations combined with the reactive force field simulation. [1]

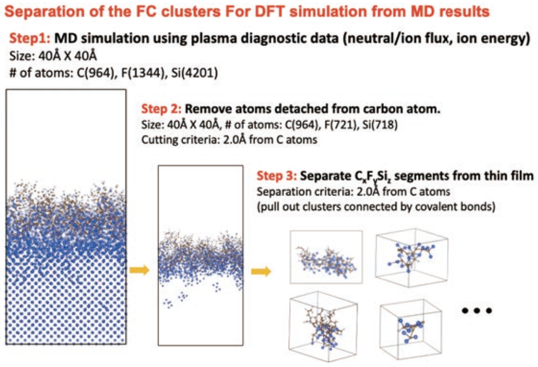

Fig 1. A schematic of the divide-and-conquer approach for split the FC polymer into small atomic clusters.

In Figure 1, we describe a representative result of the silicon etching simulation obtained with the empirical reactive bond order (REBO) method and the divide-and-conquer approach for splitting the obtained FC polymer into atomic clusters. Because the number of atoms in typical FC polymer simulation with REBO is about 10,000~40,000 atoms including carbon, fluorine and silicon atoms, the obtained results are prohibitively large for density-functional calculations. We split the FC layer (~ 4000 atoms) into many atomic clusters with selectively cutting weak and long-range interactions (so called vdW interaction) and creates many atomic clusters combined with covalent interaction between 10~200 atoms. The divided clusters are calculated by density-functional theory (DFT) with ωB97XD functional. The results give accurate atomic structures and electronic structures for carbon 1s XPS and dielectric constant presented in Figure 2.

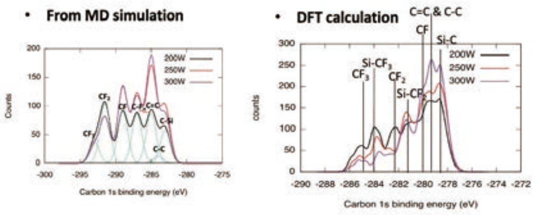

Fig 2. The simulated XPS spectra based on REBO-MD result and DFT optimized structures. The XPS spectra obtained with DFT results typically show better agreement with experimental data.

First principles calculation of exciton self-trapping in low-dimensional perovskites–

Low-dimensional perovskites are found to efficiently exhibit white broad emission with a single material in contrast to conventional three-dimensional materials. While white broad emission is attributed to self-trapped exciton (STE), detailed mechanism of STE formation is rarely explored by theoretical studies. In this project, We explored bound exciton formation in two-dimensional halide perovskites for achieving highly efficient light-emitting diode (LED) and photovoltaic devices. From the systematic study of bound exciton formation by using self-interaction corrected constraint occupation Density Functional Theory (c-DFT), electronic and structural feature of bound excitons are revealed and related outcomes such as line shape of broad emission and exciton trapping rate will be evaluated for providing practical clues for experimental design of optoelectrical and photovoltaic materials.

The exciton self-trapping calculations were performed for the $Cs_3Bi_2I_9$ which is representative 0D perovskite used for photosensors and light-emitting diodes [2].

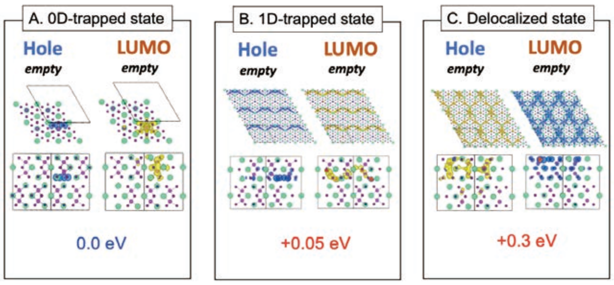

Fig 2. The simulated trapped excitons and their relative stabilities.

In results, we found three different self-trapped excitons in $Cs_3Bi_2I_9$. While the localized exciton is the ground state of the trapped-exciton state, one-dimensional and two-dimensional exciton states also exist which should be involved in broad emission and photovoltaic behavior of $Cs_3Bi_2I_9$.

References

[1] C. F. Abrams and D. B. Graves: J. Vac. Sci. Technol. A . **19** (2001) 175-181.

[2] K. M. McCall, C. C. Stoumpos, S. S. Kostina, M. G. Kanatzidis and B. W. Wessels: Chem. Mater. **29** (2017) 4129-4145.

Improvement and application of all-electron mixed basis program

Kaoru OHNO

Faculty of Engineering Science, Yokohama National University
79-5 Tokiwadai, Hodogaya-ku, Yokohama 240-8501

Using the all-electron mixed basis program TOMBO, we performed first-principles molecular dynamics simulations of Mo and Au atom vertical bombardments at the center of a six-membered ring of C_{60} to create endohedral fullerenes. With the kinetic energies of 40 eV and 80 eV, Mo and Au atoms successfully penetrated inside the C_{60}, and the endohedral fullerenes, M@C_{60} (M=Mo, Au), were created. We confirmed that the created M@C_{60} continues to exist stably without breaking. This result is currently being submitted.

On the other hand, in the Green's function method in many-body perturbation theory, all the effects of the Coulomb interaction between electrons are incorporated in the self-energy function. However, since the self-energy function depends on the energy, the quasiparticle wave functions, i.e., the basis functions, which diagonalize the Green's function, are not only effect of renormalization of the energy dependence of the self-energy has not been discussed much so far in the one-shot G_0W_0 approximation. Therefore, we discussed the effect of renormalization in the one-shot G_0W_0 approximation and the effect of linearization in the scGW approach (the scLGW method [1]) by using TOMBO, and found out that all these effects are to decrease the energy gap. According to our results, the scLGW method can improve the one-shot G_0W_0 results in many cases. Thus, linearization is very powerful and effective. The result will be submitted soon.

Lastly, we have applied our first-principle phase field method to Ti64 ternary alloys [2] and to Ni-Ti binary alloys [3], and succeeded in reproducing the experimental microstructure without introducing any empirical thermodynamic parameter. In the simulation of Ni-Ti alloys, we noticed an important tolerance behavior that the result does not depend on the assumed atomic alignment at all and found that the result does not change even if we used $NiTi_3$ instead of $NiTi_2$.

References

[1] R. Kuwahara and K. Ohno, Phys. Rev. A **90**, 032506;1-9 (2014).

[2] T. N. Pham, K. Ohno, R. Kuwahara, and S. Bhattacharyya, J. Phys.: Cond. Mat., **32**, 264001;1-9 (2020).

[3] K. Ohno, M. Tsuchiya, R. Kuwahara, R. Sahara, S. Bhattacharyya, and T. N. Pham, Comp. Mat. Sci. **191**, 110284 (2021).

Study of Efficient Training Data Generation Method for Constructing Artificial Neural Network Force Field I-II

Kohei Shimamura

Department of Physics,

Kumamoto University, 2-39-1 Kurokami, Chuo-ku, Kumamoto 860-8555

Interatomic potential using an artificial neural network (ANN potential) can not only provide high accuracy results by training first-principles molecular dynamics (FPMD) data but also have low computational cost, which allows for large scale and long-term MD simulations. In this study, we aim to finding how to efficiently generate the training data required to construct the ANN potential. Active Learning (AL) is one of the promising generation methods that we are paying attention to. In AL, firstly, several ANN potentials with different initial values of weight parameters are constructed by training with the same data. Since an output uncertainty (e.g. standard deviation) can be defined using the ANN potentials, the magnitude of the uncertainty provides us an indicator to identify the candidate data to be trained. However, there is still room for consideration of specific indicators. The indicators currently employed for AL are the uncertainty of potential energy and atomic force. This reflects the current standard training method, where ANN potentials learn the potential energy and force obtained from the FPMD.

Considering that accurate pressure is also important for MD simulations (e.g. simulations under NPT ensemble), we believe that training of pressure is indispensable and uncertainty of pressure should also be added to the indicator. We recently revealed that the pressure training is necessary to accurately calculate thermal conductivity, which is a fundamental physical quantity that characterize the thermal properties of materials [1]. There is a well-known method using long-term equilibrium MD data and Green-Kubo formula, where the thermal conductivity is calculated from the time correlation function of heat flux. It was also found that a clear relation holds between the heat flux formula and the pressure one derived from the virial theorem [1]. Since the current standard training method mentioned above does not guarantee pressure accuracy, ANN potentials with inadequate pressure accuracy are likely to show poor thermal conductivity. This result further emphasizes the importance of pressure training. We are exploring better indicators of AL including pressure uncertainty.

Reference

[1] K. Shimamura, *et al.*: J. Chem. Phys. **153**, 234301 (2020).

Refined Metadynamics and Elucidation of Reaction Mechanism of Polyalcohol Dehydration in Hot Acidic Water

Tomomi Kondo[1,2], Takehiko Sasaki[1], Motoyuki Shiga[2]

1 *Department of Complexity Science and Engineering, Graduate School of Frontier Sciences, The University of Tokyo, Kashiwa-no-ha, Kashiwa, Chiba 277-8561*

2 *Center for Computational Science and E-Systems, Japan Atomic Energy Agency 148-4 Kashiwanoha Campus, 178-4 Wakashiba, Kashiwa, Chiba, 277-0871*

Subcritical water has high solubility of organic molecules and is expected to be applied as a reaction medium. Cyclization dehydration reaction of polyalcohol in hot water has been proven to be efficient method for utilization of biomass materials [1]. In this study we proposed a new method of refinement (improved metadynamics method: Refined MTD), and applied it to cyclization dehydration of 2,5-Hexanediol (HDO) [2].

Fig. 1 Reaction for 2,5-Hexanediol (HDO)

In the metadynamics method, by adding the bias potential according to the frequency of appearance on the free energy surface characterized by the reaction coordinates (CV), a chemical reaction that does not occur on the time scale of the usual molecular dynamics method is induced. From the deposited bias potential $W(q)$, the free energy surface $A(q) = -W(q) + const$ is obtained, and the minimum and saddle points of $A(q)$ are obtained.

The activation barrier ΔA can be obtained from the difference (the point where the reaction occurred). However, the height of the bias potential represented by the Gaussian function and the frequency of addition are finite, and an error of several k_BT occurs in the free energy surface. When comparing reactions with different environmental conditions such as pressure and temperature, or when there are competitive reactions, it is necessary to estimate the accurate free energy surface with an error of several k_BT or less. In this study, we used Refined MTD, which is a method to further refine the free energy surface obtained by MTD calculation. First, the $W(q)$ deposited from the reactant to the product by metadynamics calculation is added to the potential of the system as a time-independent bias potential. Then, the canonical distribution $\rho_W(q)$ is generated by sufficiently sampling the system by molecular dynamics calculation biased by $W(q)$. $A(q)$ can be corrected using $\rho_W(q)$ as shown in the following equation [2].

$$\rho_W(q) \propto \int dr\, e^{-\beta(V(r)+W(q))}\,\delta(Q(r)-q) \propto e^{-\beta W(q)}\rho(q)$$

$$\therefore A(q) = -\beta^{-1}\ln\rho(q) \approx -W(q) - \beta^{-1}\ln\rho_W(q)$$

Sampling of the biased system must be performed sufficiently until the entire free energy surface in the CV space is sampled, and especially when the activation barrier is to be obtained, sampling not only near the minimum reaction energy point but also near the transition state is required.

Calculations were conducted using software PIMD [3] working with DFTB or VASP. The calculation system consists of 1 HDO molecule, 30 water molecules, and acidic molecules such as HCl added under the same thermodynamic conditions as in Experiment [1] (20 MPa, 523 K). CV is assumed for each product. The dihedral angle φ between the hydroxyl group and the main chain, the difference d in the O-C distances of leaving and bonding, and the proton coordination number n of the hydroxyl group were set according to the reaction path.

By using Refined MTD for the HDO system, the free energy surface of the system containing each acidic molecule was obtained. When the difference was taken before and after the correction for the minimum free energy surface of the system containing H_2CO_3, the maximum was 7.3 kcal/mol, and the average was 1.6 kcal/mol (RMSE). As a result of DFTB calculation using Refined MTD, it was confirmed that the free energy surface of the cyclization-dehydration reaction of HDO differs depending on the presence and type of acidic molecules (Fig. 3). For the higher acidic system such as a system containing H_2SO_4, metastable structure was found in the region where protons are added. In addition, the proton coordination number in the transition state was n ≈ 2.0 in the system containing acidic molecules, whereas it was n ≈ 1.4 in the pure water system, indicating that the reaction process differs depending on the acidity. The activation barrier ΔA (kcal/mol) were obtained as 50.6 (pure water), 39.6 (H_2CO_3), 35.4 (HCl), 26.3 (H_2SO_4).

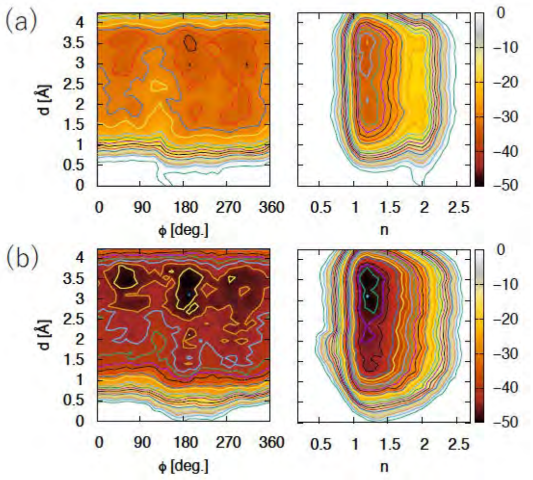

Fig. 2 Free energy surfaces obtained for HDO dehydration reaction obtained by Refined MTD.
(a) HCl aqueous solution, (b) pure water.

References

[1] A. Yamaguchi *et al.*, *Green Chem.*, **13**, 873 (2011).

[2] T. Kondo *et al.*, *J. Comput. Chem.*, **42**, 156 (2020).

[3]http://ccse.jaea.go.jp/ja/download/pimd/index.jp.html.

Ultimate impedance of coherent heat conduction in van der Waals graphene-MoS_2 heterostructures

Hu Shiqian

Department of Mechanical Engineering,

The University of Tokyo, Hongo, Bunkyo City, Tokyo 113-8654

Toward the ultimate goal of designing small thermal-conductivity materials at room temperature, herein we investigate the controllability of coherent phonon transport in van der Waals graphene-MoS_2 heterostructures with different stacking orders using non-equilibrium molecular dynamics simulations. Using Bayesian optimization–based materials informatics, the optimal stacking order of graphene and MoS_2 is efficiently identified from tens of thousands of candidates with varying degrees of phonon localization. The obtained thermal conductivity of the optimized heterostructure (0.026 W/m-K) is significantly lower than that of its building blocks, pristine MoS_2 and graphene.

There are growing efforts to control thermal transport via coherent phonons in the one-dimensional superlattice. However, in general, the difference in the intrinsic lattice structures of the constituent materials inevitably generate interface disorder during the fabrication process, greatly limiting direct experimental observation of the coherent phonon transport. The flexible integration and atomistic interlayer smoothness of van der Waals (vdW) heterostructure provide an ideal platform for the coherent phonon transport manipulation. Thus, in the current work, using the non-equilibrium molecular dynamics simulations, we investigate the coherent phonon transport in vdW graphene-MoS2 heterostructure with different stacking order.

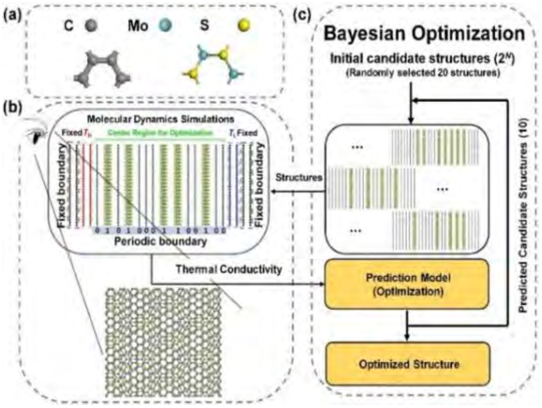

Figure. Schematics of the machine-learning method to combine the molecular dynamics (MD) and Bayesian optimization.

The histogram of the phonon transmissions in different disordered structure exhibits a log-normal distribution, which reveals the localization of the coherent phonons. Furthermore, the optimal stacking order of the graphene and MoS2 is efficiently identified from tens of thousands of candidates by machine learning. The significantly suppressed of the phonon transmission in the low frequency (<5THz) phonons of the optimized structure lead to a significant reduction of the thermal conductance compared with the pristine graphite. Finally, the effects of the defect effect on the thermal conductivity of graphite and optimized structures are also discussed. Our work provides a deep insight into the coherent phonons transport behavior in the atomistically smooth vdW structure, which is beneficial for further development of phononics.

References

[1] S. Hu, S. Ju, C. Shao, J. Guo, B. Xu, M. Ohnishi and J. Shiomi, Mater. Today Phys. **16**, 100324 (2021)

Development and applications of first principles method for light-matter interactions beyond the dipole approximation

Takeshi IWASA
Faculty of Science, Hokkaido University
N10W8, Sapporo, Hokkaido 060-0810

Near field refers to a non-propagating light field. The interaction between the near-field and molecules can overcome the diffraction limit and can induce non-dipolar excitations, offering a unique platform for nanoscale spectroscopy and microscopy [1], as well as photochemistry [2]. Due to the localization of the near-field, theoretical framework beyond the dipole approximation is required. Thus, we have developed a first principles method based on the multipolar Hamiltonian, in which, the interaction is described by coupling the electric field and the molecular polarization field integrating over the space. The method has been used to study near-field electronic excitations [3] and vibrational excitations, i.e., the near-field IR combined with electrodynamics computations [4].

In this fiscal year, we have developed a method for near-field Raman [5]. The theoretical framework we established for near-field Raman is as follows. First, the multipolar Hamiltonian is implemented into a real-time time-dependent density functional code, namely, Octopus 9.2 [6] and calculate the near-field excited electron dynamics to obtain the induced dipole moment of a molecule in the time domain, which is later Fourier transformed into the frequency domain. The induced dipole moments are calculated $6N$ times (N is the number of atom in a molecule) for distorted geometries where one of the x, y, and z coordinates of an atom is shifted slightly in either the positive and negative direction to obtain a derivative of the induced dipole moment with respect to the atomic Cartesian coordinate, which is then transformed into the normal coordinate derivative using the transformation matrix obtained by a normal mode analysis, performed separately. Finally, the Raman spectrum is obtained from the square of the absolute value of the normal coordinate derivatives.

As a demonstration, on- and off-resonance near-field Raman of benzene is studied. We showed that the obtained Raman spectra are well understood by considering both the spatial structure of the near field and the molecular vibration in the off-resonance condition. For the on-resonance condition, the Raman spectra are governed by the transition moment, in addition to the selection rule of off-resonance Raman. Interestingly, on-resonance Raman can be activated even when the near field forbids the $\pi-\pi^*$ transition at equilibrium geometry due to vibronic couplings originating from structural distortions.

References [1] R. B. Jaculbia, et al., Nat. Nanotechnol. 15, 105 (2020). [2] E. Kazuma et al., Science, 360, 521 (2018). [3] T. Iwasa and K. Nobusada, Phys. Rev. A, 80, 043409 (2009) and 82, 043411 (2010). [4] T. Iwasa, et al., J. Chem. Phys., 144, 124116 (2016) and 152, 164103 (2020). [6] M. Takenaka, T. Taketsugu, T. Iwasa, J. Chem. Phys., 154, 024104 (2021). [5] X. Andrade, et al., Phys. Chem. Chem. Phys. 17, 31371 (2015).

Theoretical analysis of influences of phonons on magnetism

Yoshihiro GOHDA
Department of Materials Science and Engineering, Tokyo Institute of Technology
J1-3, Nagatsuta-cho 4259, Midori-ku, Yokohama 226-8502, Japan

It is extremely challenging to describe magnetism at finite temperatures by first-principles electron theory. There are at least two main contributions to excitation: magnons and phonons. Even though there are attempts to include finite tempearture effects through exchange-coupling constants J_{ij} in the Heisenberg model by first-principles calculations, dependences of phonons on magnetic states has been neglected. Such an approach is also computationally challenging, because first-principles phonon calculations and Monte Carlo simulations are required for precise evaluations in addition to the standard total-energy minimization.

In this project, we propose a new first-principles scheme to evaluate the Curie temperature taking the magnetism-dependent phonons and their feedback effect to magnetism into account, and apply the scheme to bcc Fe [1] and some B2 and L1$_0$ compounds [2] as examples. In our framework, we minimize the total free energy in the explicit consideration of temperature effects, because the magnetic and vibrational free energies correlate with each other. Both the influences of magnetism on phonons and the feedback effect from phonons to magnetism are taken into account using phonon calculations by ALAMODE [3]. The feedback effect reduced the Curie temperature of bcc Fe significantly as shown in Fig. 1, where the magnetic energy is calculated by the ALPS code [4] with J_{ij} obtained by Akai-KKR [5].

In addition, first-principles computations are performed for magnetic materials including permanent magnets [6] and multiferroic materials [7]. We also improved formulations to calculate J_{ij} in OpenMX [8] by introducing the orthogonalization of localized basis sets.

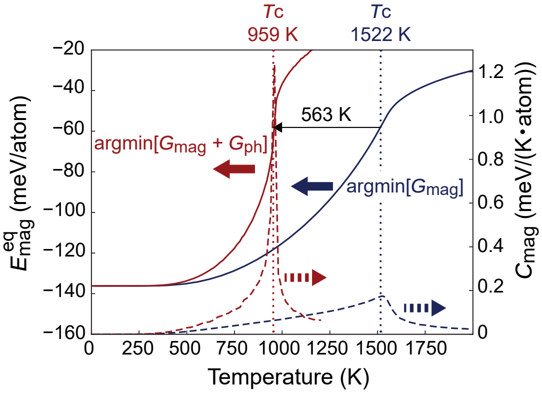

Figure 1: The equilibrium magnetic energy (solid lines) and the magnetic specific heat (dashed lines) of bcc Fe as a function of temperature obtained by the minimization of the total free energy and by the minimization of the magnetic free energy [1].

[1] T. Tanaka and Y. Gohda, npj Comput. Mater. **6**, 184 (2020).

[2] T. Tanaka and Y. Gohda, J. Phys. Soc. Jpn. **89**, 093705 (2020).

[3] T. Tadano, Y. Gohda, and S. Tsuneyuki, J. Phys.: Condens. Matter **26**, 225402 (2014).

[4] B. Bauer, S. Todo, *et al.*, J. Stat. Mech. **2011**, P05001 (2011).

[5] H. Akai, J. Phys.: Condens. Matter **1**, 8045 (1989).

[6] Y. Ainai, S. Kou, Y. Tatetsu, and Y. Gohda, Jpn. J. Appl. Phys. **59**, 060904 (2020).

[7] R. Costa–Amaral and Y. Gohda, J. Chem. Phys. **152**, 204701 (2020).

[8] T. Ozaki, Phys. Rev. B. **67**, 155108 (2003).

Microscopic simulation for ultrafast electronic and atomic response driven by strong and short laser pulses

Yasushi Shinohara[1,2], Mizuki Tani[2]
[1]*Photon Science Center,*
The University of Tokyo, Hongo, Bunkyo-ku, Tokyo 113-86562
[2]*Department of Nuclear Engineering and Management*
The University of Tokyo, Hongo, Bunkyo-ku, Tokyo 113-8656

The development of coherent light sources allows us to realize various nonequilibrium material dynamics. Such processes are initiated by electron excitation then undergoing atomic motion via the electron-phonon interaction. A theoretical description of the nonequilibrium dynamics for the whole system composed of electrons and the nucleus is one of the most challenging systems. We have investigated nonequilibrium systems along with two directions, a) electron-phonon interaction computation to understand the frequency-domain angle-resolved photoemission spectroscopy (FDARPES) under collaboration with experimentalists [1], and b) development of a theoretical framework of semiclassical modeling of the optical response for simple metals [2].

In Ta2NiSe5 (TNS), it is reported that the coexistence of insulator and semimetallic electronic structures in time-resolved angle-resolved photoemission spectroscopy (TrARPES) [3] and Coherent phonon generation in time-resolved reflectivity measurement [4]. The semimetallic phase of TNS is realized above 328 K accompanied by structural phase transition. Our coauthors conduct experiments to discover TrARPES with fine enough temporal resolution to disentangle different frequencies of coherent phonon modes. By taking the Fourier transform of the TrARPES, we obtain FDARPES in which ARPES with a phonon frequency shows electronic structure modulation by the corresponding phonon. The metallic and semiconducting electronic structures coincide with 2 and 3 THz coherent phonons. To assign phonon modes to the frequencies, we perform density-functional perturbation theory (DFPT) calculation of the FDARPES. We reveal 2 THz phonon modes are a motion connecting the two, semiconducting and semimetallic, structures.

A mean-field type quantum theory hardly captures the colliding process leading to relaxation or equilibrium among the electron subsystem. A numerically efficient scheme to describe electron scattering is a semiclassical equation of motion that the collision integral added to the Vlasov equation. The Vlasov equation can be constructed from a quantum mechanical equation of motion, such as time-dependent density-functional theory (TDDFT), by the Wigner transformation [5]. The Vlasov equation is solved by the pseudo-particle method that the distribution function is described by a sum of classical particles having finite spatial and momentum width [5]. We develop a theoretical framework for a spatially periodic system based on the Vlasov equation with the pseudo-particle method and density-dependent functional taken from TDDFT, called Vlasov-LDA hereafter. A striking advantage of Vlasov-LDA is the much lighter computational cost compared to typical time-dependent quantum mechanical simulations. We apply Vlasov-LDA to crystalline Al and compare its results with TDDFT. Optical conductivity from Vlasov-LDA perfectly coincides with TDDFT, while computational is typically 50 times lighter than TDDFT cost. We also perform systematic benchmarking for nonlinear optical responses compared with TDDFT. We are preparing the manuscript for this work.

References

[1] Takeshi Suzuki, Yasushi Shinohara, et al., Phys. Rev. B **103** (2021) L121105.

[2] M. Tani, T. Otobe, Y. Shinohara, K.L. Ishikawa, in preparation.

[3] K. Okazaki, Nature Communications volume **9** (2018) 4322.

[4] S. Y. Kim, et al., ACS Nano **10**, 8888 (2016), S. Mor, et al., Phys. Rev. B **97**, 115154 (2018).

[5] T. Fennel, et al., Eur. Phys. J. D 29, 367–378 (2004).

Ab initio Molecular Dynamics Study on Static Structure of Glass Materials

Akihide KOURA
Technical Division,
Kumamoto University, Kurokami, Chuo-ku, Kumamoto, 860-8555

We have studied condensed matter systems, which are crystal, liquid, and amorphous systems. In this project, we aimed to clarify the static structure of glass V_2O_5 under pressure using our original QXMD code, which is applicable to perform *ab initio* molecular dynamics (AIMD) and empirical molecular dynamics (MD) simulations [1].

In order to investigate the static and dynamic properties of disordered materials, we employed one of the machine learning method, the artificial neural network (ANN) technic [2]. This method enables us to perform MD simulations of the large scaled system with reasonably low calculation cost. However, the best method to construct the interatomic potential of high transferability for any calculation conditions is not established. That is, our priority mission is the establishment of construction of the ANN potential applicable for the wide range conditions based on the result of AIMD simulations. For this purpose, we try to construct new ANN potentials for different targets, liquid and crystal Na, and α- and β-phases of Ag_2Se crystals. These targets are suitable for such test because Na has only one valence electron and Ag_2Se has many electrons. The calculation cost of the former is low, therefore, it is easy to compare the result by ANN-MD with that by AIMD. While, the cost of the latter is high, hence, the efficacy of acceleration using ANN potential is checked.

In this study, it was found that an optimizing equation including the force and virial terms, which were often ignored, was needed for the phase transition [3,4].

References

[1] F. Shimojo, S. Fukushima, H. Kumazoe, M. Misawa, S. Ohmura, P. Rajak, K. Shimamura, L. Bassman, S. Tiwari, R. K. Kalia, A. Nakano, and P. Vashishta: SoftwareX **10** (2019) 100307.

[2] N. Artrith and A. Urban: Comput. Mater. Sci. **114** (2016) 135.

[3] K. Shimamura, S. Fukushima, A. Koura, F. Shimojo, M. Misawa, R. K. Kalia, A. Nakano, P. Vashishta *et al.* J. Chem. Phys. **151**, 124303 (2019).

[4] A. Irie, S. Fukushima, A. Koura, K. Shimamura, and F. Shimojo, in preparation.

Ab initio calculation for thermodynamic phase diagram

Kazuma NAKAMURA
Quantum Physics Section, Kyushu Institute of Technology
1-1 Sensui-cho, Tobata, Kitakyushu, Fukuoka, 804-8550

For the purpose of *ab initio* quantitative evaluation of thermodynamic physical properties of materials, thermodynamic phase diagrams based on first-principles calculations are calculated. Focusing on metal hydrides, which are important as hydrogen storage alloys, we will evaluate their phase diagram and pressure-composition-temperature curves. The free energy model under the regular solid solution approximation is determined from the first-principles calculation, and the phase diagram of this model is obtained with the CALPHAD method.

As the benchmark, the phase diagram of the metal hydride Ti-H sysmtem is calculated. The calculation flow is as follows: The starting point is the Gibbs free energy calculation. The free energy consists of three terms, the enthalpy term, the phonon term, and the solid-solution entropy term, all of which are evaluated by first-principles calculation. The enthalpy term is evaluated from the density-functional calculation for pure Ti and TiH systems (using xTAPP [1] and VASP [2]). The phonon term is also evaluated from the first-principles phonon calculation for Ti and TiH (using PHONOPY [3]). The solid-solution entropy term is evaluated using cluster-expansion and cluster-variational methods [4]. For these calculations, a large amount of structural data created by inserting hydrogen or voids into the tetrahedral-interstitial site is generated, where we consider a metal having a face-centered cubic (fcc) structure and the resulting structural data series is written as fcc-tetrahedron series. This structural series is generated using the software ATAT [5]. In this fcc-tetrahedron series, the total number of generated structural samples was 132. In addition to the fcc-tetrahedron series, fcc-octahedron series, body-centered-cubic (bcc)-tetrahedron series, bcc-octahedron series, hexagonal close-packed (hcp)-tetrahedral series, hcp-octahedron series, etc. are generated. First-principles calculations are performed for each structural series to obtain structural and energy data.

Next, we determine parameters of the effective model based on the regular solution approximation by fitting to the above obtained first-principles calculation data. In the first step, we use the cluster expansion method for the *ab initio* data to obtain expansion coefficients of cluster model, and then, to evaluate temperature dependence of the cluster model, cluster-variational method is performed for the cluster-expansion function of each structural series, which give the first-principles free energy surface. Finally, for the resulting free energy surface, the parameters of the regular solution model are obtained by fitting:

$$\begin{aligned}\mathcal{F}(x,T) &= xG_{\mathrm{TiH}}(T)+(1-x)G_{\mathrm{Ti}}(T)\\ &+ RT[x\ln x+(1-x)\ln(1-x)]\\ &+ x(1-x)[(1-x)-x]^0(L_0+L_0'T)\\ &+ x(1-x)[(1-x)-x]^1(L_1+L_1'T)\\ &+ x(1-x)[(1-x)-x]^2(L_2+L_2'T),\end{aligned} \tag{1}$$

where $G_{\mathrm{TiH}}(T)$ and $G_{\mathrm{Ti}}(T)$ are the free energies of TiH and Ti, respectively, and x or $1-x$ is fraction of vacancy or hydrogen in Ti. The free energy is modeled with the following function as

$$G_\alpha(T) = a_\alpha + b_\alpha T + c_\alpha T \ln T + d_\alpha T^2 + e_\alpha T^{-1}, \quad (2)$$

where the subscript α specifies TiH or Ti, and a_α, b_α, c_α, d_α, e_α in Eq. (2) are determined by fitting to the *ab initio* phonon free energy data. The third term in Eq. (1) is the mixing entropy term in the binary alloy system. The remaining terms in Eq. (1) are the interaction term and L_0, L_0', L_1, L_1', L_2, and L_2' parameters are determined by fitting to the *ab initio* cluster variational data. Table 1 lists our determined parameters in Eqs. (1) and (2).

Table 1: Determined parameters in Eqs. (1) and (2).

	bcc-tetra		fcc-tetra		hcp-tetra	
	Ti	TiH_6	Ti	TiH_2	Ti_2	Ti_2H_4
a	6413.24	60753.56	1978.90	−27924.55	−1944.38	−15163.09
b	71.017	7.801	93.111	−23.512	87.479	−18.794
c	−14.262	−1.308	−18.495	4.362	−16.921	3.644
d	−0.005	−0.009	−0.007	−0.024	−0.009	−0.024
e	0.001	0.000	0.001	0.000	0.001	0.000
L_0	−105733.39		13618.96		4345.96	
L_0’	−2.3605		−0.267		−1.7241	
L_1	−24563.95		−9933.31		−11022.69	
L_1’	−1.0794		0.1296		−1.5862	
L_2	−99788.53		−5491.55		−12354.91	
L_2’	0.0787		−0.4376		2.8456	

From the free energy curve of the regular solution model [Eq. (1)] obtained above, a phase diagram based on the CALPHAD method was calculated by using the software PANDAT [6]. Figure 1 (a) shows our calculated phase diagram of Ti-H sysmtem. The panel (b) also shows experimental phase diagram [7]. From the comparison between the two, we found that our result reasonably reproduces the experimental result. A Python Script was developed to generate PANDAT inputs from the results of the present regular solution models. We found that (i) the entropy term can be sensitive to the exchange-correlation functional used in the density-functional calculation, (ii) the phonon anharmonicity can affect the quantitative accuracy of the phase diagram boundary, and (iii) the quantitative accuracy of the interaction term depends highly on details of the cluster expansion (the cluster shape and expansion order, etc.) for the structure and energy data.

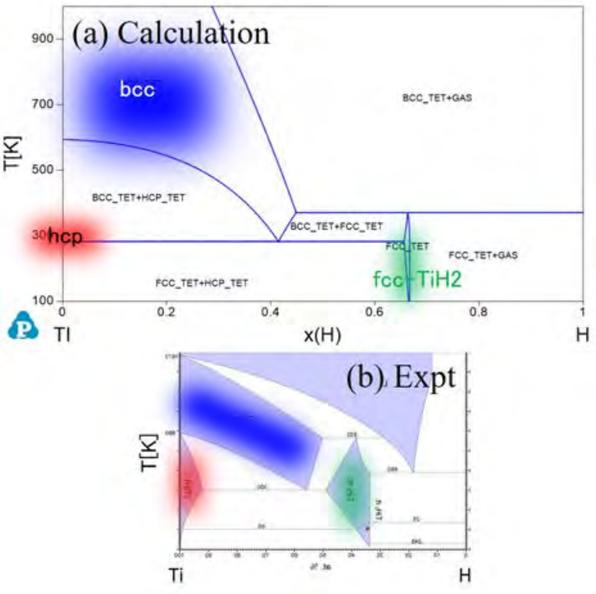

Figure 1: Thermodynamic phase diagram of TiH: (a) simulation and (b) experiment [7].

References

[1] http://xtapp.cp.is.s.u-tokyo.ac.jp

[2] https://www.vasp.at

[3] https://atztogo.github.io/phonopy

[4] M. Sluiter, D. de Fontaine, X. Q. Guo, R. Podloucky, and A.J.Freeman, Phys. Rev. B **16**, 42 10460 (1990).

[5] https://www.brown.edu/Departments/Engineering/Labs/avdw/atat/

[6] https://computherm.com/

[7] A. San-Martin, F.D. Manchester, Bulletin of Alloy Phase Diagrams **8**, 30–42 (1987).

Oxygen vacancy formation in metal-doped CeO_2 nanocrystals

Akira YOKO[1], Kazutoshi INOUE[1], Mitsuhiro SAITO[2], and Yuichi IKUHARA[1,2,*]
[1] *Advanced Institute for Materials Research, Tohoku University, Sendai, Miyagi, 980-8577*
[2] *Institute of Engineering Innovation, The University of Tokyo, Yayoi, Tokyo, 113-8656*

We studied Cr-doped cubic {100}-faceted CeO_2 nanocrystals (NCs) with an average size of 7.8 nm fabricated by a supercritical water reaction. A considerably large amount of Ce^{3+} ions was detected in the Cr-doped CeO_2 NCs by scanning transmission electron microscopy combined with electron energy loss spectroscopy (EELS). The Cr dopants substituted the Ce sites in the amount of approximately 3 mol%. We experimentally observed that the oxygen-storage capacity (OSC) was substantially improved by a low amount of Cr doping, which can be attributed to the low oxygen vacancy formation energy and high mobility of oxygen atoms by doping Cr in CeO_2.

Plane-wave basis density functional theory (DFT) simulations were performed by using the VASP code to understand the effects of the Cr dopant on oxygen vacancy (Vo) formation. A Ce atom was substituted by one Cr atom in the 96-atom $2 \times 2 \times 2$ supercell of CeO_2 ($Ce_{32}O_{64}$) with a Monkhorst–Pack k-point mesh of $4 \times 4 \times 4$, which is equivalent to the loading amount of Cr at 3 mol%. The incorporation of Cr in 3+ charge state can be compensated by the formation of an extra Vo (per two Cr^{3+} ions) or a Vo and a Ce^{3+} ion while the oxidation of Cr-doped CeO_2 NCs should create Cr^{4+} ions. Two Ce^{3+} ions were located in the next nearest neighbor positions with respect to the Vo, consistent with previous studies of CeO_2 with DFT+U. The Bader charge of the Ce^{3+} and Ce^{4+} ions was set $+2.11|e|$ and $+2.44|e|$, respectively. The Vo formation energy (E(Vo)) in the Cr-doped CeO_2 was calculated as 0.99 eV, which was substantially decreased from 2.00 eV in the non-doped case. The high OSC performance can be attributed to the contribution of the valence change of Cr to E(Vo), and the structural effect of Cr doping on E(Vo). Only 3 mol% doping improved the OSC, suggesting that Cr doping affects the structure of CeO_2 significantly. The results of layer-by-layer EELS analysis indicated a significant increase in the amount of Ce^{3+} by Cr doping particularly in the internal atomic layers, which is more than the mere compensation of Cr^{3+} with Vos. The low E(Vo) of Cr-doped CeO_2 NCs can lead to a significant increase of Ce^{3+} ions even with a low amount of Cr doping, as observed in the experiments.

In summary, DFT calculations demonstrated that the Cr dopant reduces the E(Vo), resulting in the increase of the mobility of oxygen atoms in the nano-sized CeO_2. The high concentration of Vos as well as the high oxygen diffusivity improve the OSC performance of Cr-doped CeO_2 NCs, compared with the non-doped CeO_2 NCs. These effects provides a fundamental understanding of the role of dopants in formation and distribution of Vos in the metal-doped CeO_2 NCs [1].

References

[1] X. Hao, A. Yoko, K. Inoue, Y. Xu, M. Saito, C. Chen, G. Seong, T. Tomai, S. Takami, A.L. Shluger, B. Xu, T. Adschiri, Y. Ikuhara: Acta Mater. **203**, 116473 (2021).

Oxygen vacancy formation in metal-doped CeO_2 nanocrystals

Akira YOKO[1], Kazutoshi INOUE[1], Mitsuhiro SAITO[2], and Yuichi IKUHARA[1,2,*]
[1] *Advanced Institute for Materials Research, Tohoku University, Sendai, Miyagi, 980-8577*
[2] *Institute of Engineering Innovation, The University of Tokyo, Yayoi, Tokyo, 113-8656*

We studied Cr-doped cubic {100}-faceted CeO_2 nanocrystals (NCs) with an average size of 7.8 nm fabricated by a supercritical water reaction. A considerably large amount of Ce^{3+} ions was detected in the Cr-doped CeO_2 NCs by scanning transmission electron microscopy combined with electron energy loss spectroscopy (EELS). The Cr dopants substituted the Ce sites in the amount of approximately 3 mol%. We experimentally observed that the oxygen-storage capacity (OSC) was substantially improved by a low amount of Cr doping, which can be attributed to the low oxygen vacancy formation energy and high mobility of oxygen atoms by doping Cr in CeO_2.

Plane-wave basis density functional theory (DFT) simulations were performed by using the VASP code to understand the effects of the Cr dopant on oxygen vacancy (Vo) formation. A Ce atom was substituted by one Cr atom in the 96-atom $2 \times 2 \times 2$ supercell of CeO_2 ($Ce_{32}O_{64}$) with a Monkhorst–Pack k-point mesh of $4 \times 4 \times 4$, which is equivalent to the loading amount of Cr at 3 mol%. The incorporation of Cr in 3+ charge state can be compensated by the formation of an extra Vo (per two Cr^{3+} ions) or a Vo and a Ce^{3+} ion while the oxidation of Cr-doped CeO_2 NCs should create Cr^{4+} ions. Two Ce^{3+} ions were located in the next nearest neighbor positions with respect to the Vo, consistent with previous studies of CeO_2 with DFT+U. The Bader charge of the Ce^{3+} and Ce^{4+} ions was set $+2.11|e|$ and $+2.44|e|$, respectively. The Vo formation energy (E(Vo)) in the Cr-doped CeO_2 was calculated as 0.99 eV, which was substantially decreased from 2.00 eV in the non-doped case. The high OSC performance can be attributed to the contribution of the valence change of Cr to E(Vo), and the structural effect of Cr doping on E(Vo). Only 3 mol% doping improved the OSC, suggesting that Cr doping affects the structure of CeO_2 significantly. The results of layer-by-layer EELS analysis indicated a significant increase in the amount of Ce^{3+} by Cr doping particularly in the internal atomic layers, which is more than the mere compensation of Cr^{3+} with Vos. The low E(Vo) of Cr-doped CeO_2 NCs can lead to a significant increase of Ce^{3+} ions even with a low amount of Cr doping, as observed in the experiments.

In summary, DFT calculations demonstrated that the Cr dopant reduces the E(Vo), resulting in the increase of the mobility of oxygen atoms in the nano-sized CeO_2. The high concentration of Vos as well as the high oxygen diffusivity improve the OSC performance of Cr-doped CeO_2 NCs, compared with the non-doped CeO_2 NCs. These effects provides a fundamental understanding of the role of dopants in formation and distribution of Vos in the metal-doped CeO_2 NCs [1].

References

[1] X. Hao, A. Yoko, K. Inoue, Y. Xu, M. Saito, C. Chen, G. Seong, T. Tomai, S. Takami, A.L. Shluger, B. Xu, T. Adschiri, Y. Ikuhara: Acta Mater. **203**, 116473 (2021).

van der Waals density functional study of Cu phthalocyanine adsorbed on the Au(110) surface

Yuji HAMAMOTO

Department of Precision Engineering, Graduate School of Engineering,

Osaka University, Yamada-oka, Suita, Osaka 565-0871

The lowest molecular orbital (LUMO) plays an essential role in the electronic transport across a metal-organic interface. Since surface adsorption distorts the molecular structure, influencing the properties of LUMO, it is of particular importance to understand the interface structure microscopically. Here we investigate the geometric and electronic structures at a metal-organic interface of Cu phthalocyanine (CuPc) on the Au(110) surface [1]. The (1! 2) missing-row reconstructed surface of Au(110) is modeled by removing Au atomic rows from a periodically repeated 6! 4 unit cell of the Au(110) slab composed of six atomic layers. A CuPc molecule is adsorbed on a missing row, in which *n* Au atoms with *n* = 0, 2, 4, and 6 are added below CuPc to reproduce the finding of STM measurements [1]. The van der Waals (vdW) interaction between CuPc and Au(110) is taken account of by the vdW-DF method [2].

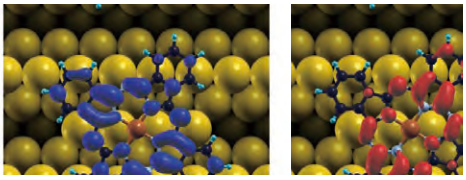

Fig. 1: Schematic views of CuPc on the m row reconstructed Au(110) surface with The blue (red) balloons show the isosurfa absolute square of $e_{g(1)}$ [$e_{g(2)}$].

Our calculated results indicate that CuPc prefers to adsorb on the center of the Au adatoms with an in-plane rotation as shown in Fig. 1, irrespective of the number of adatoms. The projected density of states (PDOS) onto the doubly degenerate LUMO, labeled as $e_{g(1)}$ and $e_{g(2)}$, of CuPc is plotted as a function of energy

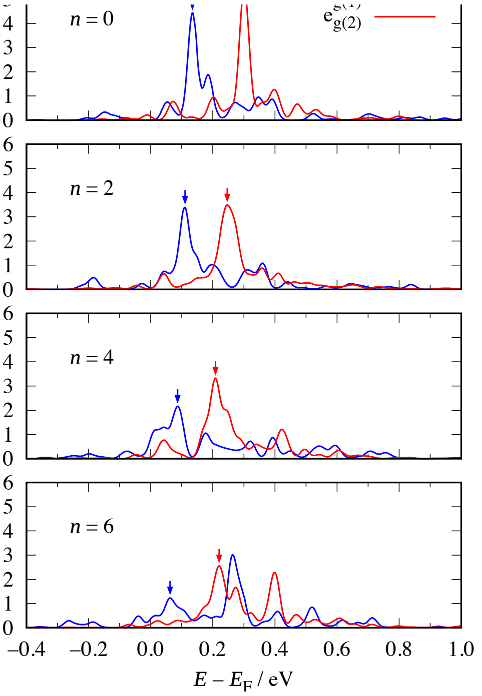

. 2: Density of states projected onto the $e_{g(1)}$ $_{2)}$] orbitals of CuPc.

in Fig. 2, where the center of the peaks for the LUMO-derived states is lowered roughly monotonically as *n* is increased, in good agreement with the results of STS measurements. The lowering of the peaks is qualitatively consistent with lowering of the effective potential of the bare surfaces as a function of *n.* The splitting of the peaks suggests that the hybridization between CuPc LUMO and surface states is enhanced for large *n*. Our results reveal that the LUMO of CuPc is sensitive to the detailed structures of the reconstructed Au(110) surfaces.

References

[1] H. Koshida, H. Okuyama, S. Hatta, T. Aruga, Y. Hamamoto, I. Hamada, and Y. Morikawa, J. Phys. Chem. C **124**, 17696 (2020).

[2] M. Dion, H. Rydberg, E. Schröder, D. C. Langreth, and B. I. Lundqvist, Phys. Rev. Lett. **92**, 246401 (2004).

First-principles study of molecule/metal interfaces

Ikutaro Hamada
Department of Precision Science and Technology, Graduate School of Engineering,
Osaka University, 2-1 Yamada-Oka, Suita, Osaka 565-0871

Carbon-based nanomaterials, such as graphene and nanographene have attracted enormous attention, owing to their fascinating electronic, optical, and magnetic properties. For precise fabrication of nanographene, on-surface synthesis has been developed, in which precursor molecules are thermally induced to react on a surface, and the technique has been proven to be powerful to fabricate graphene based nanostructures. In this work, we propose an alternative method, in which a tip of scanning tunneling microscopy/non-contact-atomic-force microscopy is utilized as a manipulable metal catalyst, which activates cyclodehydrogenation of hydrocarbons [1].

we used diazuleno[1,2-*c*:2′,1′-*g*]phenanthrene (DAPh), as well as 10,10′-dibromo-9,9′-bianthracene (DBBA) adsorbed on a Cu(100) surface, to demonstrate the tip-induced cyclodehydrogenation reaction. To investigate the mechanism of the tip-induced reaction, we performed atomistic simulations based on density functional theory (DFT) with the van der Waals (vdW) density functional (vdW-DF) [2] as implemented in our in-house DFT code STATE [3-6], to describe the interaction between organic molecule and metal accurately.

Experimentally, the DAPh molecule is thermally reacted into a cyclodehydrogenated diazulenopyrene (DAPy), but the reaction intermediate has not been determined. We performed extensive DFT calculations and successfully identified the intermediate as hydro-diazulenopyrenyl (hDAPyr). By using a Cu-terminal tip, we induced the cyclodehydrogenation of hDAPyr to form DAPyr. To understand the reaction mechanism, we used a 10-atom pyramidal model Cu tip over hDAPyr and could reproduce the tip-induced cyclodehydrogenation reaction. Furthermore, we clarified the detailed potential energy surface and by the electronic structure analysis, we revealed the electronic origin of the tip-induced catalytic dehydrogenation reaction.

References

[1] A. Shiotari et al: Nano Lett **20** (2020) 8339.

[2] M. Dion et al.: Phys. Rev Lett. **92** (2014) 246401.

[3] https://statedoc.readthedocs.io/

[4] J. Wu and F. Gygi: J. Chem. Phys **136** (2012) 224107.

[5] Y. Hamamoto, I. Hamada, K. Inagaki, and Y. Morikawa: Phys. Rev. B **93** (2016) 245440.

[6] I. Hamada: Phys. Rev. B **89** (2014) 121103(R).

Theoretical study of oxygen-redox chemistry in spinel oxides

Atsuo YAMADA
Department of Chemical System Engineering,
The University of Tokyo, Bunkyo-ku, Hongo, Tokyo 113-8656

Oxygen-redox chemistry has recently paved a path to develop large-capacity cathode materials for rechargeable batteries. Despite vast efforts on exploring oxygen-redox cathodes, few studies have been reported for the oxygen-redox reaction in spinel oxides. In this work, we theoretically uncover the oxygen-redox behavior in the stable spinel framework using the density functional theory calculations.

We performed all calculations using Vienna Ab-initio Simulation Package. The projector-augmented wave method with a plane-wave basis set was used. We applied the *U* values of 4.84 eV and 3.90 eV for Mn in the spinel and layered structures, respectively. The HSE06 hybrid functional was employed for calculating electronic structures. The crystal orbital overlap population was computed with the Lobster program and molecular orbitals were built with maximally localized Wannier functions using Wannier90 code.

The presence of ionic Mg^{2+} in spinel $LiMg_{0.5}Mn_{1.5}O_4$ brings labile O 2p states for oxygen-redox activity. However, in contrast with the dominant Mn-O interactions that could stabilize oxidized oxide ions in a typical lithium-rich layered oxide Li_2MnO_3, the spinel structure is dominated by O-O interactions near the Fermi level, which are less able to stabilize holes. Consequently, the spinel oxide is predicted to undergo structural degradation more easily during the oxygen-redox reactions.

References

[1] X.-M. Shi, E. Watanabe, M. Okubo, A. Yamada, *Chem. Mater.*, **32** (2020) 7181.

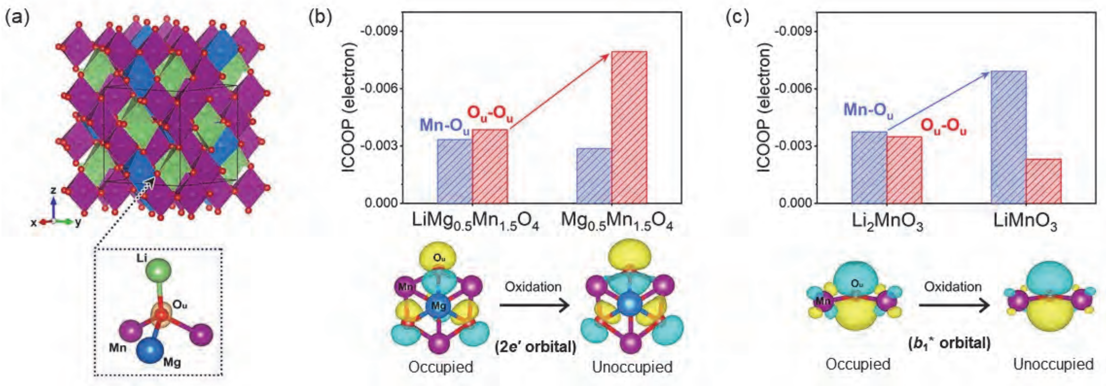

Fig. 1 (a) Spinel $LiMg_{0.5}Mn_{1.5}O_4$. Electronic structures of (b) spinel and (c) layered oxides.

Order-disorder transition in ultrahigh-pressure phase of the Na-Mg-F system

Koichiro Umemoto
Earth-Life Science Institute,
Tokyo Institute of Technology, 2-12-1 Meguro-ku, Ookayama, Tokyo 152-8550

$MgSiO_3$ bridgmanite with the orthorhombic perovskite structure is a major constituent of the lower mantle of the Earth. It takes the post-perovskite (PPV) structure near the core-mantle boundary pressure (~125 GPa). The PPV phase is the final form of $MgSiO_3$ in the Earth. However, at much higher pressures in “super-Earths” which are exoplanets expected to be terrestrial with masses much larger than the Earth, $MgSiO_3$ PPV should undergo “post-PPV” transitions. So far, first principles studies have predicted the three-stage dissociation of $MgSiO_3$ PPV: $MgSiO_3$ PPV → I-42d-type Mg_2SiO_4 + $P2_1/c$-type $MgSi_2O_5$ → Mg_2SiO_4 + Fe_2P-type SiO_2 → CsCl-type MgO + SiO_2 [1-3].

$NaMg_2F_5$ is a low-pressure analog of $MgSi_2O_5$. Theoretically $NaMgF_3$ PPV was predicted to dissociate into NaF and $NaMg_2F_5$ [4] and this prediction has been confirmed by a recent experiment [5]. There are two kinds of the Mg sites. One of them is very similar to the Na site; both Na and Mg atoms are surrounded by 9 F atoms which form tricapped triangular prisms. This similarity leads us to an idea of order-disorder transition at high temperature over the cation sublattice of Na and Mg atoms. A similar order-disorder transition has been predicted in I-42d-type Mg_2GeO_4 [6], a low-pressure analog of Mg_2SiO_4.

In this study, we investigated the order-disorder transition in $NaMg_2F_5$ by first principles [7]. To deal with the order-disorder transition, we prepared as many configurations as possible in a supercell of 64 atoms and calculated a partition function. Then, the order-disorder transition temperature (T_c) can be obtained by locating the peak temperature of heat capacity calculated from the partition function. Our calculations showed that Tc is 1500~2000 K over 20~100 GPa. The order-disorder transition was not taken into account in the experiment [5]. We expect the disordered phase may show a better explanation of the XRD pattern in the experiment.

Since $NaMg_2F_5$ is the low-pressure analog of $MgSi_2O_5$, the order-disorder transition predicted in this study is expected to occur also in $MgSi_2O_5$ and will play an important role in modeling interiors of super-Earths.

The first principles calculations in this study were performed using the Quantum-Espresso package on the supercomputer (system B) at the

Institute for Solid State Physics.

References

[1] S. Q. Wu, et al.: J. Phys.: Condens. Matter **26** (2014) 035402.

[2] H. Niu et al.: Sci. Rep. **5** (2015) 18347.

[3] K. Umemoto et al.: Earth Planet. Sci. Lett. **478** (2017) 40.

[4] K. Umemoto and R. M. Wentzcovitch: K. Umemoto and R. M. Wentzcovitch, JPS Conf. Proc. **4**, 011002 (2015).

[5] R. Dutta, et al.: Proc. Nat. Acad. Sci, **116**, 19324 (2019).

[6] K. Umemoto and R. M. Wentzcovtich: arXiv:2012.08056.

[7] K. Umemoto and R. M. Wentzcovitch, in preparation.

First principles study of effect of Al impurity on the post-post-perovskite transitions

Koichiro Umemoto
Earth-Life Science Institute,
Tokyo Institute of Technology, 2-12-1 Meguro-ku, Ookayama, Tokyo 152-8550

$MgSiO_3$ bridgmanite with the orthorhombic perovskite structure is a major constituent of the lower mantle of the Earth. It takes the post-perovskite (PPV) structure near the core-mantle boundary pressure (~125 GPa). The PPV phase is the final form of $MgSiO_3$ in the Earth. However, at much higher pressures in "super-Earths" which are exoplanets expected to be terrestrial with masses much larger than the Earth, $MgSiO_3$ PPV should undergo "post-PPV" transitions. So far, first principles studies have predicted the three-stage dissociation of $MgSiO_3$ PPV: $MgSiO_3$ PPV → I-42d-type Mg_2SiO_4 + $P2_1/c$-type $MgSi_2O_5$ → Mg_2SiO_4 + Fe_2P-type SiO_2 → CsCl-type MgO + SiO_2 [1-3].

In real super-Earths, impurities may play an important role in the above post-PPV transitions. In this study, we investigated the effect of Al atoms, one of major candidates of impurities, on the post-PPV transitions. To do it, we prepared supercells of $(Mg_{1-x}Al_x)(Si_{1-x}Al_x)O_3$, $(Mg_{2-x}Al_x)(Si_{1-x}Al_x)O_4$, and $(Mg_{1-x}Al_x)(Si_{2-x}Al_x)O_5$, for x=0.25, 0.125, and 0.0625. We found that Al atoms prefer to exist in Mg_2SiO_4 after the fist post-PPV dissociation. The presence of Al atoms decreases the transition pressure of the first dissociation. Considering effects of configuration entropy at high temperature, Al atoms start to exist also in $MgSi_2O_5$.

Recently, we predicted a new temperature-induced order-disorder transition in I-42d-type Mg_2GeO_4, a low-pressure analog of Mg_2SiO_4 [4]. The knowledge obtained in this study will be utilized for the study in the post-PPV transition at high temperature, which is expected to occur in super-Earths.

The first principles calculations in this study were performed using the Quantum-Espresso package on the supercomputer (system B) at the Institute for Solid State Physics.

References

[1] S. Q. Wu, et al.: J. Phys.: Condens. Matter **26** (2014) 035402.

[2] H. Niu et al.: Sci. Rep. **5** (2015) 18347.

[3] K. Umemoto et al.: Earth Planet. Sci. Lett. **478** (2017) 40.

[4] K. Umemoto and R. M. Wentzcovtich: arXiv:2012.08056.

First-principles molecular dynamics study of water/TiO$_2$ interfaces using hybrid functionals

Tatsuhiko OHTO

Graduate School of Engineering Science,

Osaka University, 1-3 Machikaneyama, Toyonaka, Osaka 560-8531

Density functional theory-based molecular dynamics simulations are increasingly being used for simulating aqueous interfaces. Nonetheless, the choice of the appropriate density functional, critically affecting the outcome of the simulation, has remained arbitrary. Here, we assess the performance of various exchange-correlation (XC) functionals, based on the metrics relevant to sum-frequency generation spectroscopy. The structure and dynamics of water at the water-air interface are governed by heterogeneous intermolecular interactions, therefore providing a critical benchmark for XC functionals. We find that the revPBE and revPBE0 with the dispersion correction show excellent performance. The poor performance of the empirically optimized density-functional (M06-L) manifests the importance of satisfying exact functional condition. Understanding the performance of different XC functionals can aid resolving the controversial interpretation of the interfacial water structure and direct the design of novel, improved XC functionals better suited to describe the heterogeneous interactions in condensed phases. [1]

We employed the CP2K code [2], which is based on the mixed Gaussian and plane wave basis sets. The simulation of the water/TiO2 interface is on-going.

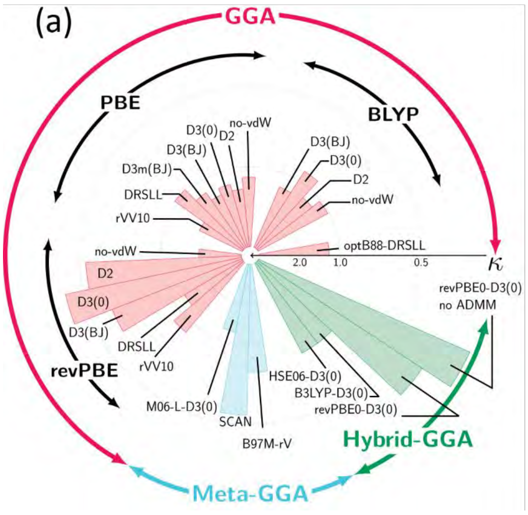

Fig. 1: The ability of different functionals to accurately predict water properties is directly compared. The smaller (larger) score κ corresponds to better (worse) predictive power of the functional [1].

References

[1] T. Ohto et al. J. Phys. Chem. Lett. **10**, 4914 (2019).

[2] The CP2K developers group, http://cp2k.berlios.de/

Ab Initio Band Structure Calculation of InAsSb Using VASP Based on Hybrid Density Functional Theory

Hiroki I. FUJISHIRO, Yoshitaka MATSUMOTO, and Akira ENDOH
Department of Applied Electronics,
Tokyo University of Science, Niijuku, Katsushika, Tokyo 125-8585

The terahertz band (0.1 to 10 THz) is the main radio resource for future high-speed large-capacity communications and sensing systems. Sb-based high electron mobility transistors (HEMTs) are one of the most promising devices that can operate in the terahertz band. In our previous works, we developed InSb [1, 2] and GaInSb [3] channel HEMTs. In order to achieve higher speed operation of HEMTs, it is desirable that the electron effective mass in the channel semiconductor is lighter and the electron concentration in the channel layer is higher. InAsSb is a semiconductor that satisfies the above conditions [4].

In 2019, we carried out ab initio band structure calculations of unstrained and compressively strained InSb using Vienna Ab initio Simulation Package (VASP) based on the method in the local density approximation to obtain band parameters [5]. We used the hybrid coefficient of the density functional [6]. The hybrid functional used in [6] was a modification of PBE0 (Perdew-Burke-Ernzerhof 0). The functional is constructed by the mixing of a fraction α of the Fock exchange with a fraction $1-\alpha$ of the PBE exchange. The exchange-correlation energy E_{xc} can be expressed by the following equation:

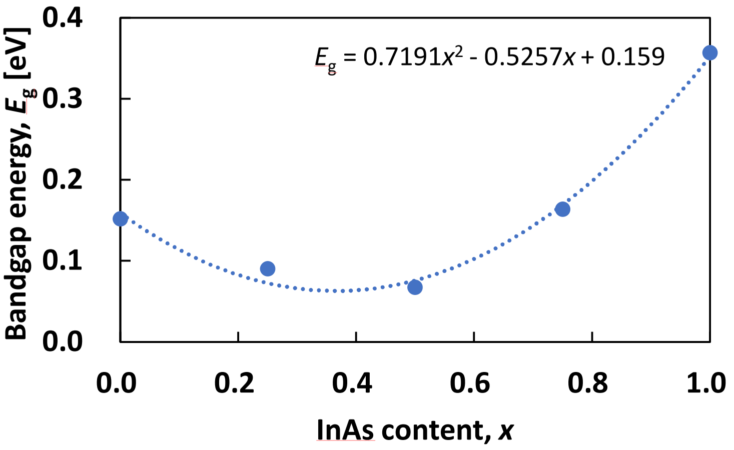

Fig. 1: InAs content x dependence of bandgap energy E_g.

$$E_{xc} = \alpha E_x + (1-\alpha)E_x^{PBE} + E_c^{PBE} \quad (1)$$

where E_x is the Fock exchange, E_x^{PBE} is the PBE exchange, and E_c^{PBE} is the PBE correlation [6]. We obtained the bandgap energy E_g closest to the literature value by using $\alpha = 0.21$ for InSb. In this work, we applied this method to InAsSb to explore the potential of InAsSb channel HEMTs.

First, we applied this method to InAs. We obtained the E_g closest to the literature one by using $\alpha = 0.24$. We carried out the band structure calculations of $InAs_xSb_{1-x}$ at $x = 0.25$, 0.50, and 0.75. For the α values of InAsSb, we used linearly interpolated values. Figure 1 shows the InAs content x dependence of bandgap energy E_g. The x-dependence of E_g is not linear and shows a downwardly convex dependency. We obtained the electron effective masses m^*'s in the Γ valley of InAsSb from the calculated band structures. Figure 2 shows the InAs content x dependence of electron effective mass in the Γ valley m^*. The x-dependence of m^*shows a tendency similar to that of E_g. The m^* values of $InAs_xSb_{1-x}$ at $x = 0.25$ and 0.50 are lighter than that of InSb. It is well known that the m^* in InSb is the lightest among group III-V compound semiconductors. According to the calculations in this study, the m^* in InAsSb is lighter than that in InSb depending on the InAs content. Therefore, InAsSb channel HEMTs have a potential to be the fastest of all HEMTs using group III-V compound semiconductors.

References

[1] K. Isono *et al.*: Proc. CSW2016, WeD1-5.
[2] N. Oka *et al.*: Abst. TWHM2017, p. 83.
[3] K. Osawa *et al.*: Abst. TWHM2019, p. 53.
[4] O. Berolo *et al.*: Phys. Rev. B **8** (1973) 3794.
[5] H. I. Fujishiro *et al.*: Activity Report 2019, p. 153.
[6] T. Garwood *et al.*: Infrared Physics & Technology, 2017.

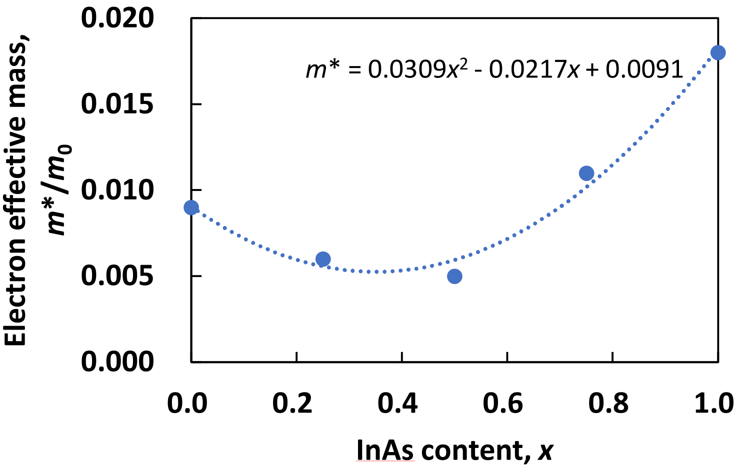

Fig. 2: InAs content x dependence of electron effective mass in Γ valley m^*. m_0 is electron rest mass.

DFT calculation of atomic displacement captured by energy dissipation channel of noncontact atomic force microscope

Toyoko ARAI[1], Takahiro Kato[1], Jun-Ichi Iwata[2], Atsushi Oshiyama[3]

[1]*Graduate school of Natural Science and Technology, Kanazawa University, Kanazawa, Ishikawa, 920-1192*

[2]*AdvanceSoft Corporation, Tokyo 101-0062*

[3]*IMaSS, Nagoya University, Nagoya, Aichi 464-8601*

In the last two decades the conservative and non-conservative (dissipative) force interactions between a tip and a sample in proximity have been intensively examined by non-contact atomic force microscopy (nc-AFM). In particular, the channel of nc-AFM to measure the energy dissipation through the non-conservative force interactions has been regarded to have great potential to explore nano-mechanical phenomena; the dissipation channel gives the change in the amount of mechanical energy to maintain the constant oscillation amplitude of an AFM cantilever. We had experimentally found that, when the nc-AFM image showed the high resolution for the individual adatoms on a Si(111)-(7×7) surface, the simultaneously obtained energy dissipation signal increased in close proximity over the hollow sites surrounded by a Si adatom and a Si rest atom with a dangling bond per each [1]. Based on the experimental results, the dynamic atomic processes responsible for the dissipation had been discussed in regard to breaking of the backbonds of the Si adatom and subsequent bond formation in an alternative atomic configuration of the Si surface atoms, including the Si atom at the apex of AFM tip. In this study, to elucidate the phenomena, the surface diffusion potentials of a Si adatom were calculated using real-space density functional theory (RSDFT) [2] when the Si tip was brought closer to the Si(111)-(7×7) surface. RSDFT is a first-principles program developed by Oshiyama and Iwata, which uses a real-space difference method and a pseudopotential method.

First, we optimized the structures of a Si(111)-(7×7) reconstructed surface consisting of 298 Si atoms and 49 H atoms and a [001] oriented Si tip by RSDFT. Then, while the tip was placed over the hollow site and brought closer from 5.0 Å to 3.0 Å, the surface diffusion potentials for a corner Si adatom were calculated from the original position of the Si adaom to the neighboring hollow site. It is known that the hollow site is a meta stable site for the adatom, and there is a diffusion barrier between the original adatom site and the hollow site. Our calculations indicated that the diffusion barrier

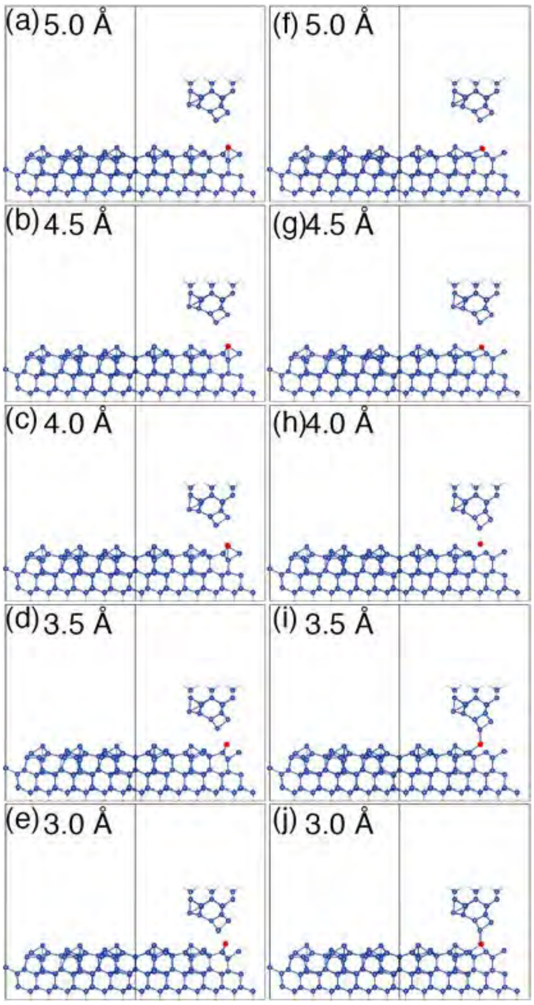

Fig. 1 Calculated structures of Si(111)-(7×7) reconstructed surface and [001] oriented Si tip. (a–e) For the Si on the adatom site, denoted by the red circles. (f–j) For the Si on the hollow site. The number shown with the unit of Å shows the vertical separation between the tip atom and the Si atom on the site.

height was lowered as the tip was approached. However, we did not obtain the evidence for promotion of the adatom diffusion from the adatom site to the hollow site only by bringing the tip closer. Next, we calculated the structure changes and the forces for two cases: the Si atom on the original adatom site or on the hollow site with the tip approaching over the hollow site, as shown in Fig. 1. Even for the Si atom on the most stable adatom site, when the tip approaches the hollow site, the Si atom was lifted up (Fig. 1(a–e)). But the Si atom did not move to the hollow site even when the tip was closer from a height of 3.0 Å (Fig. 1(e)). For the Si atom on the hollow site, it was found that the strong force acted between the tip Si atom and the Si atom on the hollow site (Fig. 1(f–j)), as a result of bonding formation between them. The paper of this study is under preparation.

References

[1] T. Arai, R. Inamura, D. Kura, and M. Tomitori, Phys. Rev. B **97**, 115428 (2018).

[2] J.-I. Iwata, D. Takahashi, A. Oshiyama et al., J. Comput. Phys. **229**, 2339 (2010).

Construction of magnetic materials database by KKR Green's function method

Tetsuya FUKUSHIMA
Institute for Solid State Physics, University of Tokyo
Kashiwa-no-ha, Kashiwa, Chiba 277-8581

We have developed an automatic exhaustive calculation tool which is based on the Korriga-Kohn-Rostoker coherent potential approximation (KKR-CPA) method. Our tool can explore the huge materials space consisting of disordered systems and construct large-scale materials databases. In this year, we implemented a new feature in our tool, where electronic structures, magnetic properties, and transport properties at finite temperature can be calculated [1].

In order to calculate electronic structures at finite temperature, we incorporate the effects of local phonon excitations and spin-wave (magnon) excitations in the framework of the KKR-CPA method. In the KKR Green's function method, the single-site t-matrix is the sum of the coefficients of partial wave expansion at each atomic position and contains information of the single-site scattering effect. We can thus replace the multiple scattering effect by an effective medium potential using CPA. We treat local phonon excitation and magnon excitation as the configuration average with respect to the local phonon displacements and local moment disorder (LMD) states, respectively.

For CPA calculation of the local phonon excitation, the probabilities of the atomic displacements must be known. Here, we employ an alloy-analogy model. The single-site t-matrix changes responding to the atomic displacements and has to be determined self-consistently. In this case, it is convenient to expand each single-site t-matrix centered on the displaced position for self-consistent calculation. However, later, we must re-expand the displaced single-site t-matrix to partial waves centered on the undisplaced atomic position, and transform the scattering matrix for the displaced potential into that defined with respect to the regular lattice position. This is possible because the effect of atomic displacement on the electronic structure is local. Accordingly, the backscattering term of the Green's function referring to the regular lattice is also obtained. In the present calculations, we take six directions (i.e., $\{0,0,1\}$ cubic directions) into consideration for the local phonon displacements of each atom.

To handle the magnon excitation, we use the LMD model. When the temperature increases, the spin tilts slightly away from the direction of the magnetization, and its effect propagates to surrounding spins, namely, spin-wave excitation. We consider the configuration average of the linear combination of the spin flips at every site. This model is called the LMD state. We estimate it from the decrease in the spontaneous magnetization observed in the experimental data. For $\mathrm{Co_2MnSi}$, for simplicity, we assume that the decrease in the magnetization originates solely from the spin-flip in the Mn atoms, and construct the LMD model as $\mathrm{Co_2Mn^{\uparrow}_{1-x/2}Mn^{\downarrow}_{x/2}Si}$, where $\mathrm{Mn^{\uparrow}}$ and $\mathrm{Mn^{\downarrow}}$ denote the up and down magnetic moments, respectively. For instance, the magnetization ratio between 0 K and 300 K is 0.983. We thus assume that 0.85% of the spins are reverse while the others are unchanged at 300 K ($Co_2Mn^{\uparrow}_{0.9915}Mn^{\downarrow}_{0.0085}Si$ random alloys).

Moreover, we calculate the conductivity using the Kubo-Greenwood formula including vertex correction, in which the vertex functions are expressed using the ladder-like approximation. The conductivity tensor is defined as follows:

$$\begin{aligned}\sigma_{\mu\nu} &= \frac{1}{4}\lim_{\eta\to 0}[\tilde{\sigma}_{\mu\nu}(\varepsilon+i\eta,\varepsilon+i\eta) \\ &+ \tilde{\sigma}_{\mu\nu}(\varepsilon-i\eta,\varepsilon-i\eta) \\ &- \tilde{\sigma}_{\mu\nu}(\varepsilon+i\eta,\varepsilon-i\eta) \\ &- \tilde{\sigma}_{\mu\nu}(\varepsilon-i\eta,\varepsilon+i\eta)]. \qquad (1)\end{aligned}$$

Here, ε is energy and $i\eta$ is an infinitesimal imaginary part. Note that $\sigma_{\mu\nu}$ depends on ε. Moreover, $\tilde{\sigma}$ is calculated by

$$\tilde{\sigma}_{\mu\nu}(z_1,z_2) = -\frac{\hbar}{\pi N\Omega}\mathrm{Tr}\langle j_\mu G(z_1) j_\nu G(z_2)\rangle_{\mathrm{CPA}}, \qquad (2)$$

where N is the number of unit cells, Ω is the unit cell volume, and $j_{\mu(\nu)}$ is the current operator. The bracket indicates the configuration average for the disordered systems by CPA.

Figure 1 shows the the temperature-dependent electrical resistivity of Co_2MnSi using the Kubo-Greenwood formula. The resistivity of Co_2MnSi derived from a local phonon is proportional to the temperature except in the low-temperature region. The resistivity originating from the magnon scattering reflects the experimentally observed magnetization curve. We determined that either local phonon displacement or LMD alone was insufficient to reproduce the experimental data. This is expected because at low temperatures, scattering due to lattice vibration and spin fluctuation is suppressed, and impurity scattering becomes dominant. It is known that there are considerable native defects in Heusler alloys, such as vacancies, interstitials, and antisite defects. For Co_2MnSi, previous works suggest the presence of antisite disorders between Co and Mn. Scattering effects from these antisite defects may be the main source of the finite resistivity at low temperature. Therefore, we attempted to calculate the resistivities considering the Mn-Co antisite disorders. Antisite effects can be easily added to the calculation in the framework of CPA. If we assume that 1.0% of the Mn-Co antisite disorders (i.e., $(Co_{0.995},Mn_{0.005})_2(Mn_{0.990},Co_{0.010})Si$) is introduced, the calculated residual resistivity is 6.47 $\mu\Omega$cm. This value is consistent with the experimental results at extremely low temperature. The pink stars in Fig. 1 represent the calculated temperature-dependent resistivity of Co_2MnSi when the Mn-Co disorders are included in addition to local phonon and magnon disorders. The result is in reasonable agreement with the experimental results. Therefore, it can be concluded that to accurately calculate the finite-temperature transport properties of Co_2MnSi, three disorders (local phonon, magnon, and Mn-Co antisite disorders) should be considered in the comprehensive procedure on the basis of CPA.

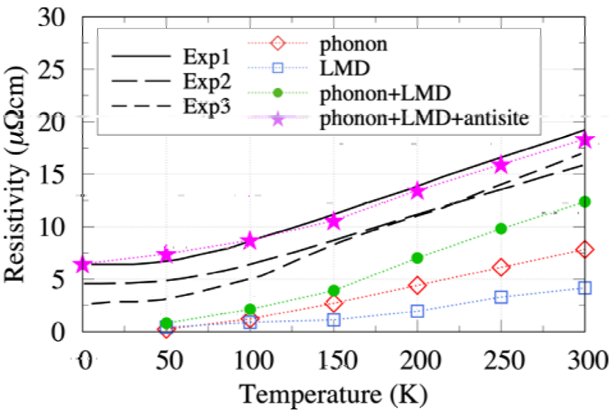

Figure 1: Temperature dependent electrical resistivity estimated by the Kubo-Greenwood formula.

References

[1] H. Shinya, S. Kou, T. Fukushima, A. Masago, K. Sato, H. Katayama-Yoshida, and H. Akai, Appl. Phys. Lett. **117** (2020) 042402.

Hybrid Ab-Initio/Machine-Learning Optimization of Nano Interfaces and Molecular Structures

Kenji TSURUTA, Md. Abdullah Al ASAD, Kyosuke SATO,
Masaaki MISAWA, and Satoshi OHMURA[a]

Graduate School of Natural Science and Technology, Okayama University, Okayama 700-8530
[a] *Department of Civil and Environmental Engineering, Hiroshima Institute of Technology, Hiroshima 731-5193*

Designing and developing functional materials/molecules often require vast searching of target properties from extra-large data set, which is far out of the capability of conventional computing algorithms. In recent years, the Deep-Learning (DL)-based molecular design methods have been extensively studied. Recently, we have reported [1] a machine learning method for predicting molecular properties by mapping a graph representation of a molecule to a latent variable space and by linking the variable to physical property of the molecule. Representing molecules in the latent space enables an efficient property search within existing data, because the DL model transforms the discrete representation of a molecular graph into a continuous variable space suitable for various numerical algorithms.

In the present study, we further improve the output rate of valid SMILES of decoder by introducing a discriminator attached to the VAE stream. Adopting a molecular-mechanics method to calculate 3D structure from SMILES, we can optimize physical properties of the molecule by other simulation methods such as density-functional-theory calculations even when there is not enough data set. The range of physical property space covered by the SMILES representation is thereby expanded and the data-driven optimization using Kernel Ridge Regression method can be performed within the search space. We have demonstrated the effectiveness of this method for optimizing a molecular HOMO-LUMO gap as an example.

Another effort is taken to perform efficient search for insertion/reaction path of an molecules on the surface of a functional materials. We computationally investigate an insertion process of water into the methylammonium lead halide perovskite ($MAPbI_3$). The rapid decomposition of $MAPbI_3$ reaction with water has been recognized to be a major obstacle to its solar-cell applications. To overcome this drawback process, it is important to identify the initial stage of water insertion into the $MAPbI_3$. The first-principles calculation based on the density-functional theory is performed to investigate the water insertion process on outer surface layer of $MAPbI_3$ slab model. Using the Nudged Elastic Band method, we find that the initial insertion process follows the three steps: approaching, re-orienting and finally sinking into the perovskite layer. This process requires approximately 0.60 eV to overcome an energy barrier, which agrees with an *in-situ* X-ray diffraction (XRD) measurement of the reaction threshold of water molecules with the $MAPbI_3$ crystal at room temperature [2]. These computations have been done in part by using the Super-computing System at SCC-ISSP

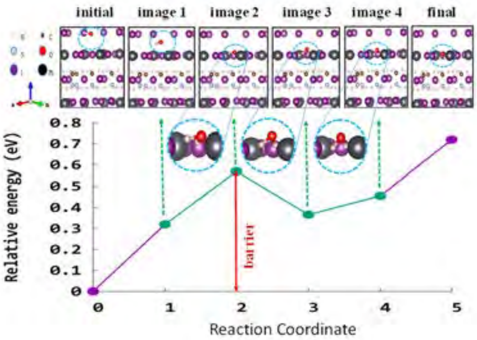

Fig. 1 Insertion path of water molecules in the $MAPbI_3$ surfaces and barrier energy variation along the path.

References

[1] K. Sato and K. Tsuruta, Mater. Sci. Forum **1016**, 1492 (2021).

[2] M. Hada, M. A. A. Asad, M. Misawa, Y. Hasegawa, R. Nagaoka, H. Suzuki, R. Mishima, H. Ota, T. Nishikawa, Y. Yamashita, Y. Hayashi, and K. Tsuruta, Appl. Phys. Lett. **117**, 253304 (2020).

Investigation on the electronic structure of photo-catalytic double-perovskite

Kazume NISHIDATE
Faculty of Science and Engineering, Iwate University
Ueda 4-3-5, Morioka, Iwate 020-8551

In recent experiments, a significant band gap widening was observed when Sb was substituted for Bi in the double-perovskite Ba_2PrBiO_6. In this work, we study a series of double-perovskites, $Ba_2Bi^{III}Bi^{V}O_6$, Ba_2PrBiO_6, and Ba_2PrSbO_6 using the first-principles density functional theory with the Heyd-Scuseria-Ernzerhof hybrid functional to investigate the substitution effect on the structural and electronic properties [1].

We use the density functional theory (DFT) as implemented in the Vienna ab-initio Simulation Package (VASP) and the projector augmented wave (PAW) potentials to study the structural and electronic properties of the double perovskite. We use the Heyd-Scuseria-Ernzerhof hybrid functional (HSE06) to account for the strong correlation effects of the system. We use an energy cutoff of 500 eV for plane wave basis set together with a 6×6×6 **k**-point grid. The rather high energy cutoff and dense **k**-point grid are necessary to predict correctly the crystal structures in the HSE06 computations. Equilibrium crystal structures were achieved so that the maximum force component was smaller than 1 meV/Å^3, and the maximum stress component smaller than 1 meV/Å^3.

In a monoclinic system, the shape of the Brillouin zone depends non-trivially on the lattice vectors. In fact, there are five possible shapes of Brillouin zones for the monoclinic crystal structure depending on the choice of lattice vectors. Where we choose the $C2/m$ which corresponds to the $MCLC_1$ lattice. To generate the set of **k**-points along the edges of the Brillouin zone, we use the code **pymatgen**. We show the obtained band structure in the Figure 1.

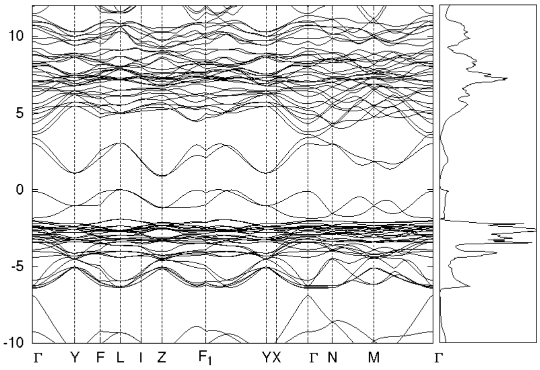

Figure 1: Band structure and density of states curve of $Ba_2Bi^{III}Bi^{V}O_6$. Fermi level is at 0 eV.

We find that the Bi^{III} 6s states at the top of valence band of $Ba_2Bi^{III}Bi^{V}O_6$ vanish on the Pr substitution for Bi at B' ^{III}-site. When Sb is substituted for Bi at B'' ^{V}-site, the Bi^{V} 6s states at the bottom of the conduction band vanish causing additional widening of the band gap.

References

[1] K. Nishidate, A. Adiko, M. Matsukawa, H. Taniguchi, A. Sato, A. Matsushita, S. Tanibayashi and M. Hasegawa, Mater. Res. Express **7** (2020) 065505.

Studies on electronic structures and optical properties in ternary oxide crystals

Takayuki Makino

Research Center for Development of Far-Infrared Region,

University of Fukui, Bunkyo Fukui, Fukui 910-8557

Lithium niobate ternary compound is known to exhibit several interesting properties such as superconducting behavior under delithiated phase. Deeper understandings for this compound are important from both technological and basic viewpoints [1]. In this research, we intend to compare calculation results on the complex dielectric function and experimental data.

We used the Quantum-ESPRESSO package to optimize the crystal structure and perform the band structure calculations. In this work, we used a set of the optimized norm-conserving pseudopotentials. The corresponding activity diagram is shown at the right hand side. We confirmed that evaluated bandgap energy (BGE in the figure) is similar to that evaluated by Ylvisaker *et al*[1].

We then moved into study on optical properties. For the optical spectra calculations such as dielectric functions, we used Respack ab-initio package [2]. Neglecting contributions from the optical anomalies, overall $\varepsilon_1(\omega)$ in the calculated spectrum is a monotonically decreasing function with upward convex in the 1.5—4-eV range (not shown in a figure). This feature is in good agreement with the experiment [3].

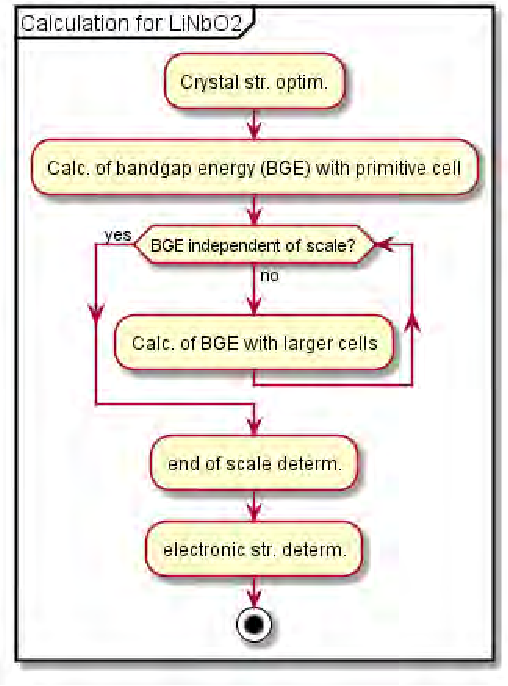

References

[1] Erik R. Ylvisaker and Warren E. Pickett: Phys. Rev. B **74** 075104 (2006).

[2] K. Nakamura *et al.*, arXiv:2001.02351 (2020).

[3] T. Kurachi *et al.*, J. Appl. Phys., submitted.

Vacancy cluster stabilization by impurities and their migration property in tungsten

Kazuhito Ohsawa

Institute for Applied Mechanics, Kyushu University,

Kasuga-koen, Kasuga, Fukuoka 816-8580

Introduction

Tungsten (W) and its alloys are plausible candidates for plasma facing materials (PFMs) used in fusion reactors because of their excellent properties, e.g. high melting point, low hydrogen (H) solubility, and toughness for irradiation. However, a large amount of H and H isotopes are retained in vacancy (V) and vacancy type lattice defects in W specimen nucleated under the irradiation circumstance. In particular, tritium (T) retention in the PFMs is a serious problem for safety operation of fusion reactors. So, the control of the vacancy type lattice defects is important subject in the field of PFMs. Vacancy clusters and their interaction with impurities included in W are investigated by experimental and computational methods. According to first-principle calculations, di-vacancy (V_2) in W are unstable compared with isolated vacancies. However, the di-vacancy and growth of vacancy clusters in W materials were observed in positron annihilation lifetime spectroscopy. In the present work, we investigated the stabilization of di-vacancy by impurities contained in the W specimen.

Simulation method

The binding energies of impurities to vacancy and stabilization of di-vacancy by the impurities were calculated in terms of first-principle calculations based on density functional theory. We used the Vienna ab-initio simulation package (VASP). A large simulation cell, composed of 6x6x6 bcc lattice (432 atoms), were used in order to reduce the effects of periodic boundary condition imposed on the simulation cell. The cut-off energy of plane wave was 520eV.

The binding energy of impurity (X) to vacancy (V) was defined as

$$E_b(\mathrm{VX})=E[\mathrm{V}]+E[\mathrm{X}]-\{E[\mathrm{VX}]+E_{\mathrm{ref}}\},$$

where E is cohesive energy of the supercell containing V, X and vacancy-impurity complex XV, and E_{ref} indicates energy of perfect lattice. Similarly, the binding energy between VX and V, stabilization of di-vacancy by impurity, was defined as

$$E_b(\mathrm{V_2X})=E[\mathrm{VX}]+E[\mathrm{V}]-\{E[\mathrm{V_2X}]+E_{\mathrm{ref}}\}.$$

Positive binding energy corresponds to attractive interaction. Besides, migration energies (E_m) of impurities and vacancy were estimated by nudged elastic band (NEB) method.

Results

We investigated interaction of vacancy with interstitial type impurities, i.e. hydrogen (H), carbon (C), nitrogen (N), and oxygen (O). As listed in Table I, the four impurities can be accommodated in a W vacancy, because the binding energies E_b(XV) are positive. While, the interaction between two vacancies is repulsive, that is, $E_b(V_2)$= -0.13eV. According to $E_b(V_2X)$, all impurities stabilize di-vacancy in W. However, the stabilization effect of H is quite small compared with those of other impurities.

Fig. 1 shows barrier height of the impurities and vacancy along the migration paths. The migration energies for H and O are quite small compared with those of C and N. The reason is that H and O are located at tetrahedral interstitial sites, while C and N are located at octahedral interstitial sites. Therefore, the migration paths between neighboring interstitial sites of H and O are shorter than those of C and N.

Table I: Binding energy of impurity to vacancy E_b(VX), stabilization of di-vacancy by impurities $E_b(V_2X)$, and migration energy of impurities and vacancy E_m.

impurity	E_b(VX)	$E_b(V_2X)$	E_m
H	1.22	0.17	0.20
C	1.97	1.09	1.48
N	2.43	1.14	0.76
O	3.04	1.39	0.18
Vacancy	-0.13	------	1.69

Discussion

Let's consider the stabilization of di-vacancy by the interstitial impurities. W specimen for the positron annihilation lifetime spectroscopy were prepared in water coolant circumstance, so impurities of low migration energy (H and O) were possible to migrate in the specimen and trapped in W vacancy to form vacancy-impurity complex VX. On the other hand, vacancy diffusion was observed at about 623K, which corresponds to migration energy for W vacancy (1.69 eV). The binging energies of H and O to vacancy were estimated to be 1.22 and 3.04 eV, respectively. Therefore, we infer that VO complex is stable at the vacancy diffusion temperature, while VH complex may be dissociated at the temperature. Therefore, O is still accommodated in W vacancy at the vacancy diffusion temperature. O is the most plausible candidate for di-vacancy stabilization among the interstitial impurities contained in W specimen.

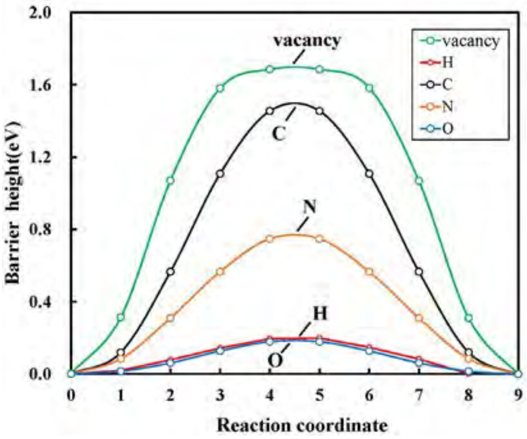

Fig. 1: Barrier height of each impurity and vacancy along migration path.

Optical gaps of metastable Ga_2O_3 and GaN with impurity doping effect

Ken-ichi SHUDO

Fac. of Eng/Sci, Yokohama Nat'l Univ.

Tokiwadai 79-5, Hodogaya-ku Yokohama 240-8501

Electronic state of Mg-doped GaN was calculated using VASP package based on local density approximation. In contrast to the most stable phase of a well-studied wurtzite GaN, thin films of haekelite phase (4|8-GaN) are suggested to show stable p-type semiconductor even with the dope.

At the same time, we calculated spin-dependent electronic structure of two-dimensional spin network of organic molecule array, made of metal-organic—framework (MOF) from Cl[5,10,15,20-tetra(4-carboxyphenyl)-porphyrin] TCPP with Mn(II) and Fe(III) at the center hole. Spin-resolved density of states for several spin-polymorph are obtained, as in Fig.1, and photo-absorption spectra were calculated. These results suggests that several spin states would coexist because the eigenenergies were mutually very close, and that ferrimeagnetic phase could be discernible when the system is cooled. The optical results are consistent with our experimental findings by means of magnetic circular dichroism (MCD) of optical transmission spectroscopy. The observed MCD signals originate from the photo-transition in the intramolecular spin states, and some signals do from Cu-ions that link the molecules in MOF formation.

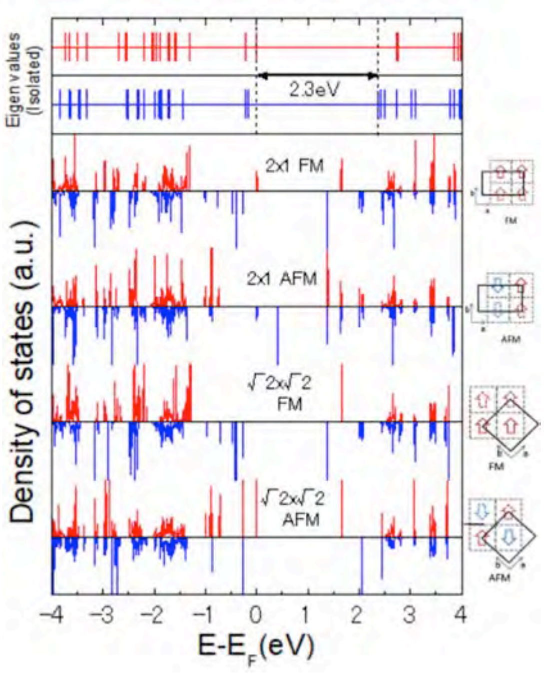

Fig 1. Calculated electronic states of an isolated molecule (top), and MOF structures of Fe-TCPP for ferro-magnetic and antiferromagnetic structures, and the latter converges at ferrimagnetic states.

Optical gaps of metastable Ga_2O_3 structures modulated by impurity dope

Ken-ichi SHUDO

Fac. of Eng/Sci, Yokohama Nat'l Univ.

Tokiwadai 79-5, Hodogaya-ku Yokohama 240-8501

Ga_2O_3 has good electrical conductivity, and its wide bandgap of 4.8 eV offers great potential for various applications. The most of researches of this oxide material are limited within the most stable β phase. We previously reported optical spectra [1] of κ- and ε-Ga_2O_3, which is widened by Co-doping. The change in the electronic states due to this Co impurity was calculated (Fig.1) to clarify the experimental photo-absorption.

The photo-absorption in Ga_2O_3:Co is difficult to be simply associated to the bandgap of oxide material. But the adjustable shift of the cutoff in the photo-absorption is accounted by the theoretical calculation in this study. The change of the experimental workfunction due to the Co doping was also explained with a band diagram of ε-phase in Fig. 2. In this phase *n*-type pinning occurs due to unintentional impurities such as Si and Ge, as is intrinsic especially ε-phase, and O-vacancy less contributes.

[1] K. Mukai, A. Tsuno, K. Shudo, and H. Otani, Jpn. J. Appl. Phys. 58, SBBK05 (2019).

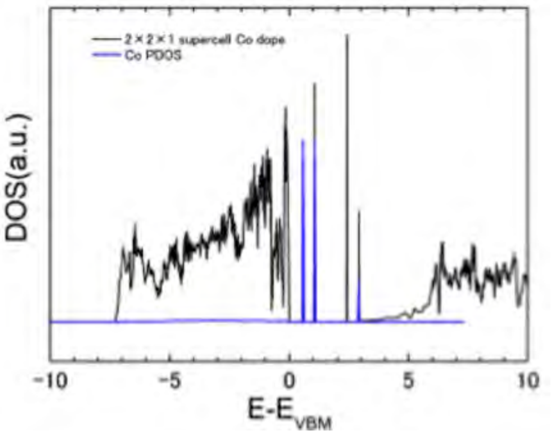

Fig.1: The density of state of Ga_2O_3:Co. Blue thin curve is the density projected to Co impurity.

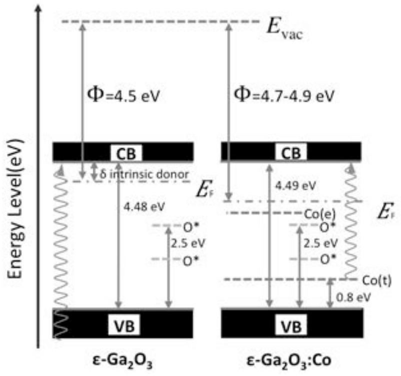

Fig.2: Calculated photoabsorption modulated by the Co-impurity dope. This accounts for the experimental optical spectra.

Effects of electron–phonon and electron–magnon scattering on finite temperature magnetic properties

H. Akai
Institute for Solid State Physics, University of Tokyo
Kashiwa-no-ha, Kashiwa, Chiba 277-8581

There are several kinds of excitations that have to be taken into account when discussing finite temperature magnetic properties of magnetic materials. Among them are phonons and magnons. Usually, single electron excitations at Fermi surfaces do not contribute significantly to the magnetic properties at the assumed temperature range of 0 ∼1500K. We have studied the effects of phonons and magnons on finite temperature magnetism, targeting at permanent magnet materials.

The effects of phonons are taken into account through random displacements of atoms around their equilibrium positions. The average displacements are estimated from either the Debye model or first-principles phonon calculations: no notable differences between the two was found. The effects of magnongs, on the other hand, are calculated by randomly flipping the local magnetic moments with probability determined self-consistently at each temperature. All the calculations were performed in the framework of first-principles calculation using KKR-CPA [1].

In the case of bcc Fe, there is a significant effect of electron–phonon scattering on the Curie temperature T_C, while that of magnons is not prominent. The effect of magnons, however, becomes remarkable in the case of $Nd_2Fe_{14}B$ permanent magnet materials. Some examples of calculated T_C are given in Table 1. The first column indicates the temperature in which the average displacement due to phonons is calculated. The experimental value of T_C is 585K.

Figure 1 shows the calculated magnetizations of $Nd_2Fe_{14}B$. Both the effects of phons and magnons are included. The theoretical curve shows a weak first-order transition at the magnetic transition temperature, which occurs as a result of electron–phonon coupling. The temperature is scaled so that T_C reproduces the experimental value of 585K although the scaling factor is close to 1. The calculated results are fairly consistent with experiments is concluded.

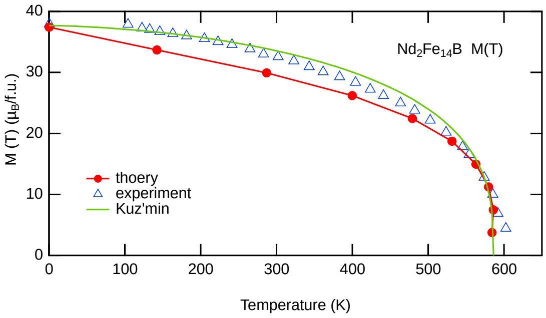

Figure 1: Calculated and experimental magnetizations vs. temperature of $Nd_2Fe_{14}B$

Table 1: Calculated T_C

	phonons only	plus magnons
0K	1062K	561K
500K	1198K	548K

References

[1] H. Akai, AkaiKKR, `http://kkr.issp.u-tokyo.ac.jp/` (2002).

Magnetic properties of $(\mathrm{Sm}_{1-x}\mathrm{Zr}_x)(\mathrm{Fe}_{0.75}\mathrm{Co}_{0.25})_{11+y}\mathrm{Ti}_{1-y}$ rare-earth magnetic materials

H. Akai
Institute for Solid State Physics, University of Tokyo
Kashiwa-no-ha, Kashiwa, Chiba 277-8581

Rare-earth permanent magnet materials of SmFe_{12} family attract much attention because expected performance using NdFe_{12} family as a main phase of permanent magnets has been recognized as hardly reached. Much work has been done to seek better intrinsic magnetic properties for SmFe_{12} by adding some elements as ingredients. In this study, we have tried several SmFe_{12} family cases, which are implied from experiments to be possible candidates for permanent magnet materials. Finite temperature properties, including the magnetizations, Curie temperatures, and magnetocrystalline anisotropy, were examined.

Figure 1 shows the calculated magnetizations as functions of temperature where the Curie temperatures are scaled so as to fit the experimental ones. More precisely, first the Curie temperatures, which are not necessarily known experimentally, are estimated by fitting the temperature dependence of magnetic moment by Kuz'min's empirical formula. On the other hand, the theoretical Curie temperatures are obtained by first-principles calculation using KKR–CPA[1]. Theoretical temperature dependence of magnetization is then obtained again using Kuz'min's formula. Finally, the temperatures are scaled using experimentally estimated Curie temperatures.

The crystalline magnetic anisotropy constant K_1 of $(\mathrm{Sm}_{1-x}\mathrm{Zr}_x)(\mathrm{Fe}_{1-y}\mathrm{Co}_y)_{11.5}\mathrm{Ti}_{0.5}$ is also calculated. Since the treatment for 4f states of Sm is still rather controversial, we neglect the contribution of 4f to magnetic anisotropy through hybridization, adopting an open core treatment. These results indicate that adding Co improves the magnetization although it degrades the magnetic anisotropy. Zr slightly contributes to improve the magnetization but not much to the anisotropy. Main contribution of Zr must be that to structural stabilization.

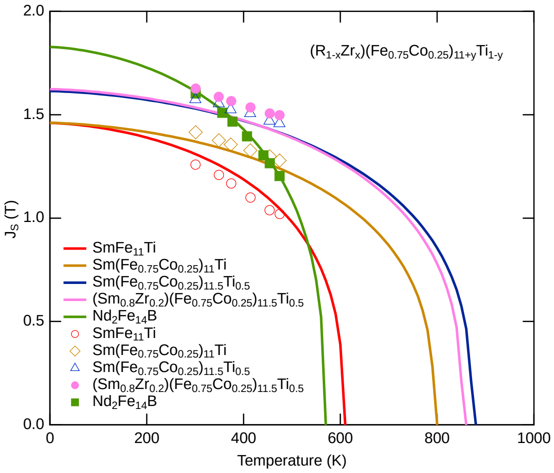

Figure 1: Temperature dependence of magnetization of various systems of SmFe_{12} family.

References

[1] H. Akai, AkaiKKR, `http://kkr.issp.u-tokyo.ac.jp/` (2002).

Theoretical Analysis of Photocatalytic Reaction Mechanism at Titanium Dioxide Interfaces

Tatsuya JOUTSUKA

Institute of Quantum Beam Science,

Graduate School of Science and Engineering, Ibaraki University, Hitachi, 316-8511 Ibaraki, Japan

We have studied the reaction mechanism of photocatalytic oxidation at anatase TiO_2 surfaces [1] using cp2k program package (MPI parallelization with multiple threads). We focused on the energetics and structure during the hole migration. This is a collaborative work with the experimentalist (Prof. Satoshi Yamauchi at Ibaraki University), who conducted the LPCVD experiment.

This experimental and theoretical study clarifies the facet dependence of the photocatalytic reaction at the anatase TiO_2 surface. The <112>-oriented anatase TiO_2 layer is deposited on the Ru(0001) substrate at 360°C by low-pressure chemical vapor deposition. The deposition rate is three times higher than that of the multi-orientation layer on the Pylex glass. The photocatalytic activity induced by ultraviolet (UV) irradiation around 365 nm in methylene blue aqueous solutions is significantly high. The density functional theory (DFT) calculations using the constrained DFT method [2] and the hybrid functionals show that the (112) surface stabilizes the adsorbed water molecule most strongly. The photogenerated hole is stably trapped not at the bare surface but at the hydroxylated surface, especially at the hydroxyl group of the hydroxylated (112) and (001) surfaces. The experimental and theoretical findings consistently elucidate the high photocatalytic activity at the anatase TiO_2(112) surface.

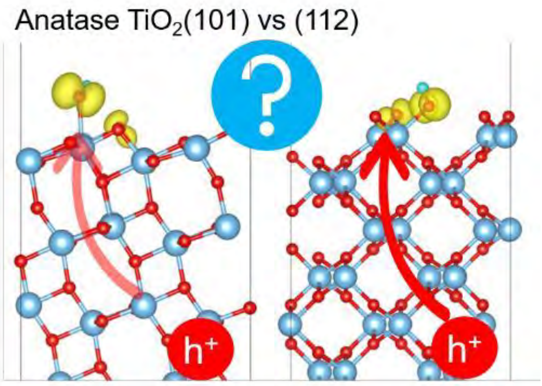

Fig. 1: Molecular mechanism of hole migration.

References

[1] T. Joutsuka, H. Yoshinari, and S. Yamauchi: Bull. Chem. Soc. Jpn., **94** (2021) 106–111. (Selected Paper, Inside Cover, Open Access).

[2] T. Joutsuka and K. Ando: J. Phys. Chem. B, **124** (2020) 8323–8330.

Ab Initio Calculation of High-Rate Deposition of Metal Films by LowPressure Chemical Vapor Deposition

Tatsuya JOUTSUKA
Institute of Quantum Beam Science,
Graduate School of Science and Engineering, Ibaraki University, Hitachi, 316-8511 Ibaraki, Japan

We have studied low-pressure chemical vapor deposition of Cu on Ru substrate using CuI [1] using cp2k program package (MPI parallelization with multiple threads). This year, we focused on the *ab initio* calculation of desorption of by-products. This is a collaborative work with the experimentalist [2] (Prof. Satoshi Yamauchi at Ibaraki University), who conducted the LPCVD experiment.

In this study, we elucidated the molecular mechanism of Cu deposition using copper(I) iodide (CuI) on Ru substrate by low-pressure chemical vapor deposition through electronic structure calculations. Figure 1 shows the molecular mechanism of Cu deposition by the LPCVD method. Using density functional theory (DFT) molecular dynamics (MD) simulations, we show that CuI molecules adsorb and decompose exothermically due to a strong adsorption of iodine atoms onto the Ru(001) surface. The rate-limiting step of the Cu deposition is found to be the desorption of iodine atoms or molecules from the Cu(111) surface by molecular dynamics simulations.

Based on this study, we are now extending our calculations to analyze the dynamical properties by the constrained DFT[3] and the dynamical reaction path analysis.[4]

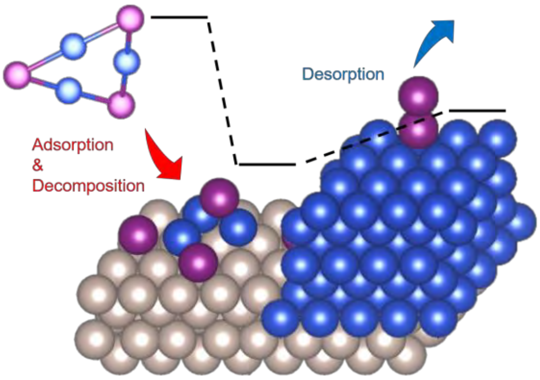

Fig. 1: Molecular mechanism of LPCVD of Cu.

References

[1] T. Joutsuka, S. Yamauchi: Chem. Phys. Lett. **741** (2020) 137108.

[2] T. Nishikawa, K. Horiuchi, T. Joutsuka and S. Yamauchi: J. Cryst. Growth, **549** (2020) 125849.

[3] T. Joutsuka and K. Ando: J. Phys. Chem. B, **124** (2020) 8323–8330.

[4] T. Joutsuka and K. Ando: J. Phys. Chem. A, **115** (2011) 678–684.

Dynamical stability of two-dimensional simple metals and ordered alloys

Shota ONO
Department of Electrical, Electronic and Computer Engineering, Gifu University
Gifu 501-1193

The family of two-dimensional (2D) materials has been expanded significantly in recent years. However, the dynamical stability as well as the synthesizability of 2D metals have not been explored in detail irrespective of the presence of the interrelationship between the energetic stability in the 2D and three-dimensional (3D) structures. In this study, we have performed high-throughput density functional theory (DFT) and density functional perturbation theory (DFPT) calculations to construct the metastability database for simple metals and ordered alloys. The database currently includes (I) the phonon dispersions of 46 simple metals from Li to Pb in the three 2D structures, including the planar hexagonal, the buckled honeycomb (BHC), and the buckled square (BSQ) lattices [1]; (II) the phonon dispersions of 2D Po, named poloniumene, in the planar square structure [2]; and (III) the formation energies of 1081 binary compounds in the 2D structures (BHC and BSQ as shown in Fig. 1) and the 3D structures (B2, L1_0, and B$_h$ corresponding to bcc, fcc, and hcp in simple metals, respectively) and the phonon dispersions of more than 50 ordered alloys in the BHC structure [3].

In Ref. [1], we have demonstrated that the trend in the dynamical stability of 2D metals is correlated with that of 3D metals. This provides design principles of ordered alloys: 2D metals are building blocks for constructing 3D alloys, where the similarity regarding the dynamical stability of different 2D metals is important for creating dynamically stable alloys.

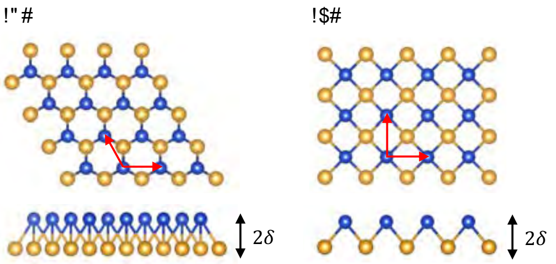

Figure 1: Schematic illustration of binary ordered alloys in the BHC and BSQ structures. After Ref. [3].

In Ref. [2], we have shown that the 2D polonium has the planar square lattice structure as its ground state and demonstrated that the spin-orbit coupling (beyond the scalar relativistic approximation) suppresses the Peierls instability and is necessary to obtain no imaginary phonon frequencies over the Brillouin zone.

In Ref. [3], by analyzing of the formation energy and the dynamical stability of binary alloys, we have demonstrated that (i) a negative formation energy is neither a sufficient nor necessary condition for producing the dynamical stability of 2D ordered alloys; and (ii) if an ordered alloy in the B$_h$ structure is synthesizable, that in the BHC structure is dynamically stable. In addition, the stability of ordered Au-Cu alloys has been studied in Ref. [4].

References

[1] S. Ono: Phys. Rev. B **102** (2020) 165424.
[2] S. Ono: Sci. Rep. **10** (2020) 11810.
[3] S. Ono and H. Satomi: Phys. Rev. B **103** (2021) L121403.
[4] S. Ono and D. Kobayashi: Phys. Rev. B **103** (2021) 094114.

Boltzmann equation solver for nonequilibrium electrons and phonons in solids (BENEP). II. Application to experiments

Shota ONO

Department of Electrical, Electronic and Computer Engineering, Gifu University
Gifu 501-1193

Understanding the ultrafast electron dynamics of laser-excited solids, where the electron-electron (e-e) and electron-phonon (e-ph) scatterings occur simultaneously within a picosecond time scale, is important to analyze the pump-probe experimental data. The author has developed the Boltzmann equation solver for nonequilibrium electrons and phonons which enables us to study the ultrafast electron and phonon dynamics [1]. We have applied our code to the calculation of the femtosecond infrared photoluminescence (PL) of silver (see Fig. 1). The preliminary results have been reported in Activity Report 2019.

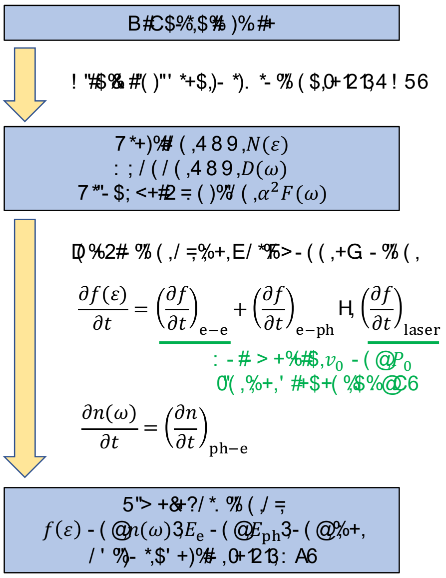

Figure 1: Flow chart describing the time-evolution calculation of the distribution functions in metals. After Ref. [2].

Figure 2 shows an application to the time-evolution of PL spectra and the transient PL at 0.9 eV in silver. The agreement between the theory and experiments is good, indicating that the effect of electron nonequilibrium is important in the PL dynamics. The disagreement may be attributed to the nanoscale roughness at metal surfaces and the e-e umklapp scattering on the ultrafast electron dynamics [2].

The author thank Prof. Tohru Suemoto for useful discussions.

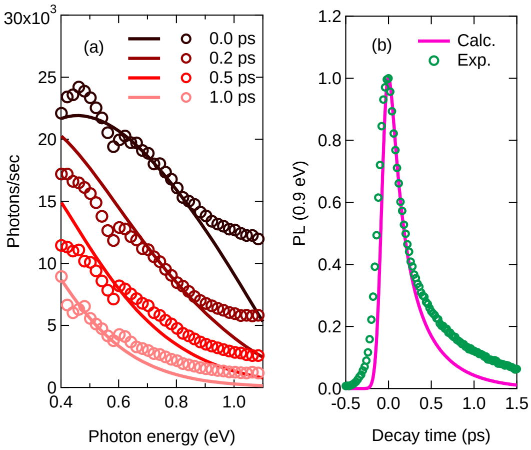

Figure 2: (a) The evolution of PL in silver: The experimental PL (circle) and the calculated PL (solid). (b) Comparison of the transient PL at 0.9 eV. After Ref. [2].

References

[1] S. Ono: Phys. Rev. B **97** (2018) 054310.
[2] S. Ono and T. Suemoto: Phys. Rev. B **102** (2020) 024308.

Noisy simulations of first-principles calculations using quantum classical hybrid algorithms

Wataru Mizukami

Center for Quantum Information and Quantum Biology, Institute for Open and Transdisciplinary Research Initiatives, Osaka University, Osaka 560-8531, Japan,

In recent years, quantum computers with dozens of qubits have been built; we now expect to see quantum devices with hundreds of qubits in the near future. Such quantum computers are often called noisy-intermediate scale quantum devices (NISQs) since they do not have quantum error correction functionality. Nonetheless, in 2019, Google showed that a NISQ with as few as 53 qubits could already outperform supercomputers when limited to a specific task. Many research projects have been currently underway to exploit the computational potential of NISQs.

One promising algorithm for NISQs is the quantum-classical hybrid algorithm, which can operate even in the short coherence time of a NISQ. Among them, the variational quantum eigensolver (VQE) can be applied to first-principles calculations of materials or molecules. An advantage of the VQE is that it can parametrize some wave functions ansatzes such as unitary coupled clusters (UCC)in polynomial time, while the UCC is exponentially computationally expensive on classical computers. However, if a NISQ is used for the VQE, the computational results are unavoidably affected by noises.

In this work, we have investigated the influence of this noise on the VQE by using a quantum circuit simulator. There are many types of noises in quantum computers, such as read-out error and amplitude damping. Since it is difficult to model all kinds of errors, we have only dealt with depolarizing noise, which is a typical error model for quantum computers, in this study. This noise can be described as Pauli operators probabilistically acting on each gate of a quantum circuit. In the presence of depolarizing noise, we can effectively say that the noise probabilistically changes the quantum circuit at each sampling. It means that the numerical simulations with depolarizing noise using classical computers, are required to simulate various quantum circuits: the simulation with depolarizing noise is much more expensive than the simulation without it. Besides, because such a simulation is a sampling problem, the individual circuits changed by the noise are independent. Hence, the VQE with depolarizing noise can be highly parallelizable.

This year, we have realized the simulation with depolarizing noise up to 1 million samples by using the MPI parallelization and the supercomputer of the ISSP. In addition, by using a many-body expansion, we have studied the effect of depolarizing errors on up-to a 100-qubits problem. We have chosen the most basic molecule, the hydrogen molecule, as the benchmark system. In our program, the PySCF quantum chemistry program library [1] is used to prepare the second quantized electronic Hamiltonian; Qulacs is employed as a quantum circuit simulator [2]. The obtained numerical results illustrate that it is impractical to achieve chemical accuracy with the error rates of today's quantum computers. This implies that an efficient way to suppress the effect of depolarizing noise is vital for the practical application of first-principles calculations using NISQs.

References

[1] Q. Sun et al., WIREs Comput. Mol. Sci. **8**, e1340 (2017).

[2] Y. Suzuki et al., arXiv:2011.13524

First principles calculations of crystals with quantum classical hybrid algorithms

Wataru Mizukami

Center for Quantum Information and Quantum Biology, Institute for Open and Transdisciplinary Research Initiatives, Osaka University, Osaka 560-8531, Japan,

First-principles calculations of solids or solid surfaces are routinely performed in materials science. They have become an indispensable tool in the fields of condensed matter physics and inorganic chemistry. The workhorse of these ab initio calculations is currently density functional theory (DFT). An approach beyond DFT is the introduction of quantum chemical methods such as the coupled-cluster theory (CC).

The problem of CC is that it works well only for weakly correlated systems. It is known to break down in systems with strong electron correlation. This issue comes from the fact that CC is not variational. Although there is a variational CC method, such a method is exponentially expensive in terms of computational costs. However, in 2014, it was shown that a kind of variational CC, the unitary CC (UCC), can be solved in polynomial time using a quantum computer.

This method is called the variational quantum eigensolver (VQE). In the VQE, the wavefunction ansatz is represented by a quantum circuit. Then, a classical computer updates the VQE's wavefunction parameters as quantum circuit parameters.

This year, we have extended the VQE to solid-state systems [1]. Specifically, we prepare a second quantized Hamiltonian in the crystal orbital representation, and make a one-to-one correspondence between crystal orbitals and qubits. The UCC ansatz in the crystal orbital representations has also been converted into the qubit representation. These mapping allows us to describe the electronic structure of a crystalline system on a quantum computer.

We have applied the developed VQE-UCC to one-dimensional hydrogen chains and calculate their potential energy surface, confirming that the VQE-UCC works in the regime where the electron correlation becomes strong so that the conventional CC does not work. We have also developed an algorithm to calculate the quasi-particle band structure from the VQE wave function based on the extended Koopman's theorem [1].

References

[1] N. Yoshioka, Y.O. Nakagawa, Y.-y. Ohnishi, W. Mizukami, arXiv:2008.09492

First-principles Calculation of Electric Field Effects in Spin-to-charge Conversion Materials

Naoya YAMAGUCHI
Nanomaterials Research Institute, Kanazawa University
Kakuma-machi, Kanazawa, Ishikawa 920-1192

We have studied materials possessing the Rashba effect that induces spin splitting, which is applicable to spin-to-charge conversion [1]. The Rashba effect originates from spin-orbit interaction and spatial inversion symmetry breaking, and is controlled by electric fields. Based on the modern theory of electric polarization, one can apply uniform electric fields even for bulk insulators in calculations with density functional theory (DFT) codes with the periodic boundary condition [2]. We have developed a linear-combination-of-pseudo-atomic-orbital (LCPAO) version of such a function making **k**-dependent potentials and implemented it to the OpenMX code. This year, we tried to focus on electric field effects in such Rashba systems with Berry phases by using the OpenMX code. Under an electric field, cations or anions are expected to shift their positions slightly, but shifts of ions' positions induce such a large electric polarization that Rashba spin splitting occurs. During structural relaxation, such ions move by following forces on themselves, but the forces are often smaller than a usual criterion of calculated forces (e.g. 10^{-4} Ha/Bohr) when we consider the realistic strength of electric fields. However, for nonorthogonal cells such as hexagonal cells, in the case of generalized gradient approximation (GGA), the “egg box effect” appeared as a difficulty because OpenMX uses PAOs expanded in the real space grid to compute physical quantities, but description of PAOs depends on the origin of the grid, that is, introducing the grid causes numerical errors. To overcome the difficulty, we added functions of calculations of a total energy and forces with several grid origins. Once calculations of electronic systems converge, one can get density matrices (DMs) and taking another real space grid with a different origin, one can evaluate an energy and forces again with the frozen DMs. In the way, we succeeded in evaluating forces under electric fields with a moderate number of grids (i.e. cutoff energy). We also added a function to change the order of the Lagrange interpolation to estimate density gradients, and it improved evaluation of forces. These two functions enabled us to predict not only relaxed structures under electric fields but also static dielectric constants and Born effective charges in any cell shape. Indeed, we confirmed that our calculated values of dielectric constants and Born effective charges for typical insulators are consistent with the prior theoretical and experimental studies. Since we encountered the problems of the "egg box effect", we have not done calculations of applications, but we have suggested a simple model of surface alloys, such as Bi/Ag surface alloys inducing giant spin splitting, based on DFT calculations [3]. This year, we also succeeded in reducing half of computational time for Berry phases averagely through tuning, and running our implemented code with up to 32^3 **k**-points for zinc blende primitive cells through efficient transfer of arrays of **k**-dependent potentials in the message passing interface (MPI).

References

[1] J. C. Rojas Sánchez et al., Nat. Commun. **4**, 2944 (2013).

[2] I. Souza, J. Íñiguez, and D. Vanderbilt, Phys. Rev. Lett. **89**, 117602 (2002).

[3] M. Nur, N. Yamaguchi, and F. Ishii, Materials **13**, 4444 (2020).

First-principles study of atomic and electronic structures of intermetallic compound catalysts

Kazuki NOZAWA
Department of Physics and Astronomy, Kagoshima University
1-21-35, Korimoto, Kagoshima 890-0065

This fiscal year, we carried out the following studies using the VASP code with the PAW method and the PBE exchange-correlation functional.

Quasicrystals (QCs) are long-range ordered materials with no translational symmetry. Partly because the atomic structure of most QCs have not been solved completely, DFT studies have usually been carried out using the surface of a crystalline phase having a close composition and common structural building unit to the quasicrystalline phase. Recently, however, single-element quasiperiodic ultra-thin films have been obtained using the Ag-In-Yb QC as a template. The Ag-In-Yb QC belongs to the only QC family whose atomic structure has been solved unambiguously. Thus, DFT studies using the actual quasiperiodic surface atomic arrangement are required to elucidate the atomic structure of the ultra-thin films. Although a straightforward way to approximate the QC surface is to use an atomic cluster extracted from the structural data of the QC, the cluster size dependence of the adsorption energy for the aperiodic surfaces has not been well studied. Therefore, this time we studied the convergence behavior of the adsorption energy of a single Bi atom concerning the cluster size [1]. Two types of clusters, the cylindrical and hemispherical clusters, are tested. Unnaturally rippled potential energy surfaces were obtained for clusters with smaller radius regardless of the cluster thickness. It was revealed that the ripples are disappeared when clusters with a sufficient cluster radius of 1.4 nm or larger are used. This trend is also confirmed in their root mean square errors. Consequently, it was concluded that both cluster models tested with a specific size are expected to give relative adsorption energy within an error of 0.15 eV. It was also pointed out that the cylindrical cluster model is relatively economical in terms of the calculation cost than the hemispherical cluster model.

We also investigated the surface atomic structure of the antiferromagnetic 1/1 Au-Al Tb approximant crystal using DFT calculation[2]. Experimentally observed stable surface atomic structure showing a linear row structure of Au/Al atoms, which is an example of a surface reconstruction in this family of QC-related systems, was found stable by the calculation.

We studied the influence of the adsorbed oxygen atoms on the surface atomic structure and electronic structure of PdZn(111) surface using DFT calculation[3].

References

[1] M. Sato, T. Hiroto, Y. Matsushita, and K. Nozawa, Mat. Trans. **62** (2021) 350.

[2] S. Coates, K. Nozawa, M. Fukami, K. Inagaki, M. Shimoda, R. McGrath, H. R. Sharma, and R. Tamura, Phys. Rev. B **102** (2020) 235419.

[3] Y. Otani, Master Thesis (Kagoshima University, 2021).

Study on Removal Mechanism of Single Crystalline Si Planarized by Catalyst-Referred Etching in Pure Water

Pho Van BUI, Kiyoto KAYAO, Kouji INAGAKI, Yoshitada MORIKAWA
Graduate School of Engineering,
Osaka University, 2-1 Yamada-oka, Suita, Osaka 565-0871

There is a growing demand on ultra-precision optical components for scientific and industrial applications, especially in extreme ultraviolet (EUV) and X-ray regimes. Using the short-wavelength light, scientific imaging of cutting-edge materials/biological samples and nanoscale lithography have become possible thanks to the ultra-precision optical components. Low thermal expansion materials such as glass and Si are still the main materials used for fabricating these optical components. Compared to glass, Si possesses more attractive properties, such as higher cleanliness, machinability, and workability. Accordingly, ultra-precision surface machining for Si surfaces has been achieved significant advances in accuracy and smoothness. A highly ordered surface with a root mean square roughness at the level of several tens of picometer is greatly desired for the highest reflectivity and the lowest unwanted scattering [1].

In this study, we apply catalyst-referred etching (CARE), an abrasive-free polishing method, to planarization of a crystalline Si surface, using Pt as the catalyst and pure water as the etching solution [2]. An atomically smooth surface with sub-Angstrom root-mean-square roughness is achieved on the Si substrate.

Our recent studies indicated that the removal mechanism of SiC and SiO_2 etching via CARE is hydrolysis reaction, in which the catalyst assists water dissociation and stabilization of hypervalent state, increasing rate of the reaction [3]. Thus, the purpose of the proposed research is to clarify the removal mechanism of Si etching via CARE using first-principles calculation. Additionally, in Si polishing, the effect of self-oxidation by oxygen and water is still not well understood due to the instability of Si under ambient condition. Thus, the oxidation effects of oxygen and water are also taken into account.

The mechanistic removal pathway of CARE for Si(111) has been clarified and shown in Fig. 1. In the pathway with the Pt catalyst, at first, a water molecule is dissociatively adsorbed on Pt. In the next step, the adsorbed OH is transferred to the targeted Si, forming the five-fold coordinated state in the metastable state (MS). At this state, the Si-Si back-bond is elongated and weekend. Finally, the Si─Si back-bond is broken by a proton transfer at the final state (FS). The activation barrier is reduced from 1.0 eV (without the Pt) to 0.6 eV (with the Pt). We expected that similar results would be observed on a Si(100).

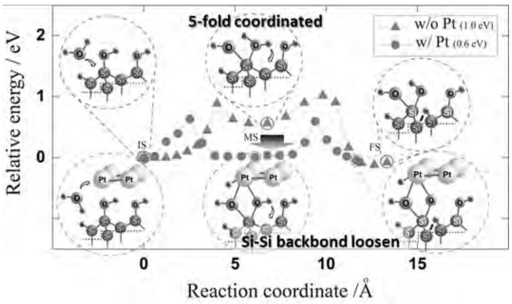

Fig. 1: A mechanistic reaction pathway of the Pt-catalyzed water etching of the Si(111) surface in comparison with the pathway without the Pt catalyst.

We consider oxidation effects by an oxygen molecule at terrace and step-edge sites on a Si(111) surface, as illustrated in Fig. 2.

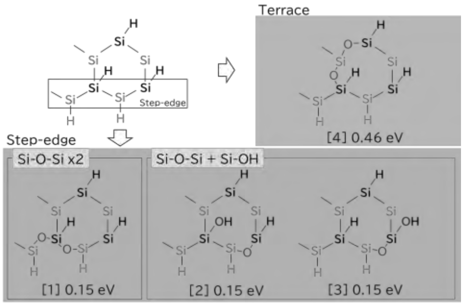

Fig. 2: Illustration of oxidation effects by an oxygen at terrace and step-edge sites on a Si(111) surface (top-view).

The activation barriers of the oxidation by an oxygen molecule are 0.46 and 0.15 eV, respectively (Fig. 3). The obtained results indicated that the oxidation might occur readily in the air at a step-edge site. However, the oxidation by oxygen at a terrace site might be difficult. The obtained results are quite consistent with the previous study [4]. The obtained results could also explained why the wettability of Si(111) surface could be lasted for several hour in the ambient conditions in the previous experimental study [5].

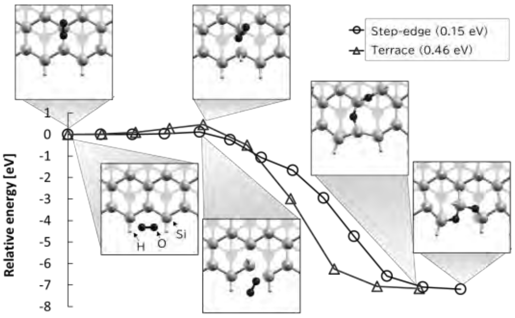

Fig. 3: Atomic configurations and energy diagrams of oxidation by an oxygen molecule at a step-edge and a terrace site.

The study has clarified the mechanistic removal pathway of CARE for Si in pure water and oxidation effect of a Si(111) surface by oxygen or water. Oxygen plays an main role in the oxidation of a Si(111) surface. Moreover, combined oxidation effects of oxygen and water might be an important factor to be considered in the future.

References

[1] R. J. Noll: Opt. Eng. **19** (1980) 249.

[2] H. Hara et al.: J. Electron Mater. **35** (2006) L11.

[3] P.V. Bui at al.: Jpn. J. Appl. Phys. **57** (2018) 055703.

[4] F. A. Soria, E. M. Patrito, and P. Paredes-Olivera: J. Phys. Chem. C **116** (2012) 24607.

[5] M. Niwano at al.: J. Appl. Phys. **76** (1994) 2157.

Doping and molecular adsorption of graphene

Yoshitaka FUJIMOTO
Depertment of Physics, Tokyo Institute of Technology
Ohokayama, Meguro, Tokyo 152-8551

Graphene is one of candidate device materials for molecular sensors using field-effect transistors due to their high charge mobility and chemical reactivity to adsorbates. Recently, we have reported the adsorption properties of environmentally polluting and/or toxic molecules (NO and NO_2 moleucles) onto boron and nitrogen-doped graphenes, and only NO and NO_2 molecules in air are strongly adsorbed on the B-doped graphenes.

We here report the adsorption property of a toxic CO molecule on the boron-doped graphene and (8,0) CNT to reveal the curvature effects of the graphene using a first-principles density-functional calculation [1, 2, 3].

Table 1 shows the adsorption energies and the binding distances between the B atom and the adsorbed molecule for the CO molecule on the B-doped monolayer and bilayer graphenes, and B-doped (8,0) CNT. The CO molecule is found to be adsorbed not strongly but weakly with short distance and small adsorption energy on the B-doped monolayer graphene. In the case of the B-doped bilayer graphene, the adsorption energy and the binding distance for the adsorption of the CO molecule show similar to those of the B-doped monolayer graphene, respectively.

Table 1: Adsorption energy E_a (eV) and binding distance d (Å) between adsorbed molecule and B atom for CO molecules adsorbed on B-doped monolayer and bilayer graphenes, and B-doped (8,0) CNT.

	E_a	d
Monolayer	-0.12	2.89
Bilayer	-0.12	2.89
CNT	-0.62	1.53

We also study the adsorption energy and the binding distance of the CO molecule on the B-doped (8,0) carbon nanotube (CNT). Unlike monolayer and bilayer graphenes, the CO molecule is found to strongly bind on the B-doped (8,0) CNT with the large adsorption energy and the short binding distance. Thus, the adsorption properties of the CO molecule on the B-doped (8,0) CNT is found to be enhanced, compared with those on the B-doped monolayer and the B-doped bilayer graphenes due to the curvature effects.

In summary, we have studied the adsorption properties of the toxic CO molecule on the B-doped monolayer and bilayer graphenes, and B-doped (8,0) CNT, using first-principles density-functional calculations. The B-doped monolayer as well as bilayer graphenes does not strongly but weakly bind with the CO molecule, while the B-doped (8,0) CNT can strongly bind with the CO molecule. The B-doped (8,0) CNT may be useful for sensor applications to detect CO molecules.

References

[1] Y. Fujimoto and S. Saito, Chem. Phys. **478**, 55 (2016).

[2] Y. Fujimoto and S. Saito, Jpn. J. Appl. Phys. **58**, 015005 (2019).

[3] Y. Fujimoto and S. Saito, Appl. Surf. Sci. Adv. **1**, 100028 (2020).

Stability and electronic structures of MoS_2 nanowires

Toshihiro SHIMADA

Division of Applied Chemistry, Faculty of Engineering,
Hokkaido University, Kita-ku, Sapporo, Hokkaido 060-8628

Nanotubes of layered materials started with the discovery of variety of helicities in carbon nanotubes. Since then, various layered materials are found to form nanotube structures. These structures show important functions such as catalytic activities, lithium ion storage, transistor action and chemical sensing. Recently, we discovered that FeO nanoparticles work as catalyst to make MoS_2 nanowires[1]. We found that the cross section of the MoS_2 nanowires show rectangular shapes. In order to investigate the mechanism of the formation and possible new functions of these nanotubes, we used VASP to calculate the stability of MoS_2 nanotubes with cylindrical and square shaped cross sections with armchair and zigzag helicities[2]. The calculation result shows that this structure has lower strain energy in the low-diameter region (~30 Å) than the conventional cylindrical nanotubes (Fig.1). The electronic structure and the surface energy per length of the square nanotubes showed unique properties because of five coordinated Mo atoms at the corner. Catalytic activities and unique sensing functions are expected.

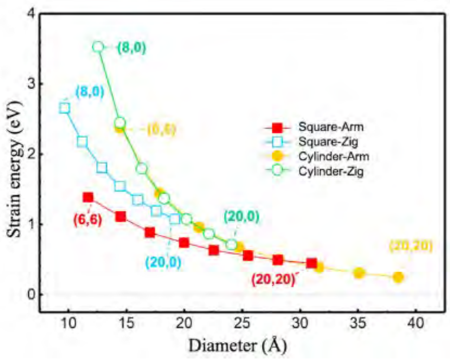

Fig. 1: Strain energy of MoS_2 nanotubes with square or cylindrical cross sections.

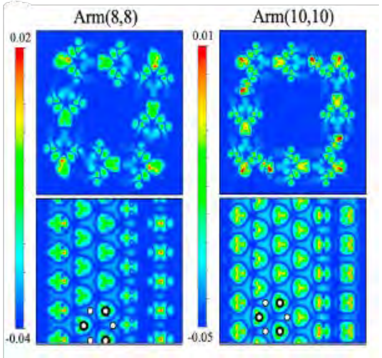

Fig. 2: 2D deformation charge density map of square-shaped nanotube.

References

[1] M. Weng, T. Yanase, F. Uehara, S. Watanabe, T. Miura, T. Nagahama, T. Shimada, CrystEngComm **19**, 3915 (2017).

[2] M. Zhang, M. Weng, T. Tamura, M. Goto, I. Yamane, T. Yanase, T. Nagahama, T. Shimada: Physica E **130**, 114693 (2021).

First-principles derivation of a many-body effective model based on PMT basis

Hirofumi SAKAKIBARA
Advanced Mechanical and Electronic System Research Center (AMES),
Tottori University, Tottori, Tottori 680-8525

To establish a construction method to obtain a model which captures the low-energy part of electronic structures obtained in first-principles calculation is an urgent problem. The model is often used to calculate physical quantities such as self-energy, conductivity, and transition temperatures of magnetism or superconductivity. The Maximally localized Wannier function (MLWF [1]) is often used to derive a tight-binding model reproducing the first-principles band structure very well. However, MLWF has a problem that it requires several optimization parameters. This requirement inhibits the automation of model construction. If the automation is achieved, we can search the materials having desirable properties from material databases. In addition, MLWF has a difficulty in the model construction for slabs and surfaces.

To overcome the problems of MLWF, we propose a construction method as Muffin-tin based Localized Orbital (MLO) based on the PMT basis function [2]. The PMT basis function is a hybrid basis between the plain wave basis and the muffin-tin basis. In the new model construction method, effects only described in the plane waves basis set are taken into account in the model Hamiltonian expressed on the muffin-tin orbital basis. Namely, we obtain a projection operator from full-space (PMT space) to the (reduced) model space, which is spanned by muffin-tin orbital. In the operator, we introduced weight function so as to reproduce the band structure of low energy region. Note that the new method does not require any handful parameters, so this can be used in the automation of model constructions.

We have applied MLO to Si crystal. The figure 1 shows the comparison of the energy eigenvalues between the first-principles calculation and MLO. We can see MLO nicely reproduce the first-principles eigenvalues. Even in other semiconductors such as GaAs and GaN, the eigenvalues are well reproduced.

In summary, MLO basis function can

accurately reproduce the eigenvalues calculated in the first-principles calculations. In the next step, we apply MLO to more difficult systems such as interfaces or slabs.

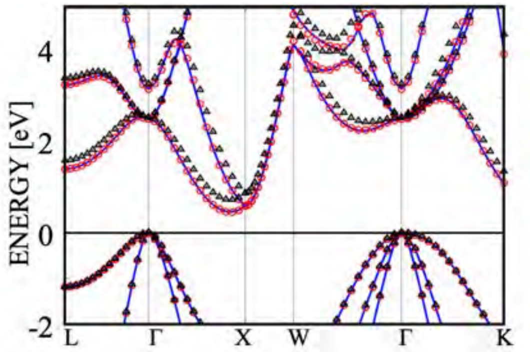

Figure 1: Result of MLO in a simple Si crystal. Solid line shows the eigenvalues obtained in first-principles calculations and circles shows the MLO results. The triangles show the result considering only the MTO basis.

References

[1] N. Marzari and D. Vanderbilt, Phys. Rev. B **56**, 12847 (1997).

[2] T. Kotani, H. Kino, and H. Akai, J. Phys. Soc. Jpn. **84**, 034720 (2015).

First-Principles Analysis of Melt Structure and Property in Na Flux GaN Growth

Takahiro KAWAMURA
Graduate School of Engineering, Mie University
1577 Kurimamachiya-cho, Tsu, Mie 514-8507

To produce high-quality III-V nitride semiconductor devices at low cost, large bulk GaN crystals for freestanding substrate are demanded. The Na-flux method is one of the most promising crystal growth technique for bulk GaN. It is known that C additives improve the growth rate and suppresses the generation of polycrystals [1]. Using first-principles calculations, we previously found that formation and dissociation of the C–N bond in the Na–Ga melt strongly affects the mechanism for enhanced GaN growth [2].

At first, graphite was used as a C source. After that Murakami et al. used methane (CH_4) gases and found they were more effective than graphite [3]. In this study, we investigated activation free energies for C–C and C–H bond dissociation in Na–Ga melts using first-principles calculations and clarified the reason why CH_4 gases are more effective than graphite.

We used the first-principles molecular dynamics (MD) simulation program STATE-Senri (Simulation Tool for Atom TEchnology), which is based on density functional theory with norm-conserving/ultrasoft pseudopotentials and plane-wave basis sets [4]. We used the generalized gradient approximation of Perdew et al. for the exchange-correlation function [5]. The cutoff energies for the wave functions and charge densities were 25 and 225 Ry, respectively. The number of k-points for Brillouin zone sampling was $1\times1\times1$.

We modeled Na–Ga (Na:Ga $\approx$ 4:1) melt models composed of about 54 atoms. A set of C and C or C and H atoms was included in the models. Periodic boundary conditions were used in all directions. We performed constrained MD simulations for 10 ps at 1073 K and at constant volume. The C–C and C–H interatomic distances were constrained to the range of 1.0–3.5 Å. By using data from the latter half of the 10 ps period, free energy profiles were calculated with the blue-moon ensemble method [6, 7].

Figures 1 show plots of the free energy profiles for C–C and C–H bond in Na–Ga melt. The horizontal axis is the constrained interatomic distance. The interatomic distance at which the free energies reach a local minimum indicates a stable bond length. The dissociation activation energies were determined from

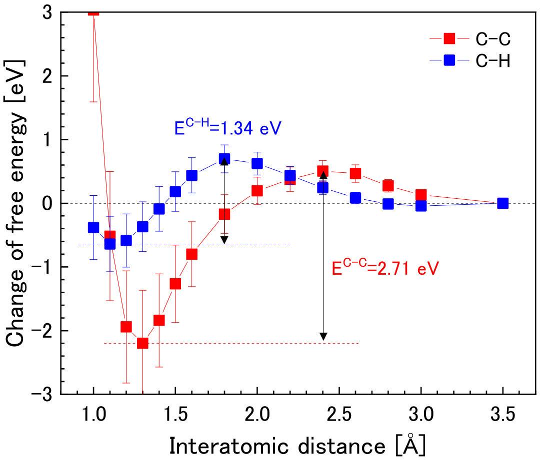

Figure 1: Free energy profiles for the C–H bond in the Na and Na–Ga melts.

the energy difference between a local maximum and a local minimum. From the result, we found that the activation free energies for C–C and C–H bond dissociation are 2.71 and 1.34 eV, respectively [8]. Because the dissociation energy of the C–H bond is lower than that for the C–C bond, CH_4 gas decomposes more easily than graphite; that is, CH_4 gas is more effective as a C additive than graphite.

References

[1] M. Imade, Y. Hirabayashi, Y. Konishi, H. Ukegawa, N. Miyoshi, M. Yoshimura, T. Sasaki, Y. Kitaoka, and Y. Mori: Appl. Phys. Express **3** (2010) 075501.

[2] T. Kawamura, H. Imabayashi, M. Maruyama, M. Imade, M. Yoshimura, Y. Mori, and Y. Morikawa: Appl. Phys. Express **9** (2016) 015601.

[3] K. Murakami, S. Ogawa, M. Imanishi, M. Imade, M. Maruyama, M. Yoshimura, and Y. Mori: Jpn. J. Appl. Phys. **56** (2017) 055502.

[4] Y. Morikawa: Phys. Rev. B **51** (1995) 14802.

[5] J. P. Perdew, K. Burke, and M. Ernzerhof: Phys. Rev. Lett. **77** (1996) 3865.

[6] E. A. Carter, G. Ciccotti, J. T. Hynes, and R. Kapral: Chem. Phys. Lett. **156**, (1989) 472.

[7] M. Sprik and G. Ciccotti: J. Chem. Phys. **109** (1998) 7737.

[8] T. Kawamura, M. Imanishi, M. Yoshimura, Y. Mori, and Y. Morikawa: Comp. Mater. Sci. **194** (2021) 110366.

Analysis on atomic and magnetic structure in magnetic molecular complex, crystal and interface and investigation of external electromagnetic field effect

Masao OBATA[1,2]

[1]*Institute of Science and Engineering, Kanazawa University, Kanazawa, Ishikawa 920-1192*

[2]*Graduate School of Natural Science and Technology, Kanazawa University, Kanazawa, Ishikawa, 920-1192*

We have investigated the electronic and magnetic structure of ferrimagnetic spinel of $NiCo_2O_4$ by using the beyond generalized gradient approximation (GGA) approach such as GGA+U or quasi-particle self-consistent GW (QSGW). The $NiCo_2O_4$ spinel has drawn a lot of attention for its material application due to its low cost with excellent electronic conductivity, redox reaction, and high electrochemical activity. However, some of the latest reports of its first-principles calculation result have some discrepancies with the experimental one. One of the reasons may come from the poor electron correlation description of GGA calculation. For this study, the first-principles calculation package ecalj [1], which adopts the mixed-based set between local orbital and plane waves, is used. We mainly focused on the inverse spinel structure containing 14 atoms, namely, eight oxygen and six cation atoms, in the primitive cell.

The results show that both GGA and QSGW gave the ferrimagnetic magnetic structure with a half-metallic electronic configuration[2]. However, some differences should be pointed out, e.g., the size of the energy gap on the majority spin. Remarkably, QSGW predicts the unoccupied energy of Ni e_g orbitals to be more than 1 eV higher than those calculated by GGA. It may affect the estimation of electric and optical properties such as reflectance or transmittance.

We also extended the QSGW calculation by combining it with the effective screened medium method [3]. It allows us to estimate the finite electric field effect of slab systems on GW level without relying on perturbation theory. We have succeeded in evaluating the dielectric constant in high accuracy [4].

References

[1] https://github.com/tkotani/ecalj/

[2] H. Al Rasyid, M. Obata, T. Kotani, T. Oda, The Science Reports of Kanazawa University, in press.

[3] M. Otani and O. Sugino, Phys. Rev. B, **73**, 115407 (2006).

[4] H. Sakakibara, T. Kotani, M. Obata, T. Oda, Phys. Rev. B, **101**, 205120(2020).

Molecular dynamics study on non-equilibrium processes of silica and silicates using first-principles calculation and machine leaning

Masaaki MISAWA

Graduate School of Natural Science and Technology, Okayama University

In this project, we studied (1) pressure-induced amorphization behavior of fayalite and (2) shock-compression behavior of quartz based on molecular dynamics simulations.

First-principles molecular dynamics simulation of pressure-induced amorphization of fayalite

Fayalite (Fe_2SiO_4), an end-member of the olivine, undergoes crystal-to-amorphous transformation at high-pressure and room-temperature conditions [1]. It was reported that this pressure-induced amorphized fayalite exhibits different features from olivine glasses synthesized by heat-and-quench processes [2]. However there are no theoretical investigations about the pressure-induced amorphization phenomenon and the pressure-induced amorphized phase yet.

In this study, we perform first-principles molecular dynamics study of fayalite to investigate energetic and structural properties of the pressure-induced amorphized fayalite. The volume-and-energy relations, partial pair distribution functions, and coordination number changes of crystalline and amorphous phases of fayalite during compression and decompression processes were obtained. We elucidated that the high-fold coordinated Si atoms exist in the amorphous phase even after decompression to an ambient conditions. Additionally, it was found that the Si atoms play a role of network-former in the amorphous phase at high-pressure, but change into network-modifier at an ambient conditions. Furthermore, it is expected that the medium- or long-range order of Fe atoms are partially remained in the amorphous phase, resulting in the appearance of its unique magnetic ordering structure.

Molecular dynamics simulation of shock-compression behavior of quartz using ANN potential

Artificial neural network (ANN) potential, which is an interatomic potential constructed by machine-leaning, attracts attention as a promising method to achieve extra-large-scale molecular dynamics (MD) simulation with first-principles accuracy [3,4]. Application of this ANN-MD to far-from-equilibrium phenomena, such as fracture and pressure-induced transformation, is important to understand structural properties of materials under extreme conditions. For this purpose, we have tried to perform ANN-MD simulation of shock-induced structural transformation of silica.

To compute shock-compression behaviors within the framework of MD method, the multiscale-shock technique [5] was employed in our simulations. Potential energy of shock-compressed α-quartz obtained by first-principles MD (FPMD) method is used as a reference data for training of ANN-potential. As a result of ANN-MD simulation for elastic shock-wave region, elastic-deformation behaviors of α-quartz was successfully reproduced with high-accuracy [6]. On the other hand, for plastic shock-wave region, the ANN-potential has completely failed on prediction of both structure and energy, because of that irregular structure appears and rapid movement of atoms occurs during the elastic-to-plastic transition process.

In order to improve the predicting ability of ANN-potential, we introduce a more accurate training method that uses not only potential energy but also atomic force and pressure as reference data [7]. Using this improved ANN-potential, it was succeeded that reproducing the elastic-to-plastic transition behavior and plastic deformation of α-quartz with an accuracy close to FPMD simulation. Thus, the ANN-potential trained with energy, force, and pressure is a potentially powerful tool to investigate wide range of far-from-equilibrium phenomena and will also provide useful information for solid earth physics field in future.

References

[1] Q. Williams et al.: J. Geophys. Res. **95** (1990) 21549.

[2] S. Kohara et al.: Science **303** (2004) 1649.

[3] J. Behler and M. Parrinello: Phys. Rev. Lett. **98** (2007) 146401.

[4] N. Artrith and A. Urban: Comput. Mater. Sci. **114** (2016) 135.

[5] E. Reed et al., Phys. Rev. Lett. **90** (2003) 235503.

[6] M. Misawa et al.: J. Phys. Chem. Lett. **11** (2020) 4536.

[7] K. Shimamura et al.: J. Chem. Phys. **153** (2020) 234301.

Search and realization of novel electronic properties of solid surfaces and interfaces and of small particles

Takeshi INAOKA
Department of Physics and Earth Sciences, Faculty of Science,
University of the Ryukyus, 1 Senbaru, Nishihara, Okinawa 903-0213

We mention two subjects which we addressed this year.

The Ni(110)-(2x1)O surface is known to have a missing-row reconstruction structure, as is shown in Fig. 1 [1]. Oxygen (O) atoms are adsorbed at bridge sites to form Ni-O-Ni atomic chains in the *y*, namely, [001] direction. The O-derived bands exist near the upper and lower edges of the substrate Ni bands. The bands around the lower edge have already been studied well by means of first-principles calculations using small-scaled slabs and some experimental studies.

This year, using a large-scaled slab composed of 21 Ni atomic layers and adsorbed O atoms at both surfaces, we investigated the upper O-derived bands, and identify them with surface states when separated up from the upper edge of the substrate bands.

We employed the program package 'Vienna Ab initio Simulation Package' (VASP) [2,3] on systems B and C.

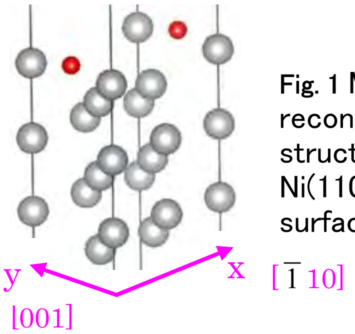

Fig. 1 Missing- row reconstruction structure at the Ni(110)-(2x1)O surface

Graphene is a very popular single-layer structure of carbon (C) atoms arranged in a hexagonal lattice. The band structure of this material is characterized by a so-called Dirac cone, and predicts an extremely high electron mobility. When this material takes a form of nanoribbons, the band structure due to π orbitals around the Fermi level depends on edge shapes. Nanoribbons with zigzag edges have localized edge states, while those with armchair edges possess no edge states.

We consider the electronic structure of graphene systems of finite area. By means of the tight-binding method, we examined if edge-localized states can be formed in finite graphene systems, and how the electronic structure of these systems depends on system shapes or areas.

(1) Identification of surface states at the Ni(110)-(2x1) O surface [4]

Assuming a slab of 21 Ni-atom layers with O atoms adsorbed at each surface and using the generalized gradient approximation, we obtained the optimized ground state structure. Figure 2 (a) shows the band dispersion on the $\bar{\Gamma}-\bar{\mathrm{Y}}$ line for majority spin. As is displayed by an arrow, there exist a pair of nearly degenerate bands that lie above the densely distributed substrate bands due to Ni *d* orbitals. Figure 2 (b) exhibits electron-density isosurfaces of the higher energy one of the above paired states at the

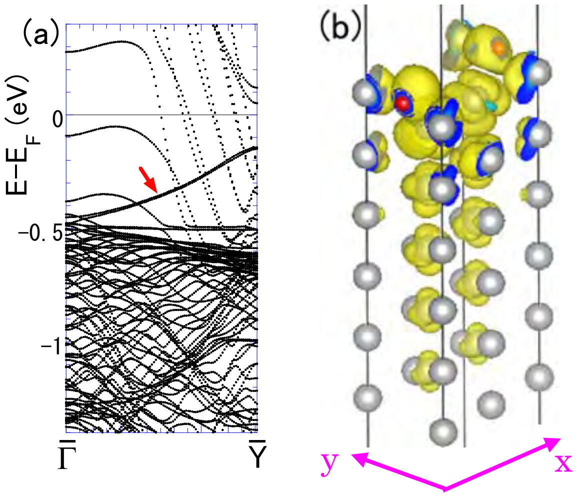

Fig. 2 (a) Band dispersion on the $\bar{\Gamma}-\bar{\mathrm{Y}}$ line for majority spin and (b) electron density isosurfaces of the state on the midpoint of the $\bar{\Gamma}-\bar{\mathrm{Y}}$ line, as is arrowed in (a).

middle point of the $\bar{\Gamma}-\bar{\mathrm{Y}}$ line. Isosurfaces of the lower one are almost the same. This isosurface map clearly indicates that this state is localized near the surface, and that the p_x orbital of an O atom, which extends in the x, namely, $[\bar{1}10]$ direction, plays a major role, and it bonds to d_{xy} orbitals of a surface Ni atom. We can recognize this tailed localization at the surface only in such a large-scaled slab as ours. However, we still have to verify that these surface states really exist even in a semi-infinite substrate. We consider that bulk which can be obtained in the limit of increasing the slab thickness, and evaluate the upper edges of those bands which correspond to the substrate bands of the slab. We find that these upper bulk-band edges are below the paired nearly degenerate bands. Through this analysis, we concluded that the surface states are really present in the semi-infinite substrate.

We made the same analysis of the O-derived bands around the upper edge of the substrate bands on the $\bar{\Gamma}-\bar{\mathrm{X}}$ line as well. We identified the surface states in which the p_y orbital of an O atom bonds to the d_{yz} orbitals of a surface Ni atom.

(2) π-band structure of finite graphene systems [5]

We examined the electronic structure of finite graphene systems for various shapes and areas. Each eigenstate is expressed in a form of a linear combination of p_z orbitals of C atoms extending in a plane-normal direction, and each component of its eigenvector represents the p_z orbital coefficient of the corresponding C atom.

As an example of the results, figure 3 displays the p_z-orbital coefficients in color scale of (a) the lowest-energy state (n=1), (b) the highest-occupied state (n=23) and (c) the highest energy state (N=46) for a parallelogram graphene with 46 C atoms. This parallelogram is quite special in having only zigzag edges.

As is shown in Fig. 3 (a), the p_z orbital coefficients in the lowest-energy state are coherent in sign. On the other hand, figure 3 (c) indicates that, in the highest-energy state, the coefficient alternates in sign along each hexagonal atom ring. In either of these states (a) and (c), the coefficient amplitude tends to decrease as we move from the center to the edge. These features are common to various shapes of finite graphene.

Figure 3 (b) shows that the highest occupied state has edge localization. Red and blue circles indicate atoms with large positive and low negative coefficients, respectively. These coefficients with large amplitudes alternate in sign along the edge line. The electron density distribution is localized around the acute-angle vertices, namely, at those edges farther away from the center. Generally, edge localization occurs at zigzag edges in specific states at or just near the Fermi level.

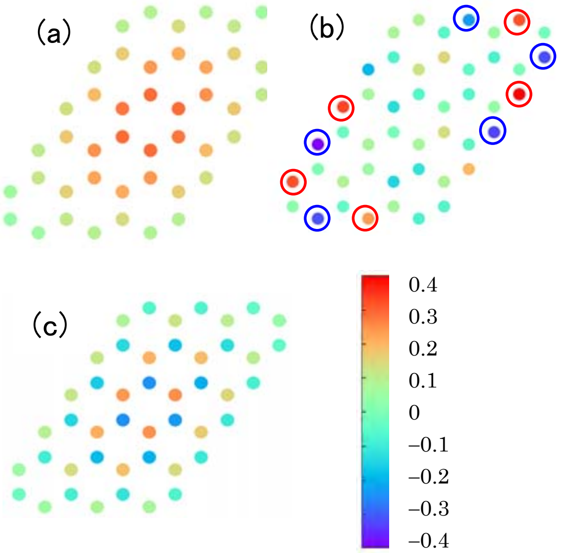

Fig. 3 p_z-orbital coefficients in color scale for a parallelogram graphene. (a) Lowest- energy state, (b) Highest-occupied state, (c) Highest-energy state.

References

[1] G. Kleinle et al., Surf. Sci. **225** (1990) 171-183.
[2] G. Kresse and J. Hafner: Phys. Rev. B **47** (1993) 558-561.
[3] G. Kresse and J. Furthmüller: Comput. Mat. Sci. **6** (1996) 15-50.
[4] T. Inaoka and Y. Uehara: Identification of surface states formed above the substrate bands of the Ni(110)-(2x1)O surface, to be submitted.
[5] T. Ohshiro and T. Inaoka: unpublished.

Theoretical Study on Electronic Properties in New Nanoscale Surfaces and Interfaces

Katsuyoshi KOBAYASHI
Department of Physics, Ochanomizu University
2-1-1 Otsuka, Bunkyo-ku, Tokyo 112-8610

In 2020 we theoretically studied one-dimensional Rashba systems. Perfect spin-polarization and spin-orientation reversal of photoelectrons have been observed in spin- and angle-resolved photoelectron spectroscopy (SARPES) of strong spin-orbit systems [1, 2]. These phenomena have theoretically been explained in terms of mirror symmetry of the systems [2, 3]. A problem, however, is that the states having mirror symmetry are restricted to lines in two-dimensional Brillouin zones. Only a small amount of photoelectrons are fully spin polarized. To improve the efficiency of spin polarization we considered a one-dimensional Rashba system and theoretically investigated it.

Mirror-symmetrical two states with respect to each other in a two-dimensional Brillouin zone form a mirror-symmetrical state by making the system finite along the direction perpendicular to a mirror symmetrical line. All states become mirror symmetrical in one-dimensional systems and all photoelectrons excited with linearly polarized light are spin-polarized. However, the wave functions are either symmetrical or anti-symmetrical, and the spin orientation of photoelectrons is determined by the symmetry of wave functions. The spinor in strong spin-orbit systems contain both type of wave functions and the magnitude of these components vary.

To investigate the spin polarization in one-dimensional Rashba systems we used a simple Rashba Hamiltonian and numerically solved it. We used both plane-wave expansion and finite difference methods, and verified that the difference between results by these methods is small. Figure 1 shows an example of calculated results. The electron spin is positively and negatively polarized for $k_x < 0$ and $k_x > 0$, respectively, where k_x is the wave number along the one-dimensional direction. The polarization decreases with decreasing $|k_x|$. However, spin polarization is not necessarily low even near $k_x \sim 0$. This is due to the properties of the Rashba Hamiltonian for the states with energy $E < 0$.

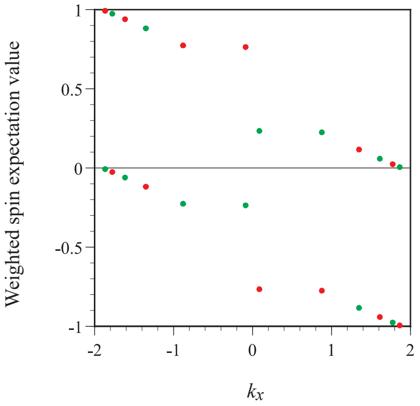

Figure 1: Spin expectation values calculated as a function of k_x for a fixed energy $E < 0$. Red and green circles show symmetrical and anti-symmetrical components of wave functions. Expectation values are weighted with the norm of each component.

References

[1] C. Jozwiak *et al.*: Nat. Phys. **9** (2013) 293.

[2] K. Yaji *et al.*: Nat. Commun. **8** (2017) 14588.

[3] K. Kobayashi *et al.*: Phys. Rev. B **95** (2017) 205436.

Study on structural elementary excitations at semiconductor surfaces and interfaces

Hiroyuki KAGESHIMA
Graduate School of Natural Science and Technology, Shimane University
1060 Nishi-Kawatsucho, Matsue, Shimane 690-8504

Our project has been focused on physical properties of structural elementary excitations of semiconductor surfaces and interfaces. We have performed one topic in this year. It is the physical properties of oxygen vacancies (V_O) in SiO_2 at interface with Si. [1] The calculations were performed based on the first-principles calculation. Program package PHASE/0 was employed.

Because of recent progress of integrated circuits, three-dimensional metal-oxide-semiconductor field-effect transistors (MOSFETs) have been attracting attention. The vertical body-channel-MOSFET has a gate insulating thermally oxide Si film around a Si pillar with a diameter of several tens of nm, but it is considered that a large stress distributes in the oxide film. When a Si nanowire with a width of 50 nm and a thickness of 30 nm is processed by dry oxidation at 1000°C for 80 min, it is known that a compressive strain of about 3% is accumulated near the interface and a tensile strain of about 3% is accumulated near the outer surface.

The strain induced in the oxide film must have an unconventional effect on the film reliability such as dielectric breakdown. It is known that the dielectric breakdown of the oxide film is triggered by V_O-related defects in the film. The V_O-related defects trap holes, and transform into 3-coordinated Si's with +1 charge. These 3-coordinated Si's diffuse and aggregate under a gate-channel electric field of MOSFET operation to create a one-dimensional conductive chain from the Si interface to the gate interface in the oxide film. Then, a gate leak current flows through this chain, and leads to the dielectric breakdown. Since the oxide film of the three-dimensional MOSFETs is subjected by the strain, it is considered that these processes are also affected by the strain.

We focused on the fundamental properties of V_O in the oxide film, and investigated the effect of strain on them using the first-principles calculation. We found that the stability of V_O increases under compression. We also found that the height of the diffusion barrier increases under compression. In addition, we found that the diffusion barrier height is determined by the Si-Si bond length of the V_O. Considering the gate oxide film in the vertical body-channel-MOSFET, the V_O density increases because the interfacial oxide film is subjected to compressive strain. This suggests that interfacial traps are more likely to occur and performance may be slightly degraded. On the other hand, tensile strain is applied to the surface oxide film to reduce the density of V_O, but diffusion of V_O is promoted. This means that the reliability of the oxide film is affected by the stain because V_O can diffuse from the interface of the oxide film to the surface.

References

[1] K. Yata and H. Kageshima, Jpn. J. Appl. Phys. **60** (2020) 035504 (6 pages).

Prediction of properties of organic ferroelectrics and piezoelectrics by first-principles calculation

Shoji ISHIBASHI
Research Center for Computational Design of Advanced Functional Materials (CD-FMat),
National Institute of Advanced Industrial Science and Technology (AIST)
Tsukuba, Ibaraki 305-8565

Organic small-molecular crystals show a variety of crystal structures and electronic properties. Among them, there is a class of compounds called "hydrogen-bonded systems", in which proton transfer causes π-bond dipole switching. Some of them show ferroelectricity or antiferroelectricity [1]. First-principles calculations toghther with the Berry phase theory successfullty predict spontaneous polarization values of such ferroelectrics [2, 3, 4, 5, 6]. Antiferroelectrics consist of polar subunits. By applying a strong electric field, some of them can be converted into ferroelectric phases. Evaluating polarization of the subunit, the total polarization can be predicted in such induced ferroelectric phases [7, 8].

In 2020, we have applied this approach in predicting electric-field-induced polarization of bis-(1H-benzimidazol-2-yl)-methane (BI2C), in which non-polar and/or polar subunits exist depending on temperture, and the obtained polarization values are in good agreemet with experimetally obtained results [9]. In addition, similarly to our previous work on antiferroelectric squaric acid [10], calculations with a computationally-applied electric field are ongoing for several hydorogen-bonded ferroelectrics and anitiferroelectics.

References

[1] S. Horiuchi and S. Ishibashi, J. Phys. Soc. Jpn. **89**, 051009 (2020).

[2] S. Horiuchi, K. Kobayashi, R. Kumai, and S. Ishibashi, Nat. Commun. **8**, 14426 (2017).

[3] F. Kagawa, S. Horiuchi, N. Minami, S. Ishibashi, K. Kobayashi, R. Kumai, Y. Murakami, and Y. Tokura, Nano Lett. **14**, 239 (2014).

[4] K. Kobayashi, S. Horiuchi, S. Ishibashi, F. Kagawa, Y. Murakami, and R. Kumai, Chem. Eur. J. **20**, 17515 (2014).

[5] S. Horiuchi, Y. Noda, T. Hasegawa, F. Kagawa, and S. Ishibashi, Chem. Mater. **27**, 6193 (2015).

[6] S. Horiuchi, S. Ishibashi, K. Kobayashi, and R. Kumai, RSC Adv. **9**, 39662 (2019).

[7] S. Horiuchi, R. Kumai, and S. Ishibashi, Chem. Sci. **9**, 425 (2018).

[8] K. Kobayashi, S. Horiuchi, S. Ishibashi, Y. Murakami, and R. Kumai, J. Am. Chem. Soc. **140**, 3842 (2018).

[9] S. Horiuchi, S. Ishibashi, R. Haruki, R. Kumai, S. Inada, and S. Aoyagi, Chem. Sci. **11**, 6183 (2020).

[10] S. Ishibashi, S. Horiuchi, and R. Kumai, Phys. Rev. B **97**, 184102 (2018).

Search of accessible surfaces for catalyst informatics

Yoyo HINUMA

Institute of Innovative Research

Tokyo Institute of Technology

4259 Nagatsuta-cho, Midori, Yokohama, Kanagawa 226-8502

High catalytic reactivity in oxides is expected in high index surfaces and at surface defects, such as corners and step edges, since there are cations and anions with more unfavorable coordination environments including low coordination number. Theoretical studies are leading experimental investigations on irregular sites because of the difficulty of the latter.

To increase the volume and variety of the data without compromising veracity, surfaces that are appropriately reconstructed need to be added. From another viewpoint, terminations that are likely to be experimentally accessible need to be distinguished from those that are not because only surfaces that can be experimentally synthesized, preferably with less effort, can be used industrially and therefore contribute to improvement of our society.

This study considered 67 terminations (34 orientations) of β-Ga_2O_3. The automated nonstoichiometric and nonpolar slab-and-model generation algorithm already developed by Hinuma et al. [1,2] was expanded to allow automatic derivation of models where the topmost and bottommost surfaces need to be reconstructed, which is the case in the normal spinel surfaces in this study [3]. Surfaces which do not have the lowest energy for a given orientation, including terminations found by genetic algorithm calculations (obtained using the USPEX code [4]), or its surface energy can be reduced by forming macroscopic facets [5], were removed.

The following orientations were found to be experimentally accessible in β-Ga_2O_3, in order of increasing surface energy: (100), (20-1), (310), (101), (11-2), (11-3), (11-1). This method can be used for other materials, and will be a powerful tool to find overlooked high-energy surfaces.

References

[1] Y. Hinuma et al.: Comp. Mater. Sci. 113 (2016) 221.

[2] Y. Hinuma et al.: Phys. Rev. Mater. 2 (2018) 124603.

[3] Y. Hinuma et al.: Mater. Trans. 61 (2020) 78.

[4] A.R. Oganov et al.: J. Chem. Phys. 124, (2006) 244704.

[5] Y. Hinuma et al.: Mater Trans.61 (2020) 143.

Calculation of multication oxide surface properties for catalyst informatics

Yoyo HINUMA

Institute of Innovative Research

Tokyo Institute of Technology

4259 Nagatsuta-cho, Midori, Yokohama, Kanagawa 226-8502

Surface point defects of metal oxides, for instance O vacancies, have a dominant effect on heterogeneous catalysis. The Mars-Van Krevelen mechanism is one of the most frequently encountered catalytic process. In one example, O vacancies on a metal oxide catalyst surface act as reaction sites. The energy minimum required to remove O from a surface, which is denoted as the surface O vacancy formation energy (E_{Ovac}), can be used to rationalize and predict catalytic performance in such a catalytic process. Calculation of E_{Ovac} requires a slab-and-vacuum model with sufficient spacing between O vacancies, hence some estimation of E_{Ovac} from less costly calculations, such as slab-and-vacuum model calculations with minimum cell size and even bulk calculations, will be effective in screening materials for a given purpose.

The E_{Ovac} of ZnM_2O_4, where M is one of Al, Ga, In, V, Cr, Mn, Fe, or Co, was calculated. These compounds take the normal spinel structure, and the (100), (110), and (111) surfaces were evaluated. The automated nonstoichiometric and nonpolar slab-and-model generation algorithm already developed by Hinuma et al. [1,2] was expanded to allow automatic derivation of models where the topmost and bottommost surfaces need to be reconstructed, which is the case in the normal spinel surfaces in this study [3]. A large variation of up to 3.6 eV in the smallest E_{Ovac} of a surface was observed for different orientations of same material. E_{Ovac} was typically higher in a more stable surface within the same compound, which is in line with chemical intuition. A good correlation between E_{Ovac} and E_{bulk}, band gap, and electron affinity was obtained between the same orientation for (100) and (110) surfaces, although the trend for the (111) surface was contradictory.

References

[1] Y. Hinuma et al.: Comp. Mater. Sci. 113 (2016) 221.

[2] Y. Hinuma et al.: Phys. Rev. Mater. 2 (2018) 124603.

[3] Y. Hinuma et al.: Mater. Trans. 61 (2020) 78.

First-principles study on complexes of impurity and dislocation in GaN p-n diodes

Yosuke HARASHIMA[1,2]
[1] *Institute of Materials and Systems for Sustainability, Nagoya University*
Furo-cho, Chikusa, Nagoya, Aichi 464-8601
[2] *Center for Computational Sciences, University of Tsukuba*
Tennodai, Tsukuba, Ibaraki, 305-8577

The development of power semiconductor devices is one of the key issues for the realization of a sustainable society. GaN has properties suitable for power devices, such as a large band gap, and is expected to be a candidate for next-generation power semiconductor materials. On the other hand, the threading dislocations generated during the synthesis of GaN become a source of leakage current, which impairs the rectifying effect, an important characteristic of the device. It has been reported that the leakage current is related to the type of threading dislocation and the condensation of impurities around the dislocation, but the microscopic mechanism of leakage current generation has not been clarified.

Power semiconductor devices consist of a combination of p-type and n-type layers, with impurities such as Si and Mg doped to each layer. To understand the mechanism of leakage current generation, it is necessary to understand the electronic state in each layer. The electronic structure of the complex of Mg and screw dislocations doped to make the p-layer has been clarified by our previous studies using first-principles calculations and atom probe tomography. [1] The purpose of this study is to analyze the interaction between Si impurities doped to make the n-layer and dislocations, and to clarify the properties of the complex consisting of Si and dislocations.

The effective mass of electrons is smaller than that of holes in GaN, and the effective Bohr radius, which indicates the width of the impurity states, is larger. Therefore, it is necessary to consider larger systems. For larger system size calculations, we use RSDFT[2, 3], a highly parallelized and efficient first-principles code. In this study, we consider a screw dislocation with the Burgers vector [0001]. The dislocations break the periodic structure and we use a supercell. In order to avoid these strains affecting each other at the periodic boundary, a vacuum layer is inserted in the lateral directions of *c*-axis.

We consider a 21 Å × 27 Å × 30 Å supercell, which includes about 800 atoms. An Si atom is substituted at a Ga site. In order to analyze the binding energy of Si, we performed calculations for several substitutional sites. We optimized the atomic positions and obtained the stable structures of the complex. We are analyzing the results for the binding energy of Si to the screw dislocation.

References

[1] T. Nakano, Y. Harahsima, *et al.*: Appl. Phys. Lett. **117** (2020) 012105.

[2] J.-I. Iwata, *et al.*: J. Comput. Phys. **229** (2010) 2339.

[3] Y. Hasegawa, *et al.*: Int. J. High Perform. Comput. Appl. **28** (2014) 335.

Simulation of scanning tunneling microscopy images of graphene ribbons with edges

Junhuan LI, Kenta ARIMA

Department of Precision Engineering, Graduate School of Engineering

Osaka University, Yamada-oka, Suita, Osaka 565-0871

We are aiming at elucidating local electronic structures of finite-size graphene sheets and their impact on scanning tunneling microscopy (STM) images. For this purpose, we have started first-principles calculations of single-layer graphene ribbons possessing either zigzag or armchair edges by the use of a simulation package named STATE (Simulation Tool for Atom TEchnology). STATE is based on the density functional theory. The exchange and correlation potential is described by the generalized gradient approximation by Perdew-Burke-Ernzerhof (GGA-PBE). We also used both a plane-wave basis set and pseudopotentials. When running STATE, we first defined the atomic structure of a finite-size graphene. This model as well as other parameters were placed as an input file on a supercomputer. The self-consistent field method was employed, which is an iterative method that involves selecting a Hamiltonian, solving the Kohn-Sham equation to obtain a more accurate set of orbitals, constructing the potential for each wave function, and solving the Kohn-Sham equation again with these until the results converge. In order to draw a map of local density of states, an electron density was integrated over a specific energy window, or a eV, below HOMO (Highest Occupied Molecular Orbital). At each (x, y) coordinate, a z-height possessing the same electron density (6.72×10^{-4} /Å^3) was investigated and its contour map was depicted. This approximates a simulated STM image at the sample bias of a V. We used the module (intel/18.0.5) for the compilers and mpt/2.16 for MPI library. The set of calculation was usually executed on F4cpu or F36cpu with suitable nodes in ISSP.

To check the performance of our calculation, we modeled a graphene nanoribbon with zigzag edges terminated by H atoms. Figure 1(a) shows a simulated STM image of a zigzag-edged ribbon named C28 at the sample bias of -1.0 V. C28 indicates the ribbon width possessing 28 dimer lines across the width. In Fig. 1(b), a hexagonal carbon network is superimposed in the image in Fig. 1(a). Figure 1 shows that either a hexagonal or a triangular pattern is formed in the interior of the ribbon whereas isolated bright spots are formed at both edges of the ribbon. The latter is caused by the localized electronic states at a zigzag edge, which agrees with literature [1]. In the next fiscal year, we are going to characterize the distribution of local charge densities of the armchair-edged graphene ribbon and to unveil its relationship with an STM image around the Fermi level.

Regarding this project, we had three oral presentations at domestic meetings in 2020 [2-4].

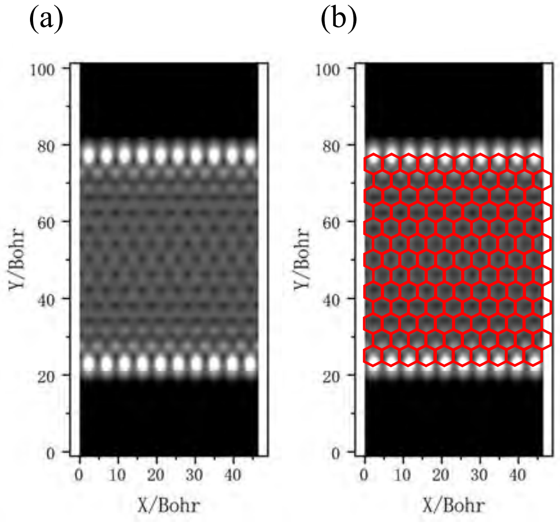

Fig. 1 (a) Simulated STM image of zigzag-edged graphene nanoribbon (C28). (b) A carbon network is superimposed in the image in (a).

References

[1] P.L. Giunta and S.P. Kelty: J. Chem. Phys., **114** (2001) 1807.

[2] J. Li, K. Arima et al.: JSAP (The Japan Society of Applied Physics) fall meeting (2020) 05-101.

[3] J. Li, K. Arima et al.: JSPE (The Japan Society for Precision Engineering) fall meeting (2020) 517.

[4] J. Li, K. Arima et al.: JVSS (The Japan Society of Vacuum and Surface Science) meeting (2020) 1Ba03.

A theoretical study on the effect of impurity doping on the thermoelectric performance of environmental friendly silicide $SrSi_2$

Tsutomu Iida, Naomi Hirayama, Daishi Shiojiri, Tomoyuki Kadono, and Masato Yamaguchi
Department of Materials Science and Technology, Faculty of Industrial Science and Technology,
Tokyo University of Science, 6-3-1 Niijyuku, Katsushika-ku, Tokyo, 125-8585, Japan

Thermoelectric semiconductors, especially those operating at low temperatures, are expected to be applied to power generation systems that utilize the vaporization of liquefied natural gas as cold heat energy sources, and to self-powered wireless sensors.

α-$SrSi_2$ has been identified as a potential TE material, and its main attributes are its light weight, its non-toxicity, and the worldwide abundance of its constituent elements. α-$SrSi_2$ has relatively good power generation performance, with a dimensionless figure of merit ZT = ~0.15 at 300 K [1] and p-type conduction when the composition is stoichiometric. For practical use, in order to further improve the p-type thermoelectric performance and achieve n-type conduction of α-$SrSi_2$ so as to configure pn devices, it would be necessary to quantitatively understand the electronic structure through experimental studies and theoretical calculations.

The electrical properties of polycrystalline α-$SrSi_2$ have been examined by M. Imai et al. [2], who revealed that α-$SrSi_2$ is a narrow-gap semiconductor with an energy gap of 35 meV and that its dominant carriers are holes. Their results, however, were not consistent with the results of previous electronic-structure calculations for which density-functional theory (DFT) with the conventional generalized gradient approximation was used. Most of the calculated bandgap values were about 0 eV or less, which is much smaller than the experimentally observed values. This difference makes it difficult to predict the thermoelectric properties from theoretical considerations.

This year, we carried out DFT calculations of the transport characteristics of α-$SrSi_2$ using the Heyd–Scuseria–Ernzerhof screened hybrid functional, and then compared the experimentally measured thermoelectric properties with the computational results.

The bandgap of the polycrystalline α-$SrSi_2$ grown by vertical Bridgman method estimated from the carrier density dependence on temperature was 13.1meV. When the mixing parameter of the Hartree-Fock contribution to the exact exchange was 18.7%, the bandgap was estimated to be 13.27 meV, which almost reproduces the experimental E_g value. Furthermore, Seebeck coefficients were calculated using the Boltzmann transport theory, and the results obtained using the chemical potential that matches the carrier concentration, which was determined experimentally, were in good agreement with the temperature dependence of the Seebeck coefficient obtained experimentally. It was concluded that first principles calculations using the hybrid functional can successfully predict the thermoelectric transport properties of narrow-gap thermoelectric semiconductors.

References

[1] S. K. Singh and M. Imai, Intermetallics 127, 106981 (2020).
[2] M. Imai, T. Naka, T. Furubayashi, H. Abe, T. Nakama, and K. Yagasaki, Appl. Phys. Lett. 86, 032102 (2005).

STM simulations for Si(111)7 × 7 surfaces

Kei TANIMOTO and Ken HATTORI

Graduate School of Science and Technology, Nara Institute of Science and Technology,
Takayama, Ikoma, Nara 630-0192

Using scanning tunneling microscopy (STM), author's group has been studied iron-silicides formation on Si(111) [1] prepared in ultra-high vacuum. In the initial stage of Si(111) 7 × 7 with isolated Fe atoms, we observed 5 different adsorption types in experimental STM images [2]. Using the super computing system in the institute for solid state physics, we carried out first principles calculations for several configurations of Fe atoms on Si(111)4 × 4 surface in the last year. The small-size 4 × 4 surface has an advantage of fast calculation compared to that in the 7 × 7 surface, maintaining the specific 7 × 7 surface property (dimer — adatom — stacking-fault structure): 4 Si adatoms on 2 × 2 T_4 sites, and 2 of 4 restatoms terminated with H atom, in a 4 × 4 unit cell.

On the basis of these results we extended the calculations to 7 × 7 surfaces in this year, firstly focusing a clean surface using the calculation package of Simulation Tool for

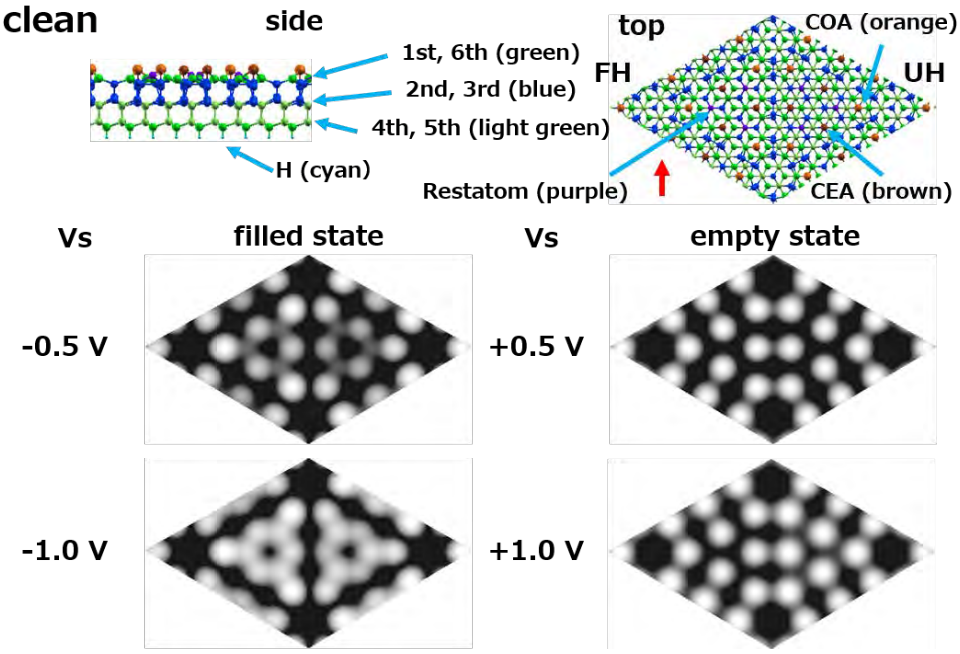

Fig. 1. Schematics of clean Si(111) 7 × 7 surface model in side (upper left) and top (upper right) views, and simulated STM images in filled states (left panel) and empty states (right panel) at different sample bias voltages (Vs). The red arrow represents side-viewing direction.

Atom TEchnology (STATE)-Senri [3]. The calculated clean 7 × 7 model consists of a Si adatom-layer, six Si-layers, and a bottom H-terminated layer, with 347 atoms. All atoms except the last Si layer and bottom H layer are fully relaxed at <0.05 eV/Å from atomic positions predicted in the 4 × 4 model, under 700 bands without spin polarization. STM images are simulated using a special STM displaying tool [4].

The obtained STM simulation images in Fig. 1 display 12 adatoms in a 7 × 7 unit cell at the all Vs, and successfully 6 restatoms at Vs = -1.0 V. We also recognize that corner adatoms (COA) are brighter (higher) than center adatoms (CEA), and atoms on a faulted half (FH) unit cell are brighter (higher) than those on an unfaulted half (UH) unit cell, in filled states. These features are consistent with the experimental results. The relaxed 7 × 7 clean surface structure can be applied for the starting structure capturing an Fe atom, extension of the Fe adsorption configurations in the 4 × 4 models.

The authors thank Profs. Morikawa, Hamada, and Inagaki in Osaka University, and Prof. Yanagisawa in Ryukyu University for their great support in STATE-Senri calculations.

References

[1] K. Kataoka, K. Hattori, Y. Miyatake, and H. Daimon, Phys. Rev. B **74** (2006) 155406.

[2] K. Kataoka, Dr.. Thesis, Nara Institute of Science and Technology, Nara (2006).

[3] Y. Morikawa, Phys. Rev. B {\bf 63} (2001) 033405, and references therein.

[4] The precise STM calculation tool has been developed by Prof. I. Hamada in Osaka University and Prof. S. Yanagisawa in Ryukyu University.

First-principles Study of Defects of Magnesium Alloys

Daisuke Matsunaka
Department of Mechanical Systems Engineering,
Shinshu University, 4-17-1 Wakasato, Nagano 380-8553

Magnesium (Mg) has been of increasingly interest from the engineering viewpoint, because of its low density and relatively high specific strength.

In this study, we calculate generalized stacking fault energy (GSFE) surface, to evaluate activation of each slip system in Mg, using first-principles calculations. In GSFE calculations for pyramidal slips, it is important to take account of relaxation of atomic configuration perpendicular to the slip direction. For the first-pyramidal slip, out-plane atomic relaxations were observed during the slip process. The out-plane atomic relaxations reduce the GSFE and cause an energy minimum on the curve, corresponding to the stable stacking fault energy (SSFE). For the second-pyramidal slip, in-plane atomic relaxation perpendicular to the slip direction was associated with the stable stacking fault.

In order to investigate effects of alloying elements, we carried out the GSFE calculations with alloy models in which one solute atom was substituted at the slip plane. The unstable stacking fault energy (USFE) and SSFE for the first-pyramidal slip were more reduced by addition of the solute atom of the larger atomic radius. On the other hand, changes in USFE and SSFE for the second-pyramidal slip were not monotonic with respect to the atomic radius of the solute atom.

In Mg-Y alloy, enhanced activation of pyramidal slips improves ductility. It has been suggested that the activation of pyramidal slips was attributed to intrinsic I_1 stacking fault (SF) energy stabilized by Yttrium addition. We investigated defect nucleation in the vicinity of a pre-existing intrinsic I_1 SF by molecular dynamics simulations. While formation of (11-21) twin was observed under shear stress on (0001) along [11-20], <c+a> partial dislocations were generated with SFs for higher resolved shear stress for pyramidal slips. The dissociation reactions of the dislocations at the side ends of the I_1 SF were energetically evaluated, and it was implied that nucleation of the <c+a> dislocations on the first-pyramidal planes is more favorable than on the second-pyramidal planes.

References

[1] R. Hori: Master Thesis, Shinshu Univ. (2021).

[2] S. Yoshikawa and D. Matsunaka: Comp. Mater. Sci. **179** (2020) 109

Elucidation of the mechanism of self-ordering phenomena at the interface between organic and inorganic materials

Tomoya Shiota,[1] Yuuichi Orimoto,[2] Yuriko Aoki[2]

[1]Department of Molecular and Material Sciences, Interdisciplinary Graduate School of Engineering Sciences, Kyushu University, Fukuoka 816-8580, Japan.

[2]Department of Material Sciences, Faculty of Engineering Sciences, Kyushu University, Fukuoka 816-8580, Japan

We have studied an interface system between an inorganic solid surface and organic molecules, PTCDAs on Ge(001) surface using the Density Functional Theory (DFT) calculations with the climbing image nudged elastic band method and kinetic Monte Carlo simulation. All MPI parallelized DFT calculations were performed using Vienna Ab initio Simulation Package (VASP) version 5.4.4 on the ISSP's new supercomputer system.

First, we elucidated the hopping mechanism of the isolated adsorbed PTCDA molecules on Ge(001) surface. [1] Subsequently, we simulated that a PTCDA molecule hops on the Ge(001) under the intermolecular interactions as shown in Fig. 1. It was found that lone adsorbed PTCDA molecules cannot hop on Ge(001). On the other hand, they can hop under the intermolecular interactions at 500K. Successively, we performed kinetic Monte Carlo simulations using the activation energies obtained by DFT calculations for the hopping of PTCDA molecules in various proximity adsorption configurations at medium coverage. As a result, the formation of one-dimensional molecular chains was confirmed.

Next, the flip-flop motion of the Ge(001) surface dimer was investigated to explicitly account for Ge(001) surface dimer conditions. On the Ge(001) clean surface, the obtained activation barriers for dimer flipping under various dimer configurations are enough small to overcome at high temperature as well known in many previous experiments. The activation barrier of surface dimers between adsorbed molecules was larger than that of the clean surface, but sufficient to overcome it at 500K.

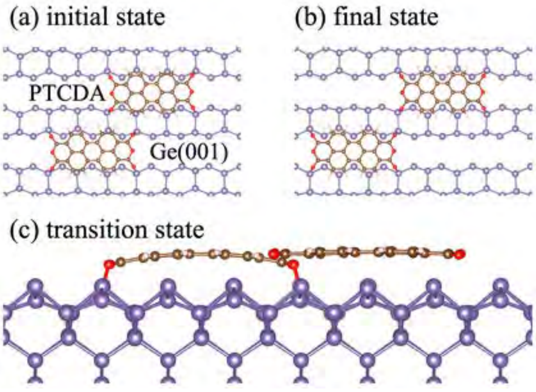

Fig. 1: The hopping of PTCDA on Ge(001) under the intermolecular interaction.

References

[1] T. Shiota, W. Mizukami, H. Tochihara, K. Yagyu, T. Suzuki, and Y. Aoki, J. Phys. Chem. C **124**, 24704 (2020)

Study on Machine Learning Model of Carrier Dynamics in Semiconductor Devices

Masakazu Muraguchi

Faculty of Engineering, Hokkaido University of Science,

Maeda, Teine, Sapporo 006-8585

In a two-dimensional nanowire system with random impurity distribution, we developed a model to predict the electron transmission probability from the impurity distribution by combining the time evolution of the electron wave function and machine learning.

Electron conduction in nanoscale two-dimensional wires with random impurity distribution is investigated. To prepare the dataset for machine learning, the time-development of an electron wave-packet is calculated, and obtain the transmission probability. The time-dependent schrödinger equation is solved where the finite difference method is employed with the second-order split operator method [1,2]. Note that a supercomputer system was used for these time-consuming time evolution calculations. Then, a model that can predict the transmission probability of electron wave packets from the space distribution of impurities build by using the machine learning. Through this process, the ways to extract the features of the transmission on this system is investigated.

The impurity distribution can be reproduced when the central coordinates are available. Therefore, this can be used as a feature. However, this does not directly include the whole shape of the potential distribution. Therefore, the features of the system were extracted by analyzing the time variation of the electron density distribution using time evolution calculations. For example, the transmission probability with impurity in the nanowire is sensitive to the position shift of impurities for y-direction (see Fig.1). As the machine learning method, a Random Forest (RF) is employed for modeling. The mean absolute error is evaluated. As the result, the accuracy of the model is improved by performing machine learning based on the extracted features. The proposed method provides a new perspective for analyzing the motion of electrons in nanoscale semiconductors.

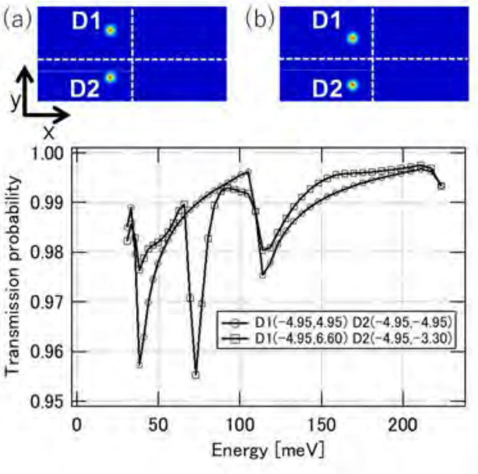

Fig.1 **Transmission probabilities with the electron energy where the positions of impurities are shifted 3.3 nm to y-direction between the case (a) and (b).**

References

[1] N. Watanabe and M. Tsukada: Phys. Rev. B 62 (2000) 2914.

[2] T.Shiokawa, M. Muraguchi and K. shiraishi, Jpn. J. Appl. Phys. 58 (2019) 112002.

Temperature dependence of liquid ethanol based on semi-classical Kramers-Heisenberg formulation

Ryosuke YAMAMURA, Kento AKIHIRO, Nozomu FUTAMATA, and Osamu TAKAHASHI

Basic Chemistry Program, Graduate School of Advanced Science and Engineering, Hiroshima University, Higashihiroshima, Hiroshima 739-8526, Japan

The hydrogen bonding in the condensed phase plays a important role in the understanding related liquid such as water and liquid alcohols. We have studied temperature dependence of liquid ethanol using X-ray emission spectroscopy (XES) theoretically and experimentally. The approach of combining theoretical and experimental methods is important for obtaining the hydrogen bonding information. The experimental XES ware carried out using the BL07SU HORNET station at SPring-8.

In theoretical method, combining molecular dynamics simulations (MD) and density functional theory (DFT) calculations performed. To construct structure of ethanol in liquid phase classical MD are adopted in the NVT ensemble at 240 K and 340K and 1 bar using GROMACS 5.1.4 with OPLS force field. To calculate the XES spectra, the DFT calculation performed using deMon2K program package. The detail of DFT calculation method are following the previous studied for methanol [1] and ethanol [2]. In short, the 17 ethanol cluster obtained from final snapshot of MD simulations are extracted randomly. The number of snapshots are 100 for each temperature. XES spectra can be calculated by applying semi-classical Kramers-Heisenberg (SCKH) formulation to the electronic state of each snapshots. Fig A shows the XES spectra based on SCKH. The calculated spectra well correspond to the experimental spectra. Now, we analyze the MD snapshots and investigate the relationship between XES spectra and hydrogen bonding.

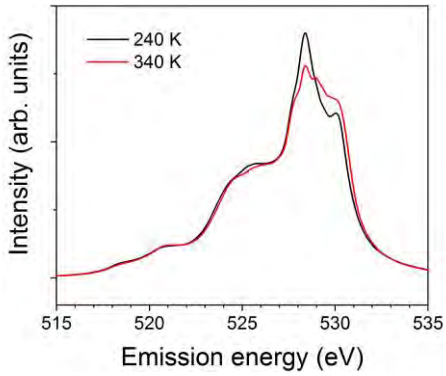

Fig A: XES spectra based on SCKH at 240K and 340K

References

[1] M. P. Ljungberget, et al.: J. Chem. Phys. **146** (2017) 134596

[2] O. Takahashi, et al.: J. Chem. Phys. B **49** (2017) 11163

Development of analysis method for molecular crystal surface using wave number space-resolved photoelectron spectroscopy

Kaori Niki

Graduate school of science

Chiba University, Yayoi-cho, Inage-ku, Chiba 263-0022

By using wave number space photoelectron spectroscopy, it has become possible to obtain a photoelectron momentum maps (PMMS) of a molecular thin film in a short time. This allowed us to obtain tomography of the wavefunction. It is suggested that more information can be obtained by analyzing PMMS in detail. We have been analyzing the surface of molecular crystals with the aim of establishing a method for analyzing momentum maps based on the multiple scattering method. For the initial state, we refer to the electronic state of the adsorption system calculated by Vienna Ab initio Simulation Packge (VASP) [1,2]. So far, we have suggested that by PMMS, it may be possible to identify the adsorption position of molecules adsorbed on the substrate surface [3].

In 2020, we expanded the sample to a more complex system. We placed VASP on the Supercomputer of Institute for Solid State Physics and performed two calculations.

1. Structural optimization and multiple scattering calculation of PTCDA / Ag (111).

The initial position of 3,4,9,10-Perylenetetracarboxylic dianhydride (PTCDA) was set to the Short-bridge site on Ag (111), and structural optimization was performed. Since PTCDA does not contain transition elements, the calculation cost is low. Periodic DFT calculations were carried out with VASP code using the projector augmented wave (PAW) method with a plane wave energy cutoff of 400 [eV] and the PBE exchange-correlation functional. The criterion convergence chosen for the SCF cycle was 10^{-8} eV, and optimization were considered converged once the forces on all atoms were lower than 10^{-8} [eV/Å] The slab was 12.1 x 12.1 [Å] large, and 10 [Å] thick (60 Ag atoms, 2PTCDA per unit cell) with a vacuum separation 20 [Å]. The three lowest layers were frozen during optimizations. The Brillouin zone was sampled with a 4x4x1 k-point grid. Electron occupancies were determined according to a Methfessel-Paxton scheme (order1) with an energy smearing of 0.2[eV].

As a result of structural optimization, PTCDA was curved in an arc with respect to the surface. PMMS calculations (using our computer) were performed using these coordinates. The PMMS has changed significantly compared to the results without the substrate. When I did the same calculation on multiple sites, I found that PMMS was different for each site. This indicates the possibility of obtaining information on the adsorption position from PMMS.

2. Structure optimization and multiple scattering calculation of CuPc and $TiSe_2$

In order to calculate the PMMS of Copper (Ⅱ) phthalocyanine (CuPc) / $TiSe_2$, the structure of CuPc and $TiSe_2$ was optimized. First, we performed structural optimization of CuPc. CuPc has a large number of constituent atoms and contains transition elements with spin. The calculation cost is high and the calculation method is complicated. Highest Occupied Molecular Orbital (HOMO) -1 was not calculated in the correct position when Generalized Gradient Approximation (GGA) was used as a functional. It has been reported that HOMO -1 can be calculated correctly using the hybrid functional according to Heyd et al. (HSE), but the calculation cost is high [4]. We also tried this, but couldn't succeed.

Next, the structure of TiSe2 was optimized. TiSe2 takes the CDW layer at low temperature and undergoes a phase transition to the normal phase at around 200 K [5]. To obtain information about the relationship between σ and temperature during smearing, we calculated the temperature dependence of the charge density wave (CDW) structure and the normal phase. Structural optimization was performed for two layers of TiSe2. The calculation conditions are the same as those described above. The normal layer extended the (1x1) structure to (2x2). For the CDW layer, the coordinates were entered based on the paper [5].

Figure 1 shows the temperature dependence of energy. The horizontal axis is temperature, and the longitudinal axis is energy, white triangles are the CDW layer, and black squares are the normal phase. From this calculation, it was found that 200K at which the phase transition occurs is approximately σ = 0.3. This calculation provided us with a guideline to use σ = 0.1 for low temperature calculations and σ = 0.4 for room temperature calculations in future.

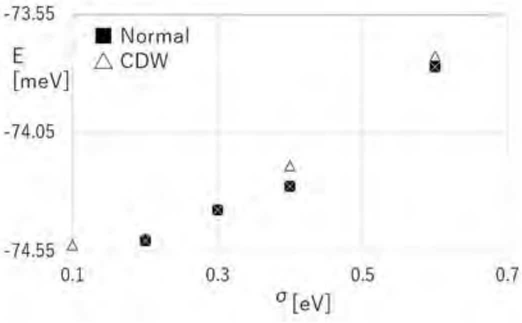

Figure 1. Energy dependence of sigma

Using these calculation results obtained, we plan to calculate the structural optimization and electronic state of the adsorption system in 2021.

References

[1] G. Kresse, and J. Furthmuller: Phys. Rev. B, **54**, (1996) 11169.

[2]G. Kresse, and J. Hafner: Phys. Rev. B, **49** (1994) 14251.

[3] K. Niki. M. Nozaki, S. Kurihara, and N. Komiya: Vac. Surf. Sci. Jpn. **63** (2020) 336.

[4] K. Sch¨onauer *et. al.*: Phys. Rev. Lett. **94** (2016) 205144.

[5] F.J. Di Salvo, D.E. Moncton, and J.V. Waszczak: Phys. Rev. B: **14** (1976) 4321.

Analysis of local quantities of electron field in material surface

Masahiro FUKUDA
Institute for Solid State Physics, University of Tokyo
Kashiwa-no-ha, Kashiwa, Chiba 277-8581

The local physical quantities, which is defined in the framework of quantum field theory (energy-momentum tensor density, current density, chiral current density, and so on), are significant to understand physical or chemical properties of surface materials, since it is not easy to be explained by bulk feature in solids such as a band structure.

In the previous work, we developed a program code which enables us to calculate local physical quantities as a post-process calculation from OpenMX [1] (DFT calculation program code) in order to evaluate the local physical quantities in large periodic systems. To proceed the discussion on a relation between the chemical bonding and the local electronic stress, recent research revealed the importance of evaluation of local physical quantities in a certain energy range. Therefore, in this project, we developed a program code which enables us to calculate local physical quantities in a specified energy range or orbitals.

The physical and chemical nature around the interaction region between atoms in Ag(FCC) were investigated as a demonstration. In Fig. 1 (a), the positive stress (tensile stress) and the eigenvectors form the spindle structure [2], which visualize a covalent bonding state. On the other hands, in Fig. 1 (b), the negative stress (compress stress) and the eigenvectors form the anti-spindle structure [2], which visualize an anti-bonding state. Moreover, the distribution of the isotropic negative stress as shown in Fig. 1 (d) reveals the "liquid" character of bulk metallicity. These characterizations will help us to understand chemical bond formation between a material surface and a molecular cluster deeply.

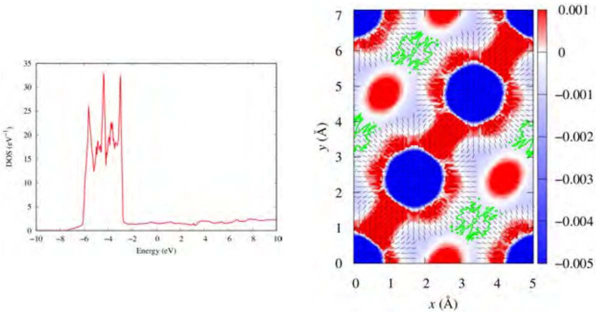

(a) DOS (b) $-5\text{eV} < E < -4\text{eV}$

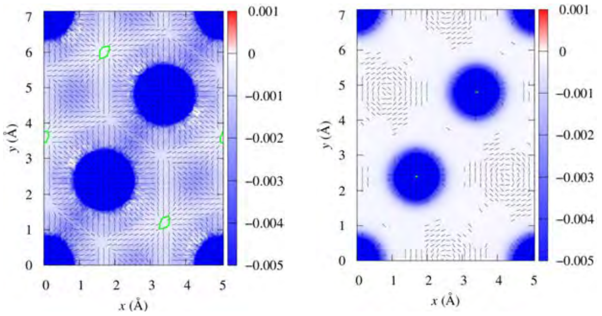

(c) $-4\text{eV} < E < -3\text{eV}$ (d) $-1\text{eV} < E < 1\text{eV}$

Figure 1: (a) Density of state, (b)-(d) distributions of maximum eigenvalues and eigenvectors of the electronic stress tensor density of Ag(FCC).

References

[1] OpenMX, http://www.openmx-square.org/.

[2] A. Tachibana, "New Aspects of Quantum Electrodynamics", Springer (2017)

3.3 Strongly Correlated Quantum Systems

Machine learning and *ab initio* analyses of cuprate high-temperature superconductors

Masatoshi IMADA

Toyota Physical and Chemical Research Institute

41-1 Yokomichi, Nagakute, Aichi, 480-1192

and

Research Institute for Sicence and Engineering, Waseda University

3-4-1 Okubo, Shinjuku-ku, Tokyo, 169-8555

Understanding physics of high-T_c cuprate superconductors remains one of the challenges in physics. In this project, we have continued efforts to clarify physics and mechanism of high-temperature superconductivity, particularly for the copper oxides. This is a combined research activity of three different approaches:

(1) Parameter search of strongly correlated electron models by using high-accuracy solvers for quantum many-body lattice Hamiltonians

(2) Parameter-free *ab initio* studies of real materials by using multi-scale *ab initio* scheme for correlated electrons (MACE) [1]

(3) Data science approaches to expose hidden physical quantities and mechanisms by combining extended experimental data such as by angle resolved photoemission spectroscopy (ARPES), quasiparticle interference (QPI) by scanning tunnel microscope (STM) and resonant inelastic X-ray scattering (RIXS) with the help of applied mathematical and information science technology such as machine-learning tools.

In the first approach, we have continued to clarify physics of electron fractionalization and formation of topological states such as quantum spin liquids (QSL). It was achieved by using the variational Monte Carlo tools (mVMC) [2] combined with the restricted Boltzmann machine developed by us [3,4], tensor network [5,6] and the Lanczos diagonalization. In the J_1J_2 Heisenberg model defined on the 2D square lattice with the nearest neighbor exchange interaction (J_1) and the next nearest neighbor exchange (J_2), we have further firmly established the existence of the QSL in the region $0.49<J_2/J_1<0.54$ [7]. The analyses were elaborated by comparing the accuracy of our solver with other tools in the literature. The accuracy and reliability of our solver were shown to be the best among existing solvers both for the ground states and the excitations. The reliability and robustness of the analyses was confirmed by (i) the size insensitivity of the correlation-ratio crossing points to identify the QSL-antiferromagnetic transition and the QSL to valence-bond-solid transition (ii) the insensitivity about the choice of the initial variational parameters for the wavefunction (iii) better size extrapolation of the level crossing point to infer the ground state phase boundary from the level crossing points of the excitation spectra, where larger size calculation has been added to enhance the accuracy of the extrapolation.

We have also been investigating the quantum ground state of the S=1/2 Heisenberg antiferromagnet on the pyrochlore lattice [8]. After investigation of various trial wave functions, we find that the singlet ground state has a linear dispersion at vanishing momentum with a finite energy gap to triplet excitations. Furthermore, it has turned out that the ground state is fully degenerate for all the point group symmetry represented by the irreducible symmetry group, which implies an emergence of the unprecedented type of quantum spin liquid.

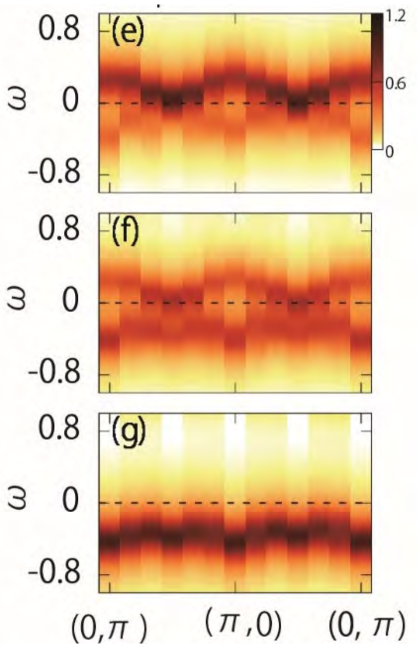

Fig.1: Spectral function along around symmetry line. (f) is closest to the symmetry line showing a large d-wave gap at (π,0) [10].

Accurate algorithms and tools for quantum dynamics were also sought for [9]. A method to calculate spectral functions measurable by the ARPES representing the imaginary part of the electron single-particle Green’s function was developed in addition to the two-particle dynamical structure factor for spin and charge [10]. The application to the Hubbard model revealed the d-wave gap structure for the first time in the superconducting state as shown in Fig.1. It has shown an unrealistically large gap of the typical Hubbard model implying an oversimplified nature of the Hubbard model as a model of the cuprate superconductors.

For the *ab initio* approaches (2), we have reproduced the experimental phase diagram of $HgBa_2CuO_{4+y}$ [11] by solving its *ab initio* low-energy effective Hamiltonian without adjustable parameters [12]. Thanks to this success, in the present project in 2020, more thorough and systematic analyses for several different copper oxide compounds have started. Derivation of *ab initio* low-energy effective Hamiltonians for the series of multi-layer compounds including Bi and solving with refined mVMC tool is under way.

The third data science approach (3) has been elaborated for the machine learning analysis of the ARPES data. The comparison with the literature has clarified the reliability of our analyses, which shows the emergence of prominent peak structures in the normal and anomalous parts of the self-energies and their cancellation in the Green's function resulting in the direct invisibility in ARPES, while the prominent peak is the origin of the high temperature superconductivity [13]. The accuracy and reliability of the present machine learning method were confirmed by several benchmark tests, which successfully reproduced the expected exact results and the established analyses in the literature. It further established the robustness against unavoidable experimental noise and extrinsic contributions to spectral functions such as background effects. The origin of the failure of previous studies which did not find the prominent structure in the self-energies are exposed by faithfully following the assumptions by the previous studies and by showing the error contained in the assumptions.

More thorough studies of the integrated spectroscopy analysis have been conducted in the combination of ARPES, and QPI or RIXS. By using the ARPES data and their machine learning analyses, a two-component fermion model is constructed to represent the fractionalization of electrons supported by the previous theoretical and experimental studies. Then the two-component Hamiltonian was analyzed to predict the RIXS data [14]. The prediction shows a substantial enhancement of the RIXS intensity in the superconducting phase in comparison to the normal phase, if the electron fractionalization correctly describes the low energy dynamics of the cuprate superconductors. Since such an enhancement does not occur in the absence of the fractionalization, it can be used as the stringent test for the occurrence of the fractionalization.

This is a combined report for E project 2020-Ea-0005 and 2020-Eb-0005 as well as shared project for Fugaku project.

This series of work has been done in collaboration with T. Misawa, M. Hirayama, K. Ido, Y. Nomura, Y. Yamaji, R. Pohle, M. Charlebois, J-B. Moree, F. Imoto, A. Fujimori and T. Yoshida. The work is also supported by JSPS Kakenhi 16H06345, the RIKEN Center for Computational Science under the HPCI project (hp200132) This project has used the software HPhi, mVMC and RESPACK.

References

[1] M. Imada and T. Miyake: J. Phys. Soc. Jpn. **79** (2010) 112001

[2] T. Misawa *et al.*: Comput. Phys. Commun. **235** (2019) 447

[3] Y. Nomura *et al.*: Phys. Rev. B.96 (2017) 205152

[4] G. Carleo *et al.*: Nat. Commun. 9 (2018) 5322

[5] H.-H. Zhao *et al.*: Phys. Rev. B.96 (2017) 085103

[6] A. S. Darmawan *et al.*: Phys. Rev. B 98 (2018) 205132.

[7] Y. Nomura and M. Imada: arXiv:2005.14142.

[8] R. Pohle, Y. Yamaji and M. Imada: unpublished.

[9] M. Charlebois and M. Imada: Phys. Rev. X 10 (2020) 041023.

[10] K. Ido, M. Imada and T, Misawa: Phys. Rev. B 101 (2020) 075124

[11] T. Ohgoe *et al.*, Phys. Rev. B **101** (2020) 045124.

[12] M. Hirayama *et al.*: Phys. Rev. B **99** (2019) 245155.

[13] Y. Yamaji et al.: arXiv:1903.08060

[14] M. Imada, arXiv:2103.10016.

Numerical studies of quantum spin liquids by quantum mutual information

Youhei YAMAJI
GREEN, National Institute for Materials Science
Namiki, Tsukuba-shi, Ibaraki, 305-0044

Recent studies on quantum spin liquids (QSLs) revealed that a wide variety of the QSLs is characterized by emergent fractionalized excitations and their topological nature, instead of an absence of spontaneous symmetry breaking at zero temperature. Entanglement entropy has been proposed to distinguish topologically trivial and non-trivial states. Although the entanglement entropy is hard to measure in experiments, it is applicable to any many-body states.

Instead of the entanglement entropy, mutual information (MI), a generalization of entanglement entropy, is useful at finite temperatures, where temperature scales characterizing the fractionalization may emerge. The MI is given as relative entropy between the density matrix and a product of reduced density matrices of a given system: When the system is devided into two subsystems, X and Y, the MI I is given as $I = \mathrm{tr}\left[\hat{\rho}\left\{\ln\hat{\rho} - \ln(\hat{\rho}^X \otimes \hat{\rho}^Y)\right\}\right]$, where $\hat{\rho}$ is the density matrix and $\hat{\rho}^X$ ($\hat{\rho}^Y$) is the reduced density matrix for the subsystem X (Y) by taking a partial trace over the complementary subsystem Y (X).

Naively, the computational and memory costs for I are higher than those for obtaining an eigenstate. However, typical state approaches enable us to estimate I with $\mathcal{O}(N_{\rm H})$ computational and memory costs, where $N_{\rm H}$ is the Hilbert space dimension of the target system, although the density matrix consisting of a typical pure state shows unphysical properties, as follows. When one define the density matrix with a canonical thermal pure quantum (cTPQ) state [1, 2] as, $\hat{\rho}_{\rm pure} = |\Phi(\beta)\rangle\langle\Phi(\beta)|/\langle\Phi(\beta)|\Phi(\beta)\rangle$, where $|\Phi(\beta)\rangle = e^{-\beta\hat{H}/2}|\Phi(0)\rangle$ and $|\Phi(0)\rangle$ is a normalized random vector. As emphasized in the literature, $\hat{\rho}_{\rm pure}$ is different from $\hat{\rho}$: any integer power of $\hat{\rho}_{\rm pure}$ is equal to $\hat{\rho}$ as $\mathbb{E}[\hat{\rho}^m_{\rm pure}] = \hat{\rho}$, where $\mathbb{E}$ is the average over distribution of the random vector $|\Phi(0)\rangle$ and $Z(\beta) = \sum_n e^{-\beta E_n}$. In contrast, the reduced ensity matrix constructed from $\hat{\rho}_{\rm pure}$ for the subsystem X (Y), $\hat{\rho}^X_{\rm pure}$ ($\hat{\rho}^Y_{\rm pure}$), satsfies $\hat{\rho}^{X/Y} = \mathbb{E}[\hat{\rho}^{X/Y}_{\rm pure}]$.

Because $\hat{\rho}^{X/Y}_{\rm pure}$ and $\hat{\rho}\ln\hat{\rho} = -S(\beta)$, where $S(\beta)$ is entropy at inverse temperatures β, are calculated by the cTPQ with $\mathcal{O}(N_{\rm H})$ computational and memory costs, $\hat{\rho}\ln(\hat{\rho}^X \otimes \hat{\rho}^Y)$ can be calculated with the similar costs. Here, we note that $\hat{\rho}$ appears only once in $\hat{\rho}\ln(\hat{\rho}^X \otimes \hat{\rho}^Y)$. The MI of an *ab initio* hamiltonian for $\mathrm{Na_2IrO_3}$ has been simulated and the temperature dependence will be published. The reduced density matrices are also useful to clarify the nature of correlated electrons such as high-temperature superconductivity [3].

References

[1] S.Lloyd: arXiv:1307.0378; Ph.D. Thesis, Rockefeller University (1988)

[2] S. Sugiura and A. Shimizu: Phys. Rev. Lett. **111** (2012) 010401.

[3] A. Iwano: master's thesis, The University of Tokyo (2020).

Numerical studies of quantum spin liquid candidates by highly accurate ab initio effective hamiltonians

Youhei YAMAJI
GREEN, National Institute for Materials Science
Namiki, Tsukuba-shi, Ibaraki, 305-0044

A Kitaev's spin liquid candidate, α-RuCl$_3$, has attracted considerable attention. Although several studies on the effective hamiltonian of α-RuCl$_3$, there is no consensus on the effective hamiltonian and no effective hamiltonian consistently explains experimentally observed specific heat and inelastic neutron scatterings. While these effective hamiltonians significantly deviate from the Kitaev model, the ruthenium halide shows experimental signatures of Majorana excitations. To refine the effective hamiltonian of the ruthenium halide and to clarify whether the ruthenium halide is in the vicinity of the Kitaev model or not, we theoretically study the series of the ruthenium halides, α-RuH_3 (H=Cl, Br, I).

Recent developments of deriving *abinitio* effective hamiltonians by using localized Wannier orbitals and constrained random phase or GW approximations [1, 2] enables us to study spin-orbit coupled Mott insulators and correlated (semi)metals. Regardless of the details of these methods, as the ionic radius of the halogen atom increases from Cl to I, the correlations in the ruthenium halides become weaker. The detailed analyses on the effective *abinitio* spin hamiltonians and itinerant electron hamiltonians are performed by using $\mathcal{H}\Phi$ [3] and mVMC [4]. The spin hamiltonian seems to be invalid for H =I and, at least, $t_{2\mathrm{g}}$ hamiltonians are required to describe the end member of the ruthenium halides.

To characterize the excitation spectra of correlated electrons, we have also developed numerical procedures to simulate *abinitio* spectral functions for the many-body Schrödinger equation, instead of the effective lattice hamiltonians, by combining variational Monte Carlo methods and Krylov subspace methods [5]. To examine the applicability of the present algorithm, it is applied to the single particle spectral functions of liquid helium 3. The self-energy is derived, which explicitly demonstrate the strongly correlated nature of liquid helium 3 in an *abinitio* fashion.

References

[1] M. Charlebois, J.-B. Morée, K. Nakamura, Y. Nomura, T. Tadano, Y. Yoshimoto, Y. Yamaji, T. Hasegawa, K. Matsuhira, M. Imada: arXiv:2103.09539.

[2] J.-B. Morée, S. Biermann, Y. Yamaji, and M. Imada: unpublished.

[3] M. Kawamura, K. Yoshimi, T. Misawa, Y. Yamaji, S. Todo, and N. Kawashima: Compt. Phys. Communi. **217** (2017) 180.

[4] T. Misawa, S. Morita, K. Yoshimi, M. Kawamura, Y. Motoyama, K. Ido, T. Ohgoe, M. Imada, and T. Kato: Compt. Phys. Communi. **235** (2019) 447.

[5] N. Okada: *Dynamical Variational Monte Carlo Approaches for Excitation Spectra of Many-Body Fermions in Continuum Space*, master's thesis, The University of Tokyo (2020).

Systematic analysis of ab initio low-energy effective Hamiltonians for Pd(dmit)$_2$ molecular conductors

Takahiro Misawa
Institute for Solid State Physics, University of Tokyo
Kashiwa-no-ha, Kashiwa, Chiba 277-8581

Quantum spin liquids, which do not show any symmetry breaking even at zero temperature, have attracted much interest since their elementary excitations in the quantum spin liquids are expected to show exotic elementary excitations such as Majorana particles. Because the exotic elementary excitations may be useful for next-generation devices such as quantum computers, a huge amount of works on searching and identifying the quantum spin liquids in solids has been done in a decade.

Among several candidates of the quantum spin liquids, the molecular solids β'-X[Pd(dmit)$_2$]$_2$ (X represents a cation) offers an ideal platform for realizing the quantum spin liquid induced by the geometrical frustration in the magnetic interactions because the geometrical frustration can be systematically controlled by changing cations X. In experiments, it has been proposed that the Neel temperatures are systematically controlled by changing cations X and the quantum spin liquid realizes in X =EtMe$_3$Sb [1, 2].

In this project, to identify the microscopic origin of the quantum spin liquid found in X =EtMe$_3$Sb, we have performed systematic and comprehensive *ab initio* derivations of low-energy effective Hamiltonians for available 9 compounds of β'-X[Pd(dmit)$_2$]$_2$ (X = Me$_4Y$, EtMe$_3Y$, Et$_2$Me$_2Y$ and , Y = As, Sb, and P) [3]. In the derivation the low-energy effective Hamiltonians, we first obtain the global band structure for dmit-salts using Quantum ESPRESSO [4]. Then, using the open-source software package RESPACK [5, 6], we evaluate the transfer integrals and two-body interactions such as the Coulomb interactions. As a result, we have found that the anisotropy of the transfer integrals and correlations effects systematically change by changing cations.

Moreover, we have analyzed the low-energy effective Hamiltonians using the exact diagonalization method [7, 8]. From the numerical exact analyzes of the low-energy effective Hamiltonians, we have shown the significant reduction of the antiferromagnetic ordered moment occurs around X =EtMe$_3$Sb. This reduction is consistent with the experimentally observed quantum spin liquid behavior in X=EtMe$_3$Sb. We have also shown that the reduction is induced by both the geometrical frustration in the hopping integrals and off-site Coulomb interactions. This result indicates that accurate evaluation of the microscopic parameters in the Hamiltonians is essential for reproducing the quantum spin liquid behavior in the dmit-salts.

In addition to the *ab initio* study for the dmit-salts, we have also analyzed the long-range spin transport in the topological Dirac semimetals [9] using the real-time evolution of the quantum systems. Furthermore, using $\mathcal{H}\Phi$ [7, 8], we have analyzed the magnetization process of the antiferromagnetic Heisenberg model on the kagome lattice [10]. We have also developed an open-source library for the shifted Krylov subspace method (Kω) [11] and an *Ab initio* tool for derivation of effective low-energy model for solids (RESPACK) [5, 6].

References

[1] R. Kato, Chem. Rev. **104**, 5319 (2004).

[2] K. Kanoda, R. Kato, Annu. Rev. Condens. Matter Phys. **2**, 167 (2011).

[3] T. Misawa, K. Yoshimi, T. Tsumuraya, Phys. Rev. Research **2**, 032072 (2020).

[4] P. Giannozzi, O. Andreussi, T. Brumme, O. Bunau, M. B. Nardelli, M. Calandra, R. Car, C. Cavazzoni, D. Ceresoli, M. Cococcioni, et al., Journal of Physics: Condensed Matter **29**, 465901 (2017).

[5] `https://sites.google.com/view/kazuma7k6r`

[6] K. Nakamura, Y. Yoshimoto, Y. Nomura, T. Tadano, M. Kawamura, T. Kosugi, K. Yoshimi, T. Misawa, Y. Motoyama, Computer Physics Communications **261**, 107781 (2021).

[7] M. Kawamura, K. Yoshimi, T. Misawa, Y. Yamaji, S. Todo, N. Kawashima, Comput. Phys. Commun. **217**, 180 (2017).

[8] `https://www.pasums.issp.u-tokyo.ac.jp/HPhi/en/`

[9] Y. Araki, T. Misawa, K. Nomura, arXiv:2103.06519.

[10] T. Misawa, Y. Motoyama, Y. Yamaji, Phys. Rev. B **102**, 094419 (2020).

[11] T. Hoshi, M. Kawamura, K. Yoshimi, Y. Motoyama, T. Misawa, Y. Yamaji, S. Todo, N. Kawashima, T. Sogabe, Computer Physics Communications **258**, 107536 (2021).

Study of phase formation, transport phenomena and effects of exceptional points in strongly correlated quantum systems

Norio KAWAKAMI

Department of Physics,

Kyoto University, Kitashirakawa, Sakyo-ku, Kyoto 606-8502

We have studied phase formation and transport phenomena in strongly correlated quantum systems. Especially, we have focused on phenomena such as the formation of magnetic phases and the effect of exceptional points when the non-Hermitian aspect of quasiparticle bands with finite lifetimes becomes essential.

(1) Open quantum systems

We have discussed the circumstances and requirements for the emergence of non-Hermitian phenomena in equilibrium single-particle properties of strongly correlated systems and their relationship to non-Hermitian phenomena in open quantum systems (OQS) experiencing gain and loss. While the necessity of postselection has limited the practicality of studying non-Hermitian phenomena in the OQS, in closed equilibrium systems, the single-particle Green's function is described by an effective non-Hermitian Hamiltonian without the need of postselection. By describing quasiparticles of strongly correlated systems as an OQS, we demonstrated that the non-Hermitian Hamiltonian arising in OQS and Green’s functions are equivalent. We have also demonstrated the necessity of considering the memory effect in the quantum master equation by comparing the spectral function in the Hubbard model computed by an OQS and equilibrium approaches.[1]

(2) Non-Hermitian phenomena

Quasiparticles described by Green's functions of equilibrium systems exhibit non-Hermitian topological phenomena because of their finite lifetime. This non-Hermitian perspective on equilibrium systems provides new insights into correlated systems. We provided a concise review of the non-Hermitian topological band structures for quantum many-body systems in equilibrium as well as their classification.[2]

Non-Hermitian phenomena offer a novel approach to analyze and interpret spectra in the presence of interactions. Using the density-matrix renormalization group (DMRG), we demonstrated the existence of exceptional points for the one-particle Green's function of the 1D alternating Hubbard chain with chiral symmetry, with a corresponding Fermi arc at zero frequency in the spectrum. They are robust and can be topologically characterized by the zeroth Chern number. This effect illustrates a case where the temperature has a strong impact in 1D beyond the simple broadening of spectral features. Furthermore, we demonstrated that exceptional points appear even in the two-particle Green's function (charge structure factor), where an effective Hamiltonian is difficult to establish.[3]

(3) Two-dimensional materials

The magnetic properties of black phosphorene nanoribbons have been investigated using static and dynamical mean-field theory. Besides confirming the existence of ferromagnetic/antiferromagnetic edge magnetism, our detailed calculations using large unit-cells find a phase transition at weak interaction strength to a novel incommensurate magnetic phase. Furthermore, we demonstrated that the difference of the ground state energies of the AFM and FM phase is exponentially small, making it possible to switch between both states by a small external field.[4]

We investigated the spin-dependent thermoelectric effect of graphene flakes with magnetic edges in the ballistic regime. Employing static and dynamical mean-field theory, we first showed that magnetism appears at the zigzag edges for a window of Coulomb interactions that increases significantly with increasing flake size. We then used the Landauer formalism in the framework of the non-equilibrium Green's function method to calculate the spin and charge currents in magnetic hexagonal graphene flakes by varying the temperature of the junction for different flake sizes. While in non-magnetic gated graphene, the temperature gradient drives a charge current, we observe a significant spin current for hexagonal graphene flakes with magnetic zigzag edges. Specifically, we showed that in the "meta" configuration of a hexagonal flake subject to weak Coulomb interactions, a pure spin current can be driven just by a temperature gradient in a temperature range that is promising for device applications.[5]

(4) Many-body localization

Strong disorder in low-dimensional strongly correlated systems has been discussed to induce many-body localization, which is the localization of all many-body eigenstates of the Hamiltonian. However, it has been an open issue to precisely determine the critical strength of disorder at the localization phase transition in one or higher spatial dimensions. We have considered the Fock-space localization of many-body wavefunctions in an all-to-all interacting model of fermions and demonstrated a quantitative agreement of the numerically obtained moments of eigenstate wavefunctions as well as the spectral statistics to analytical predictions.[6]

References

[1] Y. Michishita, and R. Peters, Phys. Rev. Lett. **124**, 196401 (2020).

[2] T. Yoshida, R. Peters, N. Kawakami, and Y. Hatsugai, Prog. Theor. Exp. Phys. 12A109 (2020).

[3] R. Rausch, R. Peters, and T. Yoshida, New J. Phys. **23**, 013001 (2021).

[4] J. Vahedi and R. Peters, Phys. Rev. B **103**, 075108 (2021).

[5] T. T. Phung, R. Peters, A. Honecker, G. T. de Laissardiere, and J. Vahedi, Phys. Rev. B **102**, 035160 (2020).

[6] F. Monteiro, T. Micklitz, M. Tezuka, and A. Altland, Phys. Rev. Research **3**, 013023 (2021).

Theoretical study of correlated electron systems with strong spin-orbit coupling

Yukitoshi MOTOME
Department of Applied Physics,
The University of Tokyo, Bunkyo, Tokyo 113-8656

We have theoretically studied a variety of intriguing phenomena in correlated electron systems with spin-orbit coupling, ranging from Mott insulators to metals. During the last fiscal year, we have achieved substantial progress on the following topics (project numbers: 2020-Ca-0059 and 2020-Cb-0038). We summarize the main results below.

(i) *Topological spin crystals*: We clarified that interplay between spin, charge, and orbital degrees of freedom plays a crucial role in stabilizing the magnetic hedgehog crystals recently found in *B*20 chiral magnets [1]. We also showed that the spin-charge interplay gives rise to a square-lattice type skyrmion crystals [2]. Based on the results, we made a collaboration with the experimental group to clarify the importance of the spin-charge coupling in $GdRu_2Si_2$ hosting the square skyrmion crystal [3,4]. We also studied the effect of anisotropy in a triangular lattice system [5]. In addition, we investigated the effects of the spatial anisotropy [6], the phase shift [7], and the twist angle [8] on the topological spin crystals. We wrote a review paper on the itinerant frustration which is a relevant mechanism to understand recent new generation of the topological spin crystals [9].

(ii) *Kitaev quantum spin liquids*: By using the quantum Monte Carlo simulation in the Majorana fermion representation, we investigated the effect of randomness on the Kitaev model for the thermodynamics and thermal transport [10] and the spin dynamics [11]. We also studied the finite-temperature phase transitions in a variety of three-dimensional extensions of the Kitaev model [12]. In addition, by using *ab initio* based calculations, we performed a systematic study of Pr-based *f*-electron compounds as new Kitaev candidates [13]. Summarizing our recent studies of the physics of Kitaev spin liquids and the material design of the Kitaev magnets, we wrote two review papers [14,15].

(iii) *Spin-orbit physics not requiring the spin-orbit coupling*: We showed that κ-type organic antiferromagnets exhibit an anomalous Hall response because of an effective spin-orbit coupling generated by glide symmetry breaking by the antiferromagnetic order [16]. We also showed that a similar mechanism predicts a spin current generation in perovskites with the

C-type antiferromagnetic order [17].

(iii) *Multipole physics*: We proposed channel-selective non-Fermi liquid behavior in the two-channel Kondo lattice model under a magnetic field [18]. We also clarified optical Hall responses in spin-orbit coupled metals with magnetic cluster multipole orders [19].

(iv) *Collaboration with experimental groups*: In addition to [3,4], we made combined studies between our theory based on the *ab initio* calculations and experiment on topological materials [20,21].

References

[1] S. Okumura, S. Hayami, Y. Kato, and Y. Motome, Phys. Rev. B **101**, 144416 (2020).

[2] S. Hayami and Y. Motome, Phys. Rev. B **103**, 024439 (2021).

[3] Y. Yasui *et al.*, Nat. Commun. **11**, 5925 (2020).

[4] 東京大学大学院工学系研究科 プレスリリース, "電荷密度波で電子構造の「ねじれ」をスイッチする ―トポロジカル状態の高速制御に向けた新しい指針を開拓―".

[5] S. Hayami and Y. Motome, Phys. Rev. B **103**, 054422 (2021).

[6] K. Shimizu, S. Okumura, Y. Kato, and Y. Motome, Phys. Rev. B **103**, 054427 (2021).

[7] S. Hayami, T. Okubo, and Y. Motome, preprint (arXiv:2005.03168).

[8] K. Shimizu, S. Okumura, Y. Kato, and Y. Motome, preprint (arXiv:2009.14569).

[9] S. Hayami and Y. Motome, preprint (arXiv:2103.10647).

[10] J. Nasu and Y. Motome, Phys. Rev. B **102**, 054437 (2020).

[11] J. Nasu and Y. Motome, preprint (arXiv:2103.10549).

[12] T. Eschmann, P. A. Mishchenko, K. O'Brien, T. A. Bojesen, Y. Kato, M. Hermanns, Y. Motome, and S. Trebst, Phys. Rev. B **102**, 075125 (2020).

[13] S.-H. Jang, R. Sano, Y. Kato, and Y. Motome, Phys. Rev. Materials **4**, 104420 (2020).

[14] Y. Motome, R. Sano, S.-H. Jang, Y. Sugita, and Y. Kato, J. Phys: Condens. Matter **32**, 404001 (2020), [Special Issue on Quantum Spin Liquids].

[15] 求 幸年, 那須 譲治, 固体物理 **55**, 297 (2020).

[16] M. Naka, S. Hayami, H. Kusunose, Y. Yanagi, Y. Motome, and H. Seo, Phys. Rev. B **102**, 075112 (2020).

[17] M. Naka, Y. Motome, and H. Seo, Phys. Rev. B **103**, 125114 (2021).

[18] K. Inui and Y. Motome, Phys. Rev. B **102**, 155126 (2020).

[19] T. Sato, Y. Umimoto, Y. Sugita, Y. Kato, and Y. Motome, Phys. Rev. B **103**, 054416 (2021).

[20] N. Mitsuishi *et al.*, Nat. Commun. **11**, 2466 (2020) [selected as FOCUS].

[21] M. Onga *et al.*, Nano Letters **20**, 4625 (2020).

Study on newly discovered nickelate superconductivity

Yusuke NOMURA

RIKEN Center for Emergent Matter Science, 2-1 Hirosawa, Wako, 351-0198

The recent discovery of superconductivity in the doped nickelate $Nd_{0.8}Sr_{0.2}NiO_2$ has attracted much attention because the nickelates may serve as a cuprate analog superconductor [1]. Indeed, the electronic structure of the nickelate is similar to that of the cuprates in the sense that the strongly correlated x^2-y^2 orbital is present. However, as a crucial difference from the cuprates, which shows Mott insulating behavior, RNiO$_2$ (R=Nd, Pr) is not a Mott insulator due to the carrier doping from the rare-earth layer (self-doping) [2].

In the present study, we investigate the following fundamental questions: (A) Is it possible to design nickelates whose electronic structure is more similar to that of the cuprates? (B) Can we expect large magnetic exchange coupling J in the cuprate-analog nickelates?

For (A), using a concept of "block layers", we perform a systematic materials design of layered nickelates. Then, we find several dynamically stable cuprate-analog nickelates [3]. In such nickelates, the self-doping is absent, and hence the x^2-y^2 orbital becomes half-filled. Therefore, the correlation effect will induce Mott insulating behavior in such d^9 nickelates. Using the d^9 nickelates, we can perform a fair comparison between the nickelates (Mott-Hubbard-type material) and cuprates (charge-transfer-type material).

(B) Then, it is of great interest to investigate the strength of magnetic exchange coupling J in the d^9 nickelates. Note that a large value of J of about 130 meV is a characteristic feature of the cuprates. We study the J value in theoretically-designed $RbCa_2NiO_3$ and $A_2NiO_2Br_2$ (A: a cation with the valence of +2.5) (Fig. 1). We show that these nickelates have a sizeable magnetic exchange coupling as large as about 80-100 meV, which is not far smaller than that of the cuprates [4].

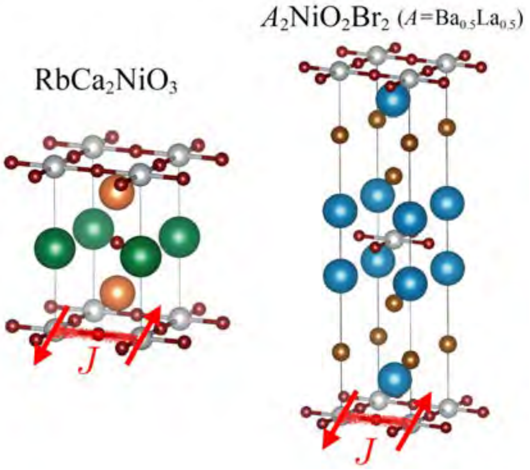

Fig. 1: Crystal structure of $RbCa_2NiO_3$ and $A_2NiO_2Br_2$ (A: a cation with the valence of +2.5).

References

[1] D. Li *et al*., Nature **572**, 624 (2019)

[2] Y. Nomura *et al*., Phys. Rev. B **100**, 205138 (2019) [Editor's suggestion]

[3] M. Hirayama and T. Tadano *et al*., Phys. Rev. B **101**, 075107 (2020)

[4] Y. Nomura *et al.*, Phys. Rev. Research **2**, 043144 (2020).

Studies on superconductivity in multiorbital systems with an incipient band and designing of new nickelate superconductors

KAZUHIKO KUROKI
Department of Physics, Osaka University
1-1 Machikaneyama, Toyonaka, Osaka, 560-0043, Japan

SUPERCONDUCTING MECHANISM OF A NEW CUPRATE SUPERCONDUCTOR $BA_2CUO_{3+\delta}$

Recently, Li et al.[1] reported high-T_c superconductivity in a new cuprate $Ba_2CuO_{3+\delta}$ with a K_2NiF_4-like layered structure. There, they find several unique features which strongly suggest that the material is a different type of cuprate superconductor that opens up a new paradigm. Namely, a large amount of oxygen vacancies are present within the CuO_2 planes, and a great amount of holes are doped which should cause a large deviation of the Cu valence from 2+. Also, the distance between Cu and the apical O is shorter than the in-plane Cu-O distance, so that the octahedron is compressed along the c axis. This should result in a crystal field very different from that of the ordinary cuprates, namely, the $3d_{3z^2-r^2}$ orbital lifted in energy above the $3d_{x^2-y^2}$ orbital. These findings suggest that the mechanism of superconductivity in the $Ba_2CuO_{3+\delta}$ may be considerably different from that for the conventional cuprates.

In 2020 fiscal year, we have studied possible superconducting mechanisms of $Ba_2CuO_{3+\delta}$[2]. In order to study the superconducting mechanism of the new superconductor, a realistic model Hamiltonian is required, which has to start with a determination of the crystal structure. For the 2-1-3 composition in particular, the chain structure is known to be stable in an actual material Sr_2CuO_3. As another possibility within the 2-1-3 composition, we considered a Lieb lattice type structure. First principles total-energy calculation performed with the VASP code shows that the chain and the Lieb lattice structures are close in the total energy, so that the latter may also be considered as a candidate.

Focusing on these two structures, we have calculated their band structures, and extracted the Wannier orbitals to construct multiorbital Hubbard models, i.e, a two-orbital model for the chain structure and a six-orbital model for the Lieb type structure. We have applied fluctuation exchange approximation to the effective models, and discuss the possibility of superconductivity by solving the linearized Eliashberg equation. We have shown that s-wave and d-wave pairings closely compete with each other and, more interestingly, that a coexistence of intra- and interorbital pairings arises. We also reveal an intriguing relation of the Lieb model with the two-orbital model for the usual K_2NiF_4-type cuprate where a close competition between s- and d-wave pairings is known to occur.

We have further shown that $s\pm$-wave superconductivity is strongly enhanced when the $d_{3z^2-r^2}$ band is raised in energy so that it become nearly incipient with the lower edge of the band close to the Fermi level within a realistic band filling regime. The enhanced superconductivity in the present model is in fact shown to be related to an enhancement found previously in the bilayer Hubbard model with an incipient band. Namely, we can show that, by orbital basis transformation[3], the two-orbital model can be transformed to the bilayer Hubbard model when all the intra and interorbital interactions have the same magnitude. In reality, the interactions are different in magnitude, but we find that the similarity between the two models holds to some extent. The strong enhancement of $s\pm$-wave superconductivity in the bilayer model with an incipient band has been shown by a number of previous studies, including our numerical study[4] based on multi-variable variational Monte Carlo method[5, 6].

DESIGNING NICKELATE SUPERCONDUCTORS

Inspired by the proposed superconducting mechanism for $Ba_2CuO_{3+\delta}$, in 2020 fiscal year, we have also theoretically designed unconventional nickelate superconductors with d^8 electron configuration[7]. Although the materials that we design apparently have nothing to do with bilayer systems at first glance, electronic structure of these materials resemble that of the bilayer Hubbard model, thereby strongly enhancing superconductivity. It is known that bilayer Hubbard model with appropriately large interlayer electron hopping exhibits $s\pm$-wave superconductivity with extremely high-T_c, but it is generally difficult to realize such a situation in actual bilayer-type materials due to various restrictions regarding the atomic orbitals. We have adopted a completely different strategy to realize the desired situation, by which we design a mixed-anion nickelates as candidates for new high-T_c superconductors.

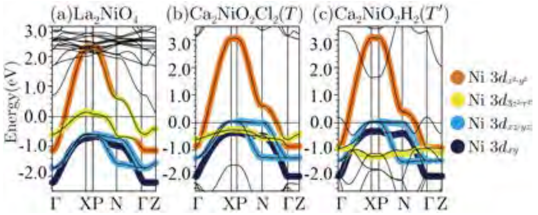

FIG. 1. Band structures of (a) La$_2$NiO$_4$, (b) Ca$_2$NiO$_2$Cl$_2$ and (c) (b) Ca$_2$NiO$_2$H$_2$ (taken from Ref.[7]).

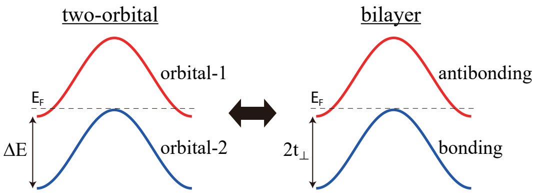

FIG. 2. Schematic figure of the correspondence between the two-orbital model and the bilayer model (taken from Ref.[7]).

More specifically, we have considered d^8 nickelates with K$_2$NiF$_4$ structure, where the apical oxygens are replaced by halogens or hydrogens. The lattice parameters are determined by structural optimization using VASP. The The band structures of two of the proposed candidates, Ca$_2$NiO$_2$Cl$_2$ and Ca$_2$NiO$_2$H$_2$, are shown in Fig.1 together with that of a reference material La$_2$NiO$_4$. The key point here is that the large crystal field splitting of the orbital energy levels, induced by replacing the apical oxygens by halogens or hydrogens, is approximately equivalent to large interlayer hopping in a bilayer system, as schematically depicted in Fig.2. Applying the fluctuation exchange approximation to the five orbital model of these materials, we have shown that the maximum superconducting transition temperature of some of them may be even higher than that of the high-T_c cuprates.

We have further found that our theory may also be related to another newly discovered superconductor (Nd,Sr)NiO$_2$[8]. In this superconductor, the nickel electron configuration is expected to be close to d^9, but this might be affected, e.g., by the reduction process during the synthesis of the material. Since the band structure of (Nd,Sr)NiO$_2$ itself, due to the absence of apical oxygens, resembles that of the proposed mixed anion-nickelates, (unintentional) reduction of the electron number in (Nd,Sr)NiO$_2$ may also result in a similar $s\pm$-wave superconductivity.

[1] W.M. Li *et al.*, Proc. Natl. Acad. Sci. USA **116**, 12156 (2019).
[2] K. Yamazaki *et al.* Phys. Rev. Res. **2**, 033356 (2020).
[3] H. Shinaoka *et al.*, Phys. Rev. B **92**, 195126 (2015).
[4] D. Kato and K. Kuroki, Phys. Rev. Res. **2**, 023156 (2020).
[5] D. Tahara and M. Imada, J. Phys. Soc. Jpn. **77**, 114701 (2008).
[6] T. Misawa *et al.*, Comp. Phys. Comm. **235**, 447 (2019).
[7] N. Kitamine, M. Ochi and K. Kuroki, Phys. Rev. Res. **2**, 042032(R).
[8] D. Li *et al.*, Nature (London) **572**, 624 (2019).

Bulk-edge correspondence for non-Hermitian topological systems

Tsuneya Yoshida
Department of Physics,
1-1-1 Tennodai, Tsukuba, Ibaraki, JAPAN 305-8571

In this year, we have studied topological phases in non-Hermitian systems [1-6]. In particular, by employing numerical diagonalization of a non-Hermitian matrix, we have elucidated the topological properties of non-Hermitian fractional quantum Hall state [1].

Specifically, we have analyzed a two-dimensional open quantum system with two-body loss. Such a system is described by Lindblad equation. Vectorizing the density matrix, we have mapped the Liouvillian to the Liouvillian matrix. Diagonalizing this matrix, we have analyzed topological properties. Our analysis elucidate that for a system with two-body loss, the Liouvillian gap remains open (see Fig. 1). In addition, introducing the pseudo-spin Chern number, we have elucidated that topology of non-Hermitian fractional quantum Hall states is maintained for this open quantum systems.

Our approach of the characterization can be also generalized to other cases of dimensions and symmetry, e.g., one dimensional open quantum systems with inversion symmetry.

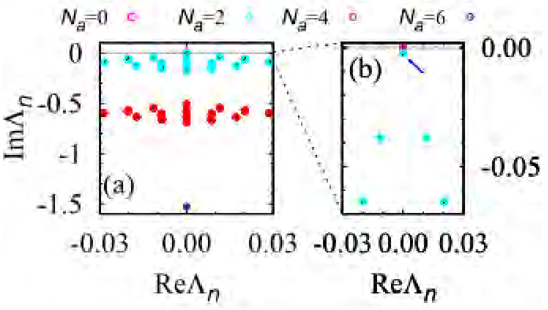

Fig.1 Spectrum of the Liouvillian matrix describing fractional non-Hermitian quantum Hall states.

We have also analyzed classical systems in term of topological band theory[7-9]. Our analysis have elucidated that topological phenomena are observed a variety of systems beyond quantum systems.

References

[1] T. Yoshida, K. Kudo, H. Katsura, and Y. Hatsugai, Phys. Rev. Research **2** 033428 (2020)

[2] T. Yoshida, Phys. Rev. B **103** 125145 (2021).

[3] H. Araki, T. Yoshida, and Y. Hatsugai, J. Phys. Soc. Jpn. **90** 053703 (2021).

[4] P. Delplace, T. Yoshida, Y. Hatsugai, arXiv: 2103.08232.

[5] R. Rausch, R. Peters, and T. Yoshida, New J. Phys. **23** 013011 (2021).

[6] T. Yoshida, T. Mizoguchi, and Y. Hatsugai Phys. Rev. Research **2** 022062 (2020).

[7] T. Yoshida, T. Mizoguchi, and Y. Hatsugai arXiv:2012.05562.

[8] T. Yoshida, T. Mizoguchi, Y. Kuno and Y. Hatsugai arXiv: 2103.11305

[9] T. Yoshida and Y. Hatsugai, Sci. Rep. **11** 888 (2021).

.

Numerical analyses on quantum spin liquids in strongly correlated electron systems

Kota IDO

Institute for Solid State Physics,

The University of Tokyo, Kashiwa-no-ha, Kashiwa, Chiba 277-8581

β '- Pd(dmit)$_2$ salts have attracted attention as candidate materials where a quantum spin liquid emerges [1]. This system consists of the dimers of two Pd(dmit)$_2$ molecules and cations. Since the dimers form an anisotropic triangular lattice, this system is considered as a two-dimensional correlated electron system with strong geometrical frustration. Although numerical studies play an important role in interpreting experimental results in the candidate materials for quantum spin liquids, it is difficult to accurately analyze large two-dimensional systems with strong frustration and many-body correlations.

In this study, to perform the ground state analysis on strongly correlated electron systems with geometrical frustration, we improved the accuracy of the trial wavefunction of the variational Monte Carlo (VMC) method. To achieve this goal, we proposed a two-component pairing wavefunction as the fermionic wavefunction. The difference from the conventional pairing wavefunction is that the strength of the pairing is dependent on the number of the local density. By using this wavefunction combined with recently developed neural network correlators [2, 3], we performed benchmarks for the *t*-*t*' Hubbard model on the square lattice and the triangular lattice with one-dimensional anisotropy. We find that the energy of quantum spin liquids using our proposed wavefunction is much lower than those using the conventional pairing wavefunction. In addition, we performed variance extrapolations of energies by using the power Lanczos method [4]. As the results, we succeed in reproducing the stability of the quantum spin liquid obtained by using the fixed-node method [5]. Our results suggest that this approach is a new efficient way to analyze the ground state in strongly correlated electron systems with the geometrical frustration and to clarify the nature of the spin liquids.

In addition, we have analyzed the ground states of an extended Kitaev model using the VMC method. It is a future issue to study not only the ground states but also nonequilibrium phenomena in quantum spin liquids.

References

[1] K. Kanoda, R. Kato, Annu. Rev. Condens. Matter Phys. **2**, 167 (2011).

[2] G. Carleo and M. Troyer, Science **355**, 602 (2017).

[3] Y. Nomura, A. S. Darmawan, Y. Yamaji, and M. Imada, Phys. Rev. B **96**, 205152 (2017).

[4] E. S. Heeb, T. M. Rice, Z. Phys. B **90**, 73 (1993).

[5] L. F. Tocchio, A. Parola, C. Gros, and F. Becca, Phys. Rev. B **80**, 064419 (2009).

Search for multiple-Q magnetic orders in systems with bond-dependent anisotropic interactions

Satoru Hayami
Department of Applied Physics, The University of Tokyo, Tokyo 113-8656

Noncoplanar spin textures have attracted considerable attention for potential applications to next-generation electronic and spintronic devices. In the project with numbers: 2020-Ca-0002 and 2020-Cb-0005, we have theoretically investigated a plethora of noncoplanar spin textures in correlated electron systems. We have presented the main results this year below.

(i) Magnetic hedgehog lattice: A magnetic hedgehog lattice (HL), which is characterized by a periodic array of magnetic monopoles and antimonopoles, is one of the noncoplanar multiple-Q states in the three-dimensional lattice system. The emergence of the HLs has been suggested in the noncentrosymmetric metal $\mathrm{MnSi}_{1-x}\mathrm{Ge}_x$ [1, 2] by experiments, but their microscopic origins have not been fully clarified owing to the unconventional short magnetic periods of the spin textures. We have investigated the stability of the HLs by analyzing an effective spin model derived from an itinerant electron model [3]. By using the variational calculations and simulated annealing, we obtained two types of HLs in the wide range of model parameters in the ground-state phase diagram. The results indicate the importance of the interplay between the Dzyaloshinskii-Moriya(DM)-type interaction by the spin-orbit coupling and the multiple-spin interactions by the spin-charge coupling.

(ii) Square skyrmion crystal: We have studied an instability toward a square skyrmion crystal (SkX), which consists of two helices with equal weight, in a centrosymmetric tetragonal lattice system [4]. We considered an effective spin model from an itinerant electron model on a square lattice. Reflecting the itinerant nature of electrons, the spin model exhibits the bilinear and biquadratic interactions in momentum space [5]. We also introduced fourfold-symmetric bond-dependent anisotropic and easy-axis anisotropic interactions to stabilize the multiple-Q states. By performing simulated annealing, we have shown that the square SkX appears by the synergy effect among the biquadratic, bond-dependent anisotropic, and easy-axis anisotropic interactions in an external magnetic field. We have also shown that the magnetic phase diagram obtained by simulated annealing well reproduces the experimental results for the SkX hosting material $\mathrm{GdRu_2Si_2}$ [6, 7].

In addition, we have investigated the vorticity and helicity of the square SkX in centrosymmetric itinerant magnets. Owing to the absence of the DM interaction in centrosymmetric magnets, the vorticity and helicity of the SkX are arbitrary. In other words, the Néel SkX, Bloch SkX, and two anti-SkXs are degenerate. In such a situation, we found that the anisotropic Ruderman-Kittel-Kasuya-Yosida (RKKY) interaction depending on the wave vectors lift the degeneracy of the SkXs with the different vorticity and helicity [8]. Our result opens a possibility of controlling the types of the SkXs through the electronic band structures.

(iii) Triangular skyrmion and meron crys-

tals: We have studied the SkXs and meron crystals in itinerant hexagonal magnets [9]. On the basis of the effective spin model with the bilinear and biquadratic interactions in momentum space [5], we examined the effect of two magnetic anisotropies on the stability of the multiple-Q states: The one is the local single-ion anisotropy and the other is the sixfold-symmetric bond-dependent anisotropy. In the case the single-ion anisotropy, we found that both the SkXs with the skyrmion number of one and two, which are denoted as the $n_{\rm sk} = 1$ SkX and $n_{\rm sk} = 2$ SkX, appear under the single-ion anisotropy, although their stability against the single-ion anisotropy is different with each other. For the $n_{\rm sk} = 2$ SkX, it is found that the stable region under the easy-axis anisotropy is wider than that for the easy-plane anisotropy at zero field. Meanwhile, the critical magnetic field to destabilize the $n_{\rm sk} = 2$ SkX is larger for the easy-plane anisotropy than that for the easy-axis anisotropy. For the $n_{\rm sk} = 1$ SkX, there is a drastic effect of the single-ion anisotropy on its stability; the $n_{\rm sk} = 1$ SkX is very weak (strong) against the easy-plane(-axis) anisotropy.

Under the bond-dependent anisotropy, we also obtained both the $n_{\rm sk} = 1$ and $n_{\rm sk} = 2$ SkXs in the wide range of model parameters. Notably, we found a variety of chiral magnetic states with nonzero scalar chirality, which is distinct from the SkXs. Especially, we obtained two types of the meron crystals: One is the $n_{\rm sk} = 1$ meron crystal, which consists of one meron-like and three antimerion-like spin textures in the magnetic unit cell and the other is the $n_{\rm sk} = 2$ meron crystal consisting of four meron-like spin textures in the magnetic unit cell.

The effective spin model in itinerant magnets will provide a deep understanding of the mechanism of the multiple-Q states, which have been recently observed in experiments, in an efficient way. Indeed, we reproduced the magnetic phase diagrams in $\mathrm{Gd_3Ru_4Al_{12}}$ [10] and $\mathrm{CeAuSb_2}$ [11], which host the multiple-Q states, by analyzing the extended effective spin model.

References

[1] T. Tanigaki *et al.*, Nano Lett. **15** (2015) 5438.

[2] Y. Fujishiro *et al.*, Nat. Commun. **10** (2019) 1059.

[3] S. Okumura, S. Hayami, Y. Kato, and Y. Motome, Phys. Rev. B **101** (2020) 144416.

[4] S. Hayami and Y. Motome, Phys. Rev. B **103** (2021) 024439.

[5] S. Hayami, R. Ozawa, and Y. Motome, Phys. Rev. B **95** (2017) 224424.

[6] N. D. Khanh *et al.*, Nat. Nanotech. **15** (2020) 444.

[7] Y. Yasui *et al.*, Nat. Commun. **11** (2020) 5925.

[8] S. Hayami and R. Yambe, J. Phys. Soc. Jpn. **89** (2020) 103702.

[9] S. Hayami and Y. Motome, Phys. Rev. B **103** (2021) 054422.

[10] M. Hirschberger, S. Hayami, and Y. Tokura, New J. Phys. **23** (2021) 023039.

[11] S. Seo *et al.*, Commun. Phys. **4** (2021) 58.

Time-Dependent DMRG Study of Spectral Shape in the Optical Conductivity of Two-Dimensional Hubbard Model

Takami TOHYAMA
Department of Applied Physics, Tokyo University of Science, Tokyo 125-8585

The parent compound of cuprate superconductors is a Mott insulator in two dimensions. The optical conductivity in the compound has been measured and its spectral features have been discussed experimentally. However, theoretical understanding of its spectral shape is still far from complete. This is due to theoretical difficulty caused by strong coupling of localized spins and holon/doublon created by photoexcitations. For example, it is unclear whether there is a magnetically induced excitonic peak at the absorption edge or not [1, 2].

In order to clarify spectral properties of the optical conductivity in two-dimensional Mott insulator, we use time-dependent density-matrix renormalization group (tDMRG) technique for a half-field Hubbard model with second-neighbor hopping (t-t'-U model) and calculate time-dependent current induced by electric field applied along the x direction, from which we can obtain the optical conductivity. In our tDMRG the time-evolution operator necessary for the calculation of time-dependent wave function is evaluated by using a kernel polynomial method [3], which is an approach good for lattices more than one dimension.

We use a 6×6 square lattice of the t-t'-U model with $U/t = 10$ under open boundary condition [4]. The number of states kept in tDMRG procedure is 4000. We note that we also use an 8×8 lattice to check size dependence for a t-U model and find that the difference of the optical conductivity in the two lattices is small. For the 6×6 lattice without t', the optical conductivity shows a prominent peak at the absorption edge followed by continuous spectral weight distribution above the peak position. The peak intensity depends on the value of t', exhibiting a maximum of the peak intensity at $t' = 0$ as a function of t'. Since t' introduces a diagonal antiferromagnetic exchange interaction, the effect of frustration competing with the nearest-neighbor exchange interaction appears. The frustration effect should not be dependent on the sign of t'. This is the case of the present result. We can say that magnetic interactions contribute to the peak at the absorption edge, indicating magnetic origin of the peak, i.e., magnetic exciton. However, we note that there is no gap between the peak and continuum mentioned above. This is different from a standard exciton where the exciton is defined as a bound state with well-defined binding energy.

References

[1] T. Tohyama, Y. Inoue, K. Tsutsui, and S. Maekawa: Phys. Rev. B **72** (2005) 045113.

[2] X.-J. Hana *et al.*: New J. Phys. **18** (2016) 103004.

[3] K. Shinjyo and T. Tohyama: Phys. Rev. B **103** (2021) 035141.

[4] K. Shinjyo, Y. Tamaki, S. Sota, and T. Tohyama, in preparation.

Development and application of DFT+DMFT software DCore

Hiroshi SHINAOKA
Department of Physics, Saitama University,
Saitama 338-8570

Dynamical mean-field theory (DMFT) has become a standard theoretical tool for studying strongly correlated electronic systems. In a DMFT calculation, an original lattice model is mapped to an effective Anderson impurity problem whose bath degrees of freedom are self-consistently determined. Although the DMFT was originally proposed for solving models such as Hubbard models, it can be combined with density functional theory (DFT) based on *ab initio* calculations for describing the electronic properties of strongly correlated materials. This composite framework, called DFT+DMFT, has been applied to various types of materials.

To make DFT+DMFT available to more users and to promote the development of a community of users and developers, we need an open-source program package with a user-friendly interface.

In this project, we have developed an open-source program, DCore v3.0.0 [1], that implements DMFT. This program features an interface based on text and HDF5 files, allowing DMFT calculations of tight-binding models to be performed on predefined lattices as well as first-principles models constructed by external DFT codes through the Wannier90 package. Furthermore, DCore provides interfaces to a variety of quantum impurity solvers such as quantum Monte Carlo codes developed in the ALPS projects. DCore is implemented on the top of the TRIQS Python library (Toolbox for Research on Interacting Quantum Systems). DCore v3.0.0 supports Python 3.x and TRIQS 3.0.

We used DCore to generate hybridization functions for a five-orbital 2 × 2 cluster impurity model for LaAsFeO [2]. The impurity model involves 40 spin orbitals. The hybridization functions computed by DCore are shown in Fig. 1. The hybridization functions have large off-diagonal elements and decay exponentially in the intermediate representation (IR) basis. We found that the exact hybridization functions with large off-diagonal elements can be fitted accurately with 332 bath sites using sparse modeling techniques.

This report is based on the collaboration with Y. Nagai, J. Otsuki, M. Kawamura, N. Takemori, K. Yoshimi.

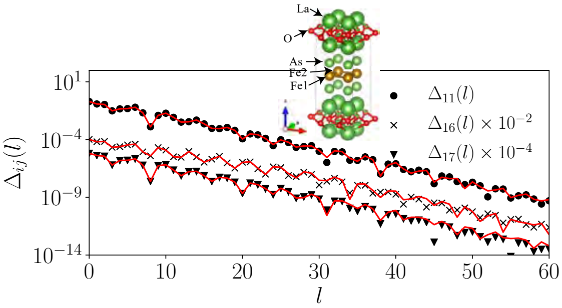

Figure 1: Illustration of the DMFT self-consistency cycle implemented in DCore

References

[1] H. Shinaoka, J. Otsuki, M. Kawamura, N. Takemori, K. Yoshimi, arXiv:2007.00901v3

[2] H. Shinaoka and Y. Nagai, PRB **103**, 045120 (2021)

Classical Monte Carlo study of J_1-J_2 Heisenberg antiferromagnet on the kagome lattice

Hiroshi SHINAOKA
Department of Physics, Saitama University,
Saitama 338-8570

Frustrated XY antiferromagnets have been investigated extensively in the past decades due to exotic phenomena induced by geometrical frustration. The classical nearest-neighbor XY antiferromagnet on the kagome lattice is a typical two-dimensional frustrated magnet. This model hosts a macroscopically degenerate ground-state manifold. Small perturbations such as thermal fluctuations lift the macroscopic degeneracy. This gives rise to various exotic phenomena. An interesting question is how next-nearest-neighbor interaction affects the competition of degenerated states at finite temperature.

In this project, we investigated the finite-temperature phase diagram of classical J_1-J_2 XY antiferromagnets on the kagome lattice through extensive Monte Carlo simulations [1, 2] using loop updates. We implemented the code in Julia, which is a modern programming language for scientific computing. The code is parallelized using MPI.jl.

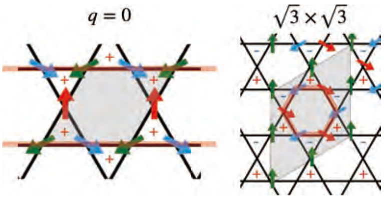

Figure 1: $q = 0$ and $\sqrt{3} \times \sqrt{3}$ spin configurations

We found that a weak antiferromagnetic J_2 induces an unconventional first-order transition at low temperatures. Furthermore, in the vicinity of the first-order transition, we find an octupole ordered phase between two competing quasi-long-range orders with different spin configurations (See Fig. 1). At antiferromatic $J_2 = -0.03$, the ground state is the $q = 0$ state. As shown in Fig. 2, there is a first-order transition between the high-temperature paramagnetic phase and the $q = 0$ quasi-long-range-ordered phase. At $J_2 = -0.005$, the Berezinskii-Kosterlitz-Thouless transition appears at a higher temperature. This report is based on the collaboration with F. Kakizawa and T. Misawa.

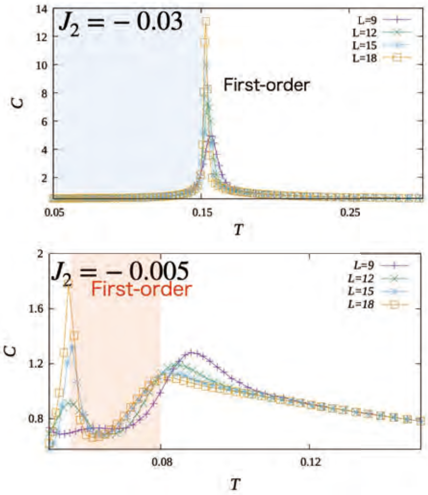

Figure 2: Temperature (T) dependence of the specific heat C computed for $J_2 = -0.03$ and $J_2 = -0.005$

References

[1] F. Kakizawa, T. Misawa, H. Shinaoka, APS March Meeting 2021, Y39.00012.

[2] 柿澤文哉, 三澤貴宏, 品岡寛, J_1–J_2古典反強磁性XYカゴメ模型における新奇相転移、日本物理学会第76回年次大会(2021年), 12pC1-8.

Research of Quantum Critical Points Emerging between Two-Channel Kondo and Fermi-Liquid States

Takashi HOTTA
Department of Physics, Tokyo Metropolitan University
1-1 Minami-Osawa, Hachioji, Tokyo 192-0397

In this research, we have investigated the emergence of quantum critical points (QCP) near a two-channel Kondo phase by evaluating an f-electron entropy of a seven-orbital impurity Anderson model hybridized with three (Γ_7 and Γ_8) conduction bands with the use of a numerical renormalization group (NRG) method.

First we consider the local f-electron Hamiltonian $H_{\rm loc}$. For the purpose, we introduce one f-electron state, which is defined by the eigenstate of spin-orbit and crystalline electric field (CEF) potential terms. Under the cubic CEF potential, we obtain Γ_7 doublet and Γ_8 quartet from $j=5/2$ sextet, whereas we find Γ_6 doublet, Γ_7 doublet, and Γ_8 quartet from $j=7/2$ octet. By using those one-electron states as bases, we describe $H_{\rm loc}$ as

$$\begin{aligned} H_{\rm loc} &= \sum_{j,\mu,\tau} (\lambda_j + B_{j,\mu} + E_f) f^{\dagger}_{j\mu\tau} f_{j\mu\tau} \\ &+ \sum_{j_1\sim j_4} \sum_{\mu_1\sim\mu_4} \sum_{\tau_1\sim\tau_4} I^{j_1 j_2, j_3 j_4}_{\mu_1\tau_1\mu_2\tau_2, \mu_3\tau_3\mu_4\tau_4} \\ &\times f^{\dagger}_{j_1\mu_1\tau_1} f^{\dagger}_{j_2\mu_2\tau_2} f_{j_3\mu_3\tau_3} f_{j_4\mu_4\tau_4}, \end{aligned} \quad (1)$$

where $f_{j\mu\tau}$ denotes the annihilation operator of a localized f electron in the bases of (j,μ,τ), j is the total angular momentum, $j=5/2$ and $7/2$ are denoted by "a" and "b", respectively, μ distinguishes the cubic irreducible representation, Γ_8 states are distinguished by $\mu=\alpha$ and β, while Γ_7 and Γ_6 states are labeled by $\mu=\gamma$ and δ, respectively, τ is the pseudo-spin which distinguishes the degeneracy concerning the time-reversal symmetry, and E_f is the f-electron level to control the local f-electron number at an impurity site.

As for the spin-orbit coupling term, we obtain $\lambda_a=-2\lambda$ and $\lambda_b=(3/2)\lambda$, where λ is the spin-orbit coupling of f electron. In this research, we set $\lambda=0.1$ and 0.11 for Pr and Nd ions, respectively. Concerning the CEF potential term for $j=5/2$, we obtain $B_{a,\alpha}=B_{a,\beta}=1320B_4^0/7$ and $B_{a,\gamma}=-2640B_4^0/7$, where B_4^0 denotes the fourth-order CEF parameter for the angular momentum $\ell=3$. Note that the sixth-order CEF potential term B_6^0 does not appear for $j=5/2$, since the maximum size of the change of the total angular momentum is less than six. On the other hand, for $j=7/2$, we obtain $B_{b,\alpha}=B_{b,\beta}=360B_4^0/7+2880B_6^0$, $B_{b,\gamma}=-3240B_4^0/7-2160B_6^0$, and $B_{b,\delta}=360B_4^0-3600B_6^0/7$. Note also that B_6^0 term appears in this case. In the present calculations, we treat B_4^0 and B_6^0 as parameters.

Now we consider the matrix element I of the Coulomb interaction. Here we skip the details of the derivation of I, but they are expressed with the use of four Slater-Condon parameters, F^0, F^2, F^4, and F^6. Although the Slater-Condon parameters of a material should be determined from experimental results, here we simply set the ratio as $F^0/10=F^2/5=F^4/3=F^6=U$, where U is the Hund's rule interaction among f orbitals. it is reasonable to set U as 1 eV in this research.

In Fig. 1, we show the local CEF ground-state phase diagram for $n=3$, obtained from

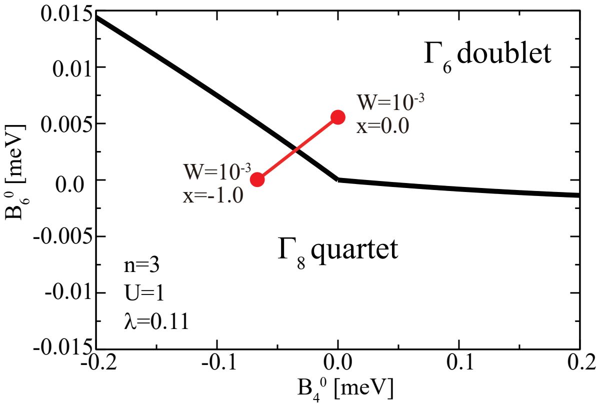

Figure 1: Local CEF ground-state phase diagram on the plane of (B_4^0, B_6^0) for $n = 3$. Red line denote the trajectory of $B_4^0 = Wx/15$ and $B_6^0 = W(1 - |x|)/180$ in the range of $-1 \leq x \leq 0$ for $W = 10^{-3}$.

the diagonalization of H_{loc}. For $n = 3$, the ground-state multiplet for $B_4^0 = B_6^0 = 0$ is characterized by total angular momentum $J = 9/2$. Under the cubic CEF potentials, the dectet of $J = 9/2$ is split into three groups as one Γ_6 doublet and two Γ_8 quartets.

Now we include the Γ_7 and Γ_8 conduction electron bands. Here we consider only the hybridization between conduction and $j = 5/2$ electrons. The Hamiltonian is given by

$$H = \sum_{\boldsymbol{k},\mu,\tau} \varepsilon_{\boldsymbol{k}} c^{\dagger}_{\boldsymbol{k}\mu\tau} c_{\boldsymbol{k}\mu\tau} + \sum_{\boldsymbol{k},\mu,\tau} V_{\mu}(c^{\dagger}_{\boldsymbol{k}\mu\tau} f_{a\gamma\tau} + \mathrm{h.c.}) + H_{\mathrm{loc}}, \tag{2}$$

where $\varepsilon_{\boldsymbol{k}}$ is the dispersion of conduction electron with wave vector $\boldsymbol{k}$, $c_{\boldsymbol{k}\gamma\tau}$ is an annihilation operator of conduction electrons, and V_μ denotes the hybridization between f electron in the μ orbital and conduction electron of the μ band. Here we set $V_\alpha = V_\beta = V_\gamma = V$.

In this research, we analyze this model by employing the NRG method [1]. We introduce a cut-off Λ for the logarithmic discretization of the conduction band. Due to the limitation of computer resources, we keep M low-energy states. Here we use $\Lambda = 8$ and $M = 5,000$. Note that the temperature T is defined as $T = D\Lambda^{-(N-1)/2}$ in the NRG calculation, where N is the number of the renormalization step and D is a half of conduction band width. Here we set $D = 1$ eV.

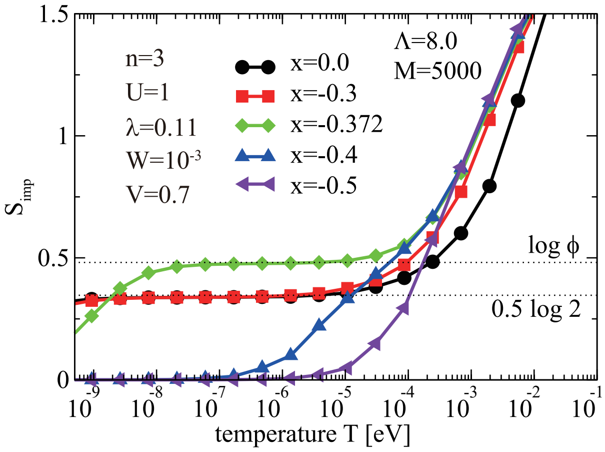

Figure 2: Entropies S_{imp} vs. temperature for $n = 3$ in the range of $-1 \leq x \leq 0$ with $W = 10^{-3}$. Note that ϕ is given by $\phi = (\sqrt{5} + 1)/2$.

Here we briefly discuss the typical results for $n = 3$ [2]. In Fig. 2, we show entropies S_{imp} vs. temperature, when we change the CEF parameters from $x = 0$ (Γ_6 doublet) to $x = -1$ (Γ_8 quartet) for $n = 3$, $W = 0.001$, and $V = 0.7$. For $x = 0$ and -0.3, we obtain the magnetic two-channel Kondo phase, while for $x = -0.4$ and -0.5, the screened Kondo phase appears, since the Γ_8 quartet effectively expressed by $S = 3/2$ spin is screened by three conduction electrons. At $x = -0.372$ between two-channel Kondo and Fermi-liquid phases, we find an entropy plateau of $\log \phi$. In this case, we could not observe the residual entropy of $\log \phi$ at low enough temperatures, but the signal of QCP is considered to be obtained.

References

[1] H. R. Krishna-murthy, J. W. Wilkins, and K. G. Wilson, Phys. Rev. B **21**, 1003 (1980).

[2] T. Hotta, J. Phys. Soc. Jpn. **89**, 114706 (2020).

Disorder effect on Kitaev quantum spin liquids

Joji Nasu
Department of Physics, Yokohama National University
Hodogaya, Yokohama 240-8501, Japan

Quantum spin liquid has been actively studied in strongly correlated electron systems. It is a state that does not show magnetic order down to the lowest temperature, which appears in insulating magnets and thought to appear owing to the cooperation of strong quantum fluctuations and many-body effects. Thus far, one considers geometrical frustration, which is essential to realize this state in the Heisenberg quantum spin model in the lattice structure. However, in this situation, one usually suffers from the negative sign problem in the quantum Monte Carlo method. Hence, the properties of quantum spin liquid have not been well understood theoretically.

On the other hand, attempts to realize quantum spin liquids other than the Heisenberg model have been made. Among them, the Kitaev model has recently attracted considerable attention because its ground state is a quantum spin liquid as an exact solution. Experimentally, many physical quantities such as specific heat, entropy, magnetic excitation, and thermal transport properties have been measured in ruthenium and iridium compounds, which are believed to be described by the Kitaev model, and have been compared with theoretical studies. In the real systems, effects of the disorder are inevitably present, which complicates extracting the nature of the Kitaev quantum spin liquid. Thus, calculations incorporating such effects are necessary to separate the properties intrinsic to Kitaev quantum spin liquids from others.

In this study, we perform numerical calculations for the Kitaev model with site dilution and bond randomness using quantum Monte Carlo simulations. The spin Hamiltonian is rewritten into the free Majorana fermion system coupled to Z_2 variables. The Majorana fermion system is diagonalized using the LAPACK library, and the configurations of the Z_2 variables are updated by the Markov chain Monte Carlo method. To avoid the freezing of the configurations, we employ the parallel tempering technique using the MPI library. Here, we calculate thermodynamic quantities such as the specific heat and thermal transport [1]. We find that the specific heat remains largely intact even in the presence of disorder at higher temperatures compared to the spin-exchange energy, while the low-temperature behavior is sensitive to the disorder. For thermal transport, the longitudinal component of the thermal conductivity is suppressed by the disorder. This behavior is common to site dilution and bond randomness. On the other hand, the thermal Hall conductivity is affected by these disorders differently. We find that the quantization of the thermal Hall conductivity is robust against the bond randomness but is fragile for the site dilution.

References

[1] J. Nasu and Y. Motome: Phys. Rev. B **102** (2020) 054437.

Effect of quenched disorder on a triangular lattice fermionic model

Chisa HOTTA

Department of Basic Science,

The University of Tokyo, Meguro-ku Komaba, Tokyo 153-8902

We studied the fermionic model on a triangular lattice with quenched disorder[1]. We are targeting the so-called tV model on a triangular lattice consisting of transfer integrals t and nearest neighbor Coulomb repulsions V, whose ground state is known to host a Pinball liquid phase [2,3] at large V/t, which is a state where part of the fermions localize on one of the three-sublattices, and form a symmetry breaking long range order. The rest of the fermions remain metallic and propagate along 2/3 of the lattice sites forming a honeycomb band. To be precise, the long range ordered fermions (pin) and metallic fermions(ball) are not fully separate, but exchange by the quantum fluctuation. In this study, we focus on the finite temperature properties of this phase, by adding a quenched disorder to the transfer integral.

However, it is quite difficult to fully solve the standard tV model at finite temperature in a reasonably large system size. Therefore, we introduce the Falikov-Kimball type of approximation and set the pins to be classical, while keep the balls to be quantum, and perform the Monte Carlo calculation. By changing the ratio of pin and ball and by moving the location of pins, and each timediagonalizing the ball-fermions under the interaction from pins, the system is safely thermalized to the pinball-liquid phase. We made full use of the ISSP supercomputing system to perform the calculation up to the system size of 24x24; the finite temperature phase transition is observed as a divergence in the specific heat. Also the low energy profile of the pinball liquid state is well reproduced. We also found that at extremely low temperature, the introduction of the quenched disorder will drive the system to some sort of a glassy phase, where there starts to appear a domain wall structure of pinball phase. This domain becomes distinct as the system size becomes larger and the degree of disorder is increased, which is detected in the broad structure of the Replica overlap distribution function.

References

[1] Keita Urakami and Chisa Hotta, in preparation.

[2] Chisa Hotta and Nobuo Furukawa , Phys. Rev. B **74**, (2006)193107.

[3] Chisa Hotta, Nobuo Furukawa, Akihiko Nakagawa, and Kenn Kubo , J. Phys. Soc. Jpn. **75**, (2006) 123704.

Ordered states in strongly correlated Dirac electron systems of organic conductors

Akito KOBAYASHI
Department of Physics, Nagoya University
Nagoya 464-8602

In the low temperature phase ($T < T_{\rm co} = 135K$) of the organic Dirac electron system α-(BEDT-TTF)$_2$I$_3$, it is believed that the electron correlation breaks the spatial inversion symmetry and transitions to a stripe charge ordered insulator. The electron correlation induces the reshaping of Dirac cones and the anomalous spin fluctuation. We investigated the electron correlation effects on the anomalous thermoelectric effects and the spin fluctuations[2, 4, 6]. In contrast, the element-substituted α-(BETS)$_2$I$_3$ shows insulating behavior at low temperatures below 50 K, but no crystal symmetry breaking or charge density change is observed in X-rays, and no sign of magnetic transition is obtained from NMR. In this study, we constructed an extended Hubbard model based on first-principles calculations and analyzed it using mean-field approximation. It was shown that a magnetic transition occurs due to a short-range Coulomb interaction as shown in Fig. 1[3]. However, since no magnetic transition was observed in the experiment, it is necessary to investigate other possibilities. In addition, we showed possible edge magnetism in Dirac nodal line systems of single component molecular conductors [1, 5].

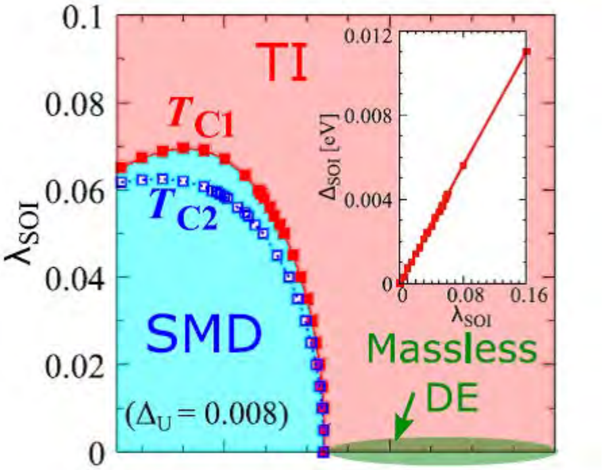

Figure 1: A candidate of ordered states in α-(BETS)$_2$I$_3$.

References

[1] T. Kawamura, B. Zhou, Akiko Kobayashi, Akito Kobayashi, accepted to J. Phys. Soc. Jpn. (2021/03/30)

[2] M. Hirata, A. Kobayashi, C. Berthier and K. Kanoda, Rep. Prog. Phys. **84** 036502 (2021)

[3] D. Ohki, K. Yoshimi, and A. Kobayashi, Phys. Rev. B **102**, 235116 (2020)

[4] D. Ohki, M. Hirata, T. Tani, Kazushi K., and A. Kobayashi, Phys. Rev. Research **2**, 033479 (2020)

[5] T. Kawamura, D. Ohki, B. Zhou, Akiko Kobayashi, Akito Kobayashi, J. Phys. Soc. Jpn. **89**, 074704 (2020)

[6] D. Ohki, Y. Omori, A. Kobayashi, Phys. Rev. B **101**, 245201 (2020)

Development of electronic structure calculation for solids with post-Hartree-Fock calculations

Kazutaka NISHIGUCHI
Department of Physics, Osaka University
Toyonaka, Osaka 560-0043, Japan

– Electronic structure calculation for solids with post-Hartree-Fock calculations –
Continuing from our preceding-term study, we have theoretically studied a new method of electronic structure calculation for solids with quantum chemistry calculations. Our proposed procedure is as follows. We first start with Hartree Fock (HF) calculation for solids and construct maximally localized Wannier functions as a localized basis set. Then we consider a real-space cluster in the Wannier representation and solve it numerically with equation-of-motion coupled cluster (EOM-CC) theory. Here we have used VASP (The Vienna Ab initio Simulation Package) [1, 2, 3, 4, 5] in the HF calculations, Wannier90 [6, 7, 8, 9] in the wannierization method, and GELLAN program [10] in the EOM-CC calculations.

We apply this method to typical semiconductors, namely, bulk Si and $SrTiO_3$, and evaluate these energy band gaps as a benchmark. Developing the preceding-term study, we use symmetry-adapted Wannier functions [9] in constructing the localized basis set with Wannier90. We then can observe that the localized basis set can be obtained stably and the band gap can be improved compared to that with the HF calculations. However, it is still insufficient because the number of the localized bases is not sufficient to take into account the electron correlations. To increase the number of the localized bases will be an interesting future work.

– Formation energy of n-type doping in $CaZn_2X_2$ (X = Sb, As, P) –
Continuing from our preceding-term study, we have numerically evaluated a formation energy of n-type doping in a strong candidate of high performance thermoelectric materials $CaZn_2X_2$ (X = Sb, As, P) by the first-principles calculations based on the density functional theory (DFT). We consider the chemical doping into the interstitial site and the element substitution of Ca, where the dopant is assumed to be the alkaline earth metals (Mg, Ca, Sr, Ba) and group 3 elements (Sc, Y, La). The ionization energy of these elements is relatively small as cations so that the smaller formation energy is expected. To take into account the chemical doping, the 3 × 3 × 2 supercell calculations are performed (Figure 1) with the Perdew Burke Ernzerhof (PBE) functional, namely, the generalized gradient approximation (GGA). Here we have used VASP [1, 2, 3, 4, 5] in the first-principles calculations.

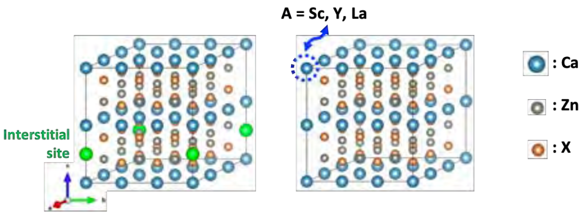

Figure 1: $3 \times 3 \times 2$ supercell of $CaZn_2X_2$ (X = Sb, As, P). (Left) Doping into the interstitial site. (Right) Element substitution of Ca.

For the interstitial doping one can observe in Figure 2 that the chemical doping of Ca and group 3 elements is favorable according to the formation energy. In addition, for the element substitution of Zn one can also see in Figure 3 that the element substitution for Sc is stable. This tendency of the formation energy is considered to depend on the ionization energy of these doping elements and the ionic radius against the interstitial site and Ca vacancy site. The improvement of the exchange correlation functional such as the hybrid functional and the inclusion of the finite-size supercell effect will be important future works.

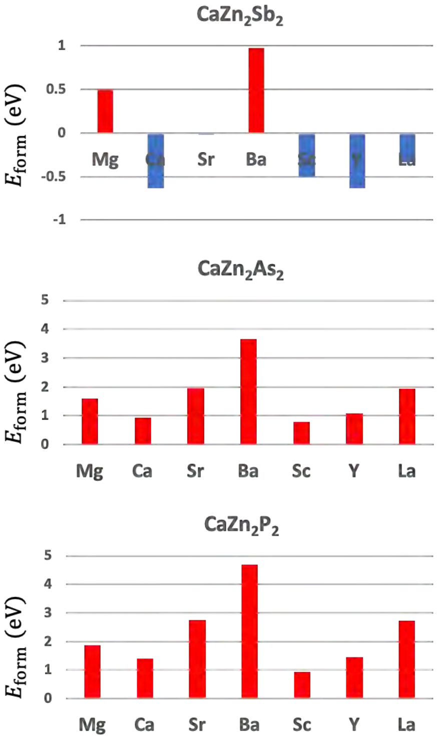

Figure 2: Formation energy of the doping into the interstitial site.

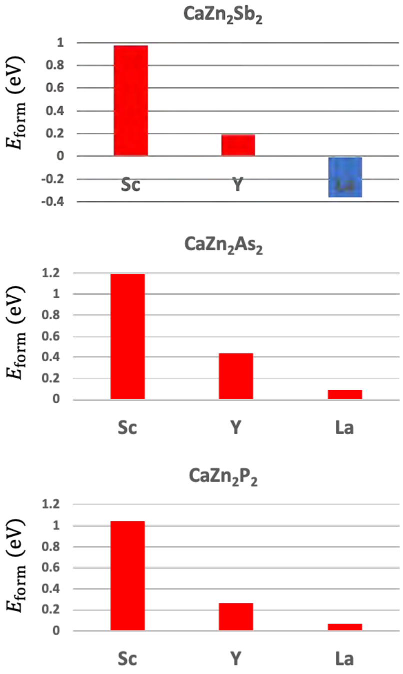

Figure 3: Formation energy of the element substitution of Ca.

References

[1] G. Kresse and J. Hafner, Phys. Rev. B **47** 558(R) (1993).

[2] G. Kresse and J. Hafner, Phys. Rev. B **49** 14251 (1994).

[3] G. Kresse and J. Furthmüller, Comput. Mater. Sci. **6** 15 (1996).

[4] G. Kresse and J. Furthmüller, Phys Rev. B **54** 11169 (1996).

[5] VASP (The Vienna Ab initio Simulation Package): https://www.vasp.at

[6] N. Marzani and D. Vanderbilt, Phys. Rev. B **56** 12847 (1997).

[7] I. Souza, N. Marzani, and D. Vanderbilt, Phys. Rev. B **65** 035109 (2001).

[8] Wannier90: http://www.wannier.org

[9] R. Sakuma, Phys. Rev. B **87** 235109 (2013).

[10] GELLAN: A hierarchical massively-parallel quantum chemistry program, Kobe University

Development of electronic structure calculation for solids with quantum chemistry calculations

Kazutaka NISHIGUCHI
Department of Physics, Osaka University
Toyonaka, Osaka 560-0043, Japan

– Electronic structure calculation for solids with quantum chemistry calculations –
A new method of electronic structure calculation for solids with quantum chemistry calculations have been studied theoretically. We first start with Hartree Fock (HF) calculation for solids and construct maximally localized Wannier functions as a localized basis set. Then we consider a real-space cluster in the Wannier representation and solve it numerically with equation-of-motion coupled cluster (EOM-CC) theory. Here we have used VASP (The Vienna Ab initio Simulation Package) [1, 2, 3, 4, 5] in the HF calculations, Wannier90 [6, 7, 8] in the wannierization method, and GELLAN program [9] in the EOM-CC calculations.

We apply this method to typical semiconductors, namely, bulk Si and $SrTiO_3$, and evaluate these energy band gaps as a benchmark. We can observe that the band gap can be improved compared to that with the HF calculations, but it is not sufficient because the localized basis set is difficult to converge stably. To achieve stable construction of the localized basis set will be an interesting future work.

– Formation energy of n-type doping in $CaZn_2Sb_2$ –
A formation energy of n-type doping in a strong candidate of high performance thermoelectric materials $CaZn_2Sb_2$ have been numerically evaluated by the first-principles calculations based on the density functional theory (DFT). We consider the chemical doping into the interstitial site and the element substitution of Zn, where the dopant is assumed to be the alkaline earth metals (Mg, Ca, Sr, Ba) and group 3 elements (Sc, Y, La). The ionization energy of these elements is relatively small as cations, so that the smaller formation energy is expected. To take into account the chemical doping, the $3 \times 3 \times 2$ supercell calculations are performed (Figure 1) with the Perdew Burke Ernzerhof (PBE) functional, namely, the generalized gradient approximation (GGA). Here we have used VASP [1, 2, 3, 4, 5] in the first-principles calculations.

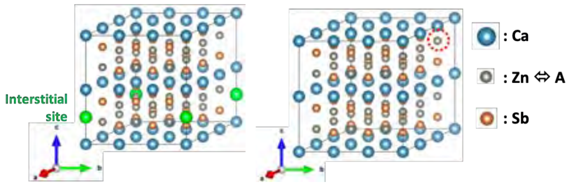

Figure 1: $3 \times 3 \times 2$ supercell of $CaZn_2Sb_2$. (Left) Doping into the interstitial site. (Right) Element substitution of Zn.

For the interstitial doping one can observe in Figure 2 that the chemical doping of Ca and group 3 elements is favorable according to the formation energy. In addition, for the element substitution of Zn one can also see in Figure 3 that the element substitution for Mg, Ca, Sr, and group 3 elements is stable. This tendency of the formation energy is considered to depend on the ionization energy of these doping elements and the ionic radius against the interstitial site and Zn vacancy site. On the other hand, the calculated formation energy is now understood to be qualitative because the PBE functional is not sufficient to evaluate the accurate energy band gap for semiconductors and the finite-size supercell effect is not included in these calculations, but the tendency of the formation energy is important for material synthesis of n-type semiconductors. The improvement of the exchange correlation functional such as the hybrid functional and the inclusion of the finite-size supercell effect will be important future works.

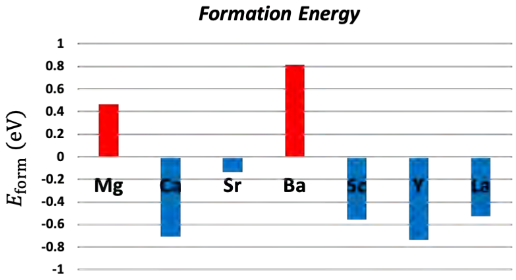

Figure 2: Formation energy of the doping into the interstitial site.

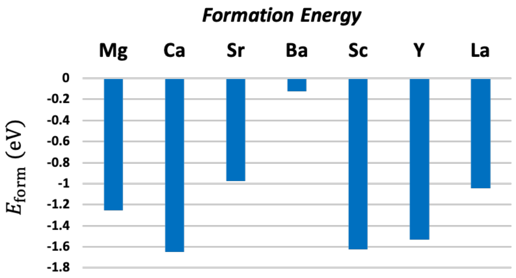

Figure 3: Formation energy of the element substitution of Zn.

References

[1] G. Kresse and J. Hafner, Phys. Rev. B **47** 558(R) (1993).

[2] G. Kresse and J. Hafner, Phys. Rev. B **49** 14251 (1994).

[3] G. Kresse and J. Furthmüller, Comput. Mater. Sci. **6** 15 (1996).

[4] G. Kresse and J. Furthmüller, Phys Rev. B **54** 11169 (1996).

[5] VASP (The Vienna Ab initio Simulation Package): https://www.vasp.at

[6] N. Marzani and D. Vanderbilt, Phys. Rev. B **56** 12847 (1997).

[7] I. Souza, N. Marzani, and D. Vanderbilt, Phys. Rev. B **65** 035109 (2001).

[8] Wannier90: http://www.wannier.org

[9] GELLAN: A hierarchical massively-parallel quantum chemistry program, Kobe University

Quantum Monte Carlo simulation and electronic state calculations in correlated electron systems

Takashi YANAGISAWA
Electronics and Photonics Research Institute
National Institute of Advanced Industrial Science and Technology (AIST)
AIST Central 2, 1-1-1 Umezono, Tsukuba 305-8568

We carried out numerical calculations on the basis of the optimized variational Monte Carlo method[1, 2, 3, 4]. We have investigated the ground-state phase diagram of the two-dimensional Hubbard model and the two-dimensional d-p model. We performed parallel computations by using a Monte Carlo algorithm. In order to reduce statistical errors, we carried out 200 $\sim$ 500 parallel calculations. Parallel computing is very necessary to reduce Monte Carlo statistical errors.

We employed the improved wave function of an $\exp(-\lambda K) - P_G$-type[1]. This wave function is a very good many-body wave function because the ground-state energy is lowered greatly and the ground-state energy is lower than those that are evaluated by any other wave functions[2]. We can improve the wave function systematically by multiplying by operators P_G and $e^{-\lambda K}$ several times.

We exhibit the condensation energy as a function of the doping rate x for the three-band d-p model in Fig. 1 where $U_d = 10t_{dp}$ and the level difference is taken as $\Delta_{dp} \equiv \epsilon_p - \epsilon_d = t_{dp}$[6]. There is the AF region when x is small and the SC region exists near the optimum region $x \sim 0.2$. We should mention that there is a phase-separated region in the low-doping region where $x < 0.07$. This indicates the existence of AF insulator phase in the low doping region. This is similar to the phase diagram of the 2D Hubbard model. The phase separation (PS) is, however, dependent on the level difference Δ_{dp}. As Δ_{dp} decreases, the phase-separated region decreases and vanishes when Δ_{dp} approaches zero. Thus the area of phase-separated region can be controlled by changing the band parameters.

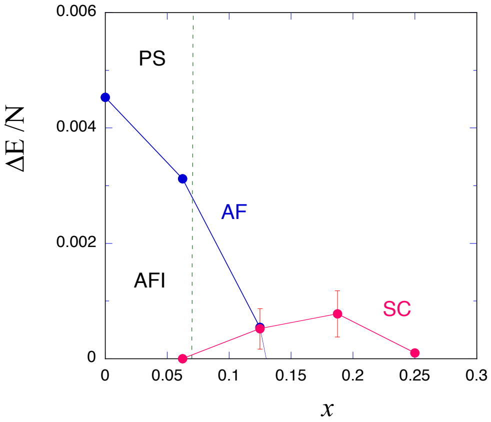

Figure 1: AF and SC condensation energies as a function of the hole doping rate x for $\Delta_{dp} = 1$ on a 8×8 lattice with $t_{pp} = 0.4$ and $U_d = 10$ in units of t_{dp}. There is a phase-separated region when x is small.

References

[1] T. Yanagisawa et al., J. Phys. Soc. Jpn. 67, 3867 (1998).

[2] T. Yanagisawa, J. Phys. Soc. Jpn. 85, 114707 (2016).

[3] T. Yanagisawa, J. Phys. Soc. Jpn. 88, 054702 (2019).

[4] T. Yanagisawa, Condensed Matter 4, 57 (2019).

[5] T. Yanagisawa, Phys. Lett. A403, 127382 (2021).

[6] T. Yanagisawa et al., EPL (2021).

Calculation of the electronic state in a large model of the organic charge ordering system using mVMC

Masatoshi SAKAI, Riku TAKEDA, Ryoma ISHII
Department of Electrical and Electronic Engineering,
Chiba University, 1-33 Yayoi-cho Inage, Chiba 263-8522

We have studied the electronic state of the large-size model of the organic charge order system by using the supercomputer. We made a base model of α-(BEDT-TTF)$_2$I$_3$ by citing reference [1] and carried out a 28 x 28 site calculation to reveal the electron number dependence of the charge order structure of the correlated electron system. The simulation software mainly used in this work was mVMC, as preinstalled in the ENAGA and OHTAKA supercomputer systems. The electron number dependence of the charge order structure is significant for us to support our experimental work. Our experimental work was the metal-insulator phase transition transistor which was observed in organic charge order material of α-(BEDT-TTF)$_2$I$_3$ near the metal-insulator phase transition at 137 K. We expect that the calculation of electron number dependence of charge order structure and energy will give a theoretical backbone to our experimental result. Our group made an effort to learn about supercomputer and mVMC, and now we are finally in routine calculation by varying electron number from 376 to 404 electrons in the system.

The other work in progress is about β-(BEDT-TTF)$_2$PF$_6$, of which metal-insulator phase transition is 297 K [2]. In this work, we could not find the physical parameters in previous works, so we began to calculate from the band structure before carrying out model calculation of correlated electronic system. We used Quantum Espresso and Respack to obtain physical parameters to build the calculation model used in mVMC or HPhi. We learned Quantum Espresso and Respack, and now we have just achieved the end of the calculation of the Respack. Therefore, we will verify the results and apply the next step by using mVMC or HPhi to reveal the physical principle of the phase transition field-effect transistor.

References

[1] Daigo Ohki, Genki Matsuno, Yukiko Omori and Akito Kobayashi: Crystals 8, (2018) 137.

[2] Hayao Kobayashi, Takehiko Mori, Reizo Kato, Akiko Kobayashi, Yukiyoshi Sasaki, Gunzi Saito and Hiroo Inokuchi: Chem. Lett. (1983) 581.

Study for high-T_c cuprates using four-band d-p model

Hiroshi WATANABE
Research Organization of Science and Technology, Ritsumeikan University
1-1-1 Noji-Higashi, Kusatsu-shi, Shiga 525-8577

The discovery of superconductivity in cuprates [1] has brought about the significant progress in strongly-correlated electron systems. However, we have not yet reached a unified understanding of their properties, including their material dependence of the superconducting transition temperature T_c. Recent development of theories and experiments sheds light on the importance of the orbital degree of freedom in cuprates [2, 3]. To elucidate the material dependence of T_c, we study the four-band d-p model for La_2CuO_4 and $HgBa_2CuO_4$ systems that properly includes the orbital degree of freedom. The ground state properties are studied with the variational Monte Carlo (VMC) method. The Gutzwiller-Jastrow type wave function is used for the VMC trial wave function. The system size for the calculation is N=24×24=576 unit cells (and thus 576×4=2304 orbitals in total), which is large enough to avoid finite size effects.

The superconducting correlation function P^{dd} vs hole doping rate δ for the La_2CuO_4 and $HgBa_2CuO_4$ systems are shown in Fig. 1. The dome-shaped behavior and the material dependence are consistent with experiments. We show that the Cu d_{z^2} orbital contribution around the Fermi energy is destructive for d-wave superconductivity, and thereby becomes a key factor to determine T_c. The energy difference Δ_{dp} between Cu $d_{x^2-y^2}$ and O p orbitals is also shown to be a key factor. Our result accounts for the empirical correlation between T_c and model parameters and gives the unified description beyond the usual one-band Hubbard, t-J, and even three-band d-p models.

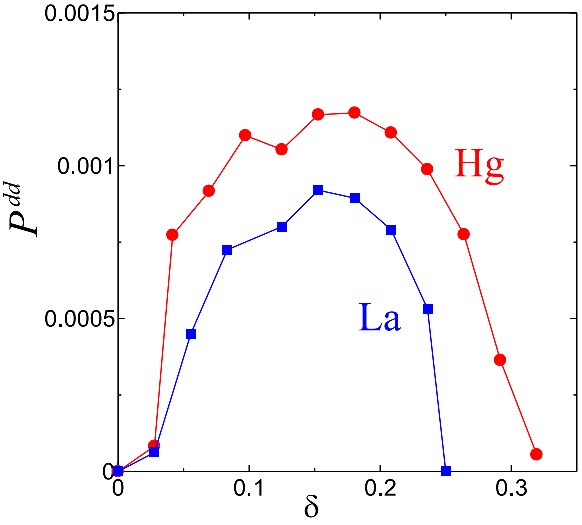

Figure 1: Superconducting correlation function P^{dd} vs hole doping rate δ for the La_2CuO_4 and $HgBa_2CuO_4$ systems.

References

[1] J. G. Bednorz and K. A. Muller, Z. Phys. B **64**, 189 (1986).

[2] H. Sakakibara et al., Phys. Rev. Lett. **105**, 057003 (2010).

[3] C. E. Matt et al., Nat. Commun. **9**, 972 (2018).

Studies of the superconductivity and magnetic states in the strongly correlated electron systems using Hubbard models.

Atsushi Yamada
Department of Physics, Chiba University
Chiba 263-8522, Japana, Chiba 277-8581

A spin liquid state has attracted a lot of interest. This state is realized in geometrically frustrated systems like the charge organic transfer salts κ-(BEDT-TTF)$_2$X[1] and Cs_2CuCl_4.[2] Hubbard model on the anisotropic triangular lattice is a simple theoretical model of these compounds, and spin liquid state is found in this model.[3] A spin liquid could arise also in the intermediate coupling region of strongly correlated systems between a semi-metal and ordered state, because in this case a correlation-driven insulating gap might open before the system becomes ordered. This possibility might be realized in the half-filled Hubbard model on the honeycomb lattice, where a semi-metal is realized at $U = 0$.

We have studied the magnetic and metal-to-insulator transitions by variational cluster approximation using 10-site and 16-site clusters as a reference system. Parts of numerical calculations were done using the computer facilities of the ISSP. We found that $U_{\rm AF} = 2.7$ and $U_{\rm MI} = 3.0$ for 10-site cluster, and $U_{\rm AF} = 2.7$ and $U_{\rm MI} = 3.2$ for 16-site cluster.[5] This result also rules out the existence of the spin liquid in this model. Our results agree with recent large scale Quantum Monte Carlo simulations.[4]

We are currently improving our program using MPI technique so that we will be able to study a larger cluster size system.

References

[1] Y. Shimizu, K. Miyagawa, K. Kanoda, M. Maesato, and G. Saito, Phys. Rev. Lett. **91**, 107001 (2003); Y. Kurosaki, Y. Shimizu, K. Miyagawa, K. Kanoda, and G. Saito, Phys. Rev. Lett. **95**, 177001 (2005).

[2] R. Coldea, D.A. Tennant, A.M. Tsvelik, and Z. Tylczynski, Phys. Rev. Lett. **86**, 1335 (2001); R. Coldea, D.A. Tennant, and Z. Tylczynski, Phys. Rev. Lett. **68**, 134424 (2003).

[3] T. Yoshioka, A. Koga, and N. Kawakami, Phys. Rev. Lett. **103**, 036401 (2009); P. Sahebsara and D. Sénéchal, Phys. Rev. Lett. **100**, 136402 (2008); L.F. Tocchio, H. Feldner, F. Becca, R. Valenti, and C. Gros, Phys. Rev. B **87**, 035143 (2013); A. Yamada, Phys. Rev. B **89**, 195108 (2014); L.F. Tocchio, C. Gros, R. Valentí, F. Becca, Phys. Rev. B **89**, 235107 (2014); A. Yamada, Phys. Rev. B **90**, 235138 (2014).

[4] S. Sorella, Y. Otsuka, and S. Yunoki, Sci. Rep. **2**, 992 (2012); F. F. Assaad and I. F. Herbut, Phys. Rev. X **3**, 031010 (2013); F. Parisen Toldin, M. Hohenadler, F. F. Assaad, and I. F. Herbut, Phys. Rev. B **91**, 165108 (2015).

[5] A. Yamada, Int. J. Mod. Phys. B **30**, 1650158 (2016).

3.4 Cooperative Phenomena in Complex Macroscopic Systems

Tensor-Network Renormalization-Group Study of Critical Phenomena

Naoki KAWASHIMA

Institute for Solid State Physics,

The University of Tokyo, Kashiwa-no-ha, Kashiwa, Chiba 277-8581

The objective of the project is to develop new methods for studying the critical phenomena, both classical and quantum, and apply them to strongly correlated systems. Especially, we aim at improving the real-space renormalization group (RSRG) method based on the tensor network representation with the hope for fuller understanding of the structure of the scaling dimensions of 2+1 or 3 dimensional fixed-point theories.

In [1], we proposed a method for obtaining an efficient low-rank approximation of a given tensor. This was motivated by the conventional RSRG methods such as the loop-TNR and entanglement filtering. In those methods, the crucial part is removal of redundancy in the tensor-network representation arising from loops. They can be regarded as a special form of low-rank approximation of a given tensor. It might then be useful also for more general class of tensors, e.g., the image data in the form of tensors. The proposed method successfully identified the redundant structure of the entanglement naturally formed in the process of the tensor renormalization group (TRG) calculation.

In [2], we studied the J-K-Γ model, a model that may represent some aspect of the compound α-$RuCl_3$, which is expected to be close to the Kitaev spin liquid and presents some features hinting a non-trivial topological structure of its state. We discovered that the chiral spin liquid phase proposed by a preceding study is realized in a narrower region than predicted. In addition, we discovered two more non-magnetic phases that our calculation suggested possesses also non-trivial topological structure.

In [3], we studied the spin-1 Kitaev model. This was motivated by the preceding work by Lee, Kaneko, Okubo and I on the conventional spin-1/2 case, in which we discovered relationship between the gapless Kitaev spin liquid and the classical loop gas model. In [3], in contrast to the S=1/2 case, we discovered the gapful spin liquid with Z_2 structure of the quasi-particles.

In [4], we improved the high-order tensor renormalization group (HOTRG), one of the conventional RSRG besed on the tensor-network representation. In the HOTRG, we bind two parallel bonds together to form one renormalized bond in much the same spirit as the Migdal-Kadanoff RG. In doing so, we need a projection operator for the rank reduction. In its simplest implementation of the HOTRG, only the local environment is taken into account in computing the projection operator, while it would obviously be better to optimize the projector in more global environment. Several methods for better optimization has been proposed at the cost of higher computational complexity. The method we proposed is based on the corner transfer-matrix technique and reduces the computational complexity without serious degrading of the accuracy.

In [5], we applied the method of variational uniform matrix-product-state (VUMPS), an MPS-based method for one-dimensional quantum systems to the 2-leg ladder system with four-body interaction, i.e., a one-dimensional analogue of the JQ model that shows a deconfined critical phenomena. While DMRG is known to be a very powerful numerical tool in investigating the one dimensional quantum systems, direct characterization of the quantum critical phenomena has been a tough problem even for DMRG. In our study, we successfully characterize various phases including symmetry protected topological phases by the 2nd cohomology group represented by the resulting fixed-point tensors. Critical behaviors between the phases are also accurately characterized.

References

[1] Hyun-Yong Lee, and Naoki Kawashima: J. Phys. Soc. Jpn. 89, 054003 (2020)

[2] Hyun-Yong Lee, Ryui Kaneko, Li Ern Chern, Tsuyoshi Okubo, Youhei Yamaji, Naoki Kawashima and Yong Baek Kim: Nature Communications 11, 1639 (2020).

[3] Hyun-Yong Lee, Naoki Kawashima and Yong Baek Kim: Phys. Rev. Res. 2, 033318 (2020).

[4] Satoshi Morita and Naoki Kawashima: Phys. Rev. B103, 045131（1-6）(2020)

[5] Takuhiro Ogino, Ryui Kaneko, Satoshi Morita, Shunsuke Furukawa and Naoki Kawashima: Phys. Rev. B 103, 085117 (2021).

Molecular Dynamics Simulations of Bio-Inspired Materials

Wataru Shinoda
Department of Materials Chemistry, Nagoya University
Nagoya 464-8603

We have studied the surface hydrophobicity of self-assembled monolayers (SAM) [1] using massive parallel computer simulations. The surface hydrophobicity was investigated for a range chemically functionalized (–CF_3, –CH_3, –OCH_3, –OH) SAMs as illustrated in Fig. 1. These SAMs have many industrial and biological applications such as for making well-defined non-fouling surfaces, cell supports, receptors, sensors, microarrays, separation devices, and for surface reactions [1, 2]. A good understanding of surface properties of these SAMs can allow us to further modify and control them for the specific uses.

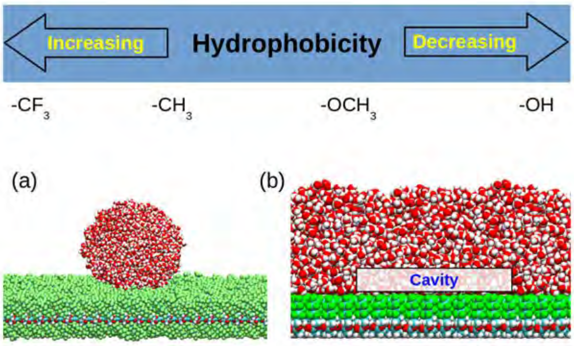

Figure 1: Surface hydrophobicity of chemically functionalized (–CF_3, –CH_3, –OCH_3, –OH) self-assembled monolayers. (a) Structure of a water droplet on the fluoroalkyl SAM surface (b) The formation of a cavity near the SAM-water interface.

The study was conducted with all-atom (AA) simulation model using the LAMMPS molecular dynamics (MD) simulation package [3]. The systems were modeled using the optimized potentials for liquid simulation (OPLS) force field [4]. SPC/E rigid-body water model was used for the water molecules [5]. A wide range of packing densities and chain lengths were considered in the study to understand their effects on the surface hydrophobicity. Analyses of the MD trajectories were done using the in-house codes. The complete details of the computational method can be found in Ref. [6, 7].

The surface hydrophobicity was investigated by means of (1) the structure, (2) the contact angle of a water droplet on the surface, and (3) the cavity formation free energy. In the structure, we mainly focused on density distribution, hydrogen-bonding, chain flexibility via root mean square displacement (RMSD), and roughness of the SAM surfaces. The free energy of cavity formation was calculated from indirect umbrella sampling methods [6, 7], in which used massive parallel computing resource. The results were found quite consistent with experiments. Through these studies, we demonstrated a systematic path to examine the hydrophobicity of such synthetic surfaces. For the hydrophobic surfaces such as for the fluorinated chains, it was found that the surface hydrophobicity is mainly governed by packing density rather than the chain length. It increases on reducing the packing density of SAMs. The SAM flexibility causes an enhancement in the surface hydrophobicity independent of chemical functional groups. These information would be certainly useful for the material design and modifying the surfaces.

Additionally, we developed a coarse-grained (CG) model for the semi-fluorocarbon diblocks and studied the hemimicelle formation of these chains at the air-water interface using ISSP supercomputer. These systems contain more than 100,000 particles even in the CG model. We showed a mechanism of micelle formation for these diblocks and successfully explained the non-coalescence behavior of micelles, which was a puzzle for the experimentalists [8]. It was found that an unique alternating P-phase forms in between the micelles, which has lateral and vertical dimensions of the nanoscale order (see Fig. 2). We believe that this P-phase could be reason for the non-coalescence behavior of micelles under strong compression.

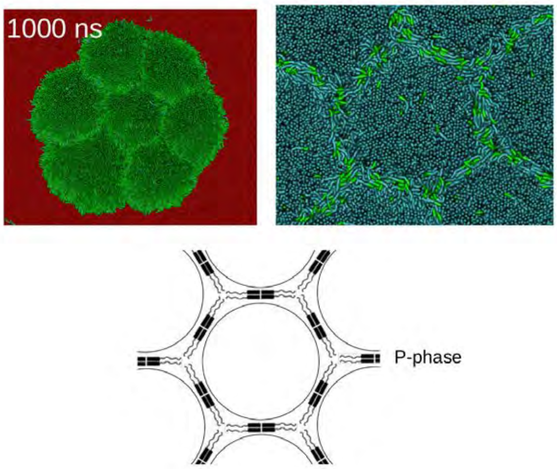

Figure 2: The hemimicelle formation of semi-fluorocarbons at the air-water interface and the structure of P-phase existing in between the hemimicelles.

More recently, we studied the amino acids and protein adsorption on the SAM surfaces (see Fig 3). We are in the process of summarizing results of these simulations for the publication. We found ISSP supercomputer really useful for conducting simulation of such large-scale complex systems. We are further looking to simulate protein adsorption on the polymers using a coarse-grained model to cover extensive time scale. In this study, we will also consider the adsorption of more larger systems such as virus capsids and organelles.

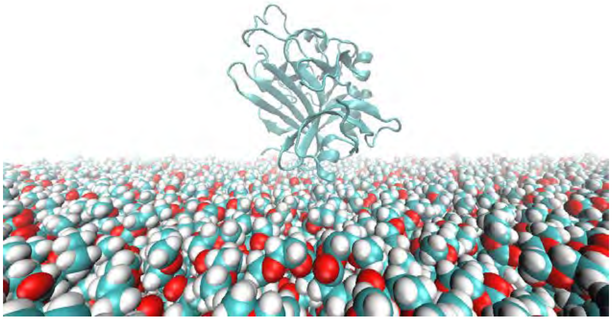

Figure 3: Adsorption of protein on synthetic SAM surfaces.

References

[1] J. C. Love, L. A. Estroff,J. K. Kriebel, R. G. Nuzzo, and G. M. Whitesides: *Chem. Rev.* 2005, **105** (2005) 1103.

[2] J. E. Raynor, J. R. Capadona, D. M. Collard, T. A. Petrie, and A. J. Garcia: *Biointerphases* **4** (2009) FA3.

[3] S. Plimpton: J. Comput. Phys. **117** (1995) 1-19.

[4] W. L. Jorgensen, D. S. Maxwell, and J. Tirado-Rives: *J. Am. Chem. Soc.* **118** (1996) 11225.

[5] H. J. C. Berendsen, J. R. Grigera, and T. P. Straatsma: *J. Phys. Chem. A.* **91** (1987) 6269.

[6] H. O. S. Yadav, A. -T. Kuo, S. Urata and W. Shinoda: *Langmuir* **35** (2019) 14316.

[7] H. O. S. Yadav, A. -T. Kuo, S. Urata and W. Shinoda: *J. Phys. Chem. C* **124** (2020) 14237.

[8] H. O. S. Yadav and S. Harada, A. -T. Kuo, S. Urata, and W. Shinoda: *Mol. Phys.* (2021) e1910355.

Construction of data assimilation in materials science

Munehisa MATSUMOTO
Institute of Materials Structure Science, High Energy Accelerator Research Organization
Oho 1-1, Tsukuba 305-0801

We have been developing methods to use both of experimental data and theoretical data to better characterize and predict good magnetic materials [1, 2]. Experimental data taken from actual materials and corresponding computational data constitute an integrated data model. The desired properties of materials are often well defined and it now looks as though it is getting more and more feasible to implement a scheme for rational materials design based on the integrated data among various experimental probes and *ab initio* materials data. However, during the course of our developments we are rather finding the relevance of stochastic aspects of the materials design.

The problem is caused by multiple requirements which are often simultaneously imposed on the target materials. For permanent magnets, a candidate compound should have strong magnetization, magnetic anisotropy, high Curie temperature, and sufficient structure stability. Unfortunately it is hardly the case that all of these can be maximized with a particular chemical composition. Trade-off's are encountered and we have to work with a good compromise. Besides, another problem is imposed by the multi-scale nature of materials. The material is put into practical use in a macroscopic world in non-equilibrium and at the moment it is hardly possible to keep all those extrinsic parameters under control in the modeling.

A starting point is to restrict the working parameter space and implement an optimization scheme therein referring to the given set of requirements for the target material [2]. Another solution which potentially has the flexibility to deal with the effect of the extrinsic parameters is a stochastic sampling over the landscape of the parameter space. A set of equivalently preferable parameter points can be sampled out and proposed as a set of candidate materials to meet the given needs. We note that the external needs can vary depending on social and economical trends. Even some unexpected requirements can pop up depending on how the material is used in practical applications. These are not predictable, which points to an unavoidable stochasticity in the materials design. Thus it seems to be a good idea to consider the materials design as a stochastic process working on the integrated data space constructed over various experimental probes and theoretical calculations. We adapt the data assimilation techniques in weather forecasts into the materials science. Developments are in progress and will be reported in detail elsewhere.

The author benefited from the online school for data assimilation in the autumn 2020 [3].

References

[1] MM, T. Hawai, K. Ono, Phys. Rev. Applied **13**, 064028 (2020).

[2] Y. Harashima, K. Tamai *et al.*, Phys. Rev. Materials **5**, 013806 (2021).

[3] `http://www.data-assimilation.riken.jp/jp/events/riken_da_tr_2020/index.html`

Data integration between experiments and calculations: the new stages

Munehisa MATSUMOTO
Institute of Materials Structure Science, High Energy Accelerator Research Organization
Oho 1-1, Tsukuba 305-0801

We have been working on magnetic materials made of transition metals and rare-earth elements. Since magnetism is a relatively low-energy phenomenon coexisting with high-energy properties of conducting electrons in the metallic parts, fundamental problems caused by the dichotomy between localized magnetic moments and delocalized electrons is already implied. On top of this, we encounter the multiple-scale problem where the intrinsic properties determined on the basis of atomic-scale structure is combined with extrinsic properties controlled by the microstructure to yield the macroscopic properties of magnetic materials. They both involve different layers of physics and we have accordingly used combined approaches such as LDA+DMFT [1] to address the magnetism of localized f-electrons embedded in the metallic environments. Here a quantum impurity problem is solved with quantum Monte Carlo method within the dynamical mean field theory (DMFT), and the realistic electronic structure is addressed with density functional theory based on local density approximation (LDA). In an analogous spirit, we have worked on a computational scheme where the electronic structure calculations for metallic ferromagnets and the input structure information taken from the Rietveld analysis of neutron diffraction data proceed via feedback to each other, which is tentatively termed "LDA+Rietveld" [2]. Here the experimental data play the role of an effective self-energy in the language of LDA+DMFT. Both approaches can be considered as developments for data integration of different types. The LDA+DMFT was originally developed for the simulation of strongly correlated electron systems which may be considered as a prototype to bridge over multiple scales in the target systems, which is often encountered in physics and materials science. While the past fiscal year 2020 was dominated by the serious pandemic problem, remote working and online learning tools have significantly improved which helped us to import several techniques from experts outside of our conventional discipline. This included the data assimilation techniques in weather forecast where unpredictable phenomenon coming from nonlinear dynamics can be put under numerical control by combining a limited number of observatory data and relatively abundant simulation data. This methodology adapted into the materials science might help the upcoming materials design and discovery to be done in an accelerated and predictable way, prospectively including a more comprehensive data integration with sample-fabrication processes. Further developments are in progress.

References

[1] MM, Phys. Rev. Materials **4**, 054401 (2020).

[2] MM, T. Hawai, K. Ono, Phys. Rev. Applied **13**, 064028 (2020).

Co-equivalent of Ce in $4f$-$3d$ intermetallics

Munehisa MATSUMOTO

Rare-earth permanent magnets based on Nd-Fe-B alloys have been widely used and expected to be even more of the key material in the upcoming decades. The weak anisotropy field at high temperatures and the relatively low Curie temperature of the main-phase compound, $Nd_2Fe_{14}B$, sometimes require supplementary rare metals in order to put the material in practical use. Since such rare metals are expensive and not always straightforwardly available, we have been in urgent quest for good ferromagnets on which permanent magnets may be developed in a cost-effective, robust, and sustainable manner. In this regard, clarification of the potential utility of Ce can be of a help. Indeed from the viewpoint of solid state physics, many interesting phenomena associated with Ce, such as valence fluctuations, heavy fermions, and unconventional superconductivity, have been known. Some of the fundamental ideas can help in answering the problems posed from material science.

We have looked into the potential utility of Ce for most of the representative properties of a ferromagnet to qualify as a constituent of a permanent magnet, namely, magnetization, magnetic anisotropy [1], Curie temperature, and structure stability. Among all these properties, we have observed that the largest merits actually seem to originate in the valence fluctuations, in particular the contribution from Ce^{4+} states to the bulk properties. One of such aspects can be illustrated with an effect of Ce substitution in $SmFe_{12}$ [2]: we can computationally get an analogue of the Slater-Pauling curve with the Ce-substituted ferromagnets. The magnetization of the Fe-based ferromagnet shows a peak as a function of the concentration of dopants, typically Co. Remarkably, the same thing can happen even when the dopant is Ce.

Obviously it is hard to observe this phenomenon in real experiments. There seems to be a strict constraint on the inter-atomic distance between the rare-earth sublattice and the transition-metal sublattice in order for the delocalized $4f$-electron to contribute to the bulk magnetization that is mostly made of $3d$-electrons. Especially for $Nd_2Fe_{14}B$ with the relatively inflated lattice, extracting the merit of Ce with the Slater-Pauling analogue is not straightforward. Nevertheless there has been some actual observation [3] confirmed both experimentally and computationally. Several findings as exemplified by these cases point to some hope for promising ferromagnets with reduced costs. So far we identified and understood several singular cases. Systematic quest to pop up further candidates on the basis of data assimilation between theory and experiments are in progress.

Helpful discussions with K. Saito, T. Ueno, and H. Shishido through the JSPS KAKENHI 15K13525 project are gratefully acknowledged.

References

[1] H. Shishido *et al.*, arXiv:2103.10202.

[2] MM, T. Hawai, K. Ono, Phys. Rev. Applied **13**, 064028 (2020).

[3] X. Tang *et al.*, Acta Materialia **175**, 1 (2019).

Finite temperature properties of frustrated systems

Tsuyoshi OKUBO
Department of Physics, The University of Tokyo
7-3-1 Hongo, Bunkyo-ku, Tokyo 133-0033

A variety of exciting phenomena, including non-collinear magnetic order, magnetization plateaus, and spin liquids, occur in the frustrated spin systems. Frustrated interactions often appear as geometrical frustrations based on the antiferromagnetic interaction on triangular units. Another origin of the frustration might be the competition of several interactions, such as the J_1-J_2 model on the square lattice. The honeycomb lattice Kitaev model could be considered as an example of the latter frustration [1]. In the Kitaev model, the interactions are Ising type, $S_i^\gamma S_j^\gamma$, and the spin component $\gamma = x, y, z$ is determined from the direction to the neighboring site. The Kitaev model is exactly solvable, and its ground state is known to be a spin liquid without long-range magnetic order. Such Kitaev interaction could appear in the realistic situation through the strong spin-orbit interaction [2]. α-RuCl$_3$ is an example of such a Kitaev compound. In this compound, the ground state is not the spin liquid: it is a magnetically ordered state. However, when we apply a magnetic field, the compound looks show the spin-liquid-like behaviors. In particular, a half-integer thermal Hall conductivity was observed at finite temperature [3], indicating the appearance of Kitaev spin liquid.

In this year's project, we investigated finite temperature properties of the Kitaev model with off-diagonal interactions motivated by the recent experiments on a Kitaev compound. The model Hamiltonian is given as

$$\mathcal{H} = \sum_{\gamma \in x,y,z} \mathcal{H}_\gamma - \frac{h}{\sqrt{3}} \sum_i (S^x + S^y + S^z), \quad (1)$$

where for $\gamma = z$,

$$\begin{aligned}\mathcal{H}_z = \sum_{\langle i,j \rangle_z} [&K S_i^z S_j^z + \Gamma(S_i^x S_j^y + S_i^y S_j^x) \\ &+ \Gamma'(S_i^z(S_j^x + S_j^y) + (S_i^x + S_i^y)S_j^z)].\end{aligned} \quad (2)$$

In the cases of $\gamma = x, y$, we consider similar interaction with cyclic rotation of x, y, z components. To numerically calculate the physical quantities at a finite temperature, we represent the system's density matrix as a tensor network and optimize its elements.

Firstly, we considered pure ferromagnetic Kitaev model ($K = -1$, $\Gamma = \Gamma' = 0$ and $h = 0$) in the thermodynamic limit. In our previous calculation using the infinite tensor product operator (iTPO) tensor network, we have found that the accuracy at the low temperature is not sufficient; we could not quantitatively reproduce the low-temperature specific heat peak previously calculated by quantum Monte Carlo [4]. In this year, we considered a cluster optimization of the tensor to improve the accuracy. In the standard optimization based on the imaginary time evolution, we perform Suzuki-Trotter decomposition and only optimize two sites simultaneously (simple update). In the new cluster optimization, we consider the imaginary time evolution of six sites and optimize them simultaneously. In Fig. 1, we plot thus obtained specific heat for the Kitaev model in the thermodynamic limit. Although both the simple update and the cluster optimization reproduce two expected peak structures of the specific heat, the lower peak height is largely increased by using the cluster optimization. Because the specific heat calculated by unbiased QMC shows a higher peak than the present data obtained by the cluster optimization, the accuracy is still not enough. However, we hope it will be improved when we consider larger bond dimensions in the future.

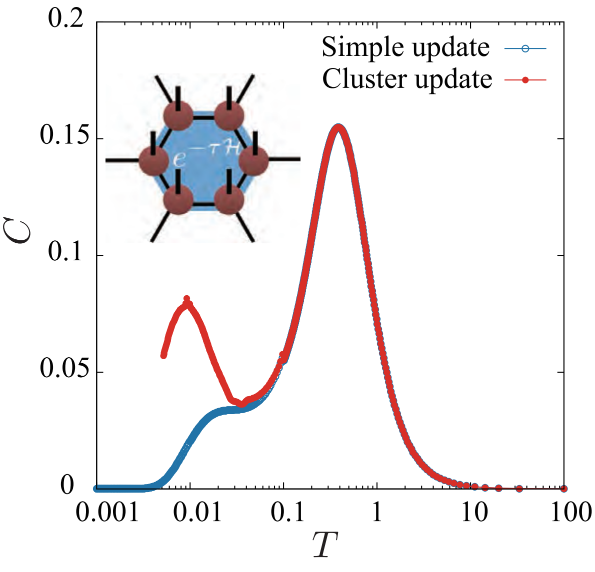

Figure 1: Specific heat of the infinite Kitaev model calculated by iTPO method. (open circle) Specific haet calculated by the standard simple update. (filled circle) Specific heat calculated by the new cluster optimization.

Secondary, we investigated the thermal Hall conductivity under a magnetic field. As we discussed, the accuracy of the infinite size simulation is still insufficient. Thus, we calculated the thermal Hall conductivity for the finite size cluster, and the density matrices are represented by matrix product operators (MPO) instead of iTPO. It has been demonstrated that by using such MPO representation, indeed, one can calculate finite temperature properties of the Kitaev model very accurately [5]. By using this MPO representation, we successfully calculated the thermal Hall conductivity under a magnetic field. For the pure Kitaev model, the thermal Hall conductivity has a peak at a finite temperature, and it overshoots the half quantized value; it is consistent with the experimental observation [3]. We also investigated the effect of the weak Γ and Γ' terms, and we found that depending on the sign of Γ and Γ', the thermal Hall conductivity is largely modified from that of the pure Kitaev model.

A part of this work has been done in collaboration with J. Nasu, T. Misawa and Y. Motome.

References

[1] A. Kitaev: Ann. Phys. **321** (2006) 2.

[2] G. Jackeli and G. Khaliullin, Phys. Rev. Lett. **102** (2009) 017205.

[3] Y. Kasahara, T. Ohnishi, Y. Mizukami, *et al.*, Nature **559** (2018) 227.

[4] J. Nasu, M. Udagawa, and Y. Motome: Phys. Rev. B **92** (2015) 115122.

[5] H. Li, D.-W. Qu, H.-K. Zhang, *et al.* Phys. Rev. ResearchBw **2** (2020) 043015.

Conformation of ultra-long-chain fatty acid in lipid bilayer

Kazutomo KAWAGUCHI[a], Koh M. NAKAGAWA[b], Satoshi NAKAGAWA[a],
Hideo SHINDOU[c], Hidemi NAGAO[a], and Hiroshi NOGUCHI[b]
[a] *Institute of Science and Engineering, Kanazawa University,*
Kanazawa, Ishikawa 920-1192, Japan
[b] *Institute for Solid State Physics, University of Tokyo, Kashiwa, Chiba 277-8581*
[c] *Department of Lipid Signaling, National Center for Global Health and Medicine,*
Shinjuku-ku, Tokyo 162-8655, Japan; Department of Lipid Science, Graduate School
of Medicine, University of Tokyo, Bunkyo-ku, Tokyo, 113-0033, Japan

In living cells, the most abundant lipids are phospholipids, which have a polar head group and two hydrocarbon tails. Each tail typically contains between 14 and 22 carbon atoms. Around C22 fatty acids such as docosahexaenoic acid (C22:6, DHA) are called very long-chain fatty acids (VLCFAs). Moreover, much longer chains, called ultra-long-chain fatty acids (ULCFAs), with 32 to 36 carbons with 6 double bonds were found at the sn-1 position of phosphatidylcholine (PC) in photoreceptors, spermatocytes, fibroblasts, and keratinocytes. However, the biosynthestic mechanisms and biological roles of ULCFAs have not understood yet. In this study, we examined the conformation of one of ULCFAs, dotriacontahexaenoic acid (C32:6) containing phosphatidylcholine (dTSPC, C32:6-C18:0), in phospholipid bilayers using all-atom molecular dynamics simulations [1].

One dTSPC is embedded in the lipid bilayer consisting of one of the following three lipids: Distearoyl PC (DSPC, C18:0-C18:0), Stearoyl-DHA PC (SDPC, C18:0-C22:6), and stearoyl-oleoyl PC (SOPC, C18:0-C18:1). Moreover, we examined the effects of the difference in lipid density between the two leaflets.

We found that the ultra-long tail of the ULCFA flips between two leaflets and fluctuates among an elongation into the opposite leaflet, lying between two leaflets, and turning back. The time scale of the conformational change between the elongated and turned shapes is $\sim$ 10 ns, so that it is quite fast. The ratio of these three states depends on the lipid-density difference between the two leaflets. The sn-1 chain is located at the opposite leaflet more frequently, as the lipid density of the opposite leaflet relatively decreases. We have clarified the linear relationships between the position of the sn-1 terminal of dTSPC and the lipid-density difference in all three types of membranes.

The main difference among the three types of host lipids is the number of the double bonds, and clear effects appear in the order profiles. Nevertheless, the conformation of dTSPC exhibits no qualitative differences. A minor influence is found in the distribution of C_{32} of dTSPC. Different shapes are obtained between SDPC and the others, whereas those of C_{18} and C_3 are not. In the SDPC membrane, C_{32} has a rounded triangular distribution. In contrast, a small peak or shoulder shape appears for the DSPC and SOPC membranes.

As described above, we revealed that ULCFA can sense and rapidly respond to the lipid-density difference to reduce such a difference. This behavior may be essential for the functions of ULCFAs in living cells.

References

[1] K. Kawaguchi, K. M. Nakagawa, S. Nakagawa, H. Shindou, H. Nagao, and H. Noguchi: J. Chem. Phys. **15**, 165101 (2020).

Giant magnetic response of hidden SU(2) symmetric antiferromagnets induced by impurity disorder

Hidemaro SUWA
Department of Physics, University of Tokyo
Hongo, Bunkyo, Tokyo 113-0033

In the research area of antiferromagnetic (AFM) spintronics, one of the most fundamental and challenging subjects is the efficient manipulation of the AFM order parameter. The key to extreme susceptibility lies in two-dimensional (2D) systems with spin isotropy. Although the ground state typically has a long-range order, any continuous symmetry is not broken at finite temperature in a 2D system with short-range interactions, according to the Mermin-Wagner theorem. As a result, the magnetic susceptibility exhibits an exponential divergence in the low-temperature region. Here the strongest divergence is obtained in the presence of the spin isotropy.

To achieve a giant magnetic response, we have proposed exploiting the hidden SU(2) symmetry built in a spin-orbit system [1]. The large spin-orbit coupling of iridates gives rise to $J_{\text{eff}} = 1/2$ quantum states and pins the $J_{\text{eff}} = 1/2$ pseudo-spins on the IrO_6 octahedral network. The octahedral rotation around the axis perpendicular to the plane can lead to a canted in-plane magnetic order and a linear coupling to uniform magnetic fields without breaking the spin isotropy. This hidden SU(2) symmetry is revealed by a staggered rotation of the spin reference frame under the frustration-free condition of the Dzyaloshinskii-Moriya interaction. Nevertheless, real materials have other perturbations to the pure 2D spin isotropic system: in particular, spin anisotropy introduced by the mixing with the $J_{\text{eff}} = 3/2$ orbitals. For efficient manipulation of the AFM order, it is crucial to make the perturbations smaller than the external fields we control.

We have shown that the AFM tunability can be systematically and significantly enhanced by introducing magnetic dilution and diminishing the spin anisotropy effect in the 2D antiferromagnets. We used ISSP System B and C in class C projects (ID: 2020-Ca-0097, 2020-Cb-0091) and calculated the large-scale quantum spin system consisting of more than one million spins using ALPS/looper (http://github.com/wistaria/alps-looper). Hybrid parallel computation was performed using up to 3,456 cores. We numerically showed that the non-magnetic substitution significantly suppresses the spin stiffness. Therefore, the perturbation of the controllable magnetic field, quantified by the ratio of the Zeeman energy to the intralayer spin stiffness, is significantly enhanced and dominant over the other perturbations. We have accomplished an extreme response of SU(2) symmetric AFM fluctuations in a diluted system close to the percolation threshold. The quasi-2D system of iridates thus represents a prototype of the magnetic dilution problem in 2D pseudo-spin-half antiferromagnets, leading to a tunability of effective spin anisotropy.

References

[1] L. Hao, D. Meyers, H. Suwa, et al., *Nat. Phys.* **14**, 806 (2018)

Development of Thermal Functional Materials Using Materials Informatics

Junichiro SHIOMI

Department of Mechanical Engineering,

The University of Tokyo, 7-3-1, Hongo, Bunkyo-ku, Tokyo 113-8656

The ability to effectively reduce a material’s thermal conductivity while keeping its electrical properties unchanged is the ultimate goal for thermoelectric materials. Due to the relative difference in the mean free paths (MFPs) of electrons and phonons, introducing nanostructures can effectively scatter phonon while affecting less to the electron transport. For example, the thermal conductivities of nanostructured materials like superlattice, nanowire, and nano-porous material are about one or two orders of magnitude lower than the bulk counterpart.

On the other hand, Silicon also has many allotropes other than the commonly seen diamond phase (referred to as Si-I phase) and has nature low thermal conductivity. Under high pressure, it can also form the body-centered cubic (BC8, referred to as Si-III) phase and rhombohedral (R8, referred to as Si-XII) phase as well as many other intermediate phases. How those multiphase nanostructure will affect the thermal conductivity remains unknown.

In this work, we utilized a multiscale modeling technique that including first-principles lattice dynamics, the Monte Carlo ray-tracing method, and effective medium theory was used to understand the mechanism of phonon transport in multiphase nanostructured silicon as well as the weak temperature dependence. The thermal conductivity values as well as its temperature dependence are also verified by the experimental measurements.

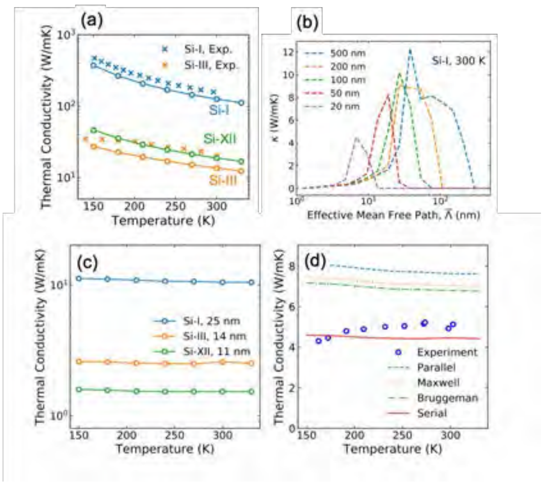

Figure 1(a) Bulk thermal conductivity of Si-I, Si-III, and Si-XII phases of silicon ure (b) The thermal conductivity spectrum as a function of effective mean free (c) The effective thermal conductivity of nanograin Si-I, Si-III, and Si-XII at different temperature. (d) The effective thermal conductivity of multiphase nanograined silicon as function of temperature.

The bulk phonon properties of the three phases are shown in Fig. 1(a), which are calculated from anharmonic lattice dynamics with interatomic force constants from first-principle calculations. The bulk phonon thermal conductivities of these three phases of silicon are quite high, which is unfavored for the thermoelectric energy conversion. Even for the Si-III phase, which has the lowest thermal conductivity among the three phases, the thermal conductivity is still above 10 W/mK at room temperature. Base on the Monte Carlo ray-tracing simulations, we found that introducing nanograin is an efficient way to reduce its lattice thermal conductivity. Taken the Si-phase as an example [Fig. 1(b)], we found that with the decreasing in the grain sizes, both the effective mean free path and the thermal conductivity will be shifted to low values. The effective thermal conductivity the nanograined silicon as a function of temperature is shown in Fig. 1(c), which shows a temperature-independent behavior. This weak temperature dependence suggests that the phonon-boundary scattering, which is a temperature-independent process in the elastic regime, is the dominate process that limits the thermal transport. To further verify the simulation, we also compared the simulation results with the experiment measurements, and the results are shown in Fig. 1(d). The inputs parameters like the volume fractions and the averaged grain sizes are extracted from the samples, and the good agreement between the simulations and the experimental measurements suggests the prediction power of our multiscale modeling scheme.

References

[1] C. Shao, K. Matsuda, S. Ju, Y. Ikoma, M. Kohno, & J. Shiomi, Journal of Applied Physics, 129(8), 085101 (2021)

Efficient Sampling Simulation of the Soft Modes Significantly Contribute to Protein Properties

K. TAKEMURA, D. TRAN, K. TAKABA, M.M. SOBEH, Y. MIYAZAWA, R. KIUCHI,
T.N. WIJAYA, T. OGAWA, Y. TAIRA, R. MISU, and A. KITAO
School of Life Science and Technology, Tokyo Institute of Technology
Ookayama, Meguro, Tokyo 152-8550

As an efficient conformation sampling method, we previously developed parallel cascade selection molecular dynamics (PaCS-MD) [1]. PaCS-MD consists of cycles of multiple independent short MD simulations. The initial structures of each cycle were selected as the closest structures to a target structure based on suitable properties such as root-mean-square-deviation (RMSD), center-of-mass distance. These selections increase the probability of rare event occurrences, and PaCS-MD enhances conformation sampling without external perturbations.

One problem in the original PaCS-MD is a requirement prior knowledge of the target structure. To address this issue, we proposed edge expansion PaCS-MD (eePaCS-MD) [2]. As illustrated in Fig. 1, eePaCS-MD requires only the initial structure (black cross). The initial structures of each cycle are randomly taken from the vertices (stars) of a multi-dimensional principal component subspace. The subspace consists of conformations sampled during previous cycles of eePaCS-MD and solving the “convex hull problem” provide the edges and vertices.

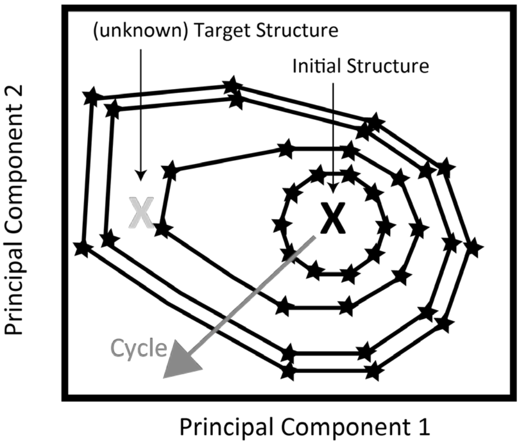

Fig. 1 Schematic illustration of the evolution of the vertices and edges in eePaCS-MD.

The sampling efficiency of the method can be examined by conducting eePaCS-MD from one state and examinimg whether the sampled conformations contain the target structures or not. For this purpose, we applied eePaCS-MD to open-close transitions (Fig.2) of glutamine binding protein (QBP), maltose/maltodextrin binding protein (MBP), adenylate kinase (ADK). We conducted eePaCS-MD from both open and close states.

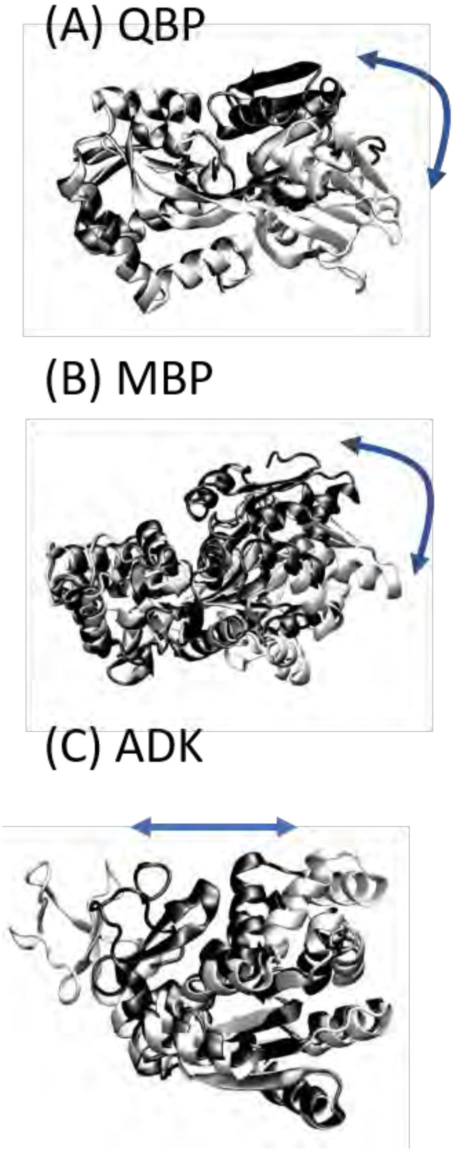

Fig. 2 Structures of target complexes. (A) Glutamine binding protein (QBP). (B) Maltose binding protein (MBP). (C) Adenylate kinase (ADK). Structures colored in black and white correspond to close and open states, respectively.

For all targets, eePaCS-MD efficiently sampled open-close transitions (generated conformations containing structures similar to the close state when simulations started from the open state). For QBP and MBP, close-open transitions were also successfully sampled. We also showed that the combination of eePaCS-MD and accelerated MD (eePaCS-aMD) achieved a further improvement of sampling efficiency. Minimum RMSD ($\mathrm{RMSD}_{\mathrm{min}}$), time to reach $\mathrm{RMSD}_{\mathrm{min}}$ (t_{min}), and the total computational cost used to reach the opposite state for the first time (T_{1st}) of eePaCS-aMD are shown in Table 1. OC and CO represent open to close and close to open transition, respectively. As shown in Table 1, open to close transitions were observed within 10 ns, which is several orders of magnitude shorter simulation time than conventional MD. Thus, eePaCS-MD is a very efficient sampling method that does not require prior knowledge.

Table 1 Summary of results (eePaCS-aMD)

Target	**$\mathrm{RMSD}_{\mathrm{min}}$ (Å)**	**t_{min} (ns)**	**T_{1st} (ns)**
QBP (OC)	1.3	4.9	40.4
QBP (CO)	1.3	6.4	52.8
MBP (OC)	1.2	6.7	41.6
MBP (CO)	1.3	7.2	49.4
ADK (OC)	1.9	8.9	114
ADK (CO)	3.2	9.3	-

References

[1] R. Harada and A. Kitao. J Chem Phys 139, 035103 (2013).

[2] K. Takaba, D.P. Tran and A. Kitao. J Chem Phys 152, 225101 (2020).

Anderson-Kitaev spin liquid

Masahiko G. YAMADA and Satoshi FUJIMOTO
Department of Materials Engineering Science, Osaka University
Toyonaka, 560-8531, Japan

More than half a century, the Anderson localization has been investegated intensively on the low-dimensional electron systems or fermionic systems. Normal magnets with a long-range order does not have a fermionic excitation, and thus the randomness effect has been investigated in a different manner. On the other hand, in Kitaev spin liquids excitations are described by Majorana fermions, and the Anderson localization of Majorana fermions can be expected. We name this new localized state Anderson-Kitaev spin liquid. This state potentially explains the experimental observation in α-RuCl$_3$ or A_3LiIr$_2$O$_6$ with $A =$ H, D, Ag.

We discovered Anderson-Kitaev spin liquid in the bond-disordererd Kitaev model with a numerical simulation. In the presense of a magnetic field, we need to recompute the flux gap of the disordered Kitaev model in the third-order perturbation. We compute this quantity in two methods. One is the exact diagonalization of the Majorana one-body Hamiltonian, and the other is the kernel polynomial method. Especially, the kernel polynomial method is very much suitable for the parallel computing, and we implement a hybrid parallelization code for this algorithm for a large-scale simulation. We note in the small scale two methods agree well.

With a massive parallel computation, we succeed in computing the flux gap, and hence the thermal Hall conductivity up to a $O(10000)$-site system for the bond-disordered Kitaev model. In the 100×100 honeycomb lattice, the thermal Hall conductivity shows a rapid decay as the disorder strength grows. After the extrapolation, the region where the thermal Hall conducitivity is quantized disappears when only 5% disorder is added. These results are published in npj Quantum Materials [1].

Overall we discover the new Anderson transition into an Anderson-Kitaev spin liquid thanks to the supercomputer in the Institute for Solid State Physics. The calculation has been done in the manner suitable for the supercomputer based on our newly established method.

References

[1] M. G. Yamada: npj Quantum Mater. **5** (2020) 82.

Analyses on complex fluids using multiscale simulation platform

Yohei MORII and Toshihiro KAWAKATSU

Department of Physics, Tohoku University, Sendai, Miyagi 980-8578

We have been developing a simulation platform named Multiscale Simulation Platform for complex fluids (MSSP), with which one can simulate macroscopic complex flows coupled with microscopic molecular simulators. MSSP uses smoothed particle hydrodynamics (SPH) method, where each hydrodynamic particle contains microscopic molecular simulator or microscopic stress calculator.

In this project, we implemented moving boundary conditions into MSSP so that we can simulate moving and deforming objects such as floating filler particles and deformable vesicles [1].

Figure 1 shows several characteristic flow properties of a viscoelastic fluid passing by a rotating cylindrical obstacle. The viscoelastic fluid is modelled as a Newtonian fluid where many dumbbells, i.e. each consists of two particles connected by a finite extensible nonlinear elastic (FENE) spring, are immersed. The obstacle is an elastic cylinder that rotates with a rotation rate (i.e. the speed at the surface of the obstacle/flow speed) 1.0, and the Reynolds number 40.0, and Weisenberg number 4.0, respectively. We used 230,000 SPH particles, each of which contains 1000 FENE dumbbells. As a result, total number of dumbbells are 230,000,000.

We can confirm that the rotation of the obstacle induces an asymmetric flow pattern around the obstacle, and that the dumbbells are strongly stretched at the obstacle surface, which is the origin of the nonlinear behavior of the viscoelastic fluid.

We also develop a simulation technique with which one can simulate an elastic membrane, i.e. a vesicle, in a channel flow. This is a preliminary work for simulating red blood cells in a blood Bessel.

References

[1] Y.Morii and T.Kawakatsu, in preparation.

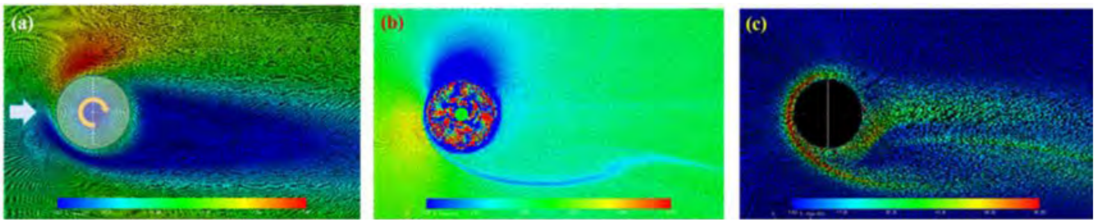

Figure 1: A FENE dumbbell flow around a rotating cylindrical obstacle. (a) Flow field, (b) pressure distribution, and (c) orientation distribution of FENE dumbbells.

Topological Order and Quantum Dynamics in Quantum Many-body Systems

Synge TODO
Department of Physics, University of Tokyo, Tokyo, 113-0033
Institute for Solid State Physics, University of Tokyo, Kashiwa, 277-8581

We have developed various novel numerical methods for quantum/classical many-body systems with strong correlations and performed large-scale simulations on ISSP supercomputer systems.

Rokhsar and Kivelson proposed the quantum dimer model in 1988 as a low-energy effective model for frustrated magnets. Although there is no negative sign problem in the Hamiltonian of the quantum dimer model, Monte Carlo simulations are challenging because of the strong geometrical restriction on the configuration of the dimers. With the help of efficient cluster update based on stochastic series expansion, we now extend our simulation to a more general class of models, including dimers and monomers and multiple interactions between them. It can include a larger Hilbert space based on the quantum dimer model, under the same framework of Monte Carlo simulation and update techniques, by which we can detect the deconfinement of monomers under the finite temperature phase transition (Fig. 1). We also implemented the exchange Monte Carlo method on the quantum dimer model to make a winding number-free simulation, with the kinetic terms to break a dimer into two monomers and still obtain the measurements for only dimer configurations.

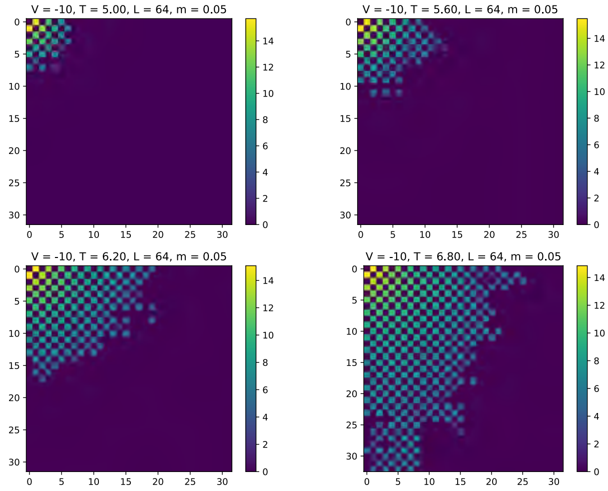

Figure 1: Deconfinement of monomers in quantum dimer model.

In the meantime, the real-space renormalization group method using tensor networks has recently been widely used as a numerical method for many-body spin systems. The tensor network method can efficiently compute the physical quantities of large-scale classical and quantum systems. However, existing methods, such as TRG and HOTRG, have a problem that the computational complexity becomes enormous as the spatial dimension increases. Our proposed Anisotropic Tensor Renormalization Group can dramatically reduce the computational complexity of high-dimensional systems such as three-dimensional quantum systems. Furthermore, by extending the tensor network to include tensors not only on the vertices but also on the lines connecting the vertices, the accuracy of the real-space renormalization method can be increased by a factor of 100 compared to existing numerical methods that require a similar amount of computation time.

Confirmation of stress-overshoot phenomena under biaxial elongational flow of ring-linear mixtures

Katsumi HAGITA[1] and Takahiro MURASHIMA[2]

[1]Department of Applied Physics, National Defense Academy, Yokosuka 239-8686

[2]Department of Physics, Tohoku University, Sendai 980-8578

Recently, we have studied (linear-rich) ring-linear mixtures [1,2] using Kremer-Grest (KG) [3] bases coarse grained molecular dynamics (CGMD) simulations. To study linear-chain penetrations into rings, we performed topology analyses based on the Gauss linking number (GLN) for all pairs of linear and ring polymers. The probability distributions of the number of linear chain penetrations per ring (n_P) were evaluated. We have investigated the possibility of increase of n_P by some conditions in order to make rings to work as a movable cross-linkers.

In the preliminary simulations at the last year, we discovered the increase of n_P under biaxial elongational flows [4]. Here, we used our extended uniform extensional flow (UEF) method [5]. We also discovered the stress overshoot under the biaxial elongational flows. Although the stress overshoot under uniaxial elongational flows were reported, that under biaxial elongational flows had been not. Thus, we proposed the D-Class project to publish a paper as quickly as possible.

In the proposed D-Class project, we started systematic preparation of ring-linear blends. Here, we treated uncatenated rings and ring complexes such as catenanes and bonded-rings consist of two or three rings per complex as shown in Fig. 1. We studied the cases with (N_{linear}, N_{ring}) = (160,40), (160,80), (160,120), (160,160), (40,160), (10,160) and ring fraction was fixed to be about 0.1. Here, N_{linear} and N_{ring} denotes number of beads per a linear chain and a ring, respectively. To keep enough statistical precisions, we used large system sizes with approximate 0.7 M beads. As the initial relaxation run, we performed a tun with 10^9 MD steps for each system. As the MD solvers, we used LAMMPS [5] for preparations at the ISSP supercomputer. At later we also used HooMD-bule [6] on the GPUs for continuous product runs.

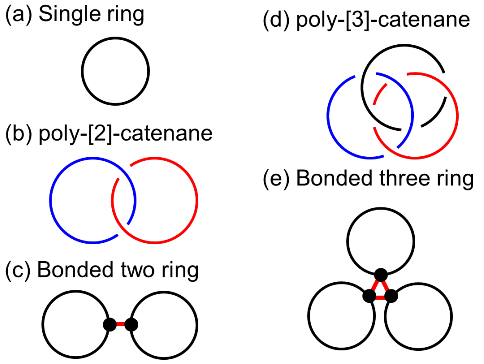

Fig. 1: Schematics of single ring, bonded-rings, poly-catenanes and ring-linear mixture.

In the present project, we developed a method to estimate $n_{\rm P}$ by using GLN. Here, the ends of linear chains are virtually connected to each other, but we prepared an extra linear chain and connected it to the original linear chain to form a cyclic chain as explained in our work [1,2]. For computation of GLN among cyclic chain and ring polymer, we used the Topoly Python package [7]. Figure 2 shows the probability distributions of linear chains penetrating into a single ring with $(N_{\rm linear}, N_{\rm ring}) = (160,40), (160,80), (160,120), (160,160)$.

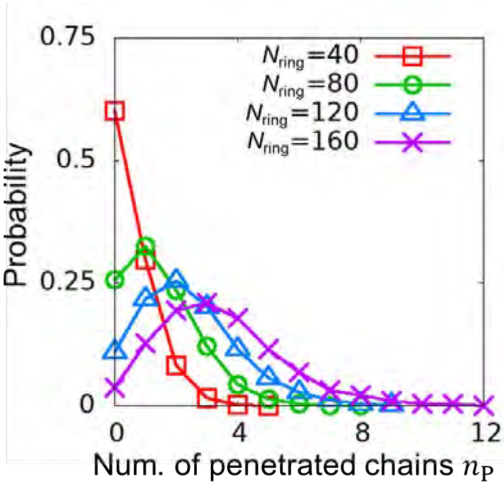

Fig. 2: Probability distributions of linear chains penetrating into a single ring with $(N_{\rm linear}, N_{\rm ring}) = (160,40), (160,80), (160,120), (160,160)$.

In this project, we also performed deformed simulations with the deformation rate of 0.001 in order to grub preliminary results. As results, we obtained the key result for biaxial elongational flows as shown in Fig. 3.

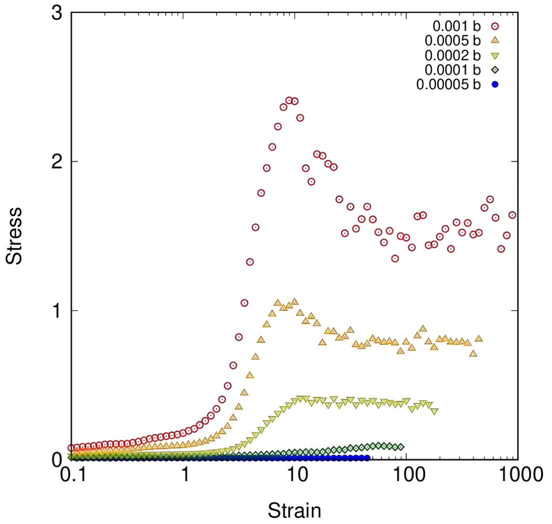

Fig. 3: Stress overshoot under biaxial elongational flows. $(N_{\rm linear}, N_{\rm ring}) = (160,40)$

References

[1] K. Hagita and T. Murashima: Polymer **218** (2021) 123493.

[2] K. Hagita and T. Murashima: Polymer **223** (2021) 123705.

[3] K. Kremer and G. S. Grest: J. Chem. Phys. **92** (1990) 5057.

[4] T. Murashima, K. Hagita, and T. Kawakatsu: Under review in Macromolecules.

[5] T. Murashima, K. Hagita, and T. Kawakatsu: Nihon Reoroji Gakkaishi (J. Soc. Rheol. Jpn.), **46** (2018) 207.

[6] S. Plimpton: J. Comp. Phys. **117** (1995) 117.

[7] J. A. Anderson, et. al.: Comput. Mat. Sci. **173** (2020) 173, 109363

[8] P. Dąbrowski-Tumański, et. al.: Brief. Bionformatics (2020) bbaa196.

Frustration-induced symmetric skyrmion lattices in three dimensions

K. MITSUMOTO[1], R. OSAMURA[2], K. AOYAMA[2] and H. KAWAMURA[1]

[1] *Molecular Photoscience Research Center, Kobe University, Kobe 657-8501*

[2] *Graduate School of Science, Osaka University, Toyonaka 560-0043*

Considerable attention has recently been paid to "skyrmion", a topologically stable nano-scale spin texture, both from fundamental interest of topology and also from possible application to spintronics. In the usual situation, skyrmion and "skyrmion lattice" are stabilized in the non-centrosymmetric magnets without the inversion center via the anti-symmetric Dzyaloshinskii-Moriya (DM) interaction, which energetically discriminates "right" and "left" spirals. Meanwhile, it was proposed in Ref.[1] that the symmetric skyrmion and skyrmion lattice might be stabilized in centrosymmetric magnets with the inversion center by the frustrated exchange interaction. Examples might be the J_1-J_3 (J_1-J_2) Heisenberg magnet on the two-dimensional (2D) triangular lattice under magnetic fields. In such frustrated magnets, in contrast to the DM case, "right" and "left" spirals are energetically equivalent, and the skyrmion with both signs of the scalar chirality (or the topological charge) is possible, giving rise to both the skyrmion and anti-skyrmion lattices. Interestingly, skyrmion and anti-skyrmion lead to the topological Hall effect of mutually opposite signs.

Real magnets are of course three-dimensional (3D) with certain amount of interlayer coupling. In this year's project, we investigate the properties of the possible skyrmion and skyrmion lattice in 3D, by performing extensive Monte Carlo simulations on the frustrated classical Heisenberg model on the 3D stacked-triangular lattice. We investigate by means of extensive Monte Carlo simulations both (i) the short-range interaction model mimicking insulators, i.e., J_1-J_3-J_{1c} Heisenberg model, and (ii) the long-range RKKY interaction (falling with $1/r^3$) model mimicking metals.

In the short-range model (i), the transition behavior of the 3D model turns out to be similar to that of the 2D model for the ferromagnetic interlayer coupling, exhibiting the skyrmion (anti-skyrmion)-lattice state, while, for the antiferromagnetic interlayer coupling, the nature of the skyrmion-lattice state changes somewhat. In the RKKY model (ii), we also find the skyrmion-lattice state, which, however, seems to accompany an exotic *replica-symmetry breaking (RSB)* unlike the short-range model.

[1] T. Okubo, S. Chung and H. Kawamura, Phys. Rev. Letters **108**, 017206 (2012).

Rotational dynamics of water molecules on the lipid membranes

Yuji HIGUCHI
Institute for Solid State Physics, The University of Tokyo
Kashiwa-no-ha, Kashiwa, Chiba 277-8581

We have studied the structures and properties of soft matter. We revealed the fracture processes of semicrystalline polymers [1] by coarse-grained molecular dynamics simulations. Understanding the mechanical properties is essential to improve the toughness of polymeric materials. This year, we study the water dynamics on the lipid membranes, which are considered as a model system for biological membranes. All atomic molecular dynamics (MD) simulations are performed on System B and C using the LAMMPS program [2] and DFTB+ software [3].

We calculate the rotational relaxation of water molecules on the lipid membranes with phosphatidylcholine (PC) and phosphatidylethanolamine (PE) head groups. The relaxation is faster in PE than that in PC (Fig. 1), which is consistent with the previous experiment [4]. To reveal the mechanism of the different relaxation, hydrogen bond (HB) networks among water molecules are analyzed. The number of HBs in PE is less than that in PC. The PE head group is strongly hydrated, which breaks the HB network. In contrast, the weaker hydration around the PC head group does not break the HB network. In DFTB-MD simulation, the head groups of PC and PE are modeled as $N(CH_3)_4^+$ and NH_4^+, respectively. The rotational relaxation of water molecules and the number of HBs around ions are consistent with those on the lipid membranes, confirming the mechanism. Thus, we successfully reveal the atomistic mechanism of the different water dynamics on the lipid membranes [5].

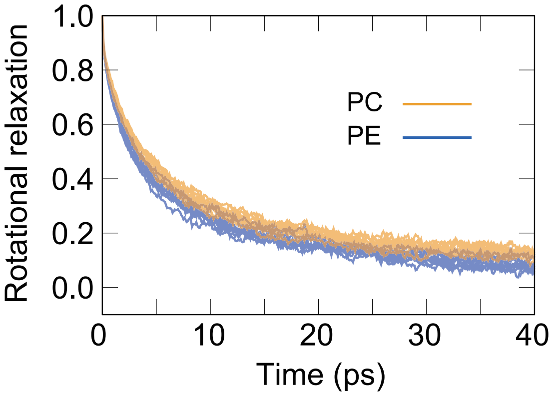

Figure 1: The rotational relaxation of water molecules just above the lipid membranes. Ten trajectories are shown, which confirms the significant difference.

References

[1] Y. Higuchi: Phys. Rev. E **103** (2021) 042502.

[2] S. Plimpton: J. Comput. Phys. **117** (1995) 1.

[3] B. Hourahine, et al.: J. Chem. Phys. **152** (2020) 124101.

[4] M. Hishida, K. Tanaka, Y. Yamamura, and K. Saito, J. Phys. Soc. Jpn. **83** (2014) 044801.

[5] Y. Higuchi, Y. Asano, T. Kuwahara, and M. Hishida: Langmuir (2021). DOI: 10.1021/acs.langmuir.1c00417

FRG study on realization of the Kitaev quantum spin liquid in condensed matter physics

Kiyu FUKUI, Yukitoshi MOTOME, and Yusuke KATO
Department of Physics, The University of Tokyo, Bunkyo, Tokyo 113-0033
Department of Applied Physics, The University of Tokyo, Bunkyo, Tokyo 113-8656
Department of Basic Science, The University of Tokyo, Meguro, Tokyo 153-8902

Frustrated quantum spin systems have been studied intensively for very long time. In general, however, it is impossible to solve them exactly mathematically. Therefore, numerical approaches to investigate them are indispensable. Numerical approaches used widely to study them are, for example, exact diagonalization (ED), quantum Monte Carlo (QMC), density matrix renormalization group (DMRG). Each method has pros and cons, of course. Since 2010s, a new method called pseudo-fermion functional renormalization group (PFFRG or pf-FRG) has been used gradually [1]. Although PFFRG overestimates ordering tendencies to magnetic orders [2], it can treat large-size systems and strongly-frustrated systems and detect quantum paramagnetism due to strong frustration. We done two studies on the feasibility of the Kitaev quantum spin liquid by PFFRG [3].

The first one is the study on the feasibility of it in ultracold molecular systems trapped in the optical lattice rather than in solids. We define dipolar Kitaev model on the honeycomb lattice as

$$\mathcal{H} = -\frac{1}{2}\sum_{i,j}^{i\neq j}\frac{1}{3r_{ij}^3} \tag{1}$$

$$\times \{J_x[1-2\cos(2\Phi_{ij}-\frac{4\pi}{3})]S_i^x S_j^x + J_y[1-2\cos(2\Phi_{ij}-\frac{2\pi}{3})]S_i^y S_j^y + J_z[1-2\cos(2\Phi_{ij})]S_i^z S_j^z\}, \tag{2}$$

based on the realization of Kitaev-type interactions proposed in 2013 [4]. In the dipolar Kitaev model, the interactions between the nearest-neighboring sites are consistent with the Kitaev model, but those between sites farther than the nearest-neighbor are more complicated. We apply PFFRG to this model to investigate the ground state at each parameter. The results show that FM order and zigzag AFM order are realized in the FM and AFM dipolar Kitaev model, respectively, for all anisotropy parameters. Furthermore, in order to investigate the connection between the (nearest-neighbor) Kitaev model and the dipolar Kitaev model, we introduce an artificial range of interactions and calculate the susceptibility when approaching the dipolar Kitaev model with long-range interactions from the Kitaev model with only nearest-neighbor interactions. From this calculation, it is clarified that the spin liquid state realized in the Kitaev model is quickly collapses, as the range of interactions is extended. After the proposals of Kitaev-type interaction in ultracold polar molecular systems by microwave irradiation in 2013, the calculation based on these proposals has not been performed, and whether Kitaev quantum spin liquid state is actually realized has remained an open question. We address this issue with PFFRG and elucidated the above results for the first time.

The other is the study on the realization of the Kitaev quantum spin liquid in the high-spin materials. We calculate the phase diagram of the spin-S Kitaev-Heisenberg model with $S = 1/2$-$5/2$ and $S = 50$. Its Hamiltonian is

$$\mathcal{H} = A \sum_{\mu} \sum_{\langle i,j \rangle_\mu} \left[2\sin(2\pi\xi) S_i^\mu S_j^\mu + \cos(2\pi\xi) \boldsymbol{S}_i \cdot \boldsymbol{S}_j \right]. \tag{3}$$

We apply the extension of PFFRG to treat spin-S systems proposed in 2017 [5]. The obtained phase diagrams of the Kitaev-Heisenberg model for $S = 1/2$ and $S = 1$ are in general good agreement with the previous studies by other numerical methods. The phase diagram for $S = 50$ is also in good agreement with the previous study on the classical Kitaev-Heisenberg model by Monte Carlo simulation, except for some special points. As a result of systematic calculations with different S, for $S \leq 3/2$, both the AFM and FM Kitaev spin liquid regions have a finite extent. For $S \geq 2$, no region showing Kitaev spin liquid state was found. Therefore, we believe that $S = 3/2$ gives an upper bound on the spins possessed by the candidate materials in which Kitaev quantum spin liquid is realized. The phase diagram calculation of the Kitaev-Heisenberg model with a systematic change of spin S, as we perform here, has not been done before. This is the first study of the application of spin-S PFFRG to the Kitaev-Heisenberg systems. The results we obtain here provide a guideline for the recent intensive search for candidate materials of $S > 1/2$ Kitaev quantum spin liquid.

References

[1] J. Reuther and P. Wölfle, Phys. Rev. B **81**, 144410 (2010).

[2] S. Göttel, S. Andergassen, C. Honerkamp, D. Schuricht, and S. Wessel, Phys. Rev. B **85**, 214406 (2012).

[3] K. Fukui, Ph.D Thesis, The University of Tokyo (2021).

[4] S. R. Manmana *et al.*, Phys. Rev. B **87**, 081106 (2013); A. V. Gorshkov, K. R. Hazzard, and A. M. Rey, Mol. Phys. **111**, 1908 (2013).

[5] M. L. Baez and J. Reuther, Phys. Rev. B **96**, 045144 (2017).

Molecular dynamics simulations for assembly and disassembly of protein aggregates

Hisashi Okumura

Exploratory Research Center on Life and Living Systems,

Institute for Molecular Science, Okazaki, Aichi 444-8585

Proteins are normally folded correctly and perform functions that are necessary to sustain life. However, when the concentration of proteins increases due to aging or other reasons, they can aggregate and cause a variety of diseases. Alzheimer's disease, which is one type of dementia, is caused by amyloid-β (Aβ) peptides, which aggregate into spherical oligomers or amyloid fibrils. We are conducting theoretical studies on the aggregation and disaggregation of Aβ peptides [1]. In this fiscal year, we investigated the destruction process of an Aβ amyloid fibril by infrared free electron laser irradiation using molecular dynamics simulation.

In recent years, Aβ aggregates have been irradiated with infrared free electron lasers and destroyed. We performed non-equilibrium molecular dynamics simulations of Aβ amyloid fibrils under a time-varying electric field mimicking that of an infrared free electron laser to clarify the destruction process and the structure of amyloid fibrils after destruction.

As a result, we have discovered a new mechanism by which water molecules destroy the Aβ amyloid fibril. Intermolecular hydrogen bonds formed between C=O and N–H in the amyloid fibril are broken with each pulse of laser irradiation. In most cases, these bonds are reformed spontaneously after the irradiation. However, if a water molecule happens to enter the gap between C=O and N–H made by the laser irradiation, the reformation of the hydrogen bonds is inhibited. This role of water molecules is quite different from other known mechanisms. This new mechanism can explain recent experiments showing that amyloid fibrils are not destroyed by laser irradiation under dry conditions [2].

Furthermore, we found that more α-helix structures are formed after the laser-irradiated amyloid-fibril destruction. This is because the α-helix structure has a different resonance frequency from the β-sheet structure. Our findings provide a theoretical basis for the application of the laser to the future treatment of amyloidosis.

References

[1] H. Okumura, S. G. Itoh, J. Am. Chem. Soc. **136** (2014) 10549-10552.

[2] T. Kawasaki, et al. Cellular and Molecular Neurobiology **38** (2018) 1039-1049.

Study on Complex Systems by Generalized-Ensemble Algorithms

Takuya HAYASHI and Yuko OKAMOTO

Department of Physics, Graduate School of Science, Nagoya University

Furo-cho, Chikusa-ku, Nagoya, Aichi 464-8602

We had two projects regarding generalized-ensemble algorithms applied to complex systems.

The density of states (DOS) is one of the most important physical quantities in statistical mechanics. Recently, we proposed a simulation protocol, REWL-MUCAREM [1], in order to obtain the DOS with high accuracy in complex systems by combining the *Replica-Exchange Wang-Landau* (REWL) method [2] and the *Multicanonical Replica-Exchange Method* (MUCAREM) [3]. The effectiveness of REWL-MUCAREM was demonstrated by using the 2-dimensional Ising model in [1].

We also applied the REWL-MUCAREM protocol to the ice Ih system in order to estimate the residual entropy with high accuracy. The residual entropy of ice has become one of good examples to test the effectiveness of sampling algorithms.

Our latest estimate of residual entropy per one water molecule [4] is:

$$W_0 = 1.507472 \pm 0.000047$$

$$S_0 = k_B \ln W_0$$

$$= 0.815615 \pm 0.000063 \ [\mathrm{cal/(mol\ K)}].$$

This estimate is in good agreement with the results of several other research groups (see Fig. 1).

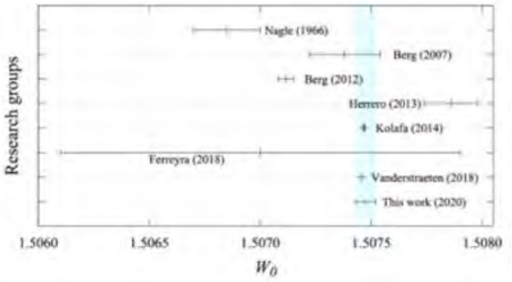

Figure 1: The estimates of residual entropy of ice Ih by several research groups.

However, our previous results disagreed with the above results [5]. We found that the discrepancy resulted from the choice of the random number generators [4]. The present

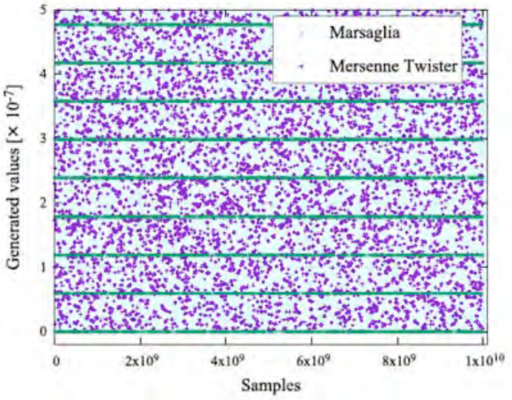

Figure 2: Generated random numbers by the Marsaglia generator (green) and Mersenne Twister generator (purple).

work used Mersenne Twister generator [6], while our previous work used Marsaglia generator [7]. In Fig. 2 we compare the two random number generators. Although the Mersenne Twister generator gives uniform distribution, Marsaglia takes on only nine values in this narrow range. We have reminded the reader that the choice of random number generators is very important.

In the second project, we studied the helix-coil transitions of homo-alanine polymers [8] based on the Microcanonical Inflection-Point Analysis (MIPA) Method [9]. Two lengths of homo-polymers were taken, N=10 and 20, and two environment conditions (in vacuum and in water) were considered. We performed the REWL-MUCAREM simulations. In Fig. 3, we compare the specific heat.

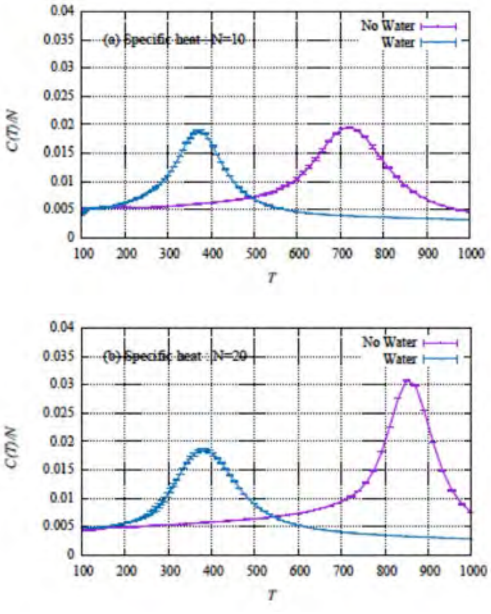

Figure 3: Specific heat as functions of temperature for N=10 and 20.

We see that the helix-coil transition temperature is higher for N=20 than for N=10. It is also shown that this transition temperature is higher for in vacuum than in water.

By calculating the microcanonical entropy and its derivative with respect to energy, we found that the latter has an inflection point in vacuum but no inflection point in water. This suggests that the helix-coil transition is first-order-like in vacuum, but it is second-order-like in water [8].

References

[1] T. Hayashi and Y. Okamoto, Phys. Rev. E. **100**, 043304 (2019).

[2] T. Vogel, Y. W. Li, T. Wüst and D. P. Landau, Phys. Rev. Lett. **110**, 210603 (2013).

[3] Y. Sugita and Y. Okamoto, Chem. Phys. Lett. **329**, 261 (2000).

[4] T. Hayashi, C. Muguruma, and Y. Okamoto, J. Chem. Phys. 154, 044503 (2021).

[5] B. A. Berg, C. Muguruma, and Y. Okamoto, Mol. Sim. **38**, 856 (2012).

[6] M. Matsumoto and T. Nishiura, ACM Trans. Modle. Comput. Simul. **8**, 3 (1998).

[7] G. Marsaglia, A. Zaman, and W. W. Tsang, Stat. Probab. Lett. **9**, 35 (1990).

[8] T. Hayashi, Y. Sakae, and Y. Okamoto, submitted for publication.

[9] K. Qi and M. Bachmann, Phys. Rev. Lett. **120**, 180601 (2018).

Numerical Diagonalization Study on the Field-Induced Spin Nematic Liquid

Tôru SAKAI[1,2], Hiroki NAKANO[1], Rito FURUCHI[1], and Tokuro SHIMOKAWA[3],
[1]*Graduate School of Material Science, University of Hyogo,*
Kouto, Kamigori, Hyogo 678-1297, Japan
[2]*Synchrotron Radiation Research Center, Kansai Photon Science Institute,*
Quantum Beam Science Research Directorate,
National Institute for Quantum and Radiological Science and Technology (QST)
SPring-8, Kouto, Sayo, Hyogo 679-5148, Japan
[3]*Okinawa Institute of Science and Technology Graduate University, Onna,*
Okinawa 904-0945, Japan

The quantum spin nematic state has attracted a lot of interest in the field of the magnetism. It is a kind of state between the conventional long-range antiferromagnetic order and the quantum spin liquid. This state has been proposed as one of mechanisms of the hidden order which was observed in some strongly correlated electron systems. The spin nematic state was theoretically predicted to be realized in several frustrated systems; the square lattice model with the ferromagnetic nearest-neighbor and antiferromagnetic next-nearest-neighbor interactions[1], the triangular lattice antiferromagnet with multi spin exchange interactions[2], and the ferromagnetic and antiferromagnetic zigzag chain[3, 4]. The previous density matrix renormalization group (DMRG) analysis[5] indicated that the field-induced spin nematic liquid phase appears in the S = 1 antiferromagnetic chain with the biquadratic interaction. Thus it would be important to investigate this system using another method, in order to confirm the spin nematic liquid phase. We investigated the magnetization process of the S = 1 antiferromagnetic chain with the biquadratic interaction, using the numerical exact diagonalization of finite-size clusters[6]. The present analysis confirmed the appearance of the field-induced spin nematic Tomonaga-Luttinger liquid phase and gives the ground state phase diagram which is qualitatively consistence with the previous DMRG study[5]

References

[1] N. Shannon, T. Momoi and P. Sindzingre, Phys. Rev. Lett. 96 (2006) 027213.

[2] T. Momoi, P. Sindzingre and N. Shannon, Phys. Rev. Lett. 97 (2006) 257204.

[3] A. V. Chubukov, Phys. Rev. B 44 (1991) R4693.

[4] T. Hikihara, I. Kecke, T. Momoi and A. Furusakai, Phys. Rev. B 78 (2008) 144404.

[5] T. S. R. Manmana, A. M. Lauchli, F. H. L. Essler and F. Mila, Phys. Rev. B 83 (2011) 184433.

[6] T. Sakai, AIP Advances 11 (2021) 015306.

Symmetry Protected Topological Phase of the S=2 Antiferromagnetic Chain

Tôru SAKAI[1,2], Hiroki NAKANO[1], Rito FURUCHI[1], and Tokuro SHIMOKAWA[3],
[1] *Graduate School of Material Science, University of Hyogo,*
Kouto, Kamigori, Hyogo 678-1297, Japan
[2] *Synchrotron Radiation Research Center, Kansai Photon Science Institute,*
Quantum Beam Science Research Directorate,
National Institute for Quantum and Radiological Science and Technology (QST)
SPring-8, Kouto, Sayo, Hyogo 679-5148, Japan
[3] *Okinawa Institute of Science and Technology Graduate University, Onna,*
Okinawa 904-0945, Japan

The spin gap of the integer-spin antiferromagnetic Heisenberg chain was proposed by Haldane[1, 2] many years ago. Recently it has been generalized as the symmetry protected topological phase[3, 4], which is the gapped phase of the odd-integer-spin antiferromagnetic chain. On the other hand, the numerical diagonalization and the level spetroscopy analyses on the $S = 2$ antiferromagnetic chain with the coupling anisotropy Δ and the single-ion anisotropy D, indicated that the symmetry protected topological phase appears at a small region in the $\Delta - D$ phase diagram[5, 6]. This phase corresponds to the intermediate D phase which had been predicted by Oshikawa[7]. In the present study, the $S = 2$ antiferromagnetic Heisenbergy chain with the biquadratic interaction $J_{\rm BQ}$ and the single-ion anisotropy D is investigated using the numerical diagonalization and the level spectroscopy analyses. As a result, it is found that the intermediate D phase appears at a wide region in the $J_{\rm BQ} - D$ phase diagram.

References

[1] F. D. M. Haldane, Phys. Lett. 93A (1983) 464.

[2] Phys. Rev. Lett. 50 (1983) 1153.

[3] F. Pollmann, A. M. Tuner, E. Berg and M. Oshikawa, Phys. Rev. B 81 (2010) 064439.

[4] F. Pollmann, E. Berg, A. M. Turner and M. Oshikawa, Phys. Rev. B 85 (2012) 075125.

[5] T. Tonegawa, K. Okamoto, H. Nakano, T. Sakai, K. Nomura and M. Kaburagi, J. Phys. Soc. Jpn. 80 (2011) 043001.

[6] K. Okamoto, T. Tonegawa and T. Sakai, J. Phys. Soc. Jpn. 85 (2016) 063704.

[7] M. Oshikawa, J. Phys.: Condens. Matter 4 (1992) 7469.

Ground-State Phase Diagram of the S=1/2 Heisenberg-Γ model on a Honeycomb Lattice

Takafumi SUZUKI
Graduate School of Engineering,
University of Hyogo, Shosha, Himeji, Hyogo 670-2280

In this study, we investigated the ground-state phase diagram of the S=1/2 Heisenberg-Γ model on a honeycomb lattice [1] by the numerical exact diagonalization method and cluster-series expansion method [2]. We focused on the effects of the anisotropic interaction; by tuning the coupling constants, the system changes between the spin-chain and isolated dimer models. We found that, in the spin-chain limit, there are three kinds of states, namely a Tomonaga-Luttinger liquid and two magnetically long-range-ordered states. All three states change two-dimensional long-range ordered states, when the interchain interaction is included infinitesimally except for the case where the Heisenberg interaction is much weaker than the off-diagonal symmetric interaction (Γ). When the antiferromagnetic Γ interaction is large enough and the system locates near the spin chain limit, we observe that there are no prominent peaks of the static structure factor and the feature of the low-energy excitation is quite similar to that in the spin chain limit. We consider that two-dimensional true-long-range-ordered state is suppressed in such parameter region. Starting from the isolated dimer limit, we found that a triplet dimer phase can survive up to the isotropically interacting system in a large part of the phase diagram, where the Heisenberg and Γ interactions are ferromagnetic and antiferromagnetic, respectively. Otherwise, a phase transition to a magnetically ordered phase takes place before the interaction becomes isotropic. This means that the quantum spin liquid discussed in the Γ model [3] is unstable against the anisotropy of the interactions. The obtained results, namely the unitability of this spin liquid and the stable triplet dimer phase, are the same as those of the previous results for the Kitaev-Γ model on a honeycomb lattice [4].

References

[1] T. Suzuki, T. Yamada, and S. Suga, in preparation.

[2] J. Oitmaa, et al., Series Expansion Methods for Strongly Interacting Lattice Models, Cambridge University Press, 2006.

[3] A. Catuneanu, et al., npj. Quantum Materials, **3** 23 (2018).

[4] T. Yamada, T. Suzuki, and S. Suga, Phys. Rev. B **102**, 024415 (2020).

Numerical analysis for nonequilibrium dynamics in electronic systems on quasicrystals & Study of new ordered phase and nonequilibrium phenomena in quasicrystals

Akihisa Koga
Department of Physics, Tokyo Institute of Technology, Meguro, Tokyo 152-8551

Recently, quasicrystals, which have no translational symmetry but have ordered lattice structures, are attracting interests in the condensed matter physics. So far, their static properties such as resistivity and specific heats have been mainly focused on. Thus, it is important to reveal nonequilibrium features of quasicrystal systems and understand how special lattice structures affect the dynamics.

Motivated by this, we studied nonequilibrium dynamics of the excitonic insulating (EI) phase described by the two-band Hubbard model on the Penrose lattice. The EI phase is the condensation of the electron-hole pairs (excitons) in semiconductors or semimetals. The EI phase is analogous to superconductors and is attracting much interests in the context of nonequilbrium condensed matter physics. By means of the real-space time-dependent mean-field theory for large systems, we revealed qualitatively different behaviors in the BCS and BEC regimes, see Fig.1. Namely, in the BCS regime, the order parameter is suppressed after a single cycle pulse, while, in the BEC regime, it is increased by the pulse. Such a behavior has been reported in a previous work on the square lattice, and its origin was discussed in the momentum space. However, in quasicrystals, one cannot define the momentum space and such argument does not apply. Our results indicate existence of a more fundamental origin regardless of the momentum picture. In addition, we revealed a characteristic dynamics in the BCS regime using the perpendicular space analysis.

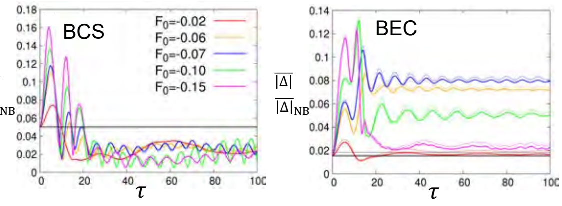

Figure 1: Dynamics of the EI order parameter for the two-band Hubbard model on the Penrose lattice. Horizontal lines indicate equilibrium values.

Another interesting topic is possible ordered phases in quasicrystals. We have clarified the nature of magnetic orders in several types of quasi-periodic lattices [2].

Furthermore, we have also studied real-space dynamics and correlations in the Kitaev spin liquid states. We revealed peculiar spin transport mediated by itinerant Majorana fermions [3] and discuss how to modify the Majorana correlations using intrinsic degrees of freedom of the Kitaev model [4].

References

[1] K. Inayoshi, Master thesis (2021); K. Inayoshi, Y. Murakami, A. Koga, in prep.

[2] A. Koga, PRB **102**, 115125 (2020): Mater. Trans. **62**, 360-366 (2021).

[3] T. Minakawa, Y. Murakami, A. Koga and J. Nasu, PRL **125**, 047204 (2020).

[4] A. Koga, Y. Murakami and J. Nasu, submitted to PRB.

Rational computational design of proteins toward drug discovery and industrial applications

Nao SATO[1], Sairi MATSUMOTO[1], Mizuki TERANISHI[1], Katsuhisa IWAYA[2],
Koji OOKA[2], Masataka YOSHIMURA[1], Shunji SUETAKA[1], Yoshiki OKA[1],
Yuuki HAYASHI[1], and Munehito ARAI[1,2]
[1]*Department of Life Sciences, Graduate School of Arts and Sciences, and*
[2]*Department of Physics, Graduate School of Science,*
The University of Tokyo, Komaba, Meguro, Tokyo 153-8902

Proteins have been extensively used in industrial and pharmaceutical applications; many protein-based drugs are among the top selling drugs. However, these proteins have been developed by experimental approaches that require a lot of time and cost. Therefore, theoretical approaches to efficiently design useful proteins are demanded. To solve this issue, we have been rationally designing various proteins, which are potentially applicable to industry and medicine, using the Rosetta 3.8 or 3.12 suite [1-3]. We have also performed experimental verification of the computational protein design.

Protein-protein interactions (PPIs) are related to many diseases, and thus designing PPI inhibitors is a promising way for drug discovery. We rationally designed inhibitors for the interactions between the KIX domain of a transcriptional coactivator CBP and transcriptional activators, which are involved in many diseases including leukemia [4]. The transactivation domain (TAD) of the transcriptional activator mixed lineage leukemia protein (MLL) was used as a template. Theoretical design of the mutants of the MLL TAD fragment that may bind KIX more tightly than the wild type was performed using Rosetta. Among the designed mutants, we could obtain the mutant that binds KIX two-fold more tightly than the wild type, suggesting that our strategy is useful for designing PPI inhibitors.

Severe acute respiratory syndrome coronavirus 2 (SARS-CoV-2), which is responsible for coronavirus disease 2019 (COVID-19), infects human cells through the PPI between the receptor-binding domain (RBD) of the viral-surface Spike protein and the cell-surface receptor angiotensin-converting enzyme 2 (ACE2) [5]. To inhibit this PPI, we have computationally designed the antibodies that can bind the ACE2-binding region of the RBD of SARS-CoV-2. We are currently producing the antibodies and the RBD proteins, to experimentally verify the predictions.

Allergic asthma is known to occur through the PPI between interleukin-33 (IL-33) released from damaged epithelial cells and the ST2 receptor of type 2 innate lymphoid cells [6]. To develop the IL-33–ST2 inhibitors, we rationally designed the IL-33 mutants that tightly bind to one of the two IL-33 binding sites on ST2 but does not to another site. The interaction of ST2 with one of the designed mutants of IL-33 was measured by fluorescence anisotropy. However, the experiment did not support the theoretical prediction, indicating the necessity of improving protein design methods.

Alkane biosynthesis has gained great attention as an alternative to fossil fuels and is expected as one of the promising ways to produce carbon-neural renewable energy. Cyanobacterial alkane biosynthesis involves two enzymes, an acyl-ACP reductase (AAR) and an aldehyde deformylating oxygenase (ADO) [7]. Interaction between these proteins allows an efficient delivery of an aldehyde from AAR to ADO [8]. To improve bioalkane production, we rationally designed the mutants of ADO that have higher affinity with AAR. Our preliminary experimental results show that some of the designed mutants enhanced alkane production as predicted.

Finally, solving the protein folding problem is important in improving rational design of proteins. The WSME model can explain the folding pathways of small proteins and is considered to be a promising model to solve the protein folding problem [9,10]. By extending this model, we have previously developed a statistical mechanical model of protein folding that can explain the folding pathways of multi-domain proteins having multiple disulfide bonds. To further extend this model for any types of proteins, here we applied this model to a protein that does not have disulfide bonds and succeeded in predicting its folding mechanism. Thus, our model may be useful for a unified theoretical description of protein folding mechanisms.

References

[1] B.J. Bender, et al.: Biochemistry, **55** (2016) 4748-4763.

[2] R. F. Alford, et al.: J Chem Theory Comput. **13** (2017) 3031-3048.

[3] J. K. Leman, et al.: Nat Methods, **17** (2020) 665-680.

[4] P. E. Wright, et al.: Nat Rev Mol Cell Biol. **16** (2015) 18-29.

[5] J. Shang, et al.: Nature, **581** (2020) 221-224.

[6] X. Liu, et al.: Proc Natl Acad Sci USA. **110** (2013) 14918-14923.

[7] M. Arai, et al.: Adv Exp Med Biol. **1080** (2018) 119-154.

[8] M. Chang, et al.: Biosci Biotech Biochem. **84** (2020) 228-237.

[9] M. Sasai, et al.: Biophys Physicobiol. **13** (2016) 281-293.

[10] M. Arai: Biophys Rev. **10** (2018) 163-181.

Development of Giant Thermal-property Databases for Amorphous Polymer Materials

Yuxuan Liao, Yoshihiro Hayashi
The Department of Mechanical Engineering
The University of Tokyo, Hongo 7-3-1, Bunkyo-ku, Tokyo, JAPAN

We intended to develop a giant thermal-property database for amorphous polymer materials. This year, we have established an automation framework for developing the giant databases, as shown in Figure 1. The automation framework allows us to generate amorphous polymer structures and calculate its thermal conductivity (TC) automatically. The steps are: 1) creation of polymer chain by random walk algorithm, 2) assignment of the force field and atomic charge into each atom, 3) generation of the amorphous polymer cell, 4) running the equilibration simulation by molecular dynamics (MD), 5) checking the convergence of total energy and density, etc. for the equilibration MD, 6) if not converged, restarting the equilibration MD, 7) running the non-equilibrium MD (NEMD) to compute the TC value, 8) collection of TC values for all polymers.

All MD calculations were performed using the corrected heat flux branch of LAMMPS package. We used an AMBER type GAFF2 forcefield. Atomic charges were derived by the Gasteiger method. The particle-particle particle-mesh (pppm) method was employed to compute the long-range Coulombic interaction. In equilibration MD, NPT calculations using Nose-Hoover thermostat and the barostat were run for 5 ns annealing and 8 ns equilibration. All bonds and angles, including those of the hydrogen atoms, were constrained by the SHAKE algorithm, and the time step was set to 1 fs. The TC is calculated by performing the reverse NEMD (RNEMD) simulation proposed by Müller-Plathe, as shown in Figure 2.

We have calculated 500 amorphous polymer systems, with an experimental validation shown in Figure 2(B). The results are organized into a paper, which will be coming online soon.

Moreover, we also calculate the thermal transport properties of amorphous materials, which is published in Nano Energy 2021 [2].

References

[1] **Yoshihiro Hayashi**, Ruimin Ma, **Yuxuan Liao**, et al, Automated calculation system of physical properties with molecular dynamics simulation for polymer informatics (Preparing for submitting)

[2] **Yuxuan Liao** et al, Heat conduction below diffusive limit in amorphous superlattice structures, Nano Energy 84, 105903.

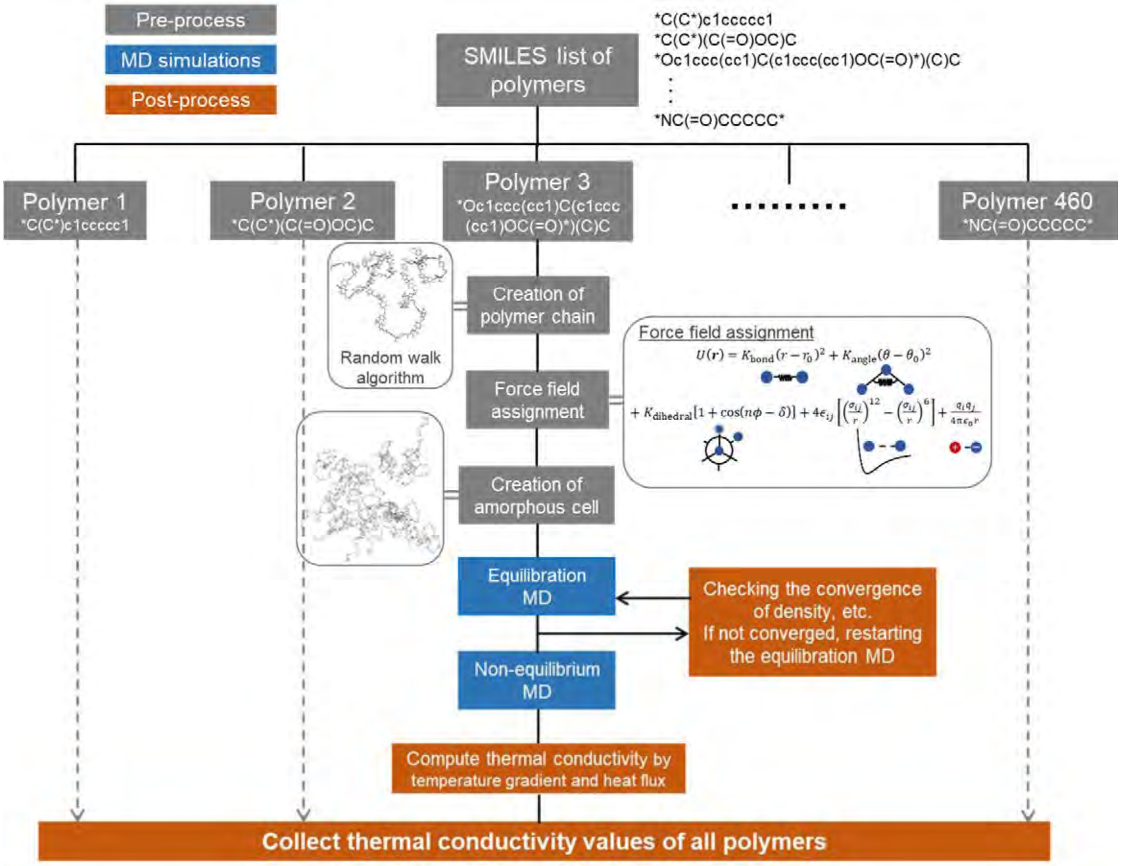

Figure 1 Automation framework for developing the giant thermal-property polymer databases

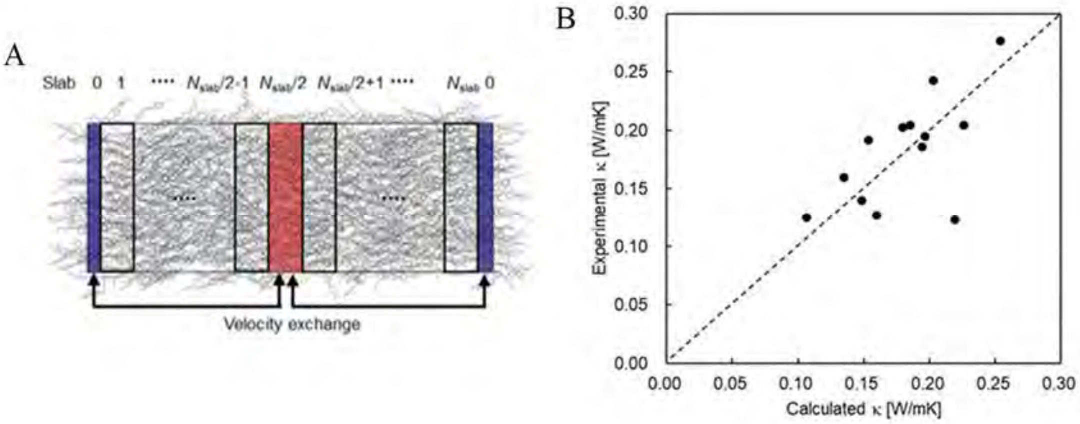

Figure 2. (a) Schematic representation of the simulation box for reverse nonequilibrium molecular dynamics (RNEMD). (b) Comparing the calculated thermal conductivity (κ) and experimental κ for 13 polymers. A dots line indicates calculated κ equal to experimental κ.

Development of Giant Thermal-property Databases for Amorphous Polymer Materials

Yuxuan Liao

The Department of Mechanical Engineering

The University of Tokyo, Hongo 7-3-1, Bunkyo-ku, Tokyo, JAPAN

We intended to develop a giant thermal-property database for amorphous polymer materials. This year, we have 1) optimized the thermal conductivity calculation method and 2) investigated the influence of the classical size effect and the chain length of polymers on the thermal conductivity of amorphous polymers.

The motivation is that 1) Since the calculation is computationally heavy, we need to find out the best NEMD method for our automation system. The Muller-Plathe (MP) method has the advantage of a rapidly converging quantity in temperature gradient rather than a slowly converging heat flux, thus, it can speed up the calculation speed. The results from the MP method are validated by comparing them with the results from the Langevin thermostat, as shown in Fig. 1. Here, a polymer with the ID of P010080 is used as an example. 2) Since the real polymer has extremely long chains consisting of over tens or hundreds of thousand atoms, which is challenging to be calculated with NEMD. The thermal conductivity of polymers typically increases with the chain length. Thus, we need to find out the converged thermal conductivity in terms of the chain length.

Figure. 1 shows the thermal conductivity as a function of chain lengths, which is characterized by the number of atoms per chain. The results show that 20000 atoms per chain are needed to obtain a converged thermal conductivity. The results indicate that heat carriers with long mean free paths (propagons) play an important role in the heat conduction of amorphous polymers.

To give a deeper insight into the underlying physics, we have explored the relaxation process and mean free path of propagons in amorphous materials. Here, we have used amorphous silicon, amorphous silica, and amorphous silicon nitride as examples. We found that the Akhiezer mechanism dominates the relaxation process of propagons [1]. The next step is how to generalize the analysis into amorphous polymers, which is still under investigation.

References

[1] **Yuxuan Liao** et al, Akhiezer Mechanism Dominates Relaxation of Propagons in Amorphous at Room Temperature, arXiv preprint arXiv:2006.07773.

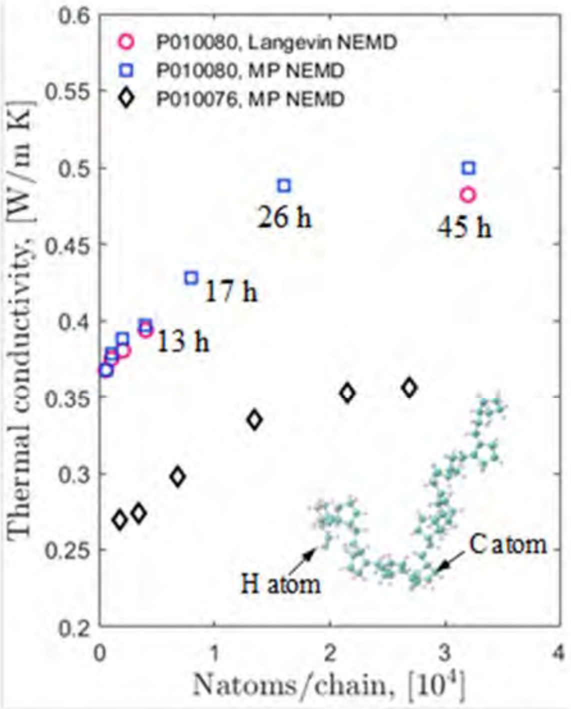

Fig. 1 Thermal conductivity as a function of chain length

Tensor renormalization-group study of spin glasses

Koji Hukushima
Department of Basic Science, University of Tokyo
3-8-1 Komaba, Meguro-ku, Tokyo 153-8902

One of the most important remaining problems in statistical physics is to clarify the low-temperature thermodynamic properties of Ising spin glasses in three dimensions. The search for the ground states is computationally intractable in the sense that it is one of the NP-hard problems in the theory of computation, and the Markov-chain Monte Carlo (MCMC) calculations at finite temperature have extremely slow relaxation phenomena, both of which make large size calculations difficult. Although many computational physical methods derived from spin-glass research, such as the extended ensemble method, have affected other research fields, they have not yet solved the spin-glass problem.

In this study, we aim to break the limit of computational size by applying the tensor renormalization group (TRG) method, which has attracted much attention in recent years, to the spin glass system instead of the MCMC method. We have previously applied TRG to a lattice glass model in two dimensions that exhibits a glass transition in the mean-field limit[1]. There have been a few previous studies that have applied the TRG to spin-glass systems, but they have not been studied extensively. One reason seems to be the problem of numerical accuracy. It has been pointed out that, as a result of frustration, a “negative partition function” appears even though it is originally positive definite, and there is another study showing that this can be solved by very high precision floating-point arithmetic. However, it has been suggested that the numerical accuracy is not realistic for such calculations at low temperature. We proposed a numerical method to detect the ordered phase in Ising spin glasses and explore the possibility of performing the calculation while avoiding the negative partition function problem in TRG. We addressed two specific issues in Ising spin glasses.

(1) Vertically of ferromagnetic phase transition and ferromagnetic limit on the Nishimori line

It is rigorously known that the ferromagnetic transition on the Nishimori line is the ferromagnetic limit on disorder. MCMC calculations suggested that the phase boundary is somewhat reentrant, but this is not definite. The negative partition function problem is considered to appear at the point where the spin glassiness is strong. Therefore, it is expected to be reduced by getting closer to the ferromagnetic side. Here, we determined the ferromagnetic transition temperature on the Nishimori line with high accuracy by calculating the free energy difference under the twisted boundary condition using TRG.

(2)Development of an algorithm to evaluate the spin-glass order parameter by TRG

Here, we developed a method to calculate the spin-glass order parameter by TRG, and performed the calculation for the Ising spin glass model. The spin-glass order parameter is an overlap function, which is defined using two independent systems with the same interactions. There are two main ways to evaluate the expectation values of physical quantities using the TRG method. One is to use the numerical derivative of the free energy, and the other is to use the impurity tensor to construct the measurement tensor of the observables. In any case, it is necessary to devise a way to calculate the spin-glass order parameter using TRG. We constructed a tensor network for a replica coupled system that introduces an interaction between two systems, and succeeded in calculating the order parameter on the Nishimori line as its derivative with respect to the coupling.

[1] K. Yoshiyama and K. Hukushima: J. Phys. Soc. Jpn. **89**, (2020) 104003.

Parallel Bayesian computation in material science

Koji Hukushima
Department of Basic Science, University of Tokyo
3-8-1 Komaba, Meguro-ku, Tokyo 153-8902

Recent development of various experimental and measurement technologies has allowed us to obtain a large amount of high-precision data, but the methodologies for data analysis have not yet caught up with the improvement of experimental techniques. On the other hand, the development of machine learning, such as deep learning, has also been remarkable in recent years, and the practical application of machine learning to materials science has attracted much attention. However, the black-boxed application of deep learning to materials science is powerful for "prediction" but not necessarily suitable for "understanding".

In this project, we attempted to apply and develop Bayesian inference based on statistical models that incorporate physical laws as much as possible, using data obtained from experiments as input. Since Bayesian statistical models using physical processes are nonlinear in general, they cannot be computed analytically. In the 1980s, the Markov-chain Monte Carlo (MCMC) method was found to be useful for Bayesian inference, and it started to be applied in large scale. In recent years, the amount of data to be analyzed has increased and the amount of computation per step has become large, and Markov chains which are bound by causality, are not necessarily easy to parallelize.

Therefor, we applied population annealing (PA), which is a population type Monte Carlo method, not based on Markov chains, to the problem of Bayesian statistics of materials science. PA, proposed by Hukushima-Iba(2003), has been introduced as a computational method for statistical mechanical models, and recently it has been working on large-scale parallel computations including GPGPU. This method has a large number of nearly independent computations and is compatible with parallel computation, which significantly reduces the computational time by parallel computation. In addition, an advantage of PA over MCMC methods is that the partition function in statistical mechanics, which is the normalization constant for the probability distribution, can be obtained as a by-product of the calculation. The partition function, which is called evidence in the context of Bayesian inference, is an important quantity that gives an indicator of model selection.

Furthermore, since the leave-one-out cross validation (LOOCV), which is one of the cross-validation methods, can be formulated by the reweighting method often used in statistical physics, its implementation is also carried out at the same time in PA. By systematically comparing the evidence and LOOCV, we developed a methodology for data analysis that integrates hyper-parameter estimation and model selection.

The proposed method has been implemented in linear regression models with noise. It has been pointed out that L_1 regularization-based methods such as LASSO lead to bias, and in order to avoid this, a direct method of analyzing sparsity as an L_0 regularization problem has been considered. However, the L_0 regularization problem is known to be NP hard, and no efficient algorithm is known. We successfully solved this problem in a realistic time using PA, and also succeeded in evaluating the magnitude of the noise by computing the evidence. This means that we have established a new data-analysis method for sparse modeling, including uncertainty evaluation. We believe that it can develop materials science through our sampling methods such as noise magnitude estimation and model selection, which are a step further than conventional Bayesian estimation usually attributed to optimization calculations.

Study on relaxations of fluctuation with the event-chain algorithm

Y. Ozeki and Y. Osada

Graduate School of Informatics and Engineering, The University of Electro-Communications

We investigate the applicability of the event chain algorithm [1, 2] to the relaxation of fluctuation for the nonequilibrium relaxation (NER) method, [3,4] which has been an efficient numerical method to evaluate critical exponents. The event-chain algorithm has introduced for the Monte Carlo (MC) simulation with a multi-spin-flip algorithm, and shows estimation of the dynamical critical exponent $z \sim 1$ [1], which indicates a faster dynamics as compared with those with a single-spin-flip algorithm such as the the Metropolis one.

Previously, we investigated it for its applicability to the NER method and estimated the dynamical exponent z by means of the dynamical scaling analysis. The initial state of relaxation is prepared as an all-aligned state. As an example, we analyze the classical XY model in three dimensions; $\mathcal{H} = -J \sum_{\langle ij \rangle} \mathbf{S}_i \cdot \mathbf{S}_j$, where summation for $\langle ij \rangle$ is taken over all nearest-neighboring sites on a simple cubic lattice. Since the relaxation is much fast in the simulation with the event chain algorithm, we proposed the relaxation of the absolute value of the magnetization as the dynamical order parameter,

$$|m(t)| = \left\langle \left(N^{-1} \sum_i \mathbf{S}_i \right)^2 \right\rangle^{1/2} \tag{1}$$

and confirmed the efficiency of it.

Let us show the result of dynamical scaling analysis. The relaxation of the order parameter $|m(t|)$ are calculated for $2.182 \le T \le 2.222$ on a 300^3 simple cubic lattice up to an observation time of 100 MCSs. About 864 samples are taken for statistical averaging. The estimations are plotted in Fig. 1. Using the improved dynamical scaling analysis for the NER data [4], we analyze the dynamical scaling form,

$$|m(t,T)| = \tau^{-\lambda} Y[t/\tau], \tag{2}$$

where $\tau(T)$ is the relaxation time and λ is a dynamical critical exponent. The result is shown in Fig. 2 with $T_{\rm c} = 2.202$ and $z = 1.47$.

The exponents estimated by dynamical scaling is used to deviate slightly because of corrections to scaling. To estimate the exponent more precisely,

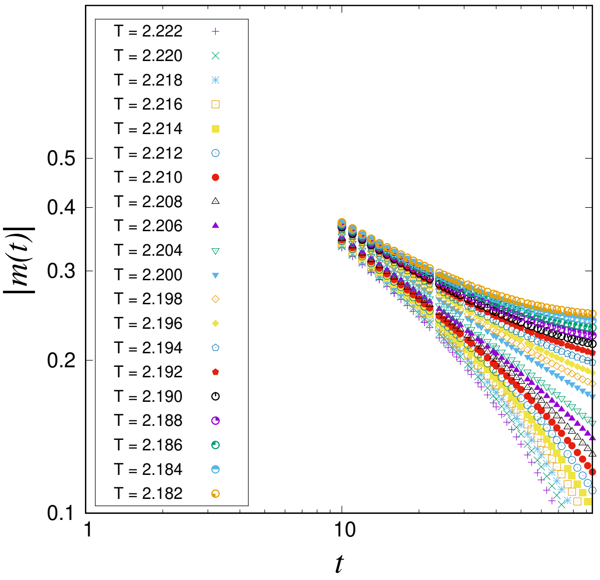

Figure 1: Relaxation of $|m(t)$ for the 3D XY model in $2.182 \le T \le 2.222$ with the interval $\Delta T = 0.002$.

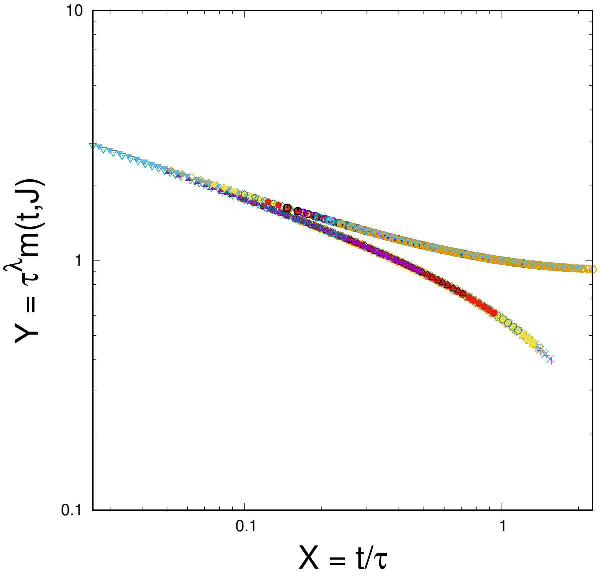

Figure 2: Scaling plot for the data in$2.182 \le T \le 2.222$ in Fig. 1

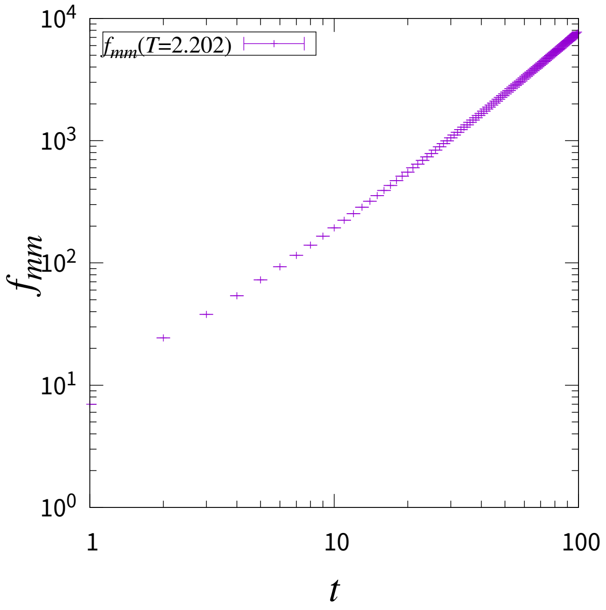

Figure 3: Relaxation of fluctuation f_{mm} calculated at $T = 2.202$

we analyze the relaxation of fluctuation,

$$f_{mm}(t) \equiv N \left[\frac{\langle |m(t)|^2 \rangle}{\langle |m(t)\rangle^2} - 1 \right], \tag{3}$$

at the transition temperature $T_c = 2.202$ estimated above. This function is expected to diverge as

$$f_{mm}(t) \sim t^{\lambda_{mm}}, \tag{4}$$

where $\lambda_{mm} = d/z$. Calculations are carried out on a 200^3 simple cubic lattice up to the observation time of 100 MCSs. About 645120 samples are taken for statistical averaging. The result is plotted in Fig. 3. We evaluate the numerical derivative

$$\lambda_{mm}(t) \equiv \frac{\mathrm{d} \log f_{mm}(t)}{\mathrm{d} \log t}, \tag{5}$$

and plot $d/\lambda_{mm}(t)$ in fig. 4, where the horizontal axis is modulated as $1/t^{0.704}$ to show a precise asymptotic value for $t \to \infty$. The result is $z = 1.67$, which is a little greater than the value obtained by the dynamical scaling. Consequently, the event-chain algorithm can be used in the NER analysis with an efficient relaxation performance, and would be applicable to various slowly relaxing problems such as frustrated and/or random systems.

References

[1] Y. Nishikawa *et. al.*, *Phys. Rev.* E**92 063306 (2015)**

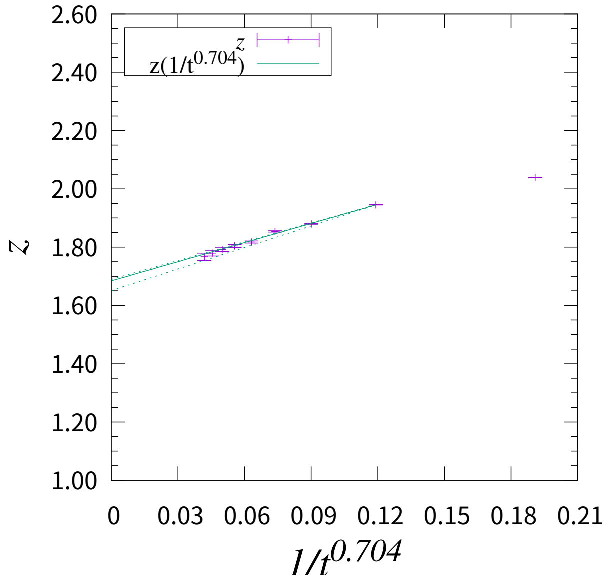

Figure 4: Critical exponent z is estimated as $t \to \infty$.

[2] **M. Michel** *et. al.*, *Europhys. Lett.* **112 20003 (2015)**

[3] **Y. Ozeki and N. Ito,** *J. Phys.: Math. Theor.* **40 R149 (2007).**

[4] **Y. Echinaka and Y. Ozeki,** *Phys. Rev.* **E94 043312 (2016).**

[5] **A. P. Aloysius and M. Harsenbusch,** *Physica* **A201 593 (1993)**

Numerical study of bulk-edge correspondence and topological phases: From quantum to classical mechanics

Y. Hatsugai
Department of Physics, University of Tsukuba
1-1-1 Tennodai, Tsukuba 305-8571, Ibaraki, Japan

As for standard topological phenomena, non trivial topology of the bulk is reflected in the boundary physics which can be, in principle, easily accessible by experiments. This is the bulk-edge correspondence[1] that is widely used for various systems from quantum to classical ones. In this project, we have tried to extend the universal feature of the bulk-edge correspondence by using numerical methods. In this context, the adiabatic pump proposed by Thouless more than 30 years ago is quite special since the center of mass of the bulk, that has topological origin, is the physical observable although the edge physics is not directly observed by a realistic finite speed. Experimental realization the adiabatic limit including the gapless edge states is difficult although it is quite useful for clear understanding of topological character of the pumping[2]. We have extended the bulk-edge correspondence of the topological pumping for various systems with strong correlation[3, 4]. Another extension of the bulk-edge correspondence for the higher order topological phases is the bulk-corner correspondence. We demonstrated its validity for classical mechanical systems on a Kagome lattice[5]. We further applied numerical methods to various topological phenomena among quantum and classical ones. [6, 7, 8].

References

[1] Y. Hatsugai, "Chern Number and Edge States in the Integer Quantum Hall effect", Phys. Rev. Lett. 71, 3697 (1993).

[2] Y. Hatsugai and T. Fukui, " Bulk-edge correspondence in topological pumping", Phys. Rev. B 94, 041102(R) (2016).

[3] Y. Kuno and Y. Hatsugai, "Interaction-induced topological charge pump", Phys. Rev. Research 2, 042024 (2020)

[4] K. Kudo and Y. Hatsugai, "Adiabatic heuristic principle on a torus and generalized Streda formula", Phys. Rev. B 102, 125108 (2020). Also K. Kudo, Y. Kuno and Y. Hatsugai in preparation.

[5] H. Wakao, T. Yoshida, H. Araki, T. Mizoguchi, and Y. Hatsugai, "Higher-order topological phases in a spring-mass model on a breathing kagome lattice", Phys. Rev. B 101, 094107 (2020).

[6] T. Mizoguchi, Y. Kuno, and Y. Hatsugai, "Detecting Bulk Topology of Quadrupolar Phase from Quench Dynamics", Phys. Rev. Lett. **126**, 016802 (2021).

[7] T. Yoshida, K. Kudo, H. Katsura, and Y. Hatsugai, "Fate of fractional quantum Hall states in open quantum systems: Characterization of correlated topological states for the full Liouvillian", Phys. Rev. Research **2**, 033428 (2020).

[8] T. Yoshida, T. Mizoguchi, and Y. Hatsugai, "Mirror skin effect and its electric circuit simulation", Phys. Rev. Research **2**, 022062(R) (2020).

Numerical study on low-energy states of quantum spin systems

Hiroki NAKANO
Graduate School of Material Science, University of Hyogo

In condensed matter physics, we often have to tackle many-body problems, in which it is difficult to estimate physical quantities precisely. Quantum spin systems are such typical cases. To examine the systems, under circumstances, numerical approaches have widely and effectively been employed in various studies. A lot of computational investigations have been carried out and gave us useful information of the target systems.

Within the field of quantum spin systems, three methods are effectively used. One is the numerical diagonalization method. The second is the quantum Monte Carlo (QMC) method. The third one is the density matrix renormalization group (DMRG) method. Each of the methods has advantages; at the same time, it also disadvantages. In the QMC simulations, large systems can be treated irrespective of the spatial dimensions of the systems although it is difficult to precisely evaluate physical quantities in frustrated systems due to the negative sign problem. When spatial dimension of a target system is one, on the other hand, the DMRG method is very useful irrespective of whether the target system includes frustration or not. For the cases when the spatial dimension is larger than one, however, this method is still under development. The numerical diagonalization method can be applied irrespective of the presence of frustrations and the spatial dimension. However, this method has a serious weak point that only very small system sizes can be treated. To overcome this disadvantage, we developed a hybrid-type parallelized code of Lanczos diagonalization[1]. This Lanczos-diagonalization code enables us to treat various large systems that have not been previously treated yet within this method. We, thus, study various quantum spin systems by this method as a primary approach in this project.

In the project in 2020, we tackled the $S = 1/2$ Heisenberg antiferromagnet on the orthogonal-dimer lattice. This system was examined based on the calculations of 36- and 40-site systems of the same Lanczos diagonalization[2], which pointed out that the third characteristic ratio defined as J_2/J_1 appears between the edge of the exact-dimer phase and the edge of the Neel-ordered phase; here, J_1 is the amplitude of the exchange coupling on orthogonal-dimer bonds and J_2 is the amplitude of the exchange coupling forming the simple square lattice. In order to clarify whether or not the behavior showing the presence of the third characteristic ratio of J_2/J_1 survives when the system becomes larger, we additionally calculated the 44-site cluster of this system, which has not been treated before. As a result, our calculations for 44-site system show the behavior that is consistent with those for 40-site system. Our examination contributes to our deeper understandings of the quantum antiferromagnets with frustrations. Further investigations would clarify nontrivial effects of quantum nature and frustration.

References

[1] H. Nakano and A. Terai: J. Phys. Soc. Jpn. **78** (2009) 014003.

[2] H. Nakano and T. Sakai, J. Phys. Soc. Jpn. **87** (2018) 123702.

Thermal effects on quantum frustrated magnetisms

Tokuro SHIMOKAWA
Theory of Quantum Matter Unit, Okinawa Institute of Science and Technology Graduate University
Onna-son, Okinawa 904-0412

Quantum frustrated magnetism is well known as a source of exotic states of matter, but investigating the true nature, particularly at finite temperatures, is still a tough and challenging problem. In this fiscal year, we investigated both the ground state and finite-temperature properties of several two-dimensional frustrated magnetism by means of exact diagonalization (ED) and quantum typicality (QT) methods. We will here briefly report our numerical activities with the ISSP supercomputer.

1) S=1/2 breathing bilayer kagome (BBK) magnets for $Ca_{10}Cr_7O_{28}$ magnet

Motivated by recent experimental results on a new quantum spin liquid candidate, $Ca_{10}Cr_7O_{28}$, we investigated the ground state and finite-T properties of the S=1/2 BBK model. We developed a new ED code specialized for high fields [1], which enables us to treat much larger system sizes at most 2000 spin clusters and compute spin dynamics without any bias in our quantum Hamiltonian. We succeeded in reproducing bow-tie and ring-like features in quantum spin dynamics, which inelastic neutron scattering (INS) measurements reported as signatures of the quantum spin liquid state of this material. We also computed the temperature dependences of specific heat and equal-time spin structure factors by means of the QT method, and we found a realization of a spiral spin liquid state at moderate temperatures having a ring-like structure in equal-time spin structure factors. [2]

2) Signatures of finite-T phase transition in S=1/2 Shastry-Sutherland model

Recent experimental results under high pressures revealed the intermediate plaquette-singlet phase in $SrCu_2(BO_3)_2$ compound. In this intermediate phase, we naturally expect to have a spontaneous mirror symmetry breaking at a finite temperature; however, detecting the possible finite-T transition has been a challenging problem, such as in the traditional ED method because of the smallness of accessible system sizes. We used the quantum typicality (QT) method for this problem and succeeded in capturing some clear signatures of the finite-T phase transition. For example, the temperature dependence of the real-space spin-spin correlation is one of the valuable quantities to see the signatures: we could see two possible mirror symmetry broken correlation patterns at low temperatures depending on the random initial spin configurations used in QT method. We also discussed the relationship to the material $SrCu_2(BO_3)_2$. These results are published in Phys. Rev. B. [3]

References

[1] H. Ueda, S. Yunoki, and T. Shimokawa, in preparation.

[2] T. Shimokawa, R. Pohle, and N. Shannon, in preparation.

[3] T. Shimokawa: Phys. Rev. B **103** (2021) 134419.

Global thermodynamic functions extended to nonequilibrium steady states

Naoko NAKAGAWA
Department of Physics, Ibaraki University
2-1-1 Bunkyo, Mito, Ibaraki 310-8512

We study spatially inhomogeneous systems, such as liquid-gas coexistence and multicomponent systems, from the viewpoint of global thermodynamics [1]. We conducted numerical research on the following two topics by utilizing the supercomputer at ISSP. In both topics, we performed molecular dynamics simulation using LAMMPS.

(1) Numerical experimental protocol to determine the standard entropy and free energy of two-component fluids:
The "standard" entropy or free energy plays a fundamental role to describe the thermodynamic properties of pure substances. This is also the case in mixtures to distinguish their variety and industrial applicability. We have developed a numerical protocol for determining the standard free energy of mixtures from thermodynamic measurements by using knowledge of fluctuating thermodynamics and information thermodynamics. The protocol is valid to numerical experiments, especially to molecular dynamics. In order to verify the validity of our protocol, we organized the molecular dynamics simulation taking a simple example on which we can make a theoretical prediction. We concluded the validity and the efficiency of our protocol as a method to determine the standard free energy, mixing entropy, solubility, and so on.

(2) Osmotic pressure in a binary mixture separated by a semipermeable membrane:
We have applied global thermodynamics to a binary mixture in thermal conduction, which is separated by a semipermeable membrane. It predicts how the osmotic pressure changes from equilibrium. One of the point to be examined is whether the osmotic pressure is deviated from a conventional expectation, which corresponds to the balance of local chemical potential. To clarify this point, we start large-scale numerical experiments. The resources used were mainly the L9 CPU of System C (because LAMMPS has not been installed in the new System B). The simulation was run on 9 nodes in 360 parallel computation using MPI. This allowed us to perform long calculations on a system with up to 10^5 particles to measure the local and global thermodynamic quantities in the steady state with a sufficient relaxation time and a sufficiently large number of samples. We are now checking the effect of the finite system size.

References

[1] N. Nakagawa and S.-i. Sasa: J. Stat. Phys. **177** (2019) 825.

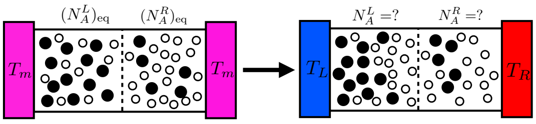

Figure 1: Configuration of the investigated system with two component fluid and a semipermeable membrane. The distribution of particles is modified by heat current.

Multiscale simulation of polymeric fluids and solids

Takahiro MURASHIMA
Department of Physics, Graduate School of Science, Tohoku University,
6-3, Aramaki-aza-Aoba, Aoba-ku, Sendai, Miyagi 980-8578

To develop multiscale simulation directly connecting macroscopic continuum system and microscopic molecular particle system, we need a suitable boundary condition for molecular dynamics simulation. For long years, extensional flows were difficult problems in molecular dynamics simulation. Recently, we have developed UEFEX algorithm [1] applicable for the Langevin thermostat. This new algorithm can solve the extensional flow problems. In this algorithm, the flow frame and the simulation frame were separately treated. In the similar way, we have developed a QR-decomposition based deformation algorithm [2] and applied to a tensile deformation of polymeric solid. In this fiscal year, we extended this QR-decomposition based algorithm to be applicable for rotational flow, rotational shear flow, pure shear flow, and so on. Fig.1 shows the rotational shear flow.

Fig. 1: Snapshots of rotational shear flow. Non-symmetric deformation rate tensor applied. Simulation box (the flow frame) is rotating clockwise. Black frame represents “the MD frame”.

The rotational shear flow is typical in cavity flow and contraction and expansion flow. I would like to apply this technique to the ring-linear polymer blend [3], where the topological constraint of ring polymer causes unique phenomena; for example, the viscosity overshoot in a biaxial elongational flow.

References

[1] T. Murashima, K. Hagita, T. Kawakatsu, J. Soc. Rheol. Jpn. 46 (2018) 207.

[2] T. Murashima, S. Urata, S. Li, Euro. Phys. J. B, 92 (2019) 211.

[3] T. Murashima, K. Hagita, T. Kawakatsu, arXiv:2102.02452.

Ground state and dynamical properties of the $J_1 J_2 K$-Heisenberg model on the square lattice

Matthias GOHLKE, Tokuro SHIMOKAWA
Theory of Quantum Matter Unit, Okinawa Institute of Science and Technology
1919-1 Tancha, Onna-son, Okinawa 904-0495

In the absence of conventional magnetic order of spin-dipolar moments, ordering with higher-order moments like spin-quadrupoles may occur. Such spin-quadrupolar—or spin-nematic (SN)—order was found theoretically in spin-1 model with biquadratic spin-exchange [1].

Magnets with spin-$\frac{1}{2}$ degrees of freedom, however, can only exhibit a SN states if two spin-$\frac{1}{2}$ are combined into an effective spin-1 [2]. In fact, such SN states on bonds has theoretically been observed in frustrated ferromagnets on the square lattice with dominant ferromagnetic Heisenberg exchange, J_1, antiferromagnetic next-nearest neighbor exchange, J_2, and cyclic permutation, K. It was found that the condensation of a two-magnon bound state, at strong magnetic fields along the z-axis, can stabilize a phase with bond-nematic order [3].

Experimentally, the nature of such a ground state is intrinsically difficult to verify, due to the lack of probes that couple directly to the spin-quadrupole moments. Instead, it is necessary to examine the dynamics of a SN: A continuous symmetry for the director of a spin-quadrupole remains, that give rise to a gapless Goldstone mode [4, 5].

We started by studying the square-lattice frustrated J_1-K model [2],

$$\begin{aligned}\mathcal{H} &= J_1 \sum_{\langle i,j\rangle} \boldsymbol{S}\cdot\boldsymbol{S} \\ &+ K \sum_{(i,j,k,l)} \left(P_{ijkl} + P_{ijkl}^{-1}\right) + h_z \sum_i S_i^z \ ,\end{aligned} \tag{1}$$

where J_1 represents dominant ferromagnetic Heisenberg exchange between nearest neighbor spins, K the cyclic ring exchange around squares, and h_z the Zeeman coupling to a magnetic field along the z-axis.

Using iDMRG and the matrix product states (MPS) framework, we confirm the existence of the bond-nematic phase in an extended range of $K/|J_1|$ while being sandwiched between the fully-polarized phase at high fields and a long-range magnetically ordered phase at low fields. A recently developed exact diagonalization method near saturation [6], shows a good agreement with iDMRG on cylindrical geometries with circumference $L_{\mathrm{circ}} \geq 6$ sites.

Given the ground state wave function as an MPS, dynamical properties can then be studied by applying a time-evolution unitary $U(dt)$ represented as a matrix product operator. In doing so, we observe the condensation of two-magnon bound state at the corresponding wave vector of the SN state. Within the SN phase, we observe a gapless mode with vanishing spectral weight in the $\boldsymbol{q} \to 0$ & $\omega \to 0$ limit as predicted by prior mean-field studies. We do, however, observe some relevant qualitative differences, whose origin we are currently investigating.

References

[1] K. Harada and N. Kawashima, Phys. Rev. B **65** (2002) 052403.

[2] A. Andreev and I. Grishchuk, Sov. Phys. JETP **60** (1984) 267.

[3] N. Shannon, T. Momoi, and P. Sindzingre, Phys. Rev. Lett. **96** (2006) 027213.

[4] R. Shindou, S. Yunoki, and T. Momoi, Phys. Rev. B **87**, (2013) 054429.

[5] A. Smerald, H. T. Ueda, and N. Shannon, Phys. Rev. B **91** (2015) 174402.

[6] H. Ueda, S. Yunoki, and T. Shimokawa, in preparation.

Development of entanglement optimization method

Kenji HARADA
Graduate School of Informatics, Kyoto University, Kyoto 606-8501, Japan

There are various interesting algorithms on tensor networks to calculate the free energy and critical properties of classical systems and the ground state of quantum systems. In these algorithms, we often need to control the entanglement structure in a tensor network. For example, we need to remove the short entanglement loop structure in grid tensor networks to calculate a critical fixed point tensor.

In this project, we try to optimize an entanglement structure in a local tensor network directly. In particular, we consider the development of a new optimization method for a branching operator[1]. To make a branching operator, we usually use the truncation optimization for a local tensor network. Instead, we directly reduce the entanglement after applying a branching operator. Combining automatic differentiation and manifold optimization techniques, we can construct an iteration method to reduce the entanglement by a branching operator.

Applying the new method to a tensor network representation of a Born machine[2, 3], we can directly transform a MPS into a MERA tensor network[4, 5]. In the case of the Born machine of the Ising model, we can construct a correct MERA tensor network from an exact MPS of the Born machine. In two-dimensional tensor networks, it is hard to transform the PEPS into a tree tensor network. We need to transform the PEPS into the MERA tensor network directly. It is also necessary to develop a similar optimization method of a branching operator for the two-dimensional network.

[1] K. Harada, “Entanglement branching operator,” Phys. Rev. B **97**,045124 (2018).

[2] Z.-Y. Han, J. Wang, H. Fan, L. Wang, and P. Zhang, “Unsupervised Generative Modeling Using Matrix Product States,” Phys. Rev. X, **8**, 031012 (2018).

[3] S. Cheng, L. Wang, T. Xiang, and P. Zhang, “Tree tensor networks for generative modeling,” Phys. Rev. B, **99**, 155131 (2019).

[4] G. Vidal, “Entanglement Renormalization,” Phys. Rev. Lett., **99**, 220405 (2007).

[5] G. Vidal, “Algorithms for entanglement renormalization,” arXiv:0707.1454v1 (2007).

Kinetics of phase transition and polyamorphism

Kazuhiro Fuchizaki, Hiroki Naruta, and Katsumi Nakamura
Department of Physics, Ehime University, Matsuyama 790-8577

In FY2020, we mainly treated the structural variation during the amorphous–amorphous transition in SnI_4. We conducted *in situ* synchrotron x-ray measurements along the isotherm at room temperature from 30 GPa down to 1.1 GPa, using a diamond anvil cell to obtain the structure factor required for the analysis. We also succeeded in applying an idea of nonequilibrium relaxation to machine learning (ML) for predicting the order-disorder transition temperature in a 2-dimensional (2D) Ising system. The last project was unscheduled at the outset. We exploited System B in the following scene.

Amorphous–amorphous transition in SnI_4 [1]

We decided to analyze the structure employing reverse Monte Carlo (RMC) simulation because it is much advantageous than a usual Fourier inversion in the following respect: we can extract 3D structural information, from which partial radial distribution functions are obtainable. Before conducting the RMC fit of the experimental structure factor $S(k)$, we had to determine the system's density and initial configuration transferred to the fit as input. For this purpose, we prepared a system, which "mimics" the actual system at the measured thermodynamic conditions, using classical isothermal and isobaric molecular dynamics simulation for a system composed of 2744 rigid regular tetrahedral molecules confined in a cubic box with periodic boundary conditions. System B took care of this process.

We call the system, whose density is to be determined, a target system. Our model system [2] was known to capture the real system below 1 GPa. Hence, we first searched in a trial-and-error manner thermodynamic conditions at which the model system "looks like" the real system, at least in the length scale k_{m}^{-1}, where k_{m} denotes the principal-peak position of $S(k)$. The conditions thus found were listed in Table 1 of Ref. [1]. The resultant model systems after equilibration were all metastable liquids.

Our method for density estimation from $S(k)$ presumes the existence of a reference state that has a similar structure on the length scale of k_{m}^{-1}. Let n_{t} be a trial number density. We redefine the system's length by multiplying $n_{\mathrm{t}}^{-1/3}$ and calculate the structure factor, $S_{\mathrm{t}}(k)$, using the scaled length. If we denote the principal-peak position of $S_{\mathrm{t}}(k)$ by k_{t}, we can define the difference, $\delta k = k_{\mathrm{t}} - k_{\mathrm{m}}$, as a function of n_{t}. The target's number density, n, is then estimated by the condition, $\delta k/\delta n_{\mathrm{t}}|_n = 0$. After finalizing the density, we resized the whole system uniformly so that not only the length of sides of the system but also the interatomic distances were updated. We transferred the configuration along with the density to the RMC program.

The RMC simulation (see Fig. 1 for an example) could reveal that the high-density amorphous (HDA) state is divided into two states: the high-pressure HDA state beyond 14 GPa containing isolated Sn atoms and the low-pressure HDA state below 14 GPa consisting of deformed molecules connected by metallic I_2 bonds. In the latter state, the molecular shape becomes C_{3v}-like just before the transition to the low-density amorphous (LDA) state, in which molecules recover the original T_d symmetry. This local symmetry change has been detected on the liquid–liquid transition of $\mathrm{SnI_4}$, suggesting the strong coupling between the local symmetry and the global order parameter of density.

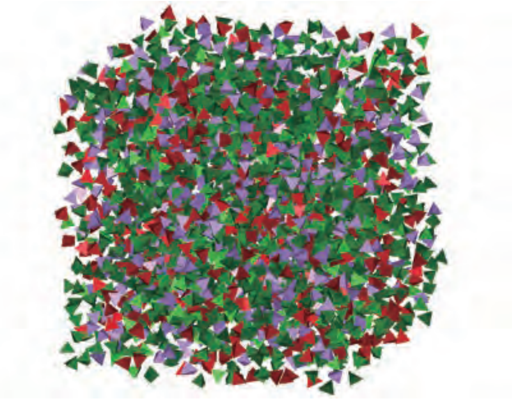

Figure 1: The RMC-simulation result obtained from $S(k)$ at 3.3 GPa, just before the transition to the LDA state on decompression, is visualized as an example. $\mathrm{SnI_4}$ units (not necessarily molecules) are depicted in red, green, and purple when they are regularly tetrahedral shaped, severely deformed, and even dissociated, respectively.

Applying nonequilibrium-relaxation scheme to ML for detecting a phase transition [3]

There seems no need to explain the significance of applying the ML technique to problems across the various disciplines today. One example in physics problems is detecting the phase transition without any information about the "answers" *a priori*, as intelligibly illustrated for a 2D Ising model [4]. Tanaka and Tomiya identified that the weights, more strictly, their sum W_{sum}, in a convolutional neural network (CNN) can play a relevant order parameter [4]. The identification then readily prompted us to apply the idea of nonequilibrium relaxation [5] to the detection.

We employed the same CNN with one hidden layer besides the input and output layers. To investigate the learning processes in detail, we realized the CNN in-house. We used the same 2D Ising system on an $L \times L$ lattice with periodic boundary conditions imposed for the examination, where $L = 32$, 64, 128, and 256. We used as training data the systems well equilibrated at the specified temperature. Here, the temperatures constituted the labels, which were one-hot encoded into the binary vector.

Initially, we set W_{sum} to zero, which corresponds to the completely "unlearned" state. W_{sum} soon evolved into one of the two states with learning, depending on the pattern's temperature, leaving W_{sum} at the transition temperature T_{c} unlearned. We could thus identify T_{c} as the fixed point in the label space. Because W_{sum} with labels on both sides of the fixed point soon bifurcates with learning, a CNN with proper filters implemented can judge the location of a T_{c} at an early stage of learning. In this context, the existence of hidden layers is practically relevant to efficiency.

However, such a T_{c} irregularly depends on L; T_{c} does not follow the relationship, $T_{\mathrm{c}}(L) \sim L^{-1}$, expected from the finite-size scaling. The unusual L-dependence happened to make such an $L = 32$ system predict the transition temperature remarkably close to the exact one, and large systems used as training data do not necessarily bring about a better result for predicting T_{c}.

References

[1] K. Fuchizaki, A. Ohmura, H. Naruta, and T. Nishioka, submitted to J. Phys.: Condens. Matter.

[2] K. Fuchizaki and Y. Asano, J. Phys. Soc. Jpn. **84**, 064601 (2015).

[3] K. Fuchizaki, K. Nakamura, and D. Hiroi, J. Phys. Soc. Jpn. **90** (2021), in press.

[4] A. Tanaka and A. Tomiya, J. Phys. Soc. Jpn. **86**, 063001 (2017).

[5] N. Ito, Physica A **192**, 604 (1993).

Investigation of the molecular origins of the mechanical and thermal properties of realistic bio-polymers using all-atomistic molecular dynamics

Okazaki Susumu

Department of Advanced Materials Science,

The University of Tokyo, Kashiwa-no-ha, Kashiwa, Chiba 277-8581

We have studied the impact fractures of amorphous glassy polymer materials using all-atomistic molecular dynamics (MD) simulations for the past few years [1, 2]. In the second half of the past year, we continued the pursuit of the molecular scale understanding of the yielding and the glass transition phenomena using the protocols employing large-scale parallel MD simulations and analyses established earlier, by utilizing the supercomputer resources at ISSP.

In the first half, we investigated the stress origins of the yielding process of the brittle material poly-(methyl methacrylate) (PMMA) using the stress decomposition method we developed previously, and found that 1) the brittle materials share the same stress origins as the ductile materials; 2) the dense and bulky sidechains of PMMA makes it a brittle material by lowering its flexibility and increasing the stress strength. [3]

In the second half, we thoroughly studied the glass transition phenomenon by analyzing the MD trajectories, and realized that various degrees of freedom, including the translation and rotation of polymer chains, the dihedral angle rotation, and some angle bending, defreeze at different temperatures, within the observation time of current MD simulation time scale. This causes the volume, the order parameter usually used to define glass transition, to show a broad glass transition over decades of kelvins. The same phenomenon is believed to occur in experimental conditions, although the impact of the faster degrees of freedom are less.

References

[1] K. Fujimoto, Z. Tang, W. Shinoda, S. Okazaki, All-atom molecular dynamics study of impact fracture of glassy polymers. I: Molecular mechanism of brittleness of pmma and ductility of pc, Polymer 178(12) (2019) 121570.

[2] Z. Tang, K. Fujimoto, S. Okazaki, All-atom molecular dynamics study of impact fracture of glassy polymers. II: Microscopic origins of stresses in elasticity, yielding, and strain hardening, Polymer 207(20) (2020) 122908.

[3] Z. Tang, K. Fujimoto, S. Okazaki, A comparison of the brittle PMMA with the ductile PC on the elasticity and yielding from a molecular dynamics perspective, Polymer (2021), in press.

Global Optimization of Tensor Renormalization Group using the Corner Transfer Matrix

Satoshi MORITA
Institute for Solid State Physics, University of Tokyo
Kashiwa-no-ha, Kashiwa, Chiba 277-8581

Tensor network methods attract much attention as powerful tools for computing strongly correlated many-body problems. The tensor renormalization group method (TRG) [1] and the higher-order TRG (HOTRG) [2] provide a way to calculate coarse-grained tensor based on the singular value decomposition. Both the methods do information compression by solving local optimization problems. Approximations in these methods are locally optimal but not so for contraction of the whole tensor network. The second renormalization group method (SRG) [3] and the higher-order SRG method (HOSRG) [2] introduce global optimization of tensor renormalization group. Although these methods drastically improve accuracy, calculation of the environment tensor requires performing the forward-backward iterations.

To resolve this problem, we propose another approximation for global optimization [5]. We replace the environment tensor with the corner transfer matrices (CTM) and the edge tensors, which can be updated by using the CTM renormalization group (CTMRG) [4]. Moreover, we introduce additional decomposition, which reduces computational cost of tensor contraction for the coarse-grained tensor. The computational time of our algorithm (CTM-TRG) in two dimensions scales as $O(\chi^6)$ against the bond dimension χ while the HOTRG and HOSRG have $O(\chi^7)$ scaling.

We perform benchmark calculations in the Ising model on the square lattice and show that the time-to-solution of the proposed algorithm is faster than that of other methods. As shown in Fig. 1, our proposed method shows better accuracy than HOTRG and compatible to HOSRG.

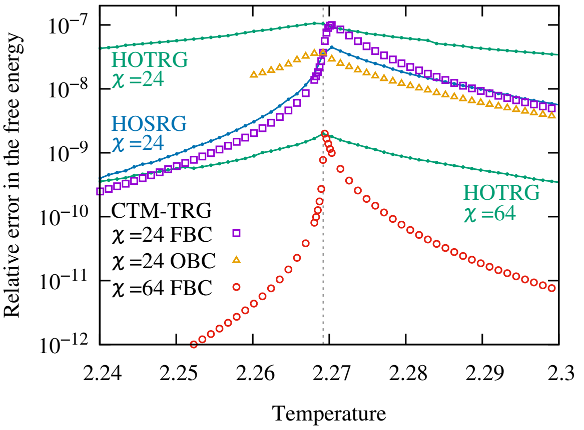

Figure 1: Relative errors in the free energy measured in the Ising model on the square lattice.

References

[1] M. Levin and C. P. Nave, Phys. Rev. Lett. **99**, 120601 (2007).

[2] Z. Y. Xie, J. Chen, M. P. Qin, J. W. Zhu, L. P. Yang, and T. Xiang, Phys. Rev. B **86**, 045139 (2012).

[3] Z. Y. Xie, H. C. Jiang, Q. N. Chen, Z. Y. Weng, and T. Xiang, Phys. Rev. Lett. **103**, 160601 (2009).

[4] T. Nishino and K. Okunishi, J. Phys. Soc. Jpn. **65**, 891 (1996).

[5] S. Morita and N. Kawashima: Phys. Rev. B **103**, 045131 (2021).

Dynamics of Phonon Entanglement Creation between Remote Electron-phonon Systems

Kunio ISHIDA

School of Engineering and Center for Optics Research and Education
Utsunomiya University, Yoto, Utsunomiya, Tochigi 321-8585

Coherent control of quantum mechanical states is important to realize various states of quantum materials. In particular, quantum entanglement is a measure for quantum mechanical features, and thus we have focused on its control method by photoirradiation[1-3]. In the present study, we study the dynamics of entanglement generation between remote systems by irradiation of a quantized light pulse by employing a model of coupled electron-phonon-photon systems described by[2]

$$\mathcal{H} = \sum_{i=1}^{3} \Omega_i {c_i}^{\dagger} c_i + \sum_{j=1}^{2} \left[\omega a_j^{\dagger} a_j + \{\mu(a_j^{\dagger} + a_j) + \varepsilon\} \frac{\sigma_z^j + 1}{2} + \{\sum_{i=1}^{3} \nu_i ({c_i}^{\dagger} + c_i) + \lambda\} \sigma_x^j \right].$$

Solving the time-dependent Schrödinger equation by numerical calculation on the System B at ISSP, we found that the quantum mutual information for phonons reveals the dynamics of phonon entanglement generation[4].

In order to investigate the dynamical behavior of phonon states in both material systems, we performed a Schmidt decomposition on the electron-phonon-photon states in which the entire system is divided into the phonons and the electrons and photons. In this case, the wavefunction $|\Phi\rangle$ is described by

$$|\Phi\rangle = \sum_{\mathrm{n}} \sqrt{\lambda_n} |\eta_n\rangle |\theta_n\rangle,$$

where $|\eta_n\rangle$ and $|\theta_n\rangle$ denote the phonon states and the electron-photon states, respectively.

We calculated the dynamical behavior of λ_n and the entanglement entropy between phonons in $|\eta_n\rangle$ as functions of time, and found that the entanglement in the singular vector $|\eta_0\rangle$ for the largest singular value λ_0 is weak, while $|\eta_1\rangle$ and $|\eta_2\rangle$ for the second and the third largest singular values λ_1 and λ_2 are strongly entangled. The phonon entanglement is generated as λ_1 and λ_2 increase, i.e., the entanglement generation process corresponds to the conversion of the phonon states from a pure decomposable state to a mixed state of entangled states.

References

[1] K. C. Lee, et al., Science **334**, 1253(2011).
[2] F. Borjans, et al., Nature **577**, 195 (2020).
[3] K. Ishida, Eur. Phys. J. **D73**, 117 (2019).
[4]K. Ishida and H. Matsueda, arXiv: 2005.14615.

A Theoretical Study for Thermal Unfolding of Proteins with Quite Similar Native Structure

Takashi YOSHIDOME

Department of Applied Physics, Graduate School of Engineering, Tohoku University,
6-6-05, Aoba, Aramaki, Aoba-ku, Sendai 980-8579

Recently, drug design for inhibiting the folding of proteins has begun. This indicates the importance of the elucidation of the molecular mechanism of folding process of proteins for drug design.

In the present study, we focused on the two proteins that have quite similar native structures but different structures at the transition state [1]. They are goat alpha-lactalbumin and human lysozyme, respectively. To elucidate the molecular mechanism of the difference in the transition state structures among goat alpha-lactalbumin and human lysozyme, we performed molecular dynamics (MD) simulations for their unfolding processes at 400 K. We successfully reproduced the experimental results for the transition state structures. By carefully analyzing the simulation results, we elucidated that the difference in the transition state structures arose from the existence of the Ca^{2+} ion in the native structure of the goat alpha-lactalbumin, and from difference in the length of the secondary structures among the two proteins.

The calculations were performed using the F4cpu and L4cpu in the system B, and L4cpu in the system C. We used Gromacs program suite [2] for the MD simulations. CHARMM22 force field [3] and TIP3P model [4] were used for the proteins and ions and for the water molecule, respectively.

References

[1] T. Oroguchi, M. Ikeguchi, M. Ota, K. Kuwajima, and A. Kidera: J. Mol. Biol. **371** (2007) 1354.

[2] H. J. C. Berendsen, D. Van der Spoel, R. van Drunen: Comput. Phys. Commu. **91** (1995) 43 (1995).

[3] A. D. MacKerell, Jr. *et al.*: J. Phys. Chem. B, **102** (1998) 3586.

[4] W. L. Jorgensen, J. Chandrasekhar, and J. D. Madura: J. Chem. Phys. **79** (1983) 926.

A Method for Analyzing Protein Dynamics: A Hybrid of Cryo-Electron Microscopy Experiment and Molecular Simulation

Takashi YOSHIDOME

Department of Applied Physics, Graduate School of Engineering, Tohoku University,
6-6-05, Aoba, Aramaki, Aoba-ku, Sendai 980-8579

Cryo-electron (Cryo-EM) microscopy is one of the methods for analyzing the three-dimensional structures of biomolecules like proteins. In this method, the three-dimensional electron density map of a protein is reconstructed using a lot of two-dimensional electron density maps of the protein projected from several projection angles. To reconstruct the three-dimensional electron density map, the projection angle for each map is necessary to estimate. A method is the "common-line method" [1], but verification method for the estimation using the common-line method has been lacking.

In the present study, we investigated whether generative topographic mapping (GTM) method [2] can be used for an estimating method. The method enables us to estimate the function describing the two-dimensional electron density maps as the function of the projection angle. Thus, the estimation of the projection angle can be possible with the GTM method. To demonstrate the possibility of the estimation, simulations for cryo-EM microscopy experiments were performed. In computing the maps, the protein was rotated by assigning the polar coordinates z=(θ, ϕ) as follows: the variable θ was fixed to 0°; and the variable ϕ was randomly assigned in the range of $0° \leq \phi \leq 360°$. It was found that estimating the projection angle for each projection image was successful using the GTM method. In future, our method will be improved in order to apply to actual cryo-electron microscopy experimental data.

The calculations were performed using the F4cpu and L4cpu in the system B, and L4cpu in the system C. We used our custom-made programs for the calculations. The program of the GTM method was implemented using the Python3 program language.

References

[1] S. J. Ludtke, P. R. Baldwin, and W. Chiu: J. Struct. Biol. **128** (1999) 82.

[2] C. M. Bishop, M. Svensén and C. K. I. Williams: Neural Comput. **10** (1998) 215.

Large-Scale Metadynamics Simulations for Water and Aqueous Solutions

Hiroki NADA

National Institute of Advanced Industrial Science and Technology (AIST),
16-1 Onogawa, Tsukuba, Ibaraki 305-8569

Phase transitions in water and aqueous solutions, such as crystallization and amorphous formation, have been studied in fields of physics and chemistry from long ago. Nevertheless, there still exist a lot of unresolved issues concerning phase transitions of water and aqueous solutions. For example, some of metastable phase transitions that are postulated to occur in water at a large supercooling, such as liquid-liquid phase separation (LLPS), have not yet been demonstrated.

Molecular dynamics (MD) simulations have often been used to study the structure of water at a large supercooling. However, evidence for the occurrence of LLPS can hardly be obtained by standard MD simulations.

In this study, a metadynamics (MTD) method was introduced to search for metastable phases of water at a large supercooling. An MD simulation in which the MTD method was implemented (MTD-MD simulation) was performed for a liquid water phase consisting of 2880 water molecules using ISSP system C with high efficiency. Following a previous study [1], two discrete oxygen-oxygen radial distribution functions represented by Gaussian window functions were used as collective variables.

A free energy landscape obtained by the MTD-MD simulation for the TIP4P/Ice model at 233 K indicated two local minima. One of the minima corresponded to a low-density water phase, and the other corresponded to a high-density water phase. The high density water phase had a structure resembling the structure of high-density ice VII. At present, it is difficult to judge whether the observed two different water phases corresponded to water phases formed by the postulated LLPS of supercooled water. More detailed studies are needed to elucidate it in the future.

References

[1] H. Nada: Sci. Rep. **10** (2020) 4708

Metadynamics Simulation Analysis of Various Cluster Structures Appearing in Calcium Carbonate Supersaturated Solution

Hiroki NADA
National Institute of Advanced Industrial Science and Technology (AIST),
16-1 Onogawa, Tsukuba, Ibaraki 305-8569

Terrestrial water on the Earth contains mineral components, such as calcium carbonate ($CaCO_3$), with a high concentration and, hence, the formation of $CaCO_3$ crystals occurs ubiquitously. Industrially, the control of $CaCO_3$ crystal nucleation is crucial in connection with issues concerning the formation of scales, causing blockage of drainage pipes and reduction of thermal efficiency of boilers. However, the control of it is quite difficult. This is because the mechanism of $CaCO_3$ crystal formation from a supersaturated solution still has remained unclear.

Atomistic simulations, such as molecular dynamics (MD) simulations, are helpful to elucidate the structure and thermodynamic stability of precursors. However, the timescale of phenomenon that can be analyzed by an MD simulation is normally on the order of microsecond or shorter. This timescale is too short to pursue all possible precursor structures that may stably appear in a solution.

In this study, a metadynamics (MTD) method was introduced to overcome the timescale problem of MD simulation [1]. An MD simulation in which the MTD method was implemented (MTD-MD simulation) was performed for a supersaturated $CaCO_3$ aqueous solution. The simulation was performed efficiently by parallel computing with multiple nodes of ISSP system B.

A free energy landscape (FEL) obtained with the MTD-MD simulation indicated stable and metastable aggregates formed in the solution, each of which correspond to a local minimum on the FEL). The results are helpful to consider the mechanism of $CaCO_3$ crystal nucleation via precursors.

References

[1] A. Laio and M. Parrinello: Proc. Natl. Acad. Sci. USA **99** (2002) 12562.

Transport properties of multiple-q states in frustrated magnets

Kazushi AOYAMA
Department of Earth and Space Science, Graduate School of Science, Osaka University
Machikaneyama-cho, Toyonaka-shi, Osaka 560-0043

Transport phenomena in magnetic systems reflect dynamical properties of interacting spins, such as magnetic excitations and fluctuations. In this work, we theoretically investigate transport properties of two-dimensional antiferromagnetic insulators, putting emphasis on how nature of spin textures characterized by more than one ordering wave vectors **Q**'s (multiple-**Q** states) is reflected in spin transport. In the J_1-J_3 classical Heisenberg model on the triangular lattice in a magnetic field, the Hamiltonian is given by

$$\mathcal{H} = \frac{1}{2}\sum_{i,j} J_{ij}\mathbf{S}_i \cdot \mathbf{S}_j - H\sum_i S_i^z \qquad (1)$$

with $J_{ij} = J_1\delta_{j\in N1(i)} + J_3\delta_{j\in N3(i)}$, where $Nn(i)$ denotes the nth nearest neighbor sites of site i. For ferromagnetic J_1 and antiferromagnetic J_3, it was shown by Okubo, Chung, and Kawamura [1] that single-**Q**, double-**Q**, and triple-**Q** states are stabilized in the low, middle, and high field regions, respectively. In particular, the triple-**Q** state is known to be the skyrmion lattice phase, and its higher-temperature region is another phase, the so-called Z phase, in which there are randomly distributed domains of the skyrmion and antiskyrmion lattices.

The spin current and the associated spin conductivity $\sigma^s_{\mu\nu}$ are respectively given by

$$\begin{aligned} \mathbf{J}_s^z(t) &= -\frac{1}{2}\sum_{i,j} J_{ij}\mathbf{r}_{ij}(\mathbf{S}_i \times \mathbf{S}_j)^z, \\ \sigma^s_{\mu\nu} &= \frac{1}{T\,L^2}\int_0^\infty dt\,\langle J^z_{s,\nu}(0)\,J^z_{s,\mu}(t)\rangle, \quad (2) \end{aligned}$$

where $\mathbf{r}_{ij}$ and L denote a vector connecting two sites i and j and the linear system size, respectively. We numerically integrate the semiclassical equation of motion with initial equilibrium spin configurations generated by Monte Carlo simulations and calculate the time correlations $\langle J^z_{s,\nu}(0)\,J^z_{s,\mu}(t)\rangle$ at each time step [2, 3].

It is found that the longitudinal spin-current conductivity σ^s_{xx} is significantly enhanced at the transition temperature between the triple-**Q** and Z phases, whereas at the higher-temperature transition between the Z and paramagnetic phases, such an anomalous behavior is not obtained. This enhancement of σ^s_{xx} is quite similar to the divergent behavior of σ^s_{xx} at the Kosterlitz-Thouless-type topological transition [2, 3] in which long-lifetime vortex excitations play a crucial role. In the present case, the topological object of the skyrmion may be relevant to the spin transport, but further analysis is necessary to understand the origin of the significant enhancement of the spin-current conductivity at the transition into the skyrmion lattice phase.

References

[1] T. Okubo, S. Chung, and H. Kawamura, Phys. Rev. Lett. **108**, 017206 (2012).

[2] K. Aoyama and H. Kawamura, Phys. Rev. B **100**, 144416 (2019).

[3] K. Aoyama and H. Kawamura, Phys. Rev. Lett. **124**, 047202 (2020).

$1/N$ bias of the hump of Binder parameter for Potts Model

Hiroshi WATANABE
Department of Applied Physics and Physico-Informatics, Keio University
Yokohama, Kanagawa 223-8522, Japan

The Binder parameter has been widely used to analyze critical phenomena [1]. Since the parameter is the dimensionless, the parameters for different system sizes are collapsed into a single curve by scaling only horizontal axis. The Binder parameter is usually a monotonic function, but it sometimes peculiar behavior. A typical example of this is the Potts model. The Binder parameter of the Potts model is non-monotonic function and exhibits a hump near the criticality. Since the hump has the system-size dependence, the Biner parameter of Potts model cannot be collapsed into a single curve by scaling only horizontal axis. The humps become larger as the system size increases and these humps interfere with the finite-size scaling analysis especially for the high-temperature side of the critical point. We also found that the peak value of the hump strongly depends on the MCs as well as the system size. In order to identify the origin of the hump, we study the Binder parameter of $Q = 3$ Potts model. We found that the Binder parameter can be decomposed into a high- and a low-temperature components, and that the humps originate from the low-temperature one. THe system size and MCs dependence of the peak value of the low-temperature component of the Binder parameter U_{low} is shown in Fig. 1. One can see that the MCs dependence becomes large as the system size increases. These MCs dependence are found to be almost independent of the relaxation time. The MCs dependence originate from the strong $1/N$ bias of the Binder parameter as it is a function of the expected value. Therefore, this bias can be removed by the jackknife resampling method. However, since the $1/N$ bias is removed and the N-infinity limit still exhibit system-size-dependence, the finite size scaling function appears to be system size dependent. The size-dependence of the peak position is stronger for larger values of Q, and the peak value is expected to be infinite at N infinity for systems involving the first-order transition. The existence of the universal finite-size scaling function in the limit of infinite system size for systems involving the continuous transitions is still non-trivial, and therefore, the further study is required.

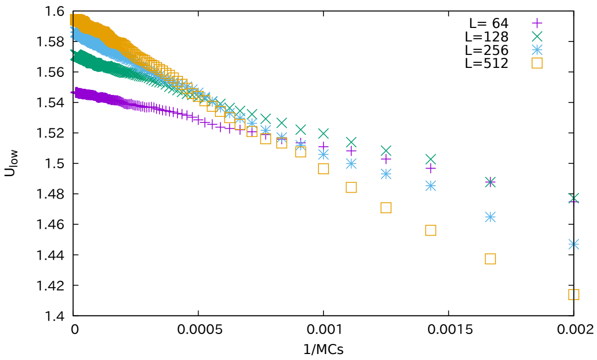

Figure 1: The system size and MCs dependence of the peak value.

References

[1] K. Binder, Z. Phys. B Cond. Matt. , vol. 43, pp. 119-140 (1981).

Magnetism in the Multiple-Spin Exchange Model on the Honeycomb Lattice

Chitoshi YASUDA
Department of Physics and Earth Sciences, Faculty of Science,
University of the Ryukyus, Okinawa 903-0213, Japan

^{3}He atoms adsorbed on graphite form the commensurate solid layer regarded as the spin-1/2 quantum spin system on a triangular lattice at a certain density of ^{3}He. There are not only an exchange of ^{3}He atoms between two neighbor atoms but also that among three or more neighbor atoms. In relation to the solid ^{3}He, the multiple-spin exchange (MSE) model on the triangular lattice has been extensively studied. Ground states and thermodynamic properties of the model have been investigated using various methods [1,2,3]. In particular, the model has attracted attention owing to the existence of novel states such as the quantum spin liquid and the spin-nematic state, and owing to the effects of fluctuations on ordered phases with chirality. Recently, a new quantum spin liquid is experimentally observed in the solid ^{3}He layer. This layer is a monolayer ^{3}He adsorbed on graphite preplated with atomic layers of deuterium hydride. At low density of ^{3}He, it was suggested that there exists the quantum spin liquid with novel dependences of the heat capacity and the magnetic susceptibility on temperature. The details of this experimental work are not yet clear, however, it is suggested that the solid ^{3}He layer forms a honeycomb lattice.

In this project, we research the classical MSE model with the two-spin and six-body ring exchange interactions on the honeycomb lattice using numerical methods. The ground state is investigated using the conjugate gradient method. In this method, we need to prepare many random spin states as the initial states because of avoidance of the trap to a metastable state. When the external magnetic field is zero, the ground state in the region where the contribution of the six-body exchange interaction is small becomes an antiferromagnetic state. This is the same ground state as the antiferromagnetic Heisenberg model on the honeycomb lattice. On the other hand, in the region where the contribution of the six-body exchange interaction is large, the eight-sublattice structure with a nearest-neighbor correlation function and a finite sublattice scalar chirality is stabilized as the ground state. When an external magnetic field is applied, the antiferromagnetic state becomes the canted state at very small fields, while the eight-sublattice structure can be maintained up to a certain finite field. When the applied magnetic field is increased, the eight-sublattice structure changes to the large sublattice structure, the four-sublattice structure, and the canted state, sequentially.

In this project, we also research thermodynamic properties of the classical MSE model using the Monte Carlo simulation with the exchange Monte Carlo method. We confirm its usefulness in the classical MSE model on the honeycomb lattice.

References

[1] C. Yasuda, D. Kinouchi, K. Kubo: J. Phys. Soc. Jpn. **75** (2006) 104705.

[2] C. Yasuda, Y. Uchihira, S. Taira, K. Kubo: J. Phys. Soc. Jpn. **87** (2018) 104704.

[3] S. Taira, C. Yasuda, T. Momoi, K. Kubo: J. Phys. Soc. Jpn. **88** (2019) 014701.

Microwave transmission through a Josephson junction array

Tsuyoshi YAMAMOTO
Institute for Solid State Physics, University of Tokyo
Kashiwa-no-ha, Kashiwa, Chiba 277-8581

Recent technological development enables us to perform quantum simulation using artificial quantum systems . Its use for solving quantum many-body problems is one of hot topics in condensed matter physics. The superconducting circuits are one of promising platforms for such an attempt. However, background random charge in superconducting circuits hinders a “good” simulation. Our study facilitates the opposite view. Namely, randomness in a circuit provides to simulate quantum disordered systems [1].

In one-dimensional systems, localization occurs no matter how the disorder is weak. While disorder in the one-dimension system with long-range interactions induces a transition into an insulating phase, its properties is known little. In this study [2], we show microwave transmission through a Josephson junction array which represents one of the simplest one-dimension disordered systems with the Coulomb interaction.

A one-dimensional nature of the system allows for the most comprehensive analytical and numerical approaches. We find signatures of the insulating modes in the microwave transmission for a wide frequency range. At high frequencies, the high accurate numerics reveals that the localization property affects the microwave transmission, which has been missed in the previous work [3], by the detailed comparison with the analytics (Fig. 1). At low frequencies, by performing the parallel computation with respect to configurations to take a disorder average, we gather several non-trivial pieces of information about statistics of the transmission.

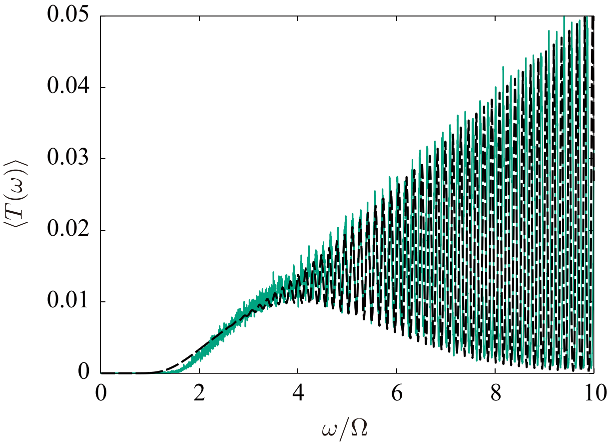

Figure 1: The frequency dependence of the transmission. The green line is the numerics and the black dashed line is the analytics.

The versatility of the design of Josephson-junction arrays motivates their further development for quantum simulation.

References

[1] R. Kuzmin *et al.*, Nat. Phys. **15**, 930 (2019).

[2] T. Yamamoto, L. I. Glazman, and M. Houzet, Phys. Rev. B **103**, 224211 (2021).

[3] M. Houzet and L. I. Glazman, Phys. Rev. Lett. **122**, 237701 (2019).

Molecular dynamics simulation of liquid $BaTiO_3$

T. Hashimoto
National Institute of Advanced Industrial Science and Technology (AIST),
Tsukuba Central 2, 1-1-1 Umezono, Tsukuba, Ibaraki 305-8568, Japan

The structure of oxides in a liquid state at high temperature is being studied by the containerless method using a floating furnace. The field strength is expressed as $F = Z_\mathrm{M}/(r_\mathrm{MO} - r_\mathrm{O})^2$, where Z_M, r_MO, and r_O are the cation charge, the bond length of the cation and oxygen, and the ionic radius of oxygen. In SiO_2, which has a large F, the coordination number of oxygen around Si, whether solid or liquid, is 4, but in ZrO_2, Y_2O_3, etc., where F is small, the coordination number of oxygen around the cation drops significantly in the case of liquids[1]. Ti has an F value in the middle of them, but in the case of $BaTi_2O_5$, it has been reported that n_TiO drops significantly from the crystalline case to the liquid case[2]. Furthermore, it has been reported that the temperature dependence of r_TiO and n_TiO is $\partial r_\mathrm{TiO}/\partial T < 0$ and $\partial r_\mathrm{TiO}/\partial T < 0$. In the case of $BaTiO_3$, it was reported by X-ray scattering and neutron scattering by ^{46}Ti-rich and ^{48}Ti-rich samples that n_TiO is reduced from 6 for crystals to about 4.4 for liquids at 2073 K[4]. However, the temperature dependences of r_TiO and n_TiO are not known. In addition, the validity of the partial radial distribution function obtained by the empirical potential structure refinement (EPSR) method using experimental data has not been fully investigated. We calculated the structure of liquid $BaTiO_3$ by first-principles molecular dynamics simulations.

The calculations were performed using the plane wave pseudopotential method (QUANTUM-ESPRESSO), ultrasoft pseudopotential (GBRV), and GGA (PBE). The density data from Paradis *et al.*[4] was extrapolated to the high temperature side and low temperature side. We calculated at 3500, 3000, 2500, 2000, 1500, 900 K using 135 atoms, using the (N, V, T) ensemble and the velocity scaling method.

The partial radial distribution functions of the liquid $BaTiO_3$ at 2000 K obtained by this study[5] were compared with those by the EPSR method at 2073 K[3]. The Ti-O results were in good agreement with each other, but Ba-Ba and Ti-Ti results were inconsistent. The reason for this is that the pair weighting factor contained in $S(Q)$ is small for both neutron scattering and X-ray scattering, especially for Ti-Ti, so there is a possibility that the interatomic interaction cannot be obtained correctly by the EPSR method. However, r_TiO and n_TiO were in good agreement with the experiment. Liquid $BaTiO_3$ had the same temperature dependence of r_TiO and n_TiO as liquid $BaTi_2O_5$.

[1] L. Skinner *et al.*, Phys. Rev. Lett. **112**, 157801 (2014).

[2] O. L. G. Alderman *et al.*, J. Phys. Chem. C **120**, 26974 (2016).

[3] O. L. G. Alderman *et al.*, J. Phys.: Condens. Matter **31**, 20LT01 (2019).

[4] P.-F. Paradis *et al.*, Appl. Phys. A **79**, 1965 (2004).

[5] T. Hashimoto *et al.*, J. Phys. Soc. Jpn **90**, 044604 (2021).

Tensor-Network Renormalization Study of Finite-Size Conformal Spectrum

Atsushi Ueda and Masaki Oshikawa
Institute for Solid State Physics, University of Tokyo
Kashiwa-no-ha, Kashiwa, Chiba 277-8581

April 30, 2021

We have studied the finite-size effects of classical 2D systems, using Tensor Network Renormalization(TNR). Based on the finite-size scaling theory of conformal field theory(CFT) [1], we demonstrated that it is possible to reconstruct an effective quantum Hamiltonian from the spectrum of the renormalized tensors. Tracking the effective Hamiltonian at each scale allows to numerically construct the renormalization group (RG) flow. We performed it for the classical Ising and XY model as concrete examples, as shown in Figs. 1 and 2.

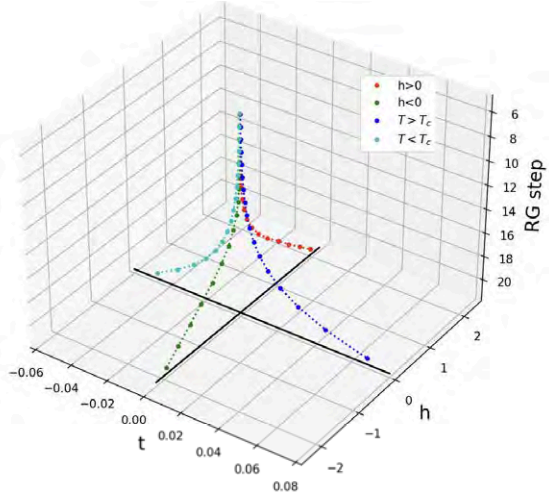

Figure 1: The numerically computed RG flow of the Ising model. t and h denote the deviations from the fixed point, corresponding to the reduced temperature $T - T_c$ and the magnetic field. The RG flows away from the fixed point induced by the relevant perturbations t and h are visualized.

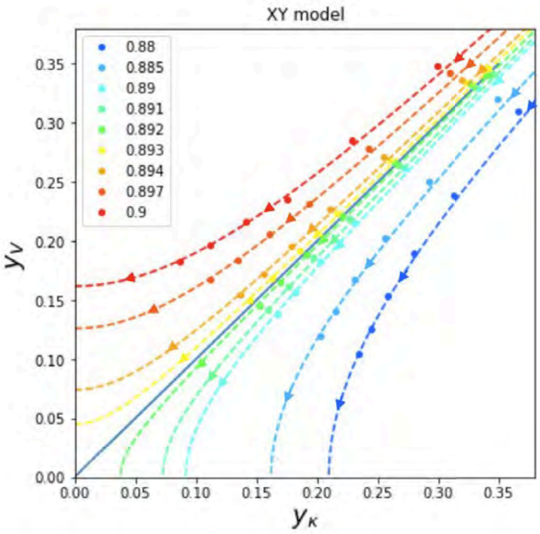

Figure 2: The numerically computed RG flow of the XY model. y_K and y_V are the perturbations corresponding to the spin-wave stiffness and the vortex fugacity, respectively. Our numerical construction gives a quantitative verification of the celebrated Kosterlitz RG flow [2].

Throughout the study above, we also investigated the effect of the finite bond cutoff, which had been often overlooked previously. We showed that there emerges an effective correlation length $\xi_D = D^\kappa$ that is observed for Matrix Product State(MPS) [3], by mapping renormalized tensors to a reduced density matrix. As the exponent κ becomes smaller when the central charge c is large, the focus of our study ($c = 2$) turns out to call for a massive calculation. Thus, we are in attempt to implement a parallel computation of TNR with the supercomputer. More details of our study will be reported elsewhere [4].

References

[1] J. L. Cardy, *Conformal invariance and universality in finite-size scaling*, Journal of Physics A: Mathematical and General 17, L385 (1984).

[2] J. M. Kosterlitz, *The critical properties of the two-dimensional xy model*, Journal of Physics C: Solid State Physics 7, 1046 (1974).

[3] Frank Pollmann, Subroto Mukerjee, Ari M Turner, and Joel E Moore, *Theory of finite-entanglement scaling at one-dimensional quantum critical points*, Physical Review Letters, 102(25):255701, (2009).

[4] A. Ueda and M. Oshikawa, in preparation.

Magnetic field dependence of the thermal Hall effect based on the augmented quasiclassical equations

Takafumi KITA
Department of Physics, Hokkaido University
Sapporo, 060-0810

Charging of vortices in the equilibrium superconducting state was studied before calculating linear responses such as the thermal Hall effect. The results are reported below.

Vortices in type-II superconductors have not only a single magnetic flux quantum but also accumulated charge. It is known that the vortex-core charging is caused by three forces: (i) the Lorentz force [1], (ii) pair-potential-gradient (PPG) force [2], and (iii) the pressure difference arising from the slope in the density of states (SDOS) [3]. Recently, augmented quasiclassical (AQC) equations with these forces were derived by incorporating the next-to-leading-order contributions in the expansion of the Gor'kov equations in terms of the quasiclassical parameter $\delta \equiv 1/k_{\rm F}\xi_0$ [4], where $k_{\rm F}$ is the Fermi wavenumber and ξ_0 is the coherence length. Numerous studies on the charging in an isolated vortex were performed [4], but the magnetic field dependence of the vortex-charging has not been fully calculated. To this end, we calculated the vortex-core charging in two-dimensional s-wave superconductors with the Abrikosov vortex lattice due to the Lorentz and PPG forces by using the AQC equations. The SDOS pressure is now absent for this case with the cylindrical Fermi surface. The fixed parameters are the magnetic penetration depth as $\lambda_0 = 5\xi_0$, Thomas–Fermi screening length as $\lambda_{\rm TF} = 0.03\xi_0$, and quasiclassical parameter as $\delta = 0.03$.

Figure 1 plots the spatial variation of the charge density due to the Lorentz and PPG forces at temperature $T = 0.2T_{\rm c}$ and the average flux densities $\bar{B} = 0.15B_{\rm c2}$, $0.42B_{\rm c2}$, and $0.88B_{\rm c2}$, respectively, where $T_{\rm c}$ is the transition temperature and $B_{\rm c2}$ is the upper critical field. Figure 2 shows the spatial variation of the charge density due to the PPG force at temperatures $T = 0.2T_{\rm c}$ and $0.5T_{\rm c}$, respectively. The charge caused by the Lorentz force has a strong field dependence with a peak and can be enhanced substantially from the value of an isolated vortex as shown in our previous work [5]. Moreover, we show in this report that the charge caused by the PPG force monotonically decreases as the magnetic field increases.

These calculations require a fine mesh of space and momenta when differentiating the Green's functions and self-energies numerically. Therefore, we performed parallel calculations using the ISSP supercomputer.

References

[1] F. London, *Superfluids* (Dover, New York, 1961), Vol. 1, p. 56.

[2] N. B. Kopnin, J. Low Temp. Phys. **97** (1994) 157.

[3] D. I. Khomskii and A. Freimuth, Phys. Rev. Lett. **75** (1995) 1384.

[4] H. Ueki, M. Ohuchi, and T. Kita, J. Phys. Soc. Jpn. **87** (2018) 044704.

[5] W. Kohno, H. Ueki, and T. Kita, J. Phys. Soc. Jpn. **85** (2016) 083705.

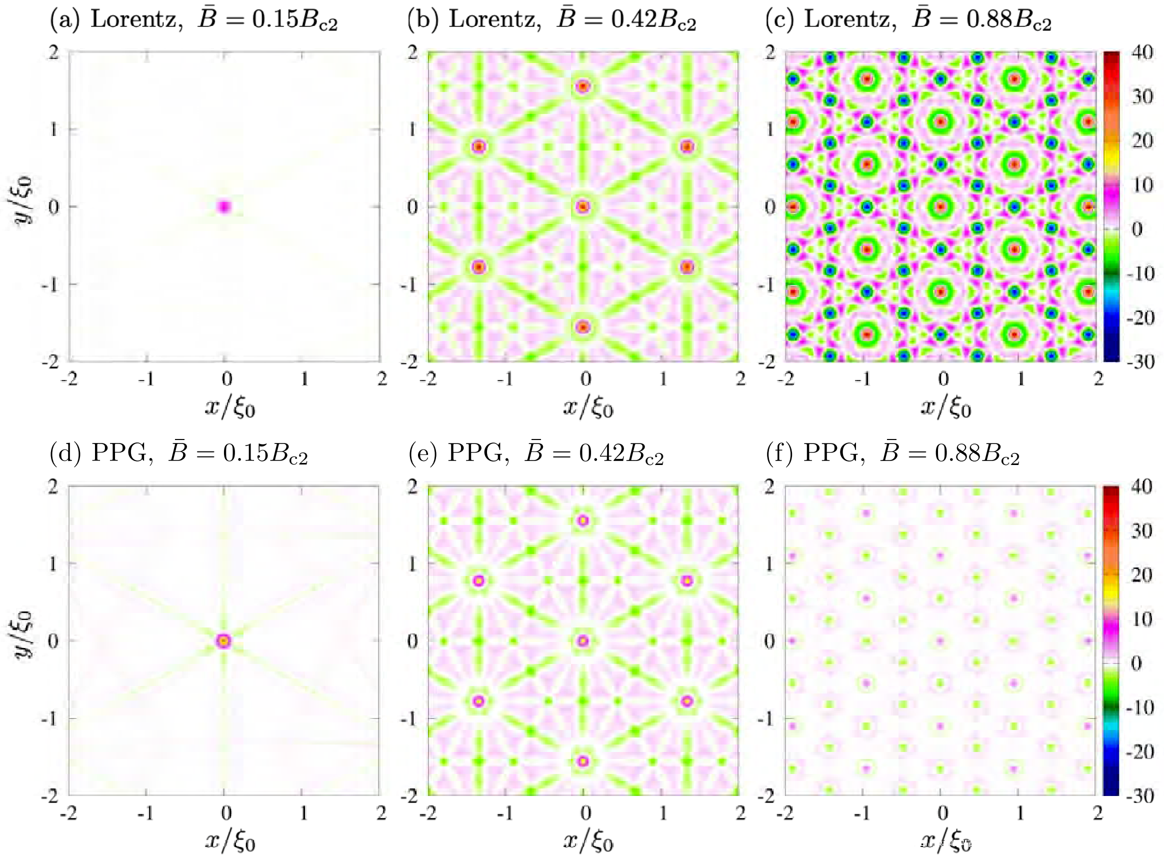

Figure 1: Spatial dependence of the charge density $\rho(\boldsymbol{r})$ due to the Lorentz force ((a), (b), and (c)), and the PPG force ((d), (e), and (f)) at temperature $T = 0.2T_{\mathrm{c}}$ in units of $\rho_0 \equiv \Delta_0\epsilon_0 d/|e|\xi_0^2$ on a square grid with x and y ranging from $[-2\xi_0, +2\xi_0]$ for the average flux densities $\bar{B} = 0.15B_{\mathrm{c2}}$, $0.42B_{\mathrm{c2}}$, and $0.88B_{\mathrm{c2}}$ from left to right, respectively. Δ_0 is the energy gap at zero temperature
0 is
the electron

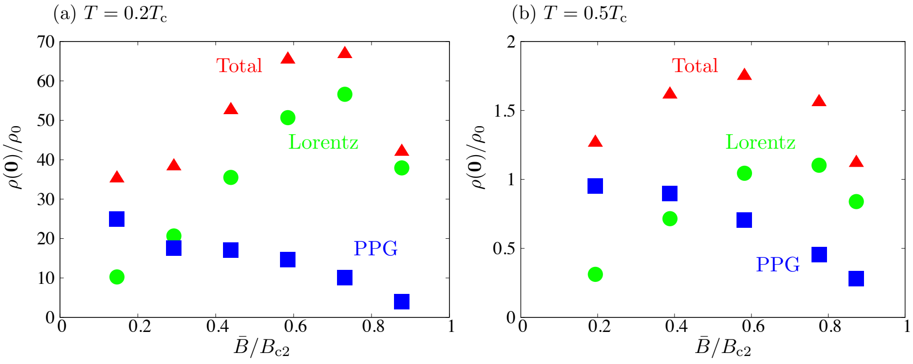

Figure 2: Magnetic field dependence of the charge density at the vortex center $\rho(\mathbf{0})$ due to the Lorentz force (green circular points), the PPG force (blue square points), and the total force (red triangular points), in units of $\rho_0 \equiv \Delta_0\epsilon_0 d/|e|\xi_0^2$ as a function of the magnetic field, at temperatures (a) $T = 0.2T_{\mathrm{c}}$ and (b) $0.5T_{\mathrm{c}}$ from left to right.

Calculation of ordered structures, dynamics and optical properties of soft materials

Jun-ichi FUKUDA

Department of Physics, Kyushu University, Motooka 744, Nishi-ku, Fukuoka 819-0395

We studied the structural properties of cholesteric blue phases, three dimensional ordered structures exhibited by a chiral liquid crystal. We particularly focused on how the cubic lattice of blue phases (BPI with O^8 symmetry and BPII with O^2 symmetry) is oriented when in contact with confining surface(s) that impose unidirectional surface alignment of the liquid crystal (unidirectional surface anchoring). Our study was motivated by a recent experimental study [1] that demonstrated specific lattice orientation of blue phases in contact with such surfaces.

Our study [2] was based on a continuum theory describing the orientational order of a liquid crystal by a second-rank tensor (Landau-de Gennes theory). The free energy of the liquid crystal was given as a functional of the tensor order parameter, and the profile of orientational order was obtained by minimizing the free energy numerically. The discretization of the liquid crystal system by a regular grid allows an efficient use of OpenMP (Our system was not large enough to require the use of MPI).

We carried out systematic evaluation of the free energy with the variation of the direction of the alignment imposed by the surface. We considered two cases commonly observed experimentally: BPI with its (110) planes parallel to the surface(s) and BPII with its (100) planes parallel to the surface(s). In both cases, the blue phase lattice adopts one specific lattice orientation that minimizes the free energy. The surface anchoring strength of 10^{-5} Jm^{-2}, easily achievable experimentally, was shown to be sufficient to lock the lattice orientation. Our finding is consistent with some of the experimental observations, but unfortunately not all. Our study provides a starting point for the understanding of how the blue phase lattice is oriented in response to the surface anchoring, which is strongly desired for practical optical application of blue phases that requires the preparation of large-scale monodomain lattices.

References

[1] M. Takahashi *et al.*: J. Phys. D: Appl. Phys. **51**, 104003 (2018).

[2] J. Fukuda and S. Zumer: Phys. Rev. Res. **2**, 033407 (2020).

Molecular simulation of colloidal particles

Takamichi TERAO
Department of Electrical, Electronic and Computer Engineering,
Gifu University, Yanagido 1-1, Gifu, 501-1132

Structural formation of colloidal particles have been studied both theoretically and experimentally for many years. In previous studies, spherical colloidal particles with isotropic interparticle interaction were investigated. Recently, there has been a great deal of research on colloidal systems with anisotropic interactions. A typical example is the so-called patchy particle system, in which anisotropic interparticle interaction exists.

The aggregation phenomena of colloidal particles have been a long-standing interest [1]. In this study, we performed computer simulations of the aggregation phenomenon in patchy particles and clarified their structure formation. In Fig. 1, an example of the snapshot of patchy particles with four patches is shown. In particular, we have quantitatively clarified the sol-gel transition and the phase diagram of the system (Figure 2). In this figure, the abscissa and the ordinate denote the rescaled dimensionless temperature and the volume fraction of the system, respectively. In this figure, the red squares show that the patchy particles form a gel network with these sets volume fraction and temperatures. The cluster size distribution and the static structure factor in aggregates were also quantitatively clarified. From these studies, we have been able to clarify the behavior of patchy particle systems with respect to the formation of various structures.

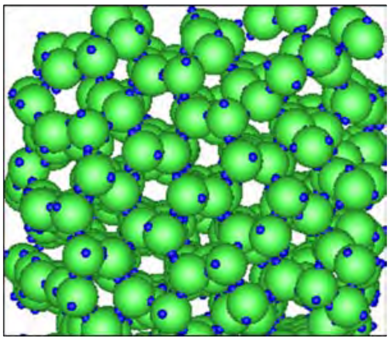

Fig. 1: Snapshot of patchy particles.

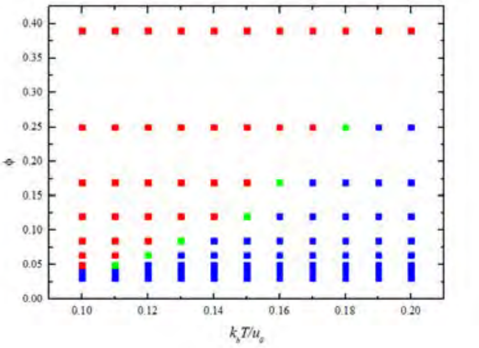

Fig. 2: Phase diagram of patchy particles.

References

[1] N. E. Valadez-Pérez, Y. Liu, and R. Castañeda-Priego: Phys. Rev. Lett. **120** (2018) 248004.

Nematic Tomonaga-Luttinger Liquid Phase in an Anisotropic $S=1/2$ Two-Leg Ladder System

Takashi Tonegawa

Professor Emeritus, Kobe Univ. and Visiting Professor, Osaka Prefecture Univ.

Recently, we [1] have explored the ground-state phase diagram of the $S=1/2$ two-leg ladder with different leg interactions, which is described by the Hamiltonian,

$$\mathcal{H}=\sum_{\ell=a,b} J_{\mathrm{l},\ell}\sum_{j=1}^{L}[\vec{S}_{j,\ell},\vec{S}_{j+1,\ell}]_{\Delta_\mathrm{l}} + J_\mathrm{r}\sum_{j=1}^{L}[\vec{S}_{j,a},\vec{S}_{j,b}]_{\Gamma_\mathrm{r}}\,,$$

where

$$\begin{aligned}[\vec{S}_{j,\ell},\vec{S}_{j+1,\ell}]_{\Delta_\mathrm{l}} &= S^x_{j,\ell}S^x_{j+1,\ell}+S^y_{j,\ell}S^y_{j+1,\ell}\\ &\quad+\Delta_\mathrm{l}S^z_{j,\ell}S^z_{j+1,\ell}\,,\end{aligned}$$

$$[\vec{S}_{j,a},\vec{S}_{j,b}]_{\Gamma_\mathrm{r}} = \Gamma_\mathrm{r}\left(S^x_{j,a}S^x_{j,b}+S^y_{j,a}S^y_{j,b}\right)+S^z_{j,\ell}S^z_{j+1,\ell}\,.$$

In these equations, $S^x_{j,\ell}$, $S^y_{j,\ell}$ and $S^z_{j,\ell}$ are, respectively, the x-, y- and z-components of the $S=1/2$ operator $\vec{S}_{j,\ell}$ at the (j,ℓ) site assigned by the jth rung and the $\ell(=a$ or $b)$ leg; $J_{\mathrm{l},a}$ and $J_{\mathrm{l},b}$ denote, respectively, the magnitudes of the a leg and b leg interactions, while J_r denotes that of the rung interaction; Δ_l and Γ_r are, respectively, the parameters representing the XXZ-type anisotropies of the former and latter interactions; L is the total number of rungs, which is assumed to be even. It is emphasized that this system has a frustration when $J_{\mathrm{l},a}J_{\mathrm{l},b}<0$ irrespective of the sign of J_r.

Using various numerical methods, we [1] have determined the phase diagram on the Δ_l versus $J_{\mathrm{l},b}$ plane in the case where $J_{\mathrm{l},a}=0.2$, $J_\mathrm{r}=-1.0$, and $\Gamma_\mathrm{r}=0.5$. Interestingly enough, we have found that the nematic Tomonaga-Luttinger Liquid (nTLL) phase appears in the unfrustrated region $(J_{\mathrm{l},b}>0)$ as well as in the frustrated one $(J_{\mathrm{l},b}<0)$. The nTLL phase is characterized not only by the formation of two-magnon bound pairs but also by the dominant nematic four-spin correlation function $\omega^{++--}(j)=\langle S^+_{j_0,a}\,S^+_{j_0,b}\,S^-_{j_0+j,a}\,S^-_{j_0+j,b}\rangle$. It is noted that the asymptotic forms of $\omega^{++--}(j)$ are given, respectively, by $\omega^{++--}(j)\propto 1/j^{\eta^{++--}}$ in the former nTLL phase and by $\omega^{++--}(j)\propto(-1)^j/j^{\eta^{++--}}$ in the latter nTLL phase. Thus, both nTLL phases are different phases, and the latter nTLL phase may be called the staggered nTLL phase.

According to the above result, it is reasonably expected that the nTLL state appears as the zero-field ground state in general $S=1/2$ unfrustrated one-dimensional systems in which pairs of $S=1/2$ spins coupled strongly with the Ising-type ferromagnetic interaction are connected by the weak XY-type antiferromagnetic interactions. Some examples of such systems are (A) the $S=1/2$ ferromagnetic-antiferromagnetic bond alternating chain, (B) the $S=1/2$ two-leg ladder with ferromagnetic rung and antiferromagnetic leg interactions, (C) the $S=1/2$ Kondo necklace chain with ferromagnetic rung and antiferromagnetic leg interactions, and so on.

This report aims at discussing the system (B) which is governed by the Hamiltonian $\mathcal{H}$ with $J_\mathrm{AF}=J_{\mathrm{l},a}=J_{\mathrm{l},b}$ and $J_\mathrm{F}=-J_\mathrm{r}$. We determine the following three ground-state phase diagrams, that is, (a) the phase diagram on the Δ_AF $(|\Delta_\mathrm{AF}|\leq 1.0)$ versus Γ_F $(0.0\leq\Gamma_\mathrm{F}\leq 1.0)$ plane for $J_\mathrm{F}=1.0$ and $J_\mathrm{AF}=0.1$, (b) the phase diagram on the Δ_AF $(-0.7\leq\Delta_\mathrm{AF}\leq 0.6)$ versus J_AF $(0.0\leq J_\mathrm{AF}\leq 0.3)$ for $J_\mathrm{F}=1.0$ and $\Gamma_\mathrm{F}=0.7$, and (c) the phase diagram on the Γ_F $(0.0\leq\Gamma_\mathrm{F}\leq 1.0)$ versus J_AF $(0.0\leq J_\mathrm{AF}\leq 1.0)$ for $J_\mathrm{F}=1.0$ and $\Delta_\mathrm{AF}=-0.12$.

The obtained results for the ground-state phase diagrams (a), (b), and (c) are presented in Fig. 1, Fig. 2, and Fig. 3, respectively. In these phase diagrams, there appear the Haldane (H), stripe Néel (sN), $XY1$ (XY1), and forromagnetic (F) phases in addition to the nTLL phase. It is expected that, at least for $J_\mathrm{F}=1.0$, $\Delta_\mathrm{AF}=-0.12$ and $0.0\leq\Gamma_\mathrm{F}\ll 1.0$, the nTLL phase survives even when the antiferromagnetic leg interactions are stronger than the ferromagnetic rung interaction (see Fig. 3).

Finally, we discuss how to obtain the phase boundary lines in these phase diagrams. All of the phase transition between the $XY1$ and H phases, that between the nTLL and H phases, and that between the nTLL and sN phases are the Berezinskii-Kosterlitz-Thouless transition [2]. As has been rigorously shown by Kitazawa *et al.* [3], the phase boundary lines for these transitions are given by $\Delta_\mathrm{AF}=0.0$. The other phase boundary lines have been numerically determined. We denote, respectively, by $E^\mathrm{P}_0(L,M)$ and $E^\mathrm{P}_1(L,M)$, the lowest and second-lowest energy eigenvalues of the Hamiltonian $\mathcal{H}$ under the periodic bound-

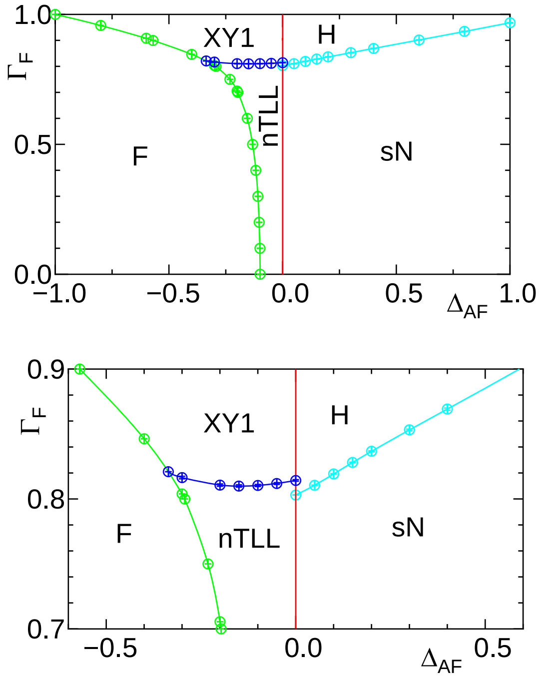

Figure 1: Ground-state phase diagram for $J_{\rm F}=1.0$ and $J_{\rm AF}=0.1$. A part of the upper figure is enlarged in the lower one.

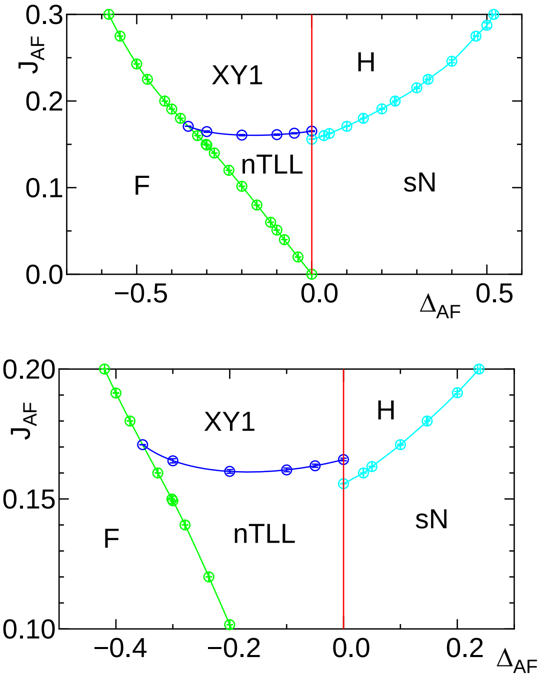

Figure 2: Ground-state phase diagram for $J_{\rm F}=1.0$ and $\Gamma_{\rm F}=0.7$. A part of the upper figure is enlarged in the lower one.

ary condition within the subspace of L and M, where M is the total magnetization ($M=0$, ± 1, $\cdots$, $\pm L$). We have numerically calculated these energies for finite-size systems with up to $L=12$ rungs by means of the exact-diagonalization method. The ground-state energy of the finite-L system is given by $E_0^{\rm P}(L,L)$ in the F region and by $E_0^{\rm P}(L,0)$ in the other regions. In the following way, we have estimated the finite-size critical values of the interaction parameters for each phase transition. Then, the phase boundary line for the transition has been obtained by connecting the results for the $L\to\infty$ extrapolation of the finite-size critical values. First, the phase transition between the H and sN phases is the 2D Ising-type transition. Then, it is well known that the phase transition line is determined by the phenomenological renormalization-group (PRG) method [4]. Then, to estimate the finite-size critical values, we solve the PRG equation, $L\,\Delta_{00}(L)=(L+2)\,\Delta_{00}(L+2)$, where $\Delta_{00}(L)=E_1^{\rm P}(L,0)-E_0^{\rm P}(L,0)$. Secondly, the nTLL state accompanies two-magnon boundstates, while the $XY1$ state does not. Then, in the ground-state magnetization curve for the finite-size system, the magnetization increases from $M=0$ to $M=2$ in the former state and from $M=0$ to $M=1$ in the latter state. Thus, the finite-size critical values are estimated from $\Delta_{10}(L)=\Delta_{20}(L)/2$, where $\Delta_{M0}(L)=E_0^{\rm P}(L,M)-E_0^{\rm P}(L,0)$. Lastly, it is apparent that the finite-size critical values for the phase transitions between the F phase and one of the nTLL and $XY1$ phases are estimated from $E_0^{\rm P}(L,L)=E_0^{\rm P}(L,0)$.

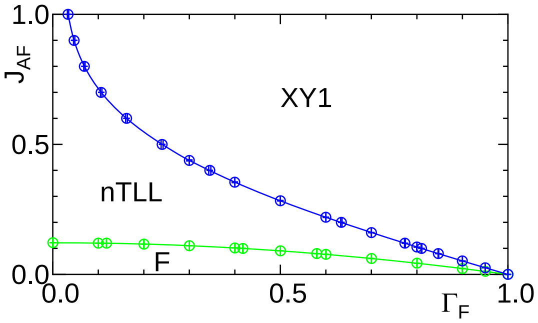

Figure 3: Ground-state phase diagram for $J_{\rm F}=1.0$ and $\Delta_{\rm AF}=-0.12$.

Invaluable discussions with K. Okamoto, K. Nomura, and T. Sakai are gratefully acknowledged.

[1] T. Tonegawa, T. Hikihara, K. Okamoto, S. C. Furuya, and T. Sakai, J. Phys. Soc. Jpn. **87**, 104002 (2018).

[2] Z. L. Berezinskii, Sov. Phys. JETP **34**, 610 (1971); J. M. Kosterlitz and D. J. Thouless, J. Phys. C **6**, 1181 (1973).

[3] A. Kitazawa, K. Hijii, and K. Nomura, J. Phys. A: Math. Gen. **36**, L351 (2003).

[4] M. P. Nightingale, Physica A **83**, 561 (1976).

Coarsening mechanism in mass-conserved reaction-diffusion systems

Michio Tateno and Shuji Ishihara
Graduate School of Arts and Sciences, The University of Tokyo
Universal Biology Institute, The University of Tokyo
Komaba 3-8-1, Meguro-ku, Tokyo 153-8902

Reaction-diffusion systems (RDs) are central mathematical scheme that comprehensively describe molecular assemblies driven by chemical reactions, and have tremendously contributed to our understanding of pattern formation observed in nature, particularly those in biological systems. Nearly 14 years ago, it was reported that in RDs satisfying the mass conservation law (MCRDs), patterns exhibit coarsening and result in formation of single isolated domain, unlike usual behavior of RDs [1]. MCRDs were originally introduced and have been discussed as models for molecular localization such as membrane-bounded GTPases which are responsible for the formation of cell polarity [1]. Recently the relevance of MCRDs has been recognized in a broad range of biological phenomena such as oscillatory motion in min-Protein and chemical turbulence (see, e.g,[2]. Despite its uniquity and fundamental importance, the physical mechanism underlying coarsening behavior in MCRDs remains elusive. This is partially because most of earlier studies only investigated one-dimensional systems. Considering the fact that morphology of the patterns is strongly influenced by spatial dimensions, an intensive study in high dimension is highly desirable.

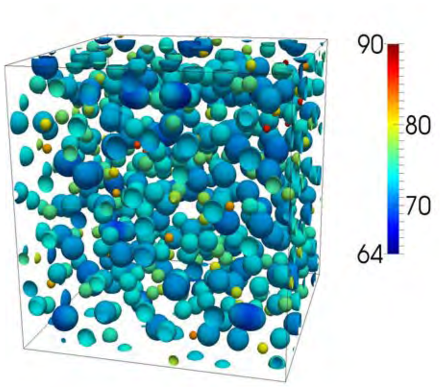

Figure 1: A spatial pattern obtained from a three-dimensional simulation. A contour surface indicates the interface between bistable states. The color is labeled according to the value of chemical-potential-like quantity in MCRDs. The numerical simulation was performed in a cubic lattice of 1024^3.

In this project, we realize a large-scale MCRD simulation in both two and three dimensions using multiple GPUs, and successfully capture coarsening dynamics of MCRDs in high dimension with statistical significance for the first time (see Fig. 1). We have an eye on similarity between coarsening dynamics in MCRDs and classical phase separation systems, and apply analysis methods established in thermodynamic phase transition (dynamic scaling law, nucleation-growth process, etc.) to the simulation results. We reveal that droplets forming in MCRDs obey the Young-Laplace law and coarsen following the evaporation-condensation (Lifshitz-Slyosov-Wagner) mechanism (see Fig. 2). These outcomes indicate that in the presence of conserved variable, a physical quantity similar to surface tension is relevant to RDs,

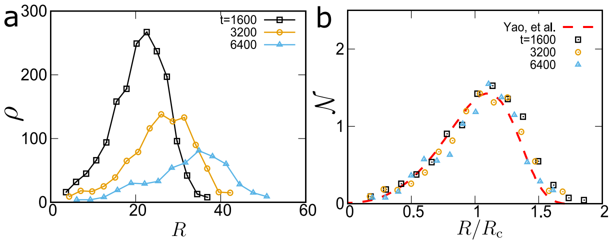

Figure 2: **a** Droplet-radius distribution $\rho(R)$ for various time t. **b.** Dynamic scaling of ρ based on Lifshitz–Slyozov–Wagner theory. The symbol shows the same simulation results as in panel a. The red dashed lines represent theoretical predictions for the scaled distribution $\mathcal{N}(R/R_{\mathrm{c}})$ [4], where R_{c} is critical radius.

which provides new insight into molecular self-assembly driven by chemical reactions. The result is now under review in an international peer reviewed journal, and the preprint is uploaded in an online paper repository [3].

References

[1] M. Otsuji, S. Ishihara, et al.: PLOS Comput. Biol. **3**, (2007) 1.; S. Ishihara, M. Otsuji and A. Mochizuki: Phys. Rev. E **75**, (2007) 015203.

[2] E. Frey, J. Halatek, et al.: *Physics of Biological Membranes*, Springer International Publishing, pp.229-260 ; J. Halatek and E. Frey: Nat. Phys. **14**, (2018) 507.

[3] http://arxiv.org/abs/2010.03900

[4] J. H. Yao, K. R. Elder, et al.: Phys. Rev. B **47**, (1993) 14110.

Multicellular simulation by phase field method

Michio Tateno and Shuji Ishihara
Graduate School of Arts and Sciences, The University of Tokyo
Universal Biology Institute, The University of Tokyo
Komaba 3-8-1, Meguro-ku, Tokyo 153-8902

The central aim of this project is to establish a multicellular simulation method that can capture multiscale dynamics, ranging from intracellular chemical concentration, shape changes of cells, to their collective motions in a tissue scale. To realize this, we adopted the phase field (PF) model, which can express cells with arbitrary shape. In this method, an auxiliary field (phase field) which obeys a bistable energy functional is introduced to distinguish the inside and outside of a cell. This procedure allows us to describe the time evolution of cell shape via interfacial dynamics without suffering from moving boundary problems.

One of the authors (SI) and coworkers combined PF model with a reaction-diffusion system, in which a bistable and excitable chemical network is incorporated to model cell migration driven by F-actin. They demonstrated that this model can precisely reproduce complex motion of amoebic cells (Dictyostelium at early starvation stage) as well as intracellular chemical waves related to actin polymerization [1]. In this term, we have made an attempt to extend this PF model to multicellular systems.

In PF model for a single cell, a square moving frame with lattice size L^2 is provided to compute the phase field. Here L should be sufficiently larger than the cell size (typically L being hundreds of order) to capture the complex morphology of a cell and avoid the cell from overhanging the frame. When increase the cells, of course, the computational cost is not simply scaled by the number of cells N; one need to deal with overlap regions among the frames for different cells, to compute intercelluar interactions such as steric effect or cell adhesion, which is a computation bottleneck. The resulting computational cost was roughly the order of $10 \times NL^2$.

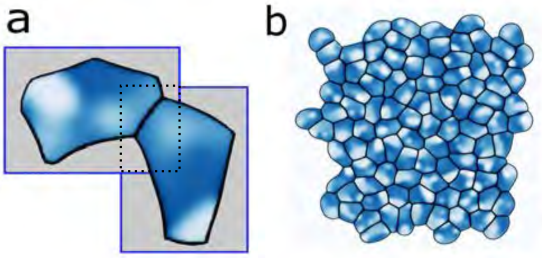

Figure 1: **a.** Adaptive moving frame (gray areas) is used in our PF model. This largely reduces the computational cost for intercellular interactions (the region surrounded by a dotted line). The white and blue regions represent the distributions of PIP3 and PTEN, respectively. **b.** A snapshot of multicelluar simulation with 100 cells.

To overcome this problem, we improve the computational efficiency by updating the moving frames to adapt to the shape of cells. Figure 1a show the computational regions for two cells (gray rectangle areas). The area surrounded by a dotted line represent the region required to compute the intercelluar interaction between the cells. Using this algorithm and GPU, we have speeded up the computation by four times and realized simulation with order of 100 cells as shown in Fig. 1b. In the further, we plan to apply our program to specific problems such fluidity transition or cell sorting of a epithelial tissue.

References

[1] D. Taniguchi, Ishihara, et al.: Proc. Natl. Acad. Sci. USA **110**, (2013) 5016.

Universal properties of dissipated many-body quantum systems

Tatsuhiko Shirai
Department of Computer Science and Communications Engineering, Waseda University
Ookubo, Shinjuku-ku, Tokyo 169-8555

We have studied two different types of nonequilibrium quantum systems: bulk-dissipated systems and boundary-dissipated systems.

1 Bulk-dissipated systems

In the bulk-dissipated systems, the dissipative environments are uniformly coupled to the system of interest. We consider that the system-envrionment coupling is weak and the environment is nonequilibrium (i.e., the detailed balance condition is broken). The reference [1] has argued that the Gibbs state at an effective temperature gives a good description of the nonequilibrium steady state provided that the system Hamiltonian obeys the eigenstate thermalization hypothesis and the perturbation theory in the weak system-environment coupling is valid in the thermodynamic limit. The numerics are based on the exact diagonalization method, which restricts the system size studied. We have developed a tensor-network approach that directly studies not only the steady states but also the relaxation dynamics in the thermodynamic limit [2]. The study reveals that when an initial state is given by a thermal Gibbs state, the states during the relaxation dynamics are well described by Gibbs states with a time-dependent effective temperature.

2 Boundary-dissipated systems

We discussed the relaxation time of the boundary-dissipated systems, where the environments with different thermodynamic potentials (e.g., temperature and chemical potential) are coupled to the edges of the non-integrable systems. The presence of the diffusive transport indicates that the relaxation time τ is proportional to the square of the system size L (i.e., $\tau \sim L^2$). The relaxation time is naively related to the gap of the time-evolution operator called the Liouvillion, but the previous studies have shown that the gap closing is slower than L^{-2} [3]. We have solved this discrepancy by numerically showing that the relaxation time is not determined by the lower-lying eigenvalues of the Liouvillion but by superexponentially large expansion coefficients for Liouvillion eigenvector with non-small eigenvalues at an initial state [4].

References

[1] T. Shirai, and T. Mori: Phys. Rev. E **101** (2020) 042116.

[2] H. Nakano, T. Shirai, and T. Mori: arXiv:2012.12274.

[3] M. Žnidarič, Phys. Rev. E **92** (2015) 042143.

[4] T. Mori, and T. Shirai: Phys. Rev. Lett. **125** (2020) 230604.

Quantum annealing in transverse-field Ising chains with a correlated disorder

Tatsuhiko Shirai
Department of Computer Science and Communications Engineering, Waseda University
Ookubo, Shinjuku-ku, Tokyo 169-8555

We have studied disordered Ising chains under transverse fields to examine the effects of a correlated disorder on quantum phase transitions. The Hamiltonian is given by

$$H = -\sum_{i=1}^{N-1} J_i \sigma_i^z \sigma_{i+1}^z - \sum_{i=1}^{N} \Gamma_i \sigma_i^x, \qquad (1)$$

where $\vec{\sigma}_i = (\sigma_i^x, \sigma_i^y, \sigma_i^z)$ are Pauli spin matrices, and J_i and Γ_i denote nearest-neighbor coupling strength and transverse-field strength, respectively. J_i is chosen from two different types of distribution: weak disorder and strong disorder. The distribution in the weak disorder case is uniform over $(J^{(0)}, 1]$ and gapped (i.e., $J^{(0)} > 0$), and thus given as

$$\pi_{\mathrm{w}}(J_i) = \begin{cases} (1 - J^{(0)})^{-1} \text{ for } J^{(0)} < J_i \le 1, \\ 0 \text{ otherwise.} \end{cases} \qquad (2)$$

On the other hand, the distribution in the strong disorder case is a gapless power-law distribution over $(0, 1]$ given as

$$\pi_{\mathrm{s}}(J_i) = \begin{cases} \frac{1}{D} J_i^{-1+\frac{1}{D}} \text{ for } 0 < J_i \le 1, \\ 0 \text{ otherwise,} \end{cases} \qquad (3)$$

where $D > 0$ denotes the disorder strength. In the correlated disorder case, the transverse-fields are given by

$$\begin{cases} \ln \frac{\Gamma_1}{\Gamma} = (1-s) \ln J_1, \\ \ln \frac{\Gamma_i}{\Gamma} = s \ln J_{i-1} + (1-s) \ln J_i \\ \qquad\qquad \text{for } 2 \le i \le N-1, \\ \ln \frac{\Gamma_N}{\Gamma} = s \ln J_{N-1}, \end{cases} \qquad (4)$$

where $s \in [0, 1]$ is a parameter for tuning the transverse fields.

In. [1], we analytically show that the dynamical critical exponents z in the system with the correlated disorder are finite: $z = 1$ in the weak disorder case and $\max(D(1/2+|s-1/2|+1/2), 1) \le z \le D+1$ in the strong-disorder case. We numerically estimate z in the strong disorder case. The numerics is based on the Jordan–Wigner transformation and an exact diagonalization method [2]. The finite z is in contrast to infinite z obtained in the uncorrelated disordered Ising chains (i.e., no correlation between the transverse fields and nearest-neighbor couplings) [2, 3]. The suppression of z is useful to enhance the performance of adiabatic quantum computations including quantum annealing with an argument based on the Kibble–Zurek mechanism.

References

[1] T. Shirai, and S. Tanaka: arXiv:2007.07439 (2020).

[2] A. P. Young and H. Rieger: Phys. Rev. B **53** (1996) 8486.

[3] D. S. Fisher: Phys. Rev. Lett. **69** (1992) 534.

Study of superstructure induced novel phenomena: stacking of atomically thin materials

Toshikaze KARIYADO
International Center for Materials Nanoarchitectonics,
National Institute for Materials Science, Namiki, Tsukuba, Ibaraki 305-0044

The purpose of this study is to propose a new design for van der Waals heterostructures of atomically thin materials to realize novel phases or phenomena. Particularly, we focus on twisted bilayers, where two layers are stacked with angle mismatch. When the relative angle is small, the system shows a long-range structure called moiré pattern that can induce novel physics. With the small relative angle, a twisted bilayer system locally resembles to a bilayer system without twist, but globally, the relative in-plane shift between two layers depends on position due to the twist. Then, it is a powerful scheme to analyze crystalline and electronic structures for untwisted bilayers and scan over the possible relative in-plane shift.

In this project, we have applied the above procedure on several candidate materials, including graphene relatives and group-IV monocalcogenide monolayers. For the analysis of crystalline and electronic structures, we have used the first-principles density functional theory method implemented in Quantum Espresso package. One of the key quantities in crystalline structure analysis is relative in-plane shift dependence of layer-layer distance, which is derived by computing the binding energy as a function of layer-layer distance with rev-vdW-DF2 type functional to take account of the van der Waal force. Once the layer-layer distance is fixed, the electronic structure is computed using PBE-GGA type functional.

Overall, we have to scan over the possible relative in-plane shift, and therefore, it is important to make a calculation for each parameter as light as possible. In that perspective, MPI parallelization implemented in Quantum Espresso package helps us a lot if it is used on a massively parallel computational system.

In addition to the above project, we have analyzed diamagnetic responses in an antiperovskite type Dirac electron system [1]. The numerically obtained susceptibility compares well with the experimental result.

References

[1] S. Suetsugu, K. Kitagawa, T. Kariyado, A. W. Rost, J. Nuss, C. Mühle, M. Ogata, and H. Takagi: Phys. Rev. B **103** (2021) 115117.

Numerical Study of One Dimensional Frustrated Quantum Spin Systems

Kazuo HIDA
Professor Emeritus, Division of Material Science,
Graduate School of Science and Engineering,
Saitama University, Saitama, Saitama 338-8570

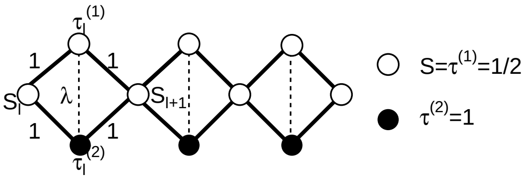

Figure 1: Structure of the diamond chain investigated in this work.

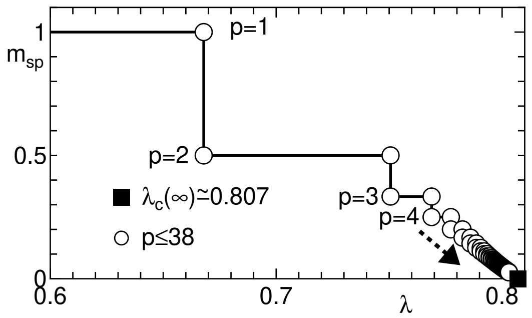

Figure 2: λ-dependence of $m_{\rm sp}$ calculated by the infinite size DMRG method.

We investigate the ground-state phases of mixed diamond chains described by the following Hamiltonian [1]:

$$\mathcal{H}=\sum_{l=1}^{L}\Big[\boldsymbol{S}_l(\boldsymbol{\tau}_l^{(1)}+\boldsymbol{\tau}_l^{(2)}) + (\boldsymbol{\tau}_l^{(1)}+\boldsymbol{\tau}_l^{(2)})\boldsymbol{S}_{l+1}+\lambda\boldsymbol{\tau}_l^{(1)}\boldsymbol{\tau}_l^{(2)}\Big], \qquad (1)$$

where $\boldsymbol{S}_l, \boldsymbol{\tau}_l^{(1)}$ and $\boldsymbol{\tau}_l^{(2)}$ are spin operators with magnitudes $S_l=\tau_l^{(1)}=1/2$ and $\tau_l^{(2)}=1$. The number of the unit cells is denoted by L. Here, the parameter λ controls the frustration as depicted in Fig. 1. Defining the composite spin operators $\boldsymbol{T}_l$ as $\boldsymbol{T}_l \equiv \boldsymbol{\tau}_l^{(1)}+\boldsymbol{\tau}_l^{(2)}$, it is evident that $\forall l$ $[\boldsymbol{T}_l^2, \mathcal{H}]=0$. Thus, we have L good quantum numbers $\boldsymbol{T}_l^2 \equiv (T_l+1)T_l$ where $T_l=1/2$ and $3/2$. The total Hilbert space of the Hamiltonian (1) consists of separated subspaces, each of which is specified by a definite set of $\{T_l\}$. For large λ, $\forall l$ $T_l=1/2$. Hence, the ground state is equivalent to that of the uniform spin 1/2 chain, namely a gapless spin liquid. For $\lambda \leq 0$, $\forall l$ $T_l=3/2$. Hence, the ground state is a Lieb-Mattis ferrimagnetic phase with spontaneous magnetization $m_{\rm sp}=1$ per unit cell. For intermediate λ, we find a series of ferrimagnetic phases with $m_{\rm sp}=1/p$ where p takes positive integer values as shown in Fig. 2 based on the infinite-size DMRG calculations for various configurations of $\{T_l\}$. The calculations for many different $\{T_l\}$ are independent from each other. Hence, they are suitable for the massively parallel system of the ISSP supercomputer center. The phases with $p \geq 2$ are accompanied by the spontaneous breakdown of the p-fold translational symmetry. It is suggested that the phase with arbitrarily large p, namely infinitesimal spontaneous magnetization, is allowed as λ approaches the transition point to the gapless spin liquid phase.

References

[1] K. Hida, arXiv:2102.02116, to be published in J. Phys. Soc. Jpn.

Development of observation-noise estimation method by machine learning

Ryo TAMURA
International Center for Materials Nanoarchitectonics,
National Institute for Materials Science,
1-1 Namiki, Tsukuba, Ibaraki, 305-0044

To know the Hamiltonian of target materials, a data-driven approach is useful, in which model parameters of Hamiltonian are determined so as to fit the experimentally measured data[1, 2, 3, 4]. In a data-driven approach, the posterior distribution is defined, and the appropriate parameters are searched by a maximum a posteriori (MAP) estimation. Thus, the Hamiltonian, which can well explain the experimental results, is obtained by the framework of MAP estimation. However, by MAP estimation, observation noise cannot be evaluated. The Hamiltonian estimation method based on Bayesian inference is formulated under the assumption of finite observation noise. Then, there must be errors in the estimated parameters. Therefore, we proposed a method to evaluate the error of the parameters by estimating the observation noise[5].

In our framework, the noise amplitude σ is considered to be a hyperparameter, and a plausible value is determined by minimizing the Bayes free energy $F(\sigma)$, defined as

$$F(\sigma) = -\log Z(\sigma), \tag{1}$$

where $Z(\sigma)$ is the normalization of the posterior distribution given by

$$Z(\sigma) = \left(\frac{1}{2\pi\sigma^2}\right)^{\frac{L}{2}} \int_{\Omega_x} d\mathbf{x} \exp\left[-E(\mathbf{x},\sigma)\right]. \tag{2}$$

Here, Ω_x is the support of the posterior distribution determined by the prior distribution. In addition, $\mathbf{x}$ is the model parameters in the Hamiltonian and $E(\mathbf{x},\sigma)$ is the energy function to be minimized in our model estimation. To evaluate $F(\sigma)$, it is convenient to extend the normalization factor with a “finite temperature”, which is defined as

$$Z_\beta(\sigma) = \left(\frac{1}{2\pi\sigma^2}\right)^{\frac{L}{2}} \int_{\Omega_x} d\mathbf{x} \exp\left[-\beta E(\mathbf{x},\sigma)\right], \tag{3}$$

where β is the inverse temperature. By using $Z_\beta(\sigma)$, the Bayesian free-energy is defined as

$$\begin{aligned} F(\sigma) &= -\int_0^1 d\beta \left(\frac{d}{d\beta}\log Z_\beta(\sigma)\right) - \log Z_0(\sigma) \\ &= \int_0^1 d\beta \langle E(\mathbf{x},\sigma)\rangle_\beta + \frac{L}{2}\log\left(2\pi\sigma^2\right) \\ &\qquad - \log\int_{\Omega_x} d\mathbf{x}, \end{aligned} \tag{4}$$

where the ensemble average $\langle E(\mathbf{x},\sigma)\rangle_\beta$ can be obtained by the MCMC method. Here, the third term on the right-hand side does not depend on σ and can be omitted. The noise amplitude of the experimental data σ^* is evaluated as the value where $F(\sigma)$ is minimized.

This noise estimation method is applied for the effective model estimation of $\mathrm{KCu_4P_3O_{12}}$. As a result, we obtained the noise amplitude, and the magnetic interactions with error bars can be estimated as $J_1 = -8.54 \pm 0.51$ meV, $J_2 = -2.67 \pm 1.13$ meV, $J_3 = -3.90 \pm 0.15$ meV, and $J_4 = 6.24 \pm 0.95$ meV, by using our noise estimation method.

This work is the collaboration work with Koji Hukushima, Akira Matsuo, Koichi Kindo, and Masashi Hase.

References

[1] R. Tamura and K. Hukushima, PLoS ONE **13**, e0193785 (2018).

[2] H. Takenaka, K. Nagata, T. Mizokawa, and M. Okada, J. Phys. Soc. Jpn. **83**, 124706 (2014).

[3] R. Tamura and K. Hukushima, Phys. Rev. B **95**, 064407 (2017).

[4] H. Fujita, Y. O. Nakagawa, S Sugiura, and M. Oshikawa, Phys. Rev. B **97**, 075114 (2018).

[5] R. Tamura, K. Hukushima, A. Matsuo, K. Kindo, and M. Hase, Phys. Rev. B **101**, 224435 (2020).

Systematic Investigation on Phonon Transport at Nanoscale Interfaces

Susumu FUJII
Nanostructures Research Laboratory, Japan Fine Ceramics Center
Mutsuno, Atsuta, Nagoya 456-8587

Grain boundaries and hetero interfaces are known to suppress lattice thermal conductivity of a material dramatically, because of their disordered structures different from the corresponding crystal structure(s). Recently, there is an increasing demand for revealing the mechanisms of interfacial thermal conduction at the nanoscale, as electronic devices have become miniaturized and nanostructuring techniques have been extensively developed. However, there is a few studies that investigate the impact of interface atomic structures or interfacial scattering mechanisms of phonons that are defined in the reciprocal space, making it difficult to obtain a guideline for controlling thermal conductivity on the basis of interfaces.

In the present study, we have mainly investigated the interfacial thermal conduction across silicon grain boundaries (Fig. 1). We chose silicon as a model material because it has many technologically important applications such as electronic devices and thermoelectrics. We performed two types of molecular dynamics simulations: (1) perturbed molecular dynamics and (2) phonon wave packet. The former adds a small magnitude of perturbation to atoms and calculate thermal conductivity from the average of heat flux of the system. The latter introduces an phonon wave packet generated from a single phonon mode from phonon dispersions and simulate its scattering process at the interface. The necessary codes were developed by the author and implemented to the Large-scale Atomic/Molecular Massively Parallel Simulator (LAMMPS) [1]. In addition, we used a machine learning potential for Si distributed in MACHINE LEARNING POTENTIAL REPOSITORY [2], which are much less computationally demanding compared with density functional theory calculations but more demanding than the empirical interatomic potentials such as Stillinger-Weber and Tersoff potentials.

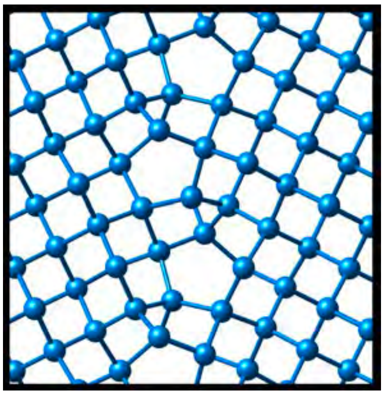

Figure 1: An example of silicon grain boundary structure derived from the machine learning potential.

The perturbed molecular dynamics simulations require a large number of timesteps more than one million and large computational cells with a few thousands of atoms. On the other hand, phonon wave packet simulations require a smaller number of timesteps less than 100000 but the computational cells must be very long for the direction perpendicular to the grain boundary plane and thus contain tens of thousands of atoms. The former were performed with five different magnitudes of perturbations, and the latter were performed for 40 - 60 different phonon modes for each grain boundary. Each of these calculations was performed in a single node.

The results perturbed molecular dynamics simulations show that thermal conductivity of Si grain boundaries significantly correlates with their microscopic atomic structures rather than their energies. On the other hand, our phonon wave packet simulations reveal that the phonon transmission (or reflaction) at the grain boundaries does not depends on the grain boundary structures much, especially for the acoustic phonons that transfer most of heat. This contradicting trends obtained from two kind of molecular dynamics simulations suggest that anharmonic effect of atomic vibrations at the grain boundaries, which is naturally included in the perturbed molecular dynamics while is intentionally neglected in the phonon wave packet simulations, is one of the dominant factors for determinig interfacial thermal conduction.

In additon, comparisons of grain boundary structures, phonon properties and thermal conductivity between the machine learning potential and a classical interatomic potential (Tersoff potential) demonstrate the high predictive power of the machine learning potential. By combining machine learning potentials with supercomputers and advanced computational programs, it is becoming possible to quantitatively analyze interfacial thermal conduction.

References

[1] S. Plimpton, J. Comput. Phys. **117** (1995) 1.

[2] A. Seko, arXiv:2007.14206.

Developing numerical tool for open quantum dynamics based on neural networks

Nobuyuki YOSHIOKA
Department of Applied Physics,
The University of Tokyo, 7-3-1 Hongo, Bunkyo-ku, Tokyo, Japan, 113-8656.

In this project, we have planned to use neural networks to study the property of open quantum many-body systems which are subject to dissipations that give rise to competition similar to “frustration” in closed quantum many-body systems. While the proposed project is currently on-going, we have achieved some other works regarding scalable simulations using neural networks. In the following, we report the results in such two works [1, 2].

In the first work, we have successfully demonstrated a novel simulation algorithm that perform first-principles calculation of solid-state systems. Namely, we have shown that the expressive power of neural networks are sufficiently high so that the essential properties of solids, the ground state and the quasiparticle band spectra, can be simulated both efficiently and accurately. The ground states are computed by the standard variational Monte Carlo manner, such that the imaginary-time evolution is realized approximately. This enables us to simulate the potential curve of various real solids including polymers, non-organic crystals, or strongly correlated systems. In particular, we have shown that, the thermodynamic limit of the strongly correlated hydrogen chain can be computed within chemical accuracy.

In the second work, we have developed two algorithms that simulates the thermal equilibrium of an isolated quantum many-body system using deep neural networks. In one method, we exploit the quantum-to-classical correspondence to construct the exact representation of Gibbs state using the deep Boltzmann machine (DBM). This demonstrates the expressibility of the DBM. In the other method, we approximate the imaginary-time evolution to generate finite-temperature density matrix starting from the infinite-temperature Gibbs state. We have numerically demonstrated that the second approach opens a door to scalable simulation even in frustrated systems where the thermal property is still under debate.

References

[1] N. Yoshioka, W. Mizukami, and F. Nori, arXiv:2010.01358 (2020).

[2] Y. Nomura, N. Yoshioka, and F. Nori, arXiv:2103.04791 (2021).

Quantum Monte Carlo study of the antiferromagnetic Ising model on a square lattice with longitudinal and transverse magnetic fields

Ryui KANEKO
Department of Physics, Kindai University
Higashi-Osaka, Osaka 577-8502, Japan

Analog quantum simulations have attracted much interest recently. Ground-state properties and nonequilibrium dynamics of quantum spin, SU(N) Heisenberg, and SU(N) Hubbard systems have been extensively studied. It is important to verify how far the simulation of the experiment is correct by comparing numerical simulations on classical computers. It is an interesting challenge to investigate the properties of complex models in static systems and those in nonequilibrium systems using numerical methods such as tensor network algorithms. On the other hand, it is also indispensable to study static properties in simple systems because it is much easier to compare the experiments and numerical simulations.

The Rydberg-atom systems are suitable for realizing the fundamental spin models. The quantum Ising models are frequently experimented with. The Hamiltonian is given as

$$H = \sum_{i,j} J_{ij} S_i^z S_j^z - h \sum_i S_i^z - \Gamma \sum_i S_i^x. \quad (1)$$

The longitudinal (transverse) field h (Γ) can be controlled by the frequency detuning (the Rabi frequency) of the laser [1]. The Ising interaction is given as van der Waals interaction, whose long-range part is often ignored for simplicity [2].

Although the ground-state phase diagram of the quantum Ising models on complex lattices have been extensively investigated, the simple model on a square lattice has yet to be explored. The ground-state phase diagram was obtained only for few dozen sites using the exact diagonalization method [3]. We investigate the ground-state phase diagram of the model on the square lattice using the quantum Monte Carlo method with the DSQSS library [4]. We typically choose 10^5 Monte Carlo steps for calculation of physical quantities and for thermalization. We use the system sizes $N_\mathrm{s} = L^2$ with $L \leq 32$ and consider the periodic-periodic boundary condition.

To determine the phase boundary, we calculate the staggered susceptibility defined as

$$\chi_\mathrm{stag}^{zz} = \frac{\langle \hat{M}^z(\boldsymbol{Q})^2 \rangle}{\beta L^d}, \quad \boldsymbol{Q} = (\pi, \pi), \quad (2)$$

$$\text{and} \quad \hat{M}^z(\boldsymbol{q}) = \int_0^\beta d\tau \sum_j \hat{S}_j^z(\tau) e^{-i\boldsymbol{q}\cdot\boldsymbol{r}_j}, \quad (3)$$

where $\boldsymbol{r}_j$ is the real space coordinate at site j, $d(=2)$ is the spatial dimension, and β is the inverse temperature.

We perform the finite-size scaling analysis to determine the phase boundary between the antiferromagnetic and disordered phases. The scaling form of χ_stag^{zz} is given as

$$\chi_\mathrm{stag}^{zz} \sim L^{2-\eta} \mathcal{F}(\delta L^{1/\nu}), \quad (4)$$

where $\mathcal{F}$ is a scaling function, η is the anomalous dimension, and ν is the correlation length exponent. The difference between the field and the critical point is given as δ. Since the dynamical exponent would satisfy $z = 1$ for the

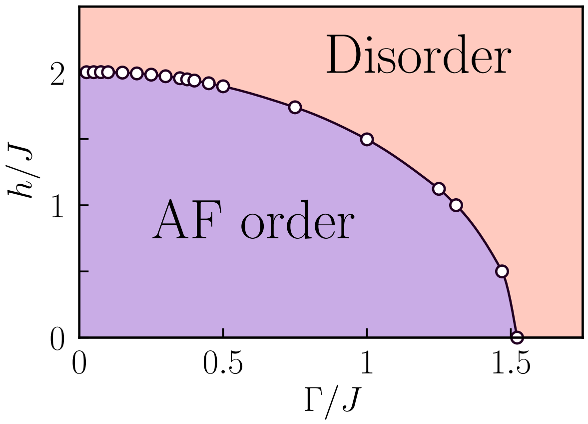

Figure 1: Phase diagram of the antiferromagnetic Ising model on a square lattice with longitudinal and transverse magnetic fields.

Ising universality class, we choose the inverse temperature β to be proportional to L during the simulation.

Figure 1 shows the ground-state phase diagram of the mixed-field Ising model on the square lattice. When the transverse field $\Gamma \sim 0$, the transition longitudinal field h_c is nearly intact as a function of Γ. On the other hand, when $h \sim 0$, h_c drops nearly vertically as a function of Γ. The latter behavior is consistent with the phase boundary obtained by the mean-field approximation [5].

By scrutinizing the phase diagram near $\Gamma \sim 0$, we have also uncovered the narrow region where the disordered phase exhibits reentrance. Our phase diagram [6] would be useful for examining the accuracy of the analog quantum simulation in the Rydberg-atom systems.

References

[1] F. Robicheaux and J. V. Hernández, Phys. Rev. A **72**, 063403 (2005).

[2] A. Browaeys and T. Lahaye, Nat. Phys. **16**, 132 (2020).

[3] V. Lienhard et al., Phys. Rev. X **8**, 021070 (2018).

[4] Y. Motoyama et al., Comput. Phys. Commun. **264**, 107944 (2021).

[5] A. A. Ovchinnikov et al., Phys. Rev. B **68**, 214406 (2003).

[6] R. Kaneko et al., arXiv:2103.12364

Theoretical study for caged compound and its conjugate acid/bases

Miyabi HIYAMA
Graduate School of Science and Technology, Gunma University,
Tenjin-cho, Kiryu, Gunma 376-8515

Caged luciferins, which can generate luciferin by UV photolytic reaction, would be useful to understand the firefly bioluminescence. We synthesized the new caged luciferin named coumarin caged luciferin and obtained its absorption spectra [1]. When we use this caged-luciferin for spectroscopic studies, we need the detail of electronic states of this molecule in aqueous solutions.

The optimization structure of ground state for coumarin caged-luciferin anion expected to be main component in the pH 8 aqueous solutions was obtained from the density functional theory. The time dependent DFT (TDDFT) calculations were carried out to estimate the theoretical absorption spectra for this structure. These theoretical spectra were used to assign the experimental spectra measured at pH 8 [2]. However, these theoretical results cannot explain the difference between the shape of absorption spectra of coumarin caged luciferin at pH 3 and those at pH 8. We expect that the main chemical species in the acidic experimental condition would be neutral coumarin caged luciferin molecule of which total charge is 0.

In this year, we performed the DFT calculations for the neutral coumarin caged luciferin molecule. The excitation energies and the oscillator strengths at the ground state were obtained using TDDFT calculations for the optimization structure of the neutral coumarin caged luciferin molecule. The polarized continuum model was used for the description of water solute molecules. We found that the absorption energy for neutral coumarin caged luciferin is larger than that for coumarin caged luciferin anion. It was also found that the shape of absorption spectra for neutral coumarin caged luciferin has a large main peak, while that for coumarin caged luciferin anion has a double peak.

All calculations were performed using the GAUSSIAN09 program [3] on system B and C of Super Computer Center in ISSP.

References

[1] Kurata et al. , J. Photochem. Photobiol. B, **189** (2018) 81.

[2] Usukura et al. Photochem. Photobiol. (2020) Photochem. Photobiol. (2020) 96, 805.

[3] Gaussian 09, Revision D.01, M. J. Frisch et al.

Exact diagonalization calculations of density of states and dynamical structure factor for the spherical-kagome spin-system $\{\mathrm{W}_{72}\mathrm{V}_{30}\}$

Yoshiyuki Fukumoto
Department of Physics, Faculty of Science and Technology, Tokyo University of Science
2641 Yamazaki, Noda, Chiba 278-8510

For the spherical-kagome cluster with thirty spin-1/2s, as well as for the 2D kagome lattice, many low-energy singlet excitations have been expected to exist in the energy region below spin gap [1], which has been actually confirmed by Kihara et al. in their specific heat measurements at low temperature in $\{\mathrm{W}_{72}\mathrm{V}_{30}\}$ [2]. However, the experimental curve of the specific heat can not be reproduced by the theoretical curve in the Heisenberg model $\mathcal{H} = J\sum_{\langle i,j\rangle} \boldsymbol{S}_i \cdot \boldsymbol{S}_j$, where $\langle i,j\rangle$ denote nearest neighbors and the exchange parameter was estimated as $J = 115$K [1]. The experimental curve does not have the peak around 2K, although the theoretical one has the 2K peak [1,2].

In last year, incorporating Dzyaloshinskii-Moriya (DM) interactions and bond randomness into our model Hamiltonian, both of which were originally proposed to explain the luck of the step-wise behaviour in the low-temperature magnetization curve of $\{\mathrm{W}_{72}\mathrm{V}_{30}\}$ [3,4], we used the method of thermal pure quantum (TPQ) state [5] to calculate the specific heat. Then, we found that 10% of randomness collapse the 2K peak.

In this year, we calculate density of states, entropy, and specific heat at low temperatures by using the Lanczos method [6]. In particular, we aim to understand low-temperature specific heat qualitatively via observation of the density of states. We find that DM interactions do not significantly affect the energy distribution of a dozen or so singlet states above the ground state, which are involved in the peak structure of the specific heat around 2K. On the other hand, we find that 10% randomness disperses this distribution to collapse the 2K peak, which is consistent with the above-mentioned TPQ result.

In conclusion, we have clarified the similarities and differences between the effects of the DM interaction and bond randomness: the DM interaction breaks the conservation of the total spin and cause magnetic components to mix dense singlet states at low energies, while the bond randomness disperses the energy distribution of singlets and triplets without breaking the conservation of the total spin, which leads to similar effects on the magnetization process but does to different effects on the specific heat.

References

[1] N. Kunisada *et al.*, PTEP 2014, 41I01 (2014).

[2] T. Kihara *et al.*, PRB 99, 064430 (2019).

[3] Y. Fukumoto *et al.*, J. Phys. Soc. Jpn. 87, 124710, 2018.

[4] J. Schnack *et al.*, arXiv:cond-mat/1304.2603v1.

[5] S. Sugiura and A.Shimizu, Phys. Rev. Lett. 108, 240401(2012).

[6] H. Otsuka, Phys. Rev. B 51, 305 (1995).

Building Algorithms for Ising Machines

Shu TANAKA
Department of Applied Physics and Physico-Informatics, Keio University
Hiyoshi, Yokohama, Kanagawa, 223-8522

We have constructed an algorithm for the Ising machines. Ising machines are expected to be highly efficient solution machines for combinatorial optimization problems, but a significant challenge is to develop an algorithm that can exploit its potential and expand its range of applications. With this background, we have studied the following three topics.

(I) Minor-embedding algorithm for simulated-annealing-based Ising machines

To input the Ising model, which represents the objective function and constraints, into the actual Ising machine to solve the combinatorial optimization problem using the Ising machine, an operation called embedding is required. The accuracy of the solution depends on the value of the hyperparameters in embedding algorithms. Therefore, appropriate hyperparameter tuning is necessary to obtain a highly accurate solution using the Ising machine. We have proposed an appropriate method for adjusting this hyperparameter based on the viewpoint of statistical mechanics. We also verified the properties of the proposed method by simulation. The results suggest that the proposed method is superior to the commonly used hyperparameter adjustment method for embedding algorithms [1]. The work was done in collaboration with Tatsuhiko Shirai (Waseda Univ.) and Nozomu Togawa (Waseda Univ.).

(II) Quantum annealing with correlated disorder transverse fields

When solving a combinatorial optimization problem in conventional quantum annealing, a uniform transverse magnetic fields are applied to all spins, and the transverse fields are gradually weakened on the same schedule. It was recently reported that the solution accuracy is improved by introducing inhomogeneity in the transverse fields. We have succeeded in obtaining rigorous inequalities for the upper and lower bounds of the dynamical critical exponents for the disordered one-dimensional transverse field Ising model, which can be analyzed rigorously through the free-fermion representation [2]. In addition, the dynamic critical exponents are confirmed by numerical calculations to see the finite size effect. The work was done in collaboration with Tatsuhiko Shirai (Waseda Univ.).

(III) Development of black-box optimization using Ising machines

We have previously proposed a method for black-box optimization using Ising machines and demonstrated it for automated metamaterial design [3]. We are currently working on expanding the scope of this method and are preparing a paper on it. The work was done in collaboration with Ryo Tamura (NIMS/Univ. of Tokyo).

References

[1] T. Shirai, S. Tanaka, and N. Togawa: IEEE Access **8** (2020) 210490.

[2] T. Shirai and S. Tanaka: Annals of Physics, Accepted.

[3] K. Kitai, J. Guo, S. Ju, S. Tanaka, K. Tsuda, J. Shiomi, and R. Tamura: Physical Review Research **2** (2020) 013319.

Diversity in memory effects of flow in paste

Akio NAKAHARA

College of Science and Technology, Nihon University
7-24-1 Narashino-dai, Funabashi, Chiba 274-8501

A dense packed colloidal suspension, called a paste, remembers the direction of its motion, and its memory is visualized as a morphology of desiccation crack patterns. When a paste remembers the direction of its vibrational motion, desiccation cracks propagate in the direction perpendicular to the direction of the vibration, while, when a paste remembers its flow motion, cracks propagate along the flow direction, as are shown in Fig. 1 [1].

Here, $CaCO_3$ paste remembers the direction of vibrational motion but cannot remember flow direction. Note that $CaCO_3$ particles are charged in water. Numerical simulations of shear motion of colloidal suspension using LAMMPS show that, for the emergence of memory of flow, the attractive interaction should be dominant in short range interaction between colloidal particles. In numerical simulations, colloidal particles attract each other via Lennard-Jones potential and receives Stokes's drag force from surrounding fluid. Elongated clusters are formed along flow direction, but when attractive interaction is eliminated in the model, colloidal particles could not form any elongated clusters along flow direction and that is why $CaCO_3$ paste cannot remember flow direction.

When NaCl is added to $CaCO_3$ paste, the paste gets the ability of remembering flow direction due to the screening effect by Cl^- ions. Recently it is experimentally found that by adding filtered starch solution into $CaCO_3$ paste, the paste also gets the ability of remembering flow direction. However, if we add more filtered starch solution into the paste, the paste loses the ability of remembering flow direction. To explain this phenomenon, the adsorption of starch polymer onto colloidal particles should be included into the model, and numerical simulations based on the model are in preparation.

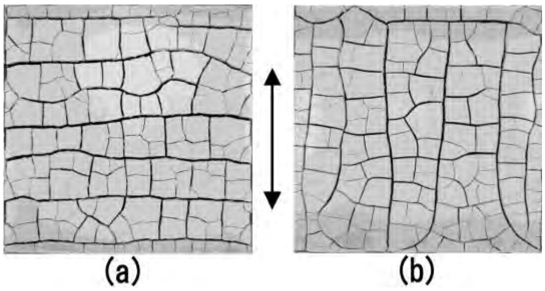

Fig. 1: Desiccation crack patterns induced by memory effect of vibration in (a) and flow in (b).

References

[1] A. Nakahara, T. Hiraoka, R. Hayashi, Y. Matsuo, S. Kitsunezaki, Phil. Trans. R. Soc. A377:20170395 (2018).

Magnetic structures under the non-equilibrium state of the magnetic thin films with the dipolar interaction

Hisato KOMATSU, Yoshihiko NONOMURA, and Masamichi NISHINO
National Institute for Materials Science, Namiki, Tsukujba, Ibaraki 305-0044

Magnetic structure of spin systems is an important subject of solid-state physics and statistical mechanics, which affects the various behaviors of systems. In particular, magnetic friction, the frictional force caused by the magnetic interaction between spins, is an example of non-equilibrium phenomena that the magnetic structure have an important role[1, 2].

We already introduced the model of magnetic friction which shows the crossover or transition from the Dieterich-Ruina law to the Stokes law in our previous study [3]. Spins of this model interact with each other by the short-range interaction, and we have not considered whether the behavior of the friction changes in the case of the long-range interaction system. However, consideration on general long-range interaction systems, including the dipolar interaction system, is difficult, because they make complicated magnetic structures depending on the condition[4] and need $O(N^2)$ computational complexity. Hence, we should first consider a relatively simple example of the long-range interaction system.

In this study, we introduce a model where the spins interact with each other by the infinite-range interaction. This model resembles that of our previous study, except for the interaction range. The reason why we choose the infinite-range interaction systems is the points that the computational complexity of the numerical simulation is $O(N)$, and the behavior at the thermodynamic limit can be investigated by mean field analysis.

According to the numerical and theoretical study, this model always obeys the Stokes law when the temperature is higher than the critical value, T_c, whereas the short-range model shows a crossover or transition from the Dieterich-Ruina law to the Stokes law even when the temperature is higher than the equilibrium transition temperature. This is because the frictional force of the present model depends directly on the long-range order and disappears when the order becomes zero. It is the large difference between two models. In the case that the temperature is lower than T_c, the model shows a crossover or transition similar to that of the short-range model when $N < \infty$, whereas it shows hysteresis dependence when $N \to \infty$. This seemingly contradictory behavior is caused by the divergence of the relaxation time in the large-N limit.

Result of this study is published as Ref. [5]. Systems with realistic long-range interaction such as the dipolar interaction should be studied in future works.

The numerical calculations of this study were mainly performed on the Numerical Materials Simulator at National Institute for Materials Science. We applied for the usage of the ISSP Supercomputer in preparation for transfer of affiliation. However, we have ended without any transfer, and have not used the ISSP Supercmputer.

References

[1] D. Kadau, A. Hucht, and D. E. Wolf: Phys. Rev. Lett. **101** (2008) 137205.

[2] M. P. Magiera, L. Brendel, D. E. Wolf, and U. Nowak: Europhys. Lett. **87** (2009) 26002.

[3] H. Komatsu: Phys. Rev. E. **100** (2019) 052130.

[4] K. De'Bell, A. B. MacIsaac, and J. P. Whitehead: Rev. Mod. Phys **72** (2000) 225.

[5] H. Komatsu: Phys. Rev. E. **102** (2020) 062131.

Establishment of new analysis method for extend X-ray absorption fine structure with sparse modeling

Hiroyuki KUMAZOE
Institute of Industrial Nanomaterials, Kumamoto University
Kurokami, Chuo-ku, Kumamoto, 860-8555

Measurement of extended X-ray absorption fine structure (EXAFS) is one of the primary methods to obtain local structure information around a specific element with atomic scale. We are building a new method for the analysis of EXAFS by the sparse modeling [1]. This year, we focused on using new basis function based on the multiple scattering theory.

To perform the sparse modeling on the EXAFS signals, we employed a new model of the EXAFS formalism based on the multiple scattering theory [3]. we consider two-body terms which are the main contribution of the EXAFS:

$$\chi(k) = \int_0^\infty \gamma^2(r,k)n(r)\,dr, \tag{1}$$

where, $\chi(k)$ is the EXAFS signal as a function of the photoelectron wavenumber; $n(r)$ is the coordination number of the distance r and $\gamma^2(r,k)$ contains the two-body scattering term corresponding to the same geometrical configuration. We use a complex Hedin–Lundqvist potential for inelastic loss effects in the framework of the multiple scattering theory. To obtain the local structure information, we solve Eq. (1) with L_1 regularization.

$$\hat{\boldsymbol{w}} = \arg\min_{\boldsymbol{w}} \left[\frac{1}{2} \|\boldsymbol{y} - \mathbf{X}\boldsymbol{w}\|_2^2 + \lambda \|\boldsymbol{w}\|_1 \right], \tag{2}$$

where the regression coefficient is $\boldsymbol{w}$. The response vector, $\boldsymbol{y}$ comes from the target data and the predictor matrix, $\mathbf{X}$ incorporates other terms in Eq. (1). In this method, some elements of the coefficient, $\boldsymbol{w}$ is are suppressed to exactly zero with the moderate value of λ.

Let us consider the sparse regression problem for the LASSO estimations within Bayesian inference to choose the regression parameter, λ. In Bayesian inference, this linear regression problem is optimized by maximizing the posterior probability. Here, we introduce the Bayesian free energy [2] as an information criterion to optimize a regularization parameter and to extract the physical model appropriately. As a result, we estimated the radial distribution function with fewer bases than in previous studies [1].

This work was supported by JST CREST Grant Number JPMJCR 1861, Japan.

References

[1] I. Akai, K. Iwamitsu, Y. Igarashi, M. Okada, H. Setoyama, T. Okajima, and Y. Hirai, J. Phys. Soc. Jpn. **87**, 074003 (2018).

[2] Y. Igarashi, H. Takenaka, Y. Nakanishi-Ohno, M. Uemura, S. Ikeda, and M. Okada, J. Phys. Soc. Jpn. **87**, 044802 (2018).

[3] F. Iesari, H. Setoyama, Y. Igarashi, M. Okada, H. Kumazoe, K. Iwamitsu, I. Akai, Y. Seno, and T. Okajima, arXiv:2104.01805 [physics.data-an].

Nonequilibrium phase transition and slow dynamics in the dense hard sphere systems

Masaharu ISOBE
Nagoya Institute of Technology
Gokiso-cho, Showa-ku, Nagoya, 466-8555

As one of the simplest models, the hard disk/sphere systems have been investigated in the field of both equilibrium and non-equilibrium statistical physics. In this project, we investigated non-equilibrium phenomena in the hard disk/sphere model system with modern algorithms, especially for Event-Chain Monte Carlo(ECMC) [1] and Event-Driven Molecular Dynamics(EDMD) [2], where we propose the "Hybrid Scheme", namely, ECMC for equilibration and EDMD for calculation of dynamical properties [3].

Direct Evidence of Void-Induced Structural Relaxations in Colloidal Glass Formers:

The mystery of the microscopic origin of kinetic arrest and slow relaxation mechanisms of glass-forming materials has puzzled scientists for decades in condensed and statistical physics. In general, when a liquid is rapidly cooled (compressed), its molecular arrangement remains disordered, and its motion becomes frozen, resulting in a glassy state. This causes "slow relaxation" due to the increase in viscosity. Most of the particles are frozen and do not move. Still, in rare cases, it is known that "active particles" that cause large displacements are generated in a spatially heterogeneous manner and move cooperatively. The cooperative motions of these "active particles" are roughly classified into two types: cooperative motions as a core-like domain region and string-like hopping chain motions, which have been observed in simulations at first. In the latter type of hopping chain motion, a void with a size of diameter is required for the initial hopping. However, in high densities, such a void does not exist, which is a paradox. One of the crucial issues is understanding whether the essential properties of glass forming materials are fundamentally thermodynamic or dynamic in origin. One perspective that favors a dynamic origin is called Dynamic Facilitation (DF) theory [4, 5]. However, the microscopic origin of structural (so-called α) slow relaxation in deeply supercooled liquids at an atomic scale has remained elusive due to the limitation of electron microscopy experiments and computer simulation.

Recently, we devoted to investigating the applicability of DF theory to athermal systems, i.e., systems of hard particles where the relevant control parameter is pressure, under "super-compressed" conditions, using "Hybrid Scheme" [6]. Besides, the optical microscopy experiments on colloidal glass former system play an important role because detailed motions of individual particles can be accessible. International collaboration project with Hong Kong, we precisely traced the movement of individual colloidal particles for a long time in experiments As a result, (A) the colloidal particles undergo a transition from collective "creeping" to the string-like "hopping" motion on approaching the glass transition, and the structural relaxation of the supercooled glass is just caused by string-like escape hopping motion. (B) In the supercooled glassy states, small fragmented voids distributed over a few particle distances, called quasi-voids, cooperatively promote the formation of large voids. (C) The voids are transported like particles, which drive a string-like hopping chain motion. In addition, we found (a) the cooperative motion of the core-like domain regions of the "active particles" observed in previous studies can be decomposed into a hopping chain motion with a higher temporal resolution, and (b) the hopping chain motion is reversed with high probability and causes a string-repetition motion, which is proved to be the leading contribution to the kinetic arrest for slow relaxation. These new findings provide fundamental insights into the structural relaxation of glass-forming materials and may pave the way for a full understanding of the microscopic mechanism [7].

Non-equilibrium response and slow equilibration in hard disk systems

The "equilibration" (relaxation toward equilibrium states) from initial non-equilibrium states in the molecular simulations is one of the crucial preliminary tasks to obtain the physical properties in "true" equilibrium. The issue such as crystallization and glass/jamming transition have been actively studied recently. It often requires a large-scale simulation in dense molecular systems, which needs a long computational cost for equilibration. In general, the equilibration of particle positions in dense systems is much difficult due to the excluded volume effect being dominant. To obtain the equilibrium states, it is a reasonable choice to use ECMC for positional relaxation at first, which is the central idea of a hybrid scheme [3]. To elucidate the microscopic origin of equilibration in a hard disk system, we investigate the relaxing process toward the liquid states as a non-equilibrium response induced by the disturbance of the homogeneous expansion. After such disturbance around the Alder transition is induced, we performed EDMD and estimated the relaxation time of four physical properties. As the preliminary results, we do not expect, an anomalous slow equilibration toward the liquid states to emerge when starting from the co-existence phase in large-scale EDMD. To identify the physical mechanism of anomalous slow equilibration, we found that the spatial inhomogeneity of the initial equilibrated phases would contribute to the relaxation time, which was confirmed by the probability distribution of local density and orientational order parameter[8]. We plan to investigate further by changing methodologies systematically.

References

[1] E. P. Bernard, W. Krauth, and D. B. Wilson: Phys. Rev. E **80** (2009) 056704.

[2] M. Isobe: Int. J. Mod. Phys. C **10** (1999) 1281.

[3] M. Isobe: Mol. Sim. **42** (2016) 1317.

[4] D. Chandler and J. P. Garrahan: Annu. Rev. Phys. Chem. **61** (2010) 191.

[5] A. S. Keys, L. O. Hedges, J. P. Garrahan, S. C. Glotzer, and D. Chandler, Phys. Rev. X, **1** (2011) 021013.

[6] M. Isobe, A. S. Keys, D. Chandler, and J. P. Garrahan: Phys. Rev. Lett. **117** (2016) 145701.

[7] C.-T. Yip, M. Isobe, C.-H. Chan, S. Ren, K.-P. Wong, Q. Huo, C.-S. Lee, Y.-H. Tsang, Y. Han, and C.-H. Lam: Phys. Rev. Lett. **125** (2020) 258001.

[8] D. Mugita and M. Isobe: EPJ Web Conferences, in press.

Quantum liquid crystals in the finite-field KΓ model for α-RuCl$_3$

Masahiko G. YAMADA and Satoshi FUJIMOTO
Department of Materials Engineering Science, Osaka University
Toyonaka, 560-8531, Japan

We study the extended Kitaev model called the KΓ model, using a perturbative expansion. From the Kitaev limit $K = 0$, the third-order perturbation in Γ leads to interacting Majorana models, which are solved by a well-controlled mean-field approximation and a cutting-edge exact diagonalization. In the exact diagonalization we use a thread parallelization up to 112 threads. By this large-scale calculation, the exact diagnolization up to 54 sites of Majorana fermions in the symmetric honeycomb geometry is possible, while usually the exact diagonalization has been done in the small system size up to 24 or 32 sites.

From the exact diagonalization combined with the mean-field theory, we found the following phases [1].

1. a Kekulé Kitaev spin liquid.
2. a non-Abelian chiral spin liquid.
3. an Abelian chiral spin liquid.
4. a nematic Kitaev spin liquid.
5. a Vijay-Hsieh-Fu surface code [2].

Especially, a Kekulé Kitaev spin liquid with a Chern number 0 and a Vijay-Hsieh-Fu surface code are new phases discovered in this large-scale calculation.

The results imply the existence of a vast region of quantum liquid crystal states (a nematic Kitaev spin liquid and a Kekulé Kitaev spin liquid). Both phases break the three-fold rotation symmetry of the system, and potentially explains the experimentally observed high-field state with zero Chern number in α-RuCl$_3$ [3]. This observation leads to a potential control of quantum states by a domain wall motion in quantum liquid crystals.

References

[1] M. G. Yamada, and S. Fujimoto: in preparation.

[2] S. Vijay, T. H. Hsieh, and L. Fu: Phys. Rev. X **5** (2020) 041038.

[3] O. Tanaka *et al.*: arXiv:2007.06757 (2020).

Crowding Movement of Cells

Katsuyoshi Matsushtia
Depertment of Biological Science, Graduate School of Science, Osaka University
Machikaneyama, Toyonaka, Osaka 560-0043

Cells are indispensable constituents of the organism's body. Cells are distributed to proper positions to function in the various organs in the developmental processes of organisms [1]. In this distribution, cells sometimes take a crowding state and move spontaneously. This crowding movement is expected to finally lead to a jamming state of cells through their steric interactions [2, 3]. In contrast to this expectation, cells smoothly move, similarly to fluid, and, further, enhances their motility as shown in the observations of Dictyostelium discodeum, neuron, and blood cells [4]. The understanding of this crowding movement is a basic common issue in the fields of soft matter physics and developmental biology.

Some of the eukaryote cells including *Dictyostelium discodeum* use the persistent memory of cell trajectory to stabilize their movements [5]. We additionally showed that the memory induces the collective movement of cells [6, 7]. The formation of collective movements is expected to have the same origin of the self-propelled disks [8]. To get hints to clarify the mechanism of the crowding movement, the comparison to the self-propelled disks is effective. The self-propelled disks have been well confirmed to stabilize collective movement in the sparse condition through the inelastic multiple collisions. In this case, the memory of trajectories aligns movement directions of disks in the collisions. In contrast, the investigation of the crowding self-propelled disks so far has clarified the destabilization of the crowding movements and take a disordered state [9]. This result is contradictory to the crowding movement of cells and implies that the crowding movements have an uncovered necessary condition.

To clarify the condition of the cellular crowding movement, we investigate the crowding movement on the basis of the cellular Potts model [10]. At the first step of this investigation, we attempt to confirm that the crowding model cells can stabilize their collective movements. To this end, we develop the model extension for dealing with the general polarity of cells [11, 12] and by using this extension remodels the memory of cell trajectory [13, 14]. By using Monte Carlo simulation based on our model, we successfully reproduced the collective movements even in crowding cells [15]. Further, the models show that the crowding state rather stabilizes the collective movement of cells. More concretely, we show that the threshold propulsion of the collective movement is reduced as the concentration of cells increases. This result at least shows that the crowding movement is possible for cells and clearly indicates that the model cells satisfies the aforementioned necessary condition of the crowding movements.

The key to clarify the condition is the origin of ordering, namely the memory of trajectories. To deeply examine effects of the memory, we try to evaluate the relation between the memory and the stability of collective movement in the crowding cells [15]. In a case, the crowding cells with movement show a solid to fluid transition, and then their configurations highly fluctuate. By using this transition, we confirm the stability in the order of movement in the crowding model cells. We can show that even at the transition point, the cells exhibit the ordering of the movement under the high fluctuation of cell configurations. To further approach the origin of this stability [16], we consider memory time dependence of this movement order. We show that the stability depends highly on the memory time. Namely, the long memory time is the origin of the stability of movements in the crowding cells.

Based on the comparison of this result and that of the self-propelled disks, we attempt to shed light on the uncovered necessary condition. For the case of the self-propelled disks, the movement has an intrinsic fluctuation. In contrast to these disks, the model cells reduce the intrinsic fluctuation in their setting to resemble the cells with the memory of cell trajectory. In the disks, the intrinsic fluctuation shortens the memory time of the disk trajectory. Thus, the disks have a possibility that the disks lose the stabilization property of the collective movements. This difference in the intrinsic fluctuation of movements reflects the difference in the stability in crowding movements between the model cells and self-propelled disks. Thus, we speculate that the reduction of intrinsic fluctuation is the necessary condition of crowding movements.

These successes of the works are attributed to kind cooperation with Prof. H. Kuwayama, Prof. S. Yabunaka, Prof. K. Fujimoto, Dr. H. Hashimura, Prof. H. Yoshino, and Prof. M. Kikuchi. The author deeply thank them.

References

[1] C. J. Weijer, J. Cell Sci. **122**, 3215 (2009).

[2] S. Henkes, Y. Fily and M. C. Marchetti, Phys. Rev. E **84**, 040301(R) (2011).

[3] L. Berthier Phys. Rev. Lett. **112**, 220602 (2014)

[4] P. Rørth, Ann. Rev. Cell Develop. Biol. **25**, 407 (2009).

[5] H. Takagi, PLoS ONE **3** e2648 (2008).

[6] K. Matsushita, *et al.*, Proc. Sympo. Traffic Flow Self-driven Parti. **24**, 5 (2018a).

[7] K. Matsushita, *et al.*, J. Phys. Soc. Jpn **88**, 103801 (2019).

[8] C. A. Weber, *et al.*, Phys. Rev. Lett. 110, 208001 (2013).

[9] T. Hanke, C. A. Weber, and E. Frey Phys. Rev. E 88, 052309 (2013).

[10] F. Graner and J. Glazier, Phys. Rev. Lett. **69**, 2013 (1992).

[11] K Matsushita, Phys. Rev. E **95**, 032415 (2017).

[12] K Matsushita, Phys. Rev. E **97**, 042413 (2018).

[13] B. Szabó, *et al.*, Phys. Rev. E, **74**, 061908 (2006).

[14] A. J. Kabla J. Royal Soc. Interface **9**, 3268 (2012).

[15] K. Matsushita, *et al.*, , Proc. Sympo. Traffic Flow Self-driven Parti. **25** 5 (2019).

[16] K. Matsushita, S. Yabunaka, K. Fujimoto J. Phys. Soc. Jpn **90**, 054801 (2021).

Multiple helical spin density waves in inversion-symmetric itinerant magnets

Takashi UCHIDA
Hokkaido University of Science
4-1, 7-15, Maeda, Teine-ku, Sapporo 006-8585

Since the discovery of magnetic skyrmions in B20 transition metal compounds, multiple helical spin density waves have attracted attention because the magnetic skyrmions emerge as 3Q multiple helical spin density waves in these materials. Typically, the magnetic skyrmions are realized in the Dzyaloshinskii-Moriya (DM) interaction driven systems under magnetic field. Recently, frustrated systems without the DM interaction have been found to reveal magnetic skyrmions [1, 2]. In order to explore theoretically the possibility of vortex-type multiple helical spin density waves such as magnetic skyrmions in the inversion-symmetric itinerant systems, we have applied the molecular spin dynamics (MSD) method [3] to the triangular-lattice single-band Hubbard model.

The MSD method is based on the functional integral method for the spin fluctuation theories and the isothermal molecular dynamics method. The method allows us to find automatically the magnetic structure of a large system with thousands of atoms in a unit cell at finite temperatures. Starting from the Hamiltonian expressed in terms of the locally rotated coordinates and by adopting the static approximation to the functional integral technique, the MSD method reduces to the generalized Hartree-Fock approximation at the ground state.

In the numerical calculations the most time-consuming process is the magnetic force calculation at each time step, where the local electronic structures are calculated in real space by means of the recursion method. We have adopted the automatic parallel calculation scheme and found it to be effective in saving both computing time and CPU resources.

We have performed the magnetic structure calculations on the supercell with 20×20 triangular lattice, which is embedded in a large cluster consisting of 3×3 supercells, each of which are connected by the periodic boundary condition. Under zero magnetic field and the fixed value of the temperature $T/t = 0.0005$, we have explored the magnetic structures changing the Coulomb interaction strength U/t and the electron number n along the antiferromagnetic (AF)-ferromagnetic (F) boundary ($n = 1.3 \sim 1.4$) . We have performed rather long-step MSD calculations (more than 15000 steps) to find the thermodynamically stable states among the various metastable multiple-Q states and have found that for $U/t = 5.0 \sim 8.0$ the 1Q helical spin density waves are stabilized in the vicinity of the AF-F boundary. To explore the possibility of 3Q multiple helical spin density waves, the MSD calculations for $U/t < 5.0$ are now in progress.

References

[1] T. Okubo, S. Chung, and H. Kawamura: Phys. Rev. Lett. **108** (2012) 017206

[2] Y. Kakehashi: J. Phys. Soc. Jpn. **89** (2020) 094710.

[3] Y. Kakehashi, S. Akbar, and N. Kimura: Phys. Rev. B**57** (1998) 8354.

Robustness of cluster states and stabilizer states for surface codes against random local fields

Tetsufumi Tanamoto
Department of Information and Electronic Engineering, Teikyo University
Utsunomiya 320-8511, Japan.

By using the ISSP supercomputer, we numerically solve a time-dependent Schrödinger equation of a many-qubit system and theoretically describe how random local fields affect cluster states and stabilizer states for surface codes [1]. While there are already several known sources of decoherence in gate operation and measurement processes, we here focus on a new source of decoherence due to effects of field fluctuations on idling qubits which should become increasingly more serious as quantum computers scale up. We find similar temporal fidelity degradation for both cluster states and stabilizer states of surface codes for up to ten qubits. We also find that the effect of local-field fluctuations is greatly mitigated if the magnitude of the fluctuations can be suppressed to below 10% of the energy gap Δ for both cluster states and stabilizer states of the surface codes. If the magnitude of the fluctuations exceeds $\Delta/2$, the state fidelities for both states deteriorate dramatically. A simple estimate based on the average fidelity up to time $t \sim 2\hbar/\Delta$ shows that the maximum number of qubits that can suppress the system infidelity below the 1% is less than 28 for the surface code stabilizer states and 21 for the cluster states when the initial states are ground states (Fig.1).

We have also used the ISSP supercomputer to calculate the sucess probability of our proposed pulse sequence in the quantum annealing mechanism [2].

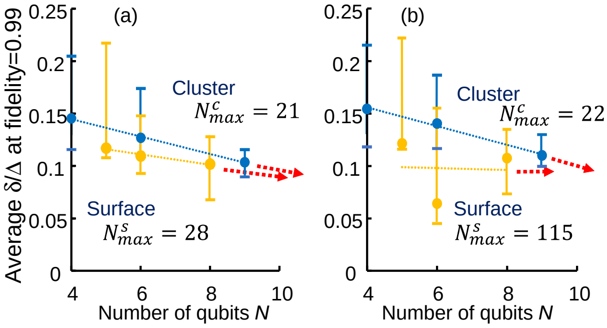

Figure 1: Average variation δ/Δ at which the fidelity is 0.99 for the cluster states and the surface-code states. The error bars are calculated from the standard deviation of δ/Δ. The extrapolation equations for the cluster states and surface-code states in (a) are given by $\delta/\Delta = -0.0053N + 0.1079$ and $\delta/\Delta = -0.0033N + 0.0924$, respectively. Those in (b) are given by $\delta/\Delta = -0.0004N + 0.0567$ and $\delta/\Delta = -0.0014N + 0.0732$, respectively. The extrapolation of these data points to the horizontal axis gives a rough estimate for the maximum number of qubits N^s_{max} and N^c_{max}, for which the errors can be corrected.

References

[1] T. Tanamoto and M Ueda: ArXiv:1910.05649

[2] T. Tanamoto: J. Appl. Phys. **84** (2015) 31415.

Development of integrated interface of eigensolvers Rokko and application to quantum spin systems

Tatsuya Sakashita
Center for Quantum Information and Quantum Biology, Osaka University
1-2 Machikaneyamachō, Toyonaka, Osaka 560-0043

To establish universal exact diagonalization package for quantum lattice models including the Heisenberg-Kitaev model, we focused on developing integrated interfaces for eigensolvers, "Rokko"[1].

In Rokko, we implemented the integrated interfaces for the following types:

- Serial solvers for dense matrices (Eigen3, LAPACK)
- MPI parallelized solvers for dense matrices (EigenExa[2], ELPA[3], Elemental[4], ScaLAPACK)
- MPI parallelized solvers for sparse matrices (Anasazi in Trilinos[5], SLEPc[6]) to cover matrix representations below:
  - CRS (Compressed Row Storage)
  - Matrix-free method (the method to give matrix-vector product routines to solvers)

Rokko has the following features:

- Integrated interfaces for eigensolvers and matrices, independent of individual eigensolver libraries
- Rokko's interfaces are implemented by utilizing factory. It enables the user to dynamically select a solver.
- C, Fortran, and Python bindings of Rokko
- Automatically detecting libraries by using CMake in building Rokko
- Unit and integrated test programs by GoogleTest
- Install scripts of eigensolvers for various architectures

We prepare a paper to report design policy, software structure, and usage examples of Rokko.

References

[1] T. Sakashita, R. Igarashi, Y. Motoyama, T. Okubo, and S. Todo. Repository of Rokko. `https://github.com/t-sakashita/rokko.git`, 2012.

[2] T. Imamura, T. Hirota, and T. Fukaya. EigenExa web page. `https://www.r-ccs.riken.jp/labs/lpnctrt/projects/eigenexa/`, 2021.

[3] ELPA Consortium. ELPA (Eigenvalue soLvers for Petaflop Applications web page). `http://elpa.rzg.mpg.de`, 2013.

[4] J. Poulson. Distributed-memory dense linear algebra Elemental web page. `https://github.com/elemental/Elemental`, 2013.

[5] M. A. Heroux, R. A. Bartlett, and V. E. Howle. Trilinos Project web page. `https://trilinos.github.io`, 2003.

[6] V. Hernandez, J. E. Roman, and V. Vidal. SLEPc web page. `http://slepc.upv.es`, 2002.

Comparison of rocking curves of 4 2 2 Bragg-reflected X-rays from thin silicon crystals calculated based on the conventional method and by solving the eigenvalue problem

Kouhei OKITSU

Institute of Engineering Innovation, School of Engineering,
The University of Tokyo, 2-11-16 Yayoi Bunkyo-ku Tokyo 113-8656

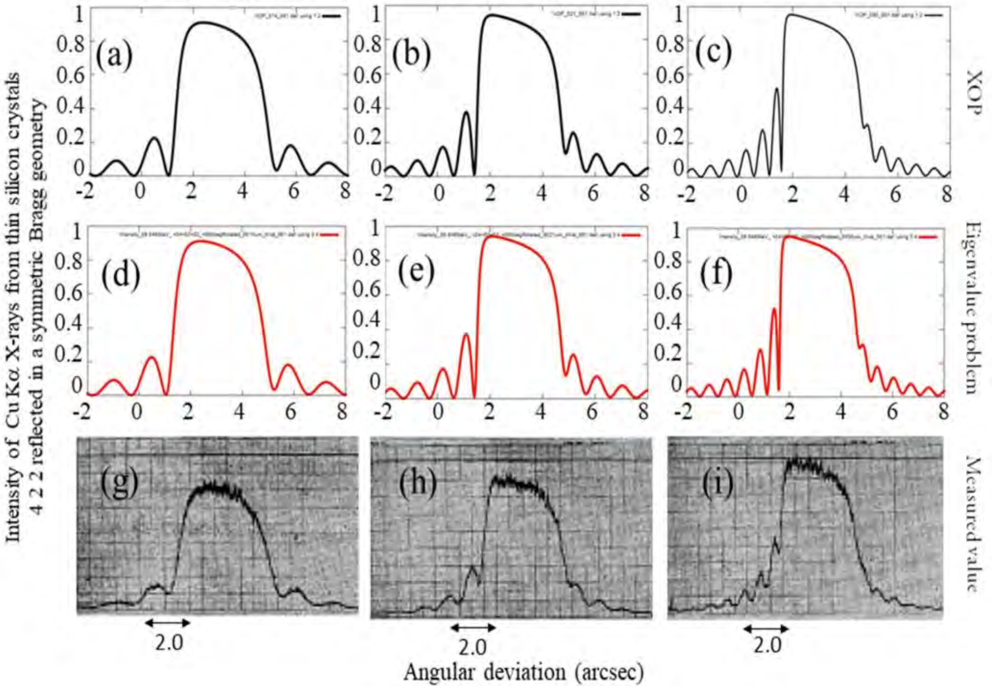

Fig. 1 Rocking curves of 4 2 2 Bragg-reflected X-rays from thin (14, 21 and 30 mm thick) silicon crystals. (a), (b) and (c) were calculated based on the conventional method. (d), (e) and (f) were obtained by solving the eigenvalue problem. (g), (h) and (i) were experimentally obtained [1]. The experiments were performed with the temperature carefully stabilized with the incidence of highly collimated and monochromatized X-rays generated from a Cu $K\alpha$ source.

The present author has worked on the n-beam Ewald-Laue (E-L) and Takagi (T-T) X-ray dynamical diffraction theories and numerical method to solve them for over twenty years [2,3]. However, this report describes two-beam rocking curves calculated based on the E-L theory and experimentally obtained over fifty years ago.

Professor H. Hashizume kindly taught the present author the existence of rocking curves experimentally obtained in 1970 [1]. He is one of the ranking authorities of the dynamical diffraction theory of X-rays. He also taught the present author that the description of the dynamical theory as the eigenvalue problem is not general and is not widely recognized.

The E-L theory was developed by Ewald (1917) and Laue (1931). The fundamental equation given by Laue is described as follows:

$$\frac{\mathbf{k}_i^2 - \mathbf{K}^2}{\mathbf{k}_i^2}\mathbf{D}_i = \sum_j \chi_{h_i - h_j} [\mathbf{D}_j]_{\perp \mathbf{k}_i} \qquad (1)$$

Here, $\mathbf{K}$ is the wave vector of the incident X-rays, $\mathbf{k}_i$ and $\mathbf{k}_j$ are the wave vectors of the Bloch wave, $\mathbf{D}_i$ and $\mathbf{D}_j$ are amplitude vectors of the ith and jth numbered Bloch wave, $\chi_{h_i - h_j}$ is the $\mathbf{h}_i - \mathbf{h}_j$ order Fourier coefficient of the electric susceptibility. $[\mathbf{D}_j]_{\perp \mathbf{k}_i}$ is the vector component of $\mathbf{D}_j$ perpendicular to $\mathbf{k}_i$.

By applying an approximation that $k_i + K \approx 2k_i$, the following equation is obtained [2,3]:

$$\xi_i D_i^{(l)} = \frac{K}{2}\sum_{j=0}^{n-1} \chi_{h_i - h_j} \sum_{m=0}^{1} C_{i,j}^{(l,m)} D_j^{(m)}. \qquad (2)$$

Here, $\xi_i = k_i - K$ (the eigenvalue), $D_i^{(l)}$ is the scalar amplitude of Bloch wave and $C_{i,j}^{(l,m)}$ is the polarization factor. The scalar amplitudes $D_i^{(l)}$ and $D_j^{(m)}$ of Bloch wave are defined as follows:

$$\mathbf{D}_i = D_i^{(0)}\mathbf{e}_i^{(0)} + D_i^{(1)}\mathbf{e}_i^{(1)}, \qquad (3a)$$

$$\mathbf{D}_j = D_j^{(0)}\mathbf{e}_j^{(0)} + D_j^{(1)}\mathbf{e}_j^{(1)}. \qquad (3b)$$

$\mathbf{e}_i^{(0)}$ and $\mathbf{e}_i^{(1)}$ are unit vectors defined such that they are perpendicular to $\mathbf{k}_i$ and mutually perpendicular to each other.

Joko and Fukuhara pointed out [4], for the first time, that eq. (2) can be described as an eigenvalue problem of a matrix for an *n*-beam dynamical theory. When *n* is 2, eq.(2) is nothing but the E-L two-beam dynamical theory that is the most wide-spread X-ray dynamical theory. This fact has been almost completely overlooked even by Ewald, Laue and many other authorities of the X-ray dynamical diffraction theory.

The conventional method to solve the X-ray two-beam dynamical theory has two steps. At first, the dispersion surfaces are calculated to give the condition that the amplitudes of Bloch wave has nonzero values. Next, for cross points (tie points) of the dispersion surfaces and the downward surface normal of the crystal, the amplitudes of Bloch wave are calculated to obtain the rocking curves.

However, eq.(2) for *n*=2 (two-beam case) can be solved directly without calculating the dispersion surfaces. The eigenvalue problem can be solved e.g. by using the LAPACK to calculate the rocking curves of Bragg-reflected X-rays as found in Figs. 1 (d), (e) and (f). They are in excellent agreement with those experimentally obtained [Figs. 1 (g), (h) and (i)] and calculated by the conventional way [Figs. 1 (a), (b) and (c)].

The present author is indebted to Mr. T. Sasaki who graduated from Tokyo Gakugei University in 2021 for his assistance when coding the program.

References

[1] H. Hashizume, K. Nakayama, T. Matsushita and K. Kohra: J. Phys. Soc. Jpn. (1970) **29** 806-807.

[2] K. Okitsu, Y. Imai, and Y. Yoda: *Recent Advances in Crystallography*, (2012) pp. 67-86. InTech Open. http://dx.doi.org/10.5772/47846.

[3] K. Okitsu: *J. Jpn. Soc. Synchrotron Rad. Res.* **33** (2020) 61-80 [Invited].

[4] T. Joko and A. Fukuhara: J. Phys.Soc. Jpn. (1967) **22** 597-604.

Non-uniform thermal transport properties in proteins

Takahisa YAMATO
Graduate School of Science,
Nagoya University, Furo-cho, Chikusa-ku, Nagoya 464-8602

We have studied thermal transport properties in proteins using molecular simulations [1-5]. Within protein molecules, tightly packed amino acid residues interact with each other through heat and energy exchanges. We illustrate non-uniform heat flow with our own model based on "local heat/energy conductivity" between each residue pair.

Native contacts in proteins are classified into nonpolar, polar, and charged types. Harmonic spring picture applies to energy transfer (ET) through nonpolar and polar contacts, and ET rates vary inversely with the variance of the contact length: whereas diffusion picture is relevant to ET through charged contacts and ET rates correlate inversely with the mean-square-distance between charged atoms of a residue pair.

The *CURP* program permits to compute inter-residue flow or energy/heat and atomic stress tensor in a protein, given atomic coordinates and velocity trajectories obtained through molecular dynamics (MD). Energy flow data permit to picture an inter-reidue Energy Exchange Network (EEN) as a graph. For interactive analysis of EEN graphs using pointing devices, a new visualization tool, *EEN VIEWER*, with JavaScript and Python codes (https://youtu.be/zCXmIXskBFE) is under development.

We implemented an accelerated *CURP* code via GPU computing with the OpenACC library. As a test calculation, this program was applied to a sensory domain of an oxygen sensor protein, FixL. As a result, the computation time of the auto-correlation function of heat currents in FixL was accelerated by 98.4%.

Human superoxide dismutase (SOD1) is known to bind metal ions for its function. To study the selective binding metal binding mechanism of SOD1, QM/MM molecular dynamics simulation using *Gromacs/DFTB* is under progress. We plan to analyze the fluctuations the metal binding sites using the *CURP* program.

References

[1] P. Humanath, K. M. Reid, T. Yamato, D. M. Leitner: J. Phys. Chem. B **124** (2020) 9852.

[2] K. M. Reid, T. Yamato, D. M. Leitner: J. Phys. B. **124** (2020) 1148.

[3] T. Yamato: Seibutsu Butsuri **60** (2020) 94.

[4] D. M. Leitner, T. Yamato: Biophys. Rev. **12** (2020) 317.

[5] T. Yamato: Biophys. Rev. **12** (2020) 291

3.5 SCCMS Projects

Development of molecular simulation framework for studying mesoscale liquid dynamics

Hayato SHIBA
Information Technology Center, University of Tokyo
Kashiwanoha, Kashiwa, Chiba 277-0882

I now work on a large-scale molecular simulation of the dynamics of liquids. This year was in the phase of developing new code. The achievements are described in two parts in the following, in which simulations on the scale of millions of atoms (particles) are enabled.

1 Development for large-scale electrolyte simulators

Dilute electrolytes, water with a small amount of dissolved ions, are indispensable for functional properties in, for example, biological function and batteries. For the purpose of elucidating many-body properties produced by correlated ions, million-atom scale molecular dynamics simulations may provide valuable insights by directly incorporating the cooperative effects induced by electrostatics.

In this year, I have developed molecular simulation code for TIP4P/2005 water + ions, based on Framework for Developing Particle Simulator (FDPS) [1], FDPS provides a library that automatically produces spatial decomposition by the recursive multi-section method associated with tree construction for for fast communication between different MPI processes, which means that the users can concentrate on implementing force fields and time development schemes. Importantly, tree method ensures scaling with $O(N \log N)$, bypassing the necessity for using FFT that prevents parallel scalability. Currently, I have achieved the speed of 12,000 steps per day for a system with 192,000 atoms. Further application tuning is ongoing, targeting 50,000 steps per day on ISSP System B (Ohtaka).

2 Development simulators for long-time correlations in glasses

When a liquid is rapidly cooled down, it turns into a glass with solidity, keeping the random atomic configurations. About two years ago, I have revealed power-law correlations in the long-time behavior of the velocity autocorrelation function in such a supercooled liquid in two dimensions. In order to fully address such a long-time correlations both in two and three dimensions, it is necessary to calculate time-dependent trajectories of each individual particle. This brings about difficulties in MPI parallelization using the spatial decomposition, because particles are no longer bound to the memory of a specific CPU. In FY2020, I have added some time-series analysis code for shared memory environment to my existing distributed parallel code for a Lennard-Jones binary mixture with Kob-Andersen parameters. The whole codes are also extended to equip CUDA routines, enabling us to calculate the autocorrelations on shared memory environment by accelerating the force-field calculation on GPUs. I am currently using this for studying space and time correlations in 2D and 3D glass-forming liquids with $O(10^7)$ particles.

References

[1] `http://fdps.jmlab.jp`

Creating a Wannier function database toward material design

Kazuyoshi YOSHIMI
Institute for Solid State Physics, University of Tokyo, Kashiwa 277-8581

As a numerical scheme for non-empirical analysis of electronic states in strongly correlated materials, the development of a calculation method based on first-principles calculations has been actively studied in recent years. In this method, the effective Hamiltonian describing the low-energy degrees of freedom is derived from the band structure obtained by the first-principles calculation [1]. The derived *ab-initio* effective Hamiltonian can be analyzed with high accuracy using low-energy solvers such as numerical exact diagonalization [2] and multivariate variational Monte Carlo methods [3] to reveal the electronic states of real solids in a non-empirical manner. On the other hand, these analyses require a high level of expertise and experience in the generation of the Wannier function, which is required in the derivation of the effective Hamiltonian. If this task can be automated, it will be possible to automatically generate model analyses for various materials, which will greatly expand the framework of material design.

In this project, we have developed a tool for automatic generation of Wannier functions and made dataset for machine learning. The Wannier functions can be calculated using the first-principles calculation software Quantum ESPRESSO (QE) [4] and Wannier90 [5]. In order to create a dataset, we have modified a tool cif2qewan [6] made by T. Koretsune group at Tohoku Univ. to output the input files for QE calculation from cif files containing crystal structures. By downloading cif files from the Materials Project [7] under certain conditions and using them with this tool, we performed comprehensive calculations of Wannier functions and created a dataset.

First, we performed exhaustive calculations for about 1000 substances as a trial calculation. As a result, the calculation was successful for about 400 materials, and about 10 Wannier functions were generated for each material. In order to increase the efficiency of data generation, it was found that it could be reduced to about 10% by controlling the parameter values. We also found that the bottleneck area, which takes a lot of computation time in Wannier90, could be speeded up by MPI parallelization, and we succeeded in achieving a 10-times speedup after making changes.

In future research, we plan to perform high-throughput calculations using the tools created and accelerated in this project to create datasets of Wannier functions, and also to try to automatically generate Wannier functions using machine learning such as deep learning. This research was done by collaboration with T. Koretsune, K. Kurita, and T. Oikawa of Tohoku Univ., T. Misawa of Beijing Academy of Quantum Information Sciences, K. Ido of Institute for Solid State Physics, and TOYOTA MORTOR CORPORATION.

References

[1] K. Nakamura, Y. Yoshimoto, Y. Nomura *et al.*, Comp. Phys. Commun. **261**, 100781(2021).

[2] M. Kawamura, K. Yoshimi, T. Misawa *et al.*, Comp. Phys. Commun. **217**, 180 (2017).

[3] T. Misawa, S. Morita, K. Yoshimi *et al.*, Comp. Phys. Commn. **235**, 447(2019).

[4] P. Giannozzi, O. Andreussi, T. Brumme *et al.*, J. Phys.: Condens. Matter **29**, 465901(2017).

[5] http://www.wannier.org

[6]https://github.com/wannier-utils-dev/cif2qewan

[7] https://materialsproject.org

Computational Investigation of Charge Photogeneration in Organic Solar Cells by Fragment-Based GW/BSE Method

Takatoshi Fujita
Institute for Molecular Science
Myodaiji, Okazaki, Aichi 444-8585

Accurate calculations of electronic states are essential for computational studies of organic materials which are directed toward understanding of fundamental processes in organic electronic devices. We have recently developed the large-scale GW method based on the fragment molecular orbital method. The fragmentation approximation for the total polarization function and the ΔCOHSEX approximation have been employed for efficient evaluations of GW quasiparticle energies from localized molecular orbitals. More recently, we have proposed the novel large-scale excited-state methods based on the FMO, exciton model, and GW/BSE with Tamm-Dancoff approximation (TDA). In this method, the excited-state Hamiltonian matrix elements at the GW/TDA-BSE level is calculated in the basis of fragment configuration state functions which describe intrafragment excitations or interfragment charge-transfer excitations. The excited-state Hamiltonian is then diagonalized to approximate the adiabatic excited states of an entire system. We have confirmed that for molecular clusters, the novel fragment-based GW/TDA-BSE can reasonably reproduce the excited states obtained from conventional GW/TDA-BSE method. Our developments enables the applications of GW/TDA-BSE method to large molecular assemblies, which will be useful for investigating charge separation in condensed phase.

As recent applications [1], we explore the energy levels and charge-transfer states of the face-on and edge-on orientations of pentacene/C60 bilayer heterojunctions. FMO-GW/BSE calculations were performed for the local interface structures in the face-on and edge-on bilayer heterojunctions, which contain approximately 2000 atoms. Calculated energy levels and charge-transfer state absorption spectra are in reasonable agreements with those obtained from experimental measurements. We found that the dependence of the energy levels on interfacial morphology is predominantly determined by the electrostatic contribution of polarization energy, while the effects of induction contribution in the edge-on interface are similar to those in the face-on. Moreover, the delocalized charge-transfer states contribute to the main absorption peak in the edge-on interface, while the face-on interface features relatively localized charge-transfer states in the main absorption peak. Our results indicate that optimizing the molecular orientation and interfacial morphologies is essential for improving the power conversion efficiency of organic solar cells.

References

[1] T. Fujita, Y. Noguchi, T. Hoshi, Materials, **13** (2020) 2728.

Promising Cathode Materials for Sodium-ion Rechargeable Batteries: *Ab initio* investigations

Huu Duc LUONG[1,2], Hiroyoshi MOMIDA[2,3], Tamio OGUCHI[2,3]
[1]*Graduate School of Engineering, Osaka University, Suita, Osaka 565-0871, Japan*
[2]*ISIR, Osaka University, Ibaraki, Osaka 567-0047, Japan*
[3]*ESICB, Kyoto University, Kyoto 615-8245, Japan*

We have studied two types of promising cathode materials applicable for sodium-ion rechargeable batteries.

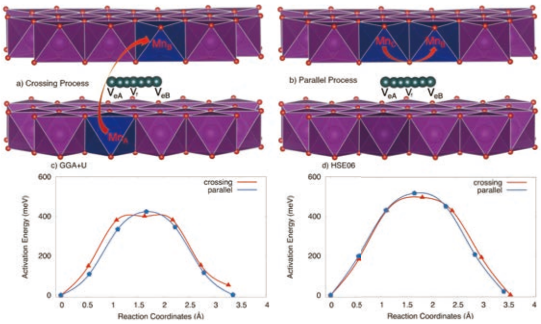

Fig. 1: Elementary diffusion processes at full charging states, including (a) crossing process and (b) parallel process and activation energy profile of Na vacancy–positive polaron complex obtained by obtained by (c) GGA+*U* and (d) HSE06 methods. The dark blue octahedrons represent the 3NN Mn sites where polaron formed, and the dark cyan balls stand for Na vacancy trace diffusion. The other Na atoms are hidden for more clarification.[1]

1. Na_xMnO_2 layered oxide

P2 layered oxide Na_xMnO_2 exhibit a voltage window from 2.0 to 3.5V and high specific capacity up to 220 mAh/g. However, the material suffers from the serious phase transformation during its charging/discharging. Using the first principles density functional theory, we explored systematically its geometric, electronic properties, phase stability and diffusion mechanism for Na^+ migration. It is found that at high or low Na concentration, Na^+ ions prefer locating only at the edge-shared prism, while at x=0.5, the material become more stable with the ratio of the Na ion at edge-shared Na_e and face-shared Na_f prism of Na_e:Na_f ≅ 2:1. When all the Na^+ ions are deintercalated from $NaMnO_2$, the conspicuous change in the lattice constant b causes an significant reduce of volume up to 20%. We pointed out that the hybridized orbitals of O's $2p_y$ states and Mn's $3d_{yz}$ and $3d_{x2-y2}$ states, play an essential role in the electronic structure of the material. We proved the polaron formation and the polaron is preferably coupling with Na^+ vacancy/ion at the third nearest neighbor sites. Two elementary diffusion processes, including parallel and crossing processes, as shown in Fig. 1, could occur and require an activation energy of 423 meV (518 meV) at high Na concentration and 273 meV (327 meV) at low Na content by GGA+U (HSE06) method. Compared to olivine phosphate, the Na^+ ion would diffuse better in Na_xMnO_2 than in polyanionic framework like $LiFePO_4$ due to the significantly lower activation energy.[1]

2. Na_xVPO_4F

A new orthorhombic phase of tavorite-like Na_xVPO_4F cathodes ($0 \leq x \leq 1$) applicable for Na-ion battery was proposed using density functional theory. We have explored the phase stability, electronic structures, electrochemical properties, and diffusion mechanisms of Na ions/vacancies of Na_xVPO_4F. No imaginary frequency in phonon dispersion provides evidence that the proposed material is thermally stable. It is suggested that the material can be synthesized from the reaction: $NaF + VPO_4 \rightarrow NaVPO_4F$ because of the negative formation energy. The material $NaVPO_4F$ would undergo bi-phase reactions upon the Na deintercalation in the ranges of $0.125 \leq x \leq 0.5$ and $0.5 \leq x \leq 1$, and show high voltages of 3.80 V and the high theoretical capacities of 143 mAhg^{-1}. The polaron migration effect on the Na^+ ion diffusion mechanism was precisely investigated. Three elementary diffusion processes, including single, crossing and parallel processes, are indicated in Fig. 2. The parallel and crossing processes require much higher activation energy for Na^+ diffusion, implying a substantial polaron migration effect. The activation barriers of Na ion diffusion gain 323 and 530 meV in the Na-rich and poor contents, respectively. Therefore, the proposed cathode can be expected to exhibit significantly faster Na-ion diffusion than that in popular cathodes such as $NaVOPO_4$ (627 meV).[2]

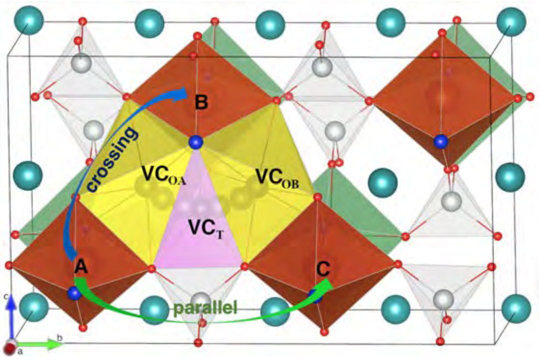

Fig. 2: Possible elementary diffusion processes of an Na vacancy (vc) accompanying by a positive polaron (pp) along the [010] direction in $NaVPO_4F$. O (red), F (blue), V (brown), P (grey), Na (cyan), and vc (black) are shown by balls, and polyhedral structural units of $V^{1NN}O_4F_2$ (brown), $V^{2NN}O_4F_2$ (green), AO_4F_2 (yellow) octahedra, and NaO_3F (purple) tetrahedra are shown. When vc moves along a path from vc$_{OA}$ to vc$_{OB}$ via vc$_T$ sites, pp can jointly hop from A to C sites (parallel process indicated by a green arrow), from A to B sites (crossing process indicated by a blue arrow), or remain at a same site (single process).

References

[1] H. D. Luong, V. A. Dinh, H. Momida, T. Oguchi, Phys. Chem. Chem. Phys. **22**, 18219 (2020).

[2] H. D. Luong, V. A. Dinh, H. Momida, T. Oguchi, J. Alloys Compd. (2021) *accepted.*

Ab initio study toward abundant element nanocatalysts with less precious metals

Tetsuya TAKETSUGU
Faculty of Science, Hokkaido University
N10W8, Sapporo, Hokkaido 060-0810

DFT computations with QuantumEspresso (QE) are used to gain chemical insights and to design novel catalysts with abundant elements such as hexagonal boron-nitride (h-BN) for reducing costs and dependences on precious metals used in various heterogeneous catalysts.

We have shown that gold clusters supported on h-BN/Au(111) are highly active catalysts for hydrogen evolution reaction (HER) [1]. It is demonstrated that the most stable gold clusters on the h-BN/Au(111) support are not necessarily the most reactive; stabilization on the surface gold clusters with the different geometries and orientation with respect to the support can form a large variety of energetically favorable H adsorption sites considerably promoting HER activity. The charge transfer between the supported gold clusters and the h-BN/Au(111) surface promotes the catalytic activity of the Au_n@h-BN/Au(111) system for HER. Therefore, h-BN/Au(111) can be considered as promising support for gold clusters as electrocatalysis [1].

Another application of BN is for oxidative dehydrogenation (ODH) of light alkanes such as olefin. Olefins are key feedstocks for range of commercially important chemicals such as polymers, fibers, and their derivatives, which are important for the energy and day to day applications. Therefore, a deeper insight into the mechanism and ways to explore catalysts for efficient oxidative dehydrogenation reaction is needed. We have proposed that oxygen functionalized h-BN with B-O-O-B sites at the zigzag edges is active catalyst for ODH. This suggestion is consistent with experimentally reported concentration of B and N atoms (high B:N ratio) to explore the ODH mechanism in a series of light alkanes [2]. DFT calculations are performed to verify our proposal. We have explored the catalytic activity of the newly proposed oxygen functionalized edges of h-BN sheets for oxidative dehydrogenation of ethylbenzene. It is demonstrated that oxygen functionalized highly defective boron-nitride can demonstrate extraordinary catalytic activity for the above reaction [2].

We have elucidated the mechanism of the novel "heterocyclic segregation" reaction of one pyrazine ring with two nitrogen atoms into two quinoline rings with one nitrogen each. Our DFT calculations showed that the intramolecular ring-forming and -opening of nitrogen-heterocycles are strongly affected by the initial hydrogen-substrate interaction [3].

References

[1] M. Gao, M. Nakahara, A. Lyalin, and T. Taketsugu, J. Phys. Chem. C **125**, 1334-1344 (2021).

[2] R. Han, J. Diao, S. Kumar, A. Lyalin, T. Taketsugu, G. Casillas, C. Richardson, F. Liu, C. W. Yoon, H. Liu, X. Sun, Z. Huang, J. Energy Chem. **57**, 477-484 (2021).

[3] K. Sun, K. Sugawara, A. Lyalin, Y. Ishigaki, K. Uosaki, T. Taketsugu, T. Suzuki, and S. Kawai, Angew. Chem. Int. Ed. **60**, 9427-9432 (2021).

Development of high-performance permanent magnets by large-scale simulation and data-driven approach

Takashi MIYAKE
CD-FMat, AIST
Umezono, Tsukuba, Ibaraki 305-8568

High-throughput first-principles calculation is a powerful tool for developing functional materials. However, systematic errors contained in computational data often prevent us from quantitative evaluation of physical properties. In order to overcome this problem, we have developed a data assimilation method in which a small number of experimental data are integrated with a large number of computational data [1]. Figure 1 is a schematic illustration of the method. Here, open circles denote accurate but a small number of data, whereas open squares are a large number of data that contain a systematic error. If we consider the former data only, we cannot estimate the target variable accurately for large x where the data do not exist, whereas accurate estimation is possible if we consider both the data. Based on this framework, we have developed a practical scheme for evaluating finite-temperature magnetization.

We have applied the scheme to $(\mathrm{Nd}_{1-\alpha-\beta-\gamma}\mathrm{Pr}_{\alpha}\,\mathrm{La}_{\beta}\,\mathrm{Ce}_{\gamma})_2\,(\mathrm{Fe}_{1-\delta-\zeta}\mathrm{Co}_{\delta}\mathrm{Ni}_{\zeta})_{14}\mathrm{B}$ [1]. In the first step, we prepared 119 experimental samples, and measured the magnetization at 3-7 temperatures within a range from 300 K to 473 K. The magnetization at zero temperature ($\mu_0 M$) and Curie temperature (T_C) are evaluated from these data by Kuzmin's formula. Independently, we performed systematic first-principles calculation for 2869 compositions using the KKR-CPA method. The saturation magnetization at zero temperature is calculated in the local spin density approximation. The intersite exchange couplings are calculated using Liechtenstein's method, from which the Curie temperature is evaluated in the mean-field approximation. We then adopted the data assimilation, and obtained $\mu_0 M$ and T_C at arbitrary composition. The magnetization at arbitrary temperature is obtained using Kuzmin's formula. Figure 2 shows the magnetization at 0 K, 300 K and 400 K. We see that the magnetization monotonically decreases with increasing Co concentration (δ) at 0 K, whereas small amount of Co doping enhances the magnetization at 400 K.

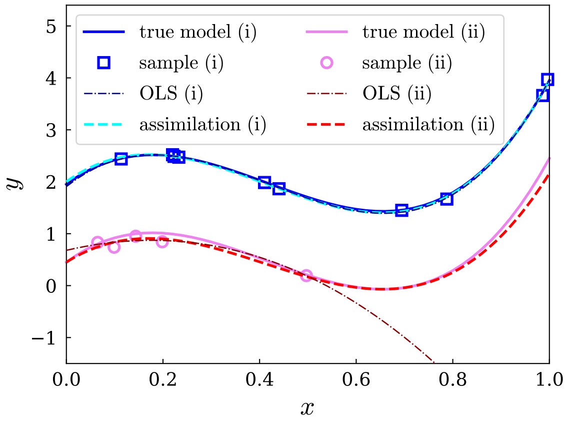

Figure 1: An example of the data assimilation.

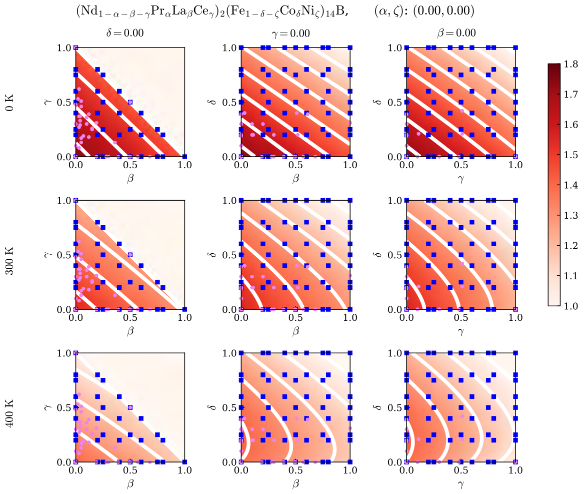

Figure 2: Magnetization of $(Nd_{1-\beta-\gamma}\ La_\beta\ Ce_\gamma)_2(Fe_{1-\delta}Co_\delta)_{14}B$.

References

[1] Yosuke Harashima, Keiichi Tamai, Shotaro Doi, Munehisa Matsumoto, Hisazumi Akai, Naoki Kawashima, Masaaki Ito, Noritsugu Sakuma, Akira Kato, Tetsuya Shoji, and Takashi Miyake, Phys. Rev. Materials **5**, 013806 (2021).

Optimized design of magnetic materials based on the integration between quantum beam experiment and first-principles calculation

Kanta Ono
Institute of Materials Structure Science, High Energy Accelerator Research Organization
Oho 1-1, Tsukuba 305-0801

We have been working on characterization and material design of rare-earth permanent magnets (REPMs) which is one of the most important materials for traction motors of vehicles and robotics. Quantification of REPMs has to be done on multiple length scales and energy scales, where our scope lies in the microscopic thermal equilibrium and off-equilibrium magnetization reversal process closer to the mesoscopic scales [1]. Since the main-phase ferromagnets in REPMs are typically made of multiple sublattices and each sublattice contributes to the bulk magnetic properties differently, it is an important problem to quantify the site-resolved contribution from the microscopic measurements to understand which sublattice can be more improved [2]. Based on the measured data from the neutron diffraction experiments, the Rietveld analysis can give us such information which so far has needed expertise of experienced practitioners. Still, unphysical solutions can be given as a metastable solution in the overall landscape of the cost function in the data fitting. In order to quickly select a physically meaningful solution and eliminate human bias as much as possible, we have been developing a data analysis technique combining Rietveld analysis and theoretical calculations [3, 4]. *Ab initio* electronic structure calculations for metallic ferromagnets can address site-specific magnetic moments based on the crystal structure data yielded by the Rietveld analysis. The output of the *ab initio* calculation can be fed back into the Rietveld analysis and such hybrid process between measured data analysis and *ab initio* calculations can be iterated until the overall convergence is reached.

While the convergence in the hybrid analysis is quite fast in the $\mathrm{ThMn_{12}}$-type ferromagnets, feasibility for the $\mathrm{Nd_2Fe_{14}B}$-type ferromagnets has been seen only recently with the new system B where the 128 cores can shorten the *ab initio* part based on AkaiKKR in less than an hour. This is in strong contrast to other electronic structure calculations for $\mathrm{Nd_2Fe_{14}B}$ which can take weeks on older machines. With the new hardware, the good *ab initio* calculation framework, and our new hybrid data analysis methodology, further developments of REPMs will be accelerated.

References

[1] H. Tsukahara, K. Iwano, T. Ishikawa, C. Mitsumata, K. Ono, NPG Asia Materials **12**, 29, (2020).

[2] K. Saito, S. Doi, T. Abe, K. Ono, J. Alloys and Compounds **721**, 476 (2017).

[3] M. Matsumoto, T. Hawai, K. Ono, Phys. Rev. Applied **13**, 064028 (2020).

[4] T. Hawai, M. Matsumoto, K. Ono, in preparation.

Evaluation of the polymer blend miscibility by using chain-increment method with all-atom molecular dynamics simulation

Kazuo YAMADA and Nobuyuki MATUBAYASI

Division of Chemical Engineering, Osaka University, Toyonaka, Osaka 560-8531

Polymer blend, a mixture of polymers, may have distinct structural and dynamical features from the component polymers and is employed in a wide variety of applications including home appliances, biomedical devices, and automotive products. The mutual miscibility of polymer species is determined by the free energy of mixing. The mixing free energy is given by the changes in the (excess) chemical potentials between the pure and mixed states of the component species, and the chemical potentials reflect sensitively the effect of intra- and intermolecular interactions in turn. To approach the chemical potential of a polymer molecule, we formulated the method of chain increment and provided a scheme to compute the free energy of incrementing a monomer with all-atom models.[1] In this work, we extended the method and treated the single-component melts of polyethylene (PE), polyvinylidene difluoride (PVDF), poly(vinyl alcohol) (PVA), polyvinylpyrrolidone (PVP) in their linear forms.

Results

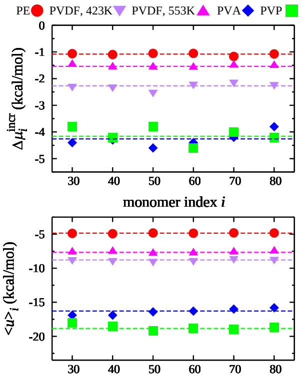

Fig 1: Incremental free energy $\Delta\mu_i^{\rm incr}$ and the average interaction energy $\langle u\rangle_i$ against the index i of the incremented monomer in the tagged polymer at $i = 30, 40, 50, 60, 70,$ and 80. The horizontal, dashed line is the averaged value of $\Delta\mu_i^{\rm incr}$ or $\langle u\rangle_i$.

The number of monomer units is fixed at 100 for all the systems. All-atom molecular dynamics simulation and free-energy calculation has been conducted at 1 bar on the supercomputer system at ISSP. We compute the incremental free energy $\Delta\mu_i^{\rm incr}$ and the averaged interaction energy of the incremented monomer with the surroundings $\langle u\rangle_i$. Figure 1 shows that $\mu_i^{\rm incr}$ stays constant within a few tenths of kcal/mol for inner monomers, demonstrating the validity of the chain-increment method. $\langle u\rangle_i$ is also constant against the index i of the incremented monomer, showing that the local environment around the monomer is independent of the monomer location along the polymer chain.

References

[1] K. Yamada and N. Matubayasi: Macromol. **53** (2020) 775-788.

Development of high-throughput calculation tools and evaluation of magnetic properties in hard magnetic materials

Tetsuya FUKUSHIMA
Institute for Solid State Physics, University of Tokyo
Kashiwa-no-ha, Kashiwa, Chiba 277-8581

In this year, we developed (i) an automatic exhaustive calculation tool and (ii) an atomistic spin Monte Carlo simulation tool for permanent magnetic materials. Our automatic exhaustive calculation tool is based on the all-electron Korringa-Kohn-Rostoker (KKR) Green's function method (AkaiKKR code). The KKR Green's function method can be combined with the coherent potential approximation (CPA) which can treat configurational disordered systems, is quite useful for investigating the electronic structures, magnetic properties, and transport properties of rare-earth transition-metal alloys. In the CPA approach, the multiple scattering effect by disordered potentials is replaced with effective medium. Therefore, we can perform the electronic structure calculations for disordered materials without supercells and decrease the computation costs dramatically. Additionally, since a Green's function is directory obtained in the KKR method, we can efficiently investigate finite temperature magnetism and transport properties by the linear response theory. We applied this tool for and high entropy alloys and rare-earth magnet Sm-Fe-N systems and, succeeded in constructing large-scale magnetic material databases.

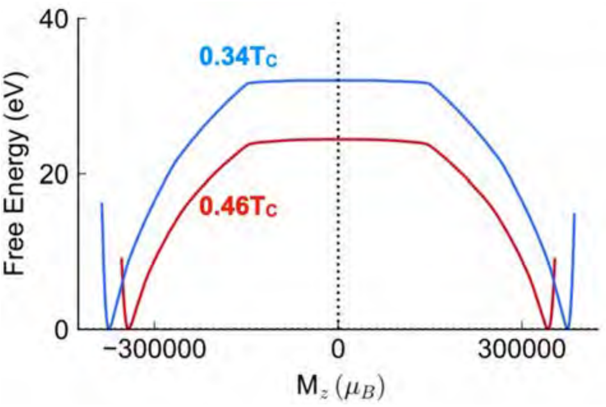

Figure 1: Free energy landscape for a isolated $Nd_2Fe_{14}B$ particle by atomistic spin model simulation. The size of the particle is 14 nm, corresponding to 212,536 spins.

Atomistic spin Monte Carlo simulation was used for investigating the temperature dependent magnetization reversal in permanent magnets. The microscopic mechanism of the coercivity at finite temperature is a crucial issue. Since the magnetization reversal is a stochastic transition from a metastable state to a stable state, we tried to capture the physical insight of the coercive force from the viewpoint of the free energy landscape. For the calculation of the free energy landscape, we developed a numerical simulation method for describing the magnetization reversal by nucleation, where highly efficient parallelization scheme (around 1,000–3,000 MPI parallelization) for the replica exchange Wang-Landau MC method and the reduction of systematic errors by the $1/t$ method are implemented.

Applying the above method to the atomistic spin model with a isolated $Nd_2Fe_{14}B$ particle, we performed the magnetization reversal anal-

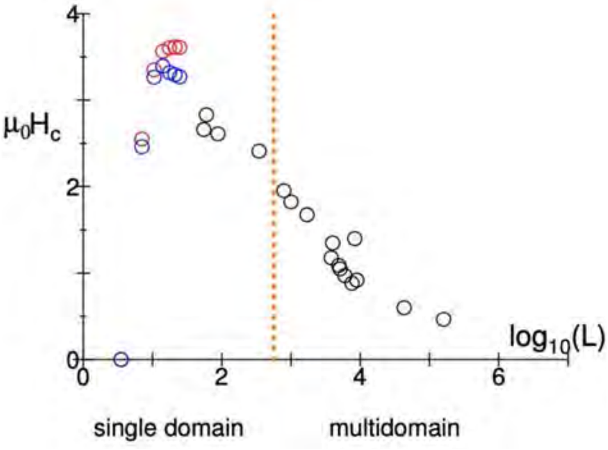

Figure 2: Coercive energy of $Nd_2Fe_{14}B$ at room temperature as a function of the size of the domain. The blue (red) circles indicate the calculation results without (with) the magnetic dipole interactions, respectively. White circles are the experimental results.

ysis for the effect of the thermal fluctuation and investigated the formation of the reverse nucleus which is a origin of the coercive force (see Fig. 1). It was considered that the barrier of the magnetization reversal is determined by the competition between the formation energy of the reverse nucleus and the Zeeman energy by external magnetic field: however, we newly proposed that the energy gain due to the expansion of the magnetization reversal region by the domain wall motion is a key role. This fact is quantitatively consistent with experimental results, where the size of the reverse nucleus dose not depend on external magnetic field.

In order to investigate the coercive force of permanent magnets quantitatively, we need to consider the effect of the magnetic dipole interactions (demagnetizing field). Although a convolution integral method (fast Fourier transform) is commonly used to incorporate long-ranged interaction, it is not effective for permanent magnet materials with low crystal symmetry such as $Nd_2Fe_{14}B$. We have developed a modified stochastic cutoff method that is applicable complex crystal structures with long-ranged interaction in computational cost $O(N\log N)$ without any approximations. This method can be combined with Monte Carlo simulation, leading to the quantitative analysis of the temperature dependent coercive forces of permanent magnets from the free energy landscape calculations with the magnetic dipole interactions (see Fig. 2). It is found that the influence of the magnetic dipole interaction (demagnetizing field) is strongly suppressed due to the surface thermal fluctuation.

References

[1] Y. Toga, S. Miyashita, A. Sakuma, and T. Miyake, Npj Comput Mater **6** (2020) 1.

[2] T. Hinokihara, M. Nishino, Y. Toga, and S. Miyashita, Phys. Rev. B **97** (2018) 104427.

Novel chloride solid electrolytes for all solid-state sodium metal battery

Masanobu NAKAYAMA

Department of Advanced Ceramics

Nagoya Institute of Technology, Gokiso-chi, Showa-ku, Nagoya, Aichi 466-8555

Using high-throughput computing and structure database (Materials Project [1]), we evaluated exhaustively migration energies of Li, Na, and Mg ion in inorganic solids. Figure 1 presents the distribution of migration energies of Li, Na, and Mg ions in oxides by using BVFF-percolation approach.[2,3] The results indicate that various factors affect the ion conducting performance. Thus, materials informatics (MI) approaches are adopted to clarify the crucial factor for ionic conductivity in oxides. Among various regression approaches, gradient boosting regression shows the best prediction performance. However, the regression performance is not sufficient from the diagnostic plots shown in Fig.2. Our tentative analysis suggests that Li-O bond length and Li-O-Li bond angles are important, i.e. structural factors are more important than compositional factors. One of the reasons for rather poor regression performance may stem from low reproducibility of universal BVFF parameters.[2] To improve, high-throughput FF approaches[4] are used for 86 Na containing materials. In this technique, DFT-MD simulations are performed just for 2 ps, and then metaheuristically optimize FF parameters, which is a derivative of original BVFF, to reproduce DFT-MD derived structural features, such as RDF and ADF. After that FF-MD approach is adopted to calculate the ion conductive performance. Figure 3 shows calculated Na ionic conductivities at room temperature for 86 compositions. We plan to verify reproducibility of present computation and apply MI approach for thus obtained data near future.

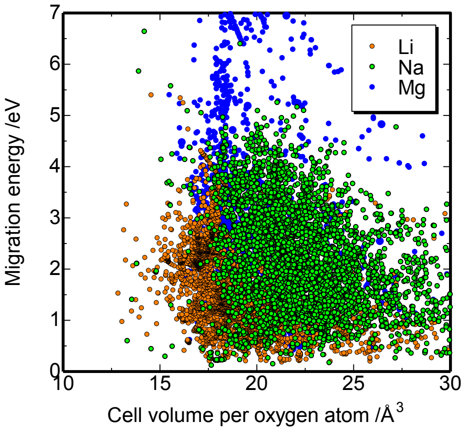

Fig. 1: Migration energies for Li, Na, and Mg ions (indicated by orange, blue, and green plots, respectively) calculated using automated exhaustive BVFF approach.

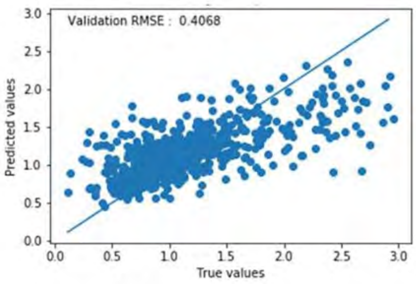

Fig. 2 diagnostic plot of the gradient boosting regression derived prediction function for Li migration energies in 711 Li-ion containing oxides.

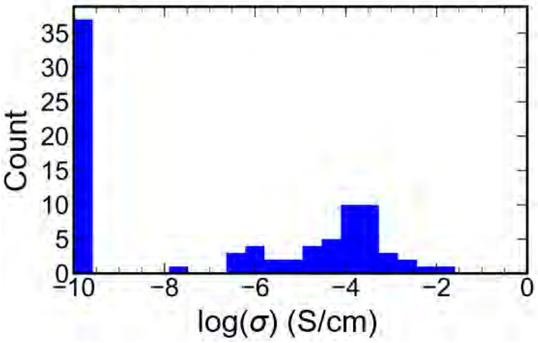

Figure 3 Histogram of room temperature Na ion conductivities for 86 samples using high-throughput FF-MD approach.

References

[1] A Jain, S. P. Ong, G. Hautier, W. Chen, W.D. Richards, S. Dacek, S. Cholia, D. Gunter, D. Skinner, G. Ceder, K.A. Persson, APL Materials, 2013, 1, 011002.

[2] S. Adams, R. P. Rao, Phys. Status Solidi Appl. Mater. Sci., 2011, 208, 1746–1753

[3] M. Nakayama, M. Kimura, R. Jalem, T. kasuga, J. Appl. Phys. 2016, 55, 01AH05

[4] R. Kobayashi, Y. Miyaji, K. Nakano and M. Nakayama, APL Mater., 2020, 8, 081111

3.6 Software Advancement Projects and Workshop Support

PHYSBO – optimization tools for PHYSics based on Bayesian Optimization–

Ryo TAMURA
International Center for Materials Nanoarchitectonics,
National Institute for Materials Science,
1-1 Namiki, Tsukuba, Ibaraki, 305-0044

Bayesian optimization (BO) is machine-learning based black-box optimization technique and has recently garnered significant attention in physics, chemistry, and materials science[1]. For example, for materials developments, the trial-and-error process to find better material is regarded as optimizing a black-box function where input is the composition, structure, and process and output will be materials property. In this algorithm, first, a Gaussian process regression that predicts the expected property and variance is constructed from the already observed input-output pairs. Next, through the trained Gaussian process, the probable input data that will yield the desired output value are also selected based on the acquisition function using expected property and variance. Then, the true output value for the selected candidate is obtained by experiments or simulations as black-box functions. BO repeats these processes to find better inputs. Although BO is powerful tool for black-box optimization, BO is generally computationally expensive in two parts: training Gaussian process regression and optimizing acquisition function.

COMBO (COMmon Bayesian Optimization) has been developed mainly for researchers in the materials science field[2]. In the Gaussian process, two hyperparameters, i.e., parameters whose values were given prior to learning, existed: the Gaussian kernel width and noise variance. Using the COMBO package, these hyperparameters were automatically determined by maximizing the Type-II likelihood. In addition, to avoid computationally expensive for training Gaussian process regression, COMBO achieves high scalability using Thompson sampling, random feature map, and one-rank Cholesky update,

To accelerate COMBO package further, PHYSBO (optimization tools for PHYSics based on Bayesian Optimization) package is developed as Python 3 code[3]. In PHYSBO, the massive parallelization using ISSP supercomputer can be performed for optimizing acquisition function, and then both computationally expensive parts in BO can be resolved. In addition, new function to perform multiobjective optimization is implemented.

In physics field, so far, BO has been applied to some problems such as autonomous X-ray scattering experiments [4], inverse scattering [5], crystal structure prediction [6], and effective model estimation[7]. Thus, PHYSBO package can accelerate these problems, and will solve more complex physical problems using supercomputer.

This package is developed with Tsuyoshi Ueno, Kei Terayama, Koji Tsuda, Yuichi Motoyama, Kazuyoshi Yoshimi, and Naoki Kawashima. We would like to thank the support from “Project for advancement of software usability in materials science” by The Institute for Solid State Physics, The University of Tokyo, for development of PHYSBO.

References

[1] K. Terayama, M. Sumita, R. Tamura, and K. Tsuda, Black-box optimization for automated discovery, Accounts of Chemical Research **54**, 1334 (2021).

[2] T. Ueno, T. D. Rhone, Z. Hou, T. Mizoguchi, and K. Tsuda, COMBO: An efficient Bayesian optimization library for materials science, Materials Discovery, **4**, 18 (2016).

[3] `https://www.pasums.issp.u-tokyo.ac.jp/physbo/`

[4] M. M. Noack, K. G. Yager, M. Fukuto, G. S. Doerk, R. Li, and J. A. Sethian, A kriging-based approach to autonomous experimentation with applications to x-ray scattering, Scientific Reports **9**, 1 (2019).

[5] R. Vargas-Hernández, Y. Guan, D. Zhang, and R. Krems, Bayesian optimization for the inverse scattering problem in quantum reaction dynamics, New Journal of Physics **21**, 022001 (2019).

[6] T. Yamashita, N. Sato, H. Kino, T. Miyake, K. Tsuda, and T. Oguchi, Crystal structure prediction accelerated by bayesian optimization, Physical Review Materials **2**, 013803 (2018).

[7] R. Tamura and K. Hukushima, Bayesian optimization for computationally extensive probability distributions, PLoS ONE **13**, e0193785 (2018).

Development of MateriApps Installer

Synge TODO[1,2], Yuichi MOTOYAMA[2], Kazuyoshi YOSHIMI[2], and Takeo KATO[2]
[1] *Department of Physics, University of Tokyo, Tokyo, 113-0033*
[2] *Institute for Solid State Physics, University of Tokyo, Kashiwa, 277-8581*

Nowadays, computer numerical computation is indispensable for theoretical researches in materials science. For the advancement of computational materials science, efficient algorithms for solving equations of materials science are essential. Many excellent applications based on state-of-the-art algorithms have been created so far. In 2013, we launched a portal site for materials science simulations, MateriApps [1], to disseminate information about the developed software to experimentalists and corporate researchers. We have been disseminating information about the application.

One of the obstacles for users to start using published applications in materials science is installing software. MateriApps LIVE! [2] is an environment that allows users to quickly try out computational materials science applications on their laptops and other devices. MateriApps LIVE! is a Virtual Hard Disk Image (OVA) of VirtualBox that includes applications, OS (Debian GNU/Linux), editors, visualization tools, and other environments needed to get started with the tutorial. Using MateriApps LIVE!, it is possible to quickly set up a computing environment for participants in classes and software training sessions.

However, the environment provided by MateriApps LIVE! is not enough to proceed with full-scale simulations. Since MateriApps LIVE! runs as a virtual machine, its computational power is somewhat limited. To support users interested in larger-scale simulations, we had started the development of MateriApps Installer in 2013.

As FY2020 Project for Advancement of Software Usability in Materials Science (PASUMS), we have made several significant updates on MateriApps Installer: i) organized directory structure and scripts, ii) added full documentation and tutorials, iii) upgraded supported software, iv) supported new hardware [ISSP system B (ohtaka)], v) supported new compilers [GCC 10 and Intel oneAPI].

Version 1.0 of MateriApps Installer was released in March 2021, which includes install scripts for ALPS, ALPSCore, DSQSS, Quantum ESPRESSO, HΦ, Kω, LAMMPS, mVMC, OpenMX, RESPACK, and TeNeS. Also, it includes scripts for the following tools and libraries: Boost, CMake, Eigen3, FFTW, GCC, Git, GSL, HDF5, LAPACK, libffi, OpenBLAS, OpenMPI, OpenSSL, Python3, ScaLAPACK, Tcl/Tk, and zlib.

Using MateriApps Installer, the above material science applications have been preinstalled on the ISSP supercomputers (ohtaka and enaga). The source code of MateriApps Installer is freely available from GitHub [4]. MateriApps Installer is distributed under the GNU General Public License version 3 (GPLv3). However, the patch files for each software are distributed under the license of the software.

[1] `https://ma.issp.u-tokyo.ac.jp/`

[2] `https://cmsi.github.io/MateriAppsLive/`

[3] `https://www.pasums.issp.u-tokyo.ac.jp/mainstaller/`

[4] `https://github.com/wistaria/MateriAppsInstaller/`

Advancement of the experimental data analysis for 2D material structure

Takeo Hoshi

Department of Applied Mathematics and Physics, Tottori University,
4-101 Koyama-Minami, Tottori 680-8550, Japan.

The open source software 2DMAT, a data-analysis software of total-reflection high-energy positron diffraction (TRHEPD) experiment, was developed in Project for Advancement of Software Usability in materials science (PASUMS) at FY2020 [1]. TRHEPD is a novel experimental technique of structure determination of two-dimensional materials and is being conducted intensively at the Slow Positron Facility of High Energy Accelerator Research Organization (KEK) [2]. We developed a python-based data analysis software of TRHEPD at 2018 and 2019 [3]. The software uses an iterative optimization (Nelder-Mead) algorithm and the grid-base search algorithm. The software was used in several application studies [4, 5] in the collaboration with experimentalists, I. Mochizuki (KEK), A. Takayama (Waseda U) and their co-workers.

In the PASUMS project at FY2020, we reorganized the software and added the Bayesian optimization algorithm, realized by the PHYSBO library [6], and the replica-exchange Monte-Carlo algorithm. The software was called 2DMAT v.1 and was published at Feb. 2021 [1]. A hands-on seminar was held at 20. April 2021 and was filled to capacity with 30 participants (https://ccms.issp.u-tokyo.ac.jp/event/4570). Several application studies with 2DMAT are currently underway.

Our successor PASUMS project started in April 2021, so as to add several parallelized algorithms and support other experimental techniques of the structure determination of two-dimensional materials, such as surface X-ray diffraction experiment and low energy electron diffraction experiment.

References

[1] https://www.pasums.issp.utokyo.ac.jp/2DMAT

[2] (Review) Y. Fukaya, *et al*, J. Phys. D: Appl. Phys. 52, 013002 (2019).

[3] K. Tanaka, *et al*, Acta. Phys. Pol. A 137, 188 (2020); JJAP Conf. Series, in press; https://arxiv.org/abs/2002.12165

[4] T. Hoshi, *et al*, Submitted; Preprint: https://arxiv.org/abs/2103.04875

[5] M. Hamada , *et al*, Poster presentation, JPS meeting, online, Mar. 2021.

[6] T. Ueno, *et al*, Materials Discovery 4, 18 (2016); https://www.pasums.issp.u-tokyo.ac.jp/physbo

Report of CCMS hands-on sessions in the 2020 fiscal year

Kota IDO
Institute for Solid State Physics, University of Tokyo
Kashiwa-no-ha, Kashiwa, Chiba 277-8581

In the 2020 fiscal year, Center for Computational Materials Science (CCMS)[1] in the Institute for Solid State Physics (ISSP) held one hands-on session using the ISSP supercomputer, which is shown in Table 1. In this report, we briefly summarize the hands-on session in Table 1.

TeNeS is open-source software based on the tensor network method[3, 4]. Users can solve two-dimensional quantum lattice models using the corner transfer matrix renormalization group method for a projected entangled pair state. Since TeNeS supports MPI/OpenMP hybrid parallelization, this software efficiently works on massively parallel machines such as enaga. Development of TeNeS was supported by "Project for advancement of software usability in materials science" (PASUMS) [5] in the 2019 fiscal year. In the hands-on session, Tsuyoshi Okubo and co-developers explained the basics of the tensor network method and gave a tutorial of TeNeS. Materials for this hands-on session are available on the official site (in Japanese) [6].

Date	Software	Main lecturer	Website
Nov. 10	TeNeS	T. Okubo	[2]

Table 1: List of CCMS hands-on sessions using ISSP supercomputer in the 2020 fiscal year.

References

[1] https://ccms.issp.u-tokyo.ac.jp

[2] https://ccms.issp.u-tokyo.ac.jp/event/3844

[3] https://www.pasums.issp.u-tokyo.ac.jp/tenes/en

[4] https://ma.issp.u-tokyo.ac.jp/en/app/2291

[5] https://www.pasums.issp.u-tokyo.ac.jp/

[6] https://www.pasums.issp.u-tokyo.ac.jp/tenes/doc/paper

Supercomputer course of Computational Materials Design (CMD®) workshop

Masaaki GESHI[1], Yoshitada MORIKAWA[2], Tomoya ONO[3]
[1]*Institute for NanoScience Design, Osaka University,*
1-2 Machikaneyama, Toyonaka, Osaka 560-0043, Japan
[2]*Department of Precision Engineering, Graduate School of Engineering,Osaka University,*
2-1 Yamada-oka, Suita, Osaka 565-0871, Japan
[3]*Department of Electrical and Electronic Engineering,*
Graduate School of Engineering, Kobe University,1-1 Rokkodaicho, Nada, Kobe 657-8501, Japan

The 37th Computational Materials Design (CMD®) workshop (CMD37) has been held from August 31st to September 4th and the 38th CMD® workshop (CMD38) has been done from February 22nd to February 26th. Both were held online. In this workshop we have the supercomputer course to train up human resources to advance research by using system B supercomputer of ISSP, the University of Tokyo.

In CMD37 eight participants took the supercomputer course and got a tutorial on STATE-Senri developed by Y. Morikawa. After giving the introductory lecture of large-scale computing by M. Geshi and explaining how to use the supercomputer of ISSP and also how to use STATE-Senri, calculation models on each research subject of the participants were built and their calculations were carried out. Concrete subjects were molecular adsorption on solid surfaces, chemical reactions at electrode interfaces, adsorption and diffusion of atoms on graphene, electronic structures of oxides for ion batteries and so on. The participants performed the calculations and examined the results.

In CMD38 four participants took the supercomputer course and used the supercomputer of ISSP. They got a tutorial on RSPACE developed by T. Ono and M. Uemoto. After giving the introductory lecture of large-scale computing by M. Geshi and describing the calculation method of electronic states and electron conduction property using RSPACE, exercises published in the manual were carried out. Then, electronic state calculations were carried out on a plurality of molecular systems, and the electronic density distribution was visualized. Finally, the atomic structure optimization of graphene blisters, SiC/SiO_2 interfaces, fullerenes, and ZnO was carried out.

We would like to thank the organizers of the MateriApps workshop at the Institute for Solid State Physics, the University of Tokyo, for providing us with useful information for holding the workshop online.

4 PUBLICATION LIST

Example:

LASTNAME, Firstname [project class; # points (B), # points (C)] (Page #)
— *Project title*

1. First paper
   Names of Authors, etc.
2. Second paper
   ...

☐ ISSP Joint Research Projects

○ B–E classes

AKAI, Hisazumi [B class; 1200 (B), 150 (C)] (141, 142)
— *Magnetic properties of rare earth magnetic materials with structural disorder*

1. Data assimilation method for experimental and first-principles data: Finite-temperature magnetization of (Nd, Pr, La, Ce)$_2$(Fe, Co, Ni)$_{14}$B
   Y. Harashima, K. Tamai, S. Doi, M. Matsumoto, H. Akai, N. Kawashima, M. Itho, N. Sakuma, K. Kato, T. Shoji, and T. Miyake Phys. Rev. Materials **5**, 013806 (2021).
   DOI:10.1103/PhysRevMaterials.5.013806

2. Spin-wave dispersion and exchange stiffness in Nd$_2$Fe$_{14}$B and RFe$_{11}$Ti (R=Y, Nd, Sm) from first-principles calculations
   T. Fukazawa, H. Akai, Y. Harashima, and T. Miyake Phys. Rev. B **103**, 024418 (2021).
   DOI:0.1103/PhysRevB.103.024418

3. Magnetic Friedel Oscillation at Fe(001) Surface: Direct Observation by Atomic-Layer-Resolved Synchrotron Radiation ^{57}Fe Mössbauer Spectroscopy
   T. Mitsui, S. Sakai, S. Li, T. Ueno, T. Watanuki, Y. Kobayashi, R. Masuda, M. Seto, and H. Akai Phys. Rev. Lett. **125**,236806 (2020).
   DOI:10.1103/PhysRevLett.125.236806

4. First-principles calculations of finite temperature electronic structures and transport properties of Heusler alloy Co$_2$MnSi
   H. Shinya, S. Kou, T. Fukushima, A. Masago, K. Sato, H. Katayama-Yoshida, and H. Akai Appl. Phys. Lett. **117**,042402 (2020).
   DOI:10.1063/5.0017862

5. Element- and orbital-selective magnetic coherent rotation at the first-order phase transition of a hard uniaxial ferrimagnet
   Sh. Yamamoto, D. I. Gorbunov, H. Akai, H. Yasumura, Y. Kotani, T. Nakamura, T. Kato, N. V. Mushnikov, A. V. Andreev, H. Nojiri, and J. Wosnitza Phys. Rev. B **101**,174430 (2020).
   DOI:10.1103/PhysRevB.101.174430

6. Calculating Curie temperatures for rare-earth permanent magnets: Ab initio inspection of localized magnetic moments in d-electron ferromagnetism
   M. Matsumoto and H. Akai Phys. Rev. B **101**, 1444402 (2020).

DOI:10.1103/PhysRevB.101.144402

AKASHI, Ryosuke [C class; 4000 (B), 750 (C)] (93)
— *First principles exploration of the metastable phases of hydrides and their superconductivity*
— *First principles exploration of the metastable phases of hydrides and their superconductivity II*

1. AtomREM: Non-empirical seeker of the minimum energy escape paths on many-dimensional potential landscapes without coarse graining
   Y. S. Nagornov and R. Akashi Comput. Phys. Commun. **254** (2020) 107260.

2. Effect of spin fluctuations on superconductivity in V and Nb: A first-principles study
   K. Tsutsumi, Y. Hizume, M. Kawamura, R. Akashi, and S. Tsuneyuki, Phys. Rev. B **102** (2020) 214515.

AKERA, Hiroshi [C class; 4000 (B), 650 (C)] (95)
— *Generation of spin and pseudospin polarizations in atomic-layer inplane heterostructures and stacked structures*

AOYAMA, Kazushi [B class; 1000 (B), 200 (C)] (280)
— *Spin transport near a phase transition in magnets*
— *Transport properties of multiple-q states in frustrated magnets*

1. Hedgehog-lattice spin texture in classical Heisenberg antiferromagnets on the breathing pyrochlore lattice
   K. Aoyama and H. Kawamura Phys. Rev. B **103** (2021) 014406.

ARAI, Munehito [C class; 4400 (B), 350 (C)] (252)
— *Computational rational design of novel proteins for industrial and pharmaceutical applications*
— *Protein design toward the development of therapeutic drugs for COVID-19*

ARAI, Toyoko [C class; 1800 (B), 400 (C)] (130)
— *DFT calculation of atomic displacement captured by energy dissipation channel of noncontact atomic force microscope*

ARIMA, Kenta [B class; 600 (B), 150 (C)] (171)
— *Analysis of electronic structures around the Fermi level of graphene nanoribbons with different widths*
— *Origin of specific dot patters on small graphene sheets observed by STM*

ARUGA, Tetsuya [B class; 200 (B), 0 (C)] ()
— *Interaction among phthalocyanine molecules adsorbed on metal surfaces*

ASANO, Yuta [E class; 22500 (B), 4000 (C)] (36)
— *Molecular dynamics simulation of cavitation in complex fluids*

1. Molecular Dynamics Simulation of Soundwave Propagation in a Simple Fluid
   Y. Asano, H. Watanabe, and H. Noguchi, J. Chem. Phys. 153, 124504 (2020).
   DOI:10.1063/5.0024150

2. Rotational Dynamics of Water at the Phospholipid Bilayer Depending on the Head Groups Studied by Molecular Dynamics Simulations
   Y. Higuchi, Y. Asano, T. Kuwahara, and M. Hishida, Langmuir **37**, 5329 (2021).
   DOI:10.1021/acs.langmuir.1c00417

3. Effects of polymers on the cavitating flow around a cylinder: A Large-scale molecular dynamics analysis

Y. Asano, H. Watanabe, and H. Noguchi, J. Chem. Phys. 155, 14905 (2021).
DOI:10.1063/5.0056988

BUI, VANPHO [C class; 1000 (B), 100 (C)] (152)
— *Study on removal mechanism in catalyst referred etching of single crystalline Si with pure water*
— *Study on removal mechanism of single crystalline Si planarized by catalyst referred etching in pure water*

EGAMI, Yoshiyuki [C class; 7200 (B), 1100 (C)] (63)
— *Development and application of algorithms for large-scale first-principles electron-transport simulation*
— *Development and application of first-principles algorithms for for long-range electron transport simulation*

1. Calculation of the Green's function in the scattering region for first-principles electron-transport simulations
   Y. Egami, S. Tsukamoto, and T. Ono, Phys. Rev. Res. **3**, 013038 (2021).
   DOI:10.1103/PhysRevResearch.3.013038

FUCHIZAKI, Kazuhiro [C class; 1800 (B), 250 (C)] (271)
— *Kinetics of phase transition and polyamorphism*

1. A unique multianvil 6–6 assembly for a cubic-type multianvil apparatus
   K. Fuchizaki, T. Wada, H. Naruta, A. Suzuki, and K. Irino Rev. Sci. Instrum. **92**, 025117 (2021).
   DOI:10.1063/5.0039306

2. Application of nonequilibrium relaxation scheme to machine learning for detecting a phase transition
   K. Fuchizaki, K. Nakamura, and D. Hiroi, J. Phys. Soc. Jpn. in press.

3. The microscopic transition process from high-density to low-density amorphous state of SnI_4
   K. Fuchizaki, A. Ohmura, H. Naruta, and T. Nishioka, submitted to J. Phys.: Condens. Matter.

FUJII, Susumu [B class; 600 (B), 0 (C)] (303)
— *Systematic Investigation on Phonon Transport at Nanoscale Interfaces*

FUJIMOTO, Satoshi [D class; 6000 (B), 1000 (C)] (236)
— *O(N) solution to the disordered Kitaev model using the large-scale parallel computing*

1. Anderson-Kitaev spin liquid
   Masahiko G. Yamada, npj Quantum Mater **5**, 82 (2020).
   DOI:10.1038/s41535-020-00285-3

FUJIMOTO, Yoshitaka [C class; 1000 (B), 0 (C)] (154)
— *Doping and molecular adsorption of graphene*

1. Stacking and curvature-dependent behaviors of electronic transport and molecular adsorptions of graphene: A comparative study of bilayer graphene and carbon nanotube
   Y. Fujimoto and S. Saito, Applied Surface Science Advances **1**, 100028 (2020).

2. Carbon annealed HPHT-Hexagonal boron nitride: Exploring defect levels using 2D materials combined through van der Waals interface
   M. Onodera, M. Isayama, T. Taniguchi, K. Watanabe, S. Masubuchi, R. Moriya, T. Haga, Y. Fujimoto, S. Saito and T. Machida, Carbon **167**, 785 (2020).

3. First-Principles Materials Design for Graphene-based Sensor Devices

Y. Fujimoto, Sustainable Materials for Next Generation Energy Devices, p.343 (Elsevier 2021).

4. Quantum transport, electronic properties and molecular adsorption in graphene
   Y. Fujimoto, Modern Physics Letters B **35**, 2130001 (2021).

5. Electronic states and modulation doping of hexagonal boron-nitride trilayer
   T. Haga, Y. Matsuura, Y. Fujimoto and S. Saito, Physical Review Materials, submitted.

6. Stability of Hydrogen Boride Sheets in Water
   K. I. Rojas, N. T. Cuong, H. Nishino et al., Communications Materials, submitted.

FUJISHIRO, Hiroki [C class; 2200 (B), 0 (C)] (128)
— *Strained Band-Structure Engineering for Antimonide-Based Terahertz Transistors*

FUKUDA, Jun-ichi [B class; 800 (B), 0 (C)] (289)
— *Calculation of ordered structures dynamics and optical properties of soft materials*

1. Lattice orientation of cholesteric blue phases in contact with surfaces enforcing unidirectional planar anchoring
   J. Fukuda and S. Žumer, Physical Review Research **2** (2020) 033407/1-11.

FUKUDA, Masahiro [B class; 300 (B), 100 (C)] (182)
— *Analysis of local quantities of electron field in material surface*

FUKUMOTO, Yoshiyuki [B class; 500 (B), 0 (C)] (309)
— *Effects of exchange randomness on magnetic properties of a spherical-kagome spin-system W72V30*
— *Exact diagonalization calculations of density of states and dynamical structure factor for the spherical-kagome spin-system* $W_{72}V_{30}$

FUKUSHIMA, Tetsuya [B,C class; 1700 (B), 300 (C)] (132)
— *Construction of magnetic materials database by KKR Green's function method*
— *Highthroughput screening calculations by KKR Green's function method*

1. Hole-mediated ferromagnetism in a high-magnetic moment material, Gd-doped GaN
   A. Masago, H. Shinya, T. Fukushima, K. Sato, and H. Katayama-Yoshida, J. Phys.: Condens. Matter **32**, 485803 (2020).
   DOI:10.1088%2F1361-648x%2Fabac8e

2. First-principles calculations of finite temperature electronic structures and transport properties of Heusler alloy Co_2MnSi
   H. Shinya, S. Kou, T. Fukushima, A. Masago, K. Sato, H. Katayama-Yoshida, and H. Akai, Appl. Phys. Lett. **117**, 042402 (2020).
   DOI:10.1063/5.0017862

GOHDA, Yoshihiro [C class; 2800 (B), 550 (C)] (112)
— *Theoretical analysis of influences of phonons on magnetism*

1. First-principles determination of intergranular atomic arrangements and magnetic properties in rare-earth permanent magnets
   Y. Gohda, Sci. Technol. Adv. Mater. **22**, 113 (2021).
   DOI:10.1080/14686996.2021.1877092

2. Prediction of the Curie temperature considering the dependence of the phonon free energy on magnetic states
   T. Tanaka and Y. Gohda, npj Comput. Mater. **6**, 184 (2020).

DOI:10.1038/s41524-020-00458-5

3. Effective quantum-well width of confined electrons in ultrathin Ag(111) films on Si(111)7x7 substrates
   K. Sugawara, I. Seo, S. Yamazaki, K. Nakatsuji, Y. Gohda, and H. Hirayama, Surf. Sci. 704, 121745 (2020).
   DOI:10.1016/j.susc.2020.121745

4. First-principles study of magnetism-dependent phonons governed by exchange ligand field
   T. Tanaka and Y. Gohda, J. Phys. Soc. Jpn. **89**, 093705 (2020).
   DOI:10.7566/JPSJ.89.093705

5. First-principles Calculations on High-temperature Desorption Loss from Iridium
   I. Seo, S. Yokota, Y. Imai, and Y. Gohda, Comput. Mater. Sci. **184**, 109897 (2020).
   DOI:10.1016/j.commatsci.2020.109897

6. First-principles study on magnetism of a crystalline grain-boundary phase in Nd–Fe–B permanent magnets
   Y. Ainai, S. Kou, Y. Tatetsu, and Y. Gohda Jpn. J. Appl. Phys. **59**, 060904 (2020).
   DOI:10.35848/1347-4065/ab9402

7. First-principles study of the adsorption of 3d transition metals on BaO- and TiO2-terminated cubic-phase BaTiO3(001) surfaces
   R. Costa-Amaral and Y. Gohda, J. Chem. Phys. **152**, 204701 (2020).
   DOI:10.1063/5.0008130

GOHLKE, Matthias [C class; 1800 (B), 400 (C)] (268)
— *Numerical study of spin-nematic order in the* $S = 1/2$ J_1J_2K*-Heisenberg model on the square lattice*

HAGITA, Katsumi [D class; 6500 (B), 0 (C)] (239)
— *Confirmation of stress-overshoot phenomena under biaxial elongational flow of ring-linear mixtures*

1. Effect of Chain-Penetration on Ring Shape for Mixtures of Rings and Linear Polymers.
   K. Hagita, T. Murashima, Polymer, 2021, 218, 123493.

2. Multi-Ring Configurations and Penetration of Linear Chains through Rings on Bonded Rings and Poly-Catenanes in Linear Chain Matrices.
   K. Hagita, T. Murashima, Polymer, 2021, 223, 123705.

3. Multi-Interval Trajectory Recording for Efficient Analyses of Time Correlations.
   K. Hagita, T. Murashima J. Phys. Soc. Jpn. 89, 024002 (2020).

HAMADA, Ikutaro [C class; 2800 (B), 0 (C)] (122)
— *First-principles study of molecule/metal interfaces*

1. Manipulable Metal Catalyst for Nanographene Synthesis
   A. Shiotari, I. Hamada, T. Nakae, S. Mori, T. Okujima, H. Uno, H. Sakaguchi, Y. Hamamoto, Y. Morikawa, and Y. Sugimoto Nano Lett. **11** (2020) 8339.

HAMAGUCHI, Satoshi [C class; 6000 (B), 1150 (C)] (68)
— *Analyses of Surface Reactions in Atomic Layer Etching Processes*

1. Self-limiting processes in thermal atomic layer etching of nickel by hexafluoroacetylacetone
   A. H. Basher, I. Hamada, and S. Hamaguchi, Jpn. J. Appl. Phys. 59, 090905 (2020).

HAMAMOTO, Yuji [C class; 2800 (B), 0 (C)] (120)
— *van der Waals density functional study of Cu phthalocyanine adsorbed on the Au(110) surface*
— *van der Waals density functional study of Cu phtyalocyanine adsorbed on the Au(110) surface*

1. Identifying Atomic-Level Correlation Between Geometric and Electronic Structure at a Metal-Organic Interface
   H. Koshida, H. Okuyama, S. Hatta, T. Aruga, Y. Hamamoto, I. Hamada, and Y. Morikawa, J. Phys. Chem. C **124**, 17696 (2020).
   DOI:10.1021/acs.jpcc.0c04678

HARADA, KENJI [C class; 1600 (B), 500 (C)] (270)
— *Development of entanglement optimization method*

HARASHIMA, Yosuke [C class; 800 (B), 0 (C)] (170)
— *First-principles study on complexes of impurity and dislocation in GaN p-n diodes*
— *leakage current on power semiconductor devices and an electronic structure on a threading dislocation*

1. Screw dislocation that converts p-type GaN to n-type: Microscopic study on Mg condensation and leakage current in p-n diodes
   T. Nakano, Y. Harashima, K. Chokawa, K. Shiraishi, A. Oshiyama, Y. Kangawa, S. Usami, N. Mayama, K. Toda, A. Tanaka, Y. Honda, and H. Amano, Appl. Phys. Lett. **117**, 012105 (2020).
   DOI:10.1063/5.0010664

HARUYAMA, Jun [C class; 6000 (B), 1100 (C)] (71)
— *Electrochemical reaction analysis using density functional calculation + implicit solvation model 2*
— *Electrochemical reaction analysis using density functional calculation + implicit solvation model 2-2*

HASHIMOTO, Tamotsu [C class; 800 (B), 150 (C)] (284)
— *Molecular dynamics simulation of liquid* $BaTiO_3$

1. Structure of Amorphous $\mathrm{BaTiO_3}$ by Molecular Dynamics Simulations Using a Shell Model
   T. Hashimoto and H. Moriwake, J. Phys. Soc. Jpn **90**, 044604 (2021).
   DOI:10.7566/JPSJ.90.044604

HATSUGAI, Yasuhiro [C class; 3600 (B), 700 (C)] (262)
— *Numerical study of bulk-edge correspondence and topological phases: From quantum to classical mechanics*

1. Adiabatic heuristic principle on a torus and generalized Streda formula
   Koji Kudo and Yasuhiro Hatsugai, Phys. Rev. B **102**, 125108 (2020).
   DOI:10.1103/PhysRevB.102.125108

2. Chiral edge modes in game theory: a kagome network of rock-paper-scissors
   Tsuneya Yoshida, Tomonari Mizoguchi, Yasuhiro Hostage, arXiv:2012.05562.

3. Fate of fractional quantum Hall states in open quantum systems: Characterization of correlated topological states for the full Liouvillian
   Tsuneya Yoshida, Koji Kudo, Hosho Katsura, and Yasuhiro Hatsugai, Phys. Rev. Research **2**, 033428 (2020).
   DOI:10.1103/PhysRevResearch.2.033428

4. Mirror skin effect and its electric circuit simulation
   Tsuneya Yoshida, Tomonari Mizoguchi, and Yasuhiro Hatsugai, Phys. Rev. Research **2**, 022062(R) (2020).
   DOI:10.1103/PhysRevResearch.2.022062

5. Higher-order topological phases in a spring-mass model on a breathing kagome lattice
   Hiromasa Wakao, Tsuneya Yoshida, Hiromu Araki, Tomonari Mizoguchi, and Yasuhiro Hatsugai, Phys. Rev. B 101, 094107 (2020).

6. Detecting Bulk Topology of Quadrupolar Phase from Quench Dynamics
   Tomonari Mizoguchi, Yoshihito Kuno, and Yasuhiro Hatsugai Phys. Rev. Lett. **126**, 016802 (2021).
   DOI:10.1103/PhysRevLett.126.016802

7. Machine Learning of Mirror Skin Effects in the Presence of Disorder
   Hiromu Araki, Tsuneya Yoshida, and Yasuhiro Hatsugai J. Phys. Soc. Jpn. **90**, 053703 (2021).
   DOI:10.7566/JPSJ.90.053703

8. Square-root topological phase with time-reversal and particle-hole symmetry
   Tsuneya Yoshida, Tomonari Mizoguchi, Yoshihito Kuno, Yasuhiro Hatsugai arXiv: 2103.11305.

9. Bulk-edge correspondence of classical diffusion phenomena
   Tsuneya Yoshida Yasuhiro Hatsugai Scientific Reports **11**, 888 (2021)
   DOI:10.1038/s41598-020-80180-w

HATTORI, Ken [B class; 500 (B), 100 (C)] (174)
— *Atomic structure and electronic states for silicide films*

HAYAMI, Satoru [C class; 5000 (B), 900 (C)] (202)
— *Search for multiple-Q magnetic orders in systems with bond-dependent anisotropic interactions*
— *Search for square-lattice skyrmion crystal in itinerant electron systems*

1. Magnetic hedgehog lattices in noncentrosymmetric metals
   S. Okumura, S. Hayami, Y. Kato, and Y. Motome Phys. Rev. B **101**, 144416 (2020).
   DOI:10.1103/PhysRevB.101.144416

2. Spontaneous antisymmetric spin splitting in noncollinear antiferromagnets without spin-orbit coupling
   S. Hayami, Y. Yanagi, and H. Kusunose Phys. Rev. B **101**, 220403(R) (2020).
   DOI:10.1103/PhysRevB.101.220403

3. Nonreciprocal magnons due to symmetric anisotropic exchange interaction in honeycomb antiferromagnets
   T. Matsumoto and S. Hayami, Phys. Rev. B **101**, 224419 (2020).
   DOI:10.1103/PhysRevB.101.224419

4. Multiple-Q magnetism by anisotropic bilinear-biquadratic interactions in momentum space
   S. Hayami, J. Magn. Magn. Mater. **513**, 167181 (2020).
   DOI:10.1016/j.jmmm.2020.167181

5. Anomalous Hall effect in κ-type organic antiferromagnets
   M. Naka, S. Hayami, H. Kusunose, Y. Yanagi, Y. Motome, and H. Seo Phys. Rev. B **102**, 075112 (2020).
   DOI:10.1103/PhysRevB.102.075112

6. Degeneracy Lifting of Neel, Bloch, and Anti-Skyrmion Crystals in Centrosymmetric Tetragonal Systems
   S. Hayami and R. Yambe, J. Phys. Soc. Jpn. **89**, 103702 (2020).
   DOI:10.7566/JPSJ.89.103702

7. Complete Multipole Basis Set for Single-Centered Electron Systems
H. Kusunose, R. Oiwa, and S. Hayami J. Phys. Soc. Jpn. **89**, 104704 (2020).
DOI:10.7566/JPSJ.89.104704

8. Bottom-up design of spin-split and reshaped electronic band structures in spin-orbit-coupling free antiferromagnets: Procedure on the basis of augmented multipoles
S. Hayami, Y. Yanagi, and H. Kusunose Phys. Rev. B **102**, 144441 (2020).
DOI:10.1103/PhysRevB.102.144441

9. Imaging the coupling between itinerant electrons and localised moments in the centrosymmetric skyrmion magnet GdRu2Si2
Y. Yasui, C. J. Butler, N. D. Khanh, S. Hayami, T. Nomoto, T. Hanaguri, Y. Motome, R. Arita, T.-h. Arima, Y. Tokura, and S. Seki Nat. Commun. **11**, 5925 (2020).
DOI:10.1038/s41467-020-19751-4

10. NQR and NMR spectra in odd-parity multipole material CeCoSi
M. Yatsushiro and S. Hayami Phys. Rev. B **102**, 195147 (2020).
DOI:10.1103/PhysRevB.102.195147

11. Square skyrmion crystal in centrosymmetric itinerant magnets
S. Hayami and Y. Motome, Phys. Rev. B **103**, 0244439 (2021).
DOI:10.1103/PhysRevB.103.024439

12. Noncoplanar multiple-Q spin textures by itinerant frustration: Effects of single-ion anisotropy and bond-dependent anisotropy
S. Hayami and Y. Motome, Phys. Rev. B **103**, 054422 (2021).
DOI:10.1103/PhysRevB.103.054422

13. Modeling a nanometric skyrmion lattice using anisotropic exchange interactions in a centrosymmetric host
M. Hirschberger, S. Hayami, and Y. Tokura New J. Phys. **23**, 023039 (2021).
DOI:10.1088/1367-2630/abdef9

14. Spin-texture-driven electrical transport in multi-Q antiferromagnets
S. Seo, S. Hayami, Y. Su, S. M. Thomas, F. Ronning, E. D. Bauer, J. D. Thompson, S.-Z. Lin and P. F. S. Rosa Commun. Phys. **4**, 58 (2021).
DOI:10.1038/s42005-021-00558-8

HIDA, Kazuo [B class; 500 (B), 150 (C)] (300)
— *Numerical Study of One Dimensional Frustrated Quantum Spin Systems*

1. Infinite Series of Ferrimagnetic Phases Emergent from the Gapless Spin Liquid Phase of Mixed Diamond Chains
K. Hida, arXiv:2102.02116, J. Phys. Soc. Jpn. in press.

HIGUCHI, Yuji [C class; 5400 (B), 850 (C)] (242)
— *Large deformation process of amphiphilic molecular aggregate*
— *Self-assemble process of amphiphilic molecules by coarse-grained molecular dynamics simulation*

1. Coarse-grained molecular dynamics simulations of void generation and growth processes in the fracture of the lamellar structure of polyethylene
Y. Higuchi, Phys. Rev. E **103**, 042502 (2021).
DOI:10.1103/PhysRevE.103.042502

2. Rotational Dynamics of Water at the Phospholipid Bilayer Depending on the Head Groups Studied by Molecular Dynamics Simulations
   Y. Higuchi, Y. Asano, T. Kuwahara, and M. Hishida, Langmuir **37**, 5329 (2021).
   DOI:10.1021/acs.langmuir.1c00417

3. 高分子材料の破壊に関する粗視化シミュレーション
   樋口祐次, 分子シミュレーション学会誌「アンサンブル」 **22**, 216-221 (2020).

HINUMA, Yoyo [B class; 800 (B), 0 (C)] (168, 169)
— *Calculation of multication oxide surface properties for catalyst informatics*
— *Search of accessible surfaces for catalyst informatics*

1. Changes in Surface Oxygen Vacancy Formation Energy at Metal/Oxide Perimeter Sites: A Systematic Study on Metal Nanoparticles Deposited on an In2O3(111) Support
   Yoyo Hinuma, Takashi Toyao, Nobutsugu Hamamoto, Motoshi Takao, Ken-ichi Shimizu, and Takashi Kamachi, J. Phys. Chem. C 2020, 124, 27621
   a
2. Surface Oxygen Vacancy Formation Energy Calculations in 34 Orientations of beta-Ga2O3 and theta-Al2O3
   Yoyo Hinuma, Takashi Kamachi, Nobutsugu Hamamoto, Motoshi Takao, Takashi Toyao, and Ken-ichi Shimizu, J. Phys. Chem. C 2020, 124, 10509
   a

HIRATSUKA, Masaki [B class; 400 (B), 100 (C)] ()
— *Estimation of Infrared and Raman spectra using ab initio calculation and machine learning*

HIYAMA, Miyabi [B class; 500 (B), 50 (C)] (308)
— *Theoretical analysis for photo absorption- and emission spectra for firefly bioluminescence related molecules*
— *Theoretical study for caged compound and its conjugate acid/bases*

1. Theoretical Study of the Wavelength Selection for the photocleavage of Coumarin-caged D-luciferin
   J. Usukura, M. Hiyama, M. Kurata, Y. Hazama, X-P. Qiu, F. M. Winnik, H. Akiyama, and N. Koga, Photochem. Photobiol. (2020) 96, 805-814

2. Quantum-Mechanical Hydration Plays Critical Role in the Stability of Firefly Oxyluciferin Isomers: State-of-the-art Calculations of the Excited States
   Y. Noguchi, M. Hiyama, M. Shiga, H. Akiyama, O. Sugino, J. Chem. Phys. (2020) 153, 201103

HORI, Yuta [B,C class; 3700 (B), 0 (C)] (98)
— *The analysis of the hydrogen-bonding structures in proton-conduction organic crystals*
— *The analysis of the local structures and molecular dynamics in proton-conduction acid-base composites*

HOSHI, Takeo [C class; 4600 (B), 850 (C)] (82, 346)
— *Fusion of computational material science and data-driven science with massively parallel computation*
— *Fusion of computational material science and data-driven science with parallel computation*

1. Development of data-analysis software for total-reflection high-energy positron diffraction (TRHEPD)

   K. Tanaka, T. Hoshi, I. Mochizuki, T. Hanada, A. Ichimiya, T. Hyodo, Acta. Phys. Pol. A 137, 188-192 (2020).

2. Two-stage data-analysis method for total-reflection high-energy positron diffraction (TRHEPD)
   K. Tanaka, I. Mochizuki, T. Hanada, A. Ichimiya, T. Hyodo, T. Hoshi, JJAP Conf. Series, in press; Preprint: https://arxiv.org/abs/2002.12165

3. Revisiting the Charge-Transfer States at Pentacene/C60 Interfaces with the GW/Bethe–Salpeter Equation Approach
   Takatoshi Fujita, Yoshifumi Noguchi, Takeo Hoshi, Materials 13, 2728/1-15 (2020).

4. An a posteriori verification method for generalized Hermitian eigenvalue problems in large-scale electronic state calculations
   Takeo Hoshi, Takeshi Ogita, Katsuhisa Ozaki, Takeshi Terao J. Comp. Appl. Math. 376, 112830/1-13 (2020).

5. Recent progress in large-scale electronic state calculations and data-driven sciences
   Takeo Hoshi and Satoshi Ito Chap. 14 of Handbook of Silicon Based MEMS Materials and Technologies 3rd Ed., Elsevier (2020).

6. Data-driven sensitivity analysis in a total-reflection high-energy positron diffraction (TRHEPD) experiment of the Si4O5N3 / 6H-SiC (0001)-($\sqrt{3} \times \sqrt{3}$) R30°
   Takeo Hoshi, Daishiro Sakata, Shotaro Oie, Izumi Mochizuki, Satoru Tanaka, Toshio Hyodo, Koji Hukushima: Submitted; Preprint:https://arxiv.org/abs/2103.04875

HOTTA, Chisa [C class; 800 (B), 800 (C)] (210)
— *Exploring chage glass phase in two-dimensional lattice models*

HOTTA, Takashi [C class; 2400 (B), 0 (C)] (207)
— *Research of Quantum Critical Points Emerging between Two-Channel Kondo and Fermi-Liquid States*

1. Two-Channel Kondo Effect Emerging from Np and Pu Ions
   Dai Matsui and Takashi Hotta, JPS Conf. Proc. **30**, 011125 (2020).
   DOI:10.7566/JPSCP.30.011125

2. Quantum Critical Point between Two-Channel Kondo and Fermi-Liquid Phases
   Takashi Hotta, J. Phys. Soc. Jpn. **89**, 114706 (2020).
   DOI:10.7566/JPSJ.89.114706

HU, Shiqian [C class; 3000 (B), 400 (C)] (109)
— *Study of Phonon Thermal Conduction in Two-dimensional (2D) Composite Materials*
— *Two-Path Phonon-Interference Resonance Induces a Stop-Band in Silicon Crystal Matrix by Embedded Nanoparticles Array*

HUKUSHIMA, Koji [C class; 4600 (B), 0 (C)] (258, 259)
— *Parallel Bayesian computation in material science*
— *Tensor renormalization-group study of spin glasses*

1. Replica Exchange Particle-Gibbs Method with Ancestor Sampling
   Hiroaki Inoue, Koji Hukushima and Toshiaki Omori J. Phys. Soc. Jpn. **89**, (2020) 104801

2. Lattice Glass Model in Three Spatial Dimensions
   Yoshihiko Nishikawa and Koji Hukushima Phys. Rev. Lett. **125**, (2020) 065501

3. Data-driven determination of the spin Hamiltonian parameters and their uncertainties: The case of the zigzag-chain compound KCu4P3O12
   Ryo Tamura, Koji Hukushima, Akira Matsuo, Koichi Kindo, and Masashi Hase Phys. Rev. B **101**, (2020) 224435

4. Maximum Separated Distribution with High Interpretability Found Using an Exhaustive Search Method –Application to Magnetocrystalline Anisotropy of Fe/Co Films–

Hiori Kino, Kohji Nakamura, Koji Hukushima, Takashi Miyake, and Dam Hieu Chi J. Phys. Soc. Jpn. **89**, 064802 (2020).

IDO, Kota [C class; 6000 (B), 900 (C)] (201)
— *Numerical analyses on quantum spin liquids in strongly correlated electron systems*
— *Spin dynamical structure factor in extended Kitaev model*

IIDA, Tsutomu [B class; 500 (B), 100 (C)] (173)
— *A theoretical study on the effect of impurity doping on the thermoelectric performance of environmental friendly silicide* $SrSi_2$

1. Re-evaluation of the electronic structure and thermoelectric properties of narrow-gap semiconducting α-SrSi2: A complementary experimental and first-principles hybrid-functional approach
   Daishi Shiojiri, Tsutomu Iida, Tomoyuki Kadono, Masato Yamaguchi, Takuya Kodama, Seiya Yamaguchi, Shinta Takahashi, Yuki Kayama, Kota Hiratsuka, Motoharu Imai, Naomi Hirayama, and Yoji Imai, J. Appl. Phys. 129(11), 115101 (2021).
   DOI:10.1063/5.0041670

IKEDA, Hiroaki [B class; 700 (B), 150 (C)] ()
— *Multipole orders and superconductivity in strongly correlated electron systems*

IKUHARA, Yuichi [C class; 2800 (B), 0 (C)] (118, 119)
— *Analysis of hetero-interface by ab-initio molecular dynamics simulations*
— *Study of atomic structure and segregation behavior in oxide interface*

1. Atomistic origin of high-concentration Ce^{3+} in {100}-faceted Cr-substituted CeO_2 nanocrystals
   X. Hao, A. Yoko, K. Inoue, Y. Xu, M. Saito, C. Chen, G. Seong, T. Tomai, S. Takami, A.L. Shluger, B. Xu, T. Adschiri, and Y. Ikuhara, Acta Mater. **203**, 116473 (2021).
   DOI:10.1016/j.actamat.2020.11.015

IMADA, Masatoshi [E class; 29000 (B), 4600 (C)] (184)
— *Exhaustive Studies on High Temperature Superconductors by Highly Accurate ab initio Scheme for Strongly Correlated Electron Systems*
— *Machine learning analyses on quasi-particle interference data of cuprate high-temperature superconductors*

1. Single-Particle Spectral Function Formulated and Calculated by Variational Monte Carlo Method with Application to d-Wave Superconducting State
   Maxime Charlebois and Masatoshi Imada, Phys. Rev. X **10** (2020) 041023.

2. Charge dynamics of correlated electrons: Variational description with inclusion of composite fermions
   Kota Ido, Masatoshi Imada, Takahiro Misawa, Phys. Rev. B **101** (2020) 075124.

3. *Ab initio* study of superconductivity and inhomogeneity in a Hg-based cuprate superconductor
   Takahiro Ohgoe, Motoaki Hirayama, Takahiro Misawa, Kota Ido, Youhei Yamaji, Masatoshi Imada, Phys. Rev. B **101** (2020) 045124.

INAOKA, Takeshi [B class; 700 (B), 150 (C)] (163)
— *Search and realization of novel electronic properties of solid surfaces and interfaces and of small particles*

1. Identification of surface states formed above the substrate bands of the Ni(110)-(2x1)O surface
   T. Inaoka and Y. Uehara, to be submitted.

ISHIBASHI, Shoji [C class; 800 (B), 0 (C)] (167)

— *Prediction of properties of organic ferroelectrics and piezoelectrics by first-principles calculation*

1. Metaelectric multiphase transitions in a highly polarizable molecular crystal
   S. Horiuchi, S. Ishibashi, R. Haruki, R. Kumai, S. Inada, and S. Aoyagi Chem. Sci. **11**, 6183 (2020).
   DOI:10.1039/d0sc01687j

ISHIDA, Kunio [B class; 1100 (B), 200 (C)] (275)

— *Dynamics of phonon entanglement creation between remote electron-phonon systems*

1. Coherent control of nonadiabatic dynamics of electron-phonon systems by quantized light field
   Kunio Ishida Progress in Ultrafast Intense Laser Science XV, 121-132, (2020).
   DOI:10.1007/978-3-030-47098-2_6

2. Two-step dynamics of photoinduced phonon entanglement generation between remote electron-phonon systems
   Kunio Ishida and Hiroaki Matsueda arXiv: 2005.14615.

ISHIHARA, Sumio [B class; 800 (B), 0 (C)] ()

— *Inhomogeneous effect in light induced nonequilibrium state*

— *Numerical study of nonequilibrium dynamics in correlated electron systems*

ISHII, Fumiyuki [C class; 6000 (B), 1100 (C)] ()

— *First-Principles Calculations of Two-Dimensional Materials and Surface Alloys*

— *First-principles calculation of anomalous Hall coefficient in metallic ferromagnet by using Berry phase approach*

ISOBE, Masaharu [B class; 400 (B), 0 (C)] (315)

— *Nonequilibrium phase transition and slow dynamics in the dense hard sphere systems*

1. Direct Evidence of Void-Induced Structural Relaxations in Colloidal Glass Formers
   C.-T. Yip, M. Isobe, C.-H. Chan, S. Ren, K.-P. Wong, Q. Huo, C.-S. Lee, Y.-H. Tsang, Y. Han, and C.-H. Lam, Phys. Rev. Lett. **125**, 258001 (2020).
   DOI:10.1103/PhysRevLett.125.258001

2. Non-equilibrium response and equilibration in hard disk systems
   D. Mugita and M. Isobe, EPJ Web Conferences, in press.

IWASA, Takeshi [C class; 2800 (B), 550 (C)] (111)

— *Development and applications of first principles methods for light-matter interactions beyond the dipole approximation*

1. Theoretical method for near-field Raman spectroscopy with multipolar Hamiltonian and real-time-TDDFT: Application to on- and off-resonance tip-enhanced Raman spectroscopy
   M. Takenaka, T. Taketsugu, T. Iwasa, J. Chem. Phys. **154**, (2021) 024104.
   DOI:10.1063/5.0034933

JESCHKE, Harald [C class; 4400 (B), 0 (C)] ()

— *Sr and Ag doped Bi_2Se_3 under pressure*

— *Theory for Superconductivity in quasi-one-dimensional Cr-based pnictides*

JOUTSUKA, Tatsuya [B class; 1300 (B), 0 (C)] (143, 144)

— *Theoretical Analysis of Photocatalytic Reaction Mechanism at Titanium Dioxide Interfaces*

— *Ab Initio Calculation of High-Rate Deposition of Metal Film by Low-Pressure Chemical Vapor Deposition*
— *Ab Initio Calculation of High-Rate Deposition of Metal Films by Low-Pressure Chemical Vapor Deposition*

1. Low-pressure chemical vapor deposition of Cu on Ru using CuI as precursor
   T. Nishikawa, K. Horiuchi, T. Joutsuka, S. Yamauchi J. Cryst. Growth **549** (2020) 125849.

2. Constrained Density Functional Theory Molecular Dynamics Simulation of Deprotonation in Aqueous Silicic Acid
   T. Joutsuka, K. Ando, J. Phys. Chem. B **124** (2020) 8323.

3. Facet Dependence of Photocatalytic Activity in Anatase TiO_2: Combined Experimental and DFT Study
   T. Joutsuka, H. Yoshinari, S. Yamauchi, Bull. Chem. Soc. Jpn. **94** (2021) 106.

KADOWAKI, Hiroaki [B class; 800 (B), 50 (C)] ()
— *Exact diagonalization and TPQ of quantum pyrochlore model*
— *Exact diagonalization of quantum pyrochlore model*

KAGESHIMA, Hiroyuki [B class; 800 (B), 0 (C)] (166)
— *Study on structural elementary excitations at semiconductor surfaces and interfaces*

1. First-principles study of strain effect on oxygen vacancy in silicon oxide
   K. Yata and H. Kageshima, Jpn. J. Appl. Phys. **60** (2020) 035504/1-6.

KANEKO, Ryui [B class; 500 (B), 50 (C)] (306)
— *tensor-network study of phase transitions in large spin systems*

1. Continuous phase transition between Néel and valence bond solid phases in a J-Q-like spin ladder system
   T. Ogino, R. Kaneko, S. Morita, S. Furukawa, and N. Kawashima, Phys. Rev. B **103**, 085117 (2021)
   DOI:10.1103/PhysRevB.103.085117

2. Multiple magnetization plateaus induced by further neighbor interaction in an $S = 1$ two-leg Heisenberg spin ladder
   H. Kohshiro, R. Kaneko, S. Morita, and N. Kawashima, submitted to Phys. Rev. B
   DOI:arXiv:2102.07473

3. Reentrance of the disordered phase in the antiferromagnetic Ising model on a square lattice with longitudinal and transverse magnetic fields
   R. Kaneko, Y. Douda, S. Goto, and I. Danshita, submitted to J. Phys. Soc. Jpn.
   DOI:arXiv:2103.12364

KARIYADO, Toshikaze [B class; 600 (B), 50 (C)] (299)
— *Study of superstructure induced novel phenomena: stacking of atomically thin materials*
— *Superstructure based band engineering and its application*

1. Giant orbital diamagnetism of three-dimensional Dirac electrons in Sr_3PbO antiperovskite
   S. Suetsugu, K. Kitagawa, T. Kariyado, A. W. Rost, J. Nuss, C. Mühle, M. Ogata, and H. Takagi, Phys. Rev. B **103**, 115117 (2021).
   DOI:10.1103/PhysRevB.103.115117

2. Selective branching and converting of topological modes
   T. Kariyado and R.-J. Slager, submitted to Phys. Rev. Research

KASAMATSU, Shusuke [C class; 5400 (B), 900 (C)] (16)
— *Analysis of disordered materials using a combination of first-principles calculations statistical physics and machine learning*
— *Thermodynamic analysis of charge-storing interfaces based on direct coupling of statistical physics and first-principles calculation*

1. Dopant arrangements in Y-doped $BaZrO_3$ under processing conditions and their impact on proton conduction: a large-scale first-principles thermodynamics study
   Shusuke Kasamatsu, Osamu Sugino, Takafumi Ogawa, and Akihide Kuwabara, J. Mater. Chem. A **8**, 12674-12686 (2020).
   DOI:10.1039/D0TA01741H

2. Theoretical study on proton diffusivity in Y-doped $BaZrO_3$ with realistic dopant configurations
   Takeo Fujii, Kazuaki Toyoura, Tetsuya Uda, and Shusuke Kasamatsu, Phys. Chem. Chem. Phys. **23**, 5908-5918 (2021).
   DOI:10.1039/D0CP06035F

3. Monte Carlo Sampling of Configuration Disorder in Crystalline Materials
   Shusuke Kasamatsu, The Brain & Neural Networks **28**, 12-19 (2021).
   DOI:10.3902/jnns.28.12

KATO, Takeo [B class; 900 (B), 100 (C)] (283)
— *Numerical Study of Adiabatic Charge Pumping through Kondo Quantum Dots*
— *Theory of Adiabatic Pumping in Mesoscopic Devices*

1. Transmission of waves through a pinned elastic medium
   T. Yamamoto, L. I. Glazman, and M. Houzet, Phys. Rev. B **103**, 224211 (2021).
   DOI:10.1103/PhysRevB.103.224211

KATO, Yusuke [C class; 5800 (B), 400 (C)] (243)
— *Dynamics of Kitaev spin liquid via functional renormalization group method*
— *Functional renormalization group approach for dynamics of Kitaev-Heisenberg model*

KAWAKAMI, Norio [C class; 9200 (B), 1350 (C)] (191)
— *Magnetism topological phase formation and transport phenomena in strongly correlated systems*
— *Study of phase formation and transport phenomena in strongly correlated quantum systems*

1. Spin-caloritronic transport in hexagonal graphene nanoflakes
   Thi. Thu Phung, Robert Peters, Andreas Honecker, Guy Trambly de Laissardiere, and Javad Vahedi, Phys. Rev. B **102** (2020) 035160.

2. Equivalence of the effective non-hermitian Hamiltonians in the context of open quantum systems and strongly-correlated electron systems
   Yoshihiro Michishita and Robert Peters, Phys. Rev. Lett. **124** (2020) 196401.

3. Exceptional band touching for strongly correlated systems in equilibrium
   Tsuneya Yoshida, Robert Peters, Norio Kawakami, and Yasuhiro Hatsugai, Prog. Theor. Exp. Phys. (2020) 12A109

4. Exceptional points in the one-dimensional Hubbard model
   Roman Rausch, Robert Peters and Tsuneya Yoshida, New J. Phys. **23** (2021) 013011.

5. Edge magnetic properties of black phosphorene nanoribbons
   Javad Vahedi and Robert Peters, Phys. Rev. B **103** (2021) 075108.

6. Minimal model of many-body localization
   F. Monteiro, T. Micklitz, Masaki Tezuka, and Alexander Altland, Phys. Rev. Research 3 (2021) 013023.

KAWAKATSU, Toshihiro [C class; 6800 (B), 0 (C)] (237)
— *Analyses on complex fluids using multiscale simulation platform*
— *Fluid-elastomer hybrid simulations using multiscale simulation platform*

KAWAMURA, Hikaru [C class; 6400 (B), 0 (C)] (241)
— *Novel order in frustrated magnets*

1. Monte Carlo studies of the spin-chirality decoupling in the three-dimensional Heisenberg spin glass
   T. Ogawa, K. Uematsu and H. Kawamura, Phys. Rev. B 101, 014434/1-16 (2020).
   DOI:10.1103/PhysRevB.101.014434

2. Spin Current as a Probe of the Z2-Vortex Topological Transition in the Classical Heisenberg Antiferromagnet on the Triangular Lattice
   K. Aoyama and H. Kawamura, Phys. Rev. Letters 124, 047202/1-6 (2020).
   DOI:10.1103/PhysRevLett.124.047202

3. Hedgehog-lattice spin texture in classical Heisenberg antiferromagnets on the breathing pyrochlore lattice
   K. Aoyama and H. Kawamura, Phys. Rev. B 131, 014406/1-15 (2021).
   DOI:10.1103/PhysRevB.103.014406

KAWAMURA, Takahiro [C class; 600 (B), 350 (C)] (158)
— *First-principles analysis of melt structure and property in Na flux GaN growth*

1. Activation free energies for formation and dissociation of N–N, C–C, and C–H bonds in a Na–Ga melt
   T. Kawamura, M. Imanishi, M. Yoshimura, Y. Mori, and Y. Morikawa Comp. Mater. Sci. **194**, 110366 (2021).
   DOI:10.1016/j.commatsci.2021.110366

KAWASHIMA, Naoki [E class; 24500 (B), 3950 (C)] (221)
— *Tensor-network study of Kitaev models*

1. DSQSS: Discrete Space Quantum Systems Solver,
   Yuichi Motoyama, Kazuyoshi Yoshimi, Akiko Masaki-Kato, Takeo Kato, Naoki Kawashima, Computational Physics Communications 264, 107944 (2021)
   DOI:10.1016/j.cpc.2021.107944

2. Multiple magnetization plateaus induced by further neighbor interaction in an S=1 two-leg Heisenberg spin ladder
   Hidehiko Kohshiro, Ryui Kaneko, Satoshi Morita, Naoki Kawashima, arXiv:2102.07473

3. Generating Function for Tensor Network Diagrammatic Summation
   Wei-Lin Tu, Huan-Kuang Wu, Norbert Schuch, Naoki Kawashima, Ji-Yao Chen, arXiv:2101.03935

4. Continuous phase transition between Néel and valence bond solid phases in a J-Q-like spin ladder system
   Takuhiro Ogino, Ryui Kaneko, Satoshi Morita, Shunsuke Furukawa, Naoki Kawashima, Phys. Rev. B 103, 085117 (2021)
   DOI:10.1103/PhysRevB.103.085117

5. Data Assimilation Method for Experimental and First-Principles Data: Finite-Temperature Magnetization of (Nd,Pr,La,Ce)$_2$(Fe,Co,Ni)$_{14}$B
   Yosuke Harashima, Keiichi Tamai, Shotaro Doi, Munehisa Matsumoto, Hisazumi Akai, Naoki Kawashima, Masaaki Ito, Noritsugu Sakuma, Akira Kato, Tetsuya Shoji, and Takashi Miyake, Physical Review Materials 5, 013806 (2021)
   DOI:10.1103/PhysRevMaterials.5.013806

6. Thermal Hall Effects of Spins and Phonons in Kagome Antiferromagnet Cd-Kapellasite
   Masatoshi Akazawa, Masaaki Shimozawa, Shunichiro Kittaka, Toshiro Sakakibara, Ryutaro Okuma, Zenji Hiroi, Hyun-Yong Lee, Naoki Kawashima, Jung Hoon Han and Minoru Yamashita, Physical Review X 10, 041059 (2020)
   DOI:10.1103/PhysRevX.10.041059

7. Global optimization of tensor renormalization group using the corner transfer matrix
   Satoshi Morita and Naoki Kawashima, Physical Review B 103, 045131 (2020)
   DOI:10.1103/PhysRevB.103.045131

8. Construction of variational matrix product states for the Heisenberg spin-1 chain
   Jintae Kim, Minsoo Kim, Naoki Kawashima, Jung Hoon Han and Hyun-Yong Lee, Phys. Rev. B 102, 085117 (2020)
   DOI:10.1103/PhysRevB.102.085117

9. Kω–Open-sourcelibraryfortheshiftedKrylovsubspacemethodoftheform(zI–H)x=b
   Takeo Hoshi, Mitsuaki Kawamura, Kazuyoshi Yoshimi, Yuichi Motoyama, Takahiro Misawa, Youhei Yamaji, Synge Todo, Naoki Kawashima, Tomohiro Sogabea Computer Physics Communications 258, 107536 (2020)
   DOI:10.1016/j.cpc.2020.107536

10. Tensor network wave function of S=1 Kitaev spin liquids
    Hyun-Yong Lee, Naoki Kawashima and Yong Baek Kim, Phys. Rev. Res. 2 033318 (2020)
    DOI:10.1103/PhysRevResearch.2.033318

11. Boundary conformal spectrum and surface critical behavior of classical spin systems:A tensor network renormalization study
    Shumpei Iino, Satoshi Morita, and Naoki Kawashima, Phys. Rev. B 101, 155418 (2020)
    DOI:10.1103/PhysRevB.101.155418

12. Magnetic field induced quantum phases in a tensor network study of Kitaev magnets
    Hyun-Yong Lee, Ryui Kaneko, Li Ern Chern, Tsuyoshi Okubo, Youhei Yamaji, Naoki Kawashima, and Yong Baek Kim, Nature Communications 11, 1639 (2020)
    DOI:10.1038/s41467-020-15320-x

13. Tensor-Ring Decomposition with Index-Splitting
    Hyun-Yong Lee, and Naoki Kawashima, J. Phys. Soc. Jpn. 89, 054003 (2020)
    DOI:10.7566/JPSJ.89.054003

KITA, Takafumi [C class; 600 (B), 200 (C)] (287)

— *Magnetic field dependence of the thermal Hall effect based on the augmented quasiclassical equations*

1. Drastic enhancement of the thermal Hall angle in a *d*-wave superconductor
   H. Ueki, H. Morita, M. Ohuchi, and T. Kita, Phys. Rev. B **101**, 184518 (2020).
   DOI:10.1103/PhysRevB.101.184518

2. Zero-Field Surface Charge Due to the Gap Suppression in *d*-Wave Superconductors

E. S. Joshua, H. Ueki, W. Kohno, and T. Kita
J. Phys. Soc. Jpn. **89**, 104702 (2020).
DOI:10.7566/JPSJ.89.104702

3. Charging in the Abrikosov lattice of type-II superconductors
   M. Ohuchi, H. Ueki, and T. Kita, submitted to Phys. Rev. B

KITAO, Akio [C class; 8000 (B), 0 (C)] (234)
— *Efficient sampling simulation of the soft modes significantly contribute to protein properties*

1. Regulation of caveolae through cholesterol-depletion-dependent tubulation mediated by PACSIN2.
   A. Gusmira, K. Takemura, S.Y. Lee, T. Inaba, K. Hanawa-Suetsugu, K. Oono-Yakura, K. Yasuhara, A. Kitao and S. Suetsugu, J Cell Sci **133** (2020) jcs246785.

2. Edge expansion parallel cascade selection molecular dynamics simulation for investigating large-amplitude collective motions of proteins.
   D.P. Tran and A Kitao, J. Chem. Phys. **152** (2020) 225101.

3. Kinetic selection and relaxation of the Intrinsically Disordered Region of a Protein upon Binding.
   K. Takaba, D.P. Tran and A. Kitao, J. Chem. Theory Comput. **16** (2020) 2835.

4. An Efficient Timer and Sizer of Biomacromolecular Motions.
   J. Chan, K. Takemura, H.R. Lin, K.C. Chang, Y.Y. Chang, Y. Joti, A. Kitao and L.W. Yang, Structure **28** (2020) 259.

5. High pressure inhibits signaling protein binding to the flagellar motor and bacterial chemotaxis through enhanced hydration.
   H. Hata, Y. Nishihara, M. Nishiyama, Y. Sowa, I. Kawagishi, A. Kitao, Sci. Rep. **10** (2020) 2351.

6. Molecular dynamics simulation of proteins under high pressure: Structure, function and thermodynamics.
   H. Hata, M. Nishiyama, A. Kitao, Biochimica et Biophysica Acta **1864** (2020) 129395.

KOBAYASHI, Akito [B class; 1000 (B), 150 (C)] (211)
— *Hidden Order in Low Temperature Phase of Organic Dirac Electron System α-(BETS)$_2I_3$*
— *Hidden Ordered State in Organic Dirac Electron System $\alpha-(BETS)_2I_3$*

1. Possible spin-density wave on Fermi arc of edge state in single-component molecular conductors [Pt(dmdt)2] and [Ni(dmdt)2]
   T. Kawamura, B. Zhou, Akiko Kobayashi, Akito Kobayashi accepted to J. Phys. Soc. Jpn. (2021/03/30)

2. Interacting chiral electrons at the 2D Dirac points: a review
   M. Hirata, A. Kobayashi, C. Berthier and K. Kanoda Rep. Prog. Phys. **84** 036502 (2021)
   DOI:10.1088/1361-6633/abc17c

3. Transport properties of the organic Dirac electron system α-(BEDT-TSeF)$_2$I$_3$
   D. Ohki, K. Yoshimi, and A. Kobayashi Phys. Rev. B 102, 235116 (2020)
   DOI:10.1103/PhysRevB.102.235116

4. Chiral excitonic instability of two-dimensional tilted Dirac cones
   D. Ohki, M. Hirata, T. Tani, Kazushi K., and A. Kobayashi Phys. Rev. Research 2, 033479 (2020)
   DOI:10.1103/PhysRevResearch.2.033479

5. Tight-binding model and electronic property of Dirac nodal line in single-component molecular conductor [Pt(dmdt)$_2$]
   T. Kawamura, D. Ohki, B. Zhou, Akiko Kobayashi, Akito Kobayashi J. Phys. Soc. Jpn. 89, 074704 (2020)
   DOI:10.7566/JPSJ.89.074704

6. Effect of Coulomb interactions on the Seebeck coefficient of the organic Dirac electron system α-(BEDT-TTF)$_2$I$_3$
   D. Ohki, Y. Omori, A. Kobayashi Phys. Rev. B 101, 245201 (2020)
   DOI:10.1103/PhysRevB.101.245201

KOBAYASHI, Katsuyoshi [B class; 700 (B), 100 (C)] (165)
— *Theoretical study on electronic properties of new nanoscale surfaces and interfaces*

1. Method of forming time-reversed LEED states from repeated-slab calculations
   K. Kobayashi, J. Phys.: Condens. Matter **32** (2020) 495002.
   DOI:10.1088/1361-648X/abb444

KOBAYASHI, Nobuhiko [C class; 3800 (B), 600 (C)] (96)
— *First-principles study of quantum transport in nanostructures*

1. SAKE: first-principles electron transport calculation code
   H. Takaki, N. Kobayashi, and K. Hirose, J. Phys.: Condens. Matter 32 (2020) 325901.

2. Charge mobility calculation of organic semiconductors without use of experimental single-crystal data
   H. Ishii, S. Obata, N. Niitsu, S. Watanabe, H. Goto, K. Hirose, N. Kobayashi, T. Okamoto, and J. Takeya, Sci Rep 10, 2524 (2020)

KOBAYASHI, Riki [B class; 500 (B), 0 (C)] ()
— *Screening of substitutable element in van der Waals coupling rare-earth compounds*
— *Screening of substitutable non-magnetic element in rare-earth inter-metallic compounds II*

KOGA, Akihisa [C class; 4200 (B), 600 (C)] (251)
— *Numerical analysis for nonequilibrium dynamics in electronic systems on quasicrystals*
— *Study of new ordered phase and nonequilibrium phenomena in quasicrystals*

1. Majorana-mediated spin transport in Kitaev quantum spin liquids
   T. Minakawa, Y. Murakami, A. Koga and J. Nasu, Phys. Rev. Lett. **125**, 047204 (2020).

2. Superlattice structure in the antiferromagnetically ordered state in the Hubbard model on the Ammann-Beenker tiling
   A. Koga, Phys. Rev. B **102**, 115125 (2020).

3. Antiferromagnetically ordered state in the half-filled Hubbard model on the Socolar dodecagonal tiling
   A. Koga, Mater. Trans. **62**, 360-366 (2021).

4. Majorana correlations in the Kitaev model with ordered-flux structure
   A. Koga, Y. Murakami, and J. Nasu, submitted to PRB.

KOMATSU, Hisato [B class; 400 (B), 100 (C)] (312)
— *Magnetic structures under the non-equilibrium state of the magnetic thin films with the dipolar in-*

teraction

KOMATSU, Yu [C class; 6200 (B), 900 (C)] (70)
— *Thermodynamic properties of icy materials in the interior of planets and satelites*

KOU, Sonju [B class; 500 (B), 0 (C)] ()
— *Development of Seebeck coefficient calculation method in the framework of density functional theory and linear response theory*

KOURA, Akihide [C class; 2600 (B), 400 (C)] (115)
— *Ab initio molecular dynamics study on static structure of glass materials*

1. Application of First-Principles-Based Artificial Neural Network Potentials to Multiscale-Shock Dynamics Simulations on Solid Materials
   M. Misawa, S. Fukushima, A. Koura, K. Shimamura, F. Shimojo, S. Tiwari, K. Nomura, R. K. Kalia, A. Nakano, and P. Vashishta, J. Phys. Chem. Lett. **11**, 4536 (2020).
   DOI:10.1021/acs.jpclett.0c00637

2. Molecular-Dynamics Study of Thermal Conductivity of Silver Chalcogenides
   S. Fukushima, K. Shimamura, A. Koura, and F. Shimojo, Phys. Status Solidi B **257**, 2000183 (2020)
   DOI:10.1002/pssb.202000183

3. Computational and training requirements for interatomic potential based on artificial neural network for estimating low thermal conductivity of silver chalcogenides
   K. Shimamura, Y. Takeshita, S. Fukushima, A. Koura, and F. Shimojo, J. Chem. Phys. **153**, 234301 (2020)
   DOI:10.1063/5.0027058

KUMAZOE, Hiroyuki [C class; 400 (B), 50 (C)] (314)
— *Establishment of new analysis method for extend X-ray absorption fine structure with sparse modeling*

KUNISADA, Yuji [C class; 5600 (B), 0 (C)] (80)
— *Reduction of Rare Metals in Formic Acid Decomposition Catalysts and Oxygen Storage Materials*

1. グラフェン担持 Pt サブナノクラスタの酸素還元反応活性
   長谷川瞬，國貞雄治，坂口紀史表面と真空 **63** (2020) 413.
   a DOI:10.1380/vss.63.413

2. Single Pt Atoms on N-Doped Graphene: Atomic Structure and Local Electronic States
   R. Sugimoto, Y. Segawa, A. Suzuta, Y. Kunisada, T. Uchida, K. Yamazaki, K. Gohara The Journal of Physical Chemistry C **125** (2021) 2900.
   DOI:10.1021/acs.jpcc.0c08811

KUROKI, Kazuhiko [C class; 7200 (B), 1100 (C)] (197)
— *Study on spin-fluctuation-mediated superconductivity enhanced by interorbital interactions*
— *Study on the enhanced superconductivity in cuprates with peculiar electronic structures*

1. Many-variable variational Monte-Carlo study of superconductivity in two-band Hubbard models with an incipient band
   D. Kato and K. Kuroki, Phys. Rev. Research **2**, 023156 (2020)
   DOI:10.1103/PhysRevResearch.2.023156

2. Superconducting mechanism for the cuprate $\mathrm{Ba_2CuO_{3+\delta}}$ based on a multiorbital Lieb lattice model
   K. Yamazaki, M. Ochi, D. Ogura, K. Kuroki, H. Eisaki, S. Uchida, and H. Aoki Phys. Rev.

Research **2**, 033356 (2020)
DOI:10.1103/PhysRevResearch.2.033356

3. Designing nickelate superconductors with d^8 configuration exploiting mixed-anion strategy
N. Kitamine, M. Ochi, and K. Kuroki, Phys.Rev.Research **2**, 042032 (2020)
DOI:10.1103/PhysRevResearch.2.042032

4. Quantifying the stability of the anion ordering in $SrVO_2H$
M. Ochi and K. Kuroki, Phys.Rev.B **102**, 134108 (2020)
DOI:10.1103/PhysRevB.102.134108

LIAO, YUXUAN [C class; 4000 (B), 700 (C)] (254, 256)
— *Machine-learning-assisted Development of Giant Thermal-Property Database for Polymer Materials*

1. Automated calculation system of physical properties with molecular dynamics simulation for polymer informatics
Yoshihiro Hayashi, Ruimin Ma, Yuxuan Liao, Tengfei Luo, Junichiro Shiomi, Ryo Yoshida, Preparing for submitting.

2. Akhiezer Mechanism Dominates Relaxation of Propagons in Amorphous at Room Temperature
Yuxuan Liao, Junichiro Shiomi, submitted to JAP

3. Ultimate suppression of thermal transport in amorphous silicon nitride by phononic nanostructure
Naoki Tambo, Yuxuan Liao, Chun Zhou, Elizabeth Michiko Ashley, Kouhei Takahashi, Paul F Nealey, Yasuyuki Naito, Junichiro Shiomi, Science Advances **6**, eabc0075 (2020).

4. Heat conduction below diffusive limit in amorphous superlattice structures
Yuxuan Liao, Sotaro Iwamoto, Michiko Sasaki, Masahiro Goto, Junichiro Shiomi, Nano Energy **84**, 105903 (2021).

MAKINO, Takayuki [B class; 1300 (B), 250 (C)] (136)
— *Calculation of electronic states in strongly-electron-correlated antiferromagnetic oxides*

1. Contactless measurement of electric field with constant-DC-reflectivity photoreflectance method
E. Kobayashi et al. Solids
DOI:10.3390/solids2020008

2. Temperature-induced localized exciton dynamics in mixed Lead-Tin based CH3NH3Pb1-xSnxI3 Perovskite materials
Md. Sherajul Islam et al. AIP Advances
DOI:10.1063/5.0007087

MASAGO, Akira [B class; 400 (B), 0 (C)] ()
— *First principles calculations of thermal dependence of conductivity and Seebeck coefficient*

MATSUKAWA, Hiroshi [C class; 0 (B), 350 (C)] ()
— *Physics of Friction*

MATSUMOTO, Munehisa [D,C class; 8100 (B), 1950 (C)] (225, 226, 227)
— *Optimal design of Ce-based magnetic compounds for rare-earth permanet magnets*
— *Optimal design of magnetic materials via data integration between experiments and theory*
— *Self-consistent analysis between ab initio data and experimental measurement results via extended dynamical mean field theory*

MATSUNAKA, Daisuke [B class; 600 (B), 0 (C)] (176)
— *First-principles Study of Defects of Magnesium Alloys*

1. Defect nucleation from a pre-existing intrinsic I1 stacking fault in magnesium by molecular dynamics simulations
   So Yoshikawa and Daisuke Matsunaka, Computational Materials Science, **179** (2020) 109644/1-5.

MATSUSHITA, Katsuyoshi [C class; 0 (B), 350 (C)] (318)
— *Construction of Response Theory for Motion of Crowding Cells*
— *Many body effects in the collective motion of crowding cells*

1. Leader-guiding collective cell rotation
   Katsuyoshi Matsushita, Sunsuke Yabunaka, Hidenori Hashimura, Hidekazu Kuwayama, Kouichi Fujimoto, Proceedings of the Symposium on Traffic Flow and Self-Driven Particles 26, 38 (2020)

2. Adhesion-stabilizing long-distance transport of cells on tissue surface
   K. Matsushita, Physical Review E 101, 052410 (2020)
   DOI:10.1103/PhysRevE.101.052410

MATSUSHITA, Yu-ichiro [C class; 8400 (B), 1300 (C)] (58)
— *Identification of interface-state defects in power semiconductors: Approach from ab-initio calculations*

1. Design and formation of SiC(0001)/SiO2 interfaces via Si deposition followed by low-temperature oxidation and high-temperature nitridation
   T. Kobayashi, T. Okuda, K. Tachiki, K. Ito, Y. Matsushita, and T. Kimoto, Applied Physics Express **13**, 091003 (2020).
   DOI:10.35848/1882-0786/ababed

2. Unraveling crystal symmetry and strain effects on electronic band structures of SiC polytypes
   Y. Kuroiwa, Y. Matsushita, and F. Oba, AIP Advances **10**, 105014 (2020).
   DOI:10.1063/5.0010512

3. Implementation of quantum imaginary-time evolution method on NISQ devices: Nonlocal approximation
   H. Nishi, T. Kosugi, and Y. Matsushita, npj quantum information in press.

4. Linear-response functions of mol;ecules on a quantum computer: Charge and spin responses and optical absorption
   T. Kosugi, and Y. Matsushita, Physical Review Research **2**, 033043 (2020).
   DOI:10.1103/PhysRevResearch.2.033043

MINAMITANI, Emi [C class; 3200 (B), 800 (C)] ()
— *Ab-initio analysis of phonon and electron-phonon interaction*

MISAWA, Masaaki [B class; 900 (B), 0 (C)] (161)
— *Molecular Dynamics Simulation on Plastic-Wave Propagation in Solid Materials Based on First-Principles Calculation and Machine Learning*
— *Molecular dynamics study on non-equilibrium processes using first-principles calculation and machine leaning*

1. Application of First-Principles-Based Artificial Neural Network Potentials to Multiscale-Shock Dynamics Simulations on Solid Materials
   Masaaki Misawa, Shogo Fukushima, Akihide Koura, Kohei Shimamura, Fuyuki Shimojo, Subodh Tiwari, Ken-ichi Nomura, Rajiv K. Kalia, Aiichiro Nakano, and Priya Vashishta, The Journal of Physical Chemistry Letters **11**, 4536 (2020).

2. First-Principles Study of Pressure-Induced Amorphization of Fe2SiO4 Fayalite
   Masaaki Misawa and Fuyuki Shimojo, Physica Status Solidi B-Basic Solid State Physics **257** 2000173 (2020).

MISAWA, Takahiro [E class; 9000 (B), 2100 (C)] (189)
— *Systematic analysis of ab initio low-energy effective Hamiltonians for Pd(dmit)*$_2$ *molecular conductors*

1. Electronic correlation and geometrical frustration in molecular solids: A systematic ab initio study of β'-X[Pd(dmit)$_2$]$_2$
   T. Misawa, K. Yoshimi, and T. Tsumuraya, Phys. Rev. Research **2**, 032072(R) (2020).
   DOI:10.1103/PhysRevResearch.2.032072

2. Asymmetric melting of a one-third plateau in kagome quantum antiferromagnets
   T. Misawa, Y. Motoyama, and Y. Yamaji, Phys. Rev. B **102**, 094419 (2020)
   DOI:10.1103/PhysRevB.102.094419

3. Kω – Open-source library for the shifted Krylov subspace method of the form $(zI - H)x = b$
   Hoshi, Takeo and Kawamura, Mitsuaki and Yoshimi, Kazuyoshi and Motoyama, Yuichi and Misawa, Takahiro and Yamaji, Youhei and Todo, Synge and Kawashima, Naoki and Sogabe, Tomohiro, Computer Physics Communications **258**, 107536 (2021)
   DOI:10.1016/j.cpc.2020.107536

4. RESPACK: An ab initio tool for derivation of effective low-energy model of material
   Nakamura, Kazuma and Yoshimoto, Yoshihide and Nomura, Yusuke and Tadano, Terumasa and Kawamura, Mitsuaki and Kosugi, Taichi and Yoshimi, Kazuyoshi and Misawa, Takahiro and Motoyama, Yuichi, Computer Physics Communications **261**, 107781 (2021)
   DOI:10.1016/j.cpc.2020.107781

MIZUGUCHI, Tomoko [C class; 0 (B), 150 (C)] ()
— *DNA unwinding mechanism studied by steered molecular dynamics simulations*

1. Icosahedral order in liquid and glassy phases of cyclohexane
   T. Mizuguchi, S. Tatsumi and S. Fujiwara, Mol. Sim. /bf 46 721 (2020).
   DOI:10.1080/08927022.2020.1757092

MIZUKAMI, Wataru [C class; 1200 (B), 0 (C)] (147, 149)
— *First principles calculations of crystals with quantum classical hybrid algorithms*
— *Noisy simulations of first-principles calculations using quantum classical hybrid algorithms*

1. Orbital optimized unitary coupled cluster theory for quantum computer
   W. Mizukami, K. Mitarai, Y.O. Nakagawa, T. Yamamoto, T. Yan, and Y.-y. Ohnishi, Phys. Rev. Research **2**, 033421 (2020)
   DOI:10.1103/PhysRevResearch.2.033421

2. Variational Quantum Simulation for Periodic Materials
   N. Yoshioka, Y.O. Nakagawa, Y.-y. Ohnishi, W. Mizukami, arXiv:2008.09492

3. Neural-Network Quantum States for the Electronic Structure of Real Solids
   N. Yoshioka, W. Mizukami, F. Nori, arXiv:2010.01358

MORIKAWA, Yoshitada [C class; 7400 (B), 1200 (C)] (61)
— *Quantum simulations on dynamical heterogeneous catalysts*

1. Blue moon ensemble simulation of aquation free energy profiles applied to mono and bifunctional platinum anticancer drugs

T. Hirakawa, D. R. Bowler, T. Miyazaki, Y. Morikawa, and L. A. Truflandier, J. Comput. Chem. **41**, 1973 (2020).
DOI:10.1002/jcc.26367

2. Identifying Atomic-Level Correlation Between Geometric and Electronic Structure at a Metal-Organic Interface
H. Koshida, H. Okuyama, S. Hatta, T. Aruga, Y. Hamamoto, I. Hamada, and Y. Morikawa, J. Phys. Chem. C **124**, 17696 (2020).
DOI:10.1021/acs.jpcc.0c04678

3. Enhanced CO tolerance of Pt clusters supported on graphene with lattice vacancies
Y. Hamamoto, S. A. Wella, K. Inagaki, F. Abild-Pedersen, T. Bligaard, I. Hamada, and Y. Morikawa, Phys. Rev. B **102**, 075408 (2020).
DOI:10.1103/PhysRevB.102.075408

4. Oxygen vacancy-induced insulator-metal transition in $LaNiO_3$ thin films
H. D. Nguyen, C. T. Bach, and Y. Morikawa, Phys. Rev. B **102**, 165411 (2020).
DOI:10.1103/PhysRevB.102.165411

5. Metal-Tip-Catalyzed Dehydrogenation of a Single Hydrocarbon Molecule
A. Shiotari, I. Hamada, T. Nakae, S. Mori, T. Okujima, H. Uno, H. Sakaguchi, Y. Hamamoto, Y. Morikawa, and Y. Sugimoto, Nano Letters **20**, 8339 (2020).
DOI:10.1021/acs.nanolett.0c03510

6. Oxidative etching mechanism of diamond (100) surface
J. I. Enriquez, F. Muttaqien, M. Michiuchi, K. Inagaki, M. Geshi, I. Hamada, and Y. Morikawa Carbon **174**, 36-51 (2021).
DOI:10.1016/j.carbon.2020.11.057

7. Density functional theory study on a nitrogen-rich carbon nitride material C_3N_5 as photocatalyst for CO_2 reduction to C1 and C2 products
Y. Wang, T. N. Pham, Y. Tian, Y. Morikawa and L. Yan J. Colloid and Interface Science **585**, 740 (2021).
DOI:10.1016/j.jcis.2020.10.054

8. Alkaline earth atom doping-induced changes in the electronic and magnetic properties of graphene: a density functional theory study
A. C. F. Serraon, J. A. D. Del Rosario, P.-Y. A. Chuang, M. N. Chong, Y. Morikawa, A. A. B. Padama, and J. D. Ocon RSC Advances **11**, 6268, (2021).
DOI:10.1039/D0RA08115A

9. Multi-scale Simulation of Equilibrium Step Fluctuations on Cu(111) Surface
H. H. Halim, S. E. M. Putra, F. Muttaqien, I. Hamada, K. Inagaki, Y. Hamamoto, and Y. Morikawa, ACS Omega **6**, 5183 (2021).
DOI:10.1021/acsomega.0c05064

10. Role of intermolecular interactions in the catalytic reaction of formic acid on Cu(111)
A. Shiotari, S. E. M. Putra, Y. Shiozawa, Y. Hamamoto, K. Inagaki, Y. Morikawa, Y. Sugimoto, J. Yoshinobu, and I. Hamada, Small, in press.
DOI:10.1002/smll.202008010

11. Activation free energies for formation and dissociation of N-N, C-C, and C-H bonds in a Na-Ga melt
T. Kawamura, M. Imanishi, M. Yoshimura, Y. Mori, and Y. Morikawa Comput. Mater. Sci. **194**, 110366 (2021).

DOI:10.1016/j.commatsci.2021.110366

MORITA, Satoshi [B class; 1200 (B), 200 (C)] (274)

— *Study of phase transitions and critical phenomena by tensor network methods*

— *Study of phase transitions and critical phenomena by tensor renormalization group*

1. Global optimization of tensor renormalization group using the corner transfer matrix
   S. Morita, and N. Kawashima, Phys. Rev. B **103**, 045131 (2021).
   DOI:10.1103/PhysRevB.103.045131

2. Continuous phase transition between Neel and valence bond solid phases in a J-Q-like spin ladder system
   T. Ogino, R. Kaneko, S. Morita, S. Furukawa, and N. Kawashima, Phys. Rev. B **103**, 085117 (2021).
   DOI:10.1103/PhysRevB.103.085117

MOTOME, Yukitoshi [C class; 8800 (B), 1350 (C)] (193)

— *Theoretical study of correlated electron systems with strong spin-orbit coupling*

1. Magnetic hedgehog lattices in noncentrosymmetric metals
   S. Okumura, S. Hayami, Y. Kato, and Y. Motome Phys. Rev. B **101**, 144416 (2020).
   DOI:10.1103/PhysRevB.101.144416

2. Switching of band inversion and topological surface states by charge density wave
   N. Mitsuishi, Y. Sugita, M. S. Bahramy, M. Kamitani, T. Sonobe, M. Sakano, T. Shimojima, H. Takahashi, H. Sakai, K. Horiba, H. Kumigashira, K. Taguchi, K. Miyamoto, T. Okuda, S. Ishiwata, Y. Motome, and K. Ishizaka Nat. Commun. **11**, 2466 (2020).
   DOI:10.1038/s41467-020-16290-w

3. Antiferromagnet-Semiconductor Van Der Waals Heterostructures: Interlayer Interplay of Exciton with Magnetic Ordering
   M. Onga, Y. Sugita, T. Ideue, Y. Nakagawa, R. Suzuki, Y. Motome, and Y. Iwasa, Nano Lett. **20**, 4625 (2020).
   DOI:10.1021/acs.nanolett.0c01493

4. Materials design of Kitaev spin liquids beyond the Jackeli-Khaliullin mechanism
   Y. Motome, R. Sano, S.-H. Jang, Y. Sugita, and Y. Kato J. Phys: Condens. Matter **32**, 404001 (2020).
   DOI:10.1088/1361-648X/ab8525

5. Anomalous Hall effect in κ-type organic antiferromagnets
   M. Naka, S. Hayami, H. Kusunose, Y. Yanagi, Y. Motome, and H. Seo Phys. Rev. B **102**, 075112 (2020).
   DOI:10.1103/PhysRevB.102.075112

6. Thermodynamic classification of three-dimensional Kitaev spin liquids
   T. Eschmann, P. A. Mishchenko, K. O'Brien, T. A. Bojesen, Y. Kato, M. Hermanns, Y. Motome, and S. Trebst Phys. Rev. B **102**, 075125 (2020).
   DOI:10.1103/PhysRevB.102.075125

7. Thermodynamic and transport properties in disordered Kitaev models
   J. Nasu and Y. Motome, Phys. Rev. B **102**, 054437 (2020).
   DOI:10.1103/PhysRevB.102.054437

8. Channel-selective non-Fermi liquid behavior in the two-channel Kondo lattice model under a

magnetic field
K. Inui and Y. Motome, Phys. Rev. B **102**, 155126 (2020).
DOI:10.1103/PhysRevB.102.155126

9. Computational design of *f*-electron Kitaev magnets: Honeycomb and hyperhoneycomb compounds A_2PrO_3 (A= alkali metals)
S.-H. Jang, R. Sano, Y. Kato, and Y. Motome, Phys. Rev. Materials **4**, 104420 (2020).
DOI:10.1103/PhysRevMaterials.4.104420

10. Imaging the coupling between itinerant electrons and localised moments in the centrosymmetric skyrmion magnet $GdRu_2Si_2$
Y. Yasui, C. J. Butler, N. D. Khanh, S. Hayami, T. Nomoto, T. Hanaguri, Y. Motome, R. Arita, T. Arima, Y. Tokura, and S. Seki Nat. Commun. **11**, 5925 (2020).
DOI:10.1038/s41467-020-19751-4

11. Optical Hall response in spin-orbit coupled metals: Comparative study of magnetic cluster monopole, quadrupole, and toroidal orders
T. Sato, Y. Umimoto, Y. Sugita, Y. Kato, and Y. Motome Phys. Rev. B **103**, 054416 (2021).
DOI:10.1103/PhysRevB.103.054416

12. Noncoplanar multiple-Q spin textures by itinerant frustration: Effects of single-ion anisotropy and bond-dependent anisotropy
S. Hayami and Y. Motome, Phys. Rev. B **103**, 054422 (2021).
DOI:10.1103/PhysRevB.103.054422

13. Phase transitions between helices, vortices, and hedgehogs driven by spatial anisotropy in chiral magnets
K. Shimizu, S. Okumura, Y. Kato, and Y. Motome, Phys. Rev. B **103**, 054427 (2021).
DOI:10.1103/PhysRevB.103.054427

14. Perovskite as a spin current generator
M. Naka, Y. Motome, and H. Seo Phys. Rev. B **103**, 125114 (2021).
DOI:10.1103/PhysRevB.103.125114

15. Phase Shift in Skyrmion Crystals
S. Hayami, T. Okubo, and Y. Motome, preprint (arXiv:2005.03168).

16. Spin Moire Engineering of Emergent Electromagnetism
K. Shimizu, S. Okumura, Y. Kato, and Y. Motome, preprint (arXiv:2009.14569).

17. Topological spin crystals by itinerant frustration
S. Hayami and Y. Motome, preprint (arXiv:2103.10647).

18. Spin dynamics in the Kitaev model with disorder: Quantum Monte Carlo study of dynamical spin structure factor, magnetic susceptibility, and NMR relaxation rate
J. Nasu and Y. Motome, preprint (arXiv:2103.10549).

MURAGUCHI, Masakazu [B class; 400 (B), 100 (C)] (178)
— *Study on machine learning model of carrier dynamics in semiconductor devices*

MURASHIMA, Takahiro [C class; 2400 (B), 450 (C)] (267)
— *Multiscale simulation of polymeric fluids and solids*

1. Viscosity Overshoot in Biaxial Elongational Flow: Coarse-Grained Molecular Dynamics Simulation of Ring-Linear Polymer Mixtures

T. Murashima, K. Hagita, and T. Kawakatsu, submitted to Macromolecules

NADA, Hiroki [B,C class; 600 (B), 650 (C)] (278, 279)
— *Large-scale metadynamics simulations for water and aqueous solutions*
— *Metadynamics Simulation Analysis of Various Cluster Structures Appearing in Calcium Carbonate Supersaturated Solution*

1. High Virus Removal by Self-Organized Nanostructured 2D Liquid-Crystalline Smectic Membranes for Water Treatment
   D. Kuo, M. Liu, K. R. S. Kumar, K. Hamaguchi, K. P. Gan, T. Sakamoto, T. Ogawa, N. Miyamoto, H. Nada, M. Kimura, M.Henmi, H. Katayama and T. Kato Small **16** (2020) 2001721.

2. High-Density Liquid Water at a Water-Ice Interface
   H. Niinomi, T. Yamazaki, H. Nada, T. Hama, A. Koichi, J. T. Okada, J. Nozawa, S. Uda and Y. Kimura J. Phys. Chem. Lett. **11** (2020) 6779.

3. Melt Crystallization Mechanism Analyzed with Dimensional Reduction of Distribution Function Geometries
   H. Nada, Sci. Rep. **10** (2020) 15465.

4. Capturing the Moment of Emergence of Crystal Nucleus from Disorder
   T. Nakamuro, M. Sakakibara, H. Nada, K. Harano and E. Nakamura J. Am. Chem. Soc. **143** (2021) 1763.

NAKAGAWA, Naoko [B,C class; 2600 (B), 450 (C)] (266)
— *Global thermodynamic functions extended to nonequilibrium steady states*

1. Effective Langevin equations leading to large deviation function of time-averaged velocity for a nonequilibrium Rayleigh piston
   Masato Itami, Yohei Nakayama, Naoko Nakagawa and Shin-ichi Sasa Phys. Rev. E **103** (2021) 022125.

NAKAHARA, Akio [B class; 400 (B), 100 (C)] (311)
— *Diversity in memory effects of flow in paste*

NAKAMURA, Kazuma [C class; 2800 (B), 0 (C)] (116)
— *Ab initio calculation for thermodynamic phase diagram: Investigation on exchange-correlation functional dependence*
projectAb initio phonon calculation for Ca5Or3O12

NAKANO, Hiroki [C class; 3000 (B), 550 (C)] (263)
— *Numerical study on low-energy states of quantum spin systems*

NAKAYAMA, Takashi [C class; 4200 (B), 900 (C)] (85)
— *First-principles study on physics of gap-state control at metal/semiconductor interfaces II*
— *First-principles study on physics of gap-state control at metal/semiconductor interfaces III: effects of electric field and alloy interface*

NASU, Joji [C class; 1800 (B), 550 (C)] (209)
— *Disorder effect on Kitaev quantum spin liquids*

1. Majorana-Magnon Crossover by a Magnetic Field in the Kitaev Model: Continuous-Time Quantum Monte Carlo Study
   J. Yoshitake, J. Nasu, Y. Kato, and Y. Motome, Phys. Rev. B **101**, 100408(R) (2020).

2. The range of non-Kitaev terms and fractional particles in α-$RuCl_3$
   Y. Wang, G. B. Osterhoudt, Y. Tian, P. Lampen-Kelley, A. Banerjee, T. Goldstein, J. Yan, J. Knolle, H. Ji, R. J. Cava, J. Nasu, Y. Motome, S. Nagler, D. Mandrus, and K. S. Burch, npj Quantum Materials **5**, 14 (2020).

3. Majorana-Magnon Crossover by a Magnetic Field in the Kitaev Model: Continuous-Time Quantum Monte Carlo Study
   J. Yoshitake, J. Nasu, Y. Kato, and Y. Motome, Phys. Rev. B **101**, 100408(R) (2020).

4. Majorana-Mediated Spin Transport in Kitaev Quantum Spin Liquids
   T. Minakawa, Y. Murakami, A. Koga, and J. Nasu, Phys. Rev. Lett. **125**, 047204 (2020).

5. Strong enhancement of magnetic susceptibility induced by spin-nematic fluctuations in an excitonic insulating system with spin-orbit coupling
   J. Nasu, M. Naka, S. Ishihara, Phys. Rev. B **102**, 045143 (2020).

6. Thermodynamic and transport properties in disordered Kitaev models
   J. Nasu and Y. Motome, Phys. Rev. B **102**, 054437/1-6 (2020).

7. Spin Seebeck effect in nonmagnetic excitonic insulators
   J. Nasu and M. Naka, Phys. Rev. B **103**, L121104/1-6 (2021).

NIKI, Kaori [C class; 0 (B), 400 (C)] (180)
— *Establishment of molecular crystal surface analysis technique using wave number space resolved photoelectron spectroscopy*

NISHIDATE, Kazume [C class; 1600 (B), 0 (C)] (135)
— *Investigation on the electronic structure of photo-catalytic double-perovskite*

1. Electronic Properties and Crystal Structures of Double-Perovskites, $Ba_2Bi^{III}Bi^{V}O_6$, Ba_2PrBiO_6, and Ba_2PrSbO_6: First-principles study
   K. Nishidate, A. Adiko, M. Matsukawa, H. Taniguchi, A. Sato, A. Matsushita, S. Tanibayashi and M. Hasegawa, Mater. Res. Express **7** (2020) 065505.

2. Hybridization versus sublattice symmetry breaking in the band gap opening in graphene on Ni(111): A first-principles study
   K. Nishidate, S. Tanibayashi, M. Matsukawa, M. Hasegawa, Surface Science, 700, October (2020) 121651.

NISHIGUCHI, Kazutaka [B class; 700 (B), 150 (C)] (212, 214)
— *Development of electronic structure calculation for solids with post-Hartree-Fock*
— *Development of electronic structure calculation for solids with quantum chemistry calculations*

NOGUCHI, Hiroshi [C class; 7400 (B), 1200 (C)] (230)
— *structure formation of biomembrane*

1. Rational Design Principles of Attenuated Cationic Lytic Peptides for Intracellular Delivery of Biomacromolecules
   N.Tamemoto, M. Akishiba, K. Sakamoto, K. Kawano, H. Noguchi, S. Futaki, Mol. Pharmaceutics 17, 2175-2185 (2020).
   DOI:10.1021/acs.molpharmaceut.0c00312

2. Pattern Formation in Reaction-Diffusion System on Membrane with Mechanochemical Feedback
   N. Tamemoto and H. Noguchi Sci. Rep. 10, 19582/1-10 (2020).
   DOI:10.1038/s41598-020-76695-x

3. Molecular Dynamics Simulation of Soundwave Propagation in a Simple Fluid
   Y. Asano, H. Watanabe, and H. Noguchi, J. Chem. Phys. 153, 124504 (2020).
   DOI:10.1063/5.0024150

4. Conformation of ultra-long-chain fatty acid in lipid bilayer: Molecular dynamics study
   K. Kawaguchi, K. M. Nakagawa, S. Nakagawa, H. Shindou, H. Nagao, and H. Noguchi, J. Chem. Phys. 153, 165101 (2020).
   DOI:10.1063/5.0026030

5. Virtual bending method to calculate bending rigidity, saddle-splay modulus, and spontaneous curvature of thin fluid membranes
   H. Noguchi, Phys. Rev. E 102, 053315 (2020).
   DOI:10.1103/PhysRevE.102.053315

6. Undulation of a moving fluid membrane pushed by filament growth
   H. Noguchi and O. Pierre-Louis Sci. Rep. 11, 7985 (2021).
   DOI:10.1038/s41598-021-87073-6

7. Binding of thermalized and active membrane curvature-inducing proteins
   Q. Goutaland, F. van Wijland, J.-B. Fournier, and H. Noguchi Soft Matter 17, 5560 (2021).
   DOI:10.1039/d1sm00027f

8. Reaction-Diffusion Waves Coupled with Membrane Curvature
   N. Tamemoto and H. Noguchi Soft Matter (2021) in press
   DOI:10.1039/d1sm00540e

9. Effects of polymers on the cavitating flow around a cylinder: A Large-scale molecular dynamics analysis
   Y. Asano, H. Watanabe, and H. Noguchi, J. Chem. Phys. 155, 14905 (2021).
   DOI:10.1063/5.0056988

NOGUCHI, Yoshifumi [C class; 5200 (B), 850 (C)] (75)
— *Development of Exact First-Principles GW+Bethe-Salpeter Method*
— *Development of GW+Bethe-Salpeter method*

1. Quantum-mechanical hydration plays critical role in the stability of firefly oxyluciferin isomers: State-of-the-art calculations of the excited states
   Yoshifumi Noguchi, Miyabi Hiyama, Hidefumi Akiyama, and Osamu Sugino, J. Chem. Phys. **153**, 201103 (2020).
   DOI:10.1063/5.0031356

NOMURA, Yusuke [C class; 7600 (B), 1150 (C)] (195)
— *Ab initio calculation for strongly-correlated nickelate superconductor*
— *Comparison between nickelate and cuprate superconductors*

1. Machine Learning Quantum States-Extensions to Fermion–Boson Coupled Systems and Excited-State Calculations
   Yusuke Nomura J. Phys. Soc. Jpn. **89**, 054706 (2020).

2. Efficient implementation of the continuous-time interaction-expansion quantum Monte Carlo method
   Hiroshi Shinaoka, Yusuke Nomura and Emanuel Gull, Computer Physics Communications **252**, 106826 (2020).

3. Higgs-mode resonance in third harmonic generation in NbN superconductors: Multiband electron-

phonon coupling, impurity scattering, and polarization-angle dependence
Naoto Tsuji and Yusuke Nomura Phys. Rev. Research **2**, 043029 (2020).

4. Efficient ab initio Migdal-Eliashberg calculation considering the retardation effect in phonon-mediated superconductors
   Tianchun Wang, Takuya Nomoto, Yusuke Nomura, Hiroshi Shinaoka, Junya Otsuki, Takashi Koretsune, and Ryotaro Arita Phys. Rev. B **102**, 134503 (2020).

5. Magnetic exchange coupling in cuprate-analog d^9 nickelates
   Yusuke Nomura, Takuya Nomoto, Motoaki Hirayama, and Ryotaro Arita, Phys. Rev. Research **2**, 043144 (2020).

6. Geometrical Hall effect and momentum-space Berry curvature from spin-reversed band pairs
   Max Hirschberger, Yusuke Nomura, Hiroyuki Mitamura, Atsushi Miyake, Takashi Koretsune, Yoshio Kaneko, Leonie Spitz, Yasujiro Taguchi, Akira Matsuo, Koichi Kindo, Ryotaro Arita, Masashi Tokunaga, and Yoshinori Tokura Phys. Rev. B **103**, L041111 (2021).

NOZAWA, Kazuki [B,C class; 800 (B), 300 (C)] (151)
— *First-principles study of atomic and electronic structures of intermetallic compound catalysts*

1. Atomic structure of the (111) surface of the antiferromagnetic 1/1 Au-Al-Tb approximant
   Sam Coates, Kazuki Nozawa, Masahiro Fukami, Kazuki Inagaki, Masahiko Shimoda, Ronan McGrath, Hem Raj Sharma, and Ryuji Tamura, Physical Review B 102 235419(2020)
   DOI:10.1103/PhysRevB.102.235419

2. Accuracy of Cluster Model Calculations for Quasicrystal Surface
   Masanori Sato, Takanobu Hiroto, Yoshitaka Matsushita, and Kazuki Nozawa, Materials Transactions, 62, 350(2021)
   DOI:10.2320/matertrans.MT-MB2020015

OBATA, Masao [B class; 700 (B), 200 (C)] (160)
— *Analysis on atomic and magnetic structure in magnetic molecular complex crystal and interface and investigation of external electric and magnetic field effect*
— *Analysis on atomic and magnetic structure in magnetic molecular complex crystal and interface and investigation of external electromagnetic field effect*

1. Anatomy of magnetic anisotropy and voltage-controlled magnetic anisotropy in metal oxide heterostructure from first principles
   Indra Pardede, Daiki Yoshikawa, Tomosato Kanagawa, Nurul Ikhsan, Masao Obata, and Tatsuki Oda, Crystals: **10**, (2020) 1118.
   DOI:10.3390/cryst10121118

2. Finite electric-field approach to evaluate the vertex correction for the screened Coulomb interaction in the quasiparticle self-consistent GW method
   Hirofumi Sakakibara, Takao Kotani, Masao Obata, and Tatsuki Oda, Phys. Rev. B **101**, (2020) 205120.
   DOI:10.1103/PhysRevB.101.205120

ODA, Tatsuki [C,E class; 16400 (B), 3200 (C)] (52)
— *Analyses on electronic structure and magnetoelectric effect in high-performance spintronics and magnetic materials*

1. Anatomy of large perpendicular magnetic anisotropy in free-standing Co/Ni (111) multilayer, Journal of Magnetism and Magnetic Materials
   Indra Pardede, Daiki Yoshikawa, Tomosato Kanagawa, Nurul Ikhsan, Itsuki Murata, Masao

Obata, Tatsuki Oda, Journal of Magnetism and Magnetic Materials **500**(2020)166357.

2. Finite electric-field approach to evaluate the vertex correction for the screened Coulomb interaction in the quasiparticle self-consistent GW method
   Hirofumi Sakakibara, Takao Kotani, Masao Obata, and Tatsuki Oda, Physical Review B, **101** (2020) 205120.

3. Electronic structure investigation of spinel NiCo2O4 from quasi-particle self-consistent GW method
   Hasan Al Rasyid, Masao Obata, Indra Pardede, Marleni Wirmas, Takao Kotani, and Tatsuki Oda, The Science Reports of Kanazawa University **64** (2020).

4. Anatomy of magnetic anisotropy and voltage-controlled magnetic anisotropy in metal oxide heterostructure from first principles
   Indra Pardede, Daiki Yoshikawa, Tomosato Kanagawa, Nurul Ikhsan, Masao Obata, and Tatsuki Oda, Crystals **10** (2020) 1118.

OGUCHI, Tamio [B,C class; 4000 (B), 250 (C)] (97)
— *Magnetocaloric Effect of Transition-Metal Alloys*

1. First-principles study of magnetism and phase stabilities of V_2 based antiferromagnetic Heusler alloys
   F. Kuroda, T. Fukushima, and T. Oguchi, J. Appl. Phys. **127**, 193904 (2020).
   DOI:10.1063/1.5143826

2. Ferroelectric atomic displacement in multiferroic tetragonal perovskite $Sr_{1/2}Ba_{1/2}MnO_3$
   D. Okuyama, K. Yamauchi, H. Sakai, Y. Taguchi, Y. Tokura, K. Sugimoto, T. J. Sato, and T. Oguchi, Phys. Rev. Research **2**, 033038 (2020).
   DOI:10.1103/PhysRevResearch.2.033038

3. Spin injection through energy-band symmetry matching with high spin polarization in atomically controlled ferromagnet/ferromagnet/semiconductor structures
   Michihiro Yamada, Fumiaki Kuroda, Makoto Tsukahara, Shinya Yamada, Tetsuya Fukushima, Kentarou Sawano, Tamio Oguchi, and Kohei Hamaya, npg Asia Materials **12**, 47 (2020).
   DOI:10.1038/s41427-020-0228-5

4. DFT-based Engineering of Dirac Surface States in Topological-insulator Multilayers
   Takao Kosaka, Kunihiko Yamauchi, and Tamio Oguchi, J. Phys. Soc. Jpn. **89**, 094701 (2020).
   DOI:10.7566/JPSJ.89.094701

5. Suppression of O-redox reactions by multivalent Cr in Li-excess $Li_{2.4}M_{0.8}M'_{0.8}O_4$ (M, M'=Cr, Mn, and Ti) cathodes with layered and cation-disordered rock-salt structures
   Motoyuki Hamaguchi, Hiroyoshi Momida, Ayuko Kitajou, Shigeto Okada, and Tamio Oguchi, Electrochimica Acta **354**, 136630 (2020).
   DOI:10.1016/j.electacta.2020.136630

6. Insight into the diffusion mechanism of sodium ion-polaron complexes in orthorhombic P2 layered cathode oxide Na_xMnO_2
   Huu Duc Luong, Van An Dinh, Hiroyoshi Momida, and Tamio Oguchi, Phys. Chem. Chem. Phys. **22**, 18219-18228 (2020).
   DOI:10.1039/d0cp03208e

7. Impact of Inter-site Spin-Orbit Coupling on Perpendicular Magnetocrystalline Anisotropy in Cobalt-Based Thin Films
   Thi Phuong Thao Nguyen, Kunihiko Yamauchi, Kohji Nakamura, and Tamio Oguchi, J. Phys. Soc. Jpn. **89**, 114710 (2020).

DOI:10.7566/JPSJ.89.114710

8. Magnetocaloric effect in MnCoGe alloys studied by first-principles calculations and Monte-Carlo simulation
   Hung Ba Tran, Tetsuya Fukushima, Yukihiro Makino, and Tamio Oguchi, Solid State Commun. **323**, 114077 (2021).
   DOI:10.1016/j.ssc.2020.114077

9. Tuning structural-transformation temperature toward giant magnetocaloric effect in MnCoGe alloy: A theoretical study
   Hung Ba Tran, Tetsuya Fukushima, Kazunori Sato, Yukihiro Makino, and Tamio Oguchi, J. Alloys Compd. **854**, 157063/1-9 (2021).
   DOI:10.1016/j.jallcom.2020.157063

OHMURA, Satoshi [C class; 5000 (B), 0 (C)] (89, 90)
— *Effects of solvents on properties of artificial-retina molecule: ab initio molecular dynamics simulations*
— *Structural and transport properties of multi-component liquid Fe mixtures under high pressure*

1. Structures of Liquid Iron–Light-Element Mixtures under High Pressure
   S. Ohmura, T. Tsuchiya and F. Shimojo, physica status solidi (b). **257**, 2000098 (2020).
   DOI:10.1002/pssb.202000098

2. Dissociation mechanism from highly charged bromophenol: ab initio molecular dynamics simulations
   S. Ohmura, K. Nagaya, F. Shimojo and M. Yao, Z. Phys. Chem. **235**, 169 (2021).
   DOI:10.1515/zpch-2020-1634

OHNISHI, Masato [C class; 5000 (B), 950 (C)] (76)
— *Analysis of Thermoelectric Properties of Clathrate Compounds with Ab Initio Calculations*

1. Ultimate impedance of coherent heat conduction in van der Waals graphene-MoS2 heterostructures
   S. Hu, S. Ju, J. Guo, B. Xu, M. Ohnishi, and J. Shiomi, Mater. Today Phys. **16**, 100324 (2021).
   DOI:10.1016/j.mtphys.2020.100324

2. Run Hu, Sotaro Iwamoto, Lei Feng, Shenghong Ju, Shiqian Hu, Masato Ohnishi, Naomi Nagai, Kazuhiko Hirakawa, Junichiro Shiomi
   Machine-learning-optimized aperiodic superlattice minimizes coherent phonon heat conduction Physical Review X **10**, 2 (2020).
   DOI:10.1103/PhysRevX.10.021050

OHNO, Akira [B class; 400 (B), 0 (C)] ()
— *Modeling and elucidation of electron transport mechanism in liquid crystals*

OHNO, Kaoru [C class; 3000 (B), 600 (C)] (105)
— *Improvement and application of all-electron mixed basis program*

1. Clear evidence of element partitioning effects in a Ti-6Al-4V alloy by the first-principles phase field method
   T N Pham, K Ohno, R Sahara, R Kuwahara, and S Bhattacharyya, J. Phys.: Cond. Mat. **32**, 264001 (2020).
   DOI:10.1088/1361-648X/ab7ad5

2. Study on Ni-Ti alloys around equiatomic composition by the first-principles phase field method
   Kaoru Ohno, Monami Tsuchiya, Riichi Kuwahara, Ryoji Sahara, Swastibrata Bhattacharyya, and Thi Nu Pham, Comp. Mat. Sci. **191**, 110284 (2021).

DOI:10.1016/j.commatsci.2021.110284

OHSAWA, Kazuhito [C class; 1200 (B), 300 (C)] (137)
— *Study of interaction between radiation damage and interstitial atom*

OHTO, Tatsuhiko [C class; 2600 (B), 0 (C)] (127)
— *First-principles molecular dynamics study of water/*TiO_2 *interfaces using hybrid functionals*

1. Acceleration of Electrochemical CO2 Reduction to Formate at the Sn/Reduced Graphene Oxide Interface
   Takuya Tsujiguchi, Yusuke Kawabe, Samuel Jeong, Tatsuhiko Ohto, Suresh Kukunuri, Hirotaka Kuramochi, Yasufumi Takahashi, Tomohiko Nishiuchi, Hideki Masuda, Mitsuru Wakisaka, Kai-long Hu, Ganesan Elumalai, Jun-ichi Fujita, and Yoshikazu Ito ACS Catal. 11, 3310 (2021).

2. Single-Molecule Conductance of a π-Hybridized Tripodal Anchor while Maintaining Electronic Communication
   Tatsuhiko Ohto, Aya Tashiro, Takuji Seo, Nana Kawaguchi, Yuichi Numai, Junpei Tokumoto, Soichiro Yamaguchi, Ryo Yamada, Hirokazu Tada, Yoshio Aso, and Yutaka Ie Small 17, 2006709 (2021).

3. Improving Intramolecular Hopping Charge Transport via Periodical Segmentation of π-Conjugation in a Molecule
   Yutaka Ie, Yuji Okamoto, Takuya Inoue, Takuji Seo, Tatsuhiko Ohto, Ryo Yamada, Hirokazu Tada, and Yoshio Aso J. Am. Chem. Soc. 143, 599 (2021).

4. Catalytic Activity of Graphene-Covered Non-Noble Metals Governed by Proton Penetration in Electrochemical Hydrogen Evolution Reaction
   Kailong Hu, Tatsuhiko Ohto, Yuki Nagata, Mitsuru Wakisaka, Yoshitaka Aoki, Jun-ichi Fujita, and Yoshikazu Ito Nat. Commun. 12, 203 (2021).

5. Correlation between the Dipole Moment of Nonfullerene Acceptors and the Active Layer Morphology of Green-Solvent Processed P3HT-based Organic Solar Cells
   Shreyam Chatterjee, Tatsuhiko Ohto, Hirokazu Tada, Seihou Jinnai, and Yutaka Ie ACS Sustain. Chem. Eng. 8, 19013 (2020)

6. Vibrational Couplings and Energy Transfer Pathways of Water's Bending Mode
   Chun-Chieh Yu, Kuo-Yang Chiang, Masanari Okuno, Takakazu Seki, Tatsuhiko Ohto, Xiaoqing Yu, Vitaly Korepanov, Hiro-o Hamaguchi, Mischa Bonn, Johannes Hunger, and Yuki Nagata Nat. Commun. 11, 5977 (2020)

7. Vibrational Mode Frequency Correction of Liquid Water in Density Functional Theory Molecular Dynamics Simulations with van der Waals Correction
   Kai Zhong, Chun-Chieh Yu, Mayank Dodia, Mischa Bonn, Yuki Nagata, and Tatsuhiko Ohto Phys. Chem. Chem. Phys. 22, 12785 (2020).

8. Decoding the molecular water structure at complex interfaces through surface-specific spectroscopy of the water bending mode
   Takakazu Seki, Chun-Chieh Yu, Xiaoqing Yu, Tatsuhiko Ohto, Shumei Sun, Konrad Meister, Ellen H. G. Backus, Mischa Bonn, and Yuki Nagata, Phys. Chem. Chem. Phys. 22, 10934 (2020).

9. Hydrogen-Bonds and Molecular Orientations of Supramolecular Structure between Barbituric Acid and Melamine Derivative at the Air/Water Interface Revealed by Heterodyne-Detected Vibrational Sum Frequency Generation Spectroscopy
   Masanari Okuno, Shuhei Yamada, Tatsuhiko Ohto, Hirokazu Tada, Waka Nakanishi, Katsuhiko Ariga, and Taka-aki Ishibashi J. Phys. Chem. Lett. 11, 2422 (2020).

10. Mechanical switching of current-voltage characteristics in spiropyran single-molecule junctions
    Takashi Tamaki, Keigo Minode, Yuichi Numai, Tatsuhiko Ohto, Ryo Yamada, Hiroshi Masai, Hirokazu Tada, and Jun Terao Nanoscale, 12, 7527 (2020).

11. Molecular Structure and Modeling of Water-Air and Ice-Air Interfaces Monitored by Sum-Frequency Generation
    Fujie Tang, Tatsuhiko Ohto, Shumei Sun, Jeremy Rouxel, Sho Imoto, Ellen H. G. Backus, Shaul Mukamel, Mischa Bonn, and Yuki Nagata Chem. Rev. 120, 3633 (2020).

12. Effect of Graphene Encapsulation of NiMo Alloys on Oxygen Evolution Reaction
    Samuel Jeong, Kailong Hu, Tatsuhiko Ohto, Yuki Nagata, Hideki Masuda, Jun-ichi Fujita, and Yoshikazu Ito ACS Catal. 10, 792 (2020).

13. Impact of intermolecular vibrational coupling effects on the sum-frequency generation spectra of the water/air interface
    Naveen Kumar Kaliannan, Andres Henao Aristizabal, Hendrik Wiebeler, Frederik Zysk, Tatsuhiko Ohto, Yuki Nagata, and Thomas D. Kuhne Mol. Phys. 118, 1620358 (2020).

OHTSUKI, Tomi [C class; 7800 (B), 700 (C)] (27)
— *Quantum phase transitions in novel disordered systems*
— *Quantum phase transitions in novel disordered topological systems*

1. Transfer matrix study of the Anderson transition in non-Hermitian systems
   Xunlong Luo, Tomi Ohtsuki, Ryuichi Shindou arXiv:2103.05239

2. Universality Classes of the Anderson Transitions Driven by Non-Hermitian Disorder
   Xunlong Luo, Tomi Ohtsuki, Ryuichi Shindou Phys. Rev. Lett. 126, 090402 (2021)
   DOI:10.1103/PhysRevLett.126.090402

3. Machine learning the dynamics of quantum kicked rotor
   Tomohiro Mano, Tomi Ohtsuki arXiv:2101.09432

4. Ballistic transport in disordered Dirac and Weyl semimetals
   Koji Kobayashi, Miku Wada, Tomi Ohtsuki Phys. Rev. Research 2, 022061(R)(2020)
   DOI:10.1103/PhysRevResearch.2.022061

OKAMOTO, Yuko [C class; 5800 (B), 0 (C)] (246)
— *Study on complex systems by generalized-ensemble algorithms*

1. Calculation of the residual entropy of Ice Ih by Monte Carlo simulation with the combination of the replica-exchange Wang–Landau algorithm and multicanonical replica-exchange method
   T. Hayashi, C. Muguruma, and Y. Okamoto, J. Chem. Phys. **154** (2021) 044503.

OKAZAKI, Susumu [C class; 1200 (B), 350 (C)] (273)
— *Investigation of the molecular origins of the mechanical and thermal properties of realistic biopolymers using all-atomistic molecular dynamics*

1. A comparison of the brittle PMMA with the ductile PC on the elasticity and yielding from a molecular dynamics perspective
   Zhiye Tang, Kazushi Fujimoto, Susumu Okazaki, Polymer **226**, 123809 (2021).

OKITSU, Kouhei [C class; 200 (B), 0 (C)] (323)
— *Study on bankruptcy of the two-beam approximation in X-ray crystal structure analysis*

OKUBO, Tsuyoshi [C class; 7400 (B), 1250 (C)] (228)
— *Finite temperature properties of frustrated spin systems*

1. Anisotropic Tensor Renormalization Group
   D. Adachi, T. Okubo and S. Todo Phys. Rev. B, **102** (2020) 054432.
   DOI:10.1103/PhysRevB.102.054432

2. Phase Shift in Skyrmion Crystals
   S. Hayami, T. Okubo, and Y. Motome, arXiv:2005.03168

OKUMURA, Hisashi [C class; 4800 (B), 1150 (C)] (245)
— *Disruption of amyloid fibril by nonequilibrium molecular dynamics simulations*
— *Molecular dynamics simulations for assembly and disassembly of protein aggregates*

1. Energetics and kinetics of substrate analog-coupled staphylococcal nuclease folding revealed by a statistical mechanical approach
   T. Mizukami, S. Furuzawa, S. G. Itoh, S. Segawa, T. Ikura, K. Ihara, H. Okumura, H. Roder, and K. Maki Proc. Natl. Acad. Sci. USA **117** (2020) 19953-19962.

2. Replica-permutation molecular dynamics simulations of an amyloid-β(16-22) peptide and polyphenols
   L. Le Nguyen Ngoc, S. G. Itoh, P. Sompornpisut, and H. Okumura : Chem. Phys. Lett. **758** (2020) 137913/1-7.

3. Involvement of pore helix in voltage-dependent inactivation of TRPM5 channel
   K. Uchida, T. Kita, M. Hatta, S. G. Itoh, H. Okumura, M. Tominaga, J. Yamazaki : Heliyon **7** (2021) e06102/1-10.

4. Structural basis for promiscuous action of monoterpenes on TRP channels
   T. H. D. Nguyen, S. G. Itoh, H. Okumura, M. Tominaga Commun. Biol. **4** (2021) 293/1-12.

5. Dimerization of α-synuclein fragments studied by isothermal-isobaric replica-permutation molecular dynamics simulation
   M. Yamauchi and H. Okumura J. Chem. Inf. Model. **61** (2021) 1307-1321.

6. Structural dynamics and susceptibility of anti-HIV drugs against HBV reverse transcriptase
   J. Kammarabutr, P. Mahalapbutr, H. Okumura, P. Wolschann, and T. Rungrotmongkol J. Biomol. Struct. Dyn. **39** (2021) 2502-2511.

7. Role of water molecules in the laser-induced disruption of amyloid fibrils observed by nonequilibrium molecular dynamics simulations
   H. Okumura, S. G. Itoh, K. Nakamura and T. Kawasaki, J. Phys. Chem. B, submitted.

ONO, Shota [B,C class; 1000 (B), 250 (C)] (145, 146)
— *A new method for exploring dynamically stable alloys from the periodic table of 2D materials*
— *Unified understanding of the femtosecond infrared luminescence for metals*
— *Unified understanding of the femtosecond infrared luminescence for metals: II*

1. Ultrafast photoluminescence in metals: Theory and its application to silver
   S. Ono and T. Suemoto, Phys. Rev. B **102**, 024308 (2020).
   DOI:10.1103/PhysRevB.102.024308

2. Two-dimensional square lattice polonium stabilized by the spin-orbit coupling
   S. Ono, Sci. Rep. **10**, 11810 (2020).
   DOI:10.1038/s41598-020-68877-4

3. Dynamical stability of two-dimensional metals in the periodic table
   S. Ono, Phys. Rev. B **102**, 165424 (2020).
   DOI:10.1103/PhysRevB.102.165424

4. High-throughput computational search for two-dimensional binary compounds: Energetic stability versus synthesizability of three-dimensional counterparts
   S. Ono and H. Satomi, Phys. Rev. B **103**, L121403 (2021).
   DOI:10.1103/PhysRevB.103.L121403

5. Lattice stability of ordered Au-Cu alloys in the warm dense matter regime
   S. Ono and D. Kobayashi, Phys. Rev. B **103**, 094114 (2021).
   DOI:10.1103/PhysRevB.103.094114

ONO, Tomoya [C class; 9400 (B), 1450 (C)] (54)
— *Development of first-principles electronic-structure and transport calculation code RSPACE and simulations for device*

1. Calculation of the Green's function in scattering region for first-principles electron-transport simulations
   Y. Egami, S. Tsukamoto, and T. Ono, Phys. Rev. Research **3** (2021) 013038.

2. Ising ferromagnetism and robust half-metallicity in two-dimensional honeycomb-kagome Cr_2O_3 layer
   A. Hashmi, K. Nakanishi, M. U. Farooq, and T. Ono, npj 2D Materials and Applications **4** (2020) 39.

ORIMOTO, Yuuichi [C class; 400 (B), 100 (C)] (177)
— *Elucidation of the mechanism of self-ordering phenomena at the interface between organic and inorganic materials*

1. Microscopic Hopping Mechanism of an Isolated PTCDA Molecule on a Reactive Ge(001) Surface
   T. Shiota, W. Mizukami, H. Tochihara, K. Yagyu, T. Suzuki, and Y. Aoki, J. Phys. Chem. C. **124**, 24704 (2020).
   DOI:10.1021/acs.jpcc.0c05858

OSHIKAWA, Masaki [B class; 800 (B), 100 (C)] (285)
— *An exploration of the topological phase transition driven by Z_2 vortex with Tensor Network Renormalization*
— *An exploration of the topological phase transition driven by Z_2 vortices with Tensor Network Renormalization*

OSHIYAMA, Atsushi [E class; 17500 (B), 2950 (C)] (49)
— *Mechanisms of Semiconductor Interface Formation and its Electronic Properties based on Quantum Theory*

1. Density-Functional Calculations for Structures and Energetics of Atomic Steps and their Implication for Surface Morphology on Si-face SiC Polar Surfaces
   K. Seino and A. Oshiyama, Phys. Rev. B **101** (2020) 195307
   DOI:10.1103/PhysRevB.101.195307

2. Absence of oxygen-vacancy-related deep levels in amorphous $(Al_2O_3)_{1-x}(SiO_2)_x$: First-principles exploration of gate oxides in GaN-based devices
   K. Chokawa, T. Narita, D. Kikuta, T. Kachi, K. Shiozaki, A. Oshiyama and K. Shiraishi, Phys. Rev. Applied **14** (2020) 014034

DOI:10.1103/PhysRevApplied.14.014034

3. Screw dislocation that converts p-type GaN to n-type: Microscopic study on Mg condensation and leakagae current in p-n diodes
T. Nakano, Y. Harashima, K. Chokawa, K. Shiraishi, A. Oshiyama, Y. Kangawa, S. Usami, N. Mayama, K. Toda, A. Tanaka, Y. Honda, and H. Amano, Appl. Phys. Lett. **117** (2020) 012105
DOI:10.1063/5.0010664

4. Gallium-gallium weak bond that incorporates nitrogen at atomic steps during GaN epitaxial growth
K. M. Bui, K. Shiraishi and A. Oshiyama, Appl. Surf. Sci. **557** (2021) 149542
DOI:10.1016/j.apsusc.2021.149542

OZEKI, Yukiyasu [C class; 4400 (B), 0 (C)] (260)
— *Dynamical scaling analysis for phase transitions and critical phenomena in frustrated systems*
— *Dynamical scaling analysis for phase transitions and critical phenomena in frustrated systems II*

1. Dynamical scaling analysis of symmetry breaking for the antiferromagnetic triangular Heisenberg model in a uniform field
K. Murayama and Y. Ozeki Phys. Rev B **101** (2020) 184427.

RAEBIGER, Hannes [C class; 3600 (B), 0 (C)] (103)
— *First principles calculation of fluorocarbon layer in dry etching process*
— *First principles theory of exciton self-trapping in low-dimensional perovskites*

1. MXene phase with C_3 structure unit: a family of 2D electrides
S. Bae, W. Espinosa-García, Y.-G. Kang, N. Egawa, J. Lee, K. Kuwahata, M. Khazaei, K. Ohno, Y.-H. Kim, M. J. Han, H. Hosono, G. M. Dalpian, and H. Raebiger, Adv. Funct. Mater. in press (2021).
DOI:10.1002/adfm.202100009

2. Electronic and magnetic properties of carbide MXenes—the role of electron correlations
S. Bae, Y.-G. Kang, M. Khazaei, K. Ohno, Y.-H. Kim, M. J. Han, K.J. Chan, and H. Raebiger, Mater. Today Adv. **9** 100118 (2021).
DOI:10.1016/j.mtadv.2020.100118

3. Electronic mechanism for resistive Switching in metal/insulator/metal nanodevices
H. Raebiger, A. C. M. Padilha, A. R. Rocha, and G. M. Dalpian Journal of Physics D: Applied Physics **53** 295302 (2020).
DOI:10.1088/1361-6463/ab7a58

SAITO, Mineo [C class; 4200 (B), 800 (C)] (88)
— *Band structure calculation based on the group theory*

1. Electronic structure of puckered group IV?VI two-dimensional monolayer materials
A. Zaharo, A. Purqon, T. Winata, and M. Saito, Jpn. J. Appl. Phys. **59**, 071006 (2020) .
DOI:10.35848/1347-4065/ab984c

2. Spin-polarized cation monovacancies in wurtzite structure semiconductors: first-principles study
M. Y. H. Widianto, H. P. Kadarisman, A. M. Yatmeidhy, and M. Saito, Jpn. J. Appl. Phys. **59**, 071001 (2020) .
DOI:10.35848/1347-4065/ab9654

SAKAGUCHI, Norihito [C class; 5200 (B), 0 (C)] (84)
— *Reduction of Rare Metals in Fuel Cell Catalysts and Hydrogen Permeable Membrane*

1. グラフェン担持 Pt サブナノクラスタの酸素還元反応活性
   長谷川瞬，國貞雄治，坂口紀史表面と真空 **63** (2020) 413.
   a DOI:10.1380/vss.63.413

2. Single Pt Atoms on N-Doped Graphene: Atomic Structure and Local Electronic States
   R. Sugimoto, Y. Segawa, A. Suzuta, Y. Kunisada, T. Uchida, K. Yamazaki, K. Gohara J. Phys. Chem. C **125** (2021) 2900.
   DOI:10.1021/acs.jpcc.0c08811

SAKAI, Masatoshi [B class; 300 (B), 50 (C)] (217)
— *Field-induced metal-insulator transition in organic charge order phase*

SAKAI, Toru [C class; 4200 (B), 750 (C)] (248, 249)
— *Numerical Diagonalization Study on the Field-Induced Spin Nematic Liquid*
— *Symmetry Protected Topological Phase of the S=2 antiferromagnetic chain*

1. Spin Nematic Liquids of the S = 1 Spin Ladder in Magnetic Field
   T. Sakai and K. Okamoto, JPS Conf. Proc. **30** (2020) 011083/1-6

2. Ground-State Phase Diagram of an Anisotropic S = 1 Ferromagnetic-Antiferromagnetic Bond-Alternating Chain
   K. Okamoto, T. Tonegawa, M. Kaburagi and T. Sakai, JPS Conf. Proc. **30** (2020) 011024/1-6

3. Quantum Phase Transition of the Twisted Spin Tube
   Y. Tachibana, Y. Ueno, T. Zenda, K. Okamoto and T. Sakai, JPS Conf. Proc. **30** (2020) 011082/1-5

4. Quantum Phase Transitions of the Distorted Diamond Spin Chain
   T. Zenda, Y. Tachibana, Y. Ueno, K. Okamoto and T. Sakai, JPS Conf. Proc. **30** (2020) 011084/1-5

5. Magnetization Plateau of the Distorted Diamond Spin Chain
   Y. Ueno, T. Zenda, Y. Tachibana, K. Okamoto and T. Sakai, JPS Conf. Proc. **30** (2020) 011085/1-5

6. Features of Chirality Generated by Paramagnetic Coupling to Magnetic Fields in the 3K-Phase of Sr_2RuO_4
   H. Kaneyasu, Y. Enokida, T. Nomura, Y. Hasegawa, T. Sakai and M. Sigrist, JPS Conf. Proc. **30** (2020) 011039/1-6

7. EPR Theories for Selection Rules to Observe the Spin Gap
   T. Sakai, Applied Magnetic Resonance **52**, 507 (2021).
   DOI:10.1007/s00723-020-01298-8

8. Quantum spin nematic liquid in the S=1 antiferromagnetic chain with the biquadratic interaction
   T. Sakai, AIP Advances **11** (2021) 015306/1-4.

SAKAKIBARA, Hirofumi [B class; 800 (B), 150 (C)] (156)
— *First-principles derivation of a many-body effective model based on PMT basis*
— *First-principles derivation of a many-body effective model based on a new basis PMT*

1. Finite electric-field approach to evaluate the vertex correction for the screened Coulomb interaction in the quasiparticle self-consistent *GW* method

H. Sakakibara, T. Kotani, M. Obata, and T. Oda, Phys. Phys. B **101** 205120 (2020).

2. Model Construction and a Possibility of Cupratelike Pairing in a New d^9 Nickelate Superconductor (Nd,Sr)NiO_2
   H. Sakakibara, H. Usui, K. Suzuki, T. Kotani, H. Aoki, and K. Kuroki, Phys. Phys. Lett. **125** 077003 (2020).

SAKASHITA, Tatsuya [B class; 100 (B), 150 (C)] (322)
— *Development of integrated interface of eigensolvers Rokko and application to quantum spin systems*

SAKURAI, Masahiro [B class; 400 (B), 50 (C)] ()
— *First-principles KKR calculations for evaluating magnetic properties*

SASAKI, Takehiko [C class; 2800 (B), 600 (C)] (107)
— *Reaction processes of polyalcohols in high temperature water by First Principles Calculations*
— *Study on cyclodehydration of sorbitol in hot water by First Principles calculations*

1. Refined metadynamics through canonical sampling using time-invariant bias potential: A study of polyalcohol dehydration in hot acidic solutions
   T. Kondo, T. Sasaki, S. Ruiz-Barragan, J. Ribas-Arino, M. Shiga, J. Comput. Chem. **42**, 156 (2020).
   DOI:10.1002/jcc.26443

SATO, Taku [B class; 400 (B), 50 (C)] ()
— *Magnetic excitations in the quantum pyrochlore magnet*

SATO, Tetsuya [C class; 5600 (B), 850 (C)] (73)
— *Study of ferromagnetism in Pt(100) thin films by first-principles calculation*

1. Appearance of ferromagnetism in Pt(100) ultrathin films originated from quantum-well states with small orbital magnetic moment
   T.Yamada, K. Ochiai, H. Kinoshita, S. Sakuragi, M. suzuki, H. Ozawa, H. Kageshima, T. Sato, submitted to Phys. Rev. B

SHAO, Cheng [C class; 5200 (B), 900 (C)] ()
— *Coupled electron-phonon transport at metal-insulator interface*
— *Phonon engineering in PbS quantum dot ligand system*

SHIMADA, Toshihiro [B class; 800 (B), 150 (C)] (155)
— *Analysis of reaction and prediction of properties of atomic layer materials*
— *Carbonization reaction and electronic structures of molecular crystals under high temperature high pressure conditions*

1. DFT Calculation of Square MoS2 Nanotubes
   Meiqi Zhang, Mengting Weng, Takahiro Tamura, Manami Goto, Ichiro Yamane, Takashi Yanase, Taro Nagahama, Toshihiro Shimada , Physica E 130, 114693 (2021)
   DOI:10.1016/j.physe.2021.114693

2. Porous Graphitic Carbon Nitride Nanoplates Obtained by A Combined Exfoliation Strategy for Enhanced Visible Light Photocatalytic Activity
   Wei Liu, Nobuhiro Iwasa, Shinichiro Fujita, Hitoshi Koizumi, Makoto Yamaguchi and Toshihiro Shimada , Applied Surface Science 499,143901 (2020).
   DOI:10.1016/j.apsusc.2019.143901

SHIMAMURA, Kohei [C class; 2600 (B), 800 (C)] (106)
— *Study of Efficient Training Data Generation Method for Constructing Artificial Neural Network Force Field*
— *Study of Efficient Training Data Generation Method for Constructing Artificial Neural Network Force Field II*

1. Computational and Training Requirements for Interatomic Potential Based on Artificial Neural Network for Estimating Low Thermal Conductivity of Silver Chalcogenides
   K. Shimamura, Y. Takeshita, S. Fukushima, A. Koura, and F. Shimojo, J. Chem. Phys. **153** (2020) 234301.

SHIMOJO, Fuyuki [C class; 7600 (B), 1150 (C)] (60)
— *First-Principles Molecular-Dynamics Study of Structural and Electronic Properties of Covalent Liquids and Glasses under Pressure*

1. Intermediate range structure of amorphous Cu_2GeTe_3: *ab initio* molecular dynamics study
   A. Koura and F. Shimojo, J. Phys.: Condens. Matter **32**, 244001 (2020)
   DOI:10.1088/1361-648X/ab7b1b

2. Structures of liquid iron-light-element mixtures under high pressure
   S. Ohmura, T. Tsuchiya, and F. Shimojo, Phys. Stat. Solidi B **257**, 2000098 (2020)
   DOI:10.1002/pssb.202000098

3. Application of First-Principles-Based Artificial Neural Network Potentials to Multiscale-Shock Dynamics Simulations on Solid Materials
   M. Misawa, S. Fukushima, A. Koura, F. Shimojo, K. Shimamura, S. Tiwari, K. Nomura, R. K. Kalia, A. Nakano, and P. Vashishta, J. Phys. Chem. Lett. **11**, 4536 (2020)
   DOI:10.1021/acs.jpclett.0c00637

4. Molecular-Dynamics Study of Thermal Conductivity of Silver Chalcogenides
   S. Fukushima, K. Shimamura, A. Koura, and F. Shimojo, Phys. Stat. Solidi B **257**, 2000183 (2020)
   DOI:10.1002/pssb.202000183

5. First-Principles Study of Pressure-Induced Amorphization of Fe_2SiO_4 Fayalite
   M. Misawa and F. Shimojo, Phys. Stat. Solidi B **257**, 2000173 (2020)
   DOI:10.1002/pssb.202000173

6. Computational and training requirements for interatomic potential based on artificial neural network for estimating low thermal conductivity of silver chalcogenides
   K. Shimamura, Y. Takeshita, S. Fukushima, A. Koura, and F. Shimojo, J. Chem. Phys. **153**, 234301 (2020)
   DOI:10.1063/5.0027058

SHIMOKAWA, Tokuro [C class; 2800 (B), 500 (C)] (265)
— *Thermal effects on quantum frustrated magnetisms*

1. Signatures of finite-temperature mirror symmetry breaking in the S=1/2 Shastry-Sutherland model
   T. Shimokawa, Phys. Rev. B **103**, 134419 (2020).
   DOI:10.1103/PhysRevB.103.134419

SHINAOKA, Hiroshi [B,C class; 2300 (B), 350 (C)] (205, 206)
— *Classical Monte Carlo study of J1-J2 Heisenberg antiferromagnet on the kagome lattice*
— *Development and application of DFT+DMFT software DCore*

1. Sparse modeling of large-scale quantum impurity models with low symmetries
   H. Shinaoka and Y. Nagai, Phys. Rev. B **103**, 045120
   DOI:10.1103/PhysRevB.103.045120

2. DCore: Integrated DMFT software for correlated electrons
   H. Shinaoka, J. Otsuki, M. Kawamura, N. Takemori, K. Yoshimi, submitted to SciPost Phys.

SHINODA, Wataru [E class; 21000 (B), 2250 (C)] (223)
— *Molecular Simulation of Soft Materials using All-Atom and Coarse-Grained Force Field*

1. pSPICA: A coarse-grained force field for lipid membranes based on a polar water model
   Y. Miyazaki, S. Okazaki, W. Shinoda, J. Chem. Theory Comput. 16, 782-793 (2020)
   DOI:10.1021/acs.jctc.9b00946

2. Monodisperse Polymer Melts Crystallize via Structurally Polydisperse Nanoscale Clusters: Insights from Polyethylene
   K. W. Hall, T. W. Sirk, S. Percec, M. L. Klein, W. Shinoda Polymers, 12, 447 (2020)
   DOI:10.3390/polym12020447

3. Effects of anion on liquid structures of ionic liquids at graphene electrode interface analyzed by molecular dynamics simulations
   S. Tsuzuki, T. Nakamura, T. Morishita, W. Shinoda, S. Seki, Y. Umebayashi, K. Ueno, K. Dokko, M. Watanabe Batteries & Supercaps, 3, 658-667 (2020)
   DOI:10.1002/batt.201900197

4. Molecular Simulation of the Shape Deformation of a Polymersome
   K. Chakraborty, W. Shinoda, S. M. Loverde Soft Matter, 16, 3234-3244 (2020)
   DOI:10.1039/C9SM02165E

5. Free energy profile of permeation of Entecavir through Hepatitis B virus capsid studied by molecular dynamics calculation
   K. Fujimoto, M. Fukai, R. Urano, W. Shinoda, T. Ishikawa, K. Omagari, Y. Tanaka, A. Nakagawa, S. Okazaki, Pure Appl. Chem. 92, 1585-1594 (2020)
   DOI:10.1515/pac-2020-0109

6. Property Decoupling across the Embryonic Nucleus-Melt Interface during Polymer Crystal Nucleation
   K. W. Hall, S. Percec, W. Shinoda, M. L. Klein J. Phys. Chem. B, 124, 4793-4804 (2020)
   DOI:10.1021/acs.jpcb.0c01972

7. Effect of Packing Density on the Surface Hydrophobicity of ω-Functionalized (–CF3, –CH3, –OCH3, and –OH) Self-assembled Monolayers: A Molecular Dynamics Study
   H. Yadav, A. Kuo, S. Urata, W. Shinoda, J. Phys. Chem. C, 124, 14237-14244 (2020)
   DOI:10.1021/acs.jpcc.0c03485

8. 脂質膜系の粗視化力場 SPICA の開発とその展望
   W. Shinoda 生物物理, 60, 157-161 (2020)
   DOI:10.2142/biophys.60.157

9. Exact Long-Range Coulombic Energy Calculation for Net Charged Systems Neutralized by Uniformly Distributed Background Charge Using Fast Multipole Method and Its Application to Efficient Free Energy Calculation
   R. Urano, W. Shinoda, N. Yoshii, S. Okazaki, J. Chem. Phys. 152, 244115 (2020)
   DOI:10.1063/5.0007957

10. Pivotal Role of Interdigitation in Interleaflet Interactions: Implications from Molecular Dynamics Simulations
    S. Seo, M. Murata, W. Shinoda, J. Phys. Chem. Lett. 11, 5171-5176 (2020)
    DOI:10.1021/acs.jpclett.0c01317

11. Conformation and orientation of branched acyl chains responsible for the physical stability of diphytanoylphosphatidylcholine
    H. Tsuchikawa, T. Ono, M. Yamagami, Y. Umegawa, W. Shinoda, M. Murata, Biochemistry, 59, 3929-3938 (2020)
    DOI:10.1021/acs.biochem.0c00589

12. Position-Dependent Diffusion Constant of Molecules in Heterogeneous Systems as Evaluated by the Local Mean Squared Displacement
    T. Nagai, S. Tsurumaki, R. Urano, K. Fujimoto, W. Shinoda, S. Okazaki, J. Chem. Theory Comput. 16, 7239-7254 (2020)
    DOI:10.1021/acs.jctc.0c00448

13. Thermodynamic aspect of sulfur, polysulfide anion and lithium polysulfide: plausible reaction path during discharge of lithium–sulfur battery
    S. Tsuzuki, T. Kaneko, K. Sodeyama, Y. Umebayashi, W. Shinoda, S. Seki, K. Ueno, K. Dokko, M. Watanabe, Phys. Chem. Chem. Phys. 23, 6832-6840 (2021)
    DOI:10.1039/D0CP04898D

14. Chain-End Modification: A Starting Point for Controlling Polymer Crystal Nucleation
    K. W. Hall, S. Percec, W. Shinoda, M. L. Klein Macromolecules, 54, 1599-1610 (2021)
    DOI:10.1021/acs.macromol.0c02398

15. Seipin accumulates and traps diacylglycerols and triglycerides in its ring-like structure
    V. Zoni, R. Khaddaj, I. Lukmantara, W. Shinoda, H. Yang, R. Schneiter, S. Vanni Proc. Natl. Acad. Sci. U.S.A. 118, e2017205118 (2021)
    DOI:10.1073/pnas.2017205118

16. Hemimicelle formation of semi-fluorocarbon chains at air–water interface: coarse-grained molecular dynamics study with an extension of the SPICA force field
    H. O. S. Yadav, S. Harada, A. Kuo, S. Urata, W. Shinoda, Mol. Phys. e1910355 (2021)
    DOI:10.1080/00268976.2021.1910355

SHINOHARA, Yasushi [C class; 3000 (B), 0 (C)] (113)
— *First-principles calculations for light absorption of crystalline solids*
— *First-principles calculations for nonlinear light absorption of insulators*

1. Detecting electron-phonon coupling during photoinduced phase transition
   Takeshi Suzuki, Yasushi Shinohara, Yangfan Lu, Mari Watanabe, Jiadi Xu, Kenichi L. Ishikawa, Hide Takagi, Minoru Nohara, Naoyuki Katayama, Hiroshi Sawa, Masami Fujisawa, Teruto Kanai, Jiro Itatani, Takashi Mizokawa, Shik Shin, and Kozo Okazaki, Phys. Rev. B **103**, L121105 (2021).
   DOI:10.1103/PhysRevB.103.L121105

SHIOMI, Junichiro [C class; 7200 (B), 1100 (C)] (232)
— *Development of Thermal Functional Materials Using Materials Informatics*

1. Phonon transport in multiphase nanostructured silicon fabricated by high-pressure torsion
   C. Shao, K. Matsuda, S. Ju, Y. Ikoma, M. Kohno, and J. Shiomi, J. Appl. Phys. **129**, 085101 (2021).
   DOI:10.1063/5.0037775

2. Scalable monolayer-functionalized nanointerface for thermal conductivity enhancement in copper/diamond composite
   B. Xu, S-W. Hung, S. Hu, C. Shao, R. Guo, J. Choi, T. Kodama, F-R. Chen, and J. Shiomi Carbon, **175**, 299-306 (2021).
   DOI:10.1016/j.carbon.2021.01.018

3. Ultimate impedance of coherent heat conduction in van der Waals graphene-MoS2 heterostructures
   S. Hu, S. Ju, J. Guo, B. Xu, M. Ohnishi, and J. Shiomi, Mater. Today Phys. **16**, 100324 (2021).
   DOI:10.1016/j.mtphys.2020.100324

4. Designing thermal functional materials by coupling thermal transport calculations and machine learning
   Shenghong Ju, Shuntaro Shimizu, Junichiro Shiomi Journal of Applied Physics, **128**, 161102 (2020).
   DOI:10.1063/5.0017042

5. Revisiting thermal conductivity and interface conductance at the nanoscale
   B. Davier, P Dollfus, S. Volz, J. Shiomi, J Saint-Martin , **175**, (2020).

6. Modulation of Interfacial Thermal Transport between Fumed Silica Nanoparticles by Surface Chemical Functionalization for Advanced Thermal Insulation
   Takashi Kodama, Nobuhiro Shinohara, Shih-Wei Hung, Masanao Obori, Donguk, Suh, Junichiro Shiomi ACS Appl. Mater. Interfaces, **13**, 15 (2021).
   DOI:10.1021/acsami.0c11066

7. Run Hu, Sotaro Iwamoto, Lei Feng, Shenghong Ju, Shiqian Hu, Masato Ohnishi, Naomi Nagai, Kazuhiko Hirakawa, Junichiro Shiomi
   Machine-learning-optimized aperiodic superlattice minimizes coherent phonon heat conduction Physical Review X, **10**, 2 (2020).
   DOI:10.1103/PhysRevX.10.021050

8. Machine learning analysis of tunnel magnetoresistance of magnetic tunnel junctions with disordered MgAl2O4
   Shenghong Ju, Yoshio Miura, Kaoru Yamamoto, Keisuke Masuda, Ken-ichi Uchida, Junichiro Shiomi Physical Review Research, **2**, 023187 (2020).
   DOI:10.1103/PhysRevResearch.2.023187

9. Two-Path Phonon-Interference Resonance Induces a Stop Band in Silicon Crystal Matrix by Embedded Nanoparticles Array
   Shiqian Hu, Lei Feng, Shao Cheng, Yuriy Kosevich, Junichiro Shiomi Physical Review B, **102**, 024301 (2020).
   DOI:10.1103/PhysRevB.102.024301

10. Design of highly-selective radiative-cooling structure accelerated by materials informatics
    Jiang Guo, Shenghong Ju, Junichiro Shiomi Optics Letters, **45**, 343 (2020).
    DOI:10.1364/OL.45.000343

SHIRAI, Tatsuhiko [B class; 700 (B), 0 (C)] (297, 298)

— *Quantum annealing with inhomogeneous fluctuations*

— *Universal properties of non-equilibrium steady states*

1. Resolving a Discrepancy between Liouvillian Gap and Relaxation Time in Boundary-Dissipated Quantum Many-Body Systems
   T. Mori and T. Shirai, Phys. Rev. Lett. **125** (2020) 230604.

DOI:10.1103/PhysRevLett.125.230604

2. Thermalization in open many-body systems based on eigenstate thermalization hypothesis
   T. Shirai and T. Mori, Phys. Rev. E **101** (2020) 042116.
   DOI:10.1103/PhysRevE.101.042116

3. Guiding Principle for Minor-Embedding in Simulated-Annealing-Based Ising Machines
   T. Shirai, S. Tanaka, and N. Togawa, IEEE Access **8** (2020), 210490
   DOI:10.1109/ACCESS.2020.3040017

4. Tensor-network approach to thermalization in open quantum many-body systems
   H. Nakano, T. Shirai, and T. Mori, Phys. Rev. E, in press.

5. Exact bounds for dynamical critical exponents of transverse-field Ising chains with a correlated disorder
   T. Shirai, and S. Tanaka, submitted to Annals of Physics

SHIRAISHI, Kenji [C class; 6600 (B), 1050 (C)] (66, 67)
— *First Principles Studies on Atomic and Electronic Structures of Impurity-screw dislocation complexes in Gan*
— *Theoretical Studies on Semiconductor MOVPE Growth Based on Multi-Physics Simulation*

1. Screw dislocation that converts p-type GaN to n-type: Microscopic study on Mg condensation and leakage current in p-n diodes
   T. Nakano, Y. Harashima, K. Chokawa, K. Shiraishi, A. Oshiyama, Y. Kangawa, S. Usami, N. Mayama, K. Toda, A. Tanaka, Y. Honda, and H. Amano, Appl. Phys. Lett. **117**, 012105 (2020).
   DOI:10.1063/5.0010664

2. Theoretical study on the effect of H_2 and NH_3 on trimethylgallium decomposition process in GaN MOVPE
   S. Sakakibara, K. Chokawa, M. Araidai, A. Kusaba, Y. Kangawa, and K. Shiraishi, Jpn. J. Appl. Phys. 60, 045507 (2021).

SHUDO, Ken-ichi [C class; 1000 (B), 400 (C)] (139, 140)
— *Optical gaps of metastable Ga2O3 and GaN with impurity doping effect*
— *Optical gaps of metastable Ga2O3 structures modulated by impurity dope*

1. Modulation of the optical absorption edge of ϵ- and κ-Ga_2O_3 due to Co impurities caused by band structure changes: Work function measurements and first-principle calculations
   K. Yamanaka, H. Raebiger, K. Mukai and K. Shudo, J. Appl. Phys. **127**, 065701/1-9 (2020).
   DOI:10.1063/1.5134521

SUGINO, Osamu [E class; 21000 (B), 4150 (C)] (48)
— *Simulation of electrochemical interfaces*
— *Computational hydrogenomics*

1. Dopant arrangements in Y-doped $BaZrO_3$ under processing conditions and their impact on proton conduction: a large-scale first-principles thermodynamics study
   Shusuke Kasamatsu, Osamu Sugino, Takafumi Ogawa, and Akihide Kuwabara, J. Mater. Chem. A **8**, 12674-12686 (2020).
   DOI:10.1039/D0TA01741H

2. Quantum-Mechanical Hydration Plays Critical Role in the Stability of Firefly Oxyluciferin Isomers: State-of-the-art Calculations of the Excited States
   Y. Noguchi, M. Hiyama, M. Shiga, H. Akiyama, O. Sugino, J. Chem. Phys. (2020) 153, 201103

DOI:10.1063/5.0031356

3. Advances and challenges for experiment and theory for multi-electron multi-proton transfer at electrified solid-liquid interfaces
   K. Sakaushi, T. Komeda, S. Hammes-Schiffer, M. M. Melander and O. Sugino Phys. Chem. Chem. Phys. 22, 19401-19442 (2021).
   DOI:10.1039/d0cp02741c

4. Hydrogen at Electrochemical Interfaces
   O. Sugino J. Phys. Soc. Jpn. 89, 051013 (2020).
   DOI:10.7566/JPSJ.89.051013

5. Surface-state Coulomb repulsion accelerates a metal-insulator transition in topological semimetal nanofilms
   S. Ito, M. Arita, J. Haruyama, B. Feng, W. -C. Chen, H. Namatame, M. Taniguchi, C. -M. Cheng, G. Bian, S. -J. Tang, T. -C. Chiang, O. Sugino, F. Komori and I. Matsuda Science Advances 6, eaaz5015 (2020).
   DOI:10.1126/sciadv.aaz5015

6. Challenge of advanced low temperature fuel cells based on high degree of freedom of group 4 and 5 metal oxides
   A. Ishihara, S. Tominaka, S. Mitsushima, H. Imai, O. Sugino and K.-I. Ota Curr. Op. ElectroChem.
   DOI:10.1016/j.coelec.2020.03.005

7. Completing density functional theory by machine learning hidden messages from molecules
   R. Nagai, R. Akashi and O. Sugino npj Comput. Mater. 6, 43 (2020).
   DOI:10.1038/s41524-020-0310-0

8. First-Principles Calculation of Copper Oxide Superconductors That Supports the Kamimura-Suwa Model
   H. Kamimura, M. Araidai, K. Ishida, S. Matsuno, H. Sakata, K. Shiraishi, O. Sugino and J.-S. Tsai Condensed Matter 5, 69 (2020).
   DOI:10.3390/condmat5040069

SUWA, Hidemaro [C class; 7800 (B), 550 (C)] (231)
— *Giant magnetic response of hidden SU(2) symmetric antiferromagnets induced by impurity disorder*
— *Impurity effect on giant magnetic response of a two-dimensional antiferromagnet*

SUZUKI, Takafumi [C class; 4200 (B), 650 (C)] (250)
— *Ground state phase diagram of extended Kitaev model II*
— *Ground-state phase diagram of extended Kitaev model on a honeycomb lattice*

1. Ground-state properties of the K–Γ model on a honeycomb lattice
   Takuto Yamada, Takafumi Suzuki and Seiichiro Suga, Phys. Rev. B **102**, 024415 (2020).
   DOI:10.1103/physrevb.102.024415

2. Frustration-induced supersolid phases of extended Bose-Hubbard model in the hard-core limit
   Wei-Lin Tu, Huan-Kuang Wu and Takafumi Suzuki J. Phys: Condens. Matter **32**, 455401 (2020).
   DOI:10.1088/1361-648x/aba383

SUZUKI, Yuji [C class; 3600 (B), 0 (C)] (101)
— *Development of High-performance Polymer Electret Using Quantum Chemical Analysis*
— *Development of High-performance Polymer Electret with the Aid of Machine Learning*

1. Solid-state Electron Affinity Analysis of Amorphous Fluorinated Polymer Electret
   Kim, S., Melnyk, A., Andrienko, D., and Suzuki, Y., J. Phys. Chem. B, 124, 46, 10507-10513 (2020)

2. Investigation of Amorphous Fluorinated Polymer for Bipolar Electret Based on Solid-state Quantum Chemical Analysis
   Mao, Z., Zhang, Y., Suzuki, K., and Suzuki, Y. 電気学会誘電・絶縁材料研究会, DEI-20-090 (2020).

TAKAHASHI, Osamu [C class; 200 (B), 250 (C)] (179)
— *Electronic state of organic compounds in aqueous solution*

1. Sub-molecular structural relaxation at physisorbed van der Waals interface with monolayer organic single crystal semiconductors
   A. Yamamura, H. Fujii, H. Ogasawara, D. Nordlund, O. Takahashi, Y. Kishi, H. Ishii, N. Kobayashi, N. Niitsu, B. Blülle, T. Okamoto, Y. Wakabayashi, S. Watanabe, J. Takeya Communications Physics, 3(1), 20/1-8 (2020)

2. Site-specificity reduction during Auger decay following Si:2p photoionization in Cl3SiSi(CH3)3 vapor: Interatomic-Coulombic-decay-like process
   S. Nagaoka, O. Takahashi, Y. Hikosaka Chem. Phys. 534, 110756/1-7 (2020)

3. Soft X-ray Absorption Spectroscopy Probes OH-π Interactions in Complex Polymer Systems
   H. Yamane, M. Oura, O. Takahashi, P. Fons, P. R. Varadwaj, Y. Shimoi, M. Ohkubo, T. Ishikawa, N. Yamazaki, K. Hasegawa, K. Takagi, T. Hatsui J. Phys. Chem. C 124, 9622-9627 (2020)

4. Dissociation and ionization dynamics of CF3I and CH3I molecules via pump and probe experiments with using soft X-ray free-electron laser
   T. Gejo, T. Nishie, T. Nagayasu, K. Tanaka, Y. Tanaka, A. Niozu, K. Nagaya, R. Yamamura, N. Futamata, T. Suenaga, O. Takahashi, T. Togashi, S. Owada, H. Fujise, A. Verna, M. Yabashi, M. Oura J. Phys. B, in press

5. Photoemission from the gas phase using soft x-ray fs pulses: An investigation of the space-charge effects
   A. Verna, G. Stefani, F. Offi, T. Gejo, Y. Tanaka, K. Tanaka, T. Nishie, K. Nagaya, A. Niozu, R. Yamamura, T. Suenaga, O. Takahashi, H. Fujise, T. Togashi, M. Yabashi, M. Oura New J Phys. 22, 123029/1-13 (2020)

6. Fragmentation pathways of methylbenzoate cations following core excitation: theoretical approach using graph theory
   N. Futamata, R. Yamamura; D. T. Ha, O. Takahashi Chem. Phys. Lett. 766, 138316/1-6 (2021)

TAMURA, Ryo [B class; 500 (B), 100 (C)] (301, 343)
— *Effective model estimation with error bars*

1. Data Integration for Accelerated Materials Design via Preference Learning
   X. Sun, Z. Hou, M. Sumita, S. Ishihara, R. Tamura, and K. Tsuda New Journal of Physics **22** (2020) 055001.

2. Experimental Establishment of Phase Diagrams Guided by Uncertainty Sampling: An Application to the Deposition of Zn–Sn–P Films by Molecular Beam Epitaxy
   R. Katsube, K. Terayama, R. Tamura, and Yoshitaro Nose ACS Materials Letters **2** (2020) 571.

3. Optimization of Heterogeneous Ternary Li3PO4-Li3BO3-Li2SO4 Mixture for Li-ion Conductivity by Machine Learning
   K. Homma, Y. Liu, M. Sumita, R. Tamura, N. Fushimi, J. Iwata, K. Tsuda, and C. Kaneta The

Journal of Physical Chemistry C **124** (2020) 12865.

4. Pushing property limits in materials discovery via boundless objective-free exploration
   K. Terayama, M. Sumita, R. Tamura, D. T. Payne, M. K. Chahal, S. Ishihara, and K. Tsuda Chemical Science **11** (2020) 5959.

5. Data-driven determination of a spin Hamiltonian of $KCu_4P_3O_{12}$ with uncertainty
   R. Tamura, K. Hukushima, A. Matsuo, K. Kindo, and M. Hase, Physical Review B **101** (2020) 224435.

6. Materials informatics approach to understand aluminum alloys
   R. Tamura, M. Watanabe, H. Mamiya, K. Washio, M. Yano, K. Danno, A. Kato, and T. Shoji Science and Technology of Advanced Materials **21** (2020) 540.

7. Dynamic Observation and Theoretical Analysis of Initial O2 Molecule Adsorption on Polar and m-Plane Surfaces of GaN
   M. Sumiya, M. Sumita, Y. Asai, R. Tamura, A. Uedono, and A. Yoshigoe The Journal of Physical Chemistry C **124** (2020) 25282.

8. Machine learning-driven optimization in powder manufacturing of Ni-Co based superalloy
   R. Tamura, T. Osada, K. Minagawa, T. Kohata, M. Hirosawa, K. Tsuda, and K. Kawagishi Materials & Design **198** (2021) 109290.

9. Mechanomics Biomarker for Cancer Cells Unidentifiable through Morphology and Elastic Modulus
   H. Wang, H. Zhang, B. Da, D. Lu, R. Tamura, K. Goto, I. Watanabe, D. Fujita, N. Hanagata, J. Kano, T. Nakagawa, and M. Noguchi Nano Letters **21** (2021) 1538.

10. Black-Box Optimization for Automated Discovery
    K. Terayama, M. Sumita, R. Tamura, and K. Tsuda Accounts of Chemical Research **54** (2021) 1334.

TANAKA, Shu [B class; 400 (B), 100 (C)] (310)
Building Algorithms for Ising Machines

1. Guiding Principle for Minor-Embedding in Simulated-Annealing-Based Ising Machines
   T. Shirai, S. Tanaka, and N. Togawa, IEEE Access **8** 210490 (2020).

2. How to Reduce the Bit-width of an Ising Model by Adding Auxiliary Spins
   D. Oku, M. Tawada, S. Tanaka, and N. Togawa to appear in IEEE Transactions on Computers.

3. Solving Constrained Slot Placement Problems Using an Ising Machine and Its Evaluations
   S. Kanamaru, K. Kawamura, S. Tanaka, Y. Tomita, and N. Togawa IEICE Transactions on Information and Systems **104** 226 (2021).

4. PyQUBO: Python Library for Mapping Combinatorial Optimization Problems to QUBO Form
   M. Zaman, K. Tanahashi, and S. Tanaka to appear in IEEE Transactions on Computers.

5. Exact bounds for dynamical critical exponents of transverse-field Ising chains with a correlated disorder
   T. Shirai and S. Tanaka, Annals of Physics, Accepted.

6. Mapping Induced Subgraph Isomorphism Problems to Ising Models and Its Evaluations by an Ising Machine
   N. Yoshimura, M. Tawada, S. Tanaka, J. Arai, S. Yagi, H. Uchiyama, and N. Togawa IEICE Transactions on Information and Systems **104** 481 (2021).

TANAMOTO, Tetsufumi [B class; 200 (B), 50 (C)] (321)
— *All to all connections in two dimensional qubit array with two-body interactions aiming at quantum annealing machine*

1. Robustness of cluster states and surface code states against random local fields
   T. Tanamoto, M. Ueda, arXiv:1910.05649

2. Generation of all-to-all connections in a two-dimensional qubit array with two-body interactions
   T. Tanamoto Journal of Applied Physics 129 (1), 014307 (2021)
   DOI:10.1063/5.0033173

TATENO, Michio [B class; 700 (B), 0 (C)] (293, 295)
— *Coarsening mechanism in mass-conserved reaction diffusion systems*
— *Multicellular simulation by phase field method*

1. Power-law coarsening in network-forming phase separation governed by mechanical relaxation
   M. Tateno and H. Tanaka, Nat. Commun. **12** (2021) 1.
   DOI:10.1038/s41467-020-20734-8

2. Interfacial-curvature-driven coarsening in mass-conserved reaction-diffusion systems
   M. Tateno and S. Ishihara, Phys. Rev. Res. under review.

TATETSU, Yasutomi [C class; 4600 (B), 850 (C)] (81)
— *First-principles study on grain boundaries in Ga-doped permanent magnets*
— *First-principles study on grain boundaries with multiple subphases in permanent magnets*

1. First-principles study on magnetism of a crystalline grain-boundary phase in Nd–Fe–B permanent magnets
   Y. Ainai, K. Sonju, Y. Tatetsu, and Y. Gohda, Jpn. J. Appl. Phys. **59** (2020) 060904.

TERAO, Takamichi [B class; 600 (B), 150 (C)] (290)
— *Molecular simulation of colloidal particles*

1. Wave propagation in double-negative acoustic metamaterial multilayers
   T. Terao, Proceedings of 14th international congress on artificial materials for novel wave phenomena (2020), in press.

2. Anomalous microion distribution of concentrated electrolytes in the underscreening regime: Monte Carlo simulations
   T. Terao, Mol. Phys. **119**, e1831634 (2021).

TERASAWA, Asako [C class; 1400 (B), 300 (C)] ()
— *first-principles calculation of exchange coupling constants and investigation of interface magnetism for various phases and their interfaces of permanent magnets*

TODO, Synge [C class; 5200 (B), 1500 (C)] (238, 345)
— *Topological Order and Quantum Dynamics in Quantum Many-body Systems*

1. Anisotropic tensor renormalization group
   D. Adachi, T. Okubo, and S. Todo Phys. Rev. B **102**, 054432 (7pp) (2020).
   DOI:10.1103/PhysRevB.102.054432

2. Sequential minimal optimization for quantum-classical hybrid algorithms
   K. M. Nakanishi, K. Fujii, and S. Todo Phys. Rev. Research **2**, 043158 (10pp) (2020)

DOI:10.1103/PhysRevResearch.2.043158

3. Multithreaded event-chain Monte Carlo with local times
   B. Li, S. Todo, A. C. Maggs, and W. Krauth Comp. Phys. Comm. **261**, 107702 (10pp) (2021)
   DOI:10.1016/j.cpc.2020.107702

4. Bond-weighted Tensor Renormalization Group
   D. Adachi, T. Okubo, and S. Todo arXiv:2103.00372

5. Neural Network Approach to Construction of Classical Integrable Systems
   F. Ishikawa, H. Suwa, and S. Todo arXiv:2011.01679

TOHYAMA, Takami [C class; 3800 (B), 550 (C)] (204)
— *Time-dependent DMRG study of spectral shape in the optical conductivity of Mott insulators*
— *Time-dependent DMRG study of spectral shape in the optical conductivity of two-dimensional Hubbard model*

1. Characterization of photoexcited states in the half-filled one-dimensional extended Hubbard model assisted by machine learning
   K. Shinjo, S. Sota, S. Yunoki, and T. Tohyama, Phys. Rev. B **101**, (2020) 195136.

2. Cluster-Based Haldane States in Spin-1/2 Cluster Chains
   T. Sugimoto, K. Morita, and T. Tohyama, Phys. Rev. Research **2**, (2020) 023420.

3. Spin dynamics in the t-t'-J model: Dynamical density-matrix renormalization group study
   T. Tohyama, S. Sota, and S. Yunoki, J. Phys. Soc. Jpn. **89**, (2020) 124709.

4. Effect of phase string on single-hole dynamics in the two-leg Hubbard ladder
   K. Shinjo, S. Sota, and T. Tohyama, Phys. Rev. B **103**, (2021) 035141.

TONEGAWA, Takashi [B class; 700 (B), 0 (C)] (291)
— *Numerical Study of the One-Dimensional Quantum Spin Systems with Spatial Structures*

TSUNEYUKI, Shinji [C class; 6600 (B), 1100 (C)] (64)
— *Development of data assimilation method for crystal structure prediction and its application to hydrogen-containing compounds*
— *Prediction of hydrogen function by advanced calculation of solids containing hydrogen*

1. Effect of spin fluctuations on superconductivity in V and Nb: A first-principles study
   K.Tsutsumi, Y. Hizume, M.Kawamura, R. Akashi, S. Tsuneyuki, Phys. Rev. B **102** (2020) 214515.
   DOI:10.1103/PhysRevB.102.214515

2. 実験とシミュレーションのデータ同化に基づく効率的結晶構造決定
   濱田幾太郎、常行真司 セラミックス **56** (2021) 100.

3. 水素の先端計算による水素機能の高精度解析
   常行真司 まてりあ **60** (2021) 176.
   DOI:10.2320/materia.60.176

4. 不完全な粉末回折実験データを用いたデータ同化結晶構造探索
   常行真司「マテリアルズ・インフォマティクス開発事例最前線」第 3 編第 1 章第 2 節 (エヌ・ティー・エス, 2021) 101-109.

TSURUTA, Kenji [C class; 1200 (B), 700 (C)] (134)
— *Hybrid Ab-Initio/Machine-Learning Optimization of Nano Interfaces and Molecular Structures*

1. Characterization of the $\Sigma5(210)$ / [001] Grain Boundary of Methyl-Ammonium Lead Triiodide Perovskite using Density Functional Theory
   M. A. A. Asad and K. Tsuruta Trans. Mater. Res. Soc. Jpn. **45**, 67 (2020).

2. A mechanistic investigation of moisture-induced degradation of methylammonium lead iodide
   M. Hada, M. A. A. Asad, M. Misawa, Y. Hasegawa, R. Nagaoka, H. Suzuki, R. Mishima, H. Ota, T. Nishikawa, Y. Yamashita, Y. Hayashi, and K. Tsuruta, App. Phys. Lett. **117**, 253304 (2020).

3. Optimization of Molecular Characteristics via Machine Learning Based on Continuous Representation of Molecules
   K. Sato and K. Tsuruta Mater. Sci. Forum **1016**, 1492 (2021).

UCHIDA, Takashi [B class; 200 (B), 100 (C)] (320)
— *Multiple helical spin density waves in inversion-symmetric itinerant magnets*
— *Multiple-Q states in two-dimensional itinerant magnets*

UMEMOTO, Koichiro [B,C class; 2300 (B), 450 (C)] (124, 126)
— *First principles study of effect of Al impurity on the post-post-perovskite transitions*
— *Order-disorder transition in ultrahigh-pressure phase of the Na-Mg-F system*

WATANABE, Haruki [B class; 800 (B), 200 (C)] ()
— *Comprehensive material search based on symmetry indicators*

WATANABE, Hiroshi [B class; 1000 (B), 150 (C)] (281)
— *Code Optimization using Machine Learning on Parallel Computer*
— *Molecular Dynamics Study of Crown Formation During the Splash*

WATANABE, Hiroshi [B class; 300 (B), 0 (C)] (218)
— *Study for stripe order and superconductivity in high-T_c cuprates by variational Monte Carlo method*

WATANABE, Satoshi [C class; 9200 (B), 1300 (C)] (56)
— *Analyses related to atomic structures and atom dynamics at complex structures such as surfaces interfaces and defects*

1. Straintronic effect for superconductivity enhancement in Li-intercalated bilayer MoS_2
   P. Mano, E. Minamitani, and S. Watanabe Nanoscale Adv. **2**, 3150 (2020).
   DOI:10.1039/D0NA00420K

2. Prediction of viscosity behavior in oxide glass materials using cation fingerprints with artificial neural networks
   J. Hwang, Y. Tanaka, S. Ishino, and S. Watanabe Sci. Tech. Adv. Mater. **21**, 492 (2020).
   DOI:10.1080/14686996.2020.1786856

3. Theoretical prediction of superconductivity in monolayer h-BN doped with alkaline-earth metals (Ca, Sr, Ba)
   N. H. Shimada, E. Minamitani, and S. Watanabe, J. Phys. Condensed Matter **32**, 435002 (2020).
   DOI:10.1088/1361-648X/aba674

4. Effects of density and composition on the properties of amorphous alumina: A high-dimensional neural network potential study
   W. Li, Y. Ando, and S. Watanabe J. Chem. Phys. **153**, 164119 (2020).
   DOI:10.1063/5.0026289

5. High-dimensional neural network atomic potentials for examining energy materials: some recent simulations
   S. Watanabe, W. Li, W. Jeong, D. Lee, K. Shimizu, E. Mimanitani, Y. Ando, and S. Han, J. Phys. Energy **3**, 012003 (2021).
   DOI:10.1088/2515-7655/abc7f3

6. Nickel-Catalyzed Acyl Group Transfer of o-Alkynylphenol Esters Accompanied by C-O Bond Fission for Synthesis of Benzo[b]furan
   R. Doi, K. Shimizu, Y. Ikemoto, M. Uchiyama, M. Koshiba, A. Furukawa, K. Maenaka, S. Watanabe, and Y. Sato ChemCatChem **13**, 1 (2021).
   DOI:10.1002/cctc.202001949

7. ニューラルネットワークを用いた原子間ポテンシャルの材料科学における応用事例
   清水康司, 渡邉聡, 日本神経回路学会誌 **28**, 3 (2021).
   DOI:10.3902/jnns.28.3

8. Tuning the Schottky Barrier Height at the Interfaces of Metals and Mixed Conductors
   K. Nishio, T. Shirasawa, K. Shimizu, N. Nakamura, S. Watanabe, R. Shimizu, and T. Hitosugi, ACS Appl. Mater. Interfaces **13**, 15746 (2021).
   DOI:10.1021/acsami.0c18656

9. Phase stability of Au-Li binary systems studied using neural network potential
   K. Shimizu, E. F. Arguelles, W. Li, Y. Ando, E. Minamitani, and S. Watanabe, Phys. Rev. B **103**, 094112 (2021).
   DOI:10.1103/PhysRevB.103.094112

YAMADA, Atsuo [C class; 2000 (B), 750 (C)] (123)
— *First principles analyses on novel materials for secondary batteries*

1. Theoretical analysis of electrode-dependent interfacial structures on hydrate-melt electrolytes
   N. Takenaka, T. Inagaki, T. Shimada, Y. Yamada, A. Yamada J. Chem. Phys. **152**, 124706 (2020).
   DOI:10.1063/5.0003196

2. Impact of anion asymmetry on local structure and supercooling behavior of water-in-salt electrolytes
   D. Reber, N. Takenaka, R.-S. Kuhnel, A. Yamada, C. Battaglia J. Phys. Chem. Lett. **11**, 4720 (2020).
   DOI:10.1021/acs.jpclett.0c00806

3. Does spinel serve as a rigid framework for oxygen redox?
   X. M. Shi, E. Watanabe, M. Okubo, A. Yamada, Chem. Mater. **32**, 7181 (2020).
   DOI:10.1021/acs.chemmater.0c00599

4. First-principles study on the cation-dependent electrochemical stabilities in Li/Na/K hydrate-melt electrolytes
   K. Miyazaki. N. Takenaka, E. Watanabe, Y. Yamada, Y. Tateyama, A. Yamada ACS Appl. Mater. Interfaces **12**, 42734 (2020).
   DOI:10.1021/acsami.0c10472

YAMADA, Atsushi [C class; 0 (B), 200 (C)] (219)
— *Studies of the superconductivity and magnetic states in the strongly correlated electron systems using Hubbard models.*

YAMADA, Masahiko [B class; 300 (B), 50 (C)] (317)
— *Numerical simulation of the spin Seebeck effect in Kitaev spin liquids*

YAMAGUCHI, Naoya [B,C class; 1000 (B), 150 (C)] (150)
— *First-principles Analysis of Band Dispersion in Bulk Insulators/Semiconductors Under Finite Electric Fields by Using the LCPAO Method*
— *First-principles Calculation of Electric Field Effects in Spin-to-charge Conversion Materials*

1. Simple Model for Corrugation in Surface Alloys Based on First-Principles Calculations
   M. Nur, N. Yamaguchi, and F. Ishii, Materials **13**, 4444 (2020).
   DOI:10.3390/ma13194444

YAMAJI, Youhei [E class; 19000 (B), 3000 (C)] (187, 188)
— *Numerical studies of quantum spin liquid candidates by highly accurate ab initio effective hamiltonians*
— *Numerical studies of quantum spin liquids by quantum mutual information*

YAMASHITA, Tomoki [C class; 3000 (B), 600 (C)] (99)
— *Development of surface and interface structure prediction methods*

1. CrySPY: a crystal structure prediction tool accelerated by machine learning
   T. Yamashita, S. Kanehira, N. Sato, H. Kino, K. Terayama, H. Sawahata, T. Sato, F. Utsuno, K. Tsuda, T. Miyake, and T. Oguchi, submitted to Sci. Technol. Adv. Mater.:Methods

YAMAUCHI, Kunihiko [C class; 4400 (B), 650 (C)] (87)
— *First-principles electronic structure calculations of non-centrosymmetric antiferromagnets*

1. Impact of Inter-site Spin-Orbit Coupling on Perpendicular Magnetocrystalline Anisotropy in Cobalt-Based Thin Films
   Thi Phuong Thao Nguyen, Kunihiko Yamauchi, Kohji Nakamura, and Tamio Oguchi Journal of the Physical Society of Japan
   DOI:10.7566/JPSJ.89.114710

YANAGISAWA, Susumu [C class; 4600 (B), 350 (C)] (91)
— *First-principles investigation on the electronic properties of polymer organic semiconductors*
— *First-principles theoretical study on the electronic structure and interface gap states of organic semiconductor polymers*

1. Quantitative analysis of the electrostatic and electronic polarization energies in molecularly mixed films of organic semiconductors
   Y. Uemura, S. A. Abd-Rahman, S. Yanagisawa, and H. Yoshida, Phys. Rev. B **102**, 125302 (2020).
   DOI:10.1103/PhysRevB.102.125302

YANAGISAWA, Takashi [B class; 600 (B), 150 (C)] (216)
— *Numerical study of strongly correlated electron systems*
— *Study of new quantum phenomena in correlated electron systems*

1. Phase diagram of cuprate high-temperature superconductors based on the optimization Monte Carlo method
   T. Yanagisawa, M. Miyazaki, K. Yamaji, Modern Phys. Lett. B34 (2020) 2040046.

2. Phase diagram and mechanism of superconductivity in strongly correlated electrons
   T. Yanagisawa, M. Miyazaki, K. Yamaji, J. Super. Novel Magne. 33 (2020) 2355.

3. Electronic structure of novel superconductor doped ZrPSe
   I. Hase, T. Yanagisawa, H. Kito et al. J. Phys. Conf. Ser. 1590 (2020) 012008.

4. Three-dimensional topological insulator in pyrochlore oxides
   I. Hase, T. Yanagisawa Symmetry 12 (2020) 1076.

5. Zero-energy modes, fractional fermion numbers and the index theorem in a vortex-idirac fermion system
   T. Yanagisawa Symmetry 12 (2020) 373.

6. Phase diagram of the three-band d-p model
   T. Yanagisawa, M. Miyazaki, K. Yamaji, EPL in press

7. On the kinetic-energy driven superconductivity in the two-dimensional Hubbard model
   T. Yanagisawa, M. Miyazaki, K. Yamaji, Condensed Matter 6 (2021) 12.

8. Enhancement of superconductivity due to kinetic energy effect in the strongly correlated phase in the two-dimensional Hubbard model
   T. Yanagisawa, Physics Letters A 403 (2021) 127382.

9. Electronic structure of novel superconductor $(\mathrm{Ca}_{1-x}\mathrm{Sr}_x)\mathrm{Pd}_3\mathrm{P}$
   I. Hase, T. Yanagisawa, A. Iyo et al. J. Phys. Conf. Ser. in press

10. Renormalization group theory of generalized multi-vertex sine-Gordon model
    T. Yanagisawa Prog. Theor. Exper. Phys. 2021 (2021) 033A01

YASUDA, Chitoshi [B class; 900 (B), 150 (C)] (282)
— *Magnetism in the multiple-spin exchange model on the honeycomb lattice*

YOKO, Akira [B,C class; 5100 (B), 650 (C)] (78)
— *First-principles calculation for low-temperature oxygen transfer in metal oxide*
— *First-principles calculation of oxygen storage capacity and structural distortion of metal doped cerium oxide*
— *Oxidative reaction of CH_4 on CeO_2 (100)*

1. Atomistic Origin of High-Concentration Ce3+ in 100-Faceted Cr-Doped CeO2 Nanocrystals
   X. Hao, A. Yoko, K. Inoue, Y. Xu, M. Saito, C. Chen, G. Seong, T. Tomai, S. Takami, A.L. Shluger, B. Xu, T. Adschiri, Y. Ikuhara, Acta Materialia. **203**, 116473 (2021).
   DOI:10.1016/j.actamat.2020.11.015

YOSHIDA, Tsuneya [C class; 7200 (B), 0 (C)] (199)
— *Bulk-edge correspondence for non-Hermitian topological systems*
— *Correlation effects on non-Hermitian topological states*

1. Mirror skin effect and its electric circuit simulation
   Tsuneya Yoshida, Tomonari Mizoguchi, and Yasuhiro Hatsugai, Phys. Rev. Research **2**, 022062 (2020).
   DOI:10.1103/PhysRevResearch.2.022062

2. Fate of fractional quantum Hall states in open quantum systems: Characterization of correlated topological states for the full Liouvillian
   Tsuneya Yoshida, Koji Kudo, Hosho Katsura, and Yasuhiro Hatsugai, Phys. Rev. Research **2**, 033428 (2020).
   DOI:10.1103/PhysRevResearch.2.033428

3. Chiral edge modes in game theory: a kagome network of rock-paper-scissors
   Tsuneya Yoshida, Tomonari Mizoguchi, Yasuhiro Hatsugai, arXiv:2012.05562.

4. Real-space dynamical mean field theory study of non-Hermitian skin effect for correlated systems: Analysis based on pseudospectrum
   Tsuneya Yoshida, Phys. Rev. B **103**, 125145 (2021).
   DOI:10.1103/PhysRevB.103.125145

5. Bulk-edge correspondence of classical diffusion phenomena
   Tsuneya Yoshida, Yasuhiro Hatsugai Sci. Rep. **11**, 888 (2021).
   DOI:10.1038/s41598-020-80180-w

6. Exceptional points in the one-dimensional Hubbard model
   Roman Rausch, Robert Peters, and Tsuneya Yoshida New J. Phys. **23**, 013011 (2021).
   DOI:10.1088/1367-2630/abd35e

7. Square-root topological phase with time-reversal and particle-hole symmetry
   Tsuneya Yoshida, Tomonari Mizoguchi, Yoshihito Kuno, Yasuhiro Hatsugai arXiv: 2103.11305.

8. Machine Learning of Mirror Skin Effects in the Presence of Disorder
   Hiromu Araki, Tsuneya Yoshida, and Yasuhiro Hatsugai J. Phys. Soc. Jpn. **90**, 053703 (2021).
   DOI:10.7566/JPSJ.90.053703

YOSHIDOME, Takashi [C class; 800 (B), 450 (C)] (276, 277)
— *A Method for Analyzing Protein Dynamics: A Hybrid of Cryo-Electron Microscopy Experiment and Molecular Simulation*
— *A theoretical study for thermal unfolding of proteins with quite similar native structure*

1. F1-ATPase Rotation and Its Inhibition from the Viewpoint of Solvent Entropy
   T. Yoshidome, Chemical Physics Letters, **757**, 137886/1-6 (2020).

YOSHIOKA, Nobuyuki [B class; 500 (B), 50 (C)] (305)
— *Developing numerical tool for open quantum dynamics based on neural networks*

1. Neural-Network Quantum States for the Electronic Structure of Real Solids
   N. Yoshioka, W. Mizukami, and F. Nori, submitted to Communications Physics

2. Purifying Deep Boltzmann Machines for Thermal Quantum States
   Y. Nomura, N. Yoshioka, and F. Nori, submitted to Phys. Rev. Lett.

○ A class

Since this class is for trial use, research reports are not required.
When other classes are also used, their publications are shown in the list of B–E classes.
Then, the pages of their reports and publications are given in ( ).

AKIYAMA, Ryota [A class; 100 (B), 50 (C)] ()
— *Band calculation in metal-intercalated graphene*

ARUGA, Tetsuya [A class; 100 (B), 50 (C)] (351)
— *Electronic structure and interaction at the interface of* π*-electron organic molecules and metals*

CHIBA, Takahiro [A class; 100 (B), 50 (C)] ()
— *Band structure and spin texture of Bi-Te/ferromagnetic-metal interface*

GONOME, Hiroki [A class; 100 (B), 50 (C)] ()
— *Study of the principle of photothermal conversion by ab initio calculations*

HATANO, Naomichi [A class; 100 (B), 50 (C)] ()
— *Molecular Dynamics Calculation of Non-equilibrium Steady State in Systems with Temperature Gradient*

HATTORI,Ken [A class; 100 (B), 0 (C)] (174, 356)
— *Atomic structure and electronic states for silicide films*

ISHIBASHI, Shoji [A class; 100 (B), 50 (C)] (167, 361)
— *Prediction of properties of organic ferroelectrics and piezoelectrics by first-principles calculation*

ISHIKAWA, Ryo [A class; 100 (B), 50 (C)] ()
— *First-principles calculation on charged defects in* α-Al_2O_3

KOTA, Yohei [A class; 100 (B), 50 (C)] ()
— *Analysis of N-doping effect on electronic structure in antiferromagnetic Cr*

1. Mechanism of highly sensitive strain response in antiferromagneitc chromium
   Yohei Kota, Eiji Niwa, and Masayuki Naoe, Journal of Applied Physics **129**, 203901 (2021)
   DOI:10.1063/5.0045728

MASAKI, Yusuke [A class; 100 (B), 50 (C)] ()
— *Microscopic calculations of non-axisymmetric vortices in topological superfluids*

OHTO, Tatsuhiko [A class; 100 (B), 0 (C)] (127, 381)
— *First-principles transport calculations for molecular junctions*

SAKAI, Masatoshi [A class; 100 (B), 50 (C)] (217, 386)
— *Excess carrier dependent electronic state in organic charge order phase*

SATO, Taku [A class; 100 (B), 50 (C)] (387)
— *Magnetic excitations in the quantum pyrochlore magnet*

TANUMA, Yasunari [A class; 100 (B), 50 (C)] ()
— *Study on numerical analysis method of superconducting junctions with broken time reversal symmetry states*

TOKUMOTO, Yuki [A class; 100 (B), 50 (C)] ()
— *Exploring dopants to improve bulk-insulation of Pb-based topological insulators*

YAMASHITA, Tomoki [A class; 100 (B), 0 (C)] (99, 400)
— *Development of surface and interface structure prediction methods*

YAMATO, Takahisa [A class; 100 (B), 50 (C)] (325)
— *Non-uniform thermal transport properties in proteins*

1. Energy transfer across nonpolar and polar contacts in proteins: role of equilibrium fluctuations
   P. Humanath, K. M. Reid, T. Yamato, and D. M. Leitner, J. Phys. Chem. B. **124**, 9852 (2020).
   DOI:10.1021/acs.jpcb.0c08091

YOSHIZAWA, Kanako [A class; 100 (B), 50 (C)] ()
— *Performance measurement of Quantum ESPRESSO*

□ SCCMS Projects

FUJITA, Takatoshi [5500 (B), 0 (C)] (330)
— *Investigation of charge photogeneration process in organic thin film solar cells by large-scale GW/Bethe-Salpeter equation method*
— *Computational Investigation of Charge Photogeneration in Organic Solar Cells by Fragment-Based GW/BSE Method*

1. Revisiting the Charge-Transfer States at Pentacene/C60 Interfaces with the GW/Bethe–Salpeter Equation Approach
   T. Fujita, Y. Noguchi, T. Hoshi Materials **13**, 2728 (2020).

2. First-Principles Investigations of Electronically Excited States in Organic Semiconductors
   T. Fujita In: M. Hiramoto, S. Izawa (eds), Organic Solar Cells, (2021) 155-194, Springer, Singapore.

3. FMO-Based Investigations of Excited-State Dynamics in Molecular Aggregates
   T. Fujita, T. Hoshi In: Y. Mochizuki, S. Tanaka, K. Fukazawa (eds), Recent Advances of the Fragment Molecular Orbital Method, (2021) 547-566, Springer, Singapore.

FUKUSHIMA, Tetsuya [4000 (B), 500 (C)] (338)
— *Large-scale simulation for permanent magnets*

1. Hole-mediated ferromagnetism in a high-magnetic moment material, Gd-doped GaN
   A. Masago, H. Shinya, T. Fukushima, K. Sato, and H. Katayama-Yoshida, J. Phys.: Condens. Matter **32**, 485803 (2020).
   DOI:10.1088%2F1361-648x%2Fabac8e

2. First-principles calculations of finite temperature electronic structures and transport properties of Heusler alloy Co_2MnSi
   H. Shinya, S. Kou, T. Fukushima, A. Masago, K. Sato, H. Katayama-Yoshida, and H. Akai, Appl. Phys. Lett. **117**, 042402 (2020).
   DOI:10.1063/5.0017862

3. Role of atomic-scale thermal fluctuations in the coercivity
   Y. Toga, S. Miyashita, A. Sakuma, and T. Miyake Npj Comput Mater **6**, 1 (2020).
   DOI:10.1038/s41524-020-0325-6

GOHDA, Yoshihiro [4000 (B), 500 (C)] (112)
— *First-principles study of magnetic materials*

1. First-principles determination of intergranular atomic arrangements and magnetic properties in rare-earth permanent magnets
   Y. Gohda, Sci. Technol. Adv. Mater. **22**, 113 (2021).
   DOI:10.1080/14686996.2021.1877092

2. Prediction of the Curie temperature considering the dependence of the phonon free energy on magnetic states
   T. Tanaka and Y. Gohda, npj Comput. Mater. **6**, 184 (2020).
   DOI:10.1038/s41524-020-00458-5

3. Effective quantum-well width of confined electrons in ultrathin Ag(111) films on Si(111)7x7 substrates
   K. Sugawara, I. Seo, S. Yamazaki, K. Nakatsuji, Y. Gohda, and H. Hirayama, Surf. Sci. 704,

121745 (2020).
DOI:10.1016/j.susc.2020.121745

4. First-principles study of magnetism-dependent phonons governed by exchange ligand field
T. Tanaka and Y. Gohda, J. Phys. Soc. Jpn. **89**, 093705 (2020).
DOI:10.7566/JPSJ.89.093705

5. First-principles Calculations on High-temperature Desorption Loss from Iridium
I. Seo, S. Yokota, Y. Imai, and Y. Gohda, Comput. Mater. Sci. **184**, 109897 (2020).
DOI:10.1016/j.commatsci.2020.109897

6. First-principles study on magnetism of a crystalline grain-boundary phase in Nd–Fe–B permanent magnets
Y. Ainai, S. Kou, Y. Tatetsu, and Y. Gohda Jpn. J. Appl. Phys. **59**, 060904 (2020).
DOI:10.35848/1347-4065/ab9402

7. First-principles study of the adsorption of 3d transition metals on BaO- and TiO2-terminated cubic-phase BaTiO3(001) surfaces
R. Costa-Amaral and Y. Gohda, J. Chem. Phys. **152**, 204701 (2020).
DOI:10.1063/5.0008130

IMADA, Masatoshi [9600 (B), 1300 (C)] (184)
— *Studies on quantum spin liquids in three dimensions*
— *Analyses on Superconducting Mechanism by Machine Learning*

1. Single-Particle Spectral Function Formulated and Calculated by Variational Monte Carlo Method with Application to d-Wave Superconducting State
Maxime Charlebois and Masatoshi Imada, Phys. Rev. X **10** (2020) 041023.

2. Charge dynamics of correlated electrons: Variational description with inclusion of composite fermions
Kota Ido, Masatoshi Imada, Takahiro Misawa, Phys. Rev. B **101** (2020) 075124.

3. *Ab initio* study of superconductivity and inhomogeneity in a Hg-based cuprate superconductor
Takahiro Ohgoe, Motoaki Hirayama, Takahiro Misawa, Kota Ido, Youhei Yamaji, Masatoshi Imada, Phys. Rev. B **101** (2020) 045124.

MATUBAYASI, Nobuyuki [8000 (B), 0 (C)] (337)
— *Evaluation of the polymer blend miscibility by using chain-increment method with all-atom molecular dynamics simulation*

MISAWA, Takahiro [2500 (B), 500 (C)] (189)
— *Systematic derivation and analysis of low-energy effective models for iron based superconductors and related materials*

1. Application of First-Principles-Based Artificial Neural Network Potentials to Multiscale-Shock Dynamics Simulations on Solid Materials
Masaaki Misawa, Shogo Fukushima, Akihide Koura, Kohei Shimamura, Fuyuki Shimojo, Subodh Tiwari, Ken-ichi Nomura, Rajiv K. Kalia, Aiichiro Nakano, and Priya Vashishta, The Journal of Physical Chemistry Letters **11**, 4536 (2020).

2. First-Principles Study of Pressure-Induced Amorphization of Fe2SiO4 Fayalite
Masaaki Misawa and Fuyuki Shimojo, Physica Status Solidi B-Basic Solid State Physics **257** 2000173 (2020).

MIYAKE, Takashi [500 (B), 500 (C)] (334)

— *Development of high-performance permanent magnets by large-scale simulation and data-driven approach*

1. Spin-wave dispersion and exchange stiffness in $Nd_2Fe_{14}B$ and $RFe_{11}Ti$ (R=Y, Nd, Sm) from first-principles calculations
   Taro Fukazawa, Hisazumi Akai, Yosuke Harashima and Takashi Miyake, Phys. Rev. B **103**, 0244187 (2021).
   DOI:10.1103/PhysRevB.103.024418

2. Data Assimilation Method for Experimental and First-Principles Data: Finite-Temperature Magnetization of $(Nd,Pr,La,Ce)_2(Fe,Co,Ni)_{14}B$
   Yosuke Harashima, Keiichi Tamai, Shotaro Doi, Munehisa Matsumoto, Hisazumi Akai, Naoki Kawashima, Masaaki Ito, Noritsugu Sakuma, Akira Kato, Tetsuya Shoji, and Takashi Miyake, Physical Review Materials **5**, 013806 (2021).
   DOI:10.1103/PhysRevMaterials.5.013806

3. Monoclinic YFe_{12} phases predicted from first principles
   Takahiro Ishikawa, Taro Fukazawa, and Takashi Miyake, Physical Review Materials **4**, 104408 (2020).
   DOI:10.1103/PhysRevMaterials.4.104408

4. Role of atomic-scale thermal fluctuations in the coercivity
   Yuta Toga, Seiji Miyashita, Akimasa Sakuma and Takashi Miyake, npj Computational Materials **6**, 67 (2020).
   DOI:10.1038/s41524-020-0325-6

NAKAYAMA, Masanobu [3000 (B), 0 (C)] (340)

— *Novel chloride solid electrolytes for all solid-state sodium metal battery*

1. Efficient Experimental Search for Discovering a Fast Li-Ion Conductor from a Perovskite-Type $Li_xLa_{(1-x)}/3NbO_3$ (LLNO) Solid- State Electrolyte Using Bayesian Optimization
   Zijian Yang, Shinya Suzuki, Naoto Tanibata, Hayami Takeda, Masanobu Nakayama, Masayuki Karasuyama, and Ichiro Takeuchi, J. Phys. Chem. C **125**, 152 (2021).
   DOI:10.1021/acs.jpcc.0c08887

2. High Formability and Fast Lithium Diffusivity in Metastable Spinel Chloride for Rechargeable All-Solid-State Lithium-Ion Batteries
   Naoto Tanibata, Masashi Kato, Shuta Takimoto, Hayami Takeda, Masanobu Nakayama, and Hirofumi Sumi, Advanced Energy & Sustainability Research (2020).
   DOI:10.1002/aesr.202000025

OGUCHI, Tamio [2500 (B), 500 (C)] (331)

— *Electron Theory on Secondary-Battery Materials*

1. First-principles study of magnetism and phase stabilities of V_2 based antiferromagnetic Heusler alloys
   F. Kuroda, T. Fukushima, and T. Oguchi, J. Appl. Phys. **127**, 193904 (2020).
   DOI:10.1063/1.5143826

2. Ferroelectric atomic displacement in multiferroic tetragonal perovskite $Sr_{1/2}Ba_{1/2}MnO_3$
   D. Okuyama, K. Yamauchi, H. Sakai, Y. Taguchi, Y. Tokura, K. Sugimoto, T. J. Sato, and T. Oguchi, Phys. Rev. Research **2**, 033038 (2020).
   DOI:10.1103/PhysRevResearch.2.033038

3. Spin injection through energy-band symmetry matching with high spin polarization in atomically controlled ferromagnet/ferromagnet/semiconductor structures
   Michihiro Yamada, Fumiaki Kuroda, Makoto Tsukahara, Shinya Yamada, Tetsuya Fukushima, Kentarou Sawano, Tamio Oguchi, and Kohei Hamaya, npg Asia Materials **12**, 47 (2020).
   DOI:10.1038/s41427-020-0228-5

4. DFT-based Engineering of Dirac Surface States in Topological-insulator Multilayers
   Takao Kosaka, Kunihiko Yamauchi, and Tamio Oguchi, J. Phys. Soc. Jpn. **89**, 094701 (2020).
   DOI:10.7566/JPSJ.89.094701

5. Suppression of O-redox reactions by multivalent Cr in Li-excess $\mathrm{Li}_{2.4}M_{0.8}M'_{0.8}\mathrm{O}_4$ (M, M'=Cr, Mn, and Ti) cathodes with layered and cation-disordered rock-salt structures
   Motoyuki Hamaguchi, Hiroyoshi Momida, Ayuko Kitajou, Shigeto Okada, and Tamio Oguchi, Electrochimica Acta **354**, 136630 (2020).
   DOI:10.1016/j.electacta.2020.136630

6. Insight into the diffusion mechanism of sodium ion-polaron complexes in orthorhombic P2 layered cathode oxide $\mathrm{Na}_x\mathrm{MnO}_2$
   Huu Duc Luong, Van An Dinh, Hiroyoshi Momida, and Tamio Oguchi, Phys. Chem. Chem. Phys. **22**, 18219-18228 (2020).
   DOI:10.1039/d0cp03208e

7. Impact of Inter-site Spin-Orbit Coupling on Perpendicular Magnetocrystalline Anisotropy in Cobalt-Based Thin Films
   Thi Phuong Thao Nguyen, Kunihiko Yamauchi, Kohji Nakamura, and Tamio Oguchi, J. Phys. Soc. Jpn. **89**, 114710 (2020).
   DOI:10.7566/JPSJ.89.114710

8. Magnetocaloric effect in MnCoGe alloys studied by first-principles calculations and Monte-Carlo simulation
   Hung Ba Tran, Tetsuya Fukushima, Yukihiro Makino, and Tamio Oguchi, Solid State Commun. **323**, 114077 (2021).
   DOI:10.1016/j.ssc.2020.114077

9. Tuning structural-transformation temperature toward giant magnetocaloric effect in MnCoGe alloy: A theoretical study
   Hung Ba Tran, Tetsuya Fukushima, Kazunori Sato, Yukihiro Makino, and Tamio Oguchi, J. Alloys Compd. **854**, 157063/1-9 (2021).
   DOI:10.1016/j.jallcom.2020.157063

ONO, Kanta [2500 (B), 500 (C)] (336)
— *Optimized design of magnetic materials based on the integration between quantum beam experiment and first-principles calculation*

1. $(\mathrm{Sm,Zr})\mathrm{Fe}_{12-x}\mathrm{M}_x$ (M=Zr,Ti,Co) for permanent-magnet applications: *Ab initio* material design integrated with experimental characterization
   Munehisa Matsumoto, Takafumi Hawai, and Kanta Ono, Phys. Rev. Applied **13**, 064028 (2020).
   DOI:10.1103/PhysRevApplied.13.064028

OSHIYAMA, Atsushi [9600 (B), 1300 (C)] (49)
— *Quantum-theory-based multiscale simulation for next-generation power devices*

1. Density-Functional Calculations for Structures and Energetics of Atomic Steps and their Implication for Surface Morphology on Si-face SiC Polar Surfaces
   K. Seino and A. Oshiyama, Phys. Rev. B **101** (2020) 195307

DOI:10.1103/PhysRevB.101.195307

2. Absence of oxygen-vacancy-related deep levels in amorphous $(\mathrm{Al_2O_3})_{1-x}(\mathrm{SiO_2})_x$: First-principles exploration of gate oxides in GaN-based devices
   K. Chokawa, T. Narita, D. Kikuta, T. Kachi, K. Shiozaki, A. Oshiyama and K. Shiraishi, Phys. Rev. Applied **14** (2020) 014034
   DOI:10.1103/PhysRevApplied.14.014034

3. Screw dislocation that converts p-type GaN to n-type: Microscopic study on Mg condensation and leakagae current in p-n diodes
   T. Nakano, Y. Harashima, K. Chokawa, K. Shiraishi, A. Oshiyama, Y. Kangawa, S. Usami, N. Mayama, K. Toda, A. Tanaka, Y. Honda, and H. Amano, Appl. Phys. Lett. **117** (2020) 012105
   DOI:10.1063/5.0010664

4. Gallium-gallium weak bond that incorporates nitrogen at atomic steps during GaN epitaxial growth
   K. M. Bui, K. Shiraishi and A. Oshiyama, Appl. Surf. Sci. **557** (2021) 149542
   DOI:10.1016/j.apsusc.2021.149542

SHIBA, Hayato [6500 (B), 1000 (C)] (327)
— *Large-scale molecular dynamics simulation of viscoelastic relaxation in a two-dimensional supercooled liquid*
— *Development of all atom molecular simulation framework on a mesoscale*

1. 大規模分子シミュレーションによるガラス・ソフトマターの連続体特性の研究
   芝 隼人, 分子シミュレーション学会会誌 “アンサンブル” **23**, 1 (2020).

2. Molecular-dynamics simulations on the mesophase transition induced by oscillatory shear in imidazolium-based ionic liquid crystals
   M. Liu, H. Shiba, H. Liu, and H. Peng Phys. Chem. Chem. Phys. **23**, 6496 (2021).

SUGINO, Osamu [4000 (B), 500 (C)] (48)
— *Functionality of transition metal oxides*

1. Dopant arrangements in Y-doped $\mathrm{BaZrO_3}$ under processing conditions and their impact on proton conduction: a large-scale first-principles thermodynamics study
   Shusuke Kasamatsu, Osamu Sugino, Takafumi Ogawa, and Akihide Kuwabara, J. Mater. Chem. A **8**, 12674-12686 (2020).
   DOI:10.1039/D0TA01741H

2. Quantum-Mechanical Hydration Plays Critical Role in the Stability of Firefly Oxyluciferin Isomers: State-of-the-art Calculations of the Excited States
   Y. Noguchi, M. Hiyama, M. Shiga, H. Akiyama, O. Sugino, J. Chem. Phys. (2020) 153, 201103
   DOI:10.1063/5.0031356

3. Advances and challenges for experiment and theory for multi-electron multi-proton transfer at electrified solid-liquid interfaces
   K. Sakaushi, T. Komeda, S. Hammes-Schiffer, M. M. Melander and O. Sugino Phys. Chem. Chem. Phys. 22, 19401-19442 (2021).
   DOI:10.1039/d0cp02741c

4. Hydrogen at Electrochemical Interfaces
   O. Sugino J. Phys. Soc. Jpn. 89, 051013 (2020).
   DOI:10.7566/JPSJ.89.051013

5. Surface-state Coulomb repulsion accelerates a metal-insulator transition in topological semimetal nanofilms
   S. Ito, M. Arita, J. Haruyama, B. Feng, W. -C. Chen, H. Namatame, M. Taniguchi, C. -M. Cheng, G. Bian, S. -J. Tang, T. -C. Chiang, O. Sugino, F. Komori and I. Matsuda Science Advances 6, eaaz5015 (2020).
   DOI:10.1126/sciadv.aaz5015

6. Challenge of advanced low temperature fuel cells based on high degree of freedom of group 4 and 5 metal oxides
   A. Ishihara, S. Tominaka, S. Mitsushima, H. Imai, O. Sugino and K.-I. Ota Curr. Op. ElectroChem.
   DOI:10.1016/j.coelec.2020.03.005

7. Completing density functional theory by machine learning hidden messages from molecules
   R. Nagai, R. Akashi and O. Sugino npj Comput. Mater. 6, 43 (2020).
   DOI:10.1038/s41524-020-0310-0

8. First-Principles Calculation of Copper Oxide Superconductors That Supports the Kamimura-Suwa Model
   H. Kamimura, M. Araidai, K. Ishida, S. Matsuno, H. Sakata, K. Shiraishi, O. Sugino and J.-S. Tsai Condensed Matter 5, 69 (2020).
   DOI:10.3390/condmat5040069

TAKETSUGU, Tetsuya [2500 (B), 500 (C)] (333)
— *Ab initio study toward abundant element nanocatalysts with less precious metals*

1. Boron nitride for enhanced oxidative dehydrogenation of ethylbenzene
   R. Han, J. Diao, S. Kumar, A. Lyalin, T. Taketsugu, G. Casillas, C. Richardson, F. Liu, C. W. Yoon, H. Liu, X. Sun, and Z. Huang J. Energy Chem. **57**, 477-484 (2021)
   DOI:10.1016/j.jechem.2020.03.027

2. Catalytic Activity of Gold Clusters Supported on h-BN/Au(111) Surface for Hydrogen Evolution Reaction
   M. Gao, M. Nakahara, A. Lyalin, and T. Taketsugu J. Phys. Chem. C **125**, 13341344 (2021)
   DOI:10.1021/acs.jpcc.0c08826

3. Heterocyclic Ring-Opening of Nanographene on Au(111)
   K. Sun, K. Sugawara, A. Lyalin, Y. Ishigaki, K. Uosaki, T. Taketsugu, T. Suzuki, and S. Kawai Angew. Chem. Int. Ed. **60**, 9427-9432 (2021)
   DOI:10.1002/anie.202017137

YAMADA, Atsuo [6500 (B), 1000 (C)] (123)
— *Theoretical analysis on ion conduction mechanism in aqueous electrolytes for sodium-ion battery*
— *Theoretical analysis of unusual ion transport mechanism in hydrate melt electrolyte*

1. Theoretical analysis of electrode-dependent interfacial structures on hydrate-melt electrolytes
   N. Takenaka, T. Inagaki, T. Shimada, Y. Yamada, A. Yamada J. Chem. Phys. **152**, 124706 (2020).
   DOI:10.1063/5.0003196

2. Impact of anion asymmetry on local structure and supercooling behavior of water-in-salt electrolytes
   D. Reber, N. Takenaka, R.-S. Kuhnel, A. Yamada, C. Battaglia J. Phys. Chem. Lett. **11**, 4720 (2020).
   DOI:10.1021/acs.jpclett.0c00806

3. Does spinel serve as a rigid framework for oxygen redox?
   X. M. Shi, E. Watanabe, M. Okubo, A. Yamada, Chem. Mater. **32**, 7181 (2020).
   DOI:10.1021/acs.chemmater.0c00599

4. First-principles study on the cation-dependent electrochemical stabilities in Li/Na/K hydrate-melt electrolytes
   K. Miyazaki. N. Takenaka, E. Watanabe, Y. Yamada, Y. Tateyama, A. Yamada ACS Appl. Mater. Interfaces **12**, 42734 (2020).
   DOI:10.1021/acsami.0c10472

YOSHIMI, Kazuyoshi [2500 (B), 500 (C)] (328)
— *Creating a Wannier function database toward material design*

□ Doctor Theses

1. **AL RASYID, Hasan**
   Electronic structures of spinel nickel cobaltite from a spin-polarized quasi-particle self-consistent GW method
   Kanazawa University, 2020-09

2. **ASAD, Md. Abdullah Al**
   First Principles Study on Water Intercalated Grain Boundary of Methyl Ammonium Lead Iodide Perovskite
   Okayama University, 2020-09

3. **FUKUI, Kiyu**
   Functional Renormalization Group Study on Kitaev Quantum Spin Liquid
   The University of Tokyo, 2021-03

4. **GUO, Jiang**
   Optimal design of spectrally selective photonic structures for thermal radiation applications
   The University of Tokyo, 2021-03

5. **HWANG, Jaekyun**
   Material Property Predictions and Discovery Using a Novel Descriptor “Elemental Fingerprints” with Neural Networks
   The University of Tokyo, 2021-03

6. **ISHIKAWA, Fumihiro**
   Exploration of Classical Integrable Systems Assisted by Neural Networks
   The University of Tokyo, 2021-03

7. **JANG, Seonghoon**
   Materials design of *f*-electron based Kitaev-type magnets
   The University of Tokyo, 2020-09

8. **KUDO, Koji**
   Topological invariants and adiabatic principle in correlated systems
   University of Tsukuba, 2021-03

9. **NGUYEN Thi Phuong Thao**
   Theoretical Study on Electric Field Control of Magnetism in 2D Materials
   Osaka University, 2021-03

10. **OCHI, Masaki**
    Statistical-Mechanical Analysis of Structures of Directed Complex Networks
    The University of Tokyo, 2021-03

11. **OHUCHI, Marie**
    Anomalous Hall effect on a vortex of supercurrent in type-II superconductors
    Hokkaido University, 2021-03

12. **OKUMURA, Shun**
    Chiral magnetism and quantum transport phenomena in noncentrosymmetric metals
    The University of Tokyo, 2020-09

13. **TAKENAKA, Masato**

Theoretical near-field vibrational spectroscopy
Hokkaido University, 2021-03

14. **TANAKA, Tomonori**
    Magnetism dependent phonons and their role in magnetic phase transition studied by first-principles thermodynamic formulation
    Tokyo Institute of Technology, 2020-9

15. **WIDIANTO, Muhammad Yusuf Hakim**
    First-Principles calculations of spin-polarized cation vacancies in wide-gap semiconductors
    Kanazawa University, 2021-03

16. **YASSIN, Abdulrahman Hikmat Basher**
    Mechanisms of Thermal Atomic Layer Etching (ALE) for Metals
    Osaka University, 2020-08

17. **YOSHIKAWA, Seiji**
    A Noise-Robust Data Assimilation Method for Crystal Structure Predictions Using Powder Diffraction Intensity
    The University of Tokyo, 2021-03

□ Master Theses

1. **CAO, Ruixiao**
   Numerical study of two-dimensional quantum dimer model
   The University of Tokyo, 2020-09

2. **CHIBANA, Yukiko**
   Classical ground states of the multiple-spin exchange model in a magnetic field on a honeycomb lattice
   University of the Ryukyus, 2021-03

3. **DOE, Ryunosuke**
   Density Functional Theory Study of Surface States at Noble Metal Surfaces
   Osaka University, 2021-03

4. **DOU, Ying**
   Theoretical approach for understanding group-III nitride device structures
   The University of Tokyo, 2020-09

5. **ENRIQUEZ, John Isaac Guinto**
   First-principles Study of the Oxidative Etching Mechanism of the Diamond (100) Surface
   Osaka University, 2020-09

6. **FUJIMORI, Shintaro**
   Non-uniform thermal transport in proteins
   Nagoya University, 2021-03

7. **FURUUCHI, Rito**
   Numerical Study on the Magnetization Process of the Heisenberg Antiferromagnet on the Floret Pentagon Lattice
   University of Hyogo, 2021-3

8. **GOTO, Manami**
   Synthesis of MoS2 nanotubes by sulfirization of oxide precursors
   Hokkaido University, 2021-03

9. **HALIM, Harry Handoko**
   Multi-scale Simulation of Equilibrium Steps Fluctuations on Cu(111) Surfaces
   Osaka University, 2020-09

10. **HAMAKAWA, Tom**
    Development of Analysis Method for Inelastic Phonon Transport
    The University of Tokyo, 2021-03

11. **HARA, Masahiro**
    Analyses of ion migration in Li_3PO_4 under electric fields using neural network potentials
    The University of Tokyo, 2021-03

12. **HARADA, Tatsuki**
    Development of highly efficient computational method for electron-phonon interaction matrix elements
    The University of Tokyo, 2021-03

13. **HATSUSHIKA, Jyunna**

First-principles study of two photon absorption spectra in perovskite semiconductors
Chiba University, 2021-03

14. **HIROSE, Tenshi**
    Isotope effects in the hydrogenation of styrene on Rh intermetallic catalysts
    Hokkaido University, 2021-03

15. **HORIKAWA, Ryo**
    Consideration on Mechanism of Superconductivity in BiS2-Based Layered Superconductors by Using Orbital Splitting Effect: Spin fluctuation and phonon mechanisms
    Tokyo Metropolitan University, 2021-03

16. **INAYOSHI, Ken**
    Theoretical Study of Equilibrium Order and Nonequilibrium Dynamics in the Quasicrystalline Excitonic Insulator
    Tokyo Institute of Technology, 2021-03

17. **IRIGUCHI, Takuya**
    Density Functional Theory Study on Dehydrogenation Reaction of Methanol on Pt Surfaces
    Osaka University, 2021-03

18. **IWANO, Akito**
    Microscopic Origin of Stable High-Temperature Superconductivity in Multilayer Copper Oxides
    The University of Tokyo, 2021-03

19. **KADONO, Tomoyuki**
    Material design of α-SrSi2 based on theoretical calculations snd structural and electronic properties of Mg2Si doped with Sb and Zn by synchrotron radiation analysis
    Tokyo University of Science, 2021-03

20. **KATAOKA, Yuta**
    Surface reconstruction of Au(111) and quantum diffusion of adsorbed hydrogen
    The University of Tokyo, 2021-03

21. **KOFUJI, Akira**
    Effect of strong correlation on the non-linear response in Weyl-Kondo semimetals
    Kyoto University, 2021-03

22. **KOJIMA, Ryota**
    A Computational Method for Constructing a Continuous Function Describing Cryo-Electron Microscopy Data: A Study using a Manifold Learning
    Tohoku University, 2021-03

23. **KOYAMA, Hiroaki**
    Implement of free volume calculation using higher neighbors and its application to the glassy systems
    Nagoya Institute of Technology, 2021-03

24. **KUBOTA, Genki**
    Scaling of thermal transport through native contacts in proteins with equilibrium fluctuations
    Nagoya University, 2021-03

25. **MANO, Poopodin**
    First-principles analyses of strain effects on properties of layered transition-metal dichalcogenides
    The University of Tokyo, 2021-03

26. **MATAYOSHI, Keita**
    Monte Carlo study of the multiple-spin exchange model in a magnetic field on a honeycomb lattice
    University of the Ryukyus, 2021-03

27. **MIZUGUCHI, Atsuki**
    Machine Learning Construction of Electron-Temperature-Dependent Interatomic Potential
    The University of Tokyo, 2021-03

28. **MIZUGUCHI, Ryunosuke**
    Theoretical study for ground-state properties of the Heisenberg antiferromagnet on the the Cairo Pentagon lattice
    Tokyo University of Science, 2021-03

29. **NAKATSU, Daisuke**
    Stability of TiAl-based multicomponent alloys from first principles
    Tokyo Institute of Technology, 2021-3

30. **NISHINO, Koki**
    Analyses of thermal transport properties of carbon-based materials using neural Network Potentials
    The University of Tokyo, 2021-03

31. **NOZAKI, Misa**
    Electronic state analysis of organic molecules in angle-resolved photoelectron spectroscopy
    Chiba University, 2021-03

32. **OIKAWA, Takuya**
    First-principles study of diffusion and distribution of oxygen vacancies in metal oxides
    Chiba University, 2021-03

33. **OKADA, Naoki**
    Dynamical Variational Monte Carlo Approaches for Excitation Spectra of Many-Body Fermions in Continuum Space
    The University of Tokyo, 2021-03

34. **OTANI, Yusuke**
    First-principles calculation of effects on PdZn surface by intermediates of methanol steam reforming
    Kagoshima University, 2021-03

35. **SEO, Insung**
    First-principles study on iridium loss at high temperatures
    Tokyo Institute of Technology, 2020-9

36. **SHIMAZU Ryoma**
    First-principles Calculation of Topological Insulator Hetero Structure with Spin Splitting Bands
    Osaka University, 2021-03

37. **SHIMIZU, Kotaro**
    Theoretical study on control of topological spin textures based on spin moire picture
    The University of Tokyo, 2021-03

38. **SHIMOMURA, Tadahisa**
    Local Atomic Structures and Magnetic Properties of Mn doped ZnSnAs2

Osaka University, 2021-03

39. **SATO, Nao**
Rational design of the peptide inhibitor targeting the interaction of the KIX domain of the transcriptional coactivator CBP with transcriptional activators
The University of Tokyo, 2021-03

40. **TAKEHANA, Hiroki**
Interaction of diamond and alkali metals and its application
Hokkaido University, 2021-03

41. **TESHIMA, Ryo**
Mechanical properties of Ir-based alloys from first principles
Tokyo Institute of Technology, 2021-3

42. **UEDA, Kayo**
First-principles study on Schottky barrier modulation at metal/Ge interfaces
Chiba University, 2021-03

43. **YAMADA, Tatsuru**
Appearance of ferromagnetism and change in magnetism in Pt(100) thin film by adsorbing organic materials: Experimental and first-principles studies
Keio University, 2021-03

44. **YAMAZAKI, Ryo**
Computational Studies on adsorption and diffusion properties of Li and Na atoms on Ti-based MXene sheets
Hokkaido University, 2021-03

45. **YOSHIDA, Akira**
Thermodynamic functions of equilibrium and nonequilibrium solutions used modern thermodynamics
Ibaraki University, 2021-03

46. **YOSHIDA, Shintaro**
Development of Prediction Model for Thermal Conductivity with Graph Structure and Transfer Learning
The University of Tokyo, 2020-09

47. **ZHANG, Peiyu**
Molecular dynamics simulation of water transport through fluorous nanochannel
The University of Tokyo, 2020-09